Response functions of correlated systems in the linear regime and beyond

Dissertation
der Mathematisch-Naturwissenschaftlichen Fakultät
der Eberhard Karls Universität Tübingen
zur Erlangung des Grades eines
Doktors der Naturwissenschaften
(Dr. rer. nat.)

vorgelegt von
M.Sc. Agnese Tagliavini
aus Ferrara, Italien

Tübingen,
2018

Gedruckt mit Genehmigung der Mathematisch-Naturwissenschaftlichen Fakultät der Eberhard Karls Universität Tübingen.

Tag der mündlichen Qualifikation:	9 November 2018
Dekan:	Prof. Dr. Wolfgang Rosenstiel
1. Berichterstatter:	Prof. Dr. Sabine Andergassen
2. Berichterstatter:	Prof. Dr. Alessandro Toschi

Abstract

The technological progress in material science has paved the way to engineer new condensed matter systems. Among those, fascinating properties are found in presence of strong correlations among the electrons. The maze of physical phenomena they exhibit is countered by the difficulty in devising accurate theoretical descriptions. This explains the plethora of approximated theories aiming at the closest reproduction of their properties.
In this respect, the response of the system to an external perturbation bridges the experimental evidence with the theoretical description, representing a testing ground to prove or disprove the validity of the latter.
In this thesis we develop a number of theoretical and numerical strategies to improve the computation of *linear* response functions in several of the forefront many-body techniques. In particular, the development of computationally efficient schemes, driven by physical arguments, has allowed (i) improvements in treating the local two-particle correlations and scattering functions, which represent essential building blocks for established non-perturbative theories, such as dynamical mean field theory (DMFT) and its diagrammatic extensions and (ii) the implementation of the groundbreaking multiloop functional renormalization group (mfRG) technique and its application to a two-dimensional Hubbard model. Together with (i), the multiloop scheme has promoted the functional RG to provide quantitative predictions. As the mfRG is able to build up a complete subset of Feynman diagrams, such as those of the parquet approximation, its results are independent on the choice of the cutoff scheme as well as on the way (direct or through a post-processing treatment) response functions are calculated. We demonstrate by hand of precise numerical calculations that both properties are fulfilled by a satisfactory degree of accuracy. We also elaborate how these properties could be exploited in the future for improving the numerical solution of parquet-based algorithms.
Finally, our study reveals that an important piece of physical information can be accessed by looking at the nonlinear response of the system to an external field. In particular, a DMFT study of the pairing response function to a superconducting probe *beyond* the linear regime, has pinpointed a simple criterion to identify the presence of a preformed pair phase. This result provides a complementary information to cutting-edge theoretical approaches and, possibly, to non-equilibrium experiments, to shed some light on the nature of the pseudogap in high-T_c superconductors.

Zusammenfassung

Der technologische Fortschritt in der Materialwissenschaft hat die Entwicklung neuartiger Systeme ermöglicht, deren starke elektronische Korrelationen faszinierende Eigenschaften aufweisen. Der Vielzahl an physikalischen Phänomenen steht die Schwierigkeit einer genauen theoretischen Beschreibung gegenüber. Das hat Anlass zur Entwicklung verschiedener theoretischer Näherungsmethoden gegeben. In diesem Zusammenhang stellt die Antwort des Systems auf eine externe Störung eine Möglichkeit dar, eine theoretische Beschreibung durch experimentelle Nachweise zu untermauern oder zu widerlegen.
In dieser Doktorarbeit entwicklen wir theoretische und numerische Ansätze, um die Berechnung der linearen Antwortfunktionen in verschiedenen modernen Quantenvielteilchenmethoden zu verbessern. Die effiziente numerische Handhabung, die durch physikalische Überlegungen inspiriert ist, gestattete einerseits (i) Verbesserungen in der Behandlung von zweiteilchen Korrelationen sowie Streufunktionen, die wiederum essentielle Bestandteile nicht-perturbativer Theorien sind, wie z.B. der dynamischen Molekularfeldtheorie (DMFT) und ihrer diagrammatischen Erweiterungen, und ermöglichte andererseits (ii) die Implementierung der wegweisenden *multiloop*-funktionalen Renormierungsgruppentheorie (mfRG) und deren Anwendung auf das zweidimensionale Hubbard Modell. Durch die Errungenschaften aus (i) und der Verwendung des Multiloopschemas ermöglicht die funktionale RG quantitative Vorhersagen. Die inhärente Eigenschaft der mfRG, eine vollständige Teilmenge der Feynmandiagramme zu erzeugen, hier insbesondere die Diagramme der parquet Näherung, fuehrt ausserdem dazu, dass ihre Resultate “cutoff” unabhängig sind und die Art und Weise der Berechnung der Antwortfunktionen (entweder mittels des Renormierungsgruppenflusses oder als “post-processing” der fRG Rechnung) keine Rolle spielen. Wir zeigen anhand numerischer Berechnungen, dass beide oben genannten analytischen Eigenschaften der mfRG erfüllt sind. Außerdem diskutieren wir, dass diese Eigenschaften einen bedeutenden Beitrag in der numerischen Konvergens parquebasierter Algorithmen liefern können.
Schließlich zeigt unsere Untersuchung, dass die nichtlineare Antwort eines Materials auf ein externes Störungsfeld wichtige physikalische Information enthält. Insbesondere hat eine Betrachtung der Antwortfunktion der Paarbildung auf ein Supraleitungsfeld im nichtlinearen Regime im Rahmen der DMFT, ein einfaches Kriterium für das Vorhandensein einer “preformed pair phase” aufgezeigt. Dieses Resultat liefert neue Einblicke in aktuelle theoretische und experimentelle Methoden der Vielteilchenphysik, um die Hintergründe der Entsehung einer *Pseudogap* in Hochtemperatursupraleitern zu beleuchten.

List of diagrammatic symbols

Self-energy: Σ

1P Green's function: G

Used in both non-interacting and interacting ("dressed") cases. The arrow specifies the direction of propagation.

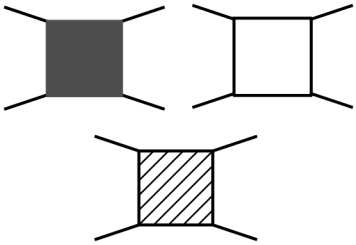

2P vertex functions:

Filled square $\rightarrow$ Full 2P vertex γ_4.
Empty square $\rightarrow$ 2P reducible vertex ϕ^r:
(a) Red framed for $r = pp$;
(b) Green framed for $r = ph$;
(c) Blue framed for $r = \overline{ph}$.
Diagonally striped square $\rightarrow$ 2PI vertex $\mathcal{I}^r$:
(a) Green-blue stripes for $r = pp$;
(b) Red-blue stripes for $r = ph$;
(c) Green-red stripes for $r = \overline{ph}$.

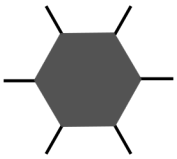

3P vertex function: γ_6

nonlocal interaction:

Filled wiggle line: nonlocal (possibly dynamic) effective interaction (V_{eff})
Simple wiggle line: nonlocal (bare) Coulomb interaction ($V(\mathbf{q})$)

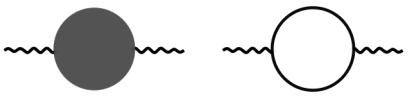

Physical susceptibility: $\chi^{\eta=\text{sc,d,m}}$

Filled circe: Full vertex-corrected susceptibility
Empty circle: Non-vertex corrected susceptibility (bare bubble) χ_0^η

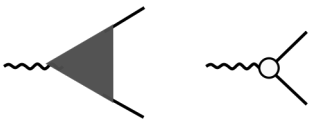

3-point vertex: $\gamma_3^{\eta=\mathrm{sc,d,m}}$

Filled triangle: Full screened 3-point fermion-boson vertex

Small empty circle: Bare 3-point fermion-boson vertex $\gamma_{0,3}^{\eta}$

4-point vertex: $\tilde{\gamma}_4^{\eta=\mathrm{sc,d,m}}$

4-point fermion-boson vertex

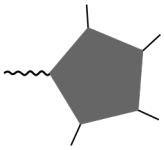

5-point vertex: $\gamma_5^{\eta=\mathrm{sc,d,m}}$

5-point fermion-boson vertex

Contents

To my grandfather Franco and his unstoppable sense of humor.

Acknowledgments

The last years have been a challenging adventure both form a scientific and, much more important, form a personal perspective.
During this journey many people have to be acknowledged and I'm not sure I can find the words to describe the importance they played along my path.
First I want to acknowledge my supervisors for the scientific guide and support. I'm thankful for their example to do science with passion, enthusiasm and respect for the others. Their "human way" of giving credits, being humble and put the love for knowledge above all is a rare quality in the nowadays tendency to acknowledge quantity instead of quality and competition instead of collaboration.
My family, despite the distance, has played a big role in my personal growth and I'm thankful for taking me out from my narrow view point and showing me new perspectives.
There are many friends form many different corners of the world who played a fundamental role in the last years process of discovering myself. I will always be grateful that our paths crossed and I can't wish myself more than having them on my side.

A special thank goes to Georg who made and makes my life beautiful.

Time is an illusion. Lunchtime doubly so.

Douglas Adams

1 Introduction

1.1 Introduction and Motivation

A crucial step common to all the existing theoretical approaches developed to describe many-body systems, consists in testing their ability to reproduce experimental measurements in order to make reliable predictions for (new) observations, yet unexplored. Generally, this is realized (i) by probing the physical system under investigation by means of an external perturbation (usually, but not always, weak compared to the internal forces of the system) and (ii) analyzing the modification occurring in the system in response to the applied perturbation. Experimentally, there are different techniques devolved to this scope, which can be classified in three broad categories: (i) Transport experiments (conductance measurements); (ii) Experiments probing thermodynamic response functions such as specific heat c_v, magnetic susceptibility χ^m, (isothermal) compressibility κ_T etc.; (iii) Spectroscopy (Raman, IR, X-Ray/ e^- spectroscopy, neutron scattering, magnetic resonance, NMR etc.). All these techniques consist in detecting the response of the system to an external perturbing force.
Formally, the application of the external perturbation corresponds to include the following term to the original many-body Hamiltonian:

$$H_{\mathrm{J}} = \int d^d r J(\mathrm{r}, t)\hat{X}(\mathrm{r}) \qquad , \tag{1.1}$$

where J represents the generalized external force applied to the sample, and $\hat{X}$ the system's operators coupling to the external perturbation. The external force drives the systems out

of its *initial* state (i.e., the one at $J = 0$), affecting the expectation value of the operator $\langle \hat{X}(\mathrm{r}) \rangle = X(\mathrm{r}, t) \neq 0$.
One of the the main scopes of the theory is, thus, to make predictions on the functional dependence of $X(\mathrm{r}, t)$ on J. In particular, if we assume the external perturbation J to be weak, then we can expect a linear functional dependence:

$$X(\mathrm{r}) = \int d^d r \int dt\, \chi(\mathrm{r}, t, \mathrm{r}', t')\, J(\mathrm{r}', t') + \mathcal{O}(J^2) \qquad , \tag{1.2}$$

where the integration kernel χ represents the linear response of the system to the external perturbation. As χ does not depend at all on J, it indicates an intrinsic property of the physical system. Therefore, the confirmation (or disprove) of a microscopical theory consists in calculating χ and testing the agreement with the observed behavior of X. Despite the conceptual simplicity of the aforementioned procedure, the calculation of response functions may pose significant challenges, especially in the case of strongly correlated materials.

In this "category" one finds several materials whose fascinating physics still challenges todays condensed matter research. In fact, despite all theoretical and algorithmic progress in the field, some of these materials still lack a comprehensive microscopical description. First in this list is the broad category of the so-called unconventional high-T_c superconductors. After appearing on the scene with the late eighties discovery by Bednorz and Müller (Bednorz & Müller, 1986), unconventional superconductivity has represented one of the most debated problem in the field ever since. Although the answer to the fundamental question about their superconducting pairing mechanism is still missing, a vast spectrum of proposals try to address the problem from different angles. In fact, as pointed out by Fisk et al. (2009), despite ".. the remarkable phase space they inhabit..", unconventional superconductors (cuprates, Fe-pnictides and chalcogenides, heavy-fermions and actinide materials) display common features. From a theoretical perspective, standard band-structure/weakly correlated theories fail to describe their properties [e.g., local (spin) density approximation (LDA) combined with random phase approximation (RPA) or fluctuation exchange (FLEX) approximation]. From an experimental perspective one observes the coexistence and the interplay of the antiferromagnet spin density wave (SDW) phases with an unconventional (d-wave, sign-change s-wave etc.) superconductivity (Scalapino, 2012).
The standard approach adopted in order to handle such systems, which eventually leads to work with the celebrated Hubbard model (Hub, 1963) or its multi-orbital extensions, consists in mapping the full Hamiltonian of our target system to an effective (low-energy) model. In the latter, the material-specific hopping integrals and effective (inter/intra-orbital and local/nonlocal) interaction parameters can be determined from *ab initio* calculations,

or just be tuned as free parameters to investigate different regimes and to make predictions. In spite of the reduced complexity with respect to (w.r.t.) the original problem, exact solutions of these low-energy models are available only in few limiting cases. For that reason, an impressive number of different theoretical and numerical approaches based on different approximation schemes have been developed in the last decades. In general, we can point out the following requirements as necessary for the forefront research in strongly correlated many-body systems. Ideally, one would need a method which: (i) goes beyond the perturbative regime, (ii) is capable of capturing simultaneously the spatial and temporal fluctuations arising when we approach phase transitions in the intermediate-to-strong coupling regimes and (iii) allows different instabilities to compete and, eventually, set in.

The first requirement (i) leads us to the dynamical mean field theory (DMFT) which represents since its formulation in 1992 (Georges et al., 1996; Georges & Kotliar, 1992), a milestone for studying strongly correlated materials. As a quantum extension of the classical mean field theories, DMFT becomes an exact theory in infinite dimensions (or infinite coordination number) (Metzner & Vollhardt, 1989). Nevertheless, even in finite dimensions, it properly captures the purely local quantum dynamics of the system, summing all local scattering processes up to infinite order in the interaction. DMFT displays several successes among which we find: the description of the metal-to-insulator transition (MIT) in V_2O_3 (Held et al., 2001a), the δ phase of Pu (Savrasov et al., 2001), the correlation effect in Fe and Ni (Lichtenstein et al., 2001), the volume collapse in Ce (Held et al., 2001b), and of a possible uncoventional superconducting mechanism in doped fullerenes (Capone et al., 2002). Moreover, DMFT has been able to reproduce the kinks in the spectral functions and the specific heat in a number of vanadates, (Byczuk et al., 2007), (Toschi et al., 2009), the spin-polaron peak structures in photo-emission (Sangiovanni et al., 2006) and optical spectroscopic data (Taranto et al., 2012) of strongly coupled antiferromagnets, anomalies of the optical spectra and sum rules in the high-temperature superconducting cuprates (Toschi et al., 2005; Comanac et al., 2008; Nicoletti et al., 2010) and some spectral (Haule et al., 2008; Craco et al., 2008) and magnetic behaviors (Haule & Kotliar, 2009; Hansmann et al., 2010; Skornyakov et al., 2011) of iron-based superconductors. Nonetheless, by looking at several DMFT studies or its combination with local density approximation (LDA+DMFT), one does observe several limitations. First, most of the comparison with experiments are limited to the one-particle correlation functions, i.e., density of states or spectral functions. Even DMFT transport surveys on optical and thermal conductivity are limited to the so-called "joint density of state", and therefore, to the one-particle level. Studies on momentum-dependent dynamical susceptibility functions within DMFT (or LDA+DMFT), have been typically restricted to the local case (Toschi et al., 2012; Hansmann et al., 2010) [1]. Nonlocal

[1] The usual procedure to probe linear response functions is to "by hand" perturbe the system by means of

effects have been included only by means of the lattice Green's functions, or via "uncontrolled" approximations (Park et al., 2011; Lin et al., 2012). Already at this level, the difficulty of computing two-particle (2P) quantities has motivated more convenient representations, e.g., Lagrangian polynomial expansion in imaginary times of one and two-particle Green's functions (Boehnke et al., 2011) and/or systematic studies of its frequency structure (Rohringer et al., 2012).

In order to include nonlocal effects at the level of the two-particle correlation function [combining requirements (i) and (ii)], cluster extensions such as (cellular) CDMFT (Kotliar et al., 2001) and dynamical cluster approximation (DCA) (Hettler et al., 2000; Maier et al., 2005), have been developed. In these approaches, however, the correlation effects are limited to the cluster size, which prevents the methods to correctly describe the physics of the system close to phase transitions, where the correlation length is expected to become infinitely large. In order to capture long-range correlations, so-called diagrammatic extensions like the dynamical vertex approximation (DΓA) (Toschi et al., 2007; Katanin, 2009; Held, 2014; Rohringer & Toschi, 2016), dual fermion theory (DF) (Rubtsov et al., 2008; Hafermann et al., 2009), one-particle irreducible approach (1PI) (Rohringer et al., 2013), dual boson (DB) theory (Rubtsov et al., 2012), DMF^{2}RG (Taranto et al., 2014) as well as the TRILEX (Ayral & Parcollet, 2015) and QUADRILEX (Ayral & Parcollet, 2016) method, have been embraced. The price of their theoretical sophistication, necessary for the inclusion of a richer physics, is the numerically challenging full treatment of the generalized two-particle correlation function[2]. On top of the difficulties already encountered at the local level, the inclusion of the momentum dependence represents a further challenge. In fact, due to the enormous numerical efforts to include nonlocal effects on top of the (local) DMFT scattering amplitude, these methods are typically limited to consider specific scattering processes ("channels"), usually of magnetic nature for repulsive interactions, disregarding the interplay of different physical mechanisms. We should also recall, in this respect, that the attempt of DΓA studies to include the interplay among the different channels by means of the so-called parquet equations, has revealed an intrinsic limitation of the diagrammatic techniques due to the occurrence of divergences of the fully two-particle irreducible vertex (Λ_{loc}) on which the parquet equations are based upon, observed in several many-electron models (Schäfer et al., 2013, 2016; Janiš & Pokorný, 2014; Ribic et al., 2016; Rohringer, 2014; Chalupa et al., 2018; Vučičević et al., 2018; Thunström et al., 2018).

The need of a controlled and unbiased treatment of all channel fluctuations [requirement

an external field, e.g., magnetic h. The correspondent spin susceptibility can be then deduced by a linear fit of the magnetization as a function of the external field, in the limit $h \to 0$ (Georges et al., 1996; Galler et al., 2015; Skornyakov et al., 2011).

[2] A problem somewhat similar to that posed by the DMFT calculations beyond photoemission spectra.

(iii)] make us turn towards (perturbative) renormalization group methods which do not require any *a priori* assumptions on the correlation-process which will eventually dominate the physics of the system. Among these, *exact* or *functional* renormalization group (fRG) turned out to be particularly convenient. Based on the original scaling theory proposed by Kadanoff (Kadanoff, 1966) and Wilson (Wilson, 1971), it has been later reformulated in terms of an infinite hierarchy of coupled integro-differential "flow" equations for the functional derivatives of the generating functional [see one-particle irreducible (1PI) fRG formulation in Metzner et al. (2012)]. The application of fRG spans across a broad class of research areas. Excluding its extensive use in fields far away (astrophysics, high-energy physics, etc.) from the one this thesis places itself, we recall applications to quantum field theory and statistical mechanics (Berges et al., 2002) and to interacting Fermi systems whose first studies allowed a comprehensive analysis of the one-band 2D Hubbard model on a square lattice (Zanchi, D., 2001; Honerkamp et al., 2001; Halboth & Metzner, 2000). From these initial studies, the target systems for the fRG approach have lifted to different levels of complexity, allowing to access the physics of unconventional lattices (Honerkamp, 2008) and multiband systems. Among the latter the iron-pnictides represent a class of materials where fRG has shown several successes in describing their underlying Fermi surface instabilities: it has confirmed the fundamental role played by the nesting property of the multi-pocket Fermi surfaces together with the multiorbital structure in arising a variety of competing pairing states characterized by different symmetry properties (Wang et al., 2009; Mazin et al., 2008; Thomale et al., 2009, 2011a; Wang & Lee, 2011; Thomale et al., 2011b; Platt et al., 2012; Khodas & Chubukov, 2012). The fRG studies on the triangular lattice model of the sodium-doped cobaltates (Kiesel et al., 2013a), on the honeycomb lattice in doped graphene (Kiesel et al., 2012) and on the analysis in kagome lattices close to van-Hove fillings (Kiesel et al., 2013b) has allowed to identify universal features related to the lattice symmetry (i.e.,chiral d-wave superconductivity). The correlation effects in quantum wires and quantum dots such as Luttinger liquid behavior and Kondo effects have been also addressed and successfully reproduced in several fRG studies (Andergassen et al., 2004, 2006; Karrasch, 2010; Kinza, 2013). In the operative use of the fRG technique, the infinite hierarchy of differential equations is usually truncated beyond the two-particle level, restricting the theory to the perturbative regime and its applicability to small values of the interaction (or to high values of T). This truncation scheme is known as one-loop approximation (1ℓ) since it retains just one topological class of differentiated two-particle vertex diagrams (with respect to an appropriately chosen scale-parameter Λ). This class is characterized by a single (diagrammatically) internal pair of fermionic propagators, i.e.,the Green's function G^{Λ} and the so-called single-scale propagator S^{Λ}. Due to the increasing number of flowing functions, the application of fRG beyond one-dimensional systems has required further approximations in the flow equations such as: the exclusion of the self-energy feedback into

the two-particle vertex flow-equation, and a static approximation for scattering amplitudes [with few exceptions, see (Vilardi et al., 2017; Uebelacker & Honerkamp, 2012)]. At the same time, the fRG community has developed a broad spectra of sophisticated treatments of the (2P) vertex momentum-dependence (Giering & Salmhofer, 2012; Honerkamp & Salmhofer, 2003; Salmhofer et al., 2004; Lichtenstein et al., 2017).

Within the fRG framework, very recent works (Kugler & von Delft, 2018c,b) have eventually clarified in a rigorous way the diagrammatic content of the standard fRG 1ℓ-approximation and extended it to the so-called multiloop scheme [beyond few already existing works (Eberlein, 2014; Katanin, 2004) restricted to the two-loop level]. This formulation yields, through an iterative cycle at every integration step of the fRG "flow" equations, the resummation of *all* diagrams of the parquet approximation (Janiš, 1999; Bickers, 1991; Li et al., 2016; Yang et al., 2009).
The insights gained by this formulation could shed light on the difficulty faced when combining (1ℓ)-fRG with DMFT, in the so-called DMF^{2}RG (Taranto et al., 2014), which could be overcome by means of a multiloop implementation of the DMF^{2}RG. In fact, the possibility to compute nonlocal effects within the multiloop-fRG on top of DMFT (requirements (i-iii)), may represent a valuable alternative to parquet DΓA, being able to circumvent the aforementioned problem of the vertex divergences in the parquet DΓA formalism. Moreover, as pointed out in (Kugler & von Delft, 2018c), the integration of the fRG differential equations may provide a more stable numerical procedure compared to the self-consistent scheme of a direct solution of the parquet equations [see (Valli et al., 2015; Schäfer et al., 2013; Li et al., 2016) and Supplement I].

For the computation of response functions, the above discussion illustrates the necessity and, at the same time, the complexity of achieving a satisfactory and unbiased calculation of two-particle vertex functions by means of the theoretical and numerical tools currently at disposal. This work provides a systematic and critical analysis of how the response functions (in the linear regime and beyond) can be accessed in different approximation schemes, conceived to fulfill, in perspective, all the aforementioned requirements.

A key step for this goal is to gain a deeper understanding of the momentum and frequency structure of the two-particle correlation functions such that efficient, and physically guided, simplified schemes can be devised. At the (local) DMFT level, for a system subjected to an instantaneous interaction, a "sparing" parametrization of the two-particle vertex in the high-frequency domain is realized by exploiting the related local response functions and fermion-boson vertices which depend on one and two frequencies, respectively (instead of three, as in the original object). This analysis, carried out in a general way in Supplement I (see Sec. 3.1) and applied to a DMFT vertex in Supplement II (see Sec. 3.2), allows us to

reduce the numerical cost of the full frequency treatment of the vertex functions.

This important information can be successfully exploited to perform a basic procedure common to several diagrammatic techniques, namely the inversion of the so-called Bethe Salpeter (BS) equations (see Sec. 3.2) in a numerically accurate way. This allows, in turn, for a proper evaluation of the response functions not only within DMFT but also in its diagrammatic extensions. The implementation of a highly simplified parametrization of the two-particle vertex in momenta, inherited from fRG studies (see above), and frequencies, as discussed in Supplements I-II, brings the fRG schemes in use to a more quantitative approach (see Supplement III). For this, the extension of the standard 1ℓ fRG to the multiloop appoach plays an important role. Its application to the calculation of linear response functions in the 2D Hubbard model, is a substantial result presented in this thesis (see Sec. 3.3 and Supplement III).

Last but not least, the study of non-linear regimes triggered by an external perturbation field might provide complementary information to interpret, as a first approximation, more complex non-equilibrium phenomena. This motivates the DMFT study carried out in Supplement IV and discussed in Sec.3.4, where the physical information contained in the *second derivative* of the order parameter to an s-wave external superconducting pairing-field is analyzed in both the attractive and the repulsive Hubbard model.

1.2 Structure of the work

In the following we schematically outline the structure of this thesis.

In Chapter 2, Section 2.1, we report the main formalism of the linear response theory. In particular, after deriving the Kubo formula, we illustrate a number of properties related to linear responses and their definition in terms of n-particle correlation functions. Moreover, we illustrate the important role played by the thermodynamic linear response to predict the occurrence of second order phase transitions within the system. Section 2.2 provides an overview on how response functions are computed in different many body solvers, such as: dynamical mean field theory (DMFT) (Sec. 2.2.1), dynamical vertex approximation (DΓA) within its ladder formulation (Sec. 2.2.2), functional renormalization group (fRG) (Sec. 2.2.3) and its merge with DMFT, the so called DMF^{2}RG, which remains since its formulation almost an unexplored ground (Sec. 2.2.4).

In Chapter 3 a general overview on my contribution to the state-of-the-art many-body methods to compute response functions is addressed. Although the full version of the papers presented in this chapter can be found in the Supplements, we aim here at presenting

them in a unified picture which should convey the gateway of this dissertation. Section 3.1 summarizes the main results obtained in the paper presented in Supplement I. This first study presents new algorithmic implementations for fRG schemes as well as for parquet-based methods that make use of the parametrization of the two-particle correlation function in the high-frequency regime. This idea, based on diagrammatic arguments, has been tested in this work on an impurity model and successively extended to solve some practical difficulties in computing response functions in DMFT as well as in DΓA implementations. This represents the main topic of Section 3.2 (for the full version of the paper, see Supplement II) which proposes two methods in order to correctly calculate two-particle irreducible vertices by means of the so-called Bethe-Salpeter equations.
In Section 3.3 we present the first application of the novel multiloop fRG to the two-dimensional Hubbard model. This work, whose correspondent full version of the paper can be found in Supplement III, extends the multiloop fRG approach to the study of response functions. Section 3.4 presents the main outcomes of the manuscript reported in Supplement IV, which provides a DMFT study of the superconducting response function in the non-linear regime. In particular the second-order derivative of the response function with respect to the external pairing field, will serve as an indicator to recognize the presence of a preformed pairs phase.

Finally, in the Conclusion section we summarize the main findings of this thesis and provide an overview of future studies on this topic.

Note that a short summary is reported within yellow boxes at the beginning of each chapter and/or main section (e.g., see the spitting of Chapter 2 in two main sections).

The importance of a physical law is not how clever we are to have found it out, but...how clever nature is to pay attention to it.

Richard Feynman

2 Theory and formalism

2.1 Response function theory: linear regime and beyond

In this section we want to recap the basic formalism of the linear response theory. The aim is to establish a connection between the response function χ [mentioned in the Introduction, see Eq. (1.2)] and the microscopic quantities accessible from specific many-body solvers. In particular we start from the Kubo formula, and proceed by discussing some general analytical properties of the response functions: Exploiting the causality principle, the so-called Kramers-Kroning relations will be derived. In order to obtain a more practical representation of the response functions in terms of n-point correlation functions of our unperturbed system, we provide the derivation of the thermodynamic generalized susceptibilities within the functional integral formalism in a nutshell.
Finally, we recall how it is possible to extract important insights on the tendency of the system to approach phase transitions/criticalities by detecting thermodynamic response functions such as specific heat c_v, isothermal compressibility κ_T and isothermal spin susceptibility χ. The latter are in fact related to the microscopic information on the energy, particle number and magnetic fluctuations of the system under investigation, respectively.

2.1.1 Microscopic Response Theory: formalism and analytical properties

Let us probe a general system, which we want to extract information from, by an external source field $J(\mathbf{r}, t)$. This results in adding to our unperturbed Hamiltonian, $\hat{H}_0$ the follow-

ing time-dependent term:

$$\hat{H}_J(t) = \int d\mathbf{r}\; J(\mathbf{r},t)\,\hat{X}(\mathbf{r})\;, \tag{2.1}$$

where $J(\mathbf{r},t)$ represents the external probe which couples to the Hermitian operator [1] $\hat{X}(\mathbf{r})$. Our goal is to study the effect of this perturbation on some measurable quantities, described by, e.g., an (Hermitian) operator $\hat{Y}(\mathbf{r})$. This results in computing its thermal average:

$$Y(\mathbf{r},t) = \langle \hat{Y}(\mathbf{r})\rangle = \mathrm{Tr}\big[\rho(t)\,\hat{Y}(\mathbf{r})\big]\;, \tag{2.2}$$

with $\rho(t)$ the time-dependent density matrix of our perturbed system.

In this case, it is convenient to write the equation of motion for the density matrix in the so-called Dirac, or interaction, picture ($\hbar = 1$):

$$i\partial_t \rho^I(t) = \big[\hat{H}_J^I(t), \rho^I(t)\big]\;, \tag{2.3}$$

where $\rho^I(t) = e^{iH_0 t}\rho(t)e^{-iH_0 t}$ [2], and we disregarded additional terms proportional to the time derivative of the perturbed Hamiltonian. By expanding the right and the left hand side in powers of the external field J and comparing order by order, we obtain an infinite hierarchy of equations of motions. The one for the first-order term is easily integrable and reads:

$$\rho_1^I(t) = i\int_{-\infty}^{t} dt'\,\big[\hat{H}_J^I(t'), \rho_0\big]\;, \tag{2.4}$$

with ρ_0 the density matrix of the unperturbed system. If we limit our analysis to the linear regime [3] we can substitute $\rho^I(t) = \rho_0^I + \rho_1^I(t)$ in Eq.(2.2) and estimate the variation of the observable $Y(t)$ due to the perturbation:

$$\begin{aligned} Y(\mathbf{r},t) - Y_0(\mathbf{r}) &= i\int_{-\infty}^{+\infty} dt' \int d\mathbf{r}'\theta(t-t')\mathrm{Tr}\Big[\hat{\rho}_0\big[\hat{Y}(\mathbf{r},t), \hat{X}(\mathbf{r}',t')\big]\Big]J(\mathbf{r}',t') \\ &= -i\int_{-\infty}^{+\infty} dt' \int d\mathbf{r}'\chi_{\mathrm{XY}}(\mathbf{r},\mathbf{r}',t,t')\;J(\mathbf{r}',t')\;. \end{aligned} \tag{2.5}$$

[1] In this case we consider a scalar perturbation field. A more general form would be a vectorial field, though. In this case χ would become a matrix/tensor.

[2] Notice: we used the superscript I to distinguish the *interaction* from the *Schrödinger* picture

[3] Notice that in some situations, e.g., imagine a laser pulse perturbing the system, the restriction to the linear response is not sufficient and one would need infinite-order resummation of this expansion.

This leads us to the so-called Kubo formula:

$$\chi_{XY}(\mathbf{r}, \mathbf{r}', t, t') = i\theta(t - t')\langle\left[\hat{Y}(\mathbf{r}, t), \hat{X}(\mathbf{r}', t')\right]\rangle_0 \ , \tag{2.6}$$

where the subscript 0 indicates that the expectation value is computed on the unperturbed quantum system.

Before entering a broader analysis of the response functions, let us list few properties of χ:

- The external field J cannot cause an effect before its action. This causality principle is explicitly expressed in Eq. (2.6) by means of the Heaviside step function $\theta(t - t')$;
- If the Hamiltonian is time-independent, the response depends just on the difference between the time coordinates, $\chi_{XY}(\mathbf{r}, \mathbf{r}', t, t') = \chi_{XY}(\mathbf{r}, \mathbf{r}', t - t')$. Therefore, it is often convenient to Fourier transform the temporal convolution in Eq. (2.5) into the frequency space:

  $$\mathcal{F}\{Y(\mathbf{r}, t) - Y_0(\mathbf{r})\}(\omega) = \Delta Y(\mathbf{r}, \omega) = \int d\mathbf{r}' \ \chi_{XY}(\mathbf{r}, \mathbf{r}', \omega) \ J(\mathbf{r}', \omega) \ . \tag{2.7}$$

  Eq. (2.7) conveys and important information: in the linear response regime, any perturbation acting at a certain frequency ω will induce a response at the same frequency. If the system responds with a frequency shift, we have triggered a non-linear effect (Alexander Altland, 2010).

- If the system is translationally invariant, the linear response depends only on the spatial difference $(\mathbf{r} - \mathbf{r}')$. Analogously to the temporal treatment, it is convenient to spatially Fourier transform Eq. (2.7) into the momentum space:

  $$\Delta Y(\mathrm{q}, \omega) = \chi_{XY}(\mathrm{q}, \omega) \ J(\mathrm{q}, \omega). \tag{2.8}$$

  We can then deduce that a peak of the observable $Y(\mathrm{q}, \omega)$ at a certain frequency-momentum value (ω, q) will indicate the presence of an intrinsic excitation with characteristic frequency and momentum (ω, q).

2.1.2 Kramers-Kronig relations

As it is known, the causality principle implies that the real and the imaginary parts of the response function in frequency space are not two independent quantities. Since this property applies to a generic function $f(\omega)$, whose inverse Fourier transform satisfies $f(t) =$

$\theta(t)f(t)$, we won't refer explicitly to the response function in the following derivation. In fact, the derived expression will apply to a generic retarded function $f(\omega)$, including -per definition- all response functions as well as, e.g., the retarded expressions of the one-particle Green's function.
By applying the convolution theorem, the Fourier transform of the function $f(t) = \theta(t)f(t)$ reads:

$$\begin{aligned} f(\omega) = \mathcal{F}\{f(t)\,\theta(t)\}(\omega) &= \int_{-\infty}^{+\infty} d\omega'\, f(\omega')\theta(\omega-\omega') \\ &= \int_{-\infty}^{+\infty} d\omega'\, f(\omega')\,\frac{1}{2}\Big[\delta(\omega-\omega') - \frac{i}{\pi}\text{p.v}\Big(\frac{1}{\omega-\omega'}\Big)\Big] \\ &= \frac{1}{2}f(\omega) - i\frac{1}{2\pi}\text{p.v.}\int_{-\infty}^{+\infty} d\omega'\frac{f(\omega')}{\omega-\omega'} \\ &= -\frac{i}{\pi}\text{p.v.}\int_{-\infty}^{+\infty} d\omega'\frac{f(\omega')}{\omega-\omega'}\,. \end{aligned} \tag{2.9}$$

Notice that in the second line we used the analytic expression for the Fourier transform of Heaviside step function, and "p.v" specifies the principal value of the intergral.
From Eq. (2.9) the so-called Kramers-Kronig relations follow:

$$\mathcal{R}e\{f(\omega)\} = f'(\omega) = -\frac{1}{\pi}\int_{-\infty}^{+\infty} d\omega'\,\frac{f''(\omega')}{\omega-\omega'} \tag{2.10}$$

$$\mathcal{I}m\{f(\omega)\} = f''(\omega) = \frac{1}{\pi}\int_{-\infty}^{+\infty} d\omega'\,\frac{f'(\omega')}{\omega-\omega'}\,. \tag{2.11}$$

2.1.3 Thermodynamic susceptibility in functional integral formalism

The formalism of the field integral represents a convenient tool to develop many-body theories and access their thermodynamic properties (Alexander Altland, 2010; J.W. Negele, 1994). Since the functional integral formalism works naturally with imaginary times, it is mandatory to derive an expression for the response functions in this framework [see (Alexander Altland, 2010)]. In the present section we will restrict ourselves to an external field coupling to (internal) bilinear fermionic fields. Therefore, the aforementioned operator $\hat{X}$ can be represented as $\hat{X}(\mathbf{r}) = \sum_{a,b} c_a^\dagger(\mathbf{r})\, X_{ab}\, c_b(\mathbf{r})$, where $c(^\dagger)$ is an annihilation (creation) fermionic operator an the subscript a stands for a possible spin and/or orbital quantum number. It is worth stressing that the previous operator $\hat{X}(\mathbf{r})$ has been implicitly shifted by its expectation value in absence of the perturbation field it couples to, $\hat{X}(\mathbf{r}) \to \hat{X}(\mathbf{r}) - X_0$

. Therefore one has:

$$\langle \hat{X}(\mathbf{r},\tau)\rangle_0 = 0 \ ,$$

where the thermal average has to be considered with respect to the unperturbed system. In the functional integral formalism, the coupling to the external field J results in the following additional term to the unperturbed action:

$$\begin{aligned}\delta S[J,\bar{\psi},\psi] &= \int d\tau \int d\mathbf{r}\, J(\tau,\mathbf{r})\, \hat{X}(\mathbf{r},\tau) \\ &= \int d\tau \int d\mathbf{r}\, J(\tau,\mathbf{r}) \sum_{a,b} \bar{\psi}_a(\mathbf{r},\tau)\, X_{ab}\, \psi_b(\mathbf{r},\tau) \\ &= (J,\hat{X}) \ .\end{aligned} \tag{2.12}$$

In Eq. (2.12) ψ ($\bar{\psi}$) represents a Grassmann variable and in the last line $(..)$ should be read as scalar product. It is convenient, as we will see more in detail in the fRG formalism, to express the expectation value of a second bilinear operator in the fermionic fields, $\hat{Y}(\mathbf{r},\tau)$, whose expectation value we want to compute, as functional derivative of the free energy. To this aim, one can formally couple this operator to a second fictitious external probe field J', so that our final action becomes $S[J,J',\bar{\psi},\psi] = S_0[\bar{\psi},\psi] + (J,\hat{X}) + (J',\hat{Y})$.
Its expectation value reads:

$$Y(\mathbf{r},\tau) = -\frac{\delta}{\delta J'(\mathbf{r},\tau)}\Big|_{J'=0} \ln \mathcal{Z}[J,J'] \ , \tag{2.13}$$

where $\mathcal{Z}[J,J'] = \int \mathcal{D}[\bar{\psi},\psi] \exp\left(-S[J,J',\bar{\psi},\psi]\right)$ is the partition function and its natural logarithm $\ln \mathcal{Z}[J,J']$, the free energy. If one assumes that the intensity of the external field J is such that Eq. (2.13) can satisfactorily be represented by the linear approximation of $\mathcal{Z}[J,J']$ in J, one obtains:

$$Y(\mathbf{r},\tau) = -\int d\tau' \int d\mathbf{r}' \Big(\frac{\delta^2}{\delta J'(\mathbf{r},\tau)\delta J(\mathbf{r}',\tau')}\Big|_{J'=J=0} \ln \mathcal{Z}[J,J'] \Big) J(\mathbf{r}',\tau') \ . \tag{2.14}$$

From the previous equation we can extract the linear response "*kernel*":

$$\begin{aligned}\chi_{XY}(\mathbf{r},\mathbf{r}',\tau,\tau') &= -\frac{\delta^2}{\delta J'(\mathbf{r},\tau)\delta J(\mathbf{r}',\tau')}\Big|_{J'=J=0} \ln \mathcal{Z}[J,J'] \\ &= -\mathcal{Z}^{-1} \frac{\delta^2}{\delta J'(\mathbf{r},\tau)\delta J(\mathbf{r}',\tau')}\Big|_{J'=J=0} \mathcal{Z}[J,J'] \ ,\end{aligned} \tag{2.15}$$

where from the first to the second line we performed the functional derivative explicitly. One observes that Eq. (2.15) is nothing but the four-point correlation function (J.W. Negele, 1994):

$$\chi_{XY}(\mathbf{r},\mathbf{r}',\tau,\tau') = -\langle(\hat{X}(\mathbf{r},\tau) - \langle\hat{X}(\mathbf{r},\tau)\rangle)(\hat{Y}(\mathbf{r},\tau) - \langle\hat{Y}(\mathbf{r}',\tau')\rangle)\rangle \ , \tag{2.16}$$

where $\langle..\rangle$ represents the functional average over the unperturbed action and we subtracted the equilibrium expectation value of $\hat{X}$ ($\hat{Y}$) which vanishes because of the previous argument. We define thermodynamic susceptibility the linear response represented by the correlation function of a bilinear operator with itself, i.e.,$\hat{X} = \hat{Y}$.
It is important to recall the symmetry properties of Eq. (2.16) in imaginary times. First, as already seen for the real-time response function, in case of space-time translational invariance, it follows:

$$\chi_{XY}(\mathbf{r},\mathbf{r}',\tau,\tau') = \chi_{XY}(\mathbf{r}-\mathbf{r}',\tau-\tau') \ .$$

Furthermore, by looking at the spectral representation of $\chi_{XY}(\mathbf{r},\tau)$ (see Appendix A), one observes that the response function in imaginary times is only defined in the interval $-\beta < \tau < +\beta$, with β the inverse temperature, and that it fulfills the following periodicity property:

$$\chi_{XY}(\tau) = \zeta_{\hat{X}}\zeta_{\hat{Y}}\ \chi_{XY}(\tau+\beta)\ \tau < 0 \ , \tag{2.17}$$

where $\xi_{\hat{X}} = \pm 1$ if the operator $\hat{X}$ follows a bosonic/fermionic algebra.
Hence, it is convenient to expand χ in a Matsubara Fourier representation, $\chi(i\omega_l) = \int_0^\beta d\tau\ \chi(\tau)e^{i\omega_l\tau}$. Since both operators $\hat{X}$ and $\hat{Y}$ have a bosonic nature, ω_m are even integer multiples of π/β and $\zeta_{\hat{X}} = 1$. Eventually, in order to relate the results of our many-body scheme with experiments, our final goal consists in calculating the retarded response function in real time or frequency. Formally this is done by performing a Wick rotation $\tau \to t$ (from imaginary to real time) or $\omega_m \to \omega$ (from Matsubara frequencies to real frequencies) to transform the calculated quantities to the real axis. This analytic continuation is, in practice, not easy to perform straightforwardly. This triggered the formulation of a number of different sophisticated techniques to respond to this challenge [4]. We conclude this section with an observation which connects two different mechanisms: energy dissipation within the system and fluctuations of physical observables. In fact, without providing a rigorous demonstration, we can connect the right-hand side (r.h.s) of Eq. (2.16), which represents,

[4] Among these techniques one finds Padé (Ferris-Prabhu & Withers, 1973; Beach et al., 2000; Vidberg & Serene, 1977), maximum entropy method (MEM) (Silver et al., 1990; Gubernatis et al., 1991; Kraberger et al., 2017), stochastic approaches (Sandvik, 1998; Mishchenko et al., 2000), and some more recent algorithm based, e.g., on machine learning (Arsenault et al., 2017).

e.g, the conductivity (linear response to an electromagnetic field), responsible for the redistribution of energy among system excitations, to the fluctuation of the observable X. This concept is known as Fluctuation-Dissipation theorem.

2.1.4 Correlation function of fermionic bilinears: from asymptotic solutions to diagrammatic approaches

In the present section we provide some examples of fermionic bilinears, whose correlation functions will be computed in almost all studies discussed in the next chapter. We will start by considering analytical expressions in the limit of non-interacting systems and in the local atomic limit, and discuss how more realistic situations deviate from these cases in different respects.
We first focus on *charge invariant* bilinears, which can be represented in fermionic Matsubara frequencies and momenta as:

$$\rho^{\mathrm{d/m}}(q) = \sum_{\sigma,\sigma'} \int dp\, c^{\dagger}_{\sigma}(p) \xi^{\mathrm{d/m}}_{\sigma\sigma'}(p,q) c_{\sigma'}(p+q) \ , \tag{2.18a}$$

where the superscript d/m refers to the charge and the spin density, respectively and $p\,(q)$ represents a fermionic (bosonic) four-momentum $p = \{p_0, \mathbf{p}\} = \{i\nu_o, \mathbf{p}\}$ ($q = \{q_0, \mathbf{q}\} = \{i\omega_l, \mathbf{q}\}$). Therefore, the integral is a short-hand form for a summation on the Matsubara frequencies multiplied by the temperature and an integral over the first Brillouine Zone (BZ) normalized over its volume ($\mathcal{V}_{\mathrm{BZ}}$). The function $\xi^{\mathrm{d/m}}_{\sigma\sigma'}(p,q)$ determines spin, momentum and dynamical structure of the bilinears. In the following examples we always consider a static perturbation such that the bilinears acquire structure in spin and momenta only:

$$\xi^{\mathrm{d/m}}_{\sigma\sigma'}(p,q) = f_n(\mathbf{p}) \xi^{\mathrm{d/m}}_{\sigma\sigma'} \qquad \text{with} \begin{cases} \xi^{\mathrm{d}}_{\sigma\sigma'} & = \boldsymbol{\sigma}^0_{\sigma\sigma'} = \mathbb{1}_{\sigma\sigma'} \\ \xi^{\mathrm{m}}_{\sigma\sigma'} & = \{\boldsymbol{\sigma}^i_{\sigma\sigma'}\}_{i=1}^{3} \ , \end{cases} \tag{2.19}$$

and $\boldsymbol{\sigma}^i$ are the three Pauli matrices and the subscript n labels momentum structure specified by the function f, which is assumed to belong to a complete set of form-factors square integrable on the first Brillouin zone, $f \in \{f_n\}_{i=0}^{\infty}$.

The pairing (or superconducting) bilinears (*non-charge invariant*) read:

$$\rho_n^{\rm sc}(q) = \int dp\, f_n(\mathbf{p}) c_\downarrow(q-p) c_\uparrow(p) \tag{2.20a}$$

$$, \rho_n^{\rm sc*}(q) = \int dp\, f_n^*(\mathbf{p}) c_\uparrow^\dagger(p) c_\downarrow^\dagger(q-p)\ . \tag{2.20b}$$

The thermodynamic susceptibility, introduced in the previous section in functional integral formalism, is nothing but the correlation function of each bilinear with itself. For the charge and spin susceptibility (d/m), it reads:

$$\begin{aligned}\chi_{nn'}^{\rm d/m}(q) =& \frac{1}{2}\int_0^\beta d\tau e^{i\omega_l\tau}\langle \mathcal{T}_\tau\{\rho_n^{\rm d/m}(\mathbf{q},\tau)\rho_{n'}^{\rm d/m\,*}(\mathbf{q},0)\}\rangle \\ =& \frac{1}{2}\int_0^\beta d\tau e^{i\omega_l\tau}\sum_{\substack{\sigma,\sigma'\\ \zeta,\zeta'}}\frac{1}{\mathcal{V}_{\rm BZ}^2}\int d\mathbf{p}\, d\mathbf{p}'\, f_n(\mathbf{p}) f_{n'}^*(\mathbf{p}')\, \boldsymbol{\sigma}_{\sigma,\sigma'}^{0/i}\, \boldsymbol{\sigma}_{\zeta,\zeta'}^{0/i} \times \\ & \langle c_\sigma^\dagger(\mathbf{p},\tau) c_{\sigma'}(\mathbf{p}+\mathbf{q},\tau) c_{\zeta'}^\dagger(\mathbf{p}'+\mathbf{q},0) c_\zeta(\mathbf{p}',0)\rangle\ ,\end{aligned} \tag{2.21}$$

where the operator $c_\sigma^{(\dagger)}(\mathbf{p},\tau) = e^{H\tau} c_\sigma^{(\dagger)}(\mathbf{p}) e^{-H\tau}$. For the pairing (superconducting) (sc) susceptibility one obtains:

$$\begin{aligned}\chi_{nn'}^{\rm sc}(q) =& \int_0^\beta d\tau e^{i\omega_l\tau}\langle \mathcal{T}_\tau\{\rho_n^{\rm sc}(\mathbf{q},\tau)\rho_{n'}^{\rm sc\,*}(\mathbf{q},0)\}\rangle \\ =& \int_0^\beta d\tau e^{i\omega_l\tau}\frac{1}{\mathcal{V}_{\rm BZ}^2}\int d\mathbf{p}\, d\mathbf{p}' f_n(\mathbf{p})\, f_{n'}^*(\mathbf{p}') \times \\ & \langle c_\uparrow^\dagger(\mathbf{p},\tau) c_\downarrow^\dagger(\mathbf{q}-\mathbf{p},\tau) c_\downarrow(\mathbf{q}-\mathbf{p}',0) c_\uparrow(\mathbf{p}',0)\rangle\ .\end{aligned} \tag{2.22}$$

Notice that in Eqs.(2.21) and (2.22) we exploited the space-temporal translational invariance of the system and Eq. (2.17).
Besides the linear response function which can be interpreted as a bosonic propagator, additional information can be extracted by the scattering amplitude between the bosonic modes and the fermionic degrees of freedom of the system. Such information can be accessed by

looking at the three-point fermion-boson vertex, which is the defined as:

$$\begin{aligned}\gamma^{\mathrm{d/m}}_{3,n}(q,p) &= \frac{1}{2}\sum_{\sigma,\sigma'} G^{-1}_{\sigma}(p)G^{-1}_{\sigma'}(p+q)\int_0^\beta d\tau_1\, d\tau_2 e^{i\nu_o\tau_1}e^{-i(\nu_o+\omega_l)\tau_2}\boldsymbol{\sigma}^{0/i}_{\sigma,\sigma'}\times \\ &\qquad \langle \mathcal{T}_\tau\{c^\dagger_\sigma(\mathbf{p},\tau)c_{\sigma'}(\mathbf{p}+\mathbf{q},\tau_2)\rho^{\mathrm{d/m}*}_n(\mathbf{q},0)\}\rangle \\ &= \frac{1}{2}\sum_{\substack{\sigma,\sigma'\\ \zeta,\zeta'}} G^{-1}_{\sigma}(p)G^{-1}_{\sigma'}(p+q)\int_0^\beta d\tau_1\, d\tau_2 e^{i\nu_o\tau_1}e^{-i(\nu_o+\omega_l)\tau_2}\boldsymbol{\sigma}^{0/i}_{\sigma,\sigma'}\boldsymbol{\sigma}^{0/i}_{\zeta,\zeta'}\times \\ &\qquad \frac{1}{\mathcal{V}_{\mathrm{BZ}}}\int d\mathbf{p}' f_n(\mathbf{p}')\langle \mathcal{T}_\tau\{c^\dagger_\sigma(\mathbf{p},\tau_1)c_{\sigma'}(\mathbf{p}+\mathbf{q},\tau_2)c^\dagger_{\zeta'}(\mathbf{p}'+\mathbf{q},0)c_\zeta(\mathbf{p}',0)\}\rangle\ ,\end{aligned} \tag{2.23a}$$

$$\begin{aligned}\gamma^{\mathrm{sc}}_{3,n}(q,p) &= G^{-1}_{\downarrow}(p)G^{-1}_{\uparrow}(q-p)\int_0^\beta d\tau_1\, d\tau_2 e^{-i\nu_o\tau_1}e^{-i(\omega_l-\nu_o)\tau_2}\times \\ &\qquad \langle \mathcal{T}_\tau\{c_\downarrow(\mathbf{p},\tau_1)c_\uparrow(\mathbf{q}-\mathbf{p},\tau_2)\rho^{\mathrm{sc}*}_n(\mathbf{q},0)\}\rangle \\ &= G^{-1}_{\downarrow}(p)G^{-1}_{\uparrow}(q-p)\int_0^\beta d\tau_1\, d\tau_2 e^{-i(i\omega_l-\nu_o)\tau_1}e^{-i\nu_o\tau_2} \\ &\qquad \frac{1}{\mathcal{V}_{\mathrm{BZ}}}\int d\mathbf{p}' f_n(\mathbf{p}')\langle \mathcal{T}_\tau\{c_\downarrow(\mathbf{q}-\mathbf{p},\tau_1)c_\uparrow(\mathbf{q},\tau_2)c^\dagger_\uparrow(\mathbf{p}',0)c^\dagger_\downarrow(\mathbf{q}-\mathbf{p}',0)\}\rangle\ .\end{aligned} \tag{2.23b}$$

Non-interacting limit

Let us first consider Eq. (2.21) in the limit of a non-interacting system, whose Hamiltonian reads:

$$H_0 = \sum_\sigma \int d\mathbf{k}\,(\epsilon_{\mathbf{k}}-\mu)c^\dagger_\sigma(\mathbf{k})c_\sigma(\mathbf{k})\ , \tag{2.24}$$

where $\epsilon_{\mathbf{k}}$ represents the energy dispersion and μ the chemical potential. In this case, Eq. (2.21) can be computed by means of the Wick's theorem by summing the two possible contractions of the fermionic operators:

$$\begin{aligned}\chi^{\mathrm{d/m}}_{nn'}(q) = \delta_{\mathbf{q},0}\langle\rho^{\mathrm{d/m}}_n\rangle\langle\rho^{\mathrm{d/m}*}_{n'}\rangle - \frac{1}{2}\sum_{\sigma,\zeta}\int dp\, dp' f_n(\mathbf{p})f^*_{n'}(\mathbf{p}')(-1)^{\epsilon_{\sigma\zeta}}\times \\ G_{\sigma\zeta}(p,p')G_{\zeta\sigma}(p'+q,p+q)\ ,\end{aligned} \tag{2.25}$$

where we exploited the SU(2) symmetry of the system such that we can choose $\boldsymbol{\sigma}^{i=3}$ and ϵ is the Levi-Civita symbol. Because we defined the operators ρ such that they represent the relative distance from their unperturbed thermal average, we have that $\langle \rho_n^{\mathrm{d/m}} \rangle = 0$.
Now, exploiting the spin conservation and the time-space translational invariance, one has:

$$G_{\sigma\zeta}(p,p') = \delta_{\sigma,\zeta}\,\delta(p-p')G_{\sigma}(p) = \delta_{\sigma,\zeta}\,\delta(p-p')G_{\bar{\sigma}}(p) = \delta_{\sigma,\zeta}\,\delta(p-p')G(p)\ , \quad (2.26)$$

where $\delta(p-p') = \beta\mathcal{V}_{\mathrm{BZ}}\,\delta_{p_0,p_0'}\delta(\mathbf{p}-\mathbf{p}')$. Hence, Eq. (2.25) simplifies:

$$\chi^{\mathrm{d/m}}_{nn'}(q) = -\int dp\, f_n(\mathbf{p}) f^*_{n'}(\mathbf{p})\, G(p)\, G(p+q)\ . \quad (2.27)$$

Let us stress that for sake of simplicity we restricted ourselves to the magnetic and charge susceptibilities, but a analogous derivation is possible for Eq. (2.22). In the non-interacting limit, the one-particle Green's function assumes the simple form:

$$G(p) = \frac{1}{p_0 - \epsilon_{\mathbf{p}} + \mu}\ . \quad (2.28)$$

Inserting Eq. (2.28) into Eq. (2.27), one can easily perform the Matsubara frequency summation (over p_0) and obtain the following analytical form:

$$\chi^{\mathrm{d/m}}_{nn'}(q) = \Pi^{\mathrm{d/m}}_{0,nn'}(q) = -\frac{1}{\mathcal{V}_{\mathrm{BZ}}}\int d\mathbf{p} f_n(\mathbf{p}) f_{n'}(\mathbf{p}) \left[\frac{\mathrm{n}(\epsilon_{\mathbf{p}}-\mu) - \mathrm{n}(\epsilon_{\mathbf{p}+\mathbf{q}}-\mu)}{q_0 - (\epsilon_{\mathbf{p}+\mathbf{q}} - \epsilon_{\mathbf{p}})}\right]\ , \quad (2.29)$$

where n represents the Fermi-Dirac distribution.
Considering $f_{n=n'=0} = 1$ and taking the static limit ($q_0 = 0, \mathbf{q} \to 0$), one recovers the well known Pauli expression for the magnetic susceptibility, which for $T \ll T_{\mathrm{F}}$ reads:

$$\lim_{\mathbf{q}\to 0} \Pi^{\mathrm{m}}_{0,00}(0,\mathbf{q}) \sim \rho(\epsilon_{\mathrm{F}})\ , \quad (2.30)$$

where $\rho(\epsilon_{\mathrm{F}})$ represents the electron density of states at the Fermi level. We notice from Eq. (2.30) that in the non-interacting limit the magnetic susceptibility depends only weakly on the temperature for $T \ll T_{\mathrm{F}}$.

Atomic limit

Let us consider the opposite case of a purely local Hamiltonian, the so-called atomic limit, which at half-filling reads:

$$H = \frac{U}{2} \sum_{\sigma} \sum_{i} c^{\dagger}_{i;\sigma} c_{i;\sigma} c^{\dagger}_{i;\bar{\sigma}} c_{i;\bar{\sigma}} = \frac{U}{2} \sum_{\sigma} n_{i;\sigma} n_{i;\bar{\sigma}} \ , \tag{2.31}$$

where $U > 0$ is the so-called *repulsive* Hubbard on-site interaction [5], $\bar{\sigma} = -\sigma$ and $n_{i;\sigma}$ represents the number operator of the i-site of the lattice with spin σ. In this situation the sites i are decoupled and Eq. (2.21) can be calculated using its spectral representation (see Appendix A) and summing over the finite number of the i-site atomic eigenstates: $\{|0\rangle, c^{\dagger}_{i\uparrow}|0\rangle, c^{\dagger}_{i\downarrow}|0\rangle, c^{\dagger}_{i\uparrow} c^{\dagger}_{i\downarrow}|0\rangle\}$.
In the static case one easily finds the following expression for the magnetic susceptibility normalized to a single atom:

$$\chi^{\mathrm{m}}_{00}(0) = \frac{\beta \, e^{\beta U/2}}{1 + e^{\beta U/2}} = \frac{\beta}{1 + e^{-\beta U/2}} \ . \tag{2.32}$$

Differently from the non-interacting case, we see that the magnetic susceptibility in the atomic limit decreases as $\sim 1/T$ down to $T = 0$.

The intermediate regime: a diagrammatic approach

In the two previous paragraphs we have discussed the exact analytical expression of χ in the cases where the n-particle which compose the physical system are decoupled: either non-interacting or spatially localized on a single site.
Although several metals and strongly electron-localized materials can be satisfactorily described by one of these limits, the physics we address in this work is observed in materials which fall in the so-called intermediate regime [e.g., cuprates, vanadates, Fe-based compounds, Ni-based compounds, adatom lattice (Li et al., 2013; Hansmann et al., 2016, 2013), etc.]. The fact that in this regime localized and delocalized effects compete with the same intensity and constructively/distructively trigger different thermodynamical phases, makes any perturbative expansion around the previous analytical solutions hardly possible.
Although Feynman diagrammatic techniques have been developed in the context of a perturbative analysis, they offer in the intermediate regime the possibility to decompose correlation functions into objects with specific diagrammatic properties (Abrikosov et al., 1975).

[5] When mapping our full (material-dependent) Hamiltonian to the model (Hubbard) Hamiltonian, U represents the local part of the expectation value of the Coulomb interaction on the localized Wannier orbitals.

Here we provide an overview over different classes of two particle correlations functions which exhibit different diagrammatic features. We start introducing the generalized susceptibility:

$$\begin{aligned}\chi^{ph}_{\sigma\sigma'\zeta'\zeta}(q,k,k') = \int \prod_{i=1}^{3} dx_i \, e^{-ikx_1} e^{i(k+q)x_2} e^{-i(k'+q)x_3} \times \\ \left[\left\langle T_\tau c^\dagger_\sigma(x_1) c_{\sigma'}(x_2) c^\dagger_{\zeta'}(x_3) c_\zeta(0)\right\rangle - \right. \\ \left. \left\langle T_\tau c^\dagger_\sigma(x_1) c_{\sigma'}(x_2)\right\rangle \left\langle T_\tau c^\dagger_{\zeta'}(x_3) c_\zeta(0)\right\rangle\right] ,\end{aligned} \tag{2.33}$$

where we assumed space and time invariance of the Hamiltonian which restricts the previous quantity to just three independent four-momenta. Let us notice that $x_i = \{\tau_i, \mathbf{r}_i\}$, which implies that the single integration symbol adopted is just a short-hand for an integration over three (independent) imaginary times τ_i and the summation over the lattice sites $\mathbf{r}_i$. The assignment of the four-momenta k, $k+q$ and $k'+q$ to the time-space coordinates x_1, x_2 and x_3, respectively, corresponds to the so-called particle-hole (ph) notation [see (Rohringer et al., 2012)].
Analogously, one can express the generalized susceptibility in the particle-hole crossed ($\overline{ph}$) or in the particle-particle (pp) notation which can be obtained from the ph one via a mere frequency-momentum shift, i.e.:

$$\begin{aligned}\chi^{\overline{ph}}_{\sigma\sigma'\zeta'\zeta}(q,k,k') &\equiv \chi^{ph}_{\sigma\sigma'\zeta'\zeta}(k'-k,k,k+q) \\ \chi^{pp}_{\sigma\sigma'\zeta'\zeta}(q,k,k') &\equiv \chi^{ph}_{\sigma\sigma'\zeta'\zeta}(q-k'-k,k,k') \ .\end{aligned}$$

Because of the spin conservation one can reduce the spin dependencies of the generalized susceptibility to just two components:

$$\chi^{r}_{\sigma\sigma'}(q,k,k') = \chi^{r}_{\sigma\sigma\sigma'\sigma'}(q,k,k') \qquad \chi^{r}_{\overline{\sigma\sigma'}}(q,k,k') = \chi^{r}_{\sigma\sigma'\sigma'\sigma}(q,k,k') \ , \tag{2.34}$$

where $r = \{ph, pp, \overline{ph}\}$. The different physical interpretations of these notations as particle-hole and particle-particle scattering amplitudes are discussed in detail in (Rohringer et al., 2012) and in Supplement I. In a spin conserving and SU(2) symmetric situation, it is convenient to decompose the two-particle correlation functions into their spin singlet- and spin triplet-components, both for the ph and the pp representation. This corresponds to the definitions of the generalized susceptibilities in the density (d), magnetic (m), particle-

particle singlet (s) and particle-particle triplet (t) channels:

$$\chi^{\mathrm{d}}(q,k,k') = \chi^{ph}_{\uparrow\uparrow}(q,k,k') + \chi^{ph}_{\uparrow\downarrow}(q,k,k'), \tag{2.35a}$$

$$\chi^{\mathrm{m}}(q,k,k') = \chi^{ph}_{\uparrow\uparrow}(q,k,k') - \chi^{ph}_{\uparrow\downarrow}(q,k,k'), \tag{2.35b}$$

$$\chi^{\mathrm{s}}(q,k,k') = \frac{1}{4}\big[-\chi^{pp}_{\uparrow\uparrow}(q,k,k') + 2\chi^{pp}_{\uparrow\downarrow}(q,k,k') - 2\Pi^{pp}(q,k,k')\big], \tag{2.35c}$$

$$\chi^{\mathrm{t}}(q,k,k') = \frac{1}{4}\big[\chi^{pp}_{\uparrow\uparrow}(q,k,k') + 2\Pi^{pp}(q,k,k')\big] \ . \tag{2.35d}$$

The bare susceptibilities in the particle-hole and particle-particle notation are given by

$$\Pi^{\mathrm{d/m}}(q,k,k') = \ \Pi^{ph}(q,k,k') = \ -\delta(k-k')\ G(k)G(k+q)\ , \tag{2.36a}$$

$$\Pi^{\mathrm{s/t}}(q,k,k') = \ \Pi^{pp}(q,k,k') = \ -\frac{1}{2}\delta(k-k')\ G(k)G(q-k)\ , \tag{2.36b}$$

where $G(k)$ is the single-particle Green's function. From the generalized susceptibilities in Eq. (2.35), the correspondent physical ones in Eqs. (2.21) and (2.22) can be obtained by performing a weighted sum on the specific momentum structure represented by the function $f_n(\mathbf{k})$ over its fermionic dependencies (k,k'):

$$\chi^{\mathrm{d/m}}_{nn'}(q) = \int dk\ dk'\ f_n(\mathbf{k})\ f^*_{n'}(\mathbf{k}')\ \chi^{\mathrm{d/m}}(q,k,k') \tag{2.37}$$

$$\chi^{\mathrm{sc}}_{nn'}(q) = \int dk\ dk'\ f_n(\mathbf{k})\ f^*_{n'}(\mathbf{k}')\ \big[\chi^{pp}_{\uparrow\downarrow}(q,k,k') - 2\Pi^{pp}(q,k,k')\big]\ . \tag{2.38}$$

In a similar fashion the fermion-boson vertex defined in Eqs. (2.23a) and (2.23b) can be written:

$$\gamma^{\mathrm{d/m}}_{3,n}(q,k) = \Pi^{\mathrm{d/m}^{-1}}(q,k,k) \int dk'\ f^*_n(\mathbf{k}')\ \chi^{\mathrm{d/m}}(q,k,k') \tag{2.39}$$

$$\gamma^{\mathrm{sc}}_{3,n}(q) = \Pi^{\mathrm{sc}^{-1}}(q,k,k) \int dk'\ f^*_n(\mathbf{k}')\ \big[\chi^{pp}_{\uparrow\downarrow}(q,k,k') - 2\Pi^{pp}(q,k,k')\big]\ . \tag{2.40}$$

From the definition of the generalized susceptibilities a number of different *vertex* functions can be derived. Of particular interest is the so-called *full* two-particle vertex which is

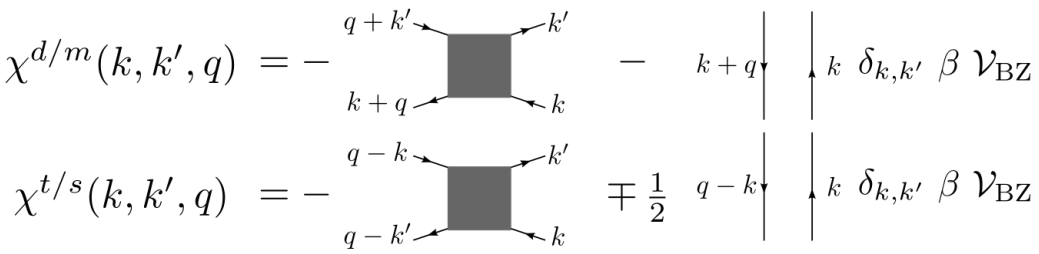

Figure 2.1: Diagrammatic representation of the generalized susceptibility $\chi^r(q,k,k')$ written in the ($r = ph$) particle-hole notation (first line) and in the ($r = pp$) particle-particle notation (second line).

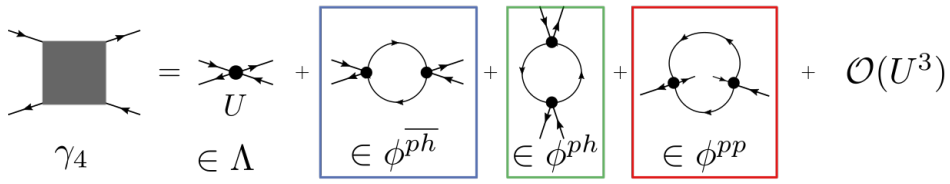

Figure 2.2: Diagrammatic representation of the full vertex γ_4 up to the second-order in the bare interaction U. In the figure, the second-order diagrams reducible in the particle-hole exchange, particle-hole and particle-particle are indicated by a blue, green and red box respectively. The fully irreducible vertex class Λ is composed by just the bare interaction U, since the next diagram in the U-expansion belonging to this class appears at fourth-order.

obtained from:

$$\begin{aligned}\gamma_4^\eta(q,k,k') &= -\frac{\chi^\eta(q,k,k') \mp \Pi^\eta(q,k,k')}{\int dk_1\, dk_2\, \Pi^\eta(q,k,k_1)\Pi^\eta(q,k_2,k')} \\ &= \frac{\chi^\eta(q,k,k') \mp \Pi^\eta(q,k,k')}{G(k)\, G(k+q)\, G(k')\, G(k'+q)}\,,\end{aligned} \tag{2.41}$$

where the minus sign has to be used for $\eta = \{\mathrm{d}, \mathrm{m}, \mathrm{t}\}$ and the plus sign for $\eta = \mathrm{s}$ and the subscript 4 indicates the number of external legs of the diagram (see Fig. 2.1). Physically, $\gamma_4^\eta(q,k,k')$ corresponds the full two-particle scattering amplitude between (quasi)particles (Abrikosov et al., 1975) which is represented by the set of *all* connected (amputated) two-particle Feynman diagrams.
So far, the superscripts particle-hole, exchange particle-hole and particle-particle have been referred to just as specific frequency-momentum notations. In the following we see how these notations end up being the most suitable ones to represent the specific subclasses of Feynman diagrams.
Within the full vertex, all scattering processes at the two-particle level can be classified by

two topologically distinguished classes of Feynman diagrams. The criterion for this classification relies on the two-particle separability[6] or, more rigorously, *reducibility* of a Feynman diagram into two distinct ones by cutting two internal propagators. We should make clear that, differently from the one-particle case, where the one-particle irreducible (amputated) Green's function is unambiguously defined as the self-energy, at the two-particle level we can distinguish three topologically diverse two-particle reducible diagrams. In fact, as shown in Fig. 2.2, the propagation direction of the two internal fermionic lines determines whether a diagram is reducible by *cutting* two longitudinal or transverse antiparallel lines, or two parallel ones. Since two antiparallel or parallel fermionic lines can be associated to a particle-hole (exchange) or particle-particle excitations, respectively, we label the sum of all separable (*reducible*) diagrams by cutting two transverse antiparallel lines, particle-hole reducible vertex ϕ^{ph}, by cutting two longitudinal antiparallel lines, particle-hole exchange reducible vertex $\phi^{\overline{ph}}$, and by cutting two parallel lines, particle-particle reducible vertex ϕ^{pp} (see Fig. 2.2). Using the same argument, one can provide a classification based on the inseparability (*irreducibility*) by cutting the aforementioned internal lines. The sum of all irreducible diagrams under cutting two specific internal lines, often referred to as scattering *channels*, goes under the name of irreducible vertices $\mathcal{I}^r$ with $r = \{ph, \overline{ph}, pp\}$. Since the reducibility and irreducibility of a diagram in a given channel are two mutually exclusive attributes (Rohringer et al., 2012), one can rewrite the full two-particle vertex, written in a specific notation $r = \{ph, \overline{ph}, pp\}$, as:

$$\gamma^r_{4;\sigma\sigma'} = \mathcal{I}^r_{\sigma\sigma'} + \phi^r_{\sigma\sigma'} \ . \tag{2.42}$$

In case of SU(2) symmetry, as done for the generalized susceptibility in Eqs. 2.35, it is convenient to introduce spin-singlet and spin-triplet components for the irreducible (as well as reducible) vertices:

$$\mathcal{I}^{\mathrm{d}}(q,k,k') = \mathcal{I}^{ph}_{\uparrow\uparrow}(q,k,k') + \mathcal{I}^{ph}_{\uparrow\downarrow}(q,k,k'), \tag{2.43a}$$

$$\mathcal{I}^{\mathrm{m}}(q,k,k') = \mathcal{I}^{ph}_{\uparrow\uparrow}(q,k,k') - \mathcal{I}^{ph}_{\uparrow\downarrow}(q,k,k'), \tag{2.43b}$$

$$\mathcal{I}^{\mathrm{s}}(q,k,k') = -\mathcal{I}^{pp}_{\uparrow\uparrow}(q,k,k') + 2\,\mathcal{I}^{pp}_{\uparrow\downarrow}(q,k,k'), \tag{2.43c}$$

$$\mathcal{I}^{\mathrm{t}}(q,k,k') = \mathcal{I}^{pp}_{\uparrow\uparrow}(q,k,k') \ . \tag{2.43d}$$

Note that here the superscript refers to both the channel r in which the vertex is irreducible (ph for $\eta = \{\mathrm{d},\ \mathrm{m}\}$ or pp for $\eta = \{\mathrm{s}, \mathrm{t}\}$) and the spin combination and the frequency-

[6] In a similar way one applies the criterion of one-particle irreducibility in order to define the self-energy from the one-particle Green's function.

momentum notation in which the vertex is represented ($\mathcal{I}^{\mathrm{d/m}}$ in the ph and $\mathcal{I}^{\mathrm{s/t}}$ in the pp notation). As a consequence of the previous discussion, one can explicitly write the irreducible vertices in Eqs. 2.43, in expressions known as *parquet* equations:

$$\mathcal{I}^{\mathrm{d}}_{q,k,k'} = \Lambda^{\mathrm{d}}_{q,k,k'} - \frac{1}{2}\phi^{\mathrm{d}}_{k'-k,k,k+q} - \frac{3}{2}\phi^{\mathrm{m}}_{k'-k,k,k+q} + \frac{1}{2}\phi^{\mathrm{s}}_{k+k'+q,k,k'} + \frac{3}{2}\phi^{\mathrm{t}}_{k+k'+q,k,k'} \ , \tag{2.44a}$$

$$\mathcal{I}^{\mathrm{m}}_{q,k,k'} = \Lambda^{\mathrm{m}}_{q,k,k'} - \frac{1}{2}\phi^{\mathrm{d}}_{k'-k,k,k+q} + \frac{1}{2}\phi^{\mathrm{m}}_{k'-k,k,k+q} - \frac{1}{2}\phi^{\mathrm{s}}_{k+k'+q,k,k'} + \frac{1}{2}\phi^{\mathrm{t}}_{k+k'+q,k,k'} \ , \tag{2.44b}$$

$$\mathcal{I}^{\mathrm{s}}_{q,k,k'} = \Lambda^{\mathrm{s}}_{q,k,k'} + \frac{1}{2}\phi^{\mathrm{d}}_{k'-k,k,q-k'} - \frac{3}{2}\phi^{\mathrm{m}}_{k'-k,k,q-k'} + \frac{1}{2}\phi^{\mathrm{d}}_{q-k-k',k,k'} - \frac{3}{2}\phi^{\mathrm{m}}_{q-k-k',k,k'} \ , \tag{2.44c}$$

$$\mathcal{I}^{\mathrm{t}}_{q,k,k'} = \Lambda^{\mathrm{t}}_{q,k,k'} - \frac{1}{2}\phi^{\mathrm{d}}_{k'-k,k,q-k'} - \frac{1}{2}\phi^{\mathrm{m}}_{k'-k,k,q-k'} + \frac{1}{2}\phi^{\mathrm{d}}_{q-k-k',k,k'} + \frac{1}{2}\phi^{\mathrm{m}}_{q-k-k',k,k'} \ , \tag{2.44d}$$

where, for a sake of conciseness, we adopt subscripts to specify the dependencies of the vertex functions, and $\Lambda^{\eta}_{q,k,k'}$ denotes the fully irreducible vertex which is defined by the sum of all diagrams which can not be separated by cutting any pair (independently to the propagation direction) of fermionic lines. In the latter, η labels the spin combination and the momentum-frequency convention (ph for $\eta = \mathrm{d/m}$ and pp for $\eta = \mathrm{s/t}$) in which this vertex is represented.
The definition of the so-called physical channels $\{\mathrm{d}, \mathrm{m}, \mathrm{s}, \mathrm{t}\}$, is particularly convenient in order to find four decoupled equations which connect each two-particle irreducible vertex $\mathcal{I}^{\eta}$ (irreducible in the channel $r = ph$ for $\eta = \mathrm{d/m}$ and $r = pp$ for $\eta = \mathrm{s/t}$) to the generalized susceptibility written in the correspondent r-notation and which accounts for the spin combination specified by η. The latter are the well known Bethe-Salpeter equations (BSE) and read:

$$\pm\chi^{\eta}(q,k,k') = \Pi^{\eta}(q,k,k') - \int dk_1\, dk_2\, \Pi^{\eta}(q,k,k_1)\mathcal{I}^{\eta}(q,k_1,k_2)\chi^{\eta}(q,k_2,k') \ . \tag{2.45}$$

In numerical solvers of many-body electron systems, one is usually forced to discretize the Brillouine zone. This is obtained by considering a finite number of lattice-sites ($\mathcal{N}$) which translates in a finite number of reciprocal vectors within the Brillouine zone ($\mathcal{N}_{\mathbf{k}} = \mathcal{N}$). Using the Einstein algebra, we can rewrite the previous frequency-momentum tensor as $(\boldsymbol{\chi}^{\eta})^{\nu\mathbf{k}}_{\nu'\mathbf{k}'}(q) = (\boldsymbol{\chi}^{\eta})^{k}_{k'}(q)$ for every possible bosonic four-momentum transfer, i.e.,q, in the

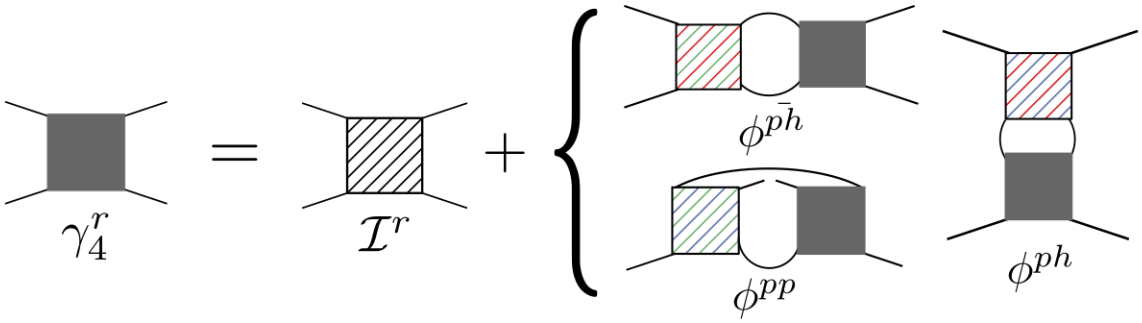

Figure 2.3: Diagrammatic representation of Eq. (2.42). See legend at page v.

specific channel η. Isolating $\mathcal{I}$ from Eq. (2.45) one recovers the following tensor expression:

$$\left(\boldsymbol{\mathcal{I}}^{\eta}\right)^{k}_{k'}(q) = \beta^2 \mathcal{N}_{\mathbf{k}}{}^2 \left[\left(\tilde{\boldsymbol{\chi}}^{\eta}\right)^{k}_{k'}(q) \mp \left(\tilde{\boldsymbol{\Pi}}^{\eta}\right)^{k}_{k'}(q)\right] , \tag{2.46}$$

where, the tensors $\tilde{\boldsymbol{\chi}}^{\eta}$, $\tilde{\boldsymbol{\Pi}}^{\eta}$ are defined such that:

$$\left(\boldsymbol{\chi}^{\eta}\right)^{k}_{k_1}\left(\tilde{\boldsymbol{\chi}}^{\eta}\right)^{k_1}_{k'} = \left(\mathbb{1}\right)^{k}_{k'} \tag{2.47}$$

$$\left(\boldsymbol{\Pi}^{\eta}\right)^{k}_{k_1}\left(\tilde{\boldsymbol{\Pi}}^{\eta}_{0}\right)^{k_1}_{k'} = \left(\mathbb{1}\right)^{k}_{k'} , \tag{2.48}$$

with $\mathbb{1}$ the unit tensor and the Einstein sum over repeated indices is implicitly assumed. This concludes our diagrammatic discussion of the two-particle correlation function which aims at providing all necessary definitions to explain how response functions are computed in the many-body solvers considered in this work (see Sec.2.2).

2.1.5 Critical phenomena: fluctuations and response functions

In this section we provide a connection between the thermodynamic susceptibility, or, more in general, two-particle correlation functions, and the theory of phase transition and critical phenomena. Although a more extensive treatment of the topic can be found in several textbooks (Binney et al., 1992; Goldenfeld, 2018) and (Schäfer, 2016), we restrict in the present section to a concise summary recalling how thermodynamic susceptibilities can be exploited not only as fingerprints of a phase transitions but also to characterize the universality class they belong to. The first quantity to be introduced in order to characterize a phase transition is the so-called order parameter. The latter is a thermodynamic state variable, e.g., magnetization, density or the order parameter amplitude for the conventional su-

perconducting phase transition. It is a matter of fact that the entire spectrum of transitions between different phases of matters can be in most cases classified in two broad classes: The first-order phase transitions, where the order parameter shows a discontinuous behavior across the transition line; The second-order phase transitions, where the order parameter exhibits a continuous, but non-analytic behavior by crossing the transition line.
The latter category displays a singular behavior of the second derivative of the free energy of the system with respect to the conjugate field coupled to the specific order parameter. In practice, as we have seen in the Sec. 2.1.3 within the linear regime, taking the second derivative of the free energy with respect to the source field J provides the thermodynamical susceptibility. Indeed, a singular behavior of the latter is the hallmark of a second-order phase transition. Depending on the nature of the source field, we are able to probe different quantum collective modes of the system under investigation. Here we will list some of the most commonly studied:

- Magnetic modes: if we assume to probe the system by means of a magnetic field, we trigger a magnetic response, whose linear order is given by the magnetic (or spin) susceptibility (χ^{m});
- Density modes: a fictitious chemical potential probe triggers a linear response function given by the density (or charge) susceptibility (χ^{d}), alternatively defined as isothermal compressibility κ_T;
- Superconducting modes: by applying a fictitious superconducting external field, the linear response of the system will be given by the superconducting (or pairing) susceptibility (χ^{sc}).

Recalling the aforementioned fluctuation dissipation theorem, we observe that a singularity of these three susceptibilities goes hand in hand with long-range fluctuations of magnetization, density of particles, and density of Cooper pairs, respectively. Another relevant quantity to detect phase transitions is the specific heat c_v, whose associate fluctuating quantity is represented by the internal energy.

Close to a transition (or to a fixed point), the divergence of the susceptibility is marked by a non-analytic or divergent behaviors of several other quantities characterizing the system. The way these quantities approach the transition is governed by characteristic power laws, whose exponents fall under the name of *critical exponents*. The peculiarity of these exponents is their ubiquitousness in different systems and for different kinds of transitions. Systems characterized by the same critical exponents belong to the same so-called *universality class*.

The critical exponents are defined in terms of the different behaviors as function of the so-called reduced temperature $t = (T - T_c)/T_c$ and are denoted as $\{\alpha, \beta, \gamma, \delta, \eta, \nu\}$ and z. Of particular interest in this work are the scaling of the magnetic susceptibility, $\chi^{\mathrm{m}} \sim |t|^{-\gamma}$ and of the correlation length, $\xi \sim |t|^{-\nu}$. The latter implies, according to the Ornstein-Zernike form (Ornstein & Zernike, 1914), the following behavior of the two-particle correlation function:

$$\chi(\mathbf{r}) \sim \begin{cases} \dfrac{1}{|\mathbf{r}|^{d-2-\eta}}, & |\mathbf{r}| \ll \xi, \\ \exp\left[-|\mathbf{r}|/\xi\right] & |\mathbf{r}| \gg \xi. \end{cases}$$

We notice that, since the correlation χ has canonical dimension $[r^{2-d}]$ (with d the system's dimension), the exponent η is referred to as anomalous dimension of the correlation function.

2.2 Investigating response functions in many-body systems: an overview

In this section we give an overview on different ways of computing linear response functions in a number of many-body solvers. All considerations provided here follow form the diagrammatic approach illustrated in Sec. 2.1.4. We will start recalling the simple ladder resummation of all "independent" excitations of electron-hole pairs, referred to as random phase approximation (RPA). Despite its simplicity, which allows for an analytic expression by means of the Lindhard function, and a description of the screening effects beyond Thomas-Fermi, RPA faces significant limitations in the description of the linear response of the system. In fact, the lack of mutual screening effects between the different channels makes the computation of physical susceptibility in this framework incorrect already at the second-order in the interaction expansion. A non-perturbative treatment is provided by dynamical mean field theory (DMFT) which yields a resummation of all local scattering processes in the description of the linear response. The recent focus on a number of diagrammatic extensions of DMFT has offered the possibility to include also nonlocal information on the scattering processes on top of the (local) DMFT description. Because of the numerical complexity of these methods, these nonlocal effects are usually included in a single channel (see, e.g., ladder dynamical vertex approximation), leading to a violation of physical sum-rules (in particular those related to the two-particle self-consistency of the theoretical description). Eventually, we will also revisit the way response functions are tackled in functional renormalization group (fRG), which is able to treat the competition between the different channels on equal footing. Though, its application is typically limited to weakly correlated systems.

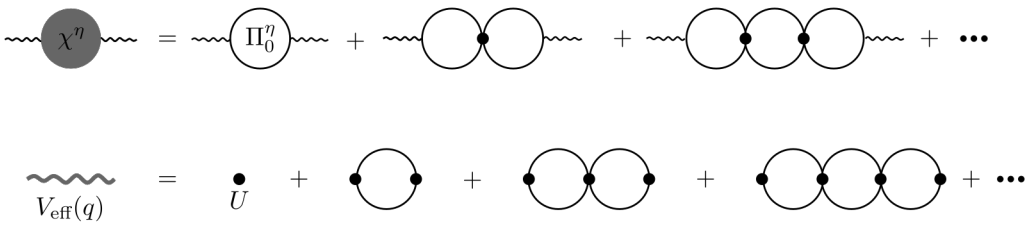

Figure 2.4: Diagrammatic representation of the RPA approximation. The first line shows the RPA susceptibility while the second represents the RPA screened interaction. In this case we assumed the Hubbard U bare interaction (black dot), but it could be replaced by a nonlocal Coulomb interaction $V(\mathbf{q})$. In this illustration, the direction of propagation of the internal fermionic lines has not been specified, nevertheless one usually assumes particle-hole internal bubbles. Consistent to the diagrammatic notation in Fig. 2.2, such ladder resummation should have developed vertically (transversely). Here we report it horizontally (longitudinally) for a sake of compactness.

2.2.1 Lindhard response theory

Let us start by considering Eq. (2.45). After isolating the generalized susceptibility on the right-hand side (r.h.s.), one can integrate out the fermionic dependencies according to Eqs. (2.37):

$$\chi_s^{\rm d/m}(q) = \int dk\, dk' \, \frac{\Pi^{ph}(q,k,k')}{1 + (\mathbf{\Pi}^{ph})^{k}_{k_1}(q)(\boldsymbol{\mathcal{I}}^{\rm d/m})^{k_1}_{k'}(q)} \,, \tag{2.49}$$

$$\chi_s^{\rm sc}(q) = -\int dk\, dk' \, \frac{\Pi^{pp}(q,k,k')}{1 - (\mathbf{\Pi}^{pp})^{k}_{k_1}(q)(\boldsymbol{\mathcal{I}}^{s})^{k_1}_{k'}(q)} \,, \tag{2.50}$$

where the integration in the denominator on the (frequency-momentum) variable k_1 has been expressed my means of the index repetition. Let us focus on the electron-hole pair excitations given in the first line of Eq. (2.49). In the weakly correlated regime we can substitute the internal bubble by its non-interacting value $\Pi \to \Pi_0$ [see Eq. (2.29)] and assuming $|\Pi_0^{\rm d/m}\mathcal{I}^{\rm d/m}| \ll 1$, we can expand the integrand as geometric series. In a single-band Hubbard model (with Hubbard interaction U), by restricting the two-particle irreducible vertex to the first-order in the interaction $\mathcal{I}^{\rm d/m}_{(1)} = \pm U$, one obtains the so-called ladder summation shown in Fig. 2.4. A notable difference between the density and the magnetic channel is given by the behavior of the integrand at the phase transition. In the magnetic channel the Stoner criterion applies [$1 = U\Pi_0^{ph}(0,\mathbf{q}^*)$], with Π_0^{ph} given by Eq. (2.29)

which leads to a breakdown of the geometric series expansion, whereas the density is always finite. Besides for the Hubbard model, the RPA is often adopted in ab-initio calculations [complementary to density functional theory (DFT)] in order to renormalize the Coulomb interaction owing to electron screening effects [$V(\mathbf{q}) \rightarrow V_{\text{eff}}(q)$] [7]. If we replace the local interaction U by the long-range Coulomb interaction $V(\mathbf{q}) = e^2/\mathbf{q}^2$, we can easily see that:

$$\frac{\chi(q)}{\Pi_0(q)} = \frac{V_{\text{eff}}(q)}{V(\mathbf{q})} = \frac{1}{1 + \Pi_0(q)V(\mathbf{q})} \,. \tag{2.51}$$

The previous expression yields the RPA expression for the dielectric constant $\epsilon(q) = 1 + \Pi_0(q)V(\mathbf{q})$. For an isotropic three-dimensional system at zero temperature, the (s-wave) Lindhard function for Π_0 in Eq. (2.29), which represents the polarization function in the RPA approximation, can be analytically estimated:

$$\Pi_0(i\omega_l, \mathbf{q}) = 2\,\rho(\epsilon_{\text{F}})\left[1 - \frac{i\omega_l}{2v_{\text{F}}|\mathbf{q}|}\ln\left(\frac{i\omega_l + v_{\text{F}}|\mathbf{q}|}{i\omega_l - v_{\text{F}}|\mathbf{q}|}\right)\right] \,, \tag{2.52}$$

where v_{F} represents the Fermi velocity. The first term on the r.h.s. of Eq. (2.52) represents the so-called static RPA polarization (with $\mathbf{q} \rightarrow 0$) which is nothing but the semi-classical expression for the polarization in the Thomas-Fermi theory of screening, where $\rho(\epsilon_{\text{F}})$ represents the density of state per spin of the non-interacting electrons at the Fermi surface. The second term, on the other hand, is responsible for the so-called Friedel-oscillations of the screened Coulomb interaction (Mahan, 2000).
Despite its simplicity, RPA completely lacks the effect of mutual screening between different channels and is restricted by construction to the case of weakly interacting systems. Therefore, in materials with strong correlations other, usually more elaborated, methods are adopted (see next subsections). Nonetheless, the RPA formalism (or, more specifically, the constrained RPA) is still broadly employed in multiband systems to estimate the screening effect of less-correlated bands onto the effective interaction of a target low-energy orbital manifold, typically affected by stronger correlations. This projection operation is a relevant step to construct the effective theory which has to be successively solved by non-perturbative methods.

2.2.2 Linear response function in dynamical mean-field theory

The main idea of dynamical mean field theory (DMFT) is to map the lattice problem we aim to solve into a single-site (impurity) system embedded and hybridized by a metallic

[7] Note that, in contrast to RPA, in the so-called Gw approximation (Aryasetiawan & Gunnarsson, 1998; Hedin, 1965) the propagator is renormalized too, i.e.,$\Pi_0^{ph} \rightarrow \Pi^{ph}$.

bath which is determined self-consistently [see (Georges et al., 1996)]. The self-consistent condition is enforced at the level of the single-impurity Green's function, which should converge, at the end of the DMFT cycle, to the local lattice Green's function "dressed" by the local self-energy of the impurity model. In infinite dimensions ($d \to \infty$), where the DMFT is exact, one can evaluate the linear response function assuming that the two-particle irreducible vertex $\mathcal{I}^{\eta} = \mathcal{I}^{\eta}_{\text{AIM}}$ (Georges et al., 1996) [8]. Clearly in finite d dimensions this argument does not apply and the DMFT response functions are affected by this approximation. Schematically, the DMFT calculation of the response function can be summarized by the following steps:

- At the end of the DMFT cycle, the two-particle Green's function of the associated impurity model (converged at the one-particle level to the lattice system) is computed. The way this evaluation is performed depends on the specific impurity solver adopted: e.g., via spectral representation in the exact diagonalization (ED) solver (Georges et al., 1996) or via a statistical approaches like continuous-time Monte Carlo CT-QMC (e.g., CT-HYB Werner & Millis (2006); Gunacker et al. (2015), CT-INT Rubtsov et al. (2005)) and Hirsch-Fye QMC algorithms (Hirsch & Fye, 1986). From the impurity two-particle Green's function, the generalized susceptibility can be extracted;

- In order to access the impurity two-particle irreducible vertex in all channels, the local version of Eq. (2.46) (where we drop the momentum-dependence) is used;

- Once the DMFT lattice Green's function $G(k)$ and the impurity two-particle irreducible vertex $\mathcal{I}^{\eta}$ are given, one can insert them in Eq. (2.45);

- The inversion of Eq. (2.45) to isolate the frequency-momentum resolved generalized susceptibility and the summation over its fermionic dependencies gives us the physical susceptibility in the different channels.

One notices that the ladder summation obtained in this framework consists of two building blocks: the lattice DMFT-approximated Green's functions and the impurity two-particle irreducible vertex (see Fig. 2.5).
The inclusion of all local correlations extends the evaluation of the linear response functions to the non-perturbative regime. Nevertheless, there are a broad class of materials where the local correlations are not sufficient to describe their physical properties, like high-temperature superconductivity (Bednorz & Müller, 1986) and quantum criticality

[8] Note that this is in general not true if one considers $\mathcal{I}^{\eta}$ itself. One can demonstrate [see (Georges et al., 1996)] that only its local part contributes to the ladder summation in (2.49).

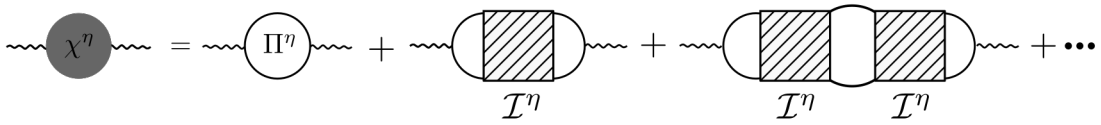

Figure 2.5: Diagrammatic representation of the susceptibility in a generic channel η within the DMFT approximation. The internal fermionic lines, are oriented according to the specific channel considered. Differently form the RPA approximation the bare interaction is here replaced by the local two-particle irreducible vertex (diagonally striped squares) calculated by the impurity solver at the end of the DMFT cycle. Moreover the RPA non-interacting internal fermionic propagators are here replaced by the lattice DMFT Green's function.

(Löhneysen et al., 2007) . Moreover, the nonlocal correlations become of particular importance in the vicinity of all second-order phase transitions (see discussion in Sec. 2.1.5). This limitation has motivated, since few years after the DMFT formulation (Schiller & Ingersent, 1995), a large variety of methods which try to include nonlocal correlations at the two-particle level [for a complete list see the introduction sections in (Rohringer et al., 2018)]. Among the latter, the work presented in this thesis has an impact (see Sec .3.2) on the so-called diagrammatic extensions of DMFT. In particular, in the following we shortly review the way to compute susceptibilities in two of these diagrammatic methods for which the present study finds a direct application: dynamical vertex approximation (DΓA).

2.2.3 Beyond DMFT: nonlocal effects at the two-particle level in DΓA

The dynamical vertex approximation method (Toschi et al., 2007) (DΓA) represents one of the most "natural" generalizations of the DMFT assumption. The latter is based on the locality of the the self-energy which, from a diagrammatic perspective, is a one-particle irreducible (1PI) vertex. What if we lift the locality approximation up to the two-particle level? According to the diagrammatic classification in Sec. 2.1.4, we have encountered the fully 2PI (Λ) as a building block of the parquet equations. Assuming the locality of this object implies that the self-energy as well as the full two-particle vertex γ_4 entering the generalized susceptibility acquires nonlocal contributions through the parquet equations. It is evident that the involved numerical effort required by the DΓA cycle is higher than its one-particle DMFT counterpart. The bottleneck of this algorithm is represented by (i) the heavy step of computing the impurity two-particle correlation function at every cycle, and (ii) the cumbersome machinery of the inverse and, above all, direct application of the

parquet equations (Janiš, 1999; Bickers, 1991) [9]. This makes the full version of the method unfeasible especially if applied to *ab-initio* calculations where multi-orbital indices are involved [see (Galler et al., 2017, 2018)] or in close proximity of phase transitions. On top of the numerical difficulties, the full DΓA method is also affected by the divergence of the local fully 2PI vertex Λ along specific lines in the DMFT phase diagram (Schäfer et al., 2013). This has turned out to be, in fact, a general feature of correlated many electron systems: It has been observed also in (cellular) CDMFT, in dynamical cluster approximation (DCA) calculations of the Hubbard model (Gunnarsson et al., 2016; Vučičević et al., 2018) as well as in the Anderson impurity model (Chalupa et al., 2018) and in the Hubbard atom (Schäfer et al., 2016; Thunström et al., 2018). Therefore, a more operative application of the DΓA algorithm has been applied in literature: the so-called ladder DΓA (Rohringer et al., 2011; Rohringer, 2014). This simplified version of DΓA gets rid of the full self-consistent cycle based on the parquet equations and computes the nonlocal self-energy and full vertex in a "one-shot" procedure after the DMFT cycle. Following the discussion in Sec. 2.2.2, we can first extract the impurity two particle irreducible vertex $\mathcal{I}^{\eta}$ by inversion of the (local) Bethe Salpeter equations, which will be inserted in their direct form in Eq. (2.45) [10]. The DMFT susceptibility in a given channel is then computed by means of a ladder resummation of the impurity irreducible vertices in the corresponding channel, connected by DMFT nonlocal fermionic propagators. The decoupling of the scattering channels at the nonlocal level results in a violation of specific sum-rules. In particular, the sum-rule concerning the total density:

$$\int dq \left[\chi^{\mathrm{d}}(q) + \chi^{\mathrm{m}}(q)\right] = \frac{n}{2}\left(1 - \frac{n}{2}\right) , \tag{2.53}$$

is not fulfilled in finite dimensional systems if the susceptibility is calculated by means of the Bethe-Salpeter equations of DMFT. To overcome this problem, one usually corrects the susceptibility by means of the so-called Moriyaesque-(λ-) correction (Rohringer et al., 2011; Rohringer, 2014). This results in the correction of $[\chi^{\eta}(q)]^{-1} \rightarrow [\chi^{\eta}(q)]^{-1} + \lambda^{\eta} = [\chi^{\lambda_{\eta},\eta}(q)]^{-1}$ by means of a correcting parameter λ determined by imposing the fulfillment of Eq. (2.53). Inserting this Moryiaesque-corrected susceptibility into the Schwinger-Dyson equations, allows to reproduce the correct $(1/k_0)$ asymptotic behavior of the self-energy. The inclusion of these corrections, although at first glance could appear as an *ad*

[9] Despite the most recent optimizations of the parquet solver [see (Li et al., 2016)], this method still remains computationally highly challenging.

[10] Note that usually, in order to avoid the aforementioned vertex divergences, an alternative procedure which avoids working explicitly with irreducible vertices as been devised in (Rohringer et al., 2013; Galler et al., 2018; Rohringer et al., 2018). It remains still unclear whether such procedure can be generalized to the parquet calculation of the full DΓA.

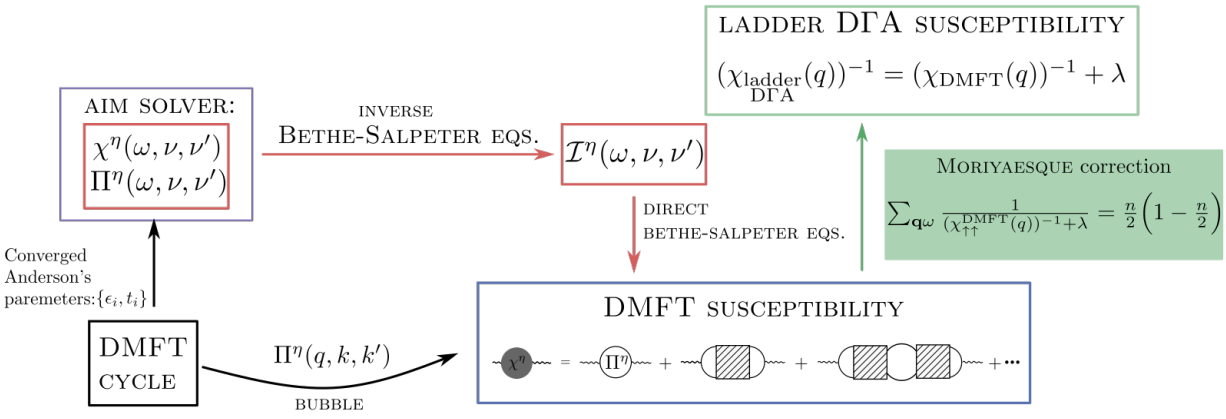

Figure 2.6: Flowchart showing how the susceptibilities are calculated in DMFT (blue block) and in ladder DΓA approximations (green block).

hoc way to correct an inconsistency of the theory, brings nonlocal information to the two-particle vertex functions. This allows to obtain critical exponents beyond the mean-field level (Rohringer et al., 2011; Del Re et al., 2018).

2.2.4 Linear response function in the functional renormalization group

In this section we provide an overview on the way response functions are computed within the functional renormalization group (fRG) method. The basic idea of fRG, inherited from the Wilsonian renormalization group techniques (Wilson, 1971), consists in successively integrating out the higher energy scales to obtain an effective lower energy theory. In fRG the access to different energy scales is controlled by a scale parameter Λ inserted in the Gaussian (non-interacting) part of the system's action and boils down to the integration of an infinite hierarchy of coupled differential equations for the n-particle vertex functions of the theory. In particular, the differential equations can be written for the 1PI vertices [see the reviews (Metzner et al., 2012; Platt et al., 2013) for a 1PI formulation of fRG]. The fRG equations have to be integrated from a high-energy scale (Λ_{init}) where (i) the system can be exactly solved and (ii) the initial condition for the 1PI vertices computed, down to low-energy scales where we expect the system to possibly encounter phase instabilities. In this section, briefly devoted to the linear response, we outline the fundamental steps to derive the differential equations of the response functions of the system [for an extensive derivation see (Metzner et al., 2012; Salmhofer & Honerkamp, 2001; Halboth & Metzner, 2000) and Appendix B in Supplement III].

First one introduces the coupling of the density operators in Eqs. (2.18) and (2.20a) to the corresponding external source fields J^η (with $\eta = \{\mathrm{d}, \mathrm{m}, \mathrm{sc}\}$), by adding the following scalar product to the original action (assumed here purely fermionic):

$$(J_n^{\mathrm{d/m}}, \rho_n^{\mathrm{d/m}}) = \int dq J_n^{\mathrm{d/m}}(q)\rho_n^{\mathrm{d/m}}(q) \ , \tag{2.54a}$$

$$(J_n^{\mathrm{sc}}, \rho_n^{\mathrm{sc}*}) + (J_n^{\mathrm{sc}*}, \rho_n^{\mathrm{sc}}) = \int dq \big[J_n^{\mathrm{sc}}(q)\rho_n^{\mathrm{sc}*}(q) + J_n^{\mathrm{sc}*}(q)\rho_n^{\mathrm{sc}}(q) \big] \ . \tag{2.54b}$$

where n specifies the momentum structure of the coupling to the external field.
It is worth stressing that, although J^η acts as a functional dependence in our derivation, it does not represent an integration variable. In the 1PI formulation of fRG, one introduces the scale parameter Λ-dependence through the kinetic term of the action. The generating functional of the one-particle irreducible vertex functions, referred to as effective action (Γ^Λ), is expanded in powers of the fermionic fields and the external bosonic source fields, giving:

$$\begin{aligned}\Gamma^\Lambda[J,\bar\psi,\psi] = \Gamma^\Lambda[\bar\psi,\psi] + \sum_\eta \sum_{y_1,y_2} \frac{\partial^{(2)}\Gamma^\Lambda[J,\bar\psi,\psi]}{\partial J_\eta(y_1)\partial J_\eta^*(y_2)}\bigg|_{\substack{\psi=\bar\psi=0\\ J=0}} J_\eta(y_1)J_\eta^*(y_2) - \\ \sum_{\eta'=\,\mathrm{d,m}} \sum_{y,x,x'} \frac{\partial^{(3)}\Gamma^\Lambda[J,\bar\psi,\psi]}{\partial J_{\eta'}(y)\partial\bar\psi(x')\psi(x)}\bigg|_{\substack{\psi=\bar\psi=0\\ J=0}} J_{\eta'}(y)\bar\psi(x')\psi(x) - \\ \sum_{y,x,x'} \frac{\partial^{(3)}\Gamma^\Lambda[J,\bar\psi,\psi]}{\partial J_{\mathrm{sc}}(y)\partial\psi(x')\partial\psi(x)}\bigg|_{\substack{\psi=\bar\psi=0\\ J=0}} J_{\mathrm{sc}}(y)\psi(x')\psi(x) + \ldots\end{aligned} \tag{2.55}$$

Notice that in Eq. (2.55), the index $x(') = \{\sigma, k\}$ combines the spin index σ and the fermionic quadrivector $k = (i\nu_l, \mathbf{k})$ (here we disregard additional quantum dependencies, e.g., orbital), $y = \{n, q\}$ refers to the momentum structure of the coupling to the bilinears, n, and to the bosonic quadrivector $q = \{i\omega_l, \mathbf{q}\}$. In Eq. (2.55) the first term on the r.h.s. represents the effective action in absence of the coupling to the external bosonic fields in Eq. (2.54). Its functional derivatives with respect to $2n$ fermionic fields correspond to the n-particle 1PI vertices, i.e.,the self-energy Σ ($n = 1$), two-particle vertex γ_4 ($n = 2$), etc. The coefficients to the fields appearing in the second term of Eq. (2.55) represent the (Λ-dependent) susceptibilities, while the coefficients appearing in the third and fourth terms represent the fermion-boson vertex (γ_3) in the density/magnetic and superconducting channels, respectively. In practice, the usual approximation done in the fRG framework

is to truncate this expansion beyond the vertex:

$$\gamma^{\eta,\Lambda}_{2n+m}(y_1..y_m;x_1...x_n;x'_1...x'_n) = \frac{\partial^{2n+m}\Gamma^{\Lambda}[J,\bar{\psi},\psi]}{\partial J_\eta(y_1)...\partial J^*_\eta(y_m)\partial\bar{\psi}(x'_1)...\partial\bar{\psi}(x'_n)...\partial\psi(x_n)}\Big|_{\psi=\bar{\psi}=J=0}, \tag{2.56}$$

with $2n+m>3$, which is known as one-loop approximation (1ℓ).
The differential equations with respect to the scale parameter Λ, the so-called "flow" equations, of the susceptibilities and the three-point fermion-boson vertices in the 1ℓ-approximation read:

$$\partial_\Lambda \chi^{\mathrm{d/m},\Lambda}_{nn'}(q) = -\int dk\, \gamma^{\mathrm{d/m},\Lambda}_{3,n}(q,k)[G^\Lambda(k)S^\Lambda(q+k)+(S\leftrightarrow G)]\gamma^{\mathrm{d/m},\Lambda,\dagger}_{3,n'}(q,k) \tag{2.57a}$$

$$\partial_\Lambda \chi^{\mathrm{sc},\Lambda}_{nn'}(q) = +\int dk\, \gamma^{\mathrm{sc},\Lambda}_{3,n}(q,k)[G^\Lambda(k)S^\Lambda(q-k)+(S\leftrightarrow G)]\gamma^{\mathrm{sc},\Lambda,\dagger}_{3,n'}(q,k)\ , \tag{2.57b}$$

and respectively

$$\partial_\Lambda \gamma^{\mathrm{d/m},\Lambda}_{3,n}(q,k) = -\int dk'\, \gamma^{\mathrm{d/m},\Lambda}_{3,n}(q,k')[G^\Lambda(k')S^\Lambda(q+k')\ +(S\leftrightarrow G)]\gamma^{\mathrm{d/m},\Lambda}_{4}(q,k',k) \tag{2.58a}$$

$$\partial_\Lambda \gamma^{\mathrm{sc},\Lambda}_{3,n}(q,k) = +\int dk'\, \gamma^{\mathrm{sc},\Lambda}_{3,n}(q,k')[G^\Lambda(k')S^\Lambda(q-k')\ +(S\leftrightarrow G)]\gamma^{\mathrm{sc},\Lambda}_{4}(q,k',k)\ , \tag{2.58b}$$

where the we assumed SU(2) symmetry as well as spin, energy and momentum conservation to hold. $S^\Lambda = \partial_\Lambda G^\Lambda|_{\Sigma=\text{ const}}$ represents the single-scale propagator (Metzner et al., 2012) and $\gamma^{\eta,\Lambda,\dagger}_{3,}(q,k,k') = \gamma^{\eta,\Lambda\,*}_{3,n'}(q,k',k)$ [with n' such that $f^*_n(\mathbf{k}) = f_{n'}(\mathbf{k})$], and the subscripts (n/n') refer to the momentum structure of the density operator coupled to the field $J_{n/n'}$. The two-particle vertex γ_4 appearing in Eq. (2.58) are given by the following

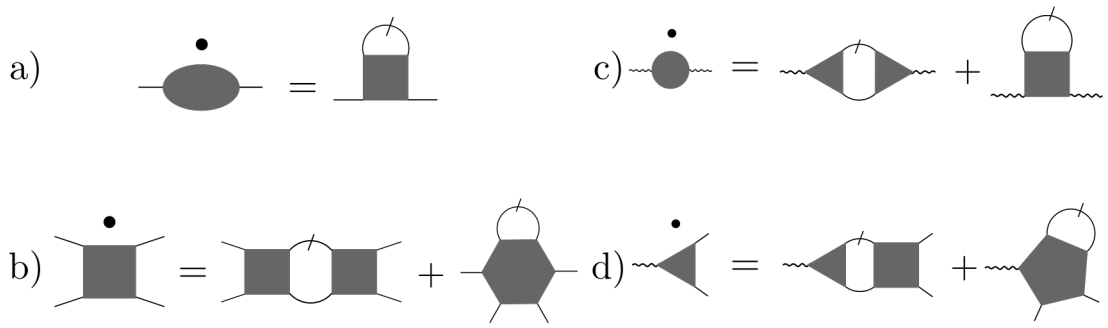

Figure 2.7: Schematic diagrammatic representation of the fRG flow equations for the self-energy (a), full vertex (b), susceptibility (c) and fermion-boson vertex (d). Notice that no propagation direction has been specified in order to make the representation schematically adequate for all channels. Lines with a dash correspond to the single scale propagator S^{Λ}. The 1ℓ approximation disregards the last diagrams on the r.h.s of (b), (c), (d). For a legend summarizing the diagrammatic symbols adopted to represent each vertex function see legend at page v.

spin combinations:

$$\gamma_{4,\mathrm{d}}(q,p,p') = \frac{1}{2}\sum_{\sigma,\sigma'} \gamma_{4;\sigma\sigma\sigma'\sigma'}(p,p+q,p'+q,p') \tag{2.59a}$$

$$\gamma_{4,\mathrm{m}}(q,p,p') = \frac{1}{2}\sum_{\sigma,\sigma'} (-1)^{\epsilon_{\sigma\sigma'}} \gamma_{4;\sigma\sigma\sigma'\sigma'}(p,p+q,p'+q,p') \tag{2.59b}$$

$$\gamma_{4,\mathrm{sc}}(q,p,p') = \gamma_{4;\uparrow\uparrow\downarrow\downarrow}(p,p',q-p,q-p') \ , \tag{2.59c}$$

where ϵ is the Levi-Civita symbol.
The integration of Eqs. (2.57) and (2.58) for the susceptibilities and the fermion-boson vertex has to be performed alongside the integration of the two-particle vertex γ_4^{Λ} and the self-energy Σ^{Λ} flow equations (see Fig. 2.7). The bottleneck of the fRG integration of all differential equations is represented by (i) the two-particle vertex γ_4 which is a function of three momenta, three frequencies and possibly four spin and/or orbital dependencies (in case of no SU(2) symmetry and/or a multi-orbital system is considered) and (ii) the evaluation of the internal differentiated bubbles which needs a high momentum resolution of the Brillouine zone. Therefore the application of the fRG solver in systems with $d > 1$ has often required massive simplifications neglecting the self-energy flow (which simplifies the S-G bubble calculation) in first place, together with an oversimplified parametrization of the frequency and momentum dependence of the two-particle vertex γ_4. The original aim of 1PI fRG scheme, in fact, was to identify the leading tendencies towards instabilities rather then

to obtain quantitative results. For the $2d$ Hubbard model and in several multi-band systems one usually finds, with few exceptions (Vilardi et al., 2017; Uebelacker & Honerkamp, 2012), a fully static approximation, which excludes any frequency dependence for the flowing vertices. The demand for a sufficiently accurate momentum resolution of the Brillouine zone, crucial for capturing the physics close to phase instabilities, has led to the N-patch momentum discretization and, more recently, to channel-decompositions in conjunction with the numerically advantageous form-factor expansion (Husemann & Salmhofer, 2009; Giering & Salmhofer, 2012; Wang et al., 2013; Lichtenstein et al., 2017).
It has to be stressed that the inclusion of Eq. (2.57) into the flow is certainly the most common and formally consistent way to compute linear response functions in fRG. However, it does not represent the only option. In fact, one could imagine to simply integrate the fRG differential equation for the self-energy and the two-particle vertex γ_4 . If no fixed points are encountered during the flow, one could use $\gamma_4^{\Lambda_{\text{fin}}}$ and $\Sigma^{\Lambda_{\text{fin}}}$ to construct the generalized susceptibility according to the exact BSE (Eq. 2.41). Eq. (2.37) can be then used to evaluate the physical susceptibilities (see Fig. 2.8 first line):

$$\chi^{\eta}_{nn'}(q) = \int dk\, dk'\, f_n(\mathbf{k})\, f^*_{n'}(\mathbf{k}')\, [\pm\Pi^{\eta,\Lambda_{\text{fin}}}(q,k,k') + \\ - \Pi^{\eta,\Lambda_{\text{fin}}}(q,k,k)\gamma_4^{\eta,\Lambda_{\text{fin}}}(q,k,k')\Pi^{\eta,\Lambda_{\text{fin}}}(q,k',k')], \tag{2.60}$$

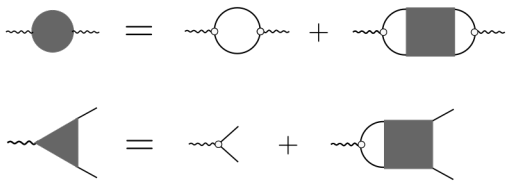

Figure 2.8: Diagrammatic representation of Eq. (2.60) (first line) and (2.61) (second line) for a generic physical channel $\eta = \{\mathrm{d}, \mathrm{m}, \mathrm{sc}\}$

This "post-processed" way of computing the susceptibility leads to different results with respect to correspondent flow calculation, obtained by solving the differential equations (2.57) and (2.58). This difference derives from the 1-loop approximation, which creates a discrepancy between the flow equation for the susceptibility and the full derivative of Eq. (2.60) with respect of the scale parameter Λ. In the latter, in fact, after introducing a scale-parameter dependence of the ("dressed") Green's functions and the two-particle vertex appearing on the r.h.s, one can take the full derivative with respect to Λ and compare it to the differential equation for the susceptibility obtained within the fRG formalism. This operation is schematically diagrammatically represented in Fig. 2.9 where Eq. (2.60) is shown within the two brackets in the first line on the r.h.s and the derivative with respect to the scale-parameter Λ is indicated by a black dot. The derivative of the self-energy as well as

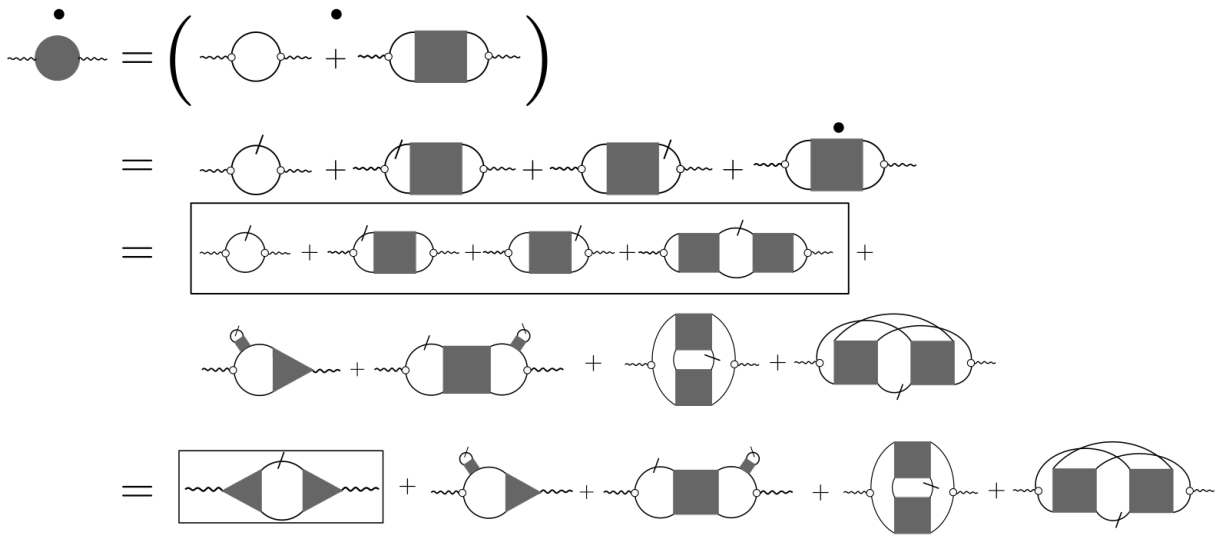

Figure 2.9: Diagrammatic representation of the scale parameter derivative of Eq. (2.60). The black dot as superscript represents the derivative with respect to the scale parameter Λ assuming the lambda dependence of all objects in the brackets. One observes that the full derivative departs from the 1ℓ approximated fRG scheme already at the second-order in the bare interaction.

the two-particle (1PI) vertex have been substituted by the 1ℓ-approximated flow equation which is schematically represented in the third line of Fig. 2.9. By recalling the definition of the three-point fermion-boson vertex in term of the two-particle vertex (see Fig. 2.8 second line):

$$\gamma^{\eta}_{3,n}(q,k) = \gamma^{\eta}_{3,0,n}(q,k) \pm \int dk_1 \gamma^{\eta}_{3,0,n}(q,k_1)\Pi^{\eta}(q,k_1,k_1)\gamma^{\eta}_{4}(q,k_1,k) \ , \tag{2.61}$$

where $\gamma^{\eta}_{3,0,n}(q,k) = f_n(\mathbf{k})$ (with the plus sign referring to $\eta = \{\mathrm{d/m}\}$ and the minus sign to $\eta = \mathrm{sc}$) represents its non-screened ("bare") value, one obtains the last line of Fig. 2.9. One observes that, in addition to the standard 1ℓ-approximated flow equation for the susceptibility as in Eqs. (2.57a) and (2.57b), one obtains further terms. The latter are responsible for a general screening of χ and γ_3 evaluated by means of Eq. (2.57) and (2.58), as shown in Appendix D of Supplement III.

2.2.5 Beyond DMFT: nonlocal effects at two-particle level in DMF^{2}RG

The fRG strength in treating competing instabilities and including successively short as well as long-range spatial correlations, albeit its limited applicability to the perturbative regime, has triggered the idea to combine it with DMFT. The synergy of these two methods, coined DMF^{2}RG, has been proposed in Taranto et al. (2014). The basic idea is to use the converged DMFT results for the two-particle vertex and the self-energy as a correlated starting point for the fRG flow. The scale parameter Λ will be deployed in this approach to interpolate between the DMFT action and the target lattice one. The nonlocal correlations, generated during the flow on top of the (purely local) DMFT ones, are introduced in a similar fashion as in the parquet equations in the DΓA approach. Nevertheless, as will be pointed out in Sec. 3.1 and formally illustrated in Sec. 3.3 following the multiloop approach by (Kugler & von Delft, 2018b), the 1ℓ-approximated fRG scheme is not capable to construct all parquet diagrams, which still makes the DMF^{2}RG, in its 1ℓ version proposed in (Taranto et al., 2014), and parquet DΓA non-equivalent. It has to be stressed that in the DMF^{2}RG application presented in (Taranto et al., 2014) to the single-band $2d$ Hubbard model at half-filling, the magnetic susceptibility has been computed by means of Eq. (2.60) at the end of the DMF^{2}RG flow.

You should never, never doubt something that no one is sure of.

Roald Dahl

3

Full many-body treatment of the response functions: from vertex corrections to higher order contributions

The formalism provided in the previous chapter and the overview on the different many-body methods constitute the basis of the works illustrated in this chapter. Here, we discuss different strategies within the state-of-the art implementation of a number of many-body techniques aiming at a more quantitative computation of linear response functions. Central to all works is the need to correctly describe, to the approximation level imposed by the theory, the two-particle scattering amplitude in different many-electron solvers. As previously discussed, the latter depends, in time-space translational invariant systems, on three independent times and spatial coordinates on top of spin and orbital dependencies. The simplification of these parameter dependence is mandatory for numerical applications, which make explicit use of the two-particle vertex functions in their algorithms. This represents the topic of the first work (Sec. 3.1 and Supplement I), which provides a diagrammatic analysis of the frequency-dependence of the local two-particle vertex of an impurity problem. This analysis unveils a simplified parametrization of the vertex in the high-frequency domain, to be used as an efficient algorithmic implementation of functional (RG) schemes and of many-body methods based on the parquet-equations. Section 3.2 (and Supplement II) addresses the correction of the common operation of inverting the Bethe-Salpeter equations by means of the asymptotic structure of the two-particle vertex. After the analysis of its frequency dependencies, we can extend our study to more challenging $2d$ calculations where nonlocal scattering processes are taken into account.

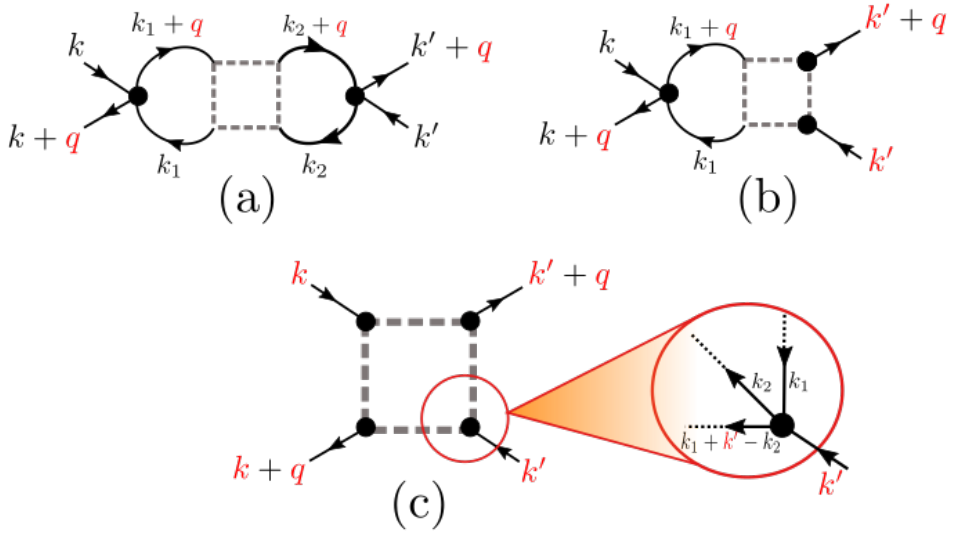

Figure 3.1: [Adaptation of Fig. 7 from (Rohringer et al., 2018)] Diagrammatic representation of Class 1 (a), Class 2 (b) and Class 3 (c) vertex functions in the particle-hole exchange notation. The dependence of the diagrams on the external four-momenta are marked in red.

Section 3.3 combines the frequency asymptotic parametrization proposed in Sec. 3.1 with an efficient momenta treatment in the fRG algorithm: the truncated unity fRG (TUfRG) proposed in Lichtenstein et al. (2017). The benefits of this efficient full frequency- and momentum-resolved fRG implementation provide fertile ground for the first $2d$ Hubbard model application of the multiloop fRG scheme (mfRG) proposed in Kugler & von Delft (2018b). Besides complementing the mfRG flow equations with those of the linear response function and the fermion-boson vertex, whose loop convergence has been addressed, the work presented in Sec. 3.3 paved the route for future applications of the mfRG method to fRG-schemes with correlated starting points. Finally, Sec. 3.4 presents a DMFT study where significant physical information beyond the linear regime is extracted from the superconducting response function of a system characterized by *attractive* or *repulsive* interaction to an external pairing field.

3.1 The high-frequency regime of the two-particle vertex: an AIM study

In this section we revisit the main idea proposed by the paper "High-frequency asymptotics of the vertex function: diagrammatic parametrization and algorithmic implementation", attached to this thesis in Supplement I. Inspired by a detailed analysis of the frequency structure of the local two-particle vertex in the context of DMFT (Rohringer et al., 2012), this work proposes an efficient parametrization of the two-particle vertex in the high-frequency regime. Such a parametrization has been incorporated explicitly into the algorithmic implementation of fRG and parquet-based schemes [see also Li et al. (2017)], but analogous extensions to different many-body solvers can be devised.
The core idea, pictorially illustrated in Fig. 3.1, is based on the diagrammatic observation that in the two-particle scattering processes, as soon as two particle lines, or a particle and a hole lines, are attached to the same bare (instantaneous) interaction (e.g., to the on-site Hubbard interaction U), the whole diagram won't depend on the four-momenta carried by those lines separately, but on their sum (or their difference in case of a particle and a hole). This is no longer the case if an external line (particle or hole) is attached by means of the bare interaction to three internal fermionic propagators. In this situation the diagram will depend explicitly on the four-momentum carried by such a line, say $k = (i\nu, \mathbf{k})$, and will exhibit a $1/i\nu$ decay going to large frequency values. Besides the trivial case, where all lines involved in the scattering process are attached to the same local and instantaneous bare interaction, which gives a constant contribution U, one can identify three classes of two-particle vertex diagrams:

- Class 1: In this case both ingoing and outgoing pair of particle-particle or particle-hole lines are attached to the same bare interaction [see Fig. 3.1 (a) for the particle-hole case]. The diagrams responding to this property depend on a single four-momentum given by the sum [or the difference in case of particle-hole exchange pair] of the four-momenta carried by the scattering lines. One easily demonstrate that such diagram is necessarily reducible by cutting the two internal fermionic propagators attached to the bare interaction. The sum of all these diagrams is referred to as $\mathcal{K}_1^r \in \phi^r(q, k, k')$;

- Class 2: If instead only one pair of particle-particle or particle-hole lines are attached to the same bare interaction U, while the two remaining lines are separately attached by means of a bare interaction to three internal lines, the diagram will depend on two independent four-momenta [see Fig. 3.1 (b)]. One is given by the sum (difference) of the four-momenta carried by the pair of particle-particle lines (particle-hole) attached to the same bare interaction, while the other is given by the four-momentum carried by one of the remaining external lines since the dependence of

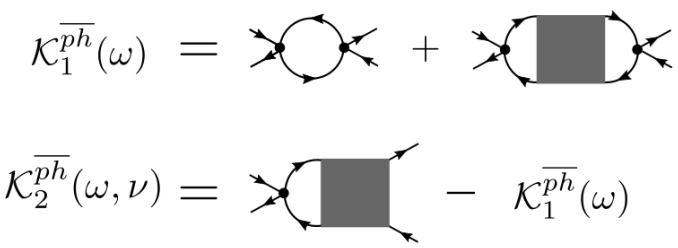

Figure 3.2: Diagrammatic representation of $\mathcal{K}_1$ (first line) and $\mathcal{K}_2$ (second line) in the exchange particle-hole channel

the last one can be recovered by energy-momentum conservation. The sum of all such diagrams are named $\mathcal{K}_2^r \in \phi^r(q,k,k')$ and $\bar{\mathcal{K}}_2^r \in \phi^r(q,k,k')$, depending if the attached particle-particle or particle-hole lines are outgoing or incoming;

- Class 3: The last class is constituted by those diagrams where each external line is attached to three internal fermionic propagators [see Fig. 3.1 (c)]. Differently from the previous two cases one cannot *a priori* deduce whether such diagrams are, or are not, two particle reducible in a specific channel. Hence, within this class, we can distinguish between those diagram which are fully two particle irreducible, Λ_{2PI}[1], and those which are two particle reducible in a specific channel, $\mathcal{R}^r(q,k,k') \in \phi^r(q,k,k')$.

Let us stress that the classification argument is possible in case the bare interaction has *no* dynamic and *no* momentum dependencies [2]. In this case, the aforementioned Class 1 and Class 2 asymptotic functions read:

$$\mathcal{K}^r_{1;\sigma\sigma'}(q) = \lim_{\substack{\nu\to\infty \\ \nu'\to\infty}} \phi^r_{\sigma\sigma'}(q,k,k') \tag{3.1a}$$

$$\mathcal{K}^r_{2;\sigma\sigma'}(q,k) = \lim_{\nu'\to\infty} \phi^r_{\sigma\sigma'}(q,k,k') - \mathcal{K}^r_{1,\sigma\sigma'}(q) \tag{3.1b}$$

$$\bar{\mathcal{K}}^r_{2;\sigma\sigma'}(q,k') = \lim_{\nu\to\infty} \phi^r_{\sigma\sigma'}(q,k,k') - \mathcal{K}^r_{1,\sigma\sigma'}(q) \quad . \tag{3.1c}$$

By looking at the diagrammatic structure of such objects (see Fig. 3.2) one notices the close similarity to the diagrammatic representation of the susceptibility and the fermion-boson

[1] Notice that the subscript has been used, differently from Sec. 2.1.4, to distinguish this symbol from the fRG parameter scale.

[2] However it could still partially apply if either a dynamic or a nonlocal bare interaction is considered.

vertex depicted in Fig. 2.8. We observe that, other then projecting $\mathcal{K}^r_{1/2;\sigma\sigma'} = \mathcal{K}^r_{\sigma\sigma'}$ onto the physical channels:

$$\mathcal{K}^{\mathrm{d/m}} = \mathcal{K}^{ph}_{\uparrow\uparrow} \pm \mathcal{K}^{ph}_{\uparrow\downarrow} \tag{3.2}$$

$$\mathcal{K}^{\mathrm{sc}} = \mathcal{K}^{pp}_{\uparrow\downarrow} \,, \tag{3.3}$$

the only significant difference consists in the bare fermion-boson vertex, $\gamma^{\eta}_{3,0,n}(q,k) = f_n(\mathbf{k})$, connecting the bosonic wiggled line to the internal fermionic lines, replaced in Fig. 3.2 by the bare interaction (here the on-site Hubbard interaction U). Thus, one identifies a connection between the $f_0(\mathbf{k}) = 1$ (s-wave) susceptibility and the fermion-boson vertex with the asymptotic functions:

$$U^2\, \chi^{\eta}_{n=0,n'=0}(q) = \mathcal{K}^{\eta}_1(q) \tag{3.4}$$

$$U\, (\gamma^{\eta}_{3,n=0}(q,k) - \gamma^{\eta}_{3,0,n=0}) = \bar{\mathcal{K}}^{\eta}_2(q,k) + \mathcal{K}^{\eta}_1(q) \tag{3.5}$$

$$U\, (\gamma^{\dagger,\eta}_{3,n=0}(q,k) - \gamma^{\dagger,\eta}_{3,0,n=0}) = \mathcal{K}^{\eta}_2(q,k) + \mathcal{K}^{\eta}_1(q) \quad . \tag{3.6}$$

The numerically efficient implementation of the asymptotic functions within codes based on fRG-schemes and parquet-decomposition have been presented in Section II of the paper. Here, we complement the numerical algorithm described there with a graphic representation in Fig. 3.3. It is worth stressing that a proper inclusion of the information carried by the asymptotic functions of the two-particle vertex it is fundamental: (i) whenever frequency summations of the latter are performed (e.g., for the calculations of physical susceptibilities) and (ii) to correctly rewrite the vertex function in different channel-related notations (e.g., in parquet-based algorithms).
To test the improvement in including the calculation of the asymptotic functions into the dynamical-fRG solver and into the parquet-approximation (PA) solver [3], we used the Anderson Impurity model (AIM). The energy levels and hybridization parameters related to the four bath sites in the latter have been chosen to simulate a box-like density of states (see Section IV in Supplement I), where the half-bandwidth D has been used as our unit of energy, i.e.,$D = 1$. The comparison of the aforementioned solvers with the exact solution, which can be computed for this simplified case, demonstrates that the role played by the inclusion of the high-frequency asymptotics for obtaining a numerically accurate result is indeed very significant. Besides the effect provided by the inclusion of $\mathcal{K}_1$ and $\mathcal{K}_2$ in the algorithm, the paper also focuses on the improvement of the fRG results by using an alternative scheme proposed in (Katanin, 2009; Eberlein, 2014), the so-called two-loop (2ℓ)-

[3] Notice that a similar parquet-approximation algorithm has been used in (Li et al., 2016) in a program package later named *Victory* (Li et al., 2017)

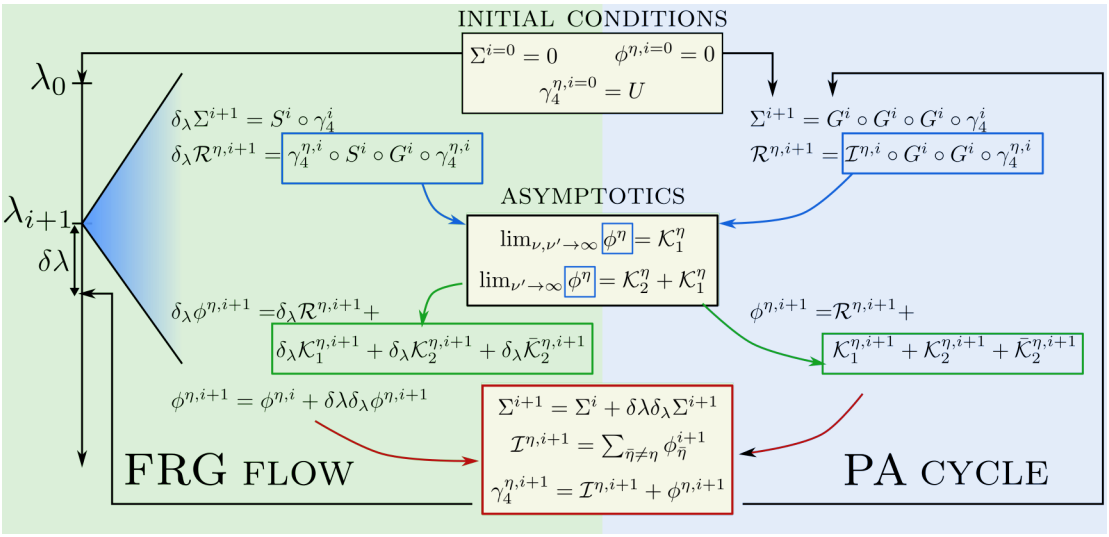

Figure 3.3: Schematic representation of the fRG (left side) and the PA (right side) algorithms. The extraction of the asymptotic vertex functions (central box) is performed by taking the numerical high frequency limit of the channel-decomposed two-particle (here 1ℓ truncated) fRG flow equations and of the two-particle parquet equations on the left and right side respectively. Although structurally quite similar, the PA solver consists of a self-consistent cycle while the fRG one in the integration of a truncated infinite hierarchy of differential equations of the 1PI vertices. Because of the truncated approximation within the fRG solver, one can demonstrate that only a subset of parquet diagrams can be generated.

approximation, and different regulators. For instance, in the following, we show data for (i) a frequency-dependent cutoff scheme, named Ω-flow, whose regulator $[R(\nu,\Lambda)]$ is given by:

$$G_0^\Lambda(k) = R(\nu,\Lambda)\, G_0(k) = \frac{\nu^2}{\nu^2+\Lambda^2}\, G_0(k) \tag{3.7}$$

where $G_0(k)$ represents the non-interacting Green's function of our system, and (ii) for a simple cutoff scheme, the so-called intercation U-flow, where $R(\nu,\Lambda) = \Lambda$.
Fig. 3.4 compares the fRG results in 1ℓ (red and orange lines for the Ω- and the U-cutoff schemes, respectively) and 2ℓ-loop approximations (dark and light green lines for the Ω- and the U-cutoff schemes, respectively) with the correspondent PA (blue hexagons) and exact (black squares) results. In Fig. 3.4, $\mathcal{K}^{ph}_{1,\uparrow\downarrow}(i\omega_l = 0)/U^3$ (left panel) and $\mathcal{K}^{ph}_{2,\uparrow\downarrow}(i\omega_l = 0, i\nu_0)/U^3$ with $i\nu_0 = i\frac{\pi}{\beta}$ (right panel) are shown as a function of different one-site Hubbard interactions U. Note that $\mathcal{K}_1$ has been shown in Fig. 3.4 with the same normalization factor of U^3 as for $\mathcal{K}_2$. In fact, although its leading order diagram in the bare interaction would be of the order U^2, as it is the case for other channels, in the specific ph-channel and spin configuration $\uparrow\downarrow$ such diagram vanishes because of the Pauli principle. In Fig. 3.4 one

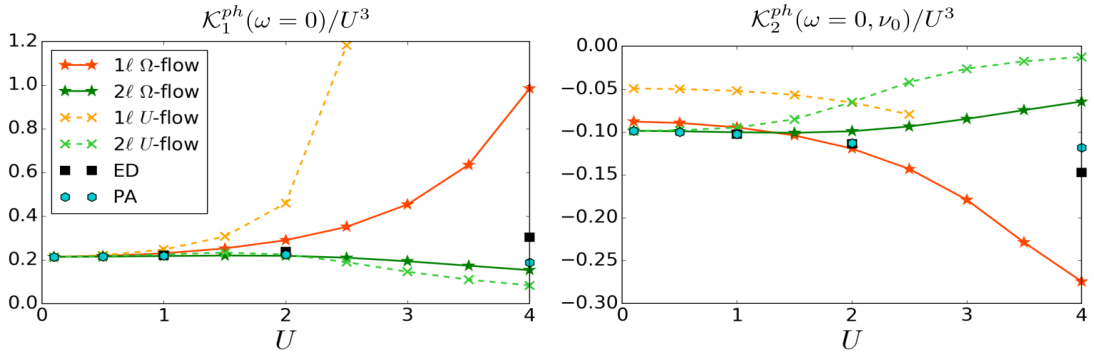

Figure 3.4: [From Supplement I Fig. 22 (left and central)] Comparison of $\mathcal{K}_1^{ph}/U^3$ and $\mathcal{K}_2^{ph}/U^3$ for fRG in the one-loop (1ℓ) and two-loop (2ℓ) implementation, for both the Ω- and U- flow, with ED and PA.

observes the improvement, for both Ω- and U-cutoff schemes, provided by the two-loop approximated fRG equations to reproduce the exact results, compared to the one-loop scheme. Furthermore, the 2ℓ results computed with different cutoff schemes are much closer, especially in the weakly correlated regime, than for the 1ℓ calculations. Differently form the one-loop results, which shown deviations to the parquet results already in the weakly correlated region, the two-loop corrections shift the offset of this discrepancies at higher U-values. Although both fRG and PA are not capable to reproduce the exact results in the intermediate-strong coupling, one notices, nonetheless, that the PA results lay closer to the ED data in the whole U-range.
A similar behaviour is observed in Fig. 3.5 for the imaginary part of the self-energy in the low-frequency region [$\mathrm{Im}\Sigma(i\nu_0)$, with $i\nu_0 = i\frac{\pi}{\beta}$ (left panel)] and in the asymptotic region [$\lim_{\nu_o\to\infty} \mathrm{Im}\Sigma(\nu_o)\ \nu_o/U^2$ (right panel)].
Last but not least, our paper shows how the fRG and PA results for the susceptibility compare with the correspondent ED data. In Fig. 3.6 we show $\chi^{ph}_{\uparrow\downarrow} = \chi^d - \chi^m$ for $U = 4D$ and $\beta = 20D^{-1}$. One observes two curves associated to the fRG solution: The green line refers to the 2ℓ fRG calculation of the susceptibility, as in Eq. (3.4) by means of $\mathcal{K}_1$, while the purple line corresponds to the calculation of the susceptibility by means of the local version of Eq. (2.60):

$$\chi^{\eta}(\omega) = \frac{1}{\beta^2}\sum_{\nu,\nu'}[\pm\Pi^{\eta,\Lambda_{\mathrm{fin}}}(\omega,\nu,\nu') + \\ - \Pi^{\eta,\Lambda_{\mathrm{fin}}}(\omega,\nu,\nu)\gamma_4^{\eta,\Lambda_{\mathrm{fin}}}(\omega,\nu,\nu')\Pi^{\eta,\Lambda_{\mathrm{fin}}}(\omega,\nu',\nu')]\ , \tag{3.8}$$

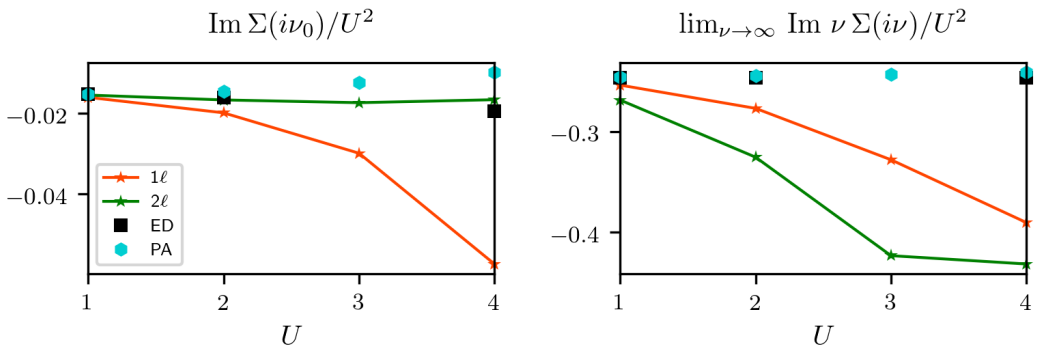

Figure 3.5: [From Supplement I Fig. 23 (left and central)] Comparison of $\mathrm{Im}\Sigma(i\nu_0)/U^2$ (left panel) and $\lim_{\nu\to\infty}\mathrm{Im}\Sigma(\nu)\,\nu/U^2$ (right panel) for fRG one-loop and two-loop using a Ω-cutoff with PA and ED.

where the positive sign refers to $\eta = \mathrm{sc}$ and the negative one to $\eta = \{\mathrm{d}, \mathrm{m}\}$. Here the functions appearing on the r.h.s. are the 2ℓ-fRG solution for the two-particle vertex γ_4^η and the "dressed" Green's function inside Π^η. One observes that the corresponding PA result (blue line) almost coincides with the fRG one calculated by means of Eq. (3.8) (purple line), while the 2ℓ result obtained during the flow (green line) is underestimated. The reason of this behavior will be clarified in Section 3.3 where the diagrammatic content of these two procedures for computing the susceptibility in fRG will become more transparent.

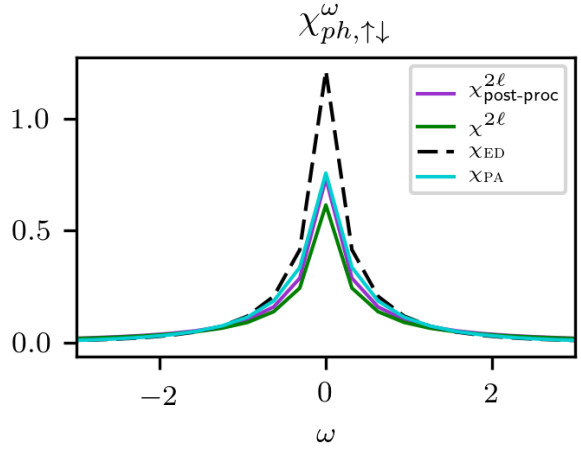

Figure 3.6: [From Supplement I. Fig. 23 (right)] Comparison of the susceptibility χ in the ph-channel for $U = 4$ obtained from the 2ℓ-fRG result for $\mathcal{K}_1^{ph}$ (see Eq. (3.4)) (green line), after the 2ℓ-fRG flow according to Eq. (3.8) ($\chi_{\text{post-proc}}$, purple line), from PA (blue line) and ED (back dashed line).

3.2 From DMFT to its diagrammatic extensions

The previous analysis on the asymptotic behavior of the two-particle vertex functions beyond its natural use in weak coupling algorithms like fRG and PA has a direct application in computing response functions in non perturbative schemes such as DMFT as well as ladder DΓA or ladder DF.
In particular, as one sees in Fig. 2.6, the evaluation of the susceptibility requires the inversion of the so-called Bethe-Salpeter (BS) equations [see Eq. (2.45)] to extract the (local) two-particle irreducible vertex of the impurity problem self-consistently connected to the lattice one. Since the (local) BS equations are integral equations w.r.t. the Matsubara frequencies, infinite internal frequency summations would be -in principle- required.
The numerical treatment of such summations, however, restricts the practical calculation to finite intervals, such that the inversion of the BS equations corresponds, in practice, to the inversion of finite-size matrices in the fermionic two-dimensional frequency space. Due to computational costs and memory constraints, the finite frequency intervals are often quite limited in size, especially in extreme situations such as low-temperature regimes, multi-orbital systems, etc. This produces an error affecting not only the (post-processing) evaluation of two-particle response functions in DMFT and DΓA but in all algorithms which make extensive use of this procedure (e.g., in parquet DΓA/QUADRILEX). The work presented in this section, "Efficient Bethe-Salpeter equations treatment in dynamical mean-field theory", whose full version is available in Supplement II, aims at curing this

source of error by using the parametric form of the vertex functions in the high-frequency region introduced in the previous section. This idea roots back to the work of Kuneš (2011), which was, nonetheless, restricted to a single channel (particle-hole) and to a single bosonic frequency $\omega = 0$, only. In our work, instead, we extend and apply the correspondent procedure to all channels and frequencies transfer.
In order to explain the essence of the method, let us start by considering the local form of Eq. (2.46):

$$\boldsymbol{\mathcal{I}}^{\eta}_{\omega} = \beta^2[(\boldsymbol{\chi}^{\eta}_{\omega})^{-1} \mp (\boldsymbol{\Pi}^{\eta}_{\omega})^{-1}], \tag{3.9}$$

where the minus/plus sign corresponds to $\eta = \{\mathrm{d,m,t}\}/\mathrm{s}$ and the bold symbol $\boldsymbol{X}^{\eta}_{\omega} \equiv X^{\eta}(\omega, \nu, \nu')$ specifies a matrix in the fermionic Matsubara frequencies ν and ν', for a given bosonic Matsubara frequency ω and the inverse of such matrix has to be assumed w.r.t. ν and ν'. Using the asymptotic expression of the two-particle reducible vertex ϕ^{η}, introduced in Eq. (3.1), and the parquet decomposition in the physical channels $\eta = \{\mathrm{d}, \mathrm{m}, \mathrm{s}, \mathrm{t}\}$ in Eq. (2.44), one can express the high-frequency behavior for the two-particle irreducible vertex $\mathcal{I}^{\eta}$ and the generalized susceptibility χ^{η} in terms of the asymptotic behavior of the two-particle vertex γ_4. As reported in section II.B of Supplement II, for $\mathcal{I}^{\eta}$ it reads:

$$\mathcal{I}^{\mathrm{d}}_{\mathrm{asym}}(\omega, \nu, \nu') = U - \frac{U^2}{2}\chi^{\mathrm{d}}_{\nu'-\nu} - \frac{3U^2}{2}\chi^{\mathrm{m}}_{\nu'-\nu} + U^2\chi^{\mathrm{sc}}_{\nu+\nu'+\omega} \ , \tag{3.10a}$$

$$\mathcal{I}^{\mathrm{m}}_{\mathrm{asym}}(\omega, \nu, \nu') = -U - \frac{U^2}{2}\chi^{\mathrm{d}}_{\nu'-\nu} + \frac{U^2}{2}\chi^{\mathrm{m}}_{\nu'-\nu} - U^2\chi^{\mathrm{sc}}_{\nu+\nu'+\omega} \ , \tag{3.10b}$$

$$\mathcal{I}^{\mathrm{s}}_{\mathrm{asym}}(\omega, \nu, \nu') = 2U + \frac{U^2}{2}\chi^{\mathrm{d}}_{\nu'-\nu} - \frac{3U^2}{2}\chi^{\mathrm{m}}_{\nu'-\nu} + \frac{U^2}{2}\chi^{\mathrm{d}}_{\omega-\nu-\nu'} - \frac{3U^2}{2}\chi^{\mathrm{m}}_{\omega-\nu-\nu'} \ , \tag{3.10c}$$

$$\mathcal{I}^{\mathrm{t}}_{\mathrm{asym}}(\omega, \nu, \nu') = -\frac{U^2}{2}\chi^{\mathrm{d}}_{\nu'-\nu} - \frac{U^2}{2}\chi^{\mathrm{m}}_{\nu'-\nu} + \frac{U^2}{2}\chi^{\mathrm{d}}_{\omega-\nu-\nu'} + \frac{U^2}{2}\chi^{\mathrm{m}}_{\omega-\nu-\nu'} \ , \tag{3.10d}$$

where on the r.h.s. the bosonic frequency dependence of the χ-functions has been specified as subscript for sake of conciseness.
Rewriting $\gamma^{\dagger,\eta}_{3,n=0}(\omega, \nu) - \gamma^{\dagger,\eta}_{3,0,n=0} = \lambda^{\eta}(\omega, \nu)$ [4] in Eqs. (3.5) and (3.6) one can derive:

[4] Note that, differently from the Moriyaesque corrections specified in Sec. 2.2.3, here λ specifies the fermion-boson vertex

$$\gamma^{\mathrm{d}}_{4,\mathrm{asym}}(\omega,\nu,\nu') = \mathcal{I}^{\mathrm{d}}_{\mathrm{asym}}(\omega,\nu,\nu') + U\lambda^{\mathrm{d}}_{\omega\nu} + U\lambda^{\mathrm{d}}_{\omega\nu'} + U^2\chi^{\mathrm{d}}_{\omega}, \tag{3.11a}$$

$$\gamma^{\mathrm{m}}_{4,\mathrm{asym}}(\omega,\nu,\nu') = \mathcal{I}^{\mathrm{m}}_{\mathrm{asym}}(\omega,\nu,\nu') + U\lambda^{\mathrm{m}}_{\omega\nu} + U\lambda^{\mathrm{m}}_{\omega\nu'} + U^2\chi^{\mathrm{m}}_{\omega}, \tag{3.11b}$$

$$\gamma^{\mathrm{s}}_{4,\mathrm{asym}}(\omega,\nu,\nu') = \mathcal{I}^{\mathrm{s}}_{\mathrm{asym}}(\omega,\nu,\nu') + 2U\lambda^{\mathrm{sc}}_{\omega\nu} + 2U\lambda^{\mathrm{sc}}_{\omega\nu'} + 2U^2\chi^{\mathrm{sc}}_{\omega}, \tag{3.11c}$$

$$\gamma^{\mathrm{t}}_{4,\mathrm{asym}}(\omega,\nu,\nu') = \mathcal{I}^{\mathrm{t}}_{\mathrm{asym}}(\omega,\nu,\nu') \quad , \tag{3.11d}$$

as well as the asymptotic form for the generalized susceptibility $\chi^{\eta}_{\mathrm{asym}}$:

$$\chi^{\eta}_{\mathrm{asym}}(\omega,\nu,\nu') = \Pi^{\eta}(\omega,\nu,\nu') - \frac{1}{\beta}\sum_{\nu_1,\nu_2}\Pi^{\eta}(\omega,\nu,\nu_1)\gamma^{\eta}_{4,\mathrm{asym}}(\omega,\nu_1,\nu_2)\Pi^{\eta}(\omega,\nu_2,\nu') \ . \tag{3.12}$$

The previous parametric from for the vertices in the high-frequency regime allows to reduce the numerical cost of computing the two-particle vertex functions. In fact, given a bosonic frequency ω, the computational effort to compute two-particle vertices in a DMFT impurity solver typically scales as $\sim N^2$, with N the number of fermionic Matsubara frequencies. The asymptotic functions χ and λ (or equivalently $\mathcal{K}_{1,2}$), are numerically cheaper to compute [5] since they depend, for a given bosonic frequency ω, at most linearly on the number of fermionic frequencies N.

Similarly as in (Kuneš, 2011), we rewrite the (infinite) matrix form in fermionic frequencies of $\mathcal{I}^{\eta}$ and χ^{η} in a block-like fashion:

$$\boldsymbol{\chi}^{\eta}_{\omega} = \begin{pmatrix} \boldsymbol{\chi}^{\eta\,00}_{\omega} & \boldsymbol{\chi}^{\eta\,01}_{\omega} \\ \boldsymbol{\chi}^{\eta\,10}_{\omega} & \boldsymbol{\chi}^{\eta\,11}_{\omega} \end{pmatrix}, \quad \boldsymbol{\mathcal{I}}^{\eta}_{\omega} = \begin{pmatrix} \boldsymbol{\mathcal{I}}^{\eta\,00}_{\omega} & \boldsymbol{\mathcal{I}}^{\eta\,01}_{\omega} \\ \boldsymbol{\mathcal{I}}^{\eta\,10}_{\omega} & \boldsymbol{\mathcal{I}}^{\eta\,11}_{\omega} \end{pmatrix}, \tag{3.13}$$

where the intervals accounted by each block are specified in Fig. 3.7. The low-frequency region (00), specified in Fig. 3.7 in red, is numerically chosen such that the two fermionic frequencies $\nu, \nu' \in I_0 = [N_{\mathrm{min}}, N_{\mathrm{max}}]$ (with $N_{\mathrm{min/max}}$ specified in Fig. 3.7). This low-frequency interval cannot be parametrized by the asymptotic functions and represents the bottleneck in the computation of the two-particle vertex from the impurity solver. On the other hand, in all other blocks such that at least one of the two fermionic frequencies belongs to $I_1 = I \backslash I_0$, with $I = [M_{\mathrm{min}}, M_{\mathrm{max}}]$, one can adopt the previous high-frequency

[5] The exact calculation of χ and λ in the exact diagonalization (ED) DMFT impurity solver is specified via their spectral representation in Appendix B of Supplement II. Other implementations in the QMC solver are specified, e.g, in (Kaufmann et al., 2017). Appendix B in Supplement I and Appendix C in Supplement II propose an alternative self-consistent evaluation of the asymptotic functions which is feasible in different vertex-based solvers.

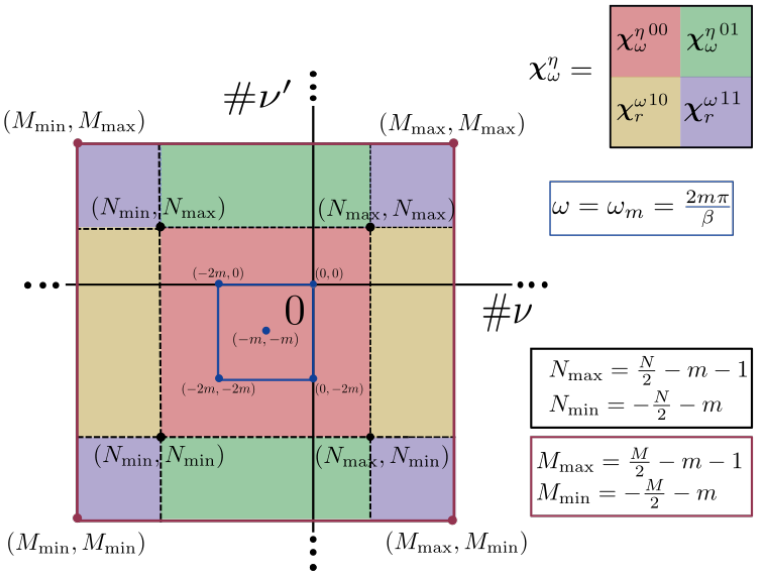

Figure 3.7: [Fig. 2 from Supplement II] Visual illustration of the block construction.

parametrization by means of χ and λ[6]. The insertion of the block decomposition into Eq. (3.9), leads (after some trivial algebraic manipulation) to the following expressions for $\boldsymbol{\mathcal{I}}_{\omega}^{\eta\,00}$:

$$\frac{1}{\beta^2}\boldsymbol{\mathcal{I}}_{\omega}^{\eta\,00} = (\boldsymbol{\chi}_{\omega}^{\eta\,00})^{-1} \mp (\boldsymbol{\Pi}_{\omega}^{\eta\,00})^{-1} + \begin{cases} +\frac{1}{\beta^2}\boldsymbol{\mathcal{I}}_{\omega}^{\eta\,01}\left[\boldsymbol{\mathcal{I}}_{\omega}^{\eta\,11} \pm \beta^2(\boldsymbol{\Pi}_{\omega}^{\eta\,11})^{-1}\right]^{-1}\boldsymbol{\mathcal{I}}_{\omega}^{\eta\,10} & \text{(3.14a)} \\ -\frac{1}{\beta^2}(\boldsymbol{\chi}_{\omega}^{\eta\,00})^{-1}\boldsymbol{\chi}_{\omega}^{\eta\,01}\boldsymbol{\mathcal{I}}_{\omega}^{\eta\,10}. & \text{(3.14b)} \end{cases}$$

The two cases listed above can be interpreted as two, formally equivalent, high-frequency corrections to the "plane" inversion of the low-frequency generalized susceptibility matrix. Despite their formal equivalence, in practice they correspond to different approximation levels once the high-frequency blocks are replaced by the asymptotic forms for the two-particle irreducible vertex and the generalized susceptibility. Eq. (3.14a) just requires the evaluation of the physical susceptibility χ, alongside the calculation of the generalized susceptibility in the low-frequency region (00), whereas Eq. (3.14b) involves the asymptotic function λ in order to parametrize the generalized susceptibility in the off-diagonal

[6] λ and χ can be calculated from the impurity solver without significant numerical effort see Appendix B in Supplement III.

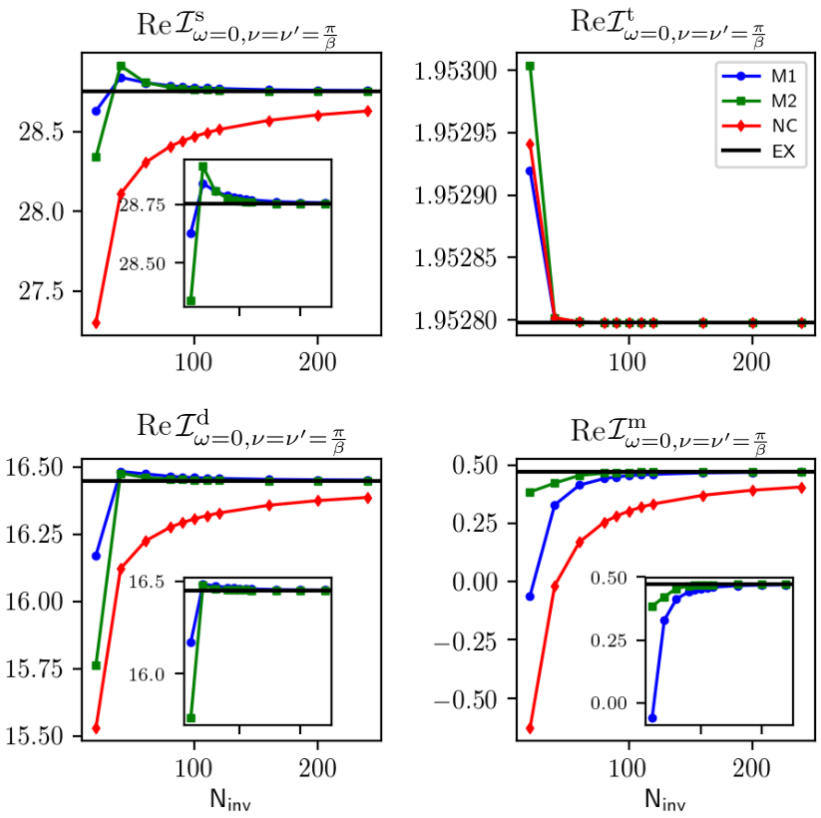

Figure 3.8: [Fig. 3 (right panel) from Supplement II] $\mathcal{I}^{\eta}_{\omega\nu\nu'}$ for $r = \{s, t, d, m\}$, evaluated at $\nu = \nu' = i\pi/\beta$ and $\omega = 0$ as a function of the inversion range N_{inv}, for $U = 1.75$. Uncorrected results (red, first part on the r.h.s of Eq. (3.14)) are compared to results corrected by the first case in Eq. (3.14a) (blue), and the second one in Eq. (3.14b) (green) and the exact result (black). The insets provide a comparison between only the two correction methods (Eqs. (3.14a) and (3.14b)) on a smaller scale.

block $\boldsymbol{\chi}^{\eta\,01}_{\omega}$. We note that, despite the additional calculation of the asymptotic function λ, which is not required in Eq. (3.14a), Eq. (3.14b) does not necessitate the inversion of the high-frequency asymptotic contribution, in contrast to the first expression in Eq. (3.14a). We tested the two methods in the case of a single-band $3d$ Hubbard model at half-filling, by varying the size of the (00)-block given by $N_{\mathrm{inv}} = N_{\mathrm{max}} - N_{\mathrm{min}}$ (notice that in the limit $N_{\mathrm{inv}} \to \infty$ the two correction terms in Eq. (3.14a) and (3.14b) vanish as expected). In Fig. 3.8 we show the results for $\mathcal{I}^{\eta}(\omega = 0, \nu = \nu' = \pi/\beta)$, with $\eta = \{\mathrm{s}, \mathrm{t}, \mathrm{d}, \mathrm{m}\}$, in the case of an intermediate Hubbard interaction $U = 1.75D$ (with $D = 2\sqrt{6}t$ twice the standard deviation of the $3d$ non-interacting density of states) and $T = 0.02D$.

One can appreciate the improvement provided by both corrective methods [Eq. (3.14a) blue line and Eq. (3.14b) green line] with respect to the plane inversion of the (00)-block of the BS equations (red line). Both methods converge very fast in the N_{inv}-size to the exact result (extrapolated for $N_{\text{inv}} \to \infty$), indicated by a black line. Additional studies on the frequency structures of the two proposed corrections has revealed that they are both almost independent of the fermionic frequencies as well as of the bosonic frequency. It turns out, in fact, that the error introduced by performing a "plane inversion" of $\boldsymbol{\chi}^{\eta}_{\omega}$ in a finite frequency window corresponds to a rigid shift of the vertex function which gets corrected by (3.14a) or (3.14b). Notable is the fact that such corrections give really good results even if the value of N_{inv} is not large enough to allow the low-frequency structures of the vertex to decay to their asymptotic values.

3.3 Nonlocal response functions in multiloop functional RG

The discussion in Sec. 3.1 has raised a number of questions regarding the connection between the fRG scheme and the parquet approximation (PA). In particular, the trend towards the PA results provided by the so-called 2ℓ-fRG approximation with respect to the 1ℓ-approximated scheme, has motivated the need to investigate more rigorously the connection between their diagrammatic content. The bridge between fRG and the PA has been recently proposed by the work of Kugler & von Delft (2018b): the so-called multiloop fRG (mfRG) method. The latter incorporates all diagrams coming from the six-point vertex contribution to the two-particle vertex flow equation, whose structure can be iteratively generated by combining the 1ℓ diagrams to construct all possible two-particle reducible contributions in the different channels. In the limit of infinite iterations, the mfRG flow equations construct the full scale-parameter derivative of the parquet approximated equations (Kugler & von Delft, 2018a). The mfRG results extend the 2ℓ-scheme proposed by Eberlein (2014) and have the great advantage of being independent from the specific choice of the cutoff scheme.

In the work presented in Supplement III, we extend the mfRG equations for the two-particle vertex and the self-energy to the correspondent multiloop equations for the boson-boson (susceptibility) and fermion-boson vertices, whose 1ℓ truncated equations have been shown in Eqs. (2.57) and (2.58). As verified in the following application to the $2d$ Hubbard model, the multiloop corrections to the response function fRG equations allow solving the ambiguity, illustrated in Sec. 2.2.4, in calculating response functions in fRG: either by tracking the renormalization group flow of the coupling to external fields or by contracting the final interaction vertex as in Eq. (2.60).

We start by providing the exact differential equations in the 1PI fRG scheme for the fermion-boson vertex and the susceptibility in all physical channels:

$$\partial_\Lambda \chi^{\mathrm{d/m},\Lambda}_{nn'}(q) = \int dk \Big[- S^\Lambda(k)\tilde{\gamma}^{\mathrm{d/m},\Lambda}_{4,nn'}(q,k) - \gamma^{\mathrm{d/m},\Lambda}_{3,n}(q,k)[G^\Lambda(k)S^\Lambda(q+k) + (S \leftrightarrow G)]\gamma^{\mathrm{d/m},\dagger,\Lambda}_{3,n'}(q,k)\Big] \tag{3.15a}$$

$$\partial_\Lambda \chi^{\mathrm{sc},\Lambda}_{nn'}(q) = \int dk \Big[- S^\Lambda(k)\tilde{\gamma}^{\mathrm{sc},\Lambda}_{4,nn'}(q,k) + \gamma^{\mathrm{sc},\Lambda}_{3,n}(q,k)[G^\Lambda(k)S^\Lambda(q-k) + (S \leftrightarrow G)]\gamma^{\mathrm{sc},\dagger,\Lambda}_{3,n'}(q,k)\Big] , \tag{3.15b}$$

and respectively

$$\partial_\Lambda \gamma^{\mathrm{d/m},\Lambda}_{3,n}(q,k) = \int dk' \Big[- S^\Lambda(k)\gamma^{\mathrm{d/m},\Lambda}_{5,n}(q,k,k') - \gamma^{\mathrm{d/m},\Lambda}_{3,n}(q,k')[G^\Lambda(k')S^\Lambda(q+k') + (S \leftrightarrow G)]\gamma^{\mathrm{d/m},\Lambda}_{4}(q,k',k)\Big] \tag{3.16a}$$

$$\partial_\Lambda \gamma^{\mathrm{sc},\Lambda}_{3,n}(q,k) = \int dk' \Big[- S^\Lambda(k)\gamma^{\mathrm{sc},\Lambda}_{5,n}(q,k,k') + \gamma^{\mathrm{sc},\Lambda}_{3,n}(q,k')[G^\Lambda(k')S^\Lambda(q-k') + (S \leftrightarrow G)]\gamma^{\mathrm{sc},\Lambda}_{4}(q,k',k)\Big] . \tag{3.16b}$$

We recall that the single scale propagator, $S^\Lambda = \partial G^\Lambda|_{\Sigma=\mathrm{const}}$, represents the partial derivative of the fermionic propagator with respect to the scale-parameter, keeping the self-energy fixed to the given Λ-scale and the subscripts (n/n') specify the momentum structure of the fermionic bilinears coupled to the external bosonic field (see Section 2.1.4). As specified in the *List of diagrammatic symbols* at page (v), $\tilde{\gamma}_4$ represents a mixed bosonic-fermionic vertex function, i.e.,with two bosonic and two fermionic legs, which, in its spin-independent form, reads:

$$\tilde{\gamma}^{\eta,\Lambda}_{4,nn'}(q,k) = \sum_\sigma \tilde{\gamma}^{\eta,\Lambda}_{4,nn';\sigma\sigma}(q,k) , \tag{3.17}$$

while the spin-independent form for γ_5 used in Eqs. (3.16) reads

$$\gamma^{\mathrm{d/m},\Lambda}_{5,n}(q,k,k') = \frac{1}{2}\sum_{\sigma',\sigma} \boldsymbol{\sigma}^{0/3}_{\sigma,\sigma'} \gamma^{\mathrm{d/m},\Lambda}_{5,n;\sigma\sigma\sigma'\sigma'}(q,k,k') \tag{3.18a}$$

$$\gamma^{\mathrm{sc},\Lambda}_{5,n}(q,k,k') = \sum_{\sigma'} \gamma^{\mathrm{sc},\Lambda}_{5,n;\uparrow\downarrow\sigma'\sigma'}(q,k,k') . \tag{3.18b}$$

After introducing the following symbol to express the $S-G$ 'bubble' within the squared brackets in Eqs. (3.15) and (3.16):

$$\dot{\Pi}_S^{\mathrm{d/m}(ph),\Lambda}(q,k) = -G^\Lambda(k)S^\Lambda(q+k) + (S \leftrightarrow G) \tag{3.19a}$$

$$\dot{\Pi}_S^{\mathrm{sc}(pp),\Lambda}(q,k) = G^\Lambda(k)S^\Lambda(q-k) + (S \leftrightarrow G)\,, \tag{3.19b}$$

one can rewrite the Eqs. (3.15) and (3.16) in the following tensor-like form:

$$\partial_\Lambda \boldsymbol{\chi}^{\eta,\Lambda} = -\boldsymbol{S}^\Lambda \circ \tilde{\boldsymbol{\gamma}}_4^{\eta,\Lambda} + \boldsymbol{\gamma}_3^{\eta,\Lambda} \circ \dot{\boldsymbol{\Pi}}_S^{\eta,\Lambda} \circ \boldsymbol{\gamma}_3^{\dagger,\eta,\Lambda} \tag{3.20}$$

$$\partial_\Lambda \boldsymbol{\gamma}_3^{\eta,\Lambda} = -\boldsymbol{S}^\Lambda \circ \tilde{\boldsymbol{\gamma}}_5^{\eta,\Lambda} + \boldsymbol{\gamma}_3^{\eta,\Lambda} \circ \dot{\boldsymbol{\Pi}}_S^{\eta,\Lambda} \circ \boldsymbol{\gamma}_4^{\eta,\Lambda} \quad , \tag{3.21}$$

with $\eta = \{\mathrm{sc}, \mathrm{d}, \mathrm{m}\}$. In a similar spirit of the derivation of the multiloop flow equations for the two-particle vertex and the self-energy (Kugler & von Delft, 2018b), in order to account for all parquet diagrams carried by the mixed fermion-boson vertices $\tilde{\gamma}_4^\Lambda$ and γ_5^Λ, we adopted the following procedure. First, we performed the so-called Katanin substitution (Katanin, 2009) $S^\Lambda \to \partial_\Lambda G^\Lambda$ ($\dot{\Pi}_S^{\eta,\Lambda} \to \dot{\Pi}^{\eta,\Lambda}$), in the one-loop flow equations [second terms on the r.h.s. of Eqs. (3.20) and (3.21)]. Since the differentiated lines with respect to the scale-parameter appear just in $\dot{\boldsymbol{\Pi}}^{\eta,\Lambda}$, one notices that no differentiated lines coming from different channels ($\bar{\eta} \neq \eta$) are included. In Appendix E of Supplement III, we demonstrate that, accounting for the leading order diagrams in the effective interaction coming from $\boldsymbol{\gamma}_5^\Lambda$ in Eq. (3.21), allows us to construct diagrams whose differentiated lines come from the complementary channels ($\bar{\eta}$). They read:

$$\dot{\boldsymbol{\gamma}}_3^{\eta,\Lambda(2)} = \boldsymbol{\gamma}_3^{\eta,\Lambda} \circ \boldsymbol{\Pi}^{\eta,\Lambda} \circ \dot{\boldsymbol{\mathcal{I}}}^{\eta,\Lambda(1)} \quad , \tag{3.22}$$

where the superscript (2) refers to the presence of two non-ladder-like bubbles appearing on the r.h.s.: One reducible in the diagrammatic channel r associated to the physical channel ($r = ph$ for $\eta = \{\mathrm{d}, \mathrm{m}\}$ and $r = pp$ for $\eta = \mathrm{sc}$), and the mixed $S-G$ bubble coming from the 1ℓ-approximated differential equation of the two-particle irreducible vertex $\dot{\boldsymbol{\mathcal{I}}}^{\eta,\Lambda(1)}$ (see Fig. 3.9 first line). Analogously to the two-loop correction for the two-particle interaction introduced by Eberlein (2014), this represents the correspondent 2ℓ approximation for the response functions. The only class of parquet diagrams missing are those where the differentiated lines coming from the complementary channels $\bar{r} \neq r$ are internally inserted to correct the bubble reducible in the particular channel $\boldsymbol{\Pi}^{\eta(r)}$. Since this bubble connects the fermion-boson vertex $\boldsymbol{\gamma}_3^\eta$ with the full vertex $\boldsymbol{\gamma}_4^\eta$, one sees that those diagrams appear only starting from the third order in the bare interaction on and are composed by two bubbles (or loops) reducible in the specific channel r considered and one (internal)

coming from $\dot{\boldsymbol{\mathcal{I}}}^{\eta,\Lambda,(1)}$ (see Fig. 3.9 second line). Moreover, replacing $\dot{\boldsymbol{\mathcal{I}}}^{\eta,\Lambda(1)}$ in Eq. (3.22) by $\dot{\boldsymbol{\mathcal{I}}}^{\eta,\Lambda(2)}$, one obtains that the three-loop diagrams are given by:

$$\begin{aligned}\dot{\boldsymbol{\gamma}}_3^{\eta,\Lambda(3)} = &\boldsymbol{\gamma}_3^{\eta,\Lambda} \circ \boldsymbol{\Pi}^{\eta,\Lambda} \circ \dot{\boldsymbol{\mathcal{I}}}^{\eta,\Lambda(2)} + \\ &\boldsymbol{\gamma}_3^{\eta,\Lambda} \circ \boldsymbol{\Pi}^{\eta,\Lambda} \circ \dot{\boldsymbol{\mathcal{I}}}^{\eta,\Lambda(1)} \circ \boldsymbol{\Pi}^{\eta,\Lambda} \circ \boldsymbol{\gamma}_4^{\eta,\Lambda} \quad .\end{aligned} \tag{3.23}$$

Following the same logic we can iteratively construct the $\ell + 2 > 3$-loop order corrections:

$$\begin{aligned}\dot{\boldsymbol{\gamma}}_3^{\eta,\Lambda(\ell+2)} = &\boldsymbol{\gamma}_3^{\eta,\Lambda} \circ \boldsymbol{\Pi}^{\eta,\Lambda} \circ \dot{\boldsymbol{\mathcal{I}}}^{\eta,\Lambda(\ell+1)} + \\ &\boldsymbol{\gamma}_3^{\eta,\Lambda} \circ \boldsymbol{\Pi}^{\eta,\Lambda} \circ \dot{\boldsymbol{\mathcal{I}}}^{\eta,\Lambda(\ell)} \circ \boldsymbol{\Pi}^{\eta,\Lambda} \circ \boldsymbol{\gamma}_4^{\eta,\Lambda} \quad .\end{aligned} \tag{3.24}$$

We can now write the multiloop flow equations for the fermion-boson vertex as:

$$\partial_\Lambda \boldsymbol{\gamma}_3^{\eta,\Lambda} = \sum_{\ell=1}^{\ell_{\max}} \dot{\boldsymbol{\gamma}}_3^{\eta,\Lambda(\ell)} \quad . \tag{3.25}$$

In the limit $\ell_{\max} \to \infty$, this method iteratively constructs the full derivative with respect to the scale parameter Λ of all diagram of the parquet approximation scheme. Considering the one-loop flow equation of the susceptibility in Eq. (3.20), we see that the $\boldsymbol{\gamma}_3^{\eta,\Lambda}$ provides the vertex corrections on both sides of the differentiated lines in $\dot{\boldsymbol{\chi}}_0^{\eta,\Lambda}$. Hence, for all higher-loop corrections, we can simply connect $\dot{\boldsymbol{\mathcal{I}}}^{\eta,\Lambda(\ell)}$ to both fermion-boson vertices, thereby raising the loop order by two. We obtain $\dot{\boldsymbol{\chi}}^{\eta,\Lambda(2)} = 0$ as well as

$$\dot{\boldsymbol{\chi}}^{\eta,\Lambda(\ell+2)} = \boldsymbol{\gamma}_3^{\eta,\Lambda} \circ \boldsymbol{\Pi}^{\eta,\Lambda} \circ \dot{\boldsymbol{\mathcal{I}}}^{\eta,\Lambda(\ell)} \circ \boldsymbol{\Pi}^{\eta,\Lambda} \circ \boldsymbol{\gamma}_3^{\eta,\Lambda,\dagger} \quad . \tag{3.26}$$

The multiloop flow equation for the susceptibility reads:

$$\partial_\Lambda \boldsymbol{\chi}^{\eta,\Lambda} = \sum_{\ell=1}^{\ell_{\max}} \dot{\boldsymbol{\chi}}^{\eta,\Lambda(\ell)} \quad . \tag{3.27}$$

For a schematic representation of Eqs. (3.27) and (3.25) at the leading order in the bare interaction, see Fig. 3.9.

The previous multiloop expressions for the response functions supplements the multiloop fRG equations for the self-energy and two-particle vertex derived in (Kugler & von Delft, 2018b). It is worth stressing the importance, in order to provide a "consistent" fRG

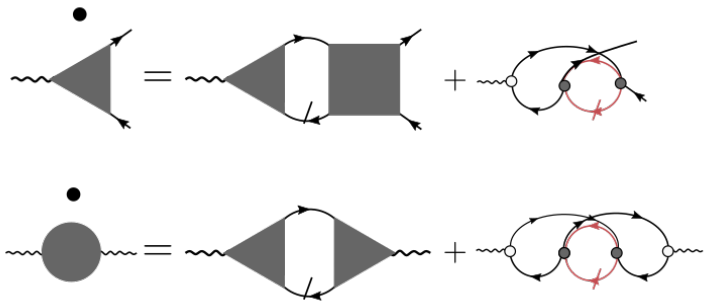

Figure 3.9: [Fig.1 from Supplement III] *multiloop* corrections for $\gamma_3^{\mathrm{d/m},\Lambda}$ (first line) and $\chi^{\mathrm{d/m},\Lambda}$ at the leading order in the bare interaction (filled black dot). The empty dot represents the "bare" 3-point vertex $\gamma_{3,0,n}^{\mathrm{d/m}} = f_n(\mathbf{k})$. The first diagram on the r.h.s. represents the usual 1ℓ-correction. In red, the contributions given by the *multiloop* corrections.

scheme, of adopting the same level of approximation, which means to truncate the sums in Eqs. (3.25) and (3.27) as well as the ones of the two-particle reducible vertices and of the self-energy at the same finite ℓ_{max}-loop level.
The multiloop corrections for the susceptibility and for the fermion-boson vertex reconstruct the *full derivative* with respect to the scale parameter of Eqs. (2.60) and (2.61), respectively. This has two important consequences: (i) in a multiloop fRG scheme whose results are converged in ℓ_{max}, the calculation of the response function via the integration of the mfRG equations and the "post-processed" scheme presented in Section 2.2.3 provide the same outcomes; (ii) As stressed in (Kugler & von Delft, 2018b), the converged (in the number of loops) results of the mfRG flow are *independent* on the regulator characterizing the fRG scheme's cutoff adopted.
In Supplement III we present the first mfRG application to the repulsive single-band $2d$ Hubbard model calculated with our new multiloop code. The solution of the latter represents, in fact, one of the most fundamental and challenging problems in many-electron physics. In the half-filled case it is well known that the physics of the single-band repulsive $2d$ Hubbard model is dominated, at low enough temperature, by antiferromagnetic fluctuations. These become infinitely large in the 1ℓ-approximated fRG scheme at a finite temperature, known as pseudocritical temperature (T_{pc}). This result reflects the violation by the 1ℓ-fRG scheme of the "Mermin-Wagner theorem" (Mermin & Wagner, 1966), which states the impossibility of any spontaneously broken continuous symmetry in $2d$ systems with short-range interactions. Since the parquet approximation has been proven to fulfill the Mermin-Wagner theorem (Vilk & Tremblay, 1996) and because of its formal equivalence with the mfRG, one expects T_{pc} to be suppressed down to zero by increasing the ℓ_{max}-loop level in a completely momentum/frequency converged mfRG calculation.

The numerical investigation of this trend, going to progressively lower T requires, however, to lift some of the common approximations done in fRG studies. In particular, the approach used in our multiloop study goes in the direction of promoting the fRG approach to more quantitative predictions. To that scope the dynamics and nonlocality of the two-particle vertex as well as the feedback of the self-energy flow have to be considered in the fRG scheme. In fact, due to numerical limitations, few are the examples in the fRG literature where non-static two-particle vertices flows, including the feedback of the self-energy, were taken into account (Uebelacker & Honerkamp, 2012; Vilardi et al., 2017). In order to overcome the numerical difficulties of treating frequencies and momenta on an equal footing, the fRG algorithm adopted in Supplement III merges the use of the vertex asymptotics developed in Supplement I (Section 3.1) with the expansion of the momentum-dependent two-particle vertices onto a form-factor basis which reflects the point symmetry of the lattice, known as truncated unity fRG (TUfRG) (Lichtenstein et al., 2017). Without entering the details of the implementation, which can be found in Supplement III, this algorithmic improvement represents an unbiased and ideal framework for the multiloop scheme.
In the following, we show and discuss mfRG results for the half-filled single-band $2d$ Hubbard model for an on-site interaction $U = 2t$ (t the hopping parameter) at different temperatures and for different choices of ℓ_{max}. If not differently specified, the mfRG calculations presented here have been obtained with a frequency-dependent cutoff (Ω-flow, see Sec. 3.1).
Fig. 3.10 shows the antiferromagnetic susceptibility $\chi_{\text{AF}} = \chi^{\text{m}}_{n=0\, n'=0}(0, \mathbf{q} = (\pi, \pi))$ and the fermion-boson vertex $\gamma_{3,\text{AF}} = \gamma^{\text{m}}_{n=0\, n'=0}(0, i\frac{\pi}{\beta}, \mathbf{q} = (\pi, \pi))$ for three selected temperatures $T = \{0.5t, 0.2t, 0.125t\}$ (left to right) as a function of different ℓ_{max}-loop approximations. In this plot, the blue line represents the susceptibility calculated by the integration of the differential Eqs. (3.20) and (3.21), while the green one is obtained by means of a "post-processed" calculation via Eqs. (2.60) and (2.61). Here, the fermionic propagators and the two-particle vertex appearing on the r.h.s. are mfRG results of the correspondent loop truncation ℓ_{max}. One sees that for $\ell_{\text{max}} = 8$ the relative difference between the two ways of computing the susceptibility, shown in the inset as ϵ_{rel}, reduces from the relatively large value of 25% for 1ℓ (in $T = 0.125t$) to less than 1%! This is consistent to the fact that the multiloop flow equation of χ constructs all non-negligible diagrams obtained by performing the full derivative of Eq. (2.60) with respect to the scale parameter. The fulfillment of this property is also verified by comparing the results obtained by means of different cutoff schemes, since the reconstruction of the full derivative should make the final outcome of the mfRG *independent* of the cutoff choice.
In Fig. 3.11 (left panel) we compared the data shown in Fig. 3.10 for $T = 0.2t$ (upper central plot), with the correspondent ones calculated using the interaction flow (U-flow). We notice that the mfRG calculations become indeed essentially independent of the cutoff

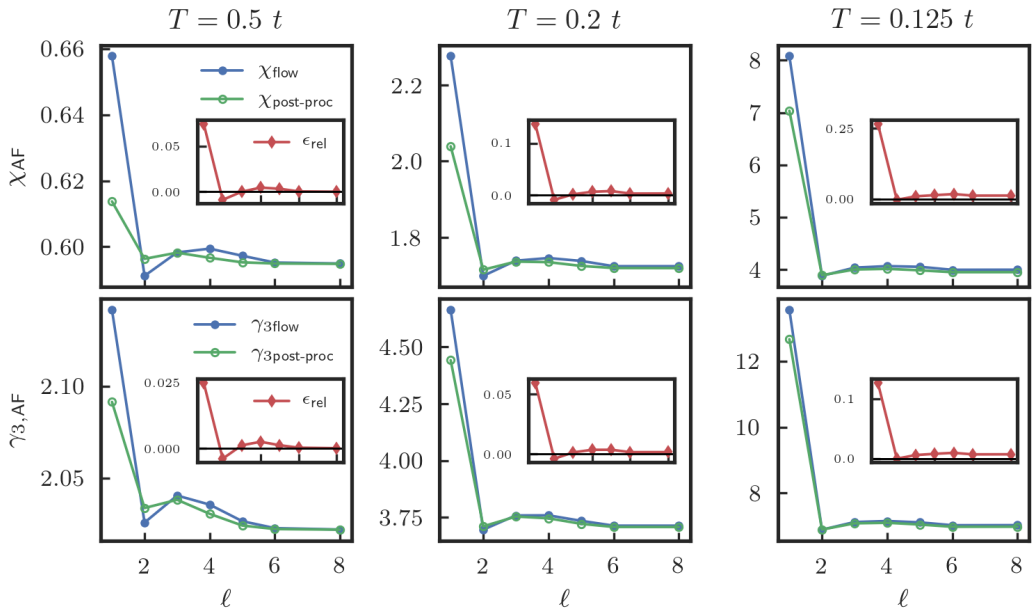

Figure 3.10: [Fig. 7 from Supplement III] Antiferromagnetic susceptibility (upper panels) and fermion-boson vertex in the magnetic channel at $\mathbf{q} = (\pi, \pi)$ ($\gamma_{3,\mathrm{AF}}$ lower panels) as a function of the number of loops, for $U = 2t$ and $T = 0.5t, 0.2t, 0.125t$ (from left to right). Each point refers to the χ value (γ_3) at bosonic frequency $\omega = 0$ (and $\nu = \pi/\beta$). The blue line shows the behavior of the integrated Eqs. (3.20) and (3.21) up to $\ell = 8$, while the green line the one obtained from the post-processed calculation by means of Eq. (2.60) for χ (as well as (2.61) for γ_3). The insets show the relative difference ϵ_{rel} between the blue and the green lines, defined for the susceptibility as $\epsilon_{\mathrm{rel}} = (\chi^{\ell}_{\mathrm{flow}} - \chi^{\ell}_{\mathrm{post\text{-}proc}})/\chi^{\ell=8}_{\mathrm{post\text{-}proc}}$.

scheme at 8ℓ, although the convergence to the asymptotic value (in the number of loops) evidently depends on the specific cutoff choice.
Finally, the expected reduction of the (Néel) pseudocritical temperature provided by the mfRG scheme with respect to the 1ℓ-fRG results can be appreciated by looking at the data in Fig. 3.11 (right panel) where the inverse antiferromagnetic susceptibility is reported as a function of the temperature. The 8ℓ data show a significant improvement w.r.t. the 1ℓ results indicating a systematic reduction of $\chi_{\mathrm{AF}}(T)$ at all T considered which corresponds to a net decrease of T_{pc}. The possibility to access the really low temperature, to confirm numerically the fulfillment of the Mermin-Wagner theorem is, however, numerically unfeasible. In the low- (but still finite) temperature regime, in fact, one would be forced to treat antiferromagnetic fluctuations with an exponentially growing correlation length (Vilk & Tremblay, 1997, 1996; Borejsza & Dupuis, 2004; Otsuki et al., 2014; Schäfer et al., 2015; Schäfer et al., 2016), which makes impossible to reach, numerically, the limit $T \to 0$, be-

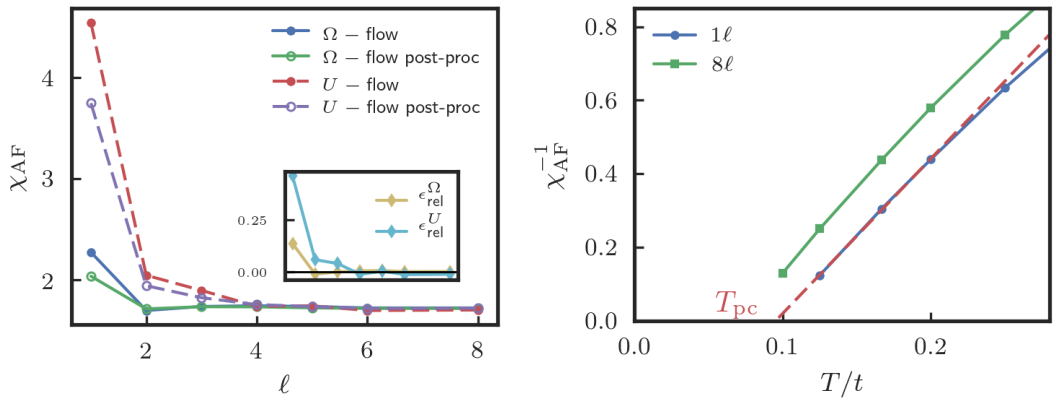

Figure 3.11: [Fig. 9-10 from Supplement III] Left panel: $\chi_{\rm AF}$ ($T = 0.2t$) as a function of the number of loops comparing the *U-flow* and the *Ω-flow*. The blue (red dashed) line shows $\chi_m(q = 0)$ computed by means of Eq. (2.60) using the so-called Ω-(interaction , U-) cutoff scheme. The inset shows the relative difference with respect to the converged value $(\chi_{\rm AF}^{\text{flow},\ell} - \chi_{\rm AF}^{\text{post-proc},\ell})/\chi_{\rm AF}^{\text{flow},8\ell}$. Right panel: Inverse antiferromagnetic susceptibility as a function of temperature. The red dashed line shows, at its crossing value with the T axis, the extrapolation of the pseudocritical temperature $T_{\rm pc}$.

cause of the finiteness of resolution in momenta.
Finally, at half-filling one expects, and numerically verifies, that the s-wave physics is sufficient to correctly capture the leading (antiferromagnetic) fluctuations, whose stability can be tested by successively including higher waves-order (d-wave, p-wave etc..). This is achieved, in practice, by enlarging the form-factor basis onto which the flowing vertex objects have been projected. In this respect, only minor variations with respect of the loop order are observed in Fig. 3.12 which shows our results for the static $i\omega_l = 0$ and uniform $\mathbf{q} = (0, 0)$ d-wave superconducting (dSC) and charge (d-wave Pomeranchuk, dPom) susceptibilities: The fluctuations with respect to the loop order are in fact on a scale of few percents.
The confirmation that the s-wave fluctuations are sufficient to obtain the correct physics is provided, however, by the comparison to the red line in Fig. 3.12. The latter represents the post-processed susceptibility calculation, according to Eq. (2.60), where the functions on the r.h.s $\boldsymbol{\gamma}_4^{\Lambda_{\rm fin}}$ and $\boldsymbol{\Pi}$ come from a mfRG flow which only includes s-wave fluctuations. It is worth stressing that the staggered $\mathbf{q} = (\pi, \pi)$ d-wave charge susceptibility, which could play a relevant role in the out-of-half-filling physics, has not been shown here because of its perfect degeneracy at half-filling with the uniform d-wave superconducting susceptibility. This degeneracy can be traced, in fact, to the underlying pseudospin SU(2) symmetry ($\text{SU}(2)_{\rm p}$) of the half-filled model as formally shown in Appendix B.

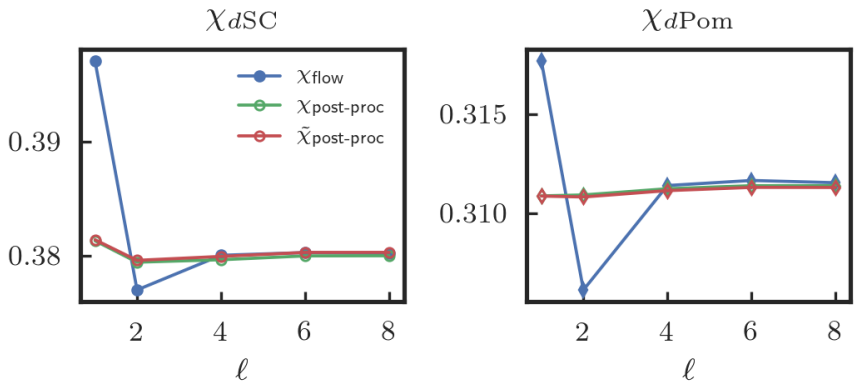

Figure 3.12: [Form Supplement III, Fig. 11] d-wave susceptibililties dSC, dPomeranchuk ($\mathbf{q} = (0, 0)$) at $i\omega_l = 0$ as a function of the number of loops, for $U = 2t$ and $T = 0.5t$. The red line has been evaluated by means of Eq. (2.60), by inserting the two-particle vertex computed from a single (s-wave) form factor.

3.4 Beyond the linear response regime: A DMFT study of the pseudogap physics

While the linear response function is associated to an observable quantity, which is directly linked to the thermodynamic fluctuations of the system, less obvious is the physical interpretation of "higher order" effects of the applied external probe. In this case, in fact, the response of the system can not be fully disentangled from the field itself. Yet, important pieces of information can be extracted by considering this regime. In particular, in the study reported in Supplement IV we address the question whether the presence of a performed pair phase can be detected unambiguously from the superconducting response function beyond the linear response regime. To this aim we used as a test bed case one of the cleanest realization of a pseudogap phase characterized by the presence of preformed pairs, namely the one observed in the *attractive* Hubbard model. By applying a (theoretical) s-wave external pairing field, we could analyze the evolution of the superconducting response as a function of the field itself. However, by applying the same perturbation to the opposite *repulsive* Hubbard model, where the electronic interaction prevents the onset of a performed (s-wave) pairs physics, we could compare the different features of the superconducting response to our external theoretical probe.
Let us look now explicitly at the two Hamiltonians considered:

$$H = -t \sum_{\langle ij \rangle \sigma} c^\dagger_{i\sigma} c_{j\sigma} + U \sum_i n_{i\uparrow} n_{i\downarrow} - \mu \sum_{i\sigma} n_{i\sigma} - \eta \sum_i (c^\dagger_{i\uparrow} c^\dagger_{\downarrow} + \text{H.c}) \ , \tag{3.28}$$

where t represents the nearest-neighbor amplitude, the on-site interaction U is positively defined in the *repulsive* and negatively defined in the *attractive* Hubbard model and $\eta =$

$-J^{\text{sc}}_{n=0} = -J^{\text{sc}}_{n=0}{}^{*}$ represents the external s-wave superconducting perturbation. For $U < 0$ and for more than two dimensions, the system displays an s-wave superconducting ground state at low temperature. While in the weak-coupling regime one witnesses a BCS-like superconducting mechanism (Bardeen et al., 1957), in the strong coupling regime preformed pairs appear far above the superconducting critical temperature T_c experiencing a Bose-Einstein condensation (BEC)-like mechanism at $T = T_c$.
For $U > 0$, instead, the s-wave superconducting order is mapped[7] onto the antiferromagnetic one and the BCS-BEC crossover (Micnas et al., 1990; Toschi et al., 2005; Strinati et al., 2018) onto a Slater mechanism at weak coupling (based on the nesting property of the Fermi surface) to a Heisenberg antiferromagnetism at high U-values. Because of the s-wave nature of our perturbation and the locality of the interaction, we restricted ourselves to a DMFT treatment, extended, however, to the broken symmetry phase, because of the presence of the pairing term in Eq. (3.28) (last term). This corresponds to recast the DMFT and its correspondent exact diagonalization (ED) solver of the auxiliary impurity in Nambu formalism (Toschi et al., 2005). In this work, we considered a semicircular density of states, the so called Bethe-lattice, whose half-bandwidth D has been taken as our energy unit throughout the paper.
The quantity we investigated is the s-wave superconducting order parameter:

$$\Delta_{\text{s-wave}}(\eta) = \langle \rho^{\text{sc}}_{n=0}(i\omega_l = 0) \rangle = \frac{1}{N} \sum_i \langle c^\dagger_{i\uparrow} c^\dagger_{i\downarrow} \rangle \ , \tag{3.29}$$

with N the number of lattice sites and where the thermal average has to be performed with respect to the system described by Eq. (3.28) and $\eta \geq 0$. In order to disentangle the effects of the superconducting probe field to the thermodynamic fluctuations in the vicinity of the phase transition, we considered a sufficiently high temperature $T = 1/7D \gg T_c$. In Fig. 3.13, we analyze the behavior of the superconducting (SC) order parameter as a function of η for different values of $U < 0$ (left panel) and $U > 0$ (right panel) at half-filling.

Let us start discussing the behavior of the superconducting order parameter in the attractive case. Here, one observes that going form small to higher U values all curves exhibit a slope which, from its highest value $\eta \to 0^+$ (corresponding to the standard superconducting susceptibility) decreases monotonically to zero at high η values, where the order parameter saturates to its maximum value $\Delta_{\text{max}} = 0.5$.
From a mathematical perspective $\Delta(\eta)$ is a *concave* function in the whole domain consid-

[7] The mapping is possible by means of the canonical transformation proposed in (Shiba, 1972). See also Appendix B.

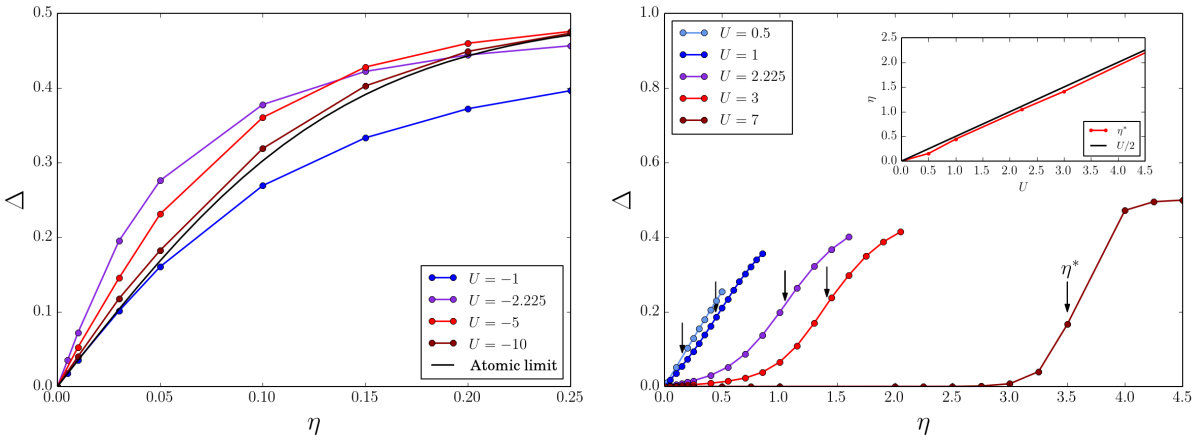

Figure 3.13: [Fig. 3 from Supplement IV] *Left panel*: s-wave superconducting order parameter as a function of the forcing pairing field η in the repulsive Hubbard model at $T = 1/7D$. The black line represents the analytical behavior in the atomic limit (see Appendix B in Supplement II). *Right panel*: Same as in the left panel but for the repulsive Hubbard model. Here η^* refers to the inflection point of the curves whose trend as a function of the coupling $U > 0$ is shown in the inset by the red curve. The correspondent value in the atomic limit $\eta^* = \frac{U}{2}$ is depicted by the black line.

ered, i.e.:

$$\frac{\partial^2 \Delta}{\partial \eta^2} < 0 \qquad \forall \eta > 0 \; . \tag{3.30}$$

The behavior of Δ displays, instead, qualitative differences in the repulsive case ($U > 0$) as shown in the right panel in Fig. 3.13. Here, while the linear response function gets, not surprisingly, progressively suppressed at higher values of U as a result of the increasing distance to the superconducting second order phase transition (which is confined in the region with $U < 0$), all curves show a peculiar behavior of the second derivative. In fact, we observe that, for all $U > 0$-values, the function $\Delta(\eta)$ shows a positive sign of the second order derivative (i.e.,is a *convex* function) up to an inflection point at $\eta = \eta^*$. For $\eta > \eta^*$ the derivative assumes a negative value and eventually saturates to its asymptotic value $\Delta = 0.5$.

The microscopic interpretation of this different behavior of the second order derivative has been possible by means of simplified analytical calculations which have been performed in selected limiting cases. In particular, the analysis of a two-sites system subjected to an on-site repulsive interaction U and to an external superconducting field η has established a connection between such behavior of the second derivative and the "nature" of the system's ground state by increasing η. Without entering the details of the calculation (see Appendix

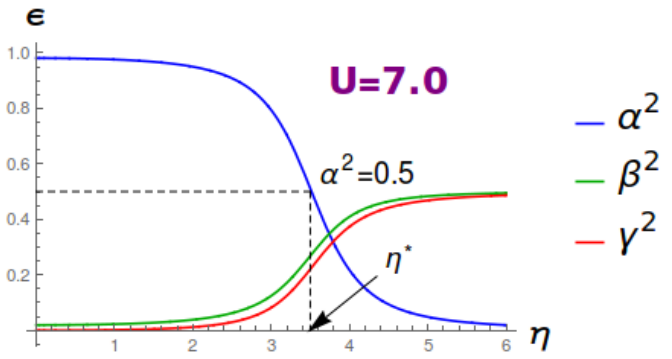

Figure 3.14: [Fig. 8 (lower panel) from Supplement IV] Ground state coefficients $|\alpha|^2$ (blue line), $|\beta|^2$ (green line) and $|\gamma|^2$ (red line) of the two-sites model for $U = 7D$ as a function of the forcing field η.

C in Supplement II) one can demonstrate that the ground state $|\psi_{GS}\rangle$ of the two-sites system subjected to the superconducting field η can be represented, in a gran canonical framework, as:

$$|\psi_{GS}\rangle = \alpha\Big(\frac{|\uparrow,\downarrow\rangle - |\downarrow,\uparrow\rangle}{\sqrt{2}}\Big) + \beta\Big(\frac{|\uparrow\downarrow,0\rangle + |0,\uparrow\downarrow\rangle}{\sqrt{2}}\Big) + \gamma\Big(\frac{|0,0\rangle + |\uparrow\downarrow,\uparrow\downarrow\rangle}{\sqrt{2}}\Big)\ , \quad (3.31)$$

where the coefficients $\{\alpha, \beta, \gamma\}$ are functions of the field η. The evolution of their squared modulus as a function of η has been explicitly studied and it is shown in Fig. 3.14 for $U = 7D$. One notices that the nature of the ground state evolves form a pure collection of localized magnetic moments for $\eta = 0$ ($|\alpha|^2 = 1$), to a mixed state for $\eta > 0$ eventually dominated by localized electron pairs for values of the field η such that $|\alpha|^2 < 0.5$. Remarkably, by looking at $\Delta(\eta)$ in the two-sites model (here not shown, see Fig. 7 in Supplement IV), one observes that the inflection point η^*, from a positive to a negative curvature does also coincide to the value of the field for which the coefficient $|\alpha|^2 = 0.5$.
Let us notice that here we just focused on the half-filled case since, as demonstrated in the paper (see Sec. III.B in Supplement IV), out-of-half filling results confirm our findings beyond the particle-hole symmetric situation.
One of the main result of our study is the identification of a general rule-of-thumb to exclude the presence of preformed pairs physics in the system: i.e., if the second derivative of $\Delta(\eta)$ is positive for relatively small (but finite) values of the superconducting field $\eta < \eta^*$ the presence of preformed pairs can be excluded. The convexity of the curve, in fact, characterizes a situation where the ground state of the system contrasts the effect of the forcing field to establish a pairing state. When the field is strong enough to "defy" the leading fluctuations of the unperturbed system, the curvature changes its sign and the supercon-

ductivity sets in. It has to be stressed, nonetheless, that the opposite regime of a negative curvature $\forall \eta > 0$ is a necessary but not sufficient condition to confirm the presence of preformed pairs. This can be seen, e.g., in Fig 3.13 (left panel) where, although the weak coupling $U = 1D$ does not display any presence of preformed pairs, the associated curvature is negative $\forall \eta > 0$.
The interpretation of our results and the conclusions might be important also in other respects: (i) by using the unitary transformation which maps the attractive Hubbard model into the repulsive and vice-versa (Shiba, 1972), our criterion could be applied to detect the presence of preformed magnetic moments, which remains a debated issue in different correlated metals (Lichtenstein et al., 2001; Anisimov et al., 2012; Antipov et al., 2012; Galler et al., 2015; Hausoel et al., 2017) and (ii) to complement the information acquired by several studies beyond DMFT to interpret the presence of a preformed pairs phase. In this context, a direct application to a dynamical cluster approximation (DCA) study (Gull & Millis, 2012) has been explicitly discussed at the end paper presented, in Sec. V.

..you'll see that things will turn out like they do, because that is what usually happens - almost always, in fact.

Jonas Jonasson

4

Conclusions and Outlook

In his lecture *Probability and uncertainty- The Quantum mechanical view of Nature*, Richard Feynman, talking about the oddly way quantum phenomena "..seem to become more and more unreasonable and more and more intuitively far from obvious", says "There is no reason why we should expect things to be otherwise, because the things of everyday experience involve large number of particles, or involve things moving very slowly, or involve other conditions that are special and represent in fact a limited experience with nature. It is a small section only of natural phenomena that one gets from direct experience...Our imagination is stretched to the utmost, not, as in fiction, to imagine things which are not really there, but just to comprehend those things which are there..". It is in this spirit that the research in strongly correlated many-electron systems has played a challenging game of the mind to develop microscopic theories to *comprehend*, if not in its totality, at least certain features of the complex reality of nature.

In this respect, the response function of a material probed by an external perturbation plays a fundamental role as test ground to confirm or disprove such microscopic theories by looking at their agreement with the experimental observations. At the linear order these objects contain intrinsic information of the specific material under survey and can be used as an indicator of its underlying scattering mechanisms and possible tendencies towards second order phase transitions. Although good theoretical descriptions are accessible by perturbative expansions in the vicinity of limiting cases (e.g., non-interacting and the atomic limit), these regimes are unfortunately still too far from a satisfactory physical description of several classes of materials at the center of the forefront research in condensed matter (high-T_c superconductors, cobaltates, nickelates, vanadates, artificially engineered hetero/or nanostructures, heavy fermion systems etc.). Since the physical properties of such materials are controlled by a delicate balance between local and nonlocal fluctuations of different nature,

which compete differently at different energy scales, we set at the beginning of this thesis three important general requirements a satisfactory microscopic theory should fulfill: (i) the ability to describe regimes beyond the perturbative one, (ii) a simultaneous description of the temporal and the spatial fluctuations, especially in the vicinity of instabilities, (iii) an unbiased inclusion of fluctuations of different nature, which compete and eventually cause the formation of a specific phase ordering.

There ain't no such thing as a free lunch and the attempts to incorporate all these requirements in a unique theory come along with a heavy computational challenge. Hence, wisely designed numerical two-particle vertex solvers are of crucial importance.
In this thesis we have shown how cheaper numerical implementations can be devised for two-particle vertex-based solvers, with the explicit application to functional renormalization group schemes and parquet solvers. In fact, a diagrammatic analysis has allowed to pinpoint a convenient high-frequency asymptotic parametrization of the two-particle vertex functions which can be computed at way lower numerical cost. The knowledge of the two-particle vertex in an infinite frequency domain, however, can be exploited in a number of different algorithmic implementations to correctly perform certain operations otherwise affected by the restriction to a finite frequency domain. This includes the inversion of the so-called Bethe-Salpeter (BS) equations, which represents a crucial step of, e.g., the dynamical vertex approximation scheme. In a DMFT study, which could be extended using the same logic to its diagrammatic extensions, we have shown how the downfolding of the high-frequency contributions of the generalized susceptibility and of the two-particle irreducible vertex into the lower frequencies (within the finite frequency domain) ameliorates substantially the inversion operation. It provides, in fact, converged results even considering cases where the two-particle correlation function is not yet decayed to its asymptotic value. This finding, together with the almost frequency- independent corrections to the inversion of the BS equations provided by the downfolding procedure, will become a crucial factor in more challenging situations, e.g., in multi-orbital and/or low-temperature calculations, where one is forced to considered only few Matsubara frequencies. Even if the algorithmic implementation of the vertex parametrization in the high-frequency regime was initially tested on a single impurity Anderson model (SIAM), its advantages are apparent in higher dimensions, where nonlocal effects have to be additionally considered. In the framework of fRG, we were able to combine the advantageous frequency treatment with an efficient way of dealing with momenta recently devised for fRG-based algorithms: the so-called truncated unity fRG (TUfRG). In our newly developed fRG algorithm, the possibility to access momentum- and frequency-dependence in a tunable, unbiased way has allowed for the first multiloop fRG (mfRG) application to the $2d$ Hubbard model. Our numerical results have shown that, even for relatively small couplings, the effect of the multiloop corrections is sizable and provides a substantial screening of the dominant channel. Although we did

not performed yet a direct comparison with parquet approximation (PA) data, there are several evidences that, as expected by its formulation, the converged (in the number of loops) mfRG results coincide with the PA ones. This is the case of the flowing fRG susceptibility in all channels, which does not only seem to converge to a plateau value (with a relative error of less than 1% at the 8^{th} loop), but it becomes also identical to a "post-processed" alternative way to compute it at the end of the mfRG flow. In fact, these different procedures to calculate susceptibilities yield the same result only if a closed subset of Feynman diagrams is built at the end of the fRG flow. In the case of mfRG considered here, the closed subset of diagrams corresponds to the one of the PA. For the same reason, we observe that the converged mfRG results become independent of the cutoff scheme considered. Another remarkable result concerns the suppression of the pseudocritical temperature, in line with the Mermin-Wagner theorem, which is known to be fulfilled by PA. At the same time, any computationally feasible momentum resolution of the Brillouin Zone prevents the access to the low-temperature regime and, at least for the parameters considered in our study, we were not able to explicitly confirm the expected exponential decay to zero temperature of the inverse antiferromagnetic susceptibility.

Let us mention here a few advantages of accessing the PA solution by means of the newly developed multiloop fRG scheme. In fact, in those cases where the solution of the ODE (ordinary differential equations) specified by the mfRG algorithm exists and is unique [see (Teschl, 2012)], it is not a priori guaranteed that such a solution can be reached by the self-consistent procedure of the PA solver. The same consideration applies to the different cutoff schemes within the mfRG implementation. In fact, although the solution has been proven to be cutoff-independent, the paths to the target system's action are non-equivalent and several of them could easily lead to "artificial" instabilities (see Fig. 4.1). One needs to recall, at this point, that one of the main strengths of the functional RG technique is the controlled way to approach and cure infrared divergences. Thus, in case of an energy scale-selective regulator, one would expect a much more controlled way to approach the final solution where eventually, in the multiloop scheme, all PA diagrams are built up. In the PA self-consistent solver, instead, all energy scales are treated on an equal footing, with the possible appearance of "pseudocritical" instabilities for certain parameter regimes. Usually the way to circumvent such spurious instabilities during the PA self-consistent cycle is to use some "damping" factor to suppress "by hand" the channels responsible for the divergence until the subleading channels grow adequately to screen it. It is clear that such a procedure is extremely uncontrolled and requires *ad hoc* recipes in order to achieve the final solution. In contrast, the intrinsic strength of the RG technique to introduce the right diagrams (or fluctuations) at the right energy scale provides, instead, a much more controlled path to the final PA solution.

These considerations bring us to another important outlook of this thesis. In fact, one

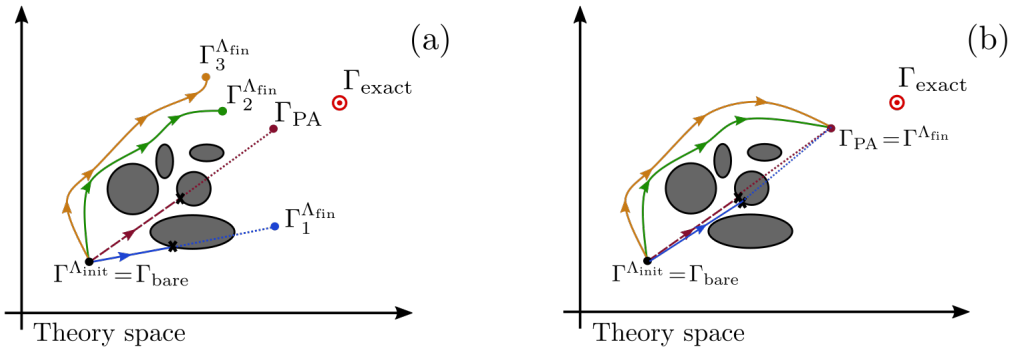

Figure 4.1: Visual representation of the different fRG schemes. (a) 1ℓ (or not converged finite-loop truncation) fRG approximation. The initial condition for the effective action is given by the bare one: $\Sigma^{\Lambda_{\rm init}} = 0, \gamma_4^{\Lambda_{\rm init}} = U$. The flow towards the final solution is cutoff dependent and brings potentially to rather different solutions (see orange, green and blue lines). Cutoff choices which are not energy-selective, i.e.,the (interaction) U-flow, could more easily lead to pseudoscritical instabilities during the flow (see blue line), which are pictorially represented by gray shapes in the phase space. (b) mfRG scheme whose solution converges to the parquet one, independently from the cutoff choice. The parquet approximation self-consistent way to approach the final solution as well as some cutoff choices not-regularizing in an RG-sense, could easily encounter infrared (pseudocritical) divergences along their path, even when a unique solution exists. However, given their formal convergence to the same PA solution, one can freely chose the most convenient regulator in order to avoid unwanted pseudocritical divergences.

could apply the multiloop fRG implementation to flows starting from correlated initial points. For instance, in the case of an initial effective action given by the DMFT solution, one could include all (non-local) parquet diagrammatic corrections to DMFT in a controlled RG-like way using a proper extension of the current multiloop fRG scheme. In fact, this would represent a multiloop extension of the already proposed DMF^{2}RG approach (which we may associate to the acronym D(MF)^{2}RG), converging in the loop order to the full parquet-DΓA method (see Fig. 4.2). This route of solving the parquet DΓA equation is particularly promising because, besides avoiding infrared instabilities, it would bypass, per construction [see also discussion in (Kugler & von Delft, 2018a)], the almost ubiquitous appearance of spurious divergences of reducible and irreducible vertex functions (Schäfer et al., 2013, 2016; Janiš & Pokorný, 2014; Ribic et al., 2016; Rohringer, 2014; Chalupa et al., 2018; Vučičević et al., 2018; Thunström et al., 2018).
It has to be stressed that, in order to study transport phenomena one would rather rely on conserving theories. The early studies by Katanin (2004), Enss (2005) and Schütz et al. (2005), in particular, have made clear that the fRG approximations violate the Ward identities typically used in condensed matter literature. Parquet approximations, on the other hand, are able to fulfill only one-particle conservation laws, while they fail at the two-particle

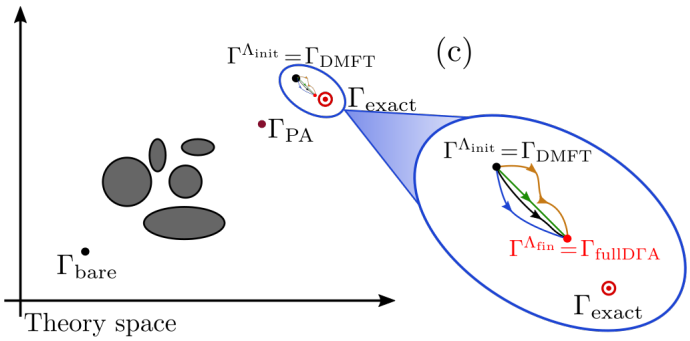

Figure 4.2: Visual representation of the mfRG application to the DMFT correlated starting point referred to as D(MF)^{2}RG. In this case, the initial condition for the effective action is the local one of DMFT, $\Sigma^{\Lambda_{\text{init}}} = \Sigma_{\text{DMFT}}$, $\gamma_4^{\Lambda_{\text{init}}} = \gamma_{4,\text{DMFT}}$. In this case the D(MF)^{2}RG should converge to the final solution of the parquet DΓA method (full DΓA). Whereas the starting point of parquet DΓA, the fully two-particle irreducible vertex Λ_{2PI}, has been explicitly proven to diverge in certain parameter regimes, on the contrary, the 1PI two-particle vertex γ_4 shows a regular behavior which assures the initial condition of D(MF)^{2}RG to be always well defined. Let us notice that infrared divergence could still be encountered while flowing towards the full DΓA solution (here not shown). Accordingly to the discussion in the text, this makes a proper regulator choice fundamental to approach the final solution in a controlled way.

level (Smith, 1992). Although some ϕ-derivable approximations (Luttinger & Ward, 1960) in exact RG literature have been formulated (Rentrop et al., 2016; Berges et al., 2005; Blaizot et al., 2011), their practical applications only restrict, to our knowledge, to some very simple systems. In the context of parquet approximation, instead, some ad hoc modifications aiming at performing conserving calculations (Baym & Kadanoff, 1961), have been recently proposed (Janis̆ et al., 2017; Kugler & von Delft, 2018a). This requires to introduce either a second auxiliary self-energy (Janis̆ et al., 2017) or a second two-particle irreducible vertex (Kugler & von Delft, 2018a) in order to obtain a thermodynamically consistent description [for details see (Janis̆ et al., 2017; Kugler & von Delft, 2018a)].
Finally, beyond the description of spectroscopic and transport properties accessible via the linear response theory, we made in this thesis a step forward by considering the effect of a finite perturbing field. In particular, we detected a possible indication of a preformed pairs phase by looking at the pairing response function beyond the linear regime. The criterion has been associated to a simple rule of thumbs which could serve to supplement the information carried by cutting-edge methods regarding the origin of the pseudogap region, which shows up as an ubiquitous feature in the phase diagram of the high-T_c superconductors. In perspective, our finding might provide an important complementary information to interpret more challenging non-equilibrium phenomena. For instance, in pump-probe

experiments where transient superconductivity is realized by coherently exciting phonon modes, we could study whether, and to which extent, these non-equilibrium phenomena can be interpreted in terms of a light-driven pairing field which favors pair formation (Fausti et al., 2011).

A

Lehmann representation of the linear response function and the fermion-boson vertex

In this section we aim at deriving the Lehmann representation of the linear response function as well as of the three-point fermion-boson vertex. Let us start from the definition of the density/magnetic as well as superconducting susceptibilities reported in Eqs. (2.21) and (2.22). For the density and the magnetic channels we can write:

$$\begin{aligned}\chi^{\mathrm{d/m}}_{nn'}(q) =& \frac{1}{2}\int_0^\beta d\tau e^{i\omega_l\tau}\sum_{\substack{\sigma,\sigma'\\ \zeta,\zeta'}}\frac{1}{\mathcal{V}^2_{\mathrm{BZ}}}\int d\mathbf{p}\, d\mathbf{p}'\; f_n(\mathbf{p})f^*_{n'}(\mathbf{p}')\,\boldsymbol{\sigma}^{0/i}_{\sigma,\sigma'}\,\boldsymbol{\sigma}^{0/i}_{\zeta,\zeta'}\times \\ & \langle c^\dagger_\sigma(\mathbf{p},\tau)c_{\sigma'}(\mathbf{p}+\mathbf{q},\tau)c^\dagger_{\zeta'}(\mathbf{p}'+\mathbf{q},0)c_\zeta(\mathbf{p}',0)\rangle \\ =& \frac{1}{2}\sum_{\substack{\sigma,\sigma'\\ \zeta,\zeta'}}\frac{1}{\mathcal{V}^2_{\mathrm{BZ}}}\int d\mathbf{p}\, d\mathbf{p}'\; f_n(\mathbf{p})f^*_{n'}(\mathbf{p}')\,\boldsymbol{\sigma}^{0/i}_{\sigma,\sigma'}\,\boldsymbol{\sigma}^{0/i}_{\zeta,\zeta'}\times \\ & \int_0^\beta d\tau e^{i\omega_l\tau}\frac{1}{\mathcal{Z}}\mathrm{Tr}\Big\{e^{-H\beta}e^{H\tau}c^\dagger_\sigma(\mathbf{p})c_{\sigma'}(\mathbf{p}+\mathbf{q})e^{-H\tau}c^\dagger_{\zeta'}(\mathbf{p}'+\mathbf{q})c_\zeta(\mathbf{p}')\Big\}\,,\end{aligned} \tag{A.1}$$

where $\mathcal{Z}$ represents the partition function and we have rewritten the thermal average in its trace-like form. By considering the full set of the Hamiltonian's eigenstates $\{|i\rangle\}_{i=0}^{\infty}$ whose

correspondent energy levels are $\{\tilde{\epsilon}_i\}_{i=0}^{\infty}$, one obtains:

$$\begin{aligned}
\chi^{\mathrm{d/m}}_{nn'}(q) =& \frac{1}{2}\sum_{\substack{\sigma,\sigma'\\ \zeta,\zeta'}} \frac{1}{\mathcal{V}^2_{\mathrm{BZ}}} \int d\mathbf{p}\, d\mathbf{p}'\, f_n(\mathbf{p}) f^*_{n'}(\mathbf{p}')\, \boldsymbol{\sigma}^{0/i}_{\sigma,\sigma'}\, \boldsymbol{\sigma}^{0/i}_{\zeta,\zeta'} \times \\
& \int_0^\beta d\tau e^{i\omega_l\tau} \frac{1}{\mathcal{Z}} \sum_{i,j} \langle i|e^{-H\beta} e^{H\tau} c^\dagger_\sigma(\mathbf{p}) c_{\sigma'}(\mathbf{p}+\mathbf{q},\tau) e^{-H\tau}|j\rangle\langle j|c^\dagger_{\zeta'}(\mathbf{p}'+\mathbf{q}) c_\zeta(\mathbf{p}')|i\rangle \\
=& \frac{1}{2}\frac{1}{\mathcal{Z}} \sum_{i,j} \langle i|\rho^{\mathrm{d/m}}_n(\mathbf{q})|j\rangle\langle j|\rho^{\mathrm{d/m}^*}_{n'}(\mathbf{q})|i\rangle \int_0^\beta d\tau e^{-\epsilon_i\beta} e^{(i\omega_l+\epsilon_i-\epsilon_j)\tau} \\
=& \frac{1}{2}\frac{1}{\mathcal{Z}} \sum_{i,j} \langle i|\rho^{\mathrm{d/m}}_n(\mathbf{q})|j\rangle\langle j|\rho^{\mathrm{d/m}^*}_{n'}(\mathbf{q})|i\rangle \, \frac{e^{-\epsilon_i\beta}(e^{(i\omega_l+\epsilon_i-\epsilon_j)\beta}-1)}{i\omega_l+\epsilon_i-\epsilon_j} \\
=& \frac{1}{2}\frac{1}{\mathcal{Z}} \sum_{i,j} \langle i|\rho^{\mathrm{d/m}}_n(\mathbf{q})|j\rangle\langle j|\rho^{\mathrm{d/m}^*}_{n'}(\mathbf{q})|i\rangle \, \frac{e^{-\epsilon_j\beta}-e^{-\epsilon_i\beta}}{i\omega_l+\epsilon_i-\epsilon_j}\,.
\end{aligned} \tag{A.2}$$

Notice that in the first line we inserted the resolution of unity $\sum_j |j\rangle\langle j| = \mathbb{1}$ and $\epsilon_i = \tilde{\epsilon}_i - \mu N_i$. Analogously, we can derive the Lehmann representation for the susceptibility in the superconducting channel:

$$\chi^{\mathrm{sc}}_{nn'}(q) = \frac{1}{\mathcal{Z}} \sum_{i,j} \langle i|\rho^{\mathrm{sc}}_n(\mathbf{q})|j\rangle\langle j|\rho^{\mathrm{sc}\,*}_{n'}(\mathbf{q})|i\rangle \, \frac{e^{-\epsilon_j\beta}-e^{-\epsilon_i\beta}}{i\omega_l+\epsilon_i-\epsilon_j}\,. \tag{A.3}$$

In a slightly more involved way, one can derive the Lehmann representation for the fermion-boson vertex γ_3. Let us start from the definition of the density/magnetic channels as in Eq. (2.23a):

$$\begin{aligned}
\gamma^{\mathrm{d/m}}_{3,n}(q,p) =& \frac{1}{2}\sum_{\sigma,\sigma'} G^{-1}_\sigma(p) G^{-1}_{\sigma'}(p+q) \int_0^\beta d\tau_1\, d\tau_2 e^{i\nu_o\tau_1} e^{-i(\nu_o+\omega_l)\tau_2} \boldsymbol{\sigma}^{0/i}_{\sigma,\sigma'} \times \\
& \langle \mathcal{T}_\tau \{ c^\dagger_\sigma(\mathbf{p},\tau) c_{\sigma'}(\mathbf{p}+\mathbf{q},\tau_2) \rho^{\mathrm{d/m}^*}_n(\mathbf{q},0)\}\rangle\,,
\end{aligned} \tag{A.4}$$

$$\begin{aligned}\gamma_{3,n}^{\mathrm{d/m}}(q,p) =&\frac{1}{2}\sum_{\sigma,\sigma'} G_{\sigma}^{-1}(p)G_{\sigma'}^{-1}(p+q)\boldsymbol{\sigma}_{\sigma,\sigma'}^{0/i}\int_0^{\beta} d\tau_1\Big[\int_0^{\tau_1} d\tau_2 e^{i\nu_o\tau_1}e^{-i(\nu_o+\omega_l)\tau_2}\times \\ &\langle\{c_{\sigma}^{\dagger}(\mathbf{p},\tau_1)c_{\sigma'}(\mathbf{p}+\mathbf{q},\tau_2)\rho_n^{\mathrm{d/m}^*}(\mathbf{q},0)\}\rangle + \\ &\int_{\tau_1}^{\beta} d\tau_2 e^{i\nu_o\tau_1}e^{-i(\nu_o+\omega_l)\tau_2}\langle\{c_{\sigma'}(\mathbf{p}+\mathbf{q},\tau_2)c_{\sigma}^{\dagger}(\mathbf{p},\tau_1)\rho_n^{\mathrm{d/m}^*}(\mathbf{q},0)\}\rangle\Big] \\ =&\frac{1}{2}\sum_{\sigma,\sigma'} G_{\sigma}^{-1}(p)G_{\sigma'}^{-1}(p+q)\boldsymbol{\sigma}_{\sigma,\sigma'}^{0/i}\Big[(\tilde{\gamma}_{3,n}^{\mathrm{d/m}})_{12}+(\tilde{\gamma}_{3,n}^{\mathrm{d/m}})_{21}\Big]\,,\end{aligned}$$

where we applied the time-ordering operator to the fermionic operators appearing in the thermal expectation value. Let us evaluate the two contributions $\tilde{\gamma}_3$ separately.

$$\begin{aligned}(\tilde{\gamma}_{3,n}^{\mathrm{d/m}})_{12} =& \int_0^{\beta} d\tau_1\int_0^{\tau_1} d\tau_2 e^{i\nu_o\tau_1}e^{-i(\nu_o+\omega_l)\tau_2}\frac{1}{\mathcal{Z}}\mathrm{Tr}\Big\{e^{-H\beta}c_{\sigma}^{\dagger}(\mathbf{p},\tau_1)c_{\sigma'}(\mathbf{p}+\mathbf{q},\tau_2)\rho_n^{\mathrm{d/m}^*}(\mathbf{q},0)\Big\} \\ =&\frac{1}{\mathcal{Z}}\sum_{i,j,k}\langle i|c_{\sigma}^{\dagger}(\mathbf{p})|j\rangle\langle j|c_{\sigma'}(\mathbf{p}+\mathbf{q})|k\rangle\langle k|\rho_n^{\mathrm{d/m}^*}(\mathbf{q},0)|i\rangle\times \\ &\int_0^{\beta} d\tau_1\int_0^{\tau_1} d\tau_2 e^{(i\nu_o+\epsilon_i-\epsilon_j)\tau_1}e^{-(i\nu_o+\omega_l-\epsilon_j+\epsilon_k)\tau_2}e^{-\epsilon_i\beta} \\ =&\frac{1}{\mathcal{Z}}\sum_{i,j,k}\frac{\langle i|c_{\sigma}^{\dagger}(\mathbf{p})|j\rangle\langle j|c_{\sigma'}(\mathbf{p}+\mathbf{q})|k\rangle\langle k|\rho_n^{\mathrm{d/m}^*}(\mathbf{q})|i\rangle}{i\nu_0+i\omega_l+\epsilon_k-\epsilon_j}\left[\frac{e^{-\epsilon_k\beta}-e^{-\epsilon_i\beta}}{i\omega_l+\epsilon_k-\epsilon_i}+\frac{e^{-\epsilon_j\beta}+e^{-\epsilon_i\beta}}{i\nu_o+\epsilon_j-\epsilon_i}\right]\,,\end{aligned} \tag{A.5}$$

while the second term reads:

$$\begin{aligned}(\tilde{\gamma}_{3,n}^{\mathrm{d/m}})_{21} =& \int_0^{\beta} d\tau_1\int_{\tau_1}^{\beta} d\tau_2 e^{i\nu_o\tau_1}e^{-i(\nu_o+\omega_l)\tau_2}\frac{1}{\mathcal{Z}}\mathrm{Tr}\Big\{e^{-H\beta}c_{\sigma'}(\mathbf{p}+\mathbf{q},\tau_2)c_{\sigma}^{\dagger}(\mathbf{p},\tau_1)\rho_n^{\mathrm{d/m}^*}(\mathbf{q},0)\Big\} \\ =&\frac{1}{\mathcal{Z}}\sum_{i,j,k}\langle i|c_{\sigma'}(\mathbf{p}+\mathbf{q})|j\rangle\langle j|c_{\sigma}^{\dagger}(\mathbf{p})|k\rangle\langle k|\rho_n^{\mathrm{d/m}^*}(\mathbf{q},0)|i\rangle\times \\ &\int_0^{\beta} d\tau_1\int_{\tau_1}^{\beta} d\tau_2 e^{(i\nu_o+\epsilon_j-\epsilon_k)\tau_1}e^{-(i\nu_o+\omega_l-\epsilon_j+\epsilon_i)\tau_2}e^{-\epsilon_i\beta} \\ =&\frac{1}{\mathcal{Z}}\sum_{i,j,k}\frac{\langle i|c_{\sigma'}(\mathbf{p}+\mathbf{q})|j\rangle\langle j|c_{\sigma}^{\dagger}(\mathbf{p})|k\rangle\langle k|\rho_n^{\mathrm{d/m}^*}(\mathbf{q})|i\rangle}{i\nu_0+i\omega_l+\epsilon_j-\epsilon_i}\left[\frac{e^{-\epsilon_i\beta}-e^{-\epsilon_k\beta}}{i\omega_l+\epsilon_k-\epsilon_i}-\frac{e^{-\epsilon_k\beta}+e^{-\epsilon_j\beta}}{i\nu_o+\epsilon_j-\epsilon_k}\right]\,.\end{aligned} \tag{A.6}$$

Following the same derivation as above, one can derive the Lehmann representation for the superconducting channel:

$$\gamma^{\text{sc}}_{3,n}(q,p) = G^{-1}_{\downarrow}(p) G^{-1}_{\uparrow}(q-p) \left[(\tilde{\gamma}^{\text{sc}}_{3,n})_{12} + (\tilde{\gamma}^{\text{sc}}_{3,n})_{21} \right] , \tag{A.7}$$

where:

$$(\tilde{\gamma}^{\text{sc}}_{3,n})_{12} = \frac{1}{\mathcal{Z}} \sum_{i,j,k} \frac{\langle i|c_{\downarrow}(\mathbf{q}-\mathbf{p})|j\rangle\langle j|c_{\uparrow}(\mathbf{p})|k\rangle\langle k|\rho^{\text{sc}*}_{n}(\mathbf{q})|i\rangle}{i\omega_l - i\nu_o + \epsilon_i - \epsilon_j} \left[\frac{e^{-\epsilon_k \beta} - e^{-\epsilon_i \beta}}{i\omega_l + \epsilon_i - \epsilon_k} - \frac{e^{-\epsilon_j \beta} + e^{-\epsilon_k \beta}}{i\nu_o + \epsilon_j - \epsilon_k} \right] , \tag{A.8}$$

$$(\tilde{\gamma}^{\text{sc}}_{3,n})_{21} = -\frac{1}{\mathcal{Z}} \sum_{i,j,k} \frac{\langle i|c_{\uparrow}(\mathbf{p})|j\rangle\langle j|c_{\downarrow}(\mathbf{q}-\mathbf{p})|k\rangle\langle k|\rho^{\text{sc}*}_{n}(\mathbf{q})|i\rangle}{i\omega_l - i\nu_o + \epsilon_j - \epsilon_k} \left[\frac{e^{-\epsilon_i \beta} - e^{-\epsilon_k \beta}}{i\omega_l + \epsilon_i - \epsilon_k} - \frac{e^{-\epsilon_i \beta} + e^{-\epsilon_j \beta}}{i\nu_o + \epsilon_i - \epsilon_j} \right] . \tag{A.9}$$

B

$\mathrm{SU}(2)_\mathrm{p}$ symmetry: degeneracy of nonlocal susceptibilities

In this appendix we want to illustrate some relevant symmetries between the charge and the superconducting susceptibilities, in particular those appearing when both particle-hole and SU(2) are symmetries of the system.
Similar considerations can be found in (Rohringer, 2014) for the two-particle correlation function of the Anderson Impurity model. Here, we generalize the derivation to a single-band d-dimensional lattice system. Its Hubbard Hamiltonian can be rearranged in a suitable form to make more transparent the particle hole-symmetry:

$$H = -t \sum_{\sigma\langle ij\rangle} (c^\dagger_{i\sigma} c_{j\sigma} + \text{h.c.}) + U \sum_i \left(n_{i\uparrow} - \frac{1}{2}\right)\left(n_{i\downarrow} - \frac{1}{2}\right) - \left(\mu - \frac{U}{2}\right) \sum_{i\sigma} n_{i,\sigma} \ . \quad \text{(B.1)}$$

Here, t represents the hopping integral between nearest neighbors, U the repulsive on-site Hubbard interaction and μ the chemical potential. One notices that at half-filling $\mu = \frac{U}{2}$ and the Hamiltonian is particle-hole symmetric as one can directly appreciate by applying the particle hole transformation (W_H) on the fermionic operators:

$$c^{\dagger\prime}_{i\sigma} = W^\dagger_\mathrm{H} c^\dagger_{i\sigma} W_\mathrm{H} = e^{\pm i\boldsymbol{\pi}\mathbf{r}_i} c_{i\sigma} \quad \text{(B.2a)}$$

$$c'_{i\sigma} = W^\dagger_\mathrm{H} c_{i\sigma} W_\mathrm{H} = e^{\mp i\boldsymbol{\pi}\mathbf{r}_i} c^\dagger_{i\sigma} \ , \quad \text{(B.2b)}$$

where the d-component wavevector $\boldsymbol{\pi} = (\pi, \pi, ...\pi)$ and the lattice vector associated to the i-site reads $\mathbf{r}_i = (r^i_1, r^i_2, ...r^i_d)$.
If one applies the particle-hole transformation to one spin component only, i.e., by means

of the operator W_{P} (Shiba, 1972):

$$c'^{\dagger}_{i\downarrow} = W_{\mathrm{P}}^{\dagger} c^{\dagger}_{i\downarrow} W_{\mathrm{P}} = e^{\pm i\boldsymbol{\pi}\mathbf{r}_i} c_{i\downarrow} \qquad c'^{\dagger}_{i\uparrow} = c^{\dagger}_{i\uparrow} \tag{B.3a}$$

$$c'_{i\downarrow} = W_{\mathrm{P}}^{\dagger} c_{i\downarrow} W_{\mathrm{P}} = e^{\mp i\boldsymbol{\pi}\mathbf{r}_i} c^{\dagger}_{i\downarrow} \qquad c'_{i\uparrow} = c_{i\uparrow} \ , \tag{B.3b}$$

one can easily demonstrate that the half-filled Hamiltonian in Eq. B.1 under such transformation gets mapped onto the correspondent half-filled Hamiltonian with negative U-interaction, i.e.,the *attractive* Hubbard model (Micnas et al., 1990):

$$W_{\mathrm{P}}^{\dagger} H(U) W_{\mathrm{P}} = H(-U) \ . \tag{B.4}$$

One notices that W_{P} does not represent a symmetry of our system by itself. Nevertheless its combination with the SU(2) symmetry can be easily proven to commute with the Hamiltonian. In fact, let us assume D a generic spin rotation [1] and let us transform it by means of W_{P}:

$$W_{\mathrm{P}}^{\dagger} D W_{\mathrm{P}} = D_{\mathrm{P}} \ , \tag{B.5}$$

we can demonstrate that $[H, D_{\mathrm{P}}] = 0$:

$$W_{\mathrm{P}}^{\dagger} D^{\dagger} W_{\mathrm{P}} H(U) W_{\mathrm{P}}^{\dagger} D W_{\mathrm{P}} = W_{\mathrm{P}}^{\dagger} D^{\dagger} H(-U) D W_{\mathrm{P}} = W_{\mathrm{P}}^{\dagger} H(-U) W_{\mathrm{P}} = H(U) \ . \tag{B.6}$$

We then conclude that the system has a pseudospin symmetry ($\mathrm{SU}(2)_{\mathrm{P}}$) D_{P} whose generators can be derived by transforming the spin operators by means of W_{P}:

$$S^x_{\mathrm{P}} = \frac{1}{2} \sum_j \left(e^{\pm i\boldsymbol{\pi}\mathbf{r}_j} c^{\dagger}_{j\uparrow} c^{\dagger}_{j\downarrow} + e^{\mp i\boldsymbol{\pi}\mathbf{r}_j} c_{j\uparrow} c_{j\downarrow} \right) \tag{B.7a}$$

$$S^y_{\mathrm{P}} = \frac{1}{2i} \sum_j \left(e^{\pm i\boldsymbol{\pi}\mathbf{r}_j} c^{\dagger}_{j\uparrow} c^{\dagger}_{j\downarrow} - e^{\mp i\boldsymbol{\pi}\mathbf{r}_j} c_{j\uparrow} c_{j\downarrow} \right) \tag{B.7b}$$

$$S^z_{\mathrm{P}} = \frac{1}{2} \sum_j \left(c^{\dagger}_{j\uparrow} c_{j\uparrow} + c^{\dagger}_{j\downarrow} c_{j\downarrow} - 1 \right) \ . \tag{B.7c}$$

[1] One can can represent the rotation operator as $D^{\phi,\hat{n}} = e^{-i\phi \mathbf{S}\cdot\hat{n}}$, where $\mathbf{S} = (S^x, S^y, S^z)$ represents a vector of the spin operators. Some relevant spin rotations are, for instance, (i) the rotation of the spin operator S^z of an angle $\phi = \pi$ around the y-axis which corresponds to a spin flip along the z direction, $D^{\pi,\hat{y}\,\dagger} S^z D^{\pi,\hat{y}} = -S^z$, or (ii) a rotation of $\phi = \frac{\pi}{2}$ w.r.t. the y-axis which transforms the spin operator along the z direction into the one along the x-direction,$D^{\frac{\pi}{2},\hat{y}\,\dagger} S^z D^{\frac{\pi}{2},\hat{y}} = -S^x$.

We will first prove that the s-wave pairing operator:

$$\Delta_{\text{s-wave}} + \Delta^{\dagger}_{\text{s-wave}} = \frac{1}{N}\sum_{j}\left[c_{j\uparrow}c_{j\downarrow} + c^{\dagger}_{j\downarrow}c^{\dagger}_{j\uparrow}\right] , \tag{B.8}$$

where N represents the number of lattice sites, can be transformed by a pseudospin rotation into the staggered ($\mathbf{q} = \boldsymbol{\pi} = (\pi, \pi ... \pi)$) density operator:

$$\rho^{\text{d}}_{\text{s-wave}}(\mathbf{q} = \boldsymbol{\pi}) = \frac{1}{N}\sum_{j}(-1)^{\mathbf{r}_j}\left[c^{\dagger}_{j\uparrow}c_{j\uparrow} - c_{j\downarrow}c^{\uparrow}_{j\downarrow}\right] . \tag{B.9}$$

Since the pseudospin rotation represents a symmetry of the system, the expectation values of the s-wave pairing operator and the s-wave staggered density operator (which are nothing but the associated order parameters) will coincide. Let us notice that this holds also for the static physical susceptibilities associated to the operators in (B.8) and (B.9) which are defines as:

$$\chi^{\text{sc}}(\mathbf{q} = \mathbf{0}) = \frac{1}{2}\int_0^{\beta} d\tau \left\langle \left[\Delta_{\text{s-wave}}(\tau) + \Delta^{\dagger}_{\text{s-wave}}(\tau)\right]\left[\Delta^{\dagger}_{\text{s-wave}}(0) + \Delta_{\text{s-wave}}(0)\right]\right\rangle , \tag{B.10}$$

$$\chi^{\text{d}}(\mathbf{q} = \boldsymbol{\pi}) = \frac{1}{2}\int_0^{\beta} d\tau \left\langle \rho^{\text{d}}_{\text{s-wave}}(\mathbf{q} = \boldsymbol{\pi}, \tau)\rho^{\text{d}}_{\text{s-wave}}{}^{\dagger}(\mathbf{q} = \boldsymbol{\pi}, 0)\right\rangle , \tag{B.11}$$

$$\chi^{\text{sc}}(\mathbf{q} = \mathbf{0}) = \chi^{\text{d}}(\mathbf{q} = \boldsymbol{\pi}) . \tag{B.12}$$

In order to prove it, let us start rewriting the operators defined in Eqs. (B.8) and (B.9) in terms of the pseudo spinors:

$$\psi_j = \begin{pmatrix} c_{j\uparrow} \\ e^{i\boldsymbol{\pi}\mathbf{r}_j}c^{\dagger}_{j\downarrow} \end{pmatrix} \qquad \psi^{\dagger}_j = \begin{pmatrix} c^{\dagger}_{j\uparrow} & e^{-i\boldsymbol{\pi}\mathbf{r}_j}c_{j\downarrow} \end{pmatrix} . \tag{B.13}$$

Let us notice that the operators in Eq. (B.7a) assume, in the pseudo spinors basis, the fol-

lowing simplified form:

$$S^x_{\mathrm{p}} = \frac{1}{2}\sum_j e^{\pm i\boldsymbol{\pi}\mathbf{r}_j}\psi^\dagger_j\boldsymbol{\sigma}_x\psi_j \ , \tag{B.14a}$$

$$S^y_{\mathrm{p}} = \frac{1}{2}\sum_j e^{\pm i\boldsymbol{\pi}\mathbf{r}_j}\psi^\dagger_j\boldsymbol{\sigma}_y\psi_j \ , \tag{B.14b}$$

$$S^z_{\mathrm{p}} = \frac{1}{2}\sum_j \psi^\dagger_j\boldsymbol{\sigma}_z\psi_j \ , \tag{B.14c}$$

where $\boldsymbol{\sigma}_{\{x,y,z\}}$ represent the three Pauli matrices:

$$\boldsymbol{\sigma}_x = \begin{pmatrix} 0 & 1 \\ 1 & 0 \end{pmatrix} \qquad \boldsymbol{\sigma}_y = \begin{pmatrix} 0 & -i \\ i & 0 \end{pmatrix} \qquad \boldsymbol{\sigma}_z = \begin{pmatrix} 1 & 0 \\ 0 & -1 \end{pmatrix} \ . \tag{B.15}$$

In the pseudo spinors basis Eq. (B.8) reads:

$$\begin{aligned} \Delta_{\text{s-wave}} + \Delta^\dagger_{\text{s-wave}} &= \frac{1}{N}\sum_j \left[-e^{i\boldsymbol{\pi}\mathbf{r}_j}\psi^\dagger_j\boldsymbol{\sigma}_-\psi_j - e^{-i\boldsymbol{\pi}\mathbf{r}_j}\psi^\dagger_j\boldsymbol{\sigma}_+\psi_j\right] \\ &= \frac{-1}{N}\sum_j (-1)^{\mathbf{r}_j}\psi^\dagger_j\boldsymbol{\sigma}_x\psi_j \ , \end{aligned} \tag{B.16}$$

where the matrices $\boldsymbol{\sigma}_+ = \begin{pmatrix} 0 & 1 \\ 0 & 0 \end{pmatrix}$ and $\boldsymbol{\sigma}_- = \begin{pmatrix} 0 & 0 \\ 1 & 0 \end{pmatrix}$.
Let us now consider a pseudospin rotation of an angle ϕ with respect to the y axis with the following matrix representation:

$$D^{\phi,\hat{y}}_{\mathrm{p}} = e^{-i\frac{\phi}{2}\boldsymbol{\sigma}_y} = \begin{pmatrix} \cos(\frac{\phi}{2}) & -\sin(\frac{\phi}{2}) \\ \sin(\frac{\phi}{2}) & \cos(\frac{\phi}{2}) \end{pmatrix} \ . \tag{B.17}$$

Considering a rotation of $\phi = \frac{\pi}{2}$ to Eq. (B.16) we have:

$$\begin{aligned} D^{\frac{\pi}{2},\hat{y}^\dagger}_{\mathrm{p}}\left[\Delta_{\text{s-wave}} + \Delta^\dagger_{\text{s-wave}}\right]D^{\frac{\pi}{2},\hat{y}}_{\mathrm{p}} &= \frac{-1}{N}\sum_j (-1)^{\mathbf{r}_j}\tilde{\psi}^\dagger_j\boldsymbol{\sigma}_z\tilde{\psi}_j \\ &= -\rho^{\mathrm{d}}_{\text{s-wave}}(\mathbf{q}=\boldsymbol{\pi}) \ , \end{aligned} \tag{B.18}$$

where $\tilde{\psi}^{(\dagger)}$ represents the rotated annihilation (creation) pseudo spinor and we used the

representation of the density operator ρ^{d} on the pseudo-spinors basis:

$$\rho^{\mathrm{d}}_{\text{s-wave}}(\mathbf{q}=\boldsymbol{\pi}) = \frac{1}{N}\sum_j (-1)^{\mathbf{r}_j}\psi_j^\dagger \boldsymbol{\sigma}_z \psi_j \ . \tag{B.19}$$

Let us now consider the pairing operators for a d-wave symmetry in a ($d = 2$) squared lattice (Khatami et al., 2015):

$$\Delta_{\text{d-wave}} = \frac{1}{2}\frac{1}{N}\sum_j\sum_{b=\pm1}\left[c_{j\uparrow}c_{j+b\hat{x}\downarrow} - c_{j\downarrow}c_{j+b\hat{x}\uparrow} - c_{j\uparrow}c_{j+b\hat{y}\downarrow} + c_{j\downarrow}c_{j+b\hat{y}\uparrow}\right] \tag{B.20a}$$

$$\Delta^\dagger_{\text{d-wave}} = \frac{1}{2}\frac{1}{N}\sum_j\sum_{b=\pm1}\left[c^\dagger_{j+b\hat{x}\downarrow}c^\dagger_{j\uparrow} - c^\dagger_{j+b\hat{x}\uparrow}c^\dagger_{j\downarrow} - c^\dagger_{j+b\hat{y}\downarrow}c^\dagger_{j\uparrow} + c^\dagger_{j+b\hat{y}\uparrow}c^\dagger_{j\downarrow}\right] \ . \tag{B.20b}$$

Taking their sum and writing them in terms of the pseudo spin, one finds:

$$\Delta_{\text{d-wave}}+\Delta^\dagger_{\text{d-wave}} = \frac{1}{2}\frac{-i}{N}\sum_j\sum_{b=\pm1}(-1)^{\mathbf{r}_j}\left[\psi_j^\dagger\boldsymbol{\sigma}_y\psi_{j+b\hat{x}} - \psi^\dagger_{j+b\hat{x}}\boldsymbol{\sigma}_y\psi_j - \psi_j^\dagger\boldsymbol{\sigma}_y\psi_{j+b\hat{y}} + \psi^\dagger_{j+b\hat{y}}\boldsymbol{\sigma}_y\psi_j\right] \ . \tag{B.21}$$

One can now apply to Eq. (B.21) a pseudospin rotation of $\phi = \frac{\pi}{2}$ around the x-axis, whose matrix representation reads:

$$D^{\phi,\hat{x}}_{\mathrm{P}} = e^{-i\frac{\phi}{2}\boldsymbol{\sigma}_x} = \begin{pmatrix} \cos(\frac{\phi}{2}) & -i\sin(\frac{\phi}{2}) \\ -i\sin(\frac{\phi}{2}) & \cos(\frac{\phi}{2}) \end{pmatrix} \ , \tag{B.22}$$

and one obtains:

$$\begin{aligned} D^{\frac{\pi}{2},\hat{x}\,\dagger}_{\mathrm{P}}\left[\Delta_{\text{d-wave}} + \Delta^\dagger_{\text{d-wave}}\right]D^{\frac{\pi}{2},\hat{x}}_{\mathrm{P}} &= \frac{i}{N}\sum_j(-1)^{\mathbf{r}_j}\Big[\tilde{\psi}_j^\dagger\boldsymbol{\sigma}_z\tilde{\psi}_{j+b\hat{x}} - \tilde{\psi}^\dagger_{j+b\hat{x}}\boldsymbol{\sigma}_z\tilde{\psi}_j - \\ &\qquad \tilde{\psi}_j^\dagger\boldsymbol{\sigma}_z\tilde{\psi}_{j+b\hat{y}} + \tilde{\psi}^\dagger_{j+b\hat{y}}\boldsymbol{\sigma}_z\tilde{\psi}_j\Big] \\ &= i\rho^{\mathrm{d}}_{\text{d-wave}}(\mathbf{q}=\boldsymbol{\pi}) \ . \end{aligned} \tag{B.23}$$

Therefore, their associated d-wave physical susceptibilities coincide:

$$\chi^{\mathrm{sc}}_{\text{d-wave}} = \chi^{\mathrm{d}}_{\text{s-wave}}(\mathbf{q}=\boldsymbol{\pi}) \ , \tag{B.24}$$

as the results in Sec. 3.3 (and in Supplement III) confirm.

Supplements

Personal contribution to publications

In the following I specify my personal contribution to the manuscripts attached to the present cumulative thesis.

I. High-frequency asymptotics of the vertex function: diagrammatic parametrization and algorithmic implementation

[**arXiv:1610.06520, Submitted to Physical Review B**]

This work results from my first approach to the functional renormalization group (fRG) method and, more in general, to the treatment of two-particle vertex functions and their inclusion into diagrammatic techniques. The idea of parametrizing the two-particle vertex functions in the high-frequency regime, in case of an instantaneous non-screened interaction, has been developed by N. Wentzell in the context of fRG, parallel to the parametrization by means of the so-called "kernel functions" proposed by G. Li in (Li et al., 2016). The idea to test and compare the two approaches has required exact calculations which have been performed for the Anderson Impurity model embedded and coupled to a non-interacting bath composed by four sites. For these I performed all exact calculations of the two-particle vertices shown in the paper (and in the Supplemental Material), which I decomposed into the different diagrammatic classes in order to extract all quantities which have been compared to the respective PA and fRG results. The latter I post-processed, together with the ED data, providing all plots presented in the paper, excluded Fig. 19,20,21 (left and central plot). I also contributed to the text of the manuscript, especially to Section VI, Appendices A, C, D. Moreover, together with N. Wentzell, I developed and implemented for the first time the idea presented in Appendix C, and derived all the symmetry relations shown in Appendix D which have been successively implemented into the fRG code.

II. Efficient Bethe-Salpeter equations treatment in dynamical mean-field theory

[**Phys. Rev. B 97, 235140 (2018)**]

The previous work inspired the idea to exploit the parametrization of the high-frequency region in other approaches which make use of the diagrammatic decomposition of the ver-

tex. Together with N. Wentzell, we had the idea of correcting the usual procedure to invert vertex functions with respect to the fermion frequencies, which is needed to calculate the two-particle reducible vertices by means of the so-called Bethe-Salpeter equations. I derived and implemented one of the techniques presented in the paper, which has been referred to as *Method 2*. Digging into the topic has made me aware of a similar approach, based, though, on different approximations and limited to the calculation of the static particle-hole susceptibility in DMFT, proposed in the work of (Kuneš, 2011). Moreover, the unpublished work of S. Hummel (Hummel, 2014) supervised by A. Toschi and G. Rohringer, had already proposed to extend this approach to dynamical susceptibilities in all channels. Therefore, I implemented this method, referred in the paper to as *Method 1*, as an alternative procedure to the one I previously derived. My interest was to understand the different approximation the two methods are based upon and try to unveil their advantages and disadvantages in different regimes and algorithmic-specific requirements. In the manuscript I elaborated, together with G. Rohringer, the theory section and the presentation of the methods. In particular, I acquired all the DMFT data as well as the their post-processed manipulation in order to invert the BS equations corrected by the two proposed approaches. I took care of the data analysis and the discussion of the results in the paper.

III. Multiloop functional renormalization group for the two-dimensional Hubbard model: Loop convergence of the response functions

[**arXiv:1807.02697, Submitted to SciPost**]

This work constitutes the core of my PhD project where I started computing linear response functions in functional RG. Although the calculation of response functions is already present in the fRG literature, none of these works gives indications on how to compute them within the framework of extended schemes like the one proposed by (Eberlein, 2014; Katanin, 2009). This has triggered the question whether a two-loop formulation for the fRG equations of the response functions was possible too. Parallel to the derivation of such scheme, I started the challenging project with C. Hille to extend the efficient fRG code inherited by N. Wentzell for local systems (`fRGdyn`), to nonlocal ones, in view of performing material calculations. This has brought us to merge the proposed efficient way of treating momenta in fRG, the so-called truncated unity fRG (Lichtenstein et al., 2017), with the frequency implementation already present in our fRG algorithm. The unbiased and versatile structure of our code has made the implementation of the recent multiloop fRG corrections proposed by Kugler & von Delft (2018b), a relatively easy task. Thanks to the collaboration with F. Kugler, we have been able to develop multiloop corrections for the flow equations of response functions on top of the two loop corrections I previously derived. This has played a crucial role in clarifying the connection between the PA and the fRG ways of computing response functions and to open fRG to new routes in order to ac-

cess non-perturbative regimes. The team work of C. Hille and me has made this challenging project possible. I contributed to the manuscript, where C. Hille and me share the first authorship, with Section II, IV.5 and with the derivations extensively reported in Appendices B C D E.

IV. Detecting a preformed pair phase: Response to a pairing forcing field

[**Phys. Rev. B 94, 155114 (2016)**]
Despite its last position in the overview on my PhD work, this paper is chronologically the first one I worked on. It roots back to the project I started for my master thesis, which I did under the supervision of M. Capone (SISSA, Trieste) and A. Toschi (TU-Wien, Vienna), and finalized during the first months of my PhD. This work represents my first approach to many-body systems solved with quantum field theory techniques. Here, I performed a DMFT study of the superconducting response of an attractive Hubbard model, as well as of its repulsive counterpart, to an external pairing field. This analysis has unveiled an unambiguous criterion, based on the superconducting response beyond the linear order, to identify the presence of preformed pairs, often associated to systems characterized by a pseudogap phase. In this work I provided all DMFT calculations necessary to the analysis of the superconducting response function and performed the analytic calculations which helped understanding their non-linear features. I contributed to the writing of the manuscript with Sections III, IV, V and with Appendices A, B, C.

I High-frequency asymptotics of the vertex function: diagrammatic parametrization and algorithmic implementation

High-frequency asymptotics of the vertex function: diagrammatic parametrization and algorithmic implementation

Nils Wentzell,[1,2] Gang Li,[1] Agnese Tagliavini,[1,2] Ciro Taranto,[3] Georg Rohringer,[1,4,5] Karsten Held,[1] Alessandro Toschi,[1] and Sabine Andergassen[2]

[1] *Institute for Solid State Physics, Vienna University of Technology, 1040 Vienna, Austria*
[2] *Institut für Theoretische Physik and Center for Quantum Science, Universität Tübingen, Auf der Morgenstelle 14, 72076 Tübingen, Germany*
[3] *Max-Planck-Institute for Solid State Research, 70569 Stuttgart, Germany*
[4] *Russian Quantum Center, 143025 Skolkovo, Russia*
[5] *Department of Physics, M.V. Lomonosov Moscow State University, 119991 Moscow, Russia*

Vertex functions are a crucial ingredient of several forefront many-body algorithms in condensed matter physics. However, the full treatment of their frequency and momentum dependence severely restricts numerical calculations. A significant advancement requires an efficient treatment of the high-frequency asymptotic behavior of the vertex functions. In this work, we first provide a detailed diagrammatic analysis of the high-frequency structures and their physical interpretation. Based on these insights, we propose a parametrization scheme, which captures the whole high-frequency domain for arbitrary values of the local Coulomb interaction and electronic density, and we discuss the details of its algorithmic implementation in many-body solvers based on parquet-equations as well as functional renormalization group schemes. Finally, we assess its validity by comparing our results for a single impurity Anderson model with exact diagonalization calculations. The proposed parametrization is pivotal for the algorithmic development of all quantum many-body methods based on vertex functions arising from local microscopic interactions, such as the diagrammatic approaches including spatial correlations beyond dynamical mean-field theory.

PACS numbers: 71.10.Fd, 71.10-w, 71.27.+a

I. INTRODUCTION

One of the most challenging aspects in contemporary condensed matter research is the theoretical treatment of correlation effects in the non-perturbative regime. While the state-of-the-art theoretical tools allow for an accurate treatment of quantum many-body correlations in specific cases, their reliability is not guaranteed in general and is often limited to particular parameter regimes. In the last decade, several promising quantum field theoretical schemes have been proposed, but their actual implementation calls for a significant improvement of the current algorithmic procedures. In particular, most of the novel non-perturbative schemes are based on a Feynman diagrammatic expansion around a correlated starting point. This means to replace the bare electronic interaction with a dynamical effective one and the bare propagators by dressed ones, which includes non-perturbatively, through the two-particle vertex function and the self-energy, a significant part of the correlations from the very beginning. The numerical treatment of these vertex functions is, however, numerically very demanding, and the development of efficient ways to include them in the current algorithms is mandatory.

The two-particle vertex, recently object of several focused studies,[1–8] depends in general on three independent frequencies and momenta, and additionally on spin and orbital variables. Even in the $SU(2)$ symmetric case, the efficient computation of two-particle vertices becomes very challenging for a reasonably large system at low temperatures. Besides the storage, the inclusion of the asymptotic structure during the computation represents a major issue and requires to exploit a detailed understanding of its underlying structure[4–7] in order to reduce the numerical effort[8].

To this aim, we begin by presenting a detailed diagrammatic analysis of the frequency and momentum structures of the vertex functions, focusing on the algorithmic aspects relevant for the development of improved parametrization schemes. After defining the general guidelines of the algorithmic implementation, we present applications for many-body solvers based on functional renormalization group[9] (fRG) schemes as well as parquet equations[1,8,10,11]. In particular, the validity of the proposed parametrization algorithm could be quantitatively assessed by comparing our results for the single impurity Anderson model (SIAM) obtained by means of fRG and the parquet approximation[12] (PA) with exact diagonalization (ED) calculations. We emphasize that the identification of the relevant asymptotic structures of the vertex functions in frequency and momentum space and the resulting reduced parametrizations are extremely valuable for an efficient implementation of several other many-body approaches beyond fRG & PA, such as the dynamical vertex approximation[13–17,8] (DΓA), the one-particle irreducible approach[18], DMF^{2}RG,[19] dual fermion[20–25] (DF), TRILEX[26,27] and QUADRILEX[28].

The paper is organized as follows: We introduce the formalism and notation at the two-particle level in Sec. II, and the parametrization of the asymptotics in Sec. III. The generic implementation is presented in Sec. IV, with some technical details specified in the appendices. After

a short discussion of analytical results obtained in the atomic limit, we describe the specific implementations for the fRG and the parquet solvers. In Sec. V we then provide a discussion of the obtained results together with a comparison to exact results of the SIAM. A conclusion and outlook is eventually provided in Sec. VI.

II. DIAGRAMMATIC FORMALISM AT THE TWO-PARTICLE LEVEL

In this section we present a concise summary of the general formalism for two-particle vertex functions and of their generic frequency and momentum structures. In particular, we recall how their high-frequency asymptotic behavior can be qualitatively related to the lowest-order perturbation theory diagrams. While a comprehensive investigation of the physical interpretation of the different structures can be found in Sec. III and in Refs. [4,7], we focus here mainly on aspects which are relevant for the algorithmic development and the applications presented in this paper.

Although most of the following considerations are valid for a wide range of many-body Hamiltonians, we will restrict ourselves, for the sake of notational simplicity, to one-band systems with a local Coulomb interaction. Specifically, we consider the following Hamiltonian:

$$\hat{\mathcal{H}} = \sum_{ij,\sigma} t_{ij}(\hat{c}^\dagger_{i\sigma}\hat{c}_{j\sigma} + \hat{c}^\dagger_{j\sigma}\hat{c}_{i\sigma}) + \sum_i U_i \hat{n}_{i\uparrow}\hat{n}_{i\downarrow}, \qquad (1)$$

where $\hat{c}^{(\dagger)}_{i\sigma}$ annihilates (creates) an electron with spin σ at the lattice site $\mathbf{R}_i$ and $\hat{n}_{i\sigma} = \hat{c}^\dagger_{i\sigma}\hat{c}_{i\sigma}$. The hopping amplitude for an electron between the lattice sites i and j is denoted by t_{ij} (for $i = j$ this corresponds to setting the energy-level for an electron at site i), while U_i is a (site-dependent) local interaction between electrons of opposite spin.

From the Hamiltonian in Eq. (1) one retains the standard Hubbard model by choosing the parameters $t_{ij} = -t$ if i and j are nearest neighbors and $t_{ij} = 0$ otherwise, and $U_i = U$ (site independent). The restriction $t_{ij} = V_j\delta_{i0}$, $t_{ii} = \varepsilon_i/2$ and $U_i = U\delta_{i0}$, on the other hand, corresponds to the SIAM, where lattice site $\mathbf{R}_0$ is the impurity.

In the following we will consider the two-particle Green's function for the model in Eq. (1), where for the SIAM we will restrict ourselves to the corresponding (purely local) correlation functions at the impurity site. Considering the time -and for the Hubbard model also space- translational invariance of the system, we can work more conveniently in frequency (and momentum) space. To this end, we will adopt both for the SIAM and the Hubbard model the following generalized notation for the frequency and momentum arguments of the Green's functions: k denotes a generalized fermionic, q a generalized bosonic index. For the Hubbard model, this corresponds to the four-vector notation $k = (\nu, \mathbf{k})$ and $q = (\Omega, \mathbf{q})$, where ν is a fermionic and Ω a bosonic Matsubara frequency and $\mathbf{k}$ and $\mathbf{q}$ are momenta in the first Brillouin zone. In the case of the SIAM, k and q correspond simply to the fermionic and bosonic Matsubara frequencies ν and Ω, respectively.

The general definition of the two-particle Green's function G_2 is given explicitly in Appendix A, together with the general relation between the two-particle Green's function and the (full) vertex function F. The latter is obtained from G_2 by first removing all unconnected parts, and by subsequently amputating all outer legs[29]. From a physical perspective, F represents the quasi-particle scattering rate between particles and holes (in parameter regimes where such excitations are well-defined[29]). Diagrammatically, F consists of all connected two-particle diagrams, i.e., all (connected) Feynman diagrams with *two incoming* and *two outgoing* lines (see leftmost diagram in Fig. 1).

One can now decompose the full vertex F into *four* distinct classes of diagrams, that differ in their two-particle irreducibility[1,10,11]. Specifically, a vertex diagram is coined *fully two-particle irreducible* if it cannot be split into two parts by cutting any two internal lines. An example for such a diagram is the second diagram in the upper line of Fig. 1. The sum of all diagrams exhibiting this property is denoted as $\Lambda_{2\mathrm{PI}}$. On the other hand, if a vertex diagram can be separated by cutting two lines, it is referred to as *two-particle reducible*. However, this notion of reducibility is obviously more complicated than in the one-particle situation. In fact, there are *three* possible scenarios for the separation of a diagram. The third, fourth and fifth diagram in the first row of Fig. 1 illustrate this state of affairs: (i) In the third diagram the two incoming particles can be separated from the two outgoing ones by cutting the two Green's functions and, hence, this diagram is coined *particle-particle* reducible. The diagrams of this type sum up to the reducible vertex function Φ_{pp}. (ii) In the fourth diagram of Fig. 1, the lower incoming particle and hole can be separated from the corresponding upper ones. The sum of all such longitudinal particle-hole reducible diagrams is referred to as Φ_{ph}. (iii) Finally, the rightmost diagram can be split in such a way, that one part contains the lower incoming particle and the upper incoming hole and vice versa for the second part. Such diagrams are reducible in the transverse particle-hole channel, and belong to the subset $\Phi_{\overline{ph}}$ of the full vertex F.

It is important to stress that each diagram for the full vertex F belongs to *exactly one* of the four classes: Either it is fully two-particle irreducible ($\Lambda_{2\mathrm{PI}}$) or it is reducible in the *pp*-channel (Φ_{pp}), in the longitudinal *ph*-channel (Φ_{ph}) or in the transverse *ph*-channel[1] ($\Phi_{\overline{ph}}$). Conse-

[1] The orientation of *ph* and $\overline{ph}$ diagrams (horizontal/vertical) is directly linked to the arrangement of the external indices, and is thus a matter of convention.

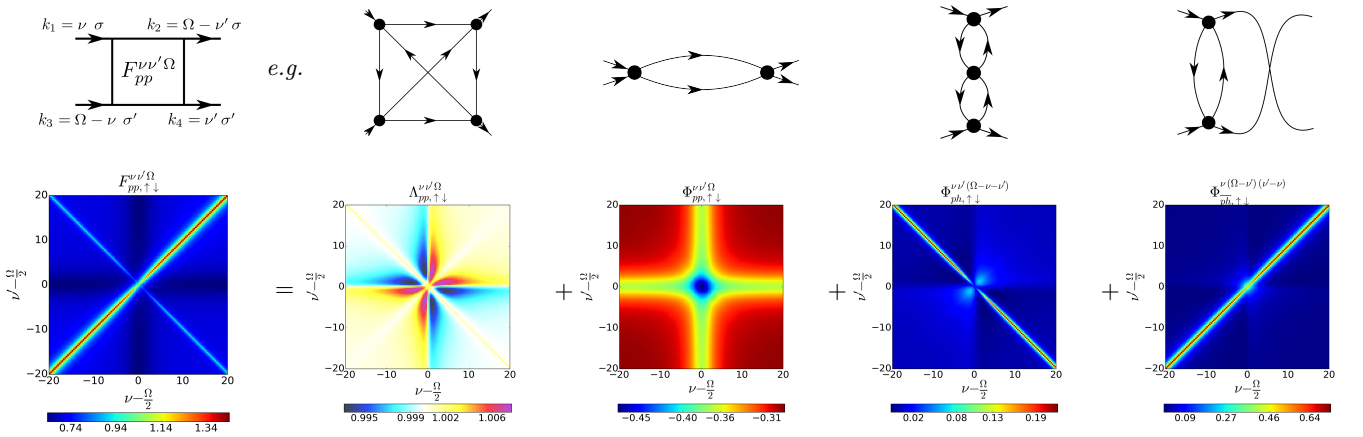

FIG. 1: The upper row shows full vertex $F_{\uparrow\downarrow}$ in *pp*-notation, and the lowest order diagrams (excluding the bare interaction) included in the contributions from the different vertex functions. The bottom row shows the numerical SIAM results for these vertices ($U = 1$, $\beta = 20$, $\Delta(0) = D = 1$) and their connection through the parquet equation (2) using *pp*-notation for vanishing transfer frequency $\Omega = 0$. Notations according to Appendix A. In the diagrammatic representations used throughout this paper, all external legs are to be considered as the remainder of the amputated propagators.

quently, by summing up all four contributions one retrieves the full two-particle scattering amplitude F:

$$F = \Lambda_{\mathrm{2PI}} + \Phi_{pp} + \Phi_{ph} + \Phi_{\overline{ph}}. \tag{2}$$

which is known as *parquet equation*[1,10,11]. It represents a *single* relation for the five quantities F, Λ_{2PI} and Φ_r, with $r \in \{pp, ph, \overline{ph}\}$. Hence, supposed that one of them is known, e.g., the full vertex F, three more relations are necessary to calculate all remaining vertices. To this end we note that we can group together all diagrams which are *not* reducible, i.e., irreducible, in a given channel r, and denote them as Γ_r:

$$\Gamma_r = \Lambda_{\mathrm{2PI}} + \sum_{r' \neq r} \Phi_{r'}, \tag{3}$$

According to Eq. (2) it is then obvious that

$$F = \Gamma_r + \Phi_r, \tag{4}$$

for all three channels r. Eqs. (4) are referred to as Bethe-Salpeter (BS) equations. The crucial observation is now that Φ_r can be expressed by means of a ladder construction in the given channel r in terms of F and Γ_r as it is depicted in Fig. 2. Schematically written, this means that $\Phi_r \sim \Gamma_r G G F$, where G denotes a single-particle Green's function (see also Appendix B). This relation closes the set of Eqs. (2) and (4). Let us note that the explicit frequency/momentum and spin dependent form of the BS equations is rather involved[4,8,18] and we refer the reader to Appendix B for its specific definitions in all three scattering channels.

Let us remark that for the most efficient treatment of the BS equations, the natural frequency (and momentum) convention in their respective channel r should be adopted. This means that the energy and momentum which is transferred via the ladder (see Fig. 2) is given by the bosonic index q. In the particle-particle notation this is exactly the case for the choice depicted in the first diagram of Fig. 1: Here, the two particles with the frequencies (momenta) k and $q-k$ scatter and transfer the energy (momentum) q to the system. Hence, we refer to the frequency convention indicated in this figure as particle-particle (*pp*) notation. The corresponding natural frequency convention for the longitudinal particle-hole channel (*ph*) can be obtained from the latter one simply by replacing $q \to q + k + k'$. Finally, for the transverse particle-hole channel ($\overline{ph}$) the natural frequency/momentum convention is derived from the *pp*-one by the shifts $k' \to k + q$ and $q \to k + k' + q$.

In their natural frequency/momentum convention the BS equations can be written as simple matrix multiplications in the frequency/momentum space[1,4]. Hence, in the following, we will assume that the corresponding irreducible and reducible vertex functions Γ_r and Φ_r in the three channels $r \in \{pp, ph, \overline{ph}\}$ always depend on their natural frequency/momentum arguments. However, for the parquet equation (2), all vertex functions must be considered in the *same* representation which, hence, re-

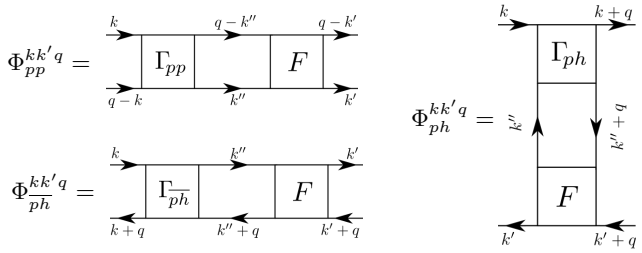

FIG. 2: Compact diagrammatic representation of the Bethe-Salpeter equations in all scattering channels. Each k'' is integrated over.

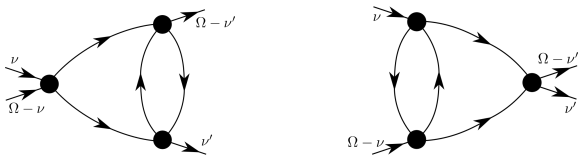

FIG. 3: The so called "eye"-diagrams in the *pp* channel.

quires the inverse of the aforementioned shifts in their frequency/momentum arguments. This corresponds exactly to the choice of frequency arguments in the vertex functions of Fig. 1.

In the lower panels of Fig. 1 the dependence of the local vertex functions $F_{\uparrow\downarrow}$, $\Lambda_{2\mathrm{PI},\uparrow\downarrow}$ and $\Phi_{r,\uparrow\downarrow}$ on the fermionic frequency arguments ν and ν' is shown, where the *pp*-notation for vanishing transfer frequency $\Omega = 0$ is used. While we restrict ourselves here to the $\uparrow\downarrow$ spin combination, we stress that analogous features are found also in $F^{\nu\nu'(\Omega=0)}_{pp,\uparrow\uparrow}$ and even at finite transfer frequencies $\Omega \neq 0$. Investigating the full vertex $F^{\nu\nu'(\Omega=0)}_{pp,\uparrow\downarrow}$ (leftmost panel) we can identify three main features: (i) There is a constant background *different* from the (constant) bare Coulomb interaction U. (ii) We observe two diagonal structures which we will refer to as main (for $\nu = \nu'$) and secondary (for $\nu = -\nu'$) diagonal. (iii) $F^{\nu\nu'(\Omega=0)}_{pp,\uparrow\downarrow}$ exhibits also a "plus"-like structure, i.e., an enhanced scattering rate along the lines $\nu = \pm\pi/\beta$ and $\nu' = \pm\pi/\beta$. Remarkably, these features do *not* decay, even in the limit of large fermionic frequencies and give, hence, rise to a highly non-trivial asymptotic behavior of the vertex functions. In order to explain their origin, we will analyze in the following the frequency structures of the four building blocks of F, i.e., of the fully irreducible vertex $\Lambda_{2\mathrm{PI}}$ and its corresponding reducible counterparts Φ_r. Our strategy will be guided by the comprehension of the frequency behavior of the lowest order perturbation diagrams for each of these sub-parts of the full vertex.

As for the fully irreducible vertex $\Lambda^{\nu\nu'(\Omega=0)}_{2\mathrm{PI},pp,\uparrow\downarrow}$, we can see that it decays uniformly in all directions of the two-dimensional (Matsubara) frequency space. Hence, $\Lambda^{\nu\nu'(\Omega=0)}_{2\mathrm{PI},pp,\uparrow\downarrow}$ does not contribute to the asymptotic structures of the two-particle scattering amplitude $F^{\nu\nu'(\Omega=0)}_{pp,\uparrow\downarrow}$ (except for the trivial constant background given by the interaction U). Beyond this numerical observation, the asymptotic behavior of $\Lambda_{2\mathrm{PI}}$ can be justified also through the analysis of its diagrammatic structure, exemplified by the "envelope"-diagram (second diagram from the left in Fig. 1). As it has been discussed in detail in Ref. [4], $\Lambda_{2\mathrm{PI},pp}$ does indeed depend explicitly on ν and ν' (and Ω) and, hence, it decays for a large value for any of its frequency arguments[2].

[2] Every frequency dependence of a diagram originates from the frequency dependence of the corresponding Green's functions. The latter decay in the asymptotic high frequency regime as $1/i\nu$.

Turning to the diagrams reducible in the particle-particle scattering channel, i.e., $\Phi^{\nu\nu'(\Omega=0)}_{pp,\uparrow\downarrow}$ (third panel in Fig. 1), they exhibit *two* of the three asymptotic frequency structures of $F^{\nu\nu'(\Omega=0)}_{pp,\uparrow\downarrow}$. Specifically, one can identify a constant background and a well-defined "plus"-structure. The background can be immediately understood by analyzing the second order diagram depicted above the plot of $\Phi_{pp,\uparrow\downarrow}$. This is given by the bubble-term

$$\frac{U^2}{\beta}\sum_{\nu_1} G(\nu_1)G(\Omega-\nu_1), \tag{5}$$

which -evidently- does not depend explicitly on ν and ν'. Hence, bubble diagrams of this type are responsible for the constant background observed in the particle-particle reducible vertex, and, consequently, in the full vertex F. The "plus"-structure, on the other hand, originates, in lowest order, from the so-called "eye"-diagrams (see Fig. 3), which either on their left or on their right hand side collapse into a bare vertex U. For this reason (as detailed in Sec. III), they cannot explicitly depend on both ν and ν', thus remaining constant upon increasing the corresponding (unnecessary) frequency[4].

Let us now consider the vertex function reducible in the particle-hole (longitudinal) channel, i.e., $\Phi^{\nu\nu'(\Omega-\nu-\nu')}_{ph,\uparrow\downarrow}$ (fourth density plot from the left in Fig. 1). One can clearly see that this vertex exhibits a secondary diagonal structure along $\nu' = -\nu$. Again, we can gain insight about the origin of this feature by analyzing the lowest order in U perturbative diagram of this vertex. For the $\uparrow\downarrow$-channel considered here, this is of third order in U, as the bare bubble term vanishes as a result of spin conservation. It is given by the fourth diagram (from the left) in Fig. 1, and reads (*pp*-notation)

$$\frac{U^3}{\beta^2}\left[\sum_{\nu_1} G(\nu_1)G(\nu_1-\Omega+\nu+\nu')\right]^2, \tag{6}$$

i.e., it depends only on the *ph* transfer frequency $\Omega - \nu - \nu'$ rather than the two fermionic frequencies ν and ν' separately. Consequently, for fixed *pp* transfer Ω, its value remains constant along a line $\Omega - \nu - \nu' = \text{const}$ and, thus, generates the secondary diagonal structure.

Finally, we turn our attention to the vertex reducible in the transverse particle-hole channel, $\Phi^{\nu(\Omega-\nu')(\nu'-\nu)}_{\overline{ph},\uparrow\downarrow}$. Obviously, it accounts for the main diagonal in the full scattering amplitude $F^{\nu\nu'(\Omega=0)}_{pp,\uparrow\downarrow}$. Once again, the analysis of its lowest order (bubble) contribution allows for an intuitive explanation of this feature. It is given by the last

diagram in Fig. 1, which reads explicitly (pp-notation)

$$\frac{U^2}{\beta}\sum_{\nu_1} G(\nu_1)G(\nu_1+\nu'-\nu), \tag{7}$$

and depends only on the $\overline{ph}$ transfer frequency $\nu'-\nu$. Consequently, its value remains constant along a line $\nu'-\nu=$ const and, hence, generates the main diagonal structure.

The above analysis demonstrates that the high-frequency asymptotic features of the vertex functions in the weak coupling regime are determined at the second and third order in U by two-particle reducible bubble- and "eye"-like diagrams. A generalization of these conclusions to the non-perturbative regime will be discussed in the following Section.

III. PARAMETRIZATION OF THE ASYMPTOTICS

In the following, we will generalize the discussion of the previous section about the main (asymptotic) structures of the various vertex functions to the non-perturbative situation. To this end, we first note that the reduced complexity of specific diagrams regarding their frequency and momentum dependence is *not* a peculiarity of low(est) order perturbation theory but rather a general consequence of the frequency and momentum independence of the bare Coulomb (Hubbard) interaction U. In fact, if any two external lines of the vertex, e.g., the incoming momenta and frequencies k_1 and k_3, are attached to the same bare vertex U, energy and momentum conservation requires $k_1+k_3=k'+k''$ where k' and k'' denote internal frequencies/momenta which are summed. Obviously, in this situation the entire diagram does depend only on the linear combination k_1+k_3 rather than k_1 and k_3 separately. Such a behavior has been already observed for lowest order perturbative (bubble and "eye") diagrams in the previous section, and does not change, as a matter of course, upon dressing these diagrams by means of vertex corrections. These insights hence suggest the following subdivision of the reducible vertex function $\Phi_{pp}^{kk'q}$ (and correspondingly for the other two channels) into three distinct classes, that are depicted diagrammatically in Fig. 4:

- Class 1: The ingoing *and* outgoing frequencies/momenta are attached to the same bare vertex. These diagrams correspond to (dressed) bubble diagrams (see first line of Fig. 4), and can hence be parametrized by a *single* (bosonic) transfer frequency and momentum $q=k_1+k_3$. The sum of all diagrams of this class will be denoted by $\mathcal{K}_{1,pp}^{q}$.
- Class 2: Either the incoming *or* the outgoing frequencies/momenta are attached to the same bare vertex. These diagrams correspond to (dressed) eye diagrams (see, e.g., Fig. 3 and first two diagrams in the second line of Fig. 4). These diagrams depend on the bosonic transfer frequency/momentum $q=k_1+k_3$ and one fermionic frequency $k=k_1$ or $k'=k_4$, respectively. The sum of such types of diagrams will be denoted as $\mathcal{K}_{2,pp}^{kq}$ and $\overline{\mathcal{K}}_{2,pp}^{k'q}$.
- Class 3: Every external frequency/momentum is attached to a different bare vertex. These diagrams depend independently on *all three* external arguments. Their sum will in the following be referred to as the "rest" function, denoted by $\mathcal{R}_{pp}^{kk'q}$. It is illustrated diagrammatically by the last diagram in the second row of Fig. 4.

Based on this classification, we can thus introduce an (a priori exact) decomposition of each reducible Φ-function into these four terms[3]. In the particle-particle channel it reads[4]

$$\Phi_{pp}^{kk'q}=\mathcal{K}_{1,pp}^{q}+\mathcal{K}_{2,pp}^{kq}+\overline{\mathcal{K}}_{2,pp}^{k'q}+\mathcal{R}_{pp}^{kk'q}. \tag{8}$$

In the same way we can decompose also the other scattering channels ph and $\overline{ph}$. It is important to note that the structures arising due to $\mathcal{K}_1$, $\mathcal{K}_2$ and $\overline{\mathcal{K}}_2$ extend to infinitely large frequencies and, hence, generate a highly non-trivial high-frequency asymptotic behavior of the corresponding vertex function.

On the contrary, the diagrammatic content of $\mathcal{R}$ implies a decay in all frequency directions, since each external fermionic frequency will enter directly one of the inner diagrammatic propagator lines by means of the frequency conservation at its attached bare vertex. These decay properties are verified numerically in Sec. V, and motivate our proposed approximation for treating the vertex asymptotics. Our strategy will be the following: We will explicitly consider the full frequency dependence of the Φ-functions only in a small frequency window, while the third class of diagrams ($\mathcal{R}$) will be neglected at larger frequencies, i.e.,

$$\Phi_{pp,\text{asympt.}}^{kk'q}\approx\mathcal{K}_{1,pp}^{q}+\mathcal{K}_{2,pp}^{kq}+\overline{\mathcal{K}}_{2,pp}^{k'q}. \tag{9}$$

One can see that the reducible vertex $\Phi_{pp}^{kk'q}$ is described by functions of *at most two* arguments in the asymptotic

---

[3] Note that for $\mathcal{K}_1$, $\mathcal{K}_2$ and $\overline{\mathcal{K}}_2$ respectively, the index denotes the reduced number of external arguments required to describe them. These shall in the following be referred to as 'necessary' arguments for the corresponding term.

[4] Let us remark that the concrete form of the argument(s) for $\mathcal{K}_{1,pp}/\mathcal{K}_{2,pp}$ depend(s) on the chosen frequency/momentum convention. The dependence on one/two *single* argument(s) becomes apparent only in its natural notation, while for other conventions, $\mathcal{K}_{1,pp}/\mathcal{K}_{2,pp}$ will depend on one/two linear combination(s) of all frequencies/momenta. Nevertheless, these functions will be constant along two-dimensional planes/one-dimensional lines in the space of three frequencies/momenta (in the natural notation these planes/lines are parallel to the coordinate axes).

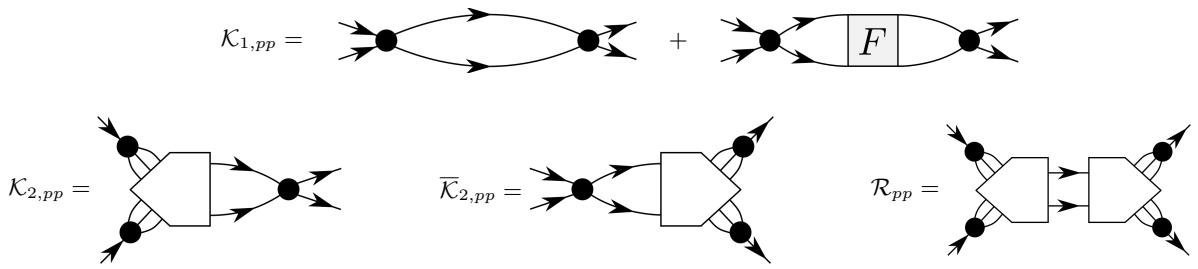

FIG. 4: Diagrammatic representation of the asymptotic functions for the particle-particle channel. For a more rigorous definition see Appendix C.

regime, which drastically lowers the cost for its numerical treatment. This way, we are able to (i) determine the reducible vertex Φ_{pp} up to arbitrarily large frequencies with a reduced computational effort, and (ii) avoid any problem arising from boundary effects due to finite-size frequency grids in vertex-based numerical algorithms.

Let us stress that, whenever momenta are considered, the decay of $\mathcal{R}$ in the frequency domain implies that the reducible vertices Φ exhibit their full momentum dependence only in the domain of small frequencies. At larger frequency values, where the reducible vertex function is determined by at most two of the asymptotic functions, the momentum dependence is reduced alongside the frequencies. This matter will become evident in the following Sec. IV. The same argument holds for the fully irreducible vertex $\Lambda_{2\mathrm{PI}}$, which decays to the value of the bare interaction in all frequency directions. As a consequence, strongly momentum dependent parts of the vertex F, e.g. the contributions responsible for a d-wave scattering amplitude, have to be localized in the frequency domain.

Let us now discuss the physical content of the asymptotic functions $\mathcal{K}_1$ and $\mathcal{K}_2$. The former is directly linked to the susceptibility in the corresponding scattering channel[3,4,7,18]. In fact, they are equal up to a prefactor U^2, i.e.

$$\mathcal{K}_1^q = -U^2 \chi^q, \tag{10}$$

with χ^q defined according to Appendix A (compare Eqs. (A8 and (.

$\mathcal{K}_2$ on the other hand encodes information about how the electrons couple to different bosonic degrees of freedom. For instance, for the generalized density in Fourier space $n_q = \int\!\!\!\!\!\!\int dk \ \sum_\sigma c_\sigma^\dagger(k) c_\sigma(k+q)$, we find the relation

$$\begin{aligned} &U \times \langle \mathcal{T} n_q c_\sigma(k+q) c_\sigma^\dagger(k) \rangle_c = \\ &G_\sigma(k) G_\sigma(k+q) \sum_{\sigma'} \left(\mathcal{K}^q_{1,ph,\sigma\sigma'} + \mathcal{K}^{kq}_{2,ph,\sigma\sigma'} \right). \end{aligned} \tag{11}$$

Here, $\langle \ldots \rangle_c$ considers only connected contractions, and the imaginary time-ordering acts inside the Fourier-integrals, and $\int\!\!\!\!\!\!\int$ denotes the generalized four-vector integration as introduced in Appendix A. The above equation identifies the sum of $\mathcal{K}_1$ and $\mathcal{K}_2$ with the expectation value $\langle \mathcal{T} n_q c_\sigma(k+q) c_\sigma^\dagger(k) \rangle_c$, which is directly related to the electron-boson coupling (three-point or Hedin) vertex as used in the ladder version of DΓA[13,30] and the recently introduced TRILEX[26,27] approach.

IV. IMPLEMENTATION

In this section, we describe how the ideas presented in the previous section can be practically exploited in analytical and numerical calculations based on two-particle vertex functions. After a general presentation of the main concepts, we will explicitly discuss the application of our scheme for analytic calculations based on the atomic limit vertex, and for numerical implementations of the fRG in its second order truncation and the parquet approximation.

The observation that any diagram vanishes if one of its necessary frequency arguments is taken to infinity allows us to select the different diagrammatic contributions by taking the corresponding limits in the frequency domain, i.e.

$$\lim_{|\nu|\to\infty} \lim_{|\nu'|\to\infty} \Phi^{kk'q}_{r,\sigma\sigma'} = \mathcal{K}^q_{1,r,\sigma\sigma'}, \tag{12a}$$

$$\lim_{|\nu'|\to\infty} \Phi^{kk'q}_{r,\sigma\sigma'} = \mathcal{K}^q_{1,r,\sigma\sigma'} + \mathcal{K}^{kq}_{2,r,\sigma\sigma'}, \tag{12b}$$

$$\lim_{|\nu|\to\infty} \Phi^{kk'q}_{r,\sigma\sigma'} = \mathcal{K}^q_{1,r,\sigma\sigma'} + \overline{\mathcal{K}}^{k'q}_{2,r,\sigma\sigma'}, \tag{12c}$$

where $r \in \{pp, ph, \overline{ph}\}$. We stress again the fact that, by taking limits in the frequency domain, we find alongside the reduced frequency dependence also a reduced momentum dependence. The remaining diagrammatic class 3 introduced in Sec. III, or rest function $\mathcal{R}$, which requires the full dependence on all arguments, can then be acquired by inverting Eq. (8)

$$\mathcal{R}^{kk'q}_{r,\sigma\sigma'} = \Phi^{kk'q}_{r,\sigma\sigma'} - \mathcal{K}^q_{1,r,\sigma\sigma'} - \mathcal{K}^{kq}_{2,r,\sigma\sigma'} - \overline{\mathcal{K}}^{k'q}_{2,r,\sigma\sigma'}. \tag{13}$$

One advantage of performing this limiting procedure based on the reducible vertex, is that Eq. (12a) holds equally if $|\nu|$ and $|\nu'|$ are taken to infinity at the same time, i.e.

$$\lim_{\substack{|\nu|\to\infty \\ |\nu'|\to\infty}} \Phi^{kk'q}_{r,\sigma\sigma'} = \mathcal{K}^q_{1,r,\sigma\sigma'}. \tag{14}$$

This property allows for a simplified scanning procedure to numerically extract asymptotic functions, which, depending on the frequency ranges and parameters, provide a good approximation.

The procedure is straightforward and applicable in all channels (see also Fig. 5 and Ref. 8):

- I: For large $|\nu|$ and $|\nu'|$ vary the transfer four-vector q to acquire $\mathcal{K}_1^q$.
- II: For large $|\nu'|$, vary k and the transfer four-vector q and subtract $\mathcal{K}_1^q$ in order to obtains $\mathcal{K}_2^{kq}$.
- III: Repeat II by replacing $\nu' \to \nu$ and $k \to k'$ to determine $\overline{\mathcal{K}}_2^{k'q}$.

The above described procedure proposed to determine $\mathcal{K}_1$ and $\mathcal{K}_2$ has some limitations. Firstly, one can easily see that if the scanning is not performed at sufficiently large $|\nu|$ ($|\nu'|$), the rest function might not be fully decayed, giving rise to an error in the $\mathcal{K}_1$ and $\mathcal{K}_2$ extraction. We found this error to be particularly pronounced in the strong coupling regime ($U = 4$ for the comparisons in Sec. V) where the rest function becomes comparable with the asymptotic functions in the domain of small frequencies. Secondly, the scanning procedure requires the knowledge of the reducible vertex functions Φ_r, which are not directly available in some algorithms, as e.g. for the exact diagonalization. This raises the question whether a similar set of limits can be formulated also for F. And in fact, as will be clarified in the following, the limits

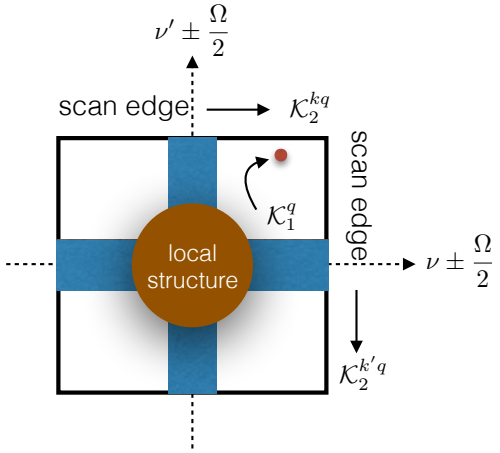

FIG. 5: Sketch of reducible vertex function in frequency space as a function of k and k' for fixed q, it consists of mainly two extensive stripes and a more dynamical structure locally centered at a position determined by the transfer frequency. The two stripes are described by $\mathcal{K}_{2,r}^{kq}$ and $\mathcal{K}_{2,r}^{k'q}$, the local structure is contained in the rest function $\mathcal{R}$. The nearly constant background is described by $\mathcal{K}_{1,r}^q$.

presented in Eq. (12) still hold, i.e.

$$\lim_{|\nu|\to\infty}\lim_{|\nu'|\to\infty} F_{r,\sigma\sigma'}^{kk'q} - (1-\delta_{\sigma,\sigma'})U = \mathcal{K}_{1,r,\sigma\sigma'}^{q}, \tag{15a}$$

$$\lim_{|\nu'|\to\infty} F_{r,\sigma\sigma'}^{kk'q} - (1-\delta_{\sigma,\sigma'})U = \mathcal{K}_{1,r,\sigma\sigma'}^{q} + \mathcal{K}_{2,r,\sigma\sigma'}^{kq}, \tag{15b}$$

$$\lim_{|\nu|\to\infty} F_{r,\sigma\sigma'}^{kk'q} - (1-\delta_{\sigma,\sigma'})U = \mathcal{K}_{1,r,\sigma\sigma'}^{q} + \overline{\mathcal{K}}_{2,r,\sigma\sigma'}^{k'q}, \tag{15c}$$

where again F_r denotes the representation of F in one of the three mixed notations. However, the numerical equivalent of the limiting procedure, i.e. the scanning procedure previously described for the Φ-functions, is not feasible in the case of F, which is directly related to the fact that Eq. (14) does not hold equally for F. In order to numerically extract the asymptotics from F directly we thus suggest an alternative approach detailed in Appendix C. We implemented this diagrammatic extraction to determine the exact asymptotic functions, as presented in Sec. V, from ED calculations.

The limiting procedure Eq. (15) is however particularly suited in the case that analytical expressions for F are available, as demonstrated for the atomic limit case in Sec. IV A. Let us thus argue why this generalization of Eq. (12) holds. It relies on the property that any reducible diagram vanishes if the corresponding transfer frequency, being a necessary argument, is sufficiently large, i.e.

$$\lim_{|\Omega|\to\infty} \Phi_{r,\sigma\sigma'}^{kk'q} = 0. \tag{16}$$

We have to further consider, that in order to take the limits in Eq. (15), we should formulate Eq. (2) in the corresponding mixed notation. E.g. for the particle-particle channel we have to translate Φ_{ph} and $\Phi_{\overline{ph}}$ to the pp-notation as follows

$$\begin{aligned} F_{pp,\sigma\sigma'}^{kk'q} = &\Phi_{pp,\sigma\sigma'}^{kk'q} + \Phi_{ph,\sigma\sigma'}^{kk'(q-k'-k)} + \Phi_{\overline{ph},\sigma\sigma'}^{k(q-k')(k'-k)} \\ &+ \Lambda_{2\mathrm{PI},pp,\sigma\sigma'}^{kk'q}. \end{aligned} \tag{17}$$

It now becomes clear that for fixed Ω and ν', the bosonic frequencies of the ph and $\overline{ph}$ channel, that is $\Omega - \nu' - \nu$ and $\nu' - \nu$, will lead to a vanishing of the respective scattering channels for $|\nu| \to \infty$. This behavior can also be observed in Fig. 1, and holds equally for the other scattering channels. Since $\Lambda_{2\mathrm{PI}}$ decays in all frequency directions to the bare interaction, we conclude that $\lim_{|\nu|\to\infty} F_{r,\sigma\sigma'}^{kk'q} - (1-\delta_{\sigma,\sigma'})U = \lim_{|\nu|\to\infty} \Phi_{r,\sigma\sigma'}^{kk'q}$, while the same argument can be made for the other limits in Eq. (15).

A. The atomic limit

As a first showcase of these ideas we discuss the vertex decomposition for a system that can be treated analyti-

cally, i.e., the atomic limit, whose Hamiltonian reads

$$\hat{\mathcal{H}} = U\left[\hat{n}_\uparrow\hat{n}_\downarrow - \frac{1}{2}(\hat{n}_\uparrow + \hat{n}_\downarrow)\right]. \tag{18}$$

Here, $\hat{n}_\sigma = \hat{c}^\dagger_\sigma\hat{c}_\sigma$ is the number operator for fermions of spin σ, and we have imposed the half-filling (particle-hole symmetry) condition $\mu = U/2$. The Hilbert space is spanned by the four eigenstates $|0\rangle$, $|\uparrow\rangle$, $|\downarrow\rangle$ and $|\uparrow\downarrow\rangle$, allowing for a direct calculation of the two-particle Green's functions by means of the Lehmann representation. The resulting two-particle vertex function[4,5,31] is, for our purposes, split into four terms (note $\mathcal{F}_r \neq F_r$)

$$F_{\uparrow\downarrow} = \mathcal{F}_{\rm odd} + \mathcal{F}_{pp} + \mathcal{F}_{ph} + \mathcal{F}_{\overline{ph}}, \tag{19}$$

which are defined in the following. The first term contains only odd orders in the interaction, and takes the most compact form in the purely fermionic notation

$$\mathcal{F}^{\nu_1\nu_2\nu_3\nu_4}_{\rm odd} = U - \frac{U^3}{8}\frac{\sum_i \nu_i^2}{\prod_i \nu_i} - \frac{3U^5}{16}\prod_i \frac{1}{\nu_i}, \tag{20}$$

while the functions $\mathcal{F}_r$ with $r \in \{pp, ph, \overline{ph}\}$ are more conveniently expressed in their respective mixed notation (see Appendix A)

$$\mathcal{F}^{\nu\nu'\Omega}_{pp} = -\beta\,\delta_{\Omega,0}\frac{U^2}{2}\mathcal{D}^{\nu\nu'} f\left(\frac{U}{2}\right), \tag{21a}$$

$$\mathcal{F}^{\nu\nu'\Omega}_{ph} = -\beta\,\delta_{\Omega,0}\frac{U^2}{4}\mathcal{D}^{\nu\nu'}\left[f\left(\frac{U}{2}\right) - f\left(-\frac{U}{2}\right)\right], \tag{21b}$$

$$\mathcal{F}^{\nu\nu'\Omega}_{\overline{ph}} = \quad\beta\,\delta_{\Omega,0}\frac{U^2}{2}\mathcal{D}^{\nu\nu'} f\left(-\frac{U}{2}\right), \tag{21c}$$

with $\mathcal{D}^{\nu\nu'} = \frac{1}{\nu^2\nu'^2}\left(\nu^2 + \frac{U^2}{4}\right)\left(\nu'^2 + \frac{U^2}{4}\right)$ and the Fermi function $f(\epsilon) = \frac{1}{1+e^{\beta\epsilon}}$. Note that, at this stage, the decomposition for the full vertex F is motivated solely by algebraic reasons, while the connection to the physical scattering channels will be established in the following.

Let us now use the limits in Eqs. (15) to identify the contributions arising from the different diagrammatic classes. This task can be performed by considering each term in Eq. (19) separately. Let us illustrate this procedure for the *pp*-channel, beginning with the first term, $\mathcal{F}_{\rm odd}$. Here, we have to translate from the purely fermionic notation to the mixed *pp*-notation:

$$\mathcal{F}^{\nu\nu'\Omega}_{\rm odd,pp} = \mathcal{F}^{\nu,\Omega-\nu',\Omega-\nu,\nu'}_{\rm odd} = U - \frac{3U^5}{16}\frac{1}{\nu(\Omega-\nu')(\Omega-\nu)\nu'} - \frac{U^3}{8}\frac{\nu^2 + (\Omega-\nu')^2 + (\Omega-\nu)^2 + \nu'^2}{\nu(\Omega-\nu')(\Omega-\nu)\nu'}. \tag{22}$$

The large frequency limits then result in

$$\lim_{|\nu|\to\infty}\lim_{|\nu'|\to\infty}\mathcal{F}^{\nu\nu'\Omega}_{\rm odd,pp} = U, \tag{23a}$$

$$\lim_{|\nu'|\to\infty}\mathcal{F}^{\nu\nu'\Omega}_{\rm odd,pp} = U - \frac{U^3}{4}\frac{1}{\nu}\frac{1}{\nu-\Omega}, \tag{23b}$$

$$\lim_{|\nu|\to\infty}\mathcal{F}^{\nu\nu'\Omega}_{\rm odd,pp} = U - \frac{U^3}{4}\frac{1}{\nu'}\frac{1}{\nu'-\Omega}. \tag{23c}$$

As for the limits of the second term, $\mathcal{F}_{pp}$, we have

$$\lim_{|\nu|\to\infty}\lim_{|\nu'|\to\infty}\mathcal{F}^{\nu\nu'\Omega}_{pp} = -\beta\,\delta_{\Omega,0}\frac{U^2}{2}f\left(\frac{U}{2}\right), \tag{24a}$$

$$\lim_{|\nu'|\to\infty}\mathcal{F}^{\nu\nu'\Omega}_{pp} = -\beta\,\delta_{\Omega,0}\frac{U^2}{2}\left[1 + \frac{U^2}{4}\frac{1}{\nu^2}\right]f\left(\frac{U}{2}\right), \tag{24b}$$

$$\lim_{|\nu|\to\infty}\mathcal{F}^{\nu\nu'\Omega}_{pp} = -\beta\,\delta_{\Omega,0}\frac{U^2}{2}\left[1 + \frac{U^2}{4}\frac{1}{\nu'^2}\right]f\left(\frac{U}{2}\right). \tag{24c}$$

Determining the contributions from the remaining terms $\mathcal{F}_{ph}$ and $\mathcal{F}_{\overline{ph}}$, which involves a translation from their respective mixed notation to the *pp*-notation, we find that their contributions vanish. This leads to the final expressions for the asymptotic functions in the *pp*-channel

$$\mathcal{K}^{\Omega}_{1,pp,\uparrow\downarrow} = -\beta\,\delta_{\Omega,0}\frac{U^2}{2}f\left(\frac{U}{2}\right), \tag{25a}$$

$$\mathcal{K}^{\nu\Omega}_{2,pp,\uparrow\downarrow} = \frac{U^2}{4}\frac{1}{\nu}\frac{1}{\nu-\Omega}\left(\mathcal{K}^{\Omega}_{1,pp,\uparrow\downarrow} - U\right), \tag{25b}$$

while the $\overline{\mathcal{K}}_2$ can be acquired by means of the symmetry properties reported in Appendix D. Performing the analogous procedure for the remaining two channels yields

$$\mathcal{K}^{\Omega}_{1,ph,\uparrow\downarrow} = -\beta\,\delta_{\Omega,0}\frac{U^2}{4}\left[f\left(\frac{U}{2}\right) - f\left(-\frac{U}{2}\right)\right], \tag{26a}$$

$$\mathcal{K}^{\nu\Omega}_{2,ph,\uparrow\downarrow} = \frac{U^2}{4}\frac{1}{\nu}\frac{1}{\nu+\Omega}\left(\mathcal{K}^{\Omega}_{1,ph,\uparrow\downarrow} - U\right), \tag{26b}$$

for the *ph*-channel, and

$$\mathcal{K}^{\Omega}_{1,\overline{ph},\uparrow\downarrow} = \beta\,\delta_{\Omega,0}\frac{U^2}{2}f\left(-\frac{U}{2}\right), \tag{27a}$$

$$\mathcal{K}^{\nu\Omega}_{2,\overline{ph},\uparrow\downarrow} = \frac{U^2}{4}\frac{1}{\nu}\frac{1}{\nu+\Omega}\left(\mathcal{K}^{\Omega}_{1,\overline{ph},\uparrow\downarrow} - U\right). \tag{27b}$$

in the $\overline{ph}$ case.

Now that we have determined all asymptotic functions of the atomic limit vertex, let us consider its structures that are localized in the frequency domain. We proceed again in a term-wise fashion, beginning with $\mathcal{F}_{\rm odd}$. By subtracting all asymptotic contributions arising from this term, we find that only the fifth order term $-\frac{3U^5}{16}\prod_i \frac{1}{\nu_i}$ survives, while it remains unclear whether this term can

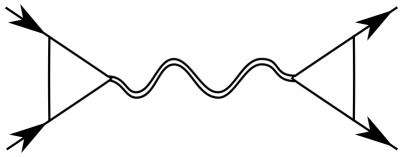

FIG. 6: Schematic diagrammatic representation of the localized structure presented in Eq. (28).

be attributed to the fully irreducible vertex function or the rest functions.

For the $\mathcal{F}_r$ terms, let us again consider the *pp*-channel as an example. Here we find

$$\mathcal{F}_{pp}^{\nu\nu'\Omega} - \lim_{|\nu'|\to\infty} \mathcal{F}_{pp}^{\nu\nu'\Omega} - \lim_{|\nu|\to\infty} \mathcal{F}_{pp}^{\nu\nu'\Omega} + \lim_{|\nu|\to\infty} \lim_{|\nu'|\to\infty} \mathcal{F}_{pp}^{\nu\nu'\Omega} = \left(\frac{U^2}{4}\frac{1}{\nu}\frac{1}{\nu-\Omega}\right) \times \mathcal{K}_{1,pp,\uparrow\downarrow}^{\Omega} \times \left(\frac{U^2}{4}\frac{1}{\nu'}\frac{1}{\nu'-\Omega}\right). \tag{28}$$

This term contains three factors, i.e. a fermion-boson vertex[28] that describes the coupling to a pairing field, the bosonic propagator in the *pp*-channel, and an additional fermion-boson vertex, as depicted schematically in Fig. 6. We can thus argue diagrammatically that this localized term belongs to the rest function $\mathcal{R}_{pp,\uparrow\downarrow}$. For the other channels, we find equally that the localized structures belong to the respective rest function, and hence $\mathcal{F}_r \in \Phi_{r,\uparrow\downarrow}$.

Note that, to obtain the full rest functions as well as the fully irreducible vertex function, it would require the analytic expressions for all the reducible Φ functions, that have so far never been reported in the literature. Their calculation requires the very involved procedure of inverting analytically the Bethe-Salpeter equations, which goes beyond the scope of this paper. The resulting expressions should reproduce the multiple vertex divergencies[32–35] appearing in the Φ functions for $T \leq \frac{\sqrt{3}}{2\pi}U$. As these divergent terms are not present in the full vertex F, they must be subjected to cancellations between Λ_{2PI} and one (or more) of rest functions.

B. Implementation for the fRG solver

The functional renormalization group approach[9,36] implements Wilson's renormalization group idea in a general field-theoretical framework. By introducing a scale-dependence into the quadratic part of the action, i.e. the non-interacting propagator

$$G_0(i\nu) \to G_0^{\Lambda}(i\nu),$$

one can derive an exact functional flow equation[37] for the 1PI generating functional, also named "effective action". This flow equation describes the gradual evolution of all correlation functions as the scale Λ is varied from the initial to the final value. Being an exact reformulation of the initial problem, it serves as a basis for further approximations, and has been used in many different applications ranging from high-energy physics to condensed matter theory. In the fRG, this approximation consists in an expansion in orders of the fields, resulting in an infinite hierarchy of coupled ordinary differential equations for all 1PI n-particle vertex functions, e.g. the self-energy Σ, the two-particle vertex F and so on. This hierarchy is typically truncated at the two-particle level, rendering the fRG perturbative in the interaction strength[38].

For the flow-parameter dependence, we consider in the following two different schemes: The so-called Ω-flow[39]:

$$G_0^{\Lambda}(i\nu) = \frac{\nu^2}{\nu^2+\Lambda^2} G_0(i\nu), \tag{29}$$

and the U-flow[40]:

$$G_0^{\Lambda}(i\nu) = \Lambda \cdot G_0(i\nu). \tag{30}$$

The Ω-flow introduces an energy cutoff into the system, that allows to successively integrate out the different energy scales from high to low. This approach is very much in the spirit of other renormalization group approaches. The U-flow on the other hand introduces a frequency-independent regulator into the Green function that treats all energy scales on a equal footing. In this sense, the U-flow is more similar to common perturbative approaches.

The flow-equations resulting from a second order truncation of the flow-equation hierarchy can be summarized as follows, where, for simplicity, we consider the $SU(2)$ symmetric case. At the level of the self-energy, the derivative takes the simple form

$$\dot{\Sigma}(k)^{\Lambda} = \sum\!\!\!\!\!\!\int dk' \; S^{\Lambda}(k') \times \left[F_{ph,\uparrow\downarrow}^{\Lambda,kk'(q=0)} + F_{ph,\uparrow\uparrow}^{\Lambda,kk'(q=0)}\right], \tag{31}$$

where we have introduced the so-called single-scale propagator

$$S^{\Lambda}(i\nu) = \partial_{\Lambda} G^{\Lambda}(i\nu)|_{\Sigma^{\Lambda}\,\mathrm{fixed}}.$$

At the level of the 1PI two-particle vertex, the flow-equation is composed of contributions from three scattering channels (particle-particle, particle-hole and transverse particle-hole)

$$\dot{F}^{\Lambda} = \mathcal{T}_{pp}^{\Lambda} + \mathcal{T}_{ph}^{\Lambda} + \mathcal{T}_{\overline{ph}}^{\Lambda}, \tag{32}$$

where

$$\mathcal{T}^{\Lambda,kk'q}_{pp,\uparrow\downarrow} = \sum\!\!\!\!\!\!\int dk'' \left[S^\Lambda(k'')G^\Lambda(q-k'') + S \leftrightarrow G\right] \times F^{\Lambda,qkk''}_{pp,\uparrow\downarrow} F^{\Lambda,qk''k'}_{pp,\uparrow\downarrow}, \tag{33a}$$

$$\mathcal{T}^{\Lambda,kk'q}_{ph,\uparrow\downarrow} = -\sum\!\!\!\!\!\!\int dk'' \left[S^\Lambda(k''+q)G^\Lambda(k'') + S \leftrightarrow G\right] \times \left[F^{\Lambda,kk''q}_{ph,\uparrow\uparrow} F^{\Lambda,k''k'q}_{ph,\uparrow\downarrow} + F_{\uparrow\uparrow} \leftrightarrow F_{\uparrow\downarrow}\right], \tag{33b}$$

$$\mathcal{T}^{\Lambda,kk'q}_{\overline{ph},\uparrow\downarrow} = \sum\!\!\!\!\!\!\int dk'' \left[S^\Lambda(k''+q)G^\Lambda(k'') + S \leftrightarrow G\right] \times F^{\Lambda,kk''q}_{\overline{ph},\uparrow\downarrow} F^{\Lambda,k''k'q}_{\overline{ph},\uparrow\downarrow}. \tag{33c}$$

These terms can be depicted diagrammatically as shown in Fig. 7 for the *pp*-channel. To understand the diagrammatic content generated by each channel let us refer to the previously introduced parquet equation, that holds for any scale Λ

$$F^\Lambda = \Lambda^\Lambda_{\text{2PI}} + \Phi^\Lambda_{pp} + \Phi^\Lambda_{ph} + \Phi^\Lambda_{\overline{ph}}. \tag{34}$$

Considering the vertex flow equation Eq. (32) (see also Fig. 7), it is obvious that at this level of truncation, the only diagrammatic content than can be generated by the flow is two-particle reducible, meaning $\Lambda^\Lambda_{\text{2PI}} = \overline{\Lambda}^{\Lambda_{\text{ini}}}_{\text{2PI}}$. We can thus separate the different two-particle reducible terms in Eq. (32), and identify

$$\dot{\Phi}^\Lambda_{pp} = \mathcal{T}_{pp}, \quad \dot{\Phi}^\Lambda_{ph} = \mathcal{T}_{ph}, \quad \dot{\Phi}^\Lambda_{\overline{ph}} = \mathcal{T}_{\overline{ph}}. \tag{35}$$

This allows us to make use of the parametrization scheme described in Sec. III during the fRG flow. While keeping track of the reducible vertex functions on a finite frequency grid, we also track the flow of the previously introduced asymptotic functions. In fact, we can directly perform the limits in Eq. (12) to compute the corresponding derivatives

$$\dot{\mathcal{K}}^{\Lambda,q}_{1,r,\sigma\sigma'} = \lim_{|\nu|\to\infty} \lim_{|\nu'|\to\infty} \dot{\Phi}^{\Lambda,kk'q}_{r,\sigma\sigma'}, \tag{36a}$$

$$\dot{\mathcal{K}}^{\Lambda,kq}_{2,r,\sigma\sigma'} = \lim_{|\nu'|\to\infty} \dot{\Phi}^{\Lambda,kk'q}_{r,\sigma\sigma'} - \dot{\mathcal{K}}^{\Lambda,q}_{1,r,\sigma\sigma'}, \tag{36b}$$

$$\dot{\overline{\mathcal{K}}}^{\Lambda,k'q}_{2,r,\sigma\sigma'} = \lim_{|\nu|\to\infty} \dot{\Phi}^{\Lambda,kk'q}_{r,\sigma\sigma'} - \dot{\mathcal{K}}^{\Lambda,q}_{1,r,\sigma\sigma'}. \tag{36c}$$

In practice, these limits are performed numerically by setting the corresponding frequency to an arbitrarily large value. In doing this, we have to determine F^Λ in the large frequency domain by making use of Eq. (9). In addition to the flow of the Φ-functions we then track, using Eqs. (36), the flow of the asymptotic functions.

Due to the numerical costs involved in treating the full argument dependence of the vertex function, a simplified parametrization scheme[41]

$$\begin{aligned}\Phi^{kk'q}_{pp} \approx \mathcal{K}^q_{\text{eff},pp} = \mathcal{K}^q_{1,pp} + \mathcal{K}^{(\lceil\Omega/2\rceil-\nu_0,\mathbf{k})q}_{2,pp} \\ + \overline{\mathcal{K}}^{(\lceil\Omega/2\rceil-\nu_0,\mathbf{k}')q}_{2,pp} + \mathcal{R}^{(\lceil\Omega/2\rceil-\nu_0,\mathbf{k})(\lceil\Omega/2\rceil-\nu_0,\mathbf{k}')q}_{pp}\end{aligned} \tag{37}$$

has found extensive use in the fRG community. Here, $\nu_0 = \frac{\pi}{\beta}$ denotes the first positive Matsubara frequency, and $\lceil\ldots\rceil$ will round up to the next bosonic Matsubara frequency [5]. This scheme considers only the dominant transfer frequency dependence of the $\mathcal{K}_2$ and $\mathcal{R}$ functions, and will be compared to the full parametrization in Sec. V 3. Performing the same approximation in the momentum domain limits the scattering to the s-wave type, while higher harmonics can be captured by means of a form-factor expansion[42].

The fRG flow equations in their second order truncated form account for the feedback of F^Λ into the flow up to the second order. If we in addition consider partially the neglected contribution of the 1PI three-particle vertex in the flow equations, it is possible to account fully for the feedback up to $\mathcal{O}[(F^\Lambda)^3]$. In practice this is achieved by taking into account both self-energy[6], and vertex corrections from diagrams with overlapping loops[43,44], which is possible with a manageable numerical effort[44]. These corrections will in the following be referred to as two-loop (2ℓ) corrections to distinguish this scheme from the conventional one-loop (1ℓ) one.

When considering the flow of the asymptotic functions, we find that including the two-loop corrections gives a substantial improvement of the two-particle vertex results. While a quantitative comparison between the one- and two-loop scheme will be presented in Sec. V 2, we can already understand from a simple diagrammatic argument that the lowest order contribution to $\mathcal{K}_2$ is not fully captured in the one-loop scheme. Here, the derivative includes four contributions, as depicted in Fig. 8.

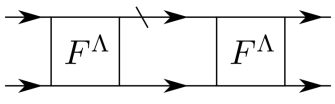

FIG. 7: Diagrammatic representation of the particle-particle contribution $\mathcal{T}_{pp}$ (33a) in the vertex flow equation. The dashed line denotes the single-scale propagator S^Λ.

[5] The parametrization scheme presented in Eq. (37) was originally implemented at zero temperature, where the flow of each channel was determined for vanishing transfer frequency of the other two channels. At finite temperature, this choice is only possible for every other transfer frequency, as the condition $\left(\frac{\beta}{2\pi}\sum_r \Omega_r\right) \bmod 2 = 1$ needs to hold. This leads to ambiguities in the definition.

[6] The self-energy correction $S \to \partial_\Lambda G^\Lambda$ is generally referred to as Katanin-substitution[43].

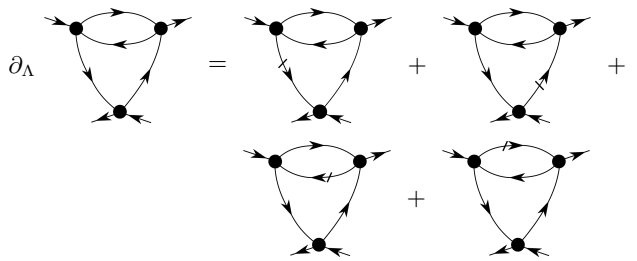

FIG. 8: Derivative of the lowest order contribution to $\mathcal{K}^{\Lambda}_{2,ph}$.

The one-loop scheme accounts only for the first two diagrams, while the two-loop scheme includes all of them. In particular for the U-flow, the contribution from all four diagrams is equal, meaning that in its one-loop implementation the flow reproduces exactly $\frac{1}{2}$ of the exact value for $U \to 0$. This is verified numerically in Sec. V 2 (see Fig. 20). A similar argument can be made for the lowest order diagram of $\mathcal{R}$, where the resulting factor is $\frac{1}{3}$.

C. Implementation for the parquet solver

In this section we discuss the implications of the asymptotic functions $\mathcal{K}_1^q$ and $\mathcal{K}_2^{kq}$ in the context of the parquet equations, that have been previously addressed from a numerical perspective[7] in Ref. 8. We further demonstrate how the diagrams of $\mathcal{K}_1$, $\mathcal{K}_2$ and $\mathcal{R}$ emerge naturally in a self-consistent solution of the parquet approximation.

Given the fully irreducible vertex function Λ_{2PI}, the parquet equations[1] form a closed set of equations for the vertex functions F, Γ_r and Φ_r as well as the self-energy Σ. They can be summarized schematically as

$$F = \Lambda_{\mathrm{2PI}} + \sum_r \Phi_r \qquad \Gamma_r = \Lambda_{\mathrm{2PI}} + \sum_{r' \neq r} \Phi_r \tag{38a}$$

$$\Phi_r = \Gamma_r GGF \qquad \Sigma = U \cdot GGG \cdot F, \tag{38b}$$

while the detailed explicit forms of these equations are presented in Appendix B.

In the following we consider the $SU(2)$ symmetric case, which allows us to decouple the Bethe-Salpeter equations by introducing the density (d), magnetic (m), singlet (s) and triplet (t) channel

$$\Phi_d = \Phi_{ph,\uparrow\uparrow} + \Phi_{ph,\uparrow\downarrow} \qquad \Phi_m = \Phi_{ph,\uparrow\uparrow} - \Phi_{ph,\uparrow\downarrow}, \tag{39a}$$

$$\Psi_s = \Phi_{pp,\uparrow\downarrow} - \Phi_{pp,\overline{\uparrow\downarrow}} \qquad \Psi_t = \Phi_{pp,\uparrow\downarrow} + \Phi_{pp,\overline{\uparrow\downarrow}}, \tag{39b}$$

and F_r, Γ_r, $\mathcal{R}_r$, $\mathcal{K}_{1,r}$ and $\mathcal{K}_{2,r}$ for $r \in \{d, m, s, t\}$ are defined in the same way.

[7] We note that the 'Kernel functions' Φ_r^q and Φ_r^{qk} introduced in Ref. 8 are related to $\mathcal{K}_1$ and $\mathcal{K}_2$ as $\Phi_r^q = \mathcal{K}_{1,r}^q$ and $\Phi_r^{qk} = \mathcal{K}_{1,r}^q + \mathcal{K}_{2,r}^{kq}$

As observed in Ref. 8 and detailed in the previous sections, the reducible two-particle vertices Φ_r play a fundamental role in the correct treatment of the two-particle vertex function F, and thus for the solution of the parquet equations. The closed set of equations (38) is solved self-consistently by using the iterative procedure described in the following. For this solution of the parquet equations, the fact that the asymptotic functions $\mathcal{K}_1$ and $\mathcal{K}_2$ allow us to determine the vertex functions on the whole frequency domain is essential, as every step of the solution requires translations between the different notations as e.g. demonstrated in Eq. (17). If the vertex functions were known only on a finite frequency grid, these translations would lead to a loss of frequencies with every iteration of the parquet equations.

The only approximation that enters in the solution of the parquet equations is the choice of the fully irreducible vertex Λ_{2PI}. In the parquet approximation, it is approximated by its lowest order contribution $\Lambda_{\mathrm{2PI}} \sim U$, while the D$\Gamma$A[8,13,45] approximates Λ_{2PI} by the local one of the effective impurity model. A typical procedure for the solution of the parquet approximation can then be outlined as follows:

1. Choose a finite but sufficiently large frequency range $[-\lambda, \lambda]$ for the problem studied

2. Initialize Σ and the vertex functions Φ_r to 0, or make some educated guess for their starting values. Initialize F and Γ_r according to Eq. (38a).

3. Calculate the reducible vertex functions $\Phi_r^{kk'q}$ with frequency arguments in the range $[-\lambda, \lambda]$ from the Bethe-Salpeter equations [Eq. (38b) left].

4. Determine the asymptotic functions using

$$\mathcal{K}_{1,r}^q = \lim_{|\nu| \to \infty} \lim_{|\nu'| \to \infty} \Phi_r^{kk'q},$$
$$\mathcal{K}_{2,r}^{kq} = \lim_{|\nu'| \to \infty} \Phi_r^{kk'q} - \mathcal{K}_{1,r}^q,$$

   where the limits are performed numerically using the Bethe-Salpeter equations. For an implementation using the scanning procedure outlined in Sec. IV, see Ref. 8.

5. Compute the vertex functions $F_r^{kk'q}$ and $\Gamma_r^{kk'q}$ using the updated values of $\Phi_r^{kk'q}$ [Eq. (38a)]. When any of the three frequency arguments of k, k' or q fall outside of the range $[-\lambda, \lambda]$, we approximate

$$\Phi^{kk'q}_{pp,\mathrm{asympt.}} \approx \mathcal{K}^q_{1,pp} + \mathcal{K}^{kq}_{2,pp} + \overline{\mathcal{K}}^{k'q}_{2,pp}.$$

6. Calculate the self-energy from F through the Schwinger-Dyson equation [Eq. (38b) right].

7. Go back to step 3 and iterate until convergence is achieved.

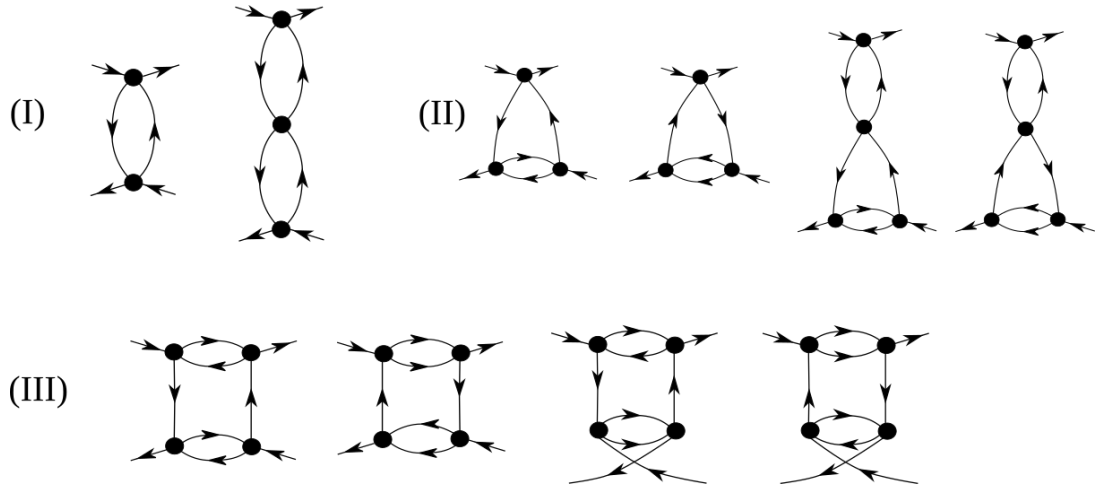

FIG. 9: Part of the Feynman diagrams for the reducible vertex function $\Phi_d^{kk'q}$ generated in the first two iterations of a parquet approximation calculation. The diagrams can be attributed to (I) $\mathcal{K}_{1,d}^q$, (II) $\mathcal{K}_{2,d}^{kq}$ and (III) $\mathcal{R}_d^{kk'q}$ respectively.

Let us now consider diagrams (see Fig. 9 for the d-channel) generated in the first iterations of the parquet approximation solution (assuming initial conditions $\Phi_r = 0$), and attribute them to the diagrammatic classes I ($\mathcal{K}_1$), II ($\mathcal{K}_2, \overline{\mathcal{K}}_2$) and III ($\mathcal{R}$). After the first iteration the reducible vertex functions $\Phi_r^{kk'q}$ read

$$\Phi_d^{kk'q} = U^2\chi_{0,ph}^q \qquad \Phi_m^{kk'q} = U^2\chi_{0,ph}^q, \tag{40a}$$

$$\Psi_s^{kk'q} = -2U^2\chi_{0,pp}^q \qquad \Psi_t^{kk'q} = 0, \tag{40b}$$

where χ_0 denotes the non-interacting bubble (see first diagram in Fig. 9 for the d case). This corresponds to the lowest order perturbation theory for Φ_r, which is only dependent on the transfer frequency and momentum q, and can thus be attributed to $\mathcal{K}_{1,r}$. The dependence of Φ on the fermionic arguments is only generated when the updated vertex functions F and Γ, e.g. for the d-channel

$$F_d^{kk'q} = U - 2U^2\chi_{0,ph}^{k'-k} - U^2\chi_{0,pp}^{k+k'+q} + U^2\chi_{0,ph}^q, \tag{41a}$$

$$\Gamma_d^{kk'q} = U - 2U^2\chi_{0,ph}^{k'-k} - U^2\chi_{0,pp}^{k+k'+q}, \tag{41b}$$

are inserted into the Bethe-Salpeter equation in the second iteration. This produces the remaining diagrams in Fig. 9, and thus the first contributions to the $\mathcal{K}_2$ (II) and $\mathcal{R}$ (III) functions. Iterating this procedure, we generate successively all reducible diagrams. Results obtained by this approach for a SIAM are presented in the following Sec. V.

V. COMPARISON TO EXACT RESULTS OF THE SIAM

In this section we illustrate the high quality of the description of the vertex asymptotics obtained using the algorithmic implementations discussed in the previous sections.

In particular, we present results for the asymptotic functions as obtained from the fRG (Ω-flow including two-loop corrections) and parquet approximation for a single impurity Anderson model and compare them with exact diagonalization data, which were acquired following the procedure outlined in Appendix C. Besides the asymptotic functions, also results for the rest function and the self-energy will be shown. In Sec. V 2 we will further discuss a detailed comparison between the fRG in its one- and two-loop implementation for both the Ω- as well as the U-flow. We first consider the regime of weak coupling where the fRG and the PA, as approximation schemes, are expected to be quantitatively correct. Hence, in this regime, the comparison with the exact results of ED will represent a stringent test for our treatment of the high-frequency asymptotics. After having demonstrated that the error introduced in the high-frequency asymptotics of the vertex function is negligible, we proceed by applying our fRG and PA algorithms, including the high-frequency treatment, to the intermediate to strong coupling regime. In this case, the comparison to the ED will allow us to assess directly the intrinsic performance of the two approximations in the non-perturbative parameter region, because no spurious effects are introduced by an incorrect treatment of the high-frequency part anymore.

The system of interest in this section is a SIAM, i.e. a single impurity site with local repulsive Coulomb interaction U coupled to a non-interacting bath (see Sec. II, Eq. (1)). In our specific case, we consider a box-like density of states

$$\rho(\omega) = \frac{1}{2D}\Theta(D - |\omega|), \tag{42}$$

where D denotes the half-bandwidth, which will be used as our unit of energy, i.e. $D = 1$. This bath is coupled to our impurity site by means of a hopping $t = \sqrt{2/\pi}$, such

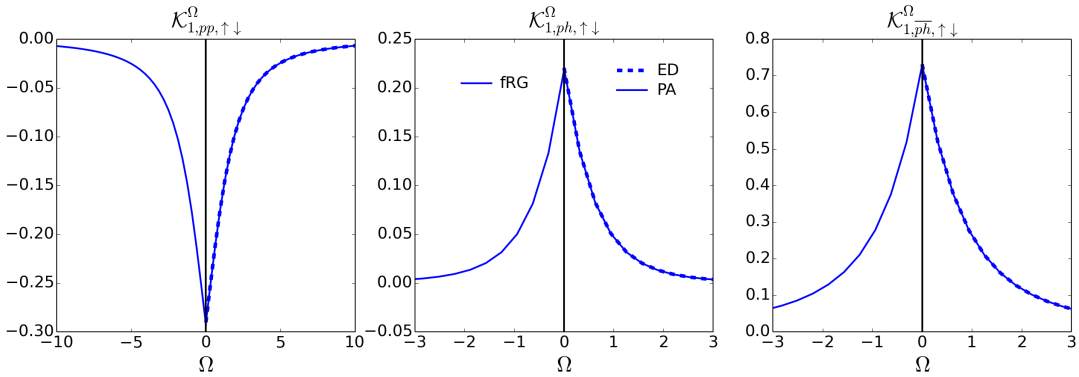

FIG. 10: $K^{\Omega}_{1,\uparrow\downarrow}$ for all three scattering channels. We present results obtained by fRG (left, solid), PA (right, solid) and ED (right, dashed) for the SIAM with $U = 1$, $\beta = 20$ and $\Delta(0) = D = 1$.

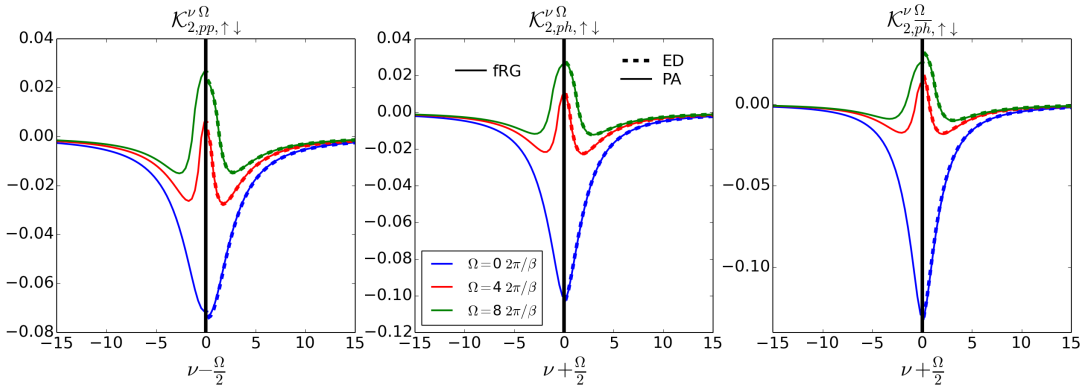

FIG. 11: $K^{\nu\Omega}_{2,\uparrow\downarrow}$ for all three scattering channels as a function of ν and for different values of Ω. We present results obtained by fRG (left, solid), PA (right, solid) and ED (right, dashed) for the SIAM with $U = 1$, $\beta = 20$ and $\Delta(0) = D = 1$.

that the resulting hybridization function reads $\Delta(\omega) = \pi t^2 \rho(\omega) = 2\rho(\omega)$. This choice results in $\Delta(0) = D = 1$, allowing us to directly relate our unit of energy to the one used in wide-band limit calculations[41], namely the hybridization function evaluated at the chemical potential.

However, the exact diagonalization of the SIAM is not possible for $\rho(\omega)$ of Eq. (42). Hence, we have determined a set of four optimized bath energy levels ϵ_n and hoppings t_n with the resulting hybridization function

$$\Delta^{\mathrm{ED}}(i\nu) = \sum_{n=1}^{4} \frac{t_n^2}{i\nu - \epsilon_n}, \tag{43}$$

in order to mimic the continuous bath of Eq. (42) in the best way possible within a discretized ED scheme. Following a somewhat similar strategy as in the ED algorithms for DMFT, we determine our bath parameters such that the norm

$$\sum_{i\nu} |\Delta^{\mathrm{ED}}(i\nu) - \Delta(i\nu)|^2 \tag{44}$$

is minimized. For an inverse temperature $\beta = 20$, which was used for all numerical calculations presented in this paper, we have $\epsilon_n = -0.7, -0.15, 0.15, 0.7$ and $t_n = 0.45, 0.34, 0.34, 0.45$. Note also that, since we are considering the particle-hole symmetric case, all two-particle quantities are purely real, while the self-energy is purely imaginary. Unless mentioned otherwise, calculations are performed with a frequency grid of $128 \times 128 \times 256$ Matsubara frequencies for the Φ-functions, while grids of 128×256 and 256 are chosen for K_2 and K_1 respectively.

Let us start considering the weak-coupling case ($U = 1$). The data for $K_{1,\uparrow\downarrow}$, $K_{2,\uparrow\downarrow}$ and $R_{\uparrow\downarrow}$ are presented in Fig. 10, Fig. 11 and Figs. 12 and 13 respectively[8]. For this parameter choice, we find an excellent agreement between the different approaches and the exact solution for all quantities. At the level of the asymptotic function $K_{1,\uparrow\downarrow}$, no distinction can be made between the results of the different schemes, while for $K_{2,\uparrow\downarrow}$ the fRG shows some minor deviations w.r.t. PA and ED in the *pp* and

[8] The contour plots are created such that every small square of equal color represents the value of the function at the bottom left corner of this square.

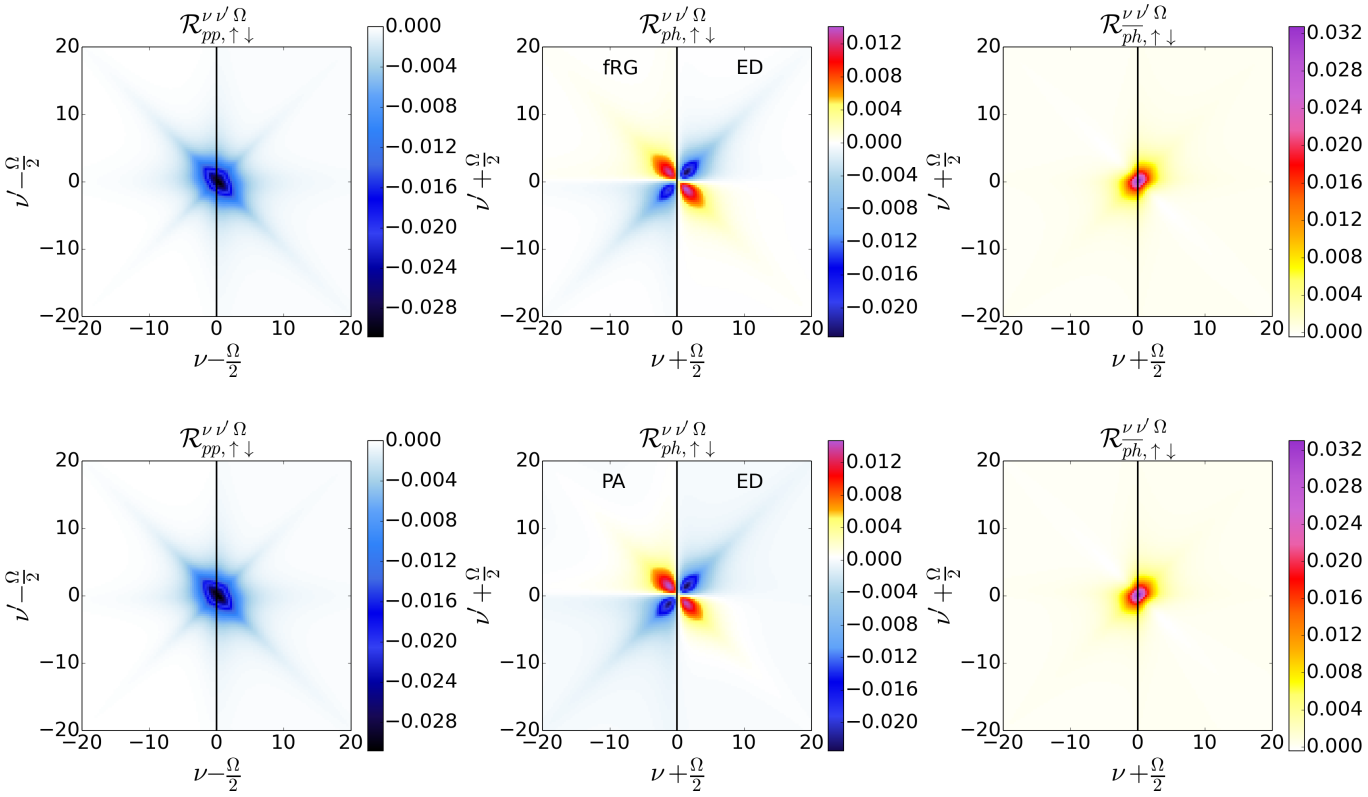

FIG. 12: Rest function $\mathcal{R}^{\nu\nu'\Omega}_{\uparrow\downarrow}$ for all three scattering channels as a function of ν and ν' plotted for $\Omega = 0$. We present results obtained by fRG (1st row, left) and PA (2nd row, left) for the SIAM with $U = 1$, $\beta = 20$ and $\Delta(0) = D = 1$. The right side always shows the corresponding ED result.

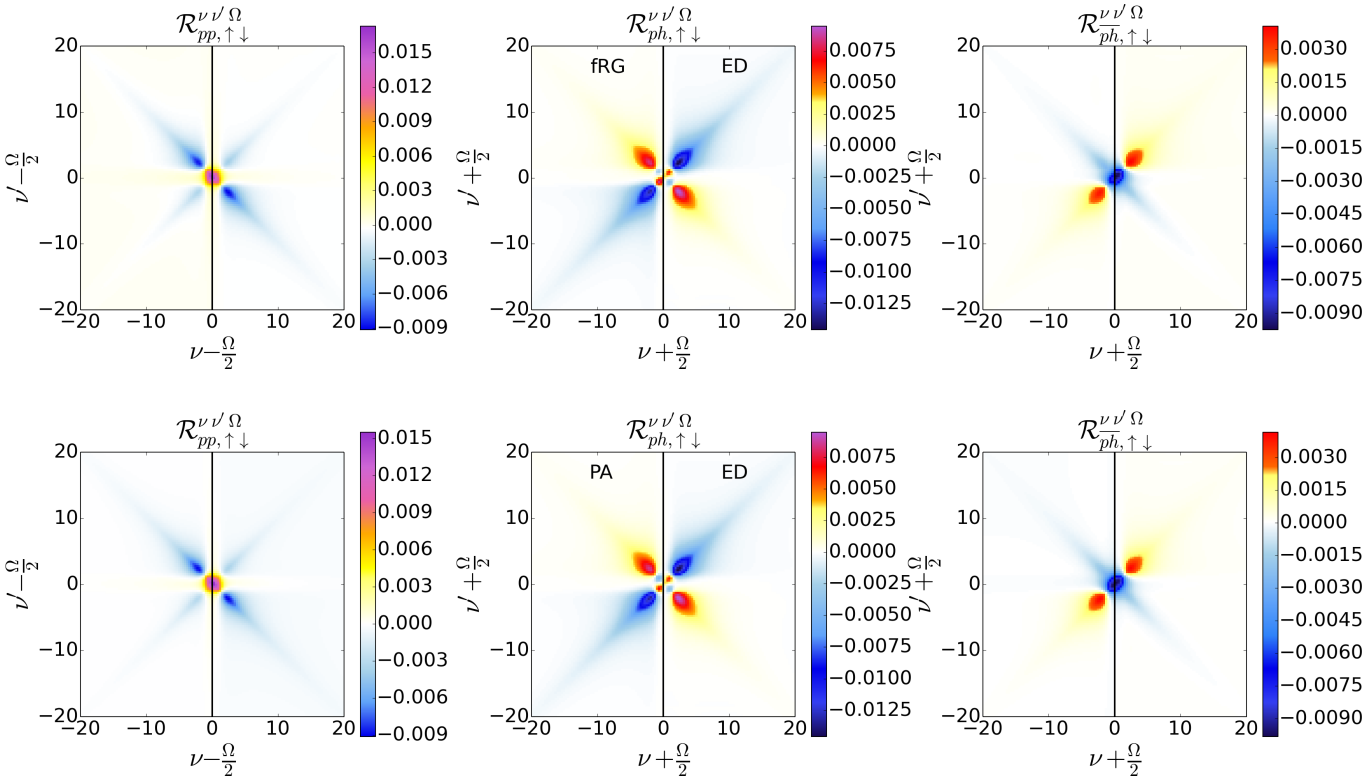

FIG. 13: Same as Fig. 12, but for a finite transfer frequency $\Omega = 8\frac{2\pi}{\beta}$.

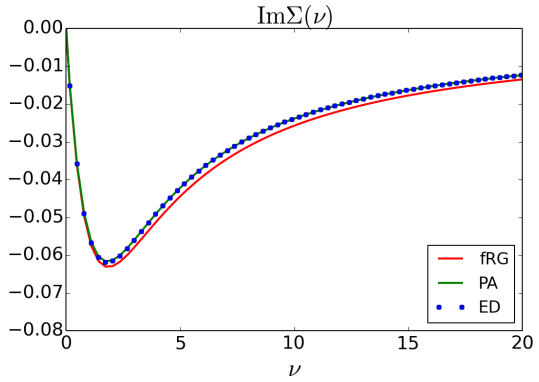

FIG. 14: $\mathrm{Im}\,\Sigma(i\nu)$ as obtained by fRG (red, solid), PA (green, solid) and ED (blue, dotted) for the SIAM with $U = 1$, $\beta = 20$ and $\Delta(0) = D = 1$.

$\overline{ph}$ channel. Even at the level of the rest function $\mathcal{R}_{\uparrow\downarrow}$, which has as a leading order U^4, we find excellent agreement between PA and ED, while only minor deviations are again observed for the fRG. Note that, contrary to the plotting conventions adopted in previous Refs. 4,8, the fermionic frequencies are shifted by $\pm\Omega/2$ for $\mathcal{K}_2$ and $\mathcal{R}$, because the main frequency structures move outwards as Ω is increased. This observation suggests to include a corresponding shift also in the notation used in the numerical implementation, such that the localized frequency structures can be more efficiently captured by means of the finite grid even in the case of finite transfer frequency. Similar trends are observed for the self-energy shown in Fig. 14. While PA and ED agree perfectly, we find that the fRG self-energy deviates from the exact results, especially in its tail.

All this numerical evidence proves the reliability of our treatment of the high frequency asymptotics within the different schemes (see also the results for $U = 2$ in the supplements), allowing us to evaluate in an unbiased way their intrinsic performance in the most challenging strong-coupling regime.

Due to the perturbative nature of fRG and PA, the situation changes drastically in the regime of stronger coupling. The corresponding results for $U = 4$ are presented for $\mathcal{K}_{1,\uparrow\downarrow}$ and $\mathcal{K}_{2,\uparrow\downarrow}$ in Figs. 15 and 16 respectively. Note that, for this value of the interaction, we are clearly in the non-perturbative regime, as divergencies[32–34,46,47] are already present in the exact vertices obtained by ED.

For both, PA and fRG, $\mathcal{K}_{1,\uparrow\downarrow}$ shows already strong deviations from the exact results, while the qualitative structures are still captured. These deviations are particularly enhanced in the ph and $\overline{ph}$ channel. In the case of $\mathcal{K}_{2,\uparrow\downarrow}$ qualitative features are missed by the PA and fRG, in particular for $\Omega = 0$, while a qualitative agreement is still achieved for finite transfer frequency. As the main structures of the rest function $\mathcal{R}$ are neither reproduced by PA nor by fRG, we show only one example for this comparison in Fig. 17 (the full vertices are reported in the supplements). Since this diagrammatic class is at least fourth order in the interaction, the strongest deviations were to be expected here. Finally, we note that for the self-energy, shown in Fig. 18, strong deviations are observed in both cases.

1. *Neglecting the asymptotics*

Let us now discuss the importance of considering asymptotic functions in numerical implementations. In this regard, we present in Fig. 19 results for $\mathrm{Im}\,\Sigma(i\nu_0)/U^2$ as a function of U calculated by fRG and PA, with and without asymptotic functions, and compare them with the exact ED data. For these calculations, a frequency grid of $64 \times 64 \times 128$ Matsubara frequencies was used for the reducible vertex functions. In the large frequency domain, we used Eq. (9) and $\Phi_{r,\mathrm{asympt.}} \approx 0$ respectively.

We observe that the results for both, fRG and PA, are strongly affected if we include the asymptotic functions in the calculations: The comparison with the exact result improves by a substantial amount. This is a strong indication of the importance of a correct description of the high-frequency part of the vertex function in all vertex-based numerical implementations.

2. *Higher order corrections in fRG*

In this subsection, we provide a quantitative comparison between the SIAM results as obtained by means of fRG in its one- and two-loop implementation[44]. To this aim, we compare in Fig. 20 the quantities $\mathcal{K}^{\Omega=0}_{1,ph,\uparrow\downarrow}$, $\mathcal{K}^{\nu_0(\Omega=0)}_{2,ph,\uparrow\downarrow}$, as well as $\max_{\nu\nu'} |\mathcal{R}^{\nu\nu'(\Omega=0)}_{ph,\uparrow\downarrow}|$ normalized by their leading order[9] in U, to the exact ED results as well as to the PA. Consistently to our expectations, we find that the two-loop corrections yield a systematic improvement of the $\mathcal{K}_1$, $\mathcal{K}_2$ and $\mathcal{R}$ functions acquired during the flow, in particular for larger values of the interaction.

More specifically, for $\mathcal{K}_{1,ph,\uparrow\downarrow}$ the two-loop corrections have a minor effect in the weak-coupling regime, whereas an excellent agreement with the exact results is achieved already at the one-loop level. At larger U, the one-loop scheme strongly overestimates $\mathcal{K}_{1,ph,\uparrow\downarrow}$. Here, the two-loop corrections yield a substantial improvement over the one-loop scheme, while underestimating $\mathcal{K}_{1,ph,\uparrow\downarrow}$. We also note the strongly improved agreement of the two-loop fRG with the PA, which is a trend to be expected, since the two-loop scheme allows to include higher orders of the reducible diagrams in an exact way.

As for $\mathcal{K}_{2,ph,\uparrow\downarrow}$, we observe that already in the limit $U \to 0$ the one-loop scheme *fails* to reproduce the exact result. This can be attributed to the fact that the lowest

[9] For the particle-hole channel in the $\uparrow\downarrow$ spin configuration the bare bubble vanishes, resulting in a leading order $\mathcal{O}(U^3)$.

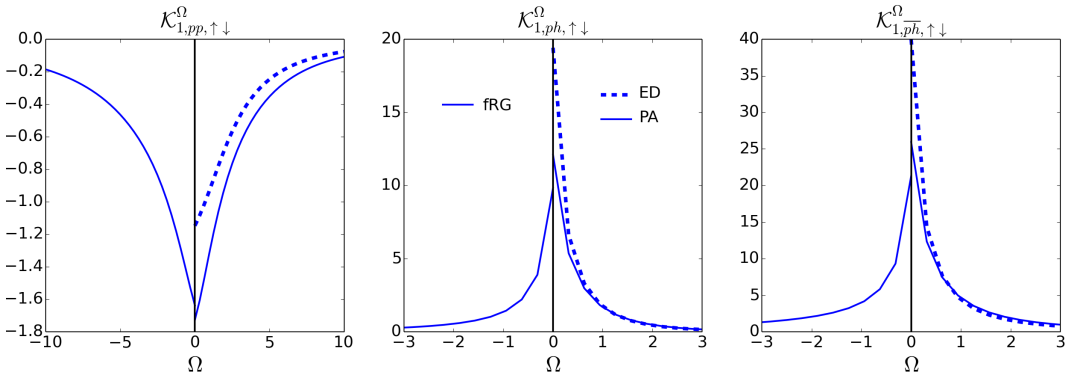

FIG. 15: Same as Fig. 10, but for $U = 4$.

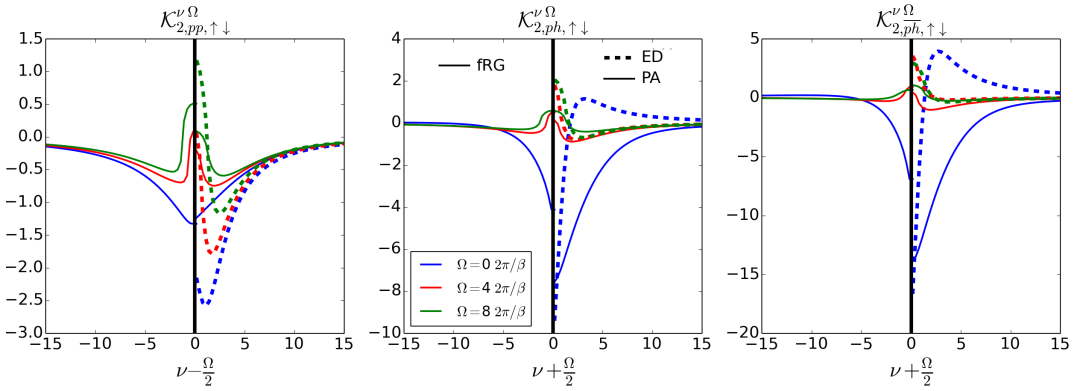

FIG. 16: Same as Fig. 11, but for $U = 4$.

order diagram in $\mathcal{K}_{2,ph,\uparrow\downarrow}$ is of order U^3, and is thus not captured exactly in the one-loop scheme. In particular for the U-flow, we numerically verify the factor $\frac{1}{2}$ (w.r.t. the exact result) already predicted diagrammatically at the end of Sec. IV B, while for the Ω-flow we find, numerically, a factor of ~ 0.89 in all channels. For larger values of U, we observe a behavior similar to the one described for $\mathcal{K}_{1,ph,\uparrow\downarrow}$, that is, a systematic improvement of the results if the two-loop corrections are included in fRG.

For $\mathcal{R}_{ph,\uparrow\downarrow}$ the trend is similar, while, being a function of $\mathcal{O}(U^4)$, the relative deviations from the exact results increase substantially. The predicted factor $\frac{1}{3}$ for $U \to 0$ is verified numerically, while for the Ω-flow we find factors 0.78, 0.25 and 0.78 in the pp, ph and $\overline{ph}$ channel respectively.

As for the comparison between the flow-schemes, consistently with the ratios in the weak-coupling regime, we

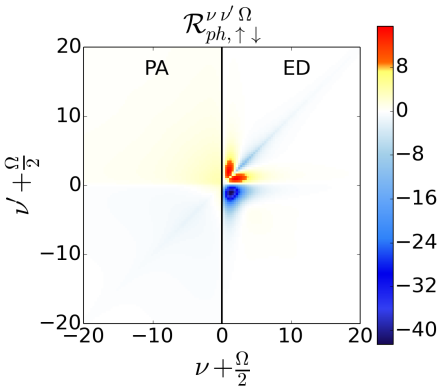

FIG. 17: Comparison of $\mathcal{R}_{ph,\uparrow\downarrow}$ obtained by means of PA with the exact result. Here, $U = 4$.

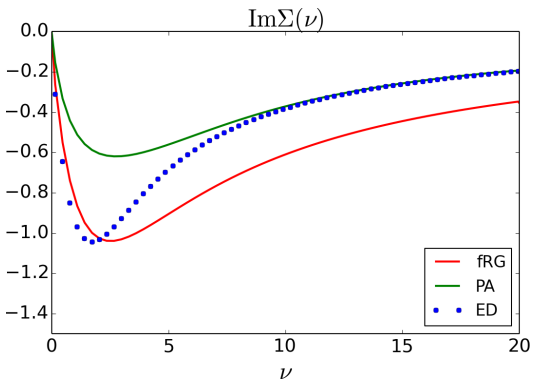

FIG. 18: Same as Fig. 14, but for $U = 4$.

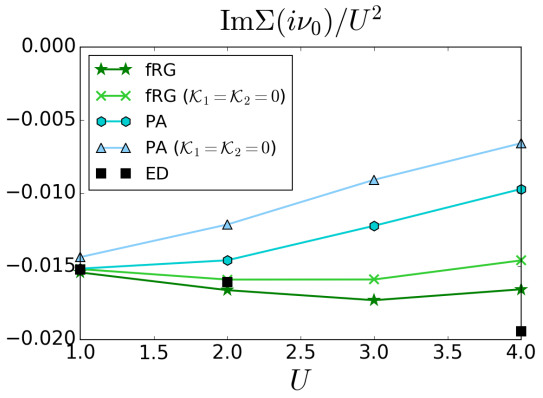

FIG. 19: Comparison of $\mathrm{Im}\,\Sigma(i\nu_0)/U^2$ for the SIAM with $\beta = 20$ and $\Delta(0) = D = 1$ as obtained by fRG and PA with and without ($\mathcal{K}_1 = \mathcal{K}_2 = 0$) high-frequency asymptotics, compared with ED for $\nu_0 = \frac{\pi}{\beta}$.

observe that the simpler U-flow performs overall worse than the Ω-flow.

3. *Efficiency of simplified parametrization schemes*

In this subsection we preset results for the simplified parametrization scheme[41] presented in Eq. (37). It has found extensive use in the fRG community, as it allows for a substantial speedup of numerical calculations. In the left two panels of Fig. 21 we compare the self-energy at the first Matsubara frequency ($\mathrm{Im}\,\Sigma(i\nu_0)/U^2$) as well as its tail ($\lim_{\nu\to\infty} \mathrm{Im}\,\nu\Sigma(i\nu)/U^2$) for fRG one-loop and two-loop in their full and simplified ($\mathcal{K}_{\mathrm{eff}}$) implementation with PA and the exact results from ED.

For the self-energy at the first Matsubara frequency, we find a good agreement between the simplified parametrization scheme and the fully parametrized fRG implementation for both the one- and two-loop scheme, while the simpler scheme performs slightly worse in reproducing the exact results. In the case of the self-energy tail, the situation is reversed. Here, the aforementioned deviations of the fRG from ED are indeed cured by the simplified parametrization scheme.

To capture the effect of the simplified approximation scheme on the two-particle quantities, we compare in the right panel of Fig. 21 the corresponding susceptibility in the *ph*-channel for the two-loop case. It is important to note that χ cannot be directly extracted from $\mathcal{K}_{\mathrm{eff}}$ using Eq. (10) due to the effective inclusion of $\mathcal{K}_2$ and $\mathcal{R}$. Instead, we calculate the susceptibility after the flow by calculating explicitly the bare and vertex-corrected bubble according to equation Eq. (C1b) (VC). This is compared, for an interaction value $U = 4$, to $\chi = \mathcal{K}_1/U^2$ and the corresponding PA and ED data. We find that the simplified parametrization fails to qualitatively reproduce the exact susceptibility, while the other approximations, although underestimating χ, compare qualitatively well with ED[10].

While the parametrization scheme of Eq. (37) performs well for one-particle quantities, we find that the qualitative features of the susceptibility are badly reproduced. Further, we observe that the ambiguities in the definition of the flow equations for the case of finite temperatures turn out to have a substantial effect on the results for larger values of the interaction. These are strong arguments for the fully parametrized schemes, that capture, consistently, all frequency structures of the two-particle vertex function.

VI. CONCLUSIONS AND OUTLOOK

We have presented a detailed analysis of the diagrammatic content of the two-particle vertex functions, focusing on the terms controlling their high frequency structures. This information is extremely valuable, also at a practical level, because the efficient algorithmic treatment of the vertex asymptotics is fundamental for several recently proposed quantum field theoretical approaches based on expansions around a correlated starting point. In particular, by focusing on the two-particle reducible parts of the vertex function, we could identify the different contributions to their high-frequency asymptotics as diagrammatic classes with a reduced frequency (and momentum) dependence, and establish a connection to the (physical) susceptibilities and the fermion-boson vertices. The gained insights are essential in order to devise efficient parametrization schemes for the two-particle vertex functions. We then discussed the algorithmic details necessary for the implementation of these ideas in numerical (and analytical) studies, considering as specific examples the functional renormalization group approach and the parquet approximation. In order to verify the correct treatment of the high frequency asymptotics, we benchmarked our numerical implementations for a SIAM against exact calculations from ED. Finally, we tested the intrinsic performance of the approaches also in the most challenging strong coupling regime.

This algorithmic progress paves the way towards a full numerical treatment of correlations at the two-particle level, which is pivotal for all vertex-based quantum many-body methods. In particular, these ideas are directly applicable in the treatment of non-local correlations beyond the dynamical mean-field theory by means of its cutting-edge diagrammatic extensions, such as the DF, the DMF2RG, the DΓA, and the recently introduced TRILEX and QUADRILEX approach.

[10] We note that χ calculated after the full two-loop flow by means of Eq. (C1) yields a result different from $\mathcal{K}_1/U^2$. This is connected to the specific approximations introduced in the fRG, and is absent in the fully self-consistent PA.

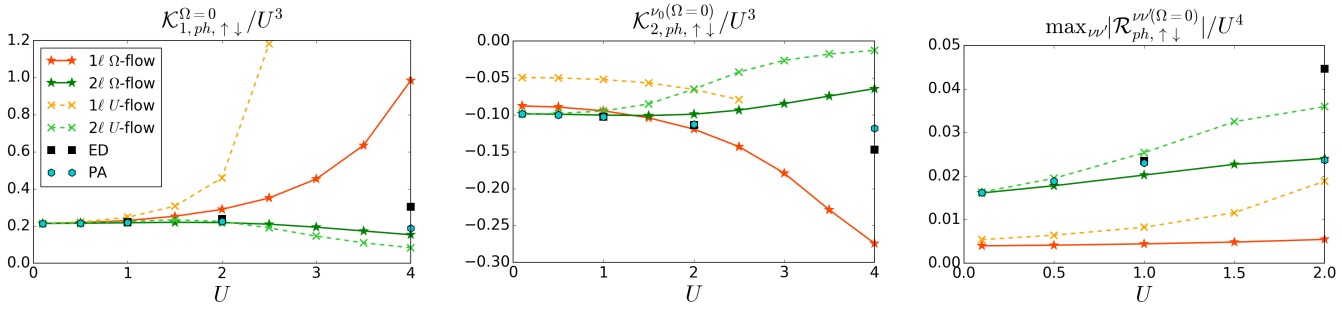

FIG. 20: Comparison of $\mathcal{K}^{\Omega=0}_{1,ph,\uparrow\downarrow}/U^3$, $\mathcal{K}^{\nu_0(\Omega=0)}_{2,ph,\uparrow\downarrow}/U^3$, and $\max_{\nu\nu'}|\mathcal{R}^{\nu\nu'(\Omega=0)}_{ph,\uparrow\downarrow}|/U^4$ ($\nu_0 = \frac{\pi}{\beta}$) for fRG in the one-loop (1ℓ) and two-loop (2ℓ) implementation, for both the Ω- and U-flow, with ED and PA. We note that the one-loop U-flow diverges for $U = 3$ or larger.

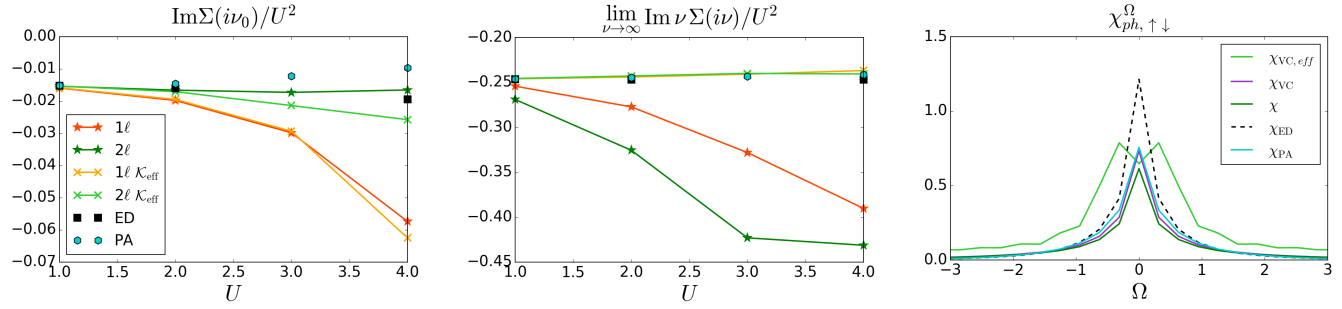

FIG. 21: Left two panels: Comparison of $\mathrm{Im}\,\Sigma(i\nu_0)/U^2$ and $\lim_{\nu\to\infty} \mathrm{Im}\,\nu\Sigma(i\nu)/U^2$ for fRG one-loop and two-loop with the corresponding simplified schemes introduced previously ($\mathcal{K}_{\mathrm{eff}}$, see Eq. (37)), PA and ED. Right panel: Comparison of the susceptibility χ in the *ph*-channel for $U = 4$ as obtained by means of Eq. (C1b) after the two-loop fRG flow (χ_{VC}) in the conventional and the simplified scheme (eff). This is compared to the susceptibility χ obtained directly from Eq. (10) as well as the PA and ED result.

Acknowledgments

We are grateful to A. Antipov, T. Ayral, E. Di Napoli, A. Eberlein, C. Honerkamp, A. Katanin, W. Metzner, O. Parcollet, D. Rohe, T. Schäfer, P. Thunström, A. Valli, and D. Vilardi for valuable discussions. We further thank A. Eberlein and T. Ayral for critical reading of the manuscript. We acknowledge financial support from the Deutsche Forschungsgemeinschaft (DFG) through FOR 723, ZUK 63, and SFB/TRR 21, the Austrian Science Fund (FWF) within the Project F41 (SFB ViCoM), and the European Research Council (ERC) under the European Unions Seventh Framework Program (FP/2007-2013)/ERC through Grant No. 306447 (G.L., K.H.). Calculations were performed on the Vienna Scientific Cluster (VSC).

Appendix A: Notations

In this appendix we present the definitions of the two-particle Green's and (1PI) vertex functions following the notation of Refs. [4,18,48], and further specify the notations used throughout this paper. Let us start by defining the two-particle Green's function G_2, which reads

$$G_{2,\sigma_1\sigma_2\sigma_3\sigma_4}(x_1,x_2,x_3,x_4) = \langle \mathcal{T}\big(c^\dagger_{\sigma_1}(x_1)c_{\sigma_2}(x_2)c^\dagger_{\sigma_3}(x_3)c_{\sigma_4}(x_4)\big)\rangle. \quad \text{(A1)}$$

Here, $c^\dagger$ (c) represent the fermionic creation (annihilation) operators with an associated spin $\sigma = \{\uparrow,\downarrow\}$, the brackets $\langle ...\rangle$ imply a thermal expectation value, $\mathcal{T}$ denotes the time-ordering operator, and $x = (\mathbf{R}_i, \tau)$ is a four-vector including the lattice site $\mathbf{R}_i$ and the imaginary time τ. First, we note that the number of spin combinations can be reduced by considering spin conservation and the antisymmetry of the two-particle Green's function, allowing us to consider only

$$G_{2,\sigma\sigma'}(x_1,x_2,x_3,x_4) = G_{2,\sigma\sigma\sigma'\sigma'}(x_1,x_2,x_3,x_4). \quad \text{(A2)}$$

Further, by making use of time and space-translational invariance, we can always shift all arguments such that $x_4 = 0$. This property can be exploited to yield momen-

tum and frequency conservation, i.e.

$$G^{k_1k_2k_3k_4}_{2,\sigma\sigma'} = \beta\, V_{\rm BZ}\, \delta_{k_1+k_3,k_2+k_4} \times \underbrace{\sum\!\!\!\!\!\!\int \prod_{i=1}^{3} dx_i\; G_{2,\sigma\sigma'}(x_1,x_2,x_3,0) e^{-ik_1x_1} e^{ik_2x_2} e^{-ik_3x_3}}_{G^{k_1k_2k_3}_{2,\sigma\sigma'}}, \tag{A3}$$

where $k = (\nu, \mathbf{k})$ represents the four-vector with momentum $\mathbf{k}$ and Matsubara frequency ν. Here, we introduced the generalized four-vector integration $\sum\!\!\!\!\!\!\int dx = \sum_{\mathbf{R}_i} \int_0^\beta d\tau$, that combines the lattice-site summation with the imaginary time integration. The corresponding object in dual space reads $\sum\!\!\!\!\!\!\int dk = \frac{1}{V_{\rm BZ}} \int_{\rm BZ} d\mathbf{k} \frac{1}{\beta} \sum_{i\nu}$, where BZ denotes the first Brillouin zone with a volume $V_{\rm BZ}$.

To obtain the two-particle vertex function F, we subtract the two possible contractions of the composite operator within the brackets (all disconnected diagrams) and subsequently cut the external fermionic legs. This yields

$$F^{k_1k_2k_3k_4}_{\sigma\sigma'} = -G^{-1}(k_1)G^{-1}(k_3)\Big[\underbrace{G^{k_1k_2k_3k_4}_{2,\sigma\sigma'} - G(k_1)G(k_3)\left(\delta_{k_1,k_2} - \delta_{k_1,k_4}\delta_{\sigma,\sigma'}\right)}_{G^{k_1k_2k_3k_4}_{2,c,\sigma\sigma'}}\Big] G^{-1}(k_2)G^{-1}(k_4). \tag{A4}$$

Here, the additional minus sign is a matter of convention, which is commonly introduced such that the lowest order contribution of F is given by U. Note that $SU(2)$ symmetry is here and in the following explicitly assumed.

While so far we considered the two-particle Green and vertex function with purely fermionic arguments, one often introduces 'mixed' notations using a bosonic and two fermionic arguments, in order to highlight a specific scattering channel. The adoption of these notations is essential for the decomposition scheme presented in this paper, in particular for the reducible vertex functions. Hence, we introduce the particle-particle (pp) notation

$$F^{kk'q}_{pp,\sigma\sigma'} = F^{k(q-k')(q-k)k'}_{\sigma\sigma'} \tag{A5}$$

the particle-hole (ph) notation

$$F^{kk'q}_{ph,\sigma\sigma'} = F^{k(k+q)(k'+q)k'}_{\sigma\sigma'} \tag{A6}$$

and the transverse particle-hole ($\overline{ph}$) notation

$$F^{kk'q}_{\overline{ph},\sigma\sigma'} = F^{kk'(k'+q)(k+q)}_{\sigma\sigma'}, \tag{A7}$$

which are defined correspondingly for G_2 and the other vertex functions ϕ, $\Lambda_{\rm 2PI}$ and Γ (see Sec.II). A diagrammatic representation of the three notations is shown in Fig. 22. Let us note that in general, for the two-particle vertex F and also for the fully irreducible vertex $\Lambda_{\rm 2PI}$, none of these notations is a priori more favorable, each of them just being an alternative way to look at the same physical object[48].

Finally, we introduce susceptibilities in all scattering

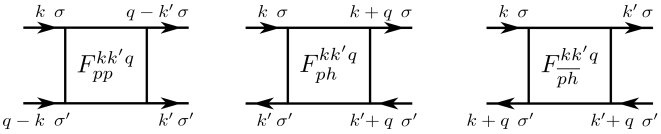

FIG. 22: Notations of the vertex functions in the three different scattering channels.

channels,

$$\chi^{kk'q}_{pp,\sigma\sigma'} = \sum\!\!\!\!\!\!\int dk\, dk'\, G^{kk'q}_{2,c,pp,\sigma\sigma'} + \sum\!\!\!\!\!\!\int dk\, G(q-k)G(k), \tag{A8a}$$

$$\chi^{kk'q}_{ph,\sigma\sigma'} = \sum\!\!\!\!\!\!\int dk\, dk'\, G^{kk'q}_{2,c,ph,\sigma\sigma'} - \delta_{\sigma,\sigma'} \sum\!\!\!\!\!\!\int dk\, G(k)G(k+q), \tag{A8b}$$

$$\chi^{kk'q}_{\overline{ph},\sigma\sigma'} = \sum\!\!\!\!\!\!\int dk\, dk'\, G^{kk'q}_{2,c,\overline{ph},\sigma\sigma'} + \sum\!\!\!\!\!\!\int dk\, G(k)G(k+q). \tag{A8c}$$

They can be easily combined to yield the physical susceptibilities in the density, magnetic, singlet and triplet channel[4].

Appendix B: Explicit equations

We here want to present some explicit forms of the parquet equations presented schematically in Sec. IV C. Let us begin by showing the Bethe Salpeter equations in

their spin-resolved version.[11]

[11] We want to point out the fond similarity between Eqs. (B1), which are the basis for the iterative parquet approximation solver, and the channel-resolved fRG flow Eqs. (33), which technically allows for very similar implementations of the two approaches.

$$\Phi_{pp,\uparrow\downarrow}^{kk'q} = \sum\!\!\!\!\!\!\int dk''\; G(k'')G(q-k'') \times \Gamma_{pp,\uparrow\downarrow}^{kk''q} F_{pp,\uparrow\downarrow}^{k''k'q}, \tag{B1a}$$

$$\Phi_{ph,\uparrow\downarrow}^{kk'q} = -\sum\!\!\!\!\!\!\int dk''\; G(k''+q)G(k'') \times \left[\Gamma_{ph,\uparrow\uparrow}^{kk''q} F_{ph,\uparrow\downarrow}^{k''k'q} + \Gamma_{ph,\uparrow\downarrow}^{kk''q} F_{ph,\uparrow\uparrow}^{k''k'q}\right], \tag{B1b}$$

$$\Phi_{\overline{ph},\uparrow\downarrow}^{kk'q} = \sum\!\!\!\!\!\!\int dk''\; G(k''+q)G(k'') \times \Gamma_{\overline{ph},\uparrow\downarrow}^{kk''q} F_{\overline{ph},\uparrow\downarrow}^{k''k'q}. \tag{B1c}$$

In the $SU(2)$ symmetric case they can be diagonalized by introducing the density (d), magnetic (m), singlet (s) and triplet (t) channel as introduced in Sec. IV C,

$$\Phi_{d/m}^{kk'q} = \sum\!\!\!\!\!\!\int dk''\; G(k''+q)G(k'') \times \Gamma_{d/m}^{kk''q} F_{d/m}^{k''k'q}, \tag{B2a}$$

$$\Psi_{t/s}^{kk'q} = \pm\frac{1}{2}\sum\!\!\!\!\!\!\int dk''\; G(k'')G(q-k'') \times \Gamma_{s/t}^{kk''q} F_{s/t}^{k''k'q}. \tag{B2b}$$

Given the fully irreducible vertex function $\Lambda^{kk'q}$, the other two-particle vertex function can be calculated through the parquet equations as shown below:

$$F_d^{kk'q} = \Lambda_d^{kk'q} + \Phi_d^{kk'q} - \frac{1}{2}\Phi_d^{k(k+q)(k'-k)} - \frac{3}{2}\Phi_m^{k(k+q)(k'-k)} + \frac{1}{2}\Psi_s^{kk'(k+k'+q)} + \frac{3}{2}\Psi_t^{kk'(k+k'+q)}, \tag{B3a}$$

$$F_m^{kk'q} = \Lambda_m^{kk'q} + \Phi_m^{kk'q} - \frac{1}{2}\Phi_d^{k(k+q)(k'-k)} + \frac{1}{2}\Phi_m^{k(k+q)(k'-k)} - \frac{1}{2}\Psi_s^{kk'(k+k'+q)} + \frac{1}{2}\Psi_t^{kk'(k+k'+q)}, \tag{B3b}$$

$$F_s^{kk'q} = \Lambda_s^{kk'q} + \Psi_s^{kk'q} + \frac{1}{2}\Phi_d^{k(q-k')(k'-k)} - \frac{3}{2}\Phi_m^{k(q-k')(k'-k)} + \frac{1}{2}\Phi_d^{kk'(q-k-k')} - \frac{3}{2}\Phi_m^{kk'(q-k-k')}, \tag{B3c}$$

$$F_t^{kk'q} = \Lambda_t^{kk'q} + \Psi_t^{kk'q} - \frac{1}{2}\Phi_d^{k(q-k')(k'-k)} - \frac{1}{2}\Phi_m^{k(q-k')(k'-k)} + \frac{1}{2}\Phi_d^{kk'(q-k-k')} + \frac{1}{2}\Phi_m^{kk'(q-k-k')}. \tag{B3d}$$

Similarly, the channel-dependent irreducible two-particle vertex $\Gamma_r^{kk'q}$ is obtained as $\Gamma_r^{kk'q} = F_r^{kk'q} - \Phi_r^{kk'q}$.

Appendix C: Extracting asymptotics from F

In this part we describe an approach that extracts the asymptotic functions directly from the full vertex function F. This procedure was employed to acquire all presented high-frequency results for the ED vertices, and is based on the fact that one can write down explicit Feynman diagrams for all asymptotic functions. These consist of all possible ways of pinching two external legs of F into one bare vertex U[6,30]. Since the latter is purely local in space and time, the dependence on two fermionic arguments is replaced by a single bosonic (transfer) one. The resulting diagrams for $\mathcal{K}_1$ are shown in Fig. 23, and read explicitly

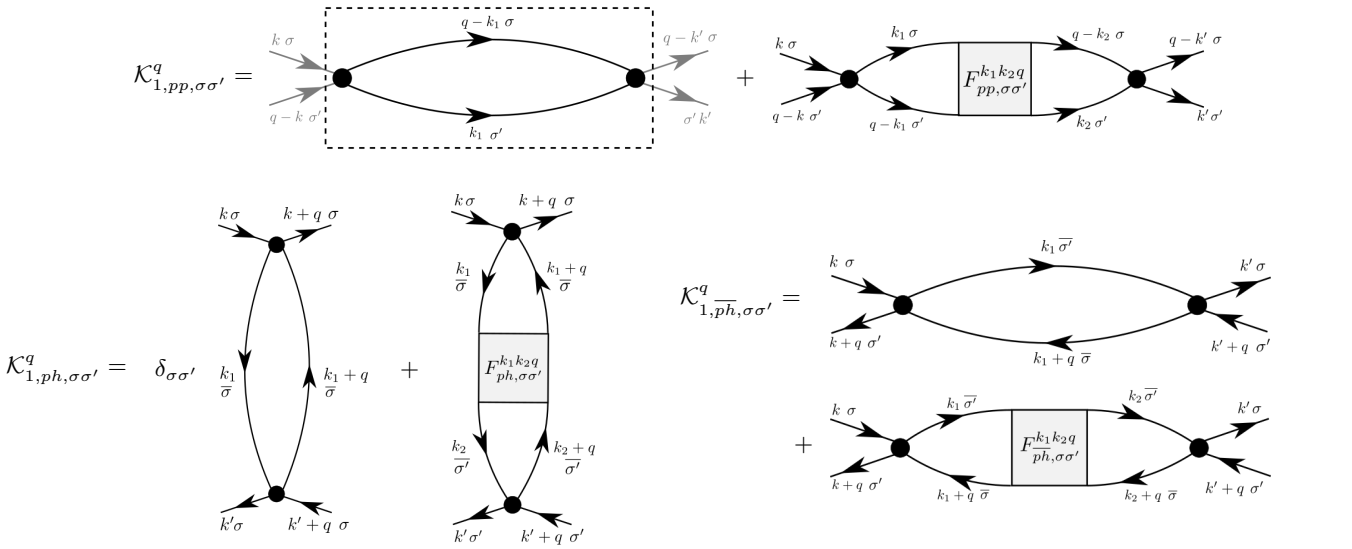

FIG. 23: Diagrammatic representation of the $\mathcal{K}_1$ functions in the three different channels. As denoted in the first diagram, the external lines are to be excluded, making the k and k' arguments redundant. Here, $\overline{\sigma}$ denotes the opposite spin of σ, and $SU(2)$ symmetry is explicitly assumed.

$$\mathcal{K}^q_{1,pp,\sigma\sigma'} = U^2 \iint dk_i\, G(k_1)G(q-k_1)F^{k_1k_2q}_{pp,\sigma\sigma'}G(q-k_2)G(k_2) - U^2 \int dk_1\, G(q-k_1)G(k_1), \tag{C1a}$$

$$\mathcal{K}^q_{1,ph,\sigma\sigma'} = U^2 \iint dk_i\, G(k_1)G(k_1+q)F^{k_1k_2q}_{ph,\sigma\sigma'}G(k_2)G(k_2+q) + U^2\delta_{\sigma,\sigma'} \int dk_1\, G(k_1)G(k_1+q), \tag{C1b}$$

$$\mathcal{K}^q_{1,\overline{ph},\sigma\sigma'} = U^2 \iint dk_i\, G(k_1)G(k_1+q)F^{k_1k_2q}_{\overline{ph},\sigma\sigma'}G(k_2)G(k_2+q) - U^2 \int dk_1\, G(k_1)G(k_1+q). \tag{C1c}$$

Here $\overline{\sigma}$ denotes the opposite spin of σ, and $SU(2)$ symmetry is explicitly assumed. In the case of $\mathcal{K}_2$ one introduces just one additional bare vertex, as shown in Fig. 24. Note that here, the previously determined $\mathcal{K}_1$ has to be subtracted. The equations in all scattering channels then read

$$\mathcal{K}^{kq}_{2,pp,\sigma\sigma'} = -U \int dk_1\, G(q-k_1)F^{kk_1q}_{pp,\sigma\sigma'}G(k_1) - \mathcal{K}^q_{1,pp,\sigma\sigma'}, \tag{C2a}$$

$$\mathcal{K}^{kq}_{2,ph,\sigma\sigma'} = \ U \int dk_1\, G(k_1)F^{kk_1q}_{ph,\sigma\overline{\sigma'}}G(k_1+q) - \mathcal{K}^q_{1,ph,\sigma\sigma'}, \tag{C2b}$$

$$\mathcal{K}^{kq}_{2,\overline{ph},\sigma\sigma'} = -U \int dk_1\, G(k_1)G(k_1+q) \times \left[\delta_{\sigma\sigma'}F^{kk_1q}_{\overline{ph},\uparrow\downarrow} + (1-\delta_{\sigma\sigma'})F^{kk_1q}_{\overline{ph},\uparrow\downarrow}\right] - \mathcal{K}^q_{1,\overline{ph},\sigma\sigma'}. \tag{C2c}$$

Further, by exploiting the symmetry relations shown in Appendix D, one can easily derive $\overline{\mathcal{K}}_2$ from $\mathcal{K}_2$.[b]

As it is typical within an ED algorithm for a SIAM, the values for F are known numerically for a finite grid in the frequency domain. Thus, in the first calculation of the aforementioned diagrams according to Eqs. (C1) and (C2) we have to make a rough approximation for F (i.e. $F = U$) in the large-frequency domain, which will introduce an error. To improve on this 'one-shot' calculation of the diagrams, we exploit a self-consistent scheme:

- I: Initialize the $\mathcal{K}_1$'s and $\mathcal{K}_2$'s to 0. Their grids may deviate from the grid for F.
- II: Calculate a set of new $\mathcal{K}_1$'s and $\mathcal{K}_2$'s according to Eqs. (C1) and (C2).
- III: Rebuild the vertex in an arbitrarily large region (as needed) using the updated asymptotic functions.
- IV: Continue from II till convergence

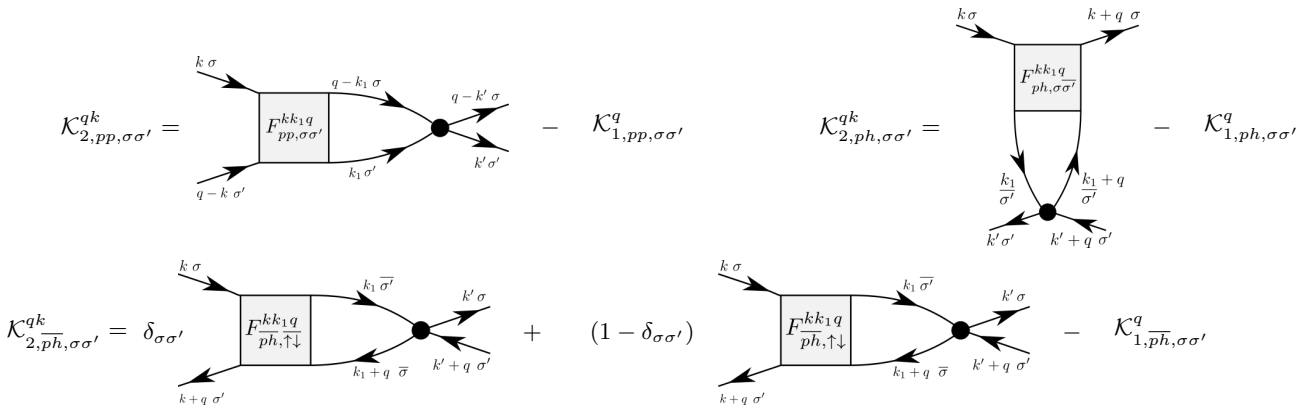

FIG. 24: Diagrammatic representation of the $\mathcal{K}_2$ functions in the three different channels. Here, $\overline{\sigma}$ denotes the opposite spin of σ, while $SU(2)$ symmetry is explicitly assumed.

Once the asymptotic functions are fully converged, we can directly determine the localized structures using

$$\Lambda_{\mathrm{2PI}} + \sum_r \mathcal{R}_r = F - \left(\sum_r \mathcal{K}_{1,r} + \mathcal{K}_{2,r} + \overline{\mathcal{K}}_{2,r} \right). \quad \text{(C3)}$$

Further, since, at this point, we have F available in the full frequency domain, we can use this additional information to determine also all the Φ functions on an arbitrarily large frequency grid by means of the Bethe-Salpeter equations (4). If needed, $\mathcal{R}$ and Λ_{2PI} can then be determined by Eq. (13) and Eq. (2) respectively.

The approach described in this section was used to compute all the exact asymptotic functions and reducible vertices presented in Sec. V, from ED calculations, originally performed on a fermionic frequency grid of $128 \times 128 \times 128$ Matsubara frequencies. While here we are dealing with a purely local vertex, we stress that this approach is equally applicable in the non-local case.

Appendix D: Symmetries

1. Symmetries of $\mathcal{K}_1$ and $\mathcal{K}_2$

In this section we summarize the symmetries of the previously introduced asymptotic functions. Before addressing the specific physical symmetries of the system of our interest, which provide useful relations for $\mathcal{K}_1$ and $\mathcal{K}_2$, we provide some fundamental relations which hold[1,4,6] independently of the system under analysis. First, we consider the exchange of two (fermionic) annihilation operators in the time-ordered matrix element of Eq. (A3), which, as a consequence of the Pauli-principle, yields a minus sign (also referred to as 'crossing symmetry'[1,4,6]). Diagrammatically speaking, this corresponds to an exchange of two outgoing lines. For $\mathcal{K}_1$, this operation leads to the following relations:

$$\mathcal{K}^{q}_{1,pp,\sigma\sigma'} = -\mathcal{K}^{q}_{1,pp,\overline{\sigma\sigma'}} \quad \text{(D1a)}$$
$$\mathcal{K}^{q}_{1,ph,\sigma\sigma'} = -\mathcal{K}^{q}_{1,\overline{ph},\overline{\sigma\sigma'}} \quad \text{(D1b)}$$
$$\mathcal{K}^{q}_{1,\overline{ph},\sigma\sigma'} = -\mathcal{K}^{q}_{1,ph,\overline{\sigma\sigma'}}. \quad \text{(D1c)}$$

Here, $\overline{\sigma\sigma'}$ denotes a spin configuration of the external indices where spins are crossing. While for the pp channel one finds relations between different spin configurations within the same channel, the ph and $\overline{ph}$-channel are interchanged. Similarly, for $\mathcal{K}_2$ one finds:

$$\mathcal{K}^{kq}_{2,pp,\sigma\sigma'} = -\mathcal{K}^{kq}_{2,pp,\overline{\sigma\sigma'}} \quad \text{(D2a)}$$
$$\mathcal{K}^{kq}_{2,ph,\sigma\sigma'} = -\mathcal{K}^{kq}_{2,\overline{ph},\overline{\sigma\sigma'}} \quad \text{(D2b)}$$
$$\mathcal{K}^{kq}_{2,\overline{ph},\sigma\sigma'} = -\mathcal{K}^{kq}_{2,ph,\overline{\sigma\sigma'}}. \quad \text{(D2c)}$$

A second generic operation involves the simultaneous exchange of both annihilation and creation operators in Eq. A3. Diagrammatically, this corresponds to an exchange of both the incoming and outgoing particles. In this case we end up with the following relations for $\mathcal{K}_1$:

$$\mathcal{K}^{q}_{1,pp,\sigma\sigma'} = \mathcal{K}^{q}_{1,pp,\sigma'\sigma} \quad \text{(D3a)}$$
$$\mathcal{K}^{q}_{1,ph,\sigma\sigma'} = \mathcal{K}^{-q}_{1,ph,\sigma'\sigma} \quad \text{(D3b)}$$
$$\mathcal{K}^{q}_{1,\overline{ph},\sigma\sigma'} = \mathcal{K}^{-q}_{1,\overline{ph},\sigma'\sigma}. \quad \text{(D3c)}$$

For $\mathcal{K}_2$ one obtains:

$$\mathcal{K}^{kq}_{2,pp,\sigma\sigma'} = \mathcal{K}^{(q-k)q}_{2,pp,\sigma'\sigma} \quad \text{(D4a)}$$
$$\mathcal{K}^{kq}_{2,ph,\sigma\sigma'} = \mathcal{K}^{(k+q)(-q)}_{2,ph,\sigma'\sigma} \quad \text{(D4b)}$$
$$\mathcal{K}^{kq}_{2,\overline{ph},\sigma\sigma'} = \mathcal{K}^{(k+q)(-q)}_{2,\overline{ph},\sigma'\sigma}. \quad \text{(D4c)}$$

While for this operation all the corresponding channels are conserved, the diagrammatic class changes from $\mathcal{K}_2$ to $\overline{\mathcal{K}}_2$ in the case of the ph and $\overline{ph}$ channel.

Symmetries	$\mathcal{K}_{1,r}$	$\mathcal{K}_{2,r}$
SU(2)	$\mathcal{K}^{q}_{1,r,\sigma\sigma'} = \mathcal{K}^{q}_{1,r,\overline{\sigma}\,\overline{\sigma'}}$ $\mathcal{K}^{q}_{1,r,\sigma\sigma} = \mathcal{K}^{q}_{1,r,\sigma\sigma'} + \mathcal{K}^{q}_{1,r,\overline{\sigma\sigma'}}$	$\mathcal{K}^{kq}_{2,r,\sigma\sigma'} = \mathcal{K}^{kq}_{2,r,\overline{\sigma}\,\overline{\sigma'}}$ $\mathcal{K}^{kq}_{2,r,\sigma\sigma} = \mathcal{K}^{kq}_{2,r,\sigma\sigma'} + \mathcal{K}^{kq}_{2,r,\overline{\sigma\sigma'}}$
Time reversal	$\mathcal{K}^{q}_{1,r,\sigma\sigma'} = \mathcal{K}^{q}_{1,r,\sigma'\sigma}$	$\mathcal{K}^{kq}_{2,r,\sigma\sigma'} = \overline{\mathcal{K}}^{kq}_{2r,\sigma\sigma'}$
Particle hole	$\left(\mathcal{K}^{q}_{1,r,\sigma\sigma'}\right)^* = \mathcal{K}^{(\Omega,-\mathbf{q})}_{1,r,\sigma\sigma'}$	$\left(\mathcal{K}^{kq}_{2,r,\sigma\sigma'}\right)^* = \mathcal{K}^{(\nu,\mathbf{\Pi}-\mathbf{k})(\Omega,-\mathbf{q})}_{2,r,\sigma\sigma'}$

TABLE I: Symmetry table for $\mathcal{K}_1$ and $\mathcal{K}_2$. Here, $\mathbf{\Pi} = (\pi, \pi, ...)$ represents the (d-dimensional) 'antiferromagnetic momentum' in the case of a simple (hyper)cubic lattice with lattice constant $a = 1$.

To conclude the discussion of the fundamental relations, we consider the complex conjugation operation, that leads to the following relations for $\mathcal{K}_1$:

$$\left(\mathcal{K}^{q}_{1,pp,\sigma\sigma'}\right)^* = \mathcal{K}^{-q}_{1,pp,\sigma'\sigma} \tag{D5a}$$

$$\left(\mathcal{K}^{q}_{1,ph,\sigma\sigma'}\right)^* = \mathcal{K}^{-q}_{1,ph,\sigma'\sigma} \tag{D5b}$$

$$\left(\mathcal{K}^{q}_{1,\overline{ph},\sigma\sigma'}\right)^* = \mathcal{K}^{q}_{1,\overline{ph},\sigma'\sigma}, \tag{D5c}$$

and for $\mathcal{K}_2$:

$$\left(\mathcal{K}^{kq}_{2,pp,\sigma\sigma'}\right)^* = \mathcal{K}^{(-k)(-q)}_{2,pp,\sigma'\sigma} \tag{D6a}$$

$$\left(\mathcal{K}^{kq}_{2,ph,\sigma\sigma'}\right)^* = \mathcal{K}^{(-k)(-q)}_{2,ph,\sigma'\sigma} \tag{D6b}$$

$$\left(\mathcal{K}^{kq}_{2,\overline{ph},\sigma\sigma'}\right)^* = \mathcal{K}^{(-k-q)q}_{2,\overline{ph},\sigma'\sigma}. \tag{D6c}$$

Using these fundamental relations, we can formulate the system-related physical symmetries, namely $SU(2)$, time reversal and particle-hole symmetry, in a channel-independent way. The results are summarized in Table I. Note that for the particle-hole symmetry, the relations differ for the frequency and momentum dependence. While in the purely local case, this symmetry implies a vanishing imaginary part of all two-particle quantities, this holds only for specific lattice-dependent $\mathbf{k}$ vectors in the non-local case.

2. Symmetries of $\mathcal{R}$

For the sake of completeness we report the symmetries of the remaining diagrammatic class, namely the rest function $\mathcal{R}$, which hold equally for the reducible vertex functions Φ. As shown above, the first set of fundamental relations results from exchanging two outgoing particles. We find the following relations for $\mathcal{R}$ in the different channels:

$$\mathcal{R}^{kk'q}_{pp,\sigma\sigma'} = -\mathcal{R}^{(k)(q-k')q}_{pp,\overline{\sigma\sigma'}} \tag{D7a}$$

$$\mathcal{R}^{kk'q}_{ph,\sigma\sigma'} = -\mathcal{R}^{kk'q}_{\overline{ph},\overline{\sigma\sigma'}} \tag{D7b}$$

$$\mathcal{R}^{kk'q}_{\overline{ph},\sigma\sigma'} = -\mathcal{R}^{kk'q}_{ph,\overline{\sigma\sigma'}}. \tag{D7c}$$

By means of the simultaneous exchange of both incoming and outgoing particles we obtain:

$$\mathcal{R}^{kk'q}_{pp,\sigma\sigma'} = \mathcal{R}^{(q-k)(q-k')q}_{pp,\sigma'\sigma} \tag{D8a}$$

$$\mathcal{R}^{kk'q}_{ph,\sigma\sigma'} = \mathcal{R}^{(k'+q)(k+q)(-q)}_{ph,\sigma'\sigma} \tag{D8b}$$

$$\mathcal{R}^{kk'q}_{\overline{ph},\sigma\sigma'} = \mathcal{R}^{(k'+q)(k+q)(-q)}_{\overline{ph},\sigma'\sigma}. \tag{D8c}$$

Finally, the complex conjugation operation leads to the following relations:

$$\left(\mathcal{R}^{kk'q}_{pp,\sigma\sigma'}\right)^* = \mathcal{R}^{(-k')(-k)(-q)}_{pp,\sigma'\sigma} \tag{D9a}$$

$$\left(\mathcal{R}^{kk'q}_{ph,\sigma\sigma'}\right)^* = \mathcal{R}^{(-k')(-k)(-q)}_{ph,\sigma'\sigma} \tag{D9b}$$

$$\left(\mathcal{R}^{kk'q}_{\overline{ph},\sigma\sigma'}\right)^* = \mathcal{R}^{(-k-q)(-k'-q)q}_{\overline{ph},\sigma'\sigma}. \tag{D9c}$$

In the same way as for $\mathcal{K}_1$ and $\mathcal{K}_2$, the fundamental relations for $\mathcal{R}$ allow us to express the physical symmetries in a channel-independent way, see Table II.

Symmetries	$\mathcal{R}_r$
SU(2)	$\mathcal{R}^{kk'q}_{r,\sigma\sigma'} = \mathcal{R}^{kk'q}_{r,\overline{\sigma}\,\overline{\sigma'}}$ $\mathcal{R}^{kk'q}_{r,\sigma\sigma} = \mathcal{R}^{kk'q}_{r,\sigma\sigma'} + \mathcal{R}^{kk'q}_{r,\overline{\sigma\sigma'}}$
Time reversal	$\mathcal{R}^{kk'q}_{r,\sigma\sigma'} = \mathcal{R}^{k'kq}_{r,\sigma'\sigma}$
Particle hole	$(\mathcal{R}^{kk'q}_{r,\sigma\sigma'})^* = \mathcal{R}^{(\nu,\mathbf{\Pi}-\mathbf{k})(\nu',\mathbf{\Pi}-\mathbf{k}')(\Omega,-\mathbf{q})}_{r,\sigma\sigma'}$

[1] N. Bickers, in *Theoretical Methods for Strongly Correlated Electrons*, edited by D. Sènèchal, A.-M. Tremblay, and C. Bourbonnais (Springer New York, 2004), CRM Series in Mathematical Physics, pp. 237–296, ISBN 978-0-387-00895-0.

[2] A. N. Tahvildar-Zadeh, J. K. Freericks, and M. Jarrell, Phys. Rev. B **55**, 942 (1997).

[3] J. Kuneš, Phys. Rev. B **83**, 085102 (2011).

[4] G. Rohringer, A. Valli, and A. Toschi, Phys. Rev. B **86**, 125114 (2012).

[5] M. Kinza, J. Ortloff, J. Bauer, and C. Honerkamp, Phys. Rev. B **87**, 035111 (2013).

[6] G. Rohringer, Ph.D. thesis, Vienna University of Technology (2014).

[7] S. Hummel, Master's thesis, Vienna University of Technology (2014).

[8] G. Li, N. Wentzell, P. Pudleiner, P. Thunström, and K. Held, Phys. Rev. B **93**, 165103 (2016).

[9] W. Metzner, M. Salmhofer, C. Honerkamp, V. Meden, and K. Schönhammer, Rev. Mod. Phys. **84**, 299 (2012).

[10] C. D. Dominicis and P. C. Martin, J. Math. Phys. **5**, 14 (1964).

[11] C. D. Dominicis and P. C. Martin, J. Math. Phys. **5**, 31 (1964).

[12] V. Janiš , Phys Rev. B **60**, 11345 (1999).

[13] A. Toschi, A. A. Katanin, and K. Held, Phys. Rev. B **75**, 045118 (2007).

[14] A. A. Katanin, A. Toschi, and K. Held, Phys. Rev. B **80**, 075104 (2009).

[15] G. Rohringer, A. Toschi, A. Katanin, and K. Held, Phys. Rev. Lett. **107**, 256402 (2011).

[16] T. Schäfer, F. Geles, D. Rost, G. Rohringer, E. Arrigoni, K. Held, N. Blümer, M. Aichhorn, and A. Toschi, Phys. Rev. B **91**, 125109 (2015).

[17] A. Valli, T. Schäfer, P. Thunström, G. Rohringer, S. Andergassen, G. Sangiovanni, K. Held, and A. Toschi, Phys. Rev. B **91**, 115115 (2015).

[18] G. Rohringer, A. Toschi, H. Hafermann, K. Held, V. I. Anisimov, and A. A. Katanin, Phys. Rev. B **88**, 115112 (2013).

[19] C. Taranto, S. Andergassen, J. Bauer, K. Held, A. Katanin, W. Metzner, G. Rohringer, and A. Toschi, Phys. Rev. Lett. **112**, 196402 (2014).

[20] A. E. Antipov, E. Gull, and S. Kirchner, Phys. Rev. Lett. **112**, 226401 (2014).

[21] A. N. Rubtsov, M. I. Katsnelson, and A. I. Lichtenstein, Phys. Rev. B **77**, 033101 (2008).

[22] A. N. Rubtsov, M. I. Katsnelson, A. I. Lichtenstein, and A. Georges, Phys. Rev. B **79**, 045133 (2009).

[23] H. Hafermann, G. Li, A. N. Rubtsov, M. I. Katsnelson, A. I. Lichtenstein, and H. Monien, Phys. Rev. Lett. **102**, 206401 (2009).

[24] N. Wentzell, C. Taranto, A. Katanin, A. Toschi, and S. Andergassen, Phys. Rev. B **91**, 045120 (2015).

[25] G. Li, Phys. Rev. B **91**, 165134 (2015).

[26] T. Ayral and O. Parcollet, Phys. Rev. B **92**, 115109 (2015).

[27] T. Ayral and O. Parcollet, Phys. Rev. B **93**, 235124 (2016), 1512.06719.

[28] T. Ayral and O. Parcollet, Phys. Rev. B **94**, 075159 (2016).

[29] A. A. Abrikosov, *Methods of Quantum Field Theory in Statistical Physics (Dover Books on Physics)* (Dover Publications, 1975), rev. english ed., ISBN 9780486632285.

[30] G. Rohringer and A. Toschi, Phys. Rev. B **94**, 125144 (2016).

[31] H. Hafermann, S. Brener, A. N. Rubtsov, M. I. Katsnelson, and A. I. Lichtenstein, JETP Lett. **86**, 677 (2008).

[32] T. Schäfer, G. Rohringer, O. Gunnarsson, S. Ciuchi, G. Sangiovanni, and A. Toschi, Phys. Rev. Lett. **110**, 246405 (2013).

[33] E. Kozik, M. Ferrero, and A. Georges, Phys. Rev. Lett. **114**, 156402 (2015).

[34] T. Schäfer, S. Ciuchi, M. Wallerberger, P. Thunstrm, O. Gunnarsson, G. Sangiovanni, G. Rohringer, and A. Toschi, arXiv:1606.03393 (2016).

[35] T. Ribic, G. Rohringer, and K. Held, Phys Rev. B **93**, 195105 (2016).

[36] M. Salmhofer, *Renormalization: An Introduction (Theoretical and Mathematical Physics)* (Springer, Berlin and Heidelberg, 1999), corrected ed., ISBN 9783540646662.

[37] C. Wetterich, Phys. Lett. B **301**, 90 (1993).

[38] M. Salmhofer and C. Honerkamp, Prog. Theor. Phys. **105**, 1 (2001).

[39] K.-U. Giering and M. Salmhofer, Phys. Rev. B **86**, 245122 (2012).

[40] C. Honerkamp, D. Rohe, S. Andergassen, and T. Enss, Phys. Rev. B **70**, 235115 (2004).

[41] C. Karrasch, A. Oguri, and V. Meden, Phys. Rev. B **77**, 024517 (2008).

[42] C. Husemann and M. Salmhofer, Phys. Rev. B **79**, 195125 (2009).

[43] A. A. Katanin, Phys. Rev. B **70**, 115109 (2004).

[44] A. Eberlein, Phys. Rev. B **90**, 115125 (2014).

[45] A. A. Katanin, Phys. Rev. B **79**, 235119 (2009).

[46] S.-X. Yang, H. Fotso, H. Hafermann, K.-M. Tam, J. Moreno, T. Pruschke, and M. Jarrell, Phys. Rev. B **84**, 155106 (2011).

[47] V. Janiš and V. Pokorný, Phys. Rev. B **90**, 045143 (2014).

[48] O. Gunnarsson, T. Schäfer, J. P. F. LeBlanc, E. Gull, J. Merino, G. Sangiovanni, G. Rohringer, and A. Toschi, Phys. Rev. Lett. **114**, 236402 (2015).

II Efficient Bethe-Salpeter equations treatment in dynamical mean-field theory

Efficient Bethe-Salpeter equation treatment in dynamical mean-field theory

Agnese Tagliavini,[1,2] Stefan Hummel,[3] Nils Wentzell,[1,4] Sabine Andergassen,[2] Alessandro Toschi,[1] and Georg Rohringer[5]

[1]*Institute for Solid State Physics, Technische Universität Wien, 1040 Vienna, Austria*

[2]*Institut für Theoretische Physik and Center for Quantum Science, Universität Tübingen, Auf der Morgenstelle 14, 72076 Tübingen, Germany*

[3]*Physics of Nanostructured Materials, Faculty of Physics, University of Vienna, 1090 Vienna, Austria*

[4]*Institut de Physique Théorique (IPhT), CEA, CNRS, 91191 Gif-sur-Yvette, France*

[5]*Russian Quantum Center, 143025 Skolkovo, Russia*

(Received 9 March 2018; revised manuscript received 1 June 2018; published 22 June 2018)

We present here two alternative schemes designed to correct the high-frequency truncation errors in the numerical treatment of the Bethe-Salpeter equations. The schemes are applicable to all Bethe-Salpeter calculations with a local two-particle irreducible vertex, which is relevant, e.g., for the dynamical mean-field theory (DMFT) and its diagrammatic extensions. In particular, within a purely diagrammatic framework, we could extend existing algorithms for treating the static case in the particle-hole sector to more general procedures applicable to *all bosonic frequencies* and *all* channels. After illustrating the derivation and the theoretical interrelation of the two proposed schemes, these have been applied to the Bethe-Salpeter equations for the auxiliary Anderson impurity models of selected DMFT calculations, where results can be compared against a numerically "exact" solution. The successful performance of the proposed schemes suggests that their implementation can significantly improve the accuracy of DMFT calculations at the two-particle level, in particular for more realistic multiorbital calculations where the large number of degrees of freedom substantially restricts the actual frequency range for numerical calculations, as well as—on a broader perspective—of the diagrammatic extensions of DMFT.

DOI: 10.1103/PhysRevB.97.235140

I. INTRODUCTION

Scattering experiments have always been of utmost importance for gaining new insights into the laws of physics. Among the most famous findings which have been achieved by this technique are the unveiling of the structure of the atom [1] or the discovery of the Higgs boson [2], which confirmed one of the major predictions of the standard model of particle theory. On the theoretical side, Feynman diagrammatic perturbation theory turned out to be a powerful tool to calculate the corresponding two-particle scattering amplitudes. This technique has been particularly successful in theories such as quantum electrodynamics where a small expansion parameter (like the fine structure constant α) allows to truncate the perturbation series at low order.

The situation is, however, very different for highly correlated (lattice) electrons where the strong interaction between the particles prevents any finite-order perturbative treatment. In fact, a rich spectrum of correlation-driven phenomena, like the celebrated Mott metal-to-insulator transition [3,4] (MIT) or the high-temperature superconductivity in the cuprates [5,6], are inaccessible by finite diagrammatic expansion. In this respect, significant progress has been achieved by the dynamical mean-field theory [7–9] (DMFT), which can describe all purely local correlations in the system. DMFT has several successes, like the understanding of realistic correlated materials [10,11]. However, it still exhibits a number of limitations which prevent a complete description of (realistic) correlated electron systems. Two of them are of particular importance:

(i) Hitherto, DMFT calculations have been often restricted to the one-particle level, i.e., to the calculation of the self-energy and the spectral function of the system. While the latter provide crucial information about the one-particle excitations and can be compared to (angular resolved) photoemission spectroscopy (ARPES), the insights that can be gained from two-particle correlation functions are certainly of equal (or even higher) significance. Among the latter are the optical conductivity and the magnetic, charge, or particle-particle susceptibility which describe the linear response of the system to an external (electric, magnetic or pairing) source field. In the case of strong correlations, an accurate evaluation of these response functions requires the inclusion of vertex corrections [12,13]. These have been in most cases neglected with the exception of few recent calculations [14–18]. Moreover, an improved treatment of two-particle vertex functions will be also highly beneficial for the so-called "fluctuation diagnostics" method [19], which has been applied to the self-energy or spectral function to disentangle features originated from different collective fluctuations in the system.

(ii) An intrinsic limitation of DMFT is the locality of the self-energy which, hence, includes only local correlations effects. However, neglecting the impact of nonlocal collective modes on the spectral function yields often poor results at low temperature where long-range order parameter fluctuations dominate the physics. In order to overcome these difficulties, so-called cluster, e.g., cellular DMFT [20] and dynamical cluster approximation [21–23] (DCA), as well as diagrammatic extensions of DMFT [24] have been developed. The most important among the latter are the diagrammatic vertex approximation [25–27] (DΓA), the dual fermion (DF) theory [28], the one-particle irreducible approach [29] (1PI), the dual

boson (DB) theory [30], DMF^{2}RG [31], as well as the TRILEX [32,33] and the QUADRILEX [34] method.

Both (i) the calculation of vertex corrections within DMFT and (ii) the inclusion of nonlocal correlation effects beyond DMFT in the self-energy require the calculation of (nonlocal) ladder diagrams. This is achieved by DMFT building blocks, i.e., the nonlocal DMFT Green's function and the (local) two-particle irreducible vertex (in a given channel), which makes an accurate determination of the latter indispensable. In practice, this local irreducible vertex is obtained from inverting the so-called (local) Bethe-Salpeter (BS) equations which are integral equations with respect to (w.r.t.) the fermionic Matsubara frequency arguments of the local one- and two-particle DMFT correlation functions. While, in principle, the "internal" fermionic frequency sums run on an infinite range, in practice, one has to restrict oneself to a finite frequency interval. This transforms the inversion of the BS equations into the inversion of a finite matrix in the fermionic frequency space, whose size is, due to the numerical computational cost and possibly memory constraints, rather small. This limitation is particularly severe when the parquet formalism [35–37] is used. Obviously, such a cut-off procedure in the frequency space produces an error which might drastically limit the accuracy of two-particle response functions or results of diagrammatic extensions of DMFT based on these irreducible vertices.

In this paper, we present new schemes to correct the errors, which arise from the restriction of the BS equations to a finite frequency grid. The proposed procedures are based on the observation that the complexity of the frequency dependence of the DMFT two-particle vertex functions is drastically reduced for large values of these frequencies [37–39]. In fact, in the asymptotic high-frequency regime the DMFT scattering amplitude can be represented by related response functions and fermion-boson vertices which depend on one and two (instead of three) frequencies, respectively. Hence they can be evaluated numerically on a much larger frequency grid, and we can approximate the full two-particle correlation functions of DMFT by these so-called asymptotic functions outside the (possibly rather small) frequency regime where the full three-frequency objects have to be calculated. A similar procedure has been already proposed in Ref. [40] where, however, the asymptotic functions have been obtained by means of functional derivatives of the normal self-energy, restricting the method to BS equations in the particle-hole channels at bosonic transfer frequency $\omega=0$. Here, instead, we adopt a diagrammatic analysis of the two-particle vertices of DMFT, put forward in Refs. [37–39], which provides the high-frequency behavior of the vertex for *all* channels and also for $\omega\neq 0$. Besides extending the method presented in Ref. [40], this also allows us to develop a new approach based on the asymptotics of the full two-particle correlations functions.

The paper is organized in the following way. In Sec. II, we give the explicit expressions of all local DMFT two-particle correlations functions used throughout the paper and discuss their high-frequency asymptotic behavior. This is then used in Sec. III for the two newly proposed methods for accurately solving the BS equations. In Sec. IV, numerical results are presented for both approaches and Sec. V is devoted to conclusions and an outlook.

II. THEORY AND FORMALISM

In this section, we will give all necessary definitions and recall the asymptotic high-frequency behavior of local two-particle correlation functions which are relevant for the main goal of this paper, i.e., a consistent and numerically stable calculation of the irreducible vertex functions of DMFT. More specifically, in Sec. II A, we introduce the model, for which the applicability of our new approach has been tested, and the general two-particle formalism which is required for the development of our new methods. In Sec. II B, we revisit [37,39,41] the diagrammatic techniques for analyzing the frequency structure of the different two-particle vertex functions and present their high-frequency behavior in terms of collective modes (described by physical susceptibilities) and their interaction with the particles of the system (fermion-boson vertex).

A. Definitions and notation

We consider the single-band Hubbard model for a generic lattice in d dimensions,

$$\hat{\mathcal{H}} = -t \sum_{\langle ij\rangle,\sigma} \hat{c}^{\dagger}_{i\sigma}\hat{c}_{j\sigma} + U\sum_{i}\hat{n}_{i\uparrow}\hat{n}_{i\downarrow} - \mu\sum_{i,\sigma}\hat{n}_{i\sigma}, \quad (1)$$

where $\hat{c}^{(\dagger)}_{i\sigma}$ annihilates (creates) an electron with spin σ at the lattice site $\mathbf{R}_i$ ($\hat{n}_{i\sigma}=\hat{c}^{\dagger}_{i\sigma}\hat{c}_{i\sigma}$), t is the hopping amplitude for electrons between neighboring sites, μ the chemical potential, and U the on-site Coulomb interaction. Here, we adopt DMFT to treat this model and, hence, we consider the purely local one- and two-particle correlation and (reducible as well as irreducible) vertex functions of the Anderson impurity model (AIM) related to the DMFT solution of the Hamiltonian given in Eq. (1). The basic two-particle correlation function, from which the irreducible vertices can be derived, is the generalized susceptibility defined by

$$\begin{aligned}\chi^{\nu\nu'\omega}_{ph,\sigma\sigma'} = \int_0^{\beta} d\tau_1 d\tau_2 d\tau_3\, e^{-i\nu\tau_1} e^{i(\nu+\omega)\tau_2} e^{-i(\nu'+\omega)\tau_3} \\ \times [\langle T_\tau c^{\dagger}_{\sigma}(\tau_1)c_{\sigma}(\tau_2)c^{\dagger}_{\sigma'}(\tau_3)c_{\sigma'}(0)\rangle \\ - \langle T_\tau c^{\dagger}_{\sigma}(\tau_1)c_{\sigma}(\tau_2)\rangle\langle T_\tau c^{\dagger}_{\sigma'}(\tau_3)c_{\sigma'}(0)\rangle], \end{aligned} \quad (2)$$

where $\nu(\nu')=\frac{\pi}{\beta}(2n(n')+1)$, $n,n'\in\mathbb{Z}$, is a fermionic and $\omega=\frac{\pi}{\beta}2m$, $m\in\mathbb{Z}$, a bosonic Matsubara frequency. T_τ is the time-ordering operator and $\langle\ldots\rangle = Z^{-1}\mathrm{Tr}(e^{-\beta\hat{\mathcal{H}}}\ldots)$ denotes the thermal expectation value, with $Z=\mathrm{Tr}(e^{-\beta\hat{\mathcal{H}}})$. $\beta=1/T$ is the inverse temperature of the system. The assignment of the frequencies ν, $\nu+\omega$, and $\nu'+\omega$ to the imaginary times τ_1, τ_2, and τ_3, respectively, corresponds to the so-called particle-hole (ph) notation [37]. Analogously, one can express the generalized susceptibility in the transverse particle-hole ($\overline{ph}$) or in the particle-particle (pp) notation which can be obtained from the ph one by a mere frequency shift, i.e., $\chi^{\nu\nu'\omega}_{\overline{ph},\sigma\sigma'} \equiv \chi^{\nu(\nu+\omega)(\nu'-\nu')}_{ph,\sigma\sigma'}$ and $\chi^{\nu\nu'\omega}_{pp,\sigma\sigma'} \equiv \chi^{\nu\nu'(\omega-\nu-\nu')}_{ph,\sigma\sigma'}$, respectively. The different physical interpretations of these notations as particle-hole and particle-particle scattering amplitude are discussed in detail in Refs. [37] and [39] (see, in particular, Figs. 1 and 2 in the former).

In the SU(2) symmetric situation considered here, it is convenient to decompose the two-particle correlation functions into their spin singlet- and spin triplet-components, both for the *ph* and the *pp* representation. This corresponds to the definitions of the generalized susceptibilities in the density (d), magnetic (m), particle-particle singlet (s), and particle-particle triplet (t) channels:[1]

$$\chi_d^{\nu\nu'\omega} = \chi_{ph,\uparrow\uparrow}^{\nu\nu'\omega} + \chi_{ph,\uparrow\downarrow}^{\nu\nu'\omega}, \tag{3a}$$

$$\chi_m^{\nu\nu'\omega} = \chi_{ph,\uparrow\uparrow}^{\nu\nu'\omega} - \chi_{ph,\uparrow\downarrow}^{\nu\nu'\omega}, \tag{3b}$$

$$\chi_s^{\nu\nu'\omega} = \tfrac{1}{4}\big(-\chi_{pp,\uparrow\uparrow}^{\nu\nu'\omega} + 2\chi_{pp,\uparrow\downarrow}^{\nu\nu'\omega} - 2\chi_{0,pp}^{\nu\nu'\omega}\big), \tag{3c}$$

$$\chi_t^{\nu\nu'\omega} = \tfrac{1}{4}\big(\chi_{pp,\uparrow\uparrow}^{\nu\nu'\omega} + 2\chi_{0,pp}^{\nu\nu'\omega}\big). \tag{3d}$$

The bare susceptibilities in the particle-hole and particle-particle notation are given by

$$\chi_{0,d/m}^{\nu\nu'\omega} = \chi_{0,ph}^{\nu\nu'\omega} = -\beta G(\nu)G(\nu+\omega)\delta_{\nu\nu'}, \tag{4a}$$

$$\chi_{0,s/t}^{\nu\nu'\omega} = \chi_{0,pp}^{\nu\nu'\omega} = -\frac{\beta}{2}G(\nu)G(\omega-\nu)\delta_{\nu\nu'}, \tag{4b}$$

where $G(\nu)$ is the local single-particle DMFT Green's function. From the generalized susceptibilities in Eqs. (3) the corresponding physical ones can be obtained by summing the former over the fermionic Matsubara frequencies ν and ν'. They explicitly read [see Fig. 7(a)]

$$\chi_{d/m}^{\omega} = \frac{1}{\beta^2}\sum_{\nu\nu'}\chi_{d/m}^{\nu\nu'\omega},$$

$$\chi_{pp,\uparrow\downarrow}^{\omega} = \frac{2}{\beta^2}\sum_{\nu\nu'}\chi_s^{\nu\nu'\omega} = \frac{1}{\beta^2}\sum_{\nu\nu'}\big(\chi_{pp,\uparrow\downarrow}^{\nu\nu'\omega} - 2\chi_{0,pp}^{\nu\nu'\omega}\big), \tag{5}$$

and describe the physical response to a (local) chemical potential, a magnetic and a singlet ($\uparrow\downarrow$) pairing field, respectively. The last equality in Eq. (5) follows from $\sum_{\nu\nu'}(\chi_t^{\nu\nu'\omega} - \chi_{0,pp}^{\nu\nu'\omega}) = 0$, which is a consequence of the Pauli principle and reflects the fact, that in a purely local (single-orbital) model no triplet superconductivity is possible.

From the definition of the generalized susceptibilities a number of different *vertex* functions can be derived. By removing all unconnected parts and amputating the outer legs from $\chi_r^{\nu\nu'\omega}$ the so-called *full* two-particle vertex is obtained as

$$F_r^{\nu\nu'\omega} = -\frac{\chi_r^{\nu\nu'\omega} \mp \chi_{0,r}^{\nu\nu'\omega}}{\frac{1}{\beta^2}\sum_{\nu_1\nu_2}\chi_{0,r}^{\nu\nu_1\omega}\chi_{0,r}^{\nu_2\nu'\omega}}, \tag{6}$$

where the minus sign has to be used for $r = d,m,t$ and the plus sign for $r = s$. Physically, $F_r^{\nu\nu'\omega}$ corresponds the full two-particle scattering amplitude between (quasi)particles [42], which is represented by the set of *all* connected (amputated) two-particle Feynman diagrams.

Diagrammatically, by "gluing" together the outgoing (or the incoming) outer legs of a generalized susceptibility (i.e., summing over the respective fermionic frequency) and amputating the two remaining outer legs, one obtains the fermion-boson vertices[2] [see also Fig. 7(b)]

$$\lambda_{d/m}^{\nu\omega} = \mp\frac{1}{\beta}\frac{\sum_{\nu'}\chi_{d/m}^{\nu\nu'\omega}}{G(\nu)G(\nu+\omega)} \mp 1,$$

$$\lambda_{pp,\uparrow\downarrow}^{\nu\omega} = \frac{2}{\beta}\frac{\sum_{\nu'}\chi_s^{\nu\nu'\omega}}{G(\nu)G(\omega-\nu)} - 1 = \frac{1}{\beta}\frac{\sum_{\nu'}\chi_{pp,\uparrow\downarrow}^{\nu\nu'\omega}}{G(\nu)G(\omega-\nu)}, \tag{7}$$

and $\lambda_r^{\nu'\omega}$ is obtained by exchanging ν and ν'. The fermion-boson vertices $\lambda_r^{\nu\omega}$ are related to the interaction between a fermion with energy ν and a collective charge, spin or singlet ($\uparrow\downarrow$) particle-particle excitations with frequency ω, respectively. The last equality in Eq. (7) as well as the vanishing of a triplet particle-particle fermion-boson vertex, i.e., $\lambda_{t=\uparrow\uparrow}^{\nu\omega} = 0$, again follow from the Pauli principle.

Let us finally turn our attention to the central objects of this paper, i.e., the vertices $\Gamma_r^{\nu\nu'\omega}$ which are two-particle irreducible in channel r. A Feynman diagram for the two-particle vertex is called irreducible in channel $r = ph, \overline{ph}, pp$, if it *cannot* be split into two separated diagrams by cutting two internal fermionic lines in such a way that one of the two contains the outer frequencies $(\nu, \pm\nu+\omega)$ and the other $(\nu', \pm\nu'+\omega)$ w.r.t. the corresponding natural frequency convention [see discussion below Eq. (2)]. The sum of all diagrams of a certain type then yields the irreducible vertices $\Gamma_{ph,\sigma\sigma'}^{\nu\nu'\omega}$, $\Gamma_{\overline{ph},\sigma\sigma'}^{\nu\nu'\omega}$, and $\Gamma_{pp,\sigma\sigma'}^{\nu\nu'\omega}$ (which are always assumed to be represented in their corresponding frequency notation). Due to the crossing and SU(2) symmetry [35,37], $\Gamma_{\overline{ph},\sigma\sigma'}^{\nu\nu'\omega}$ can be expressed in terms of $\Gamma_{ph,\sigma\sigma'}^{\nu\nu'\omega}$ and, hence, we can restrict ourselves to $\Gamma_{ph,\sigma\sigma'}^{\nu\nu'\omega}$ and $\Gamma_{pp,\sigma\sigma'}^{\nu\nu'\omega}$ in the following. Moreover, in the SU(2) symmetric case, where $\uparrow\uparrow = \downarrow\downarrow$ and $\uparrow\downarrow = \downarrow\uparrow$, it is convenient to introduce spin-singlet and spin-triplet components for the irreducible vertices [37] [analogously as for the generalized susceptibilities in Eq. (3)]

$$\Gamma_d^{\nu\nu'\omega} = \Gamma_{ph,\uparrow\uparrow} + \Gamma_{ph,\uparrow\downarrow}, \tag{8a}$$

$$\Gamma_m^{\nu\nu'\omega} = \Gamma_{ph,\uparrow\uparrow} - \Gamma_{ph,\uparrow\downarrow}, \tag{8b}$$

$$\Gamma_s^{\nu\nu'\omega} = -\Gamma_{pp,\uparrow\uparrow} + 2\Gamma_{pp,\uparrow\downarrow}, \tag{8c}$$

$$\Gamma_t^{\nu\nu'\omega} = \Gamma_{pp,\uparrow\uparrow}. \tag{8d}$$

Note that here (in contrast to the corresponding definitions for $\chi_r^{\nu\nu'\omega}$), the index r refers to *both* the channel in which the vertex is irreducible (ph for $r = d,m$ or pp for $r = s,t$) as well as the spin combination and the frequency notation in which the vertex is represented ($\Gamma_{d,m}^{\nu\nu'\omega}$ in the ph and $\Gamma_{s,t}^{\nu\nu'\omega}$ in the pp frequency notation).

The irreducible vertex functions can be now obtained from the generalized susceptibilities via the BS equation

$$\pm\chi_r^{\nu\nu'\omega} = \chi_{0,r}^{\nu\nu'\omega} - \frac{1}{\beta^2}\sum_{\nu_1\nu_2}\chi_{0,r}^{\nu\nu_1\omega}\Gamma_r^{\nu_1\nu_2\omega}\chi_r^{\nu_2\nu'\omega}, \tag{9}$$

[1]Note that the definitions for the singlet(s) and triplet(t) susceptibilities slightly differ from the corresponding ones given in Ref. [37] [Eqs. (B19) therein] in order to obtain a unified form for the BS equation in all channels.

[2]Note that the fermion-boson vertices in Eqs. (7) differ from the corresponding definitions in the dual boson [30] and TRILEX [32,33] theories by a factor $1 \pm U\chi_r^{\omega}$. Physically, this means that the $\lambda_r^{\nu\omega}$'s as given in Eqs. (7) still contain contributions from collective modes [27].

with the plus for $r=d,m,t$ and the minus for $r=s$. By solving Eq. (9) for the irreducible vertex $\Gamma_r^{\nu\nu'\omega}$, we obtain

$$\underline{\underline{\Gamma_r^\omega}} = \beta^2\left[\left(\underline{\underline{\chi_r^\omega}}\right)^{-1} \mp \left(\underline{\underline{\chi_{0,r}^\omega}}\right)^{-1}\right], \tag{10}$$

with the minus for $r=d,m,t$ and the plus sign for $r=s$. $\underline{\underline{X_r^\omega}} \equiv X_r^{\nu\nu'\omega}$ indicates a (infinite) matrix in the fermionic frequencies ν and ν' (for a given value of the bosonic frequency ω) and $(\underline{\underline{X_r^\omega}})^{-1}$ is its inverse (w.r.t. ν and ν').

B. Asymptotics of the vertex functions

In this section, we review the behavior [37,39,41] of the irreducible vertex $\Gamma_r^{\nu\nu'\omega}$ and the generalized susceptibility $\chi_r^{\nu\nu'\omega}$ for large values of ν and ν' (for a fixed value of the bosonic Matsubara frequency ω). As it has been discussed extensively in Refs. [37,39,43], this high-frequency asymptotics can be expressed in terms of the physical susceptibilities χ_r^ω [Eq. (5)] and the fermion-boson vertices $\lambda_r^{\nu\omega}$ [Eq. (7)]. Here we present just the final expressions for $\Gamma_{r,\text{asym}}^{\nu\nu'\omega}$ and $\chi_{r,\text{asym}}^{\nu\nu'\omega}$ (or $F_{r,\text{asymp}}^{\nu\nu'\omega}$) and refer the reader to Appendix A for their explicit derivations.

The vertex $\Gamma_r^{\nu\nu'\omega}$ contains all diagrams which are not reducible in channel r. Its asymptotic high-frequency behavior for $\nu,\nu'\to\infty$ and a fixed value of ω is, hence, determined by the fully irreducible vertex $\Lambda_r^{\nu\nu'\omega}$ and the reducible vertices $\Phi_{r'}^{\nu\nu'\omega}$ with $r'\neq r$ [see parquet Eqs. (A1) in Appendix A]. The former contributes just via the bare interaction, i.e., by a term $\propto U$ (where the prefactor depends on the channel r), while the high-frequency behavior of the latter can be expressed in terms of the physical susceptibilities χ_r^ω [Eq. (5)]. Following the discussion in Appendix A, we explicitly obtain for $\Gamma_{r,\text{asym}}^{\nu\nu'\omega}$,

$$\Gamma_{d,\text{asym}}^{\nu\nu'\omega} = U + \frac{U^2}{2}\chi_d^{\nu'-\nu} + \frac{3U^2}{2}\chi_m^{\nu'-\nu} - U^2\chi_{pp,\uparrow\downarrow}^{\nu+\nu'+\omega}, \tag{11a}$$

$$\Gamma_{m,\text{asym}}^{\nu\nu'\omega} = -U + \frac{U^2}{2}\chi_d^{\nu'-\nu} - \frac{U^2}{2}\chi_m^{\nu'-\nu} + U^2\chi_{pp,\uparrow\downarrow}^{\nu+\nu'+\omega}, \tag{11b}$$

$$\Gamma_{s,\text{asym}}^{\nu\nu'\omega} = 2U - \frac{U^2}{2}\chi_d^{\nu'-\nu} + \frac{3U^2}{2}\chi_m^{\nu'-\nu} - \frac{U^2}{2}\chi_d^{\omega-\nu-\nu'} + \frac{3U^2}{2}\chi_m^{\omega-\nu-\nu'}, \tag{11c}$$

$$\Gamma_{t,\text{asym}}^{\nu\nu'\omega} = \frac{U^2}{2}\chi_d^{\nu'-\nu} + \frac{U^2}{2}\chi_m^{\nu'-\nu} - \frac{U^2}{2}\chi_d^{\omega-\nu-\nu'} - \frac{U^2}{2}\chi_m^{\omega-\nu-\nu'}. \tag{11d}$$

We note that this asymptotic expansion corresponds to the one presented in Ref. [39], where the susceptibilities χ_r^ω (multiplied by U^2) have been referred to as Kernel-one functions $\mathcal{K}_{1,r}^\omega$.

In order to obtain the high-frequency asymptotics of the full vertex we use that $F_r^{\nu\nu'\omega} = \Gamma_r^{\nu\nu'\omega} + \Phi_r^{\nu\nu'\omega}$. Hence we only have to add the high-frequency contributions of $\Phi_r^{\nu\nu'\omega}$ to the corresponding ones of $\Gamma_r^{\nu\nu'\omega}$ in Eqs. (11). As discussed in detail in Appendix A, the former correspond to the fermion-boson vertex $\lambda_r^{\nu\omega}$ [see Eqs. (7) and (A3)], which leads to the following expressions for the high-frequency behavior of $F_r^{\nu\nu'\omega}$ for $\nu,\nu'\to\infty$ (with ω fixed):

$$F_{d,\text{asym}}^{\nu\nu'\omega} = U + \frac{U^2}{2}\chi_d^{\nu'-\nu} + \frac{3U^2}{2}\chi_m^{\nu'-\nu} - U^2\chi_{pp,\uparrow\downarrow}^{\nu+\nu'+\omega} + U\lambda_d^{\nu\omega} + U\lambda_d^{\nu'\omega} + U^2\chi_d^\omega, \tag{12a}$$

$$F_{m,\text{asym}}^{\nu\nu'\omega} = -U + \frac{U^2}{2}\chi_d^{\nu'-\nu} - \frac{U^2}{2}\chi_m^{\nu'-\nu} + U^2\chi_{pp,\uparrow\downarrow}^{\nu+\nu'+\omega} + U\lambda_m^{\nu\omega} + U\lambda_m^{\nu'\omega} + U^2\chi_m^\omega, \tag{12b}$$

$$F_{s,\text{asym}}^{\nu\nu'\omega} = 2U - \frac{U^2}{2}\chi_d^{\nu'-\nu} + \frac{3U^2}{2}\chi_m^{\nu'-\nu} - \frac{U^2}{2}\chi_d^{\omega-\nu-\nu'} + \frac{3U^2}{2}\chi_m^{\omega-\nu-\nu'} + 2U\lambda_{pp,\uparrow\downarrow}^{\nu\omega} + 2U\lambda_{pp,\uparrow\downarrow}^{\nu'\omega} + 2U^2\chi_{pp,\uparrow\downarrow}^\omega, \tag{12c}$$

$$F_{t,\text{asym}}^{\nu\nu'\omega} = \frac{U^2}{2}\chi_d^{\nu'-\nu} + \frac{U^2}{2}\chi_m^{\nu'-\nu} - \frac{U^2}{2}\chi_d^{\omega-\nu-\nu'} - \frac{U^2}{2}\chi_m^{\omega-\nu-\nu'}. \tag{12d}$$

We note that $\lambda_r^{\nu\omega}$ is related to the so-called Kernel-two functions of Ref. [39] by $\mathcal{K}_{2,r}^{\nu\omega} \sim U\lambda_r^{\nu'\omega} + U^2\chi_r^\omega$.

From $F_{r,\text{asym}}^{\nu\nu'\omega}$ and Eq. (6), we can now easily obtain $\chi_{d,\text{asym}}^{\nu\nu'\omega}$ as

$$\chi_{r,\text{asym}}^{\nu\nu'\omega} = \chi_{0,r}^{\nu\nu'\omega} - \frac{1}{\beta^2}\sum_{\nu_1\nu_2}\chi_{0,r}^{\nu\nu_1\omega}F_{r,\text{asym}}^{\nu_1\nu_2\omega}\chi_{0,r}^{\nu_2\nu'\omega}, \tag{13}$$

which completes our analysis of the high-frequency asymptotic behavior of two-particle correlation functions.

III. NUMERICAL IMPLEMENTATIONS

In order to calculate $\underline{\underline{\Gamma_r^\omega}}$ according to Eq. (10), one has to invert the two-dimensional infinite matrix $\underline{\underline{\chi_r^\omega}}$. In practice, $\chi_r^{\nu\nu'\omega}$, as obtained from a DMFT impurity solver such as exact diagonalization (ED) or quantum Monte Carlo (QMC), is available only on a finite frequency grid with a rather limited number of frequencies. In fact, for a given bosonic frequency ω, the numerical cost for obtaining $\chi_r^{\nu\nu'\omega}$ numerically exactly with any of the current state-of-the-art impurity solvers (ED, QMC, etc..) is typically at least proportional to $\sim N^2$, where N is the number of fermionic frequencies. Hence one has to restrict oneself to a rather small number of frequencies for performing the inversion of Eq. (10), which might introduce a non-negligible truncation error in the results for $\Gamma_r^{\nu\nu'\omega}$. On the other hand, for large values of the frequencies ν and ν', the functions $\chi_r^{\nu\nu'\omega}$ and $\Gamma_r^{\nu\nu'\omega}$ can be replaced by their asymptotic forms (13) and (11), respectively. The latter are given in terms of the physical susceptibilities χ_r^ω and the fermion-boson vertex $\lambda_r^{\nu\omega}$ which depend on a *single* (fermionic or bosonic) frequency argument (for a fixed value of ω). Hence the cost of calculating them by means of the impurity solver grows only linearly with the number of frequencies and therefore they can be obtained for a much larger frequency grid (see Appendix B for technical details on the calculation of χ_r^ω and $\lambda_r^{\nu\omega}$ within ED).

The above discussion suggests the following procedure to determine $\Gamma_r^{\nu\nu'\omega}$ from $\chi_r^{\nu\nu\omega}$: we start by specifying the frequency interval $I = [M_{\min}, M_{\max}]$, with $M_{\min}, M_{\max} \in \mathbb{Z}$ (for the fermionic Matsubara indices n and n', i.e., $n,n' \in I$), for which these functions should be computed. We then split it into a (small) low- and (large) high-frequency part $I_0 = [N_{\min}, N_{\max}]$, with $M_{\min} < N_{\min} < N_{\max} < M_{\max} \in \mathbb{Z}$, and $I_1 = I \backslash I_0$, respectively (for an illustration see Fig. 2). Following Ref. [40] we can rewrite the matrices $\underline{\underline{\chi_r^\omega}}$ and $\underline{\underline{\Gamma_r^\omega}}$ as

$$\underline{\underline{\chi_r^\omega}} = \begin{pmatrix} \underline{\underline{\chi_r^{\omega 00}}} & \underline{\underline{\chi_r^{\omega 01}}} \\ \underline{\underline{\chi_r^{\omega 10}}} & \underline{\underline{\chi_r^{\omega 11}}} \end{pmatrix}, \quad \underline{\underline{\Gamma_r^\omega}} = \begin{pmatrix} \underline{\underline{\Gamma_r^{\omega 00}}} & \underline{\underline{\Gamma_r^{\omega 01}}} \\ \underline{\underline{\Gamma_r^{\omega 10}}} & \underline{\underline{\Gamma_r^{\omega 11}}} \end{pmatrix}, \tag{14}$$

where the 00 block contains the values of the respective function for $\nu,\nu' \in I_0$, the 01 block for $\nu \in I_0$ and $\nu' \in I_1$, the 10 block for $\nu \in I_1$ and $\nu' \in I_0$, and the 11 block for both $\nu,\nu' \in I_1$. In the blocks 10, 01, and 11 (i.e., where at least one of the frequencies ν or ν' is in the region I_1 and, hence, "large") we can then replace the exact values for $\chi_r^{\nu\nu'\omega}$ and $\Gamma_r^{\nu\nu'\omega}$ by their asymptotic functions given in Eqs. (13) and (11), limiting the numerical treatment of the full frequency dependence to the 00 region, i.e., for low frequencies $\nu,\nu' \in I_0$. The goal is then to compute the low-frequency part of $\Gamma_r^{\nu\nu'\omega}$, i.e., $\underline{\underline{\Gamma_r^{\omega 00}}}$ from Eq. (10).

An important question concerns the choice of the intervals I_0 and I. As detailed in Ref. [37], the main low-energy structures that are not captured by the asymptotic functions $\Gamma_{r,\text{asym}}$ and $\chi_{r,\text{asym}}$ arise in a frequency box $I_{\text{low-energy}}$ spanned by[3] the corners (0,0), (0,$\pm\omega$), ($\pm\omega$,0), and ($\pm\omega$,$\pm\omega$) (with $-$ for $r = d,m$ and $+$ for $r = s,t$). In order to take them into account exactly, the inner frequency interval I_0 has to be larger than ω. For numerical convenience, it is advantageous to choose I_0 and I symmetrically around $I_{\text{low-energy}}$.

If we now multiply Eq. (10) with $\underline{\underline{\chi_r^\omega}}$ from the left, we obtain a matrix equation for $\underline{\underline{\Gamma_r^\omega}}$. Using the block representation of Eq. (14) to separate $\underline{\underline{\chi_r^\omega}}$ and $\underline{\underline{\Gamma_r^\omega}}$ into low- and high-frequency contributions, we get

$$\begin{aligned} &\frac{1}{\beta^2}\begin{pmatrix} \underline{\underline{\chi_r^{\omega 00}}} & \underline{\underline{\chi_r^{\omega 01}}} \\ \underline{\underline{\chi_r^{\omega 10}}} & \underline{\underline{\chi_r^{\omega 11}}} \end{pmatrix} \cdot \begin{pmatrix} \underline{\underline{\Gamma_r^{\omega 00}}} & \underline{\underline{\Gamma_r^{\omega 01}}} \\ \underline{\underline{\Gamma_r^{\omega 10}}} & \underline{\underline{\Gamma_r^{\omega 11}}} \end{pmatrix} \\ &= \begin{pmatrix} \underline{\underline{\mathbb{1}}} & \underline{\underline{\mathbb{0}}} \\ \underline{\underline{\mathbb{0}}} & \underline{\underline{\mathbb{1}}} \end{pmatrix} \mp \begin{pmatrix} \underline{\underline{\chi_r^{\omega 00}}} & \underline{\underline{\chi_r^{\omega 01}}} \\ \underline{\underline{\chi_r^{\omega 10}}} & \underline{\underline{\chi_r^{\omega 11}}} \end{pmatrix} \cdot \begin{pmatrix} \underline{\underline{\chi_{r,0}^{\omega\ 00}}} & \underline{\underline{\mathbb{0}}} \\ \underline{\underline{\mathbb{0}}} & \underline{\underline{\chi_{r,0}^{\omega\ 11}}} \end{pmatrix}^{-1}, \end{aligned} \tag{15}$$

which leads to four coupled equations for the different blocks [40,43]. Here we report the first two:

$$\frac{1}{\beta^2}\left[\underline{\underline{\chi_r^{\omega 00}}}\,\underline{\underline{\Gamma_r^{\omega 00}}} + \underline{\underline{\chi_r^{\omega 01}}}\,\underline{\underline{\Gamma_r^{\omega 10}}}\right] = \mathbb{1} \mp \underline{\underline{\chi_r^{\omega 00}}}\left(\underline{\underline{\chi_{0,r}^{\omega\ 00}}}\right)^{-1}, \tag{16a}$$

$$\frac{1}{\beta^2}\left[\underline{\underline{\chi_r^{\omega 00}}}\,\underline{\underline{\Gamma_r^{\omega 01}}} + \underline{\underline{\chi_r^{\omega 01}}}\,\underline{\underline{\Gamma_r^{\omega 11}}}\right] = \mp\underline{\underline{\chi_r^{\omega 01}}}\left(\underline{\underline{\chi_{0,r}^{\omega\ 11}}}\right)^{-1}, \tag{16b}$$

since they are the only ones needed for the derivation of our methods. We note that in these equations all quantities can be extracted directly from the impurity solver (note that $\underline{\underline{\Gamma_r^{\omega 01}}}$, $\underline{\underline{\Gamma_r^{\omega 10}}}$ and $\underline{\underline{\Gamma_r^{\omega 11}}}$ are replaced by their asymptotic functions), except for $\underline{\underline{\Gamma_r^{\omega 00}}}$, i.e., $\Gamma_r^{\nu\nu'\omega}$ in the low-frequency regime ($\nu,\nu' \in I_0$), which should be calculated by means of these relations. In fact, from Eq. (16), one can derive various schemes to determine $\underline{\underline{\Gamma_r^{\omega 00}}}$, two of which will be illustrated in the following two subsections.

A. Method 1: Γ's asymptotics

The first method for obtaining $\Gamma_r^{\nu\nu'\omega}$ in the low-frequency regime is based on both Eq. (16) and uses only the high-frequency asymptotic functions for $\Gamma_r^{\nu\nu'\omega}$. It was first put forward by J. Kuneš in Ref. [40] for the particle-hole channels ($r = d,m$) at $\omega = 0$ only. In this work, the high-frequency behavior of the irreducible vertex was derived by a functional derivative of the self-energy, which leads to the aforementioned restrictions. Our diagrammatic analysis of the vertex asymptotics instead allows for a general formulation including the particle-particle channels and finite frequencies.

Let us briefly recall how this approach can be derived [40]. From Eq. (16a), one obtains $\underline{\underline{\Gamma_r^{\omega 00}}}$ by applying the inverse of $\underline{\underline{\chi_r^{\omega 00}}}$ on both sides of the equation. In order to get rid of the asymptotic function $\underline{\underline{\chi_r^{\omega 01}}}$, one uses Eq. (16b) which can be recasted into

$$\frac{1}{\beta^2}\underline{\underline{\chi_r^{\omega 01}}} = -\underline{\underline{\chi_r^{\omega 00}}}\,\underline{\underline{\Gamma_r^{\omega 01}}}\left[\underline{\underline{\Gamma_r^{\omega 11}}} \pm \beta^2\left(\underline{\underline{\chi_{0,r}^{\omega\ 11}}}\right)^{-1}\right]^{-1}. \tag{17}$$

Inserting this into Eq. (16a) yields

$$\begin{aligned} \frac{1}{\beta^2}\underline{\underline{\Gamma_r^{\omega 00}}} &= \left(\underline{\underline{\chi_r^{\omega 00}}}\right)^{-1} \mp \left(\underline{\underline{\chi_{0,r}^{\omega\ 00}}}\right)^{-1} \\ &\quad + \frac{1}{\beta^2}\underline{\underline{\Gamma_r^{\omega 01}}}\left[\underline{\underline{\Gamma_r^{\omega 11}}} \pm \beta^2\left(\underline{\underline{\chi_{0,r}^{\omega\ 11}}}\right)^{-1}\right]^{-1}\underline{\underline{\Gamma_r^{\omega 10}}}. \end{aligned} \tag{18}$$

The right-hand side (r.h.s.) of this equation can be interpreted straightforwardly: the first line corresponds to the calculation of $\Gamma_r^{\nu\nu'\omega}$ in the low-frequency regime (without higher frequencies), while the second line represents a correction due to the high-frequency asymptotic contributions. We note that the calculation of this correction term requires also an additional inversion of the high-frequency parts of $\Gamma_r^{\nu\nu'\omega}$ and $\chi_r^{\nu\nu'\omega}$ (i.e., of the term in the square brackets). However, the latter can be obtained at much lower cost compared to the full vertex function and, hence, they are available for a much larger frequency grid which reduces the error of this inversion. Moreover, the advantage of the approach is that it does not require the calculation of the fermion boson couplings $\lambda_r^{\nu\omega}$ but only the determination of χ_r^ω, which is numerically significantly less demanding.

[3] Following the discussion in Ref. [37], the position of the main asymptotic structures of a purely local vertex function in the ν-ν' frequency space is determined by the maxima of the physical susceptibilities $\chi_d(\nu-\nu')$, $\chi_m(\nu-\nu')$ and $\chi_{pp,\uparrow\downarrow}(\nu+\nu'+\omega)$ (for the *ph* channels d and m). The latter *always* take their largest value at zero frequency, i.e., for the static limit. This leads indeed to the condition $\nu,\nu' = -\omega/2$ for the *ph* channels d and m. Analogous arguments apply to the *pp* channels s and t. Let us, however, mention that the inclusion of nonlocal correlations could induce a broadening [44] of the frequency structures, which might require a slightly different choice of the frequency interval.

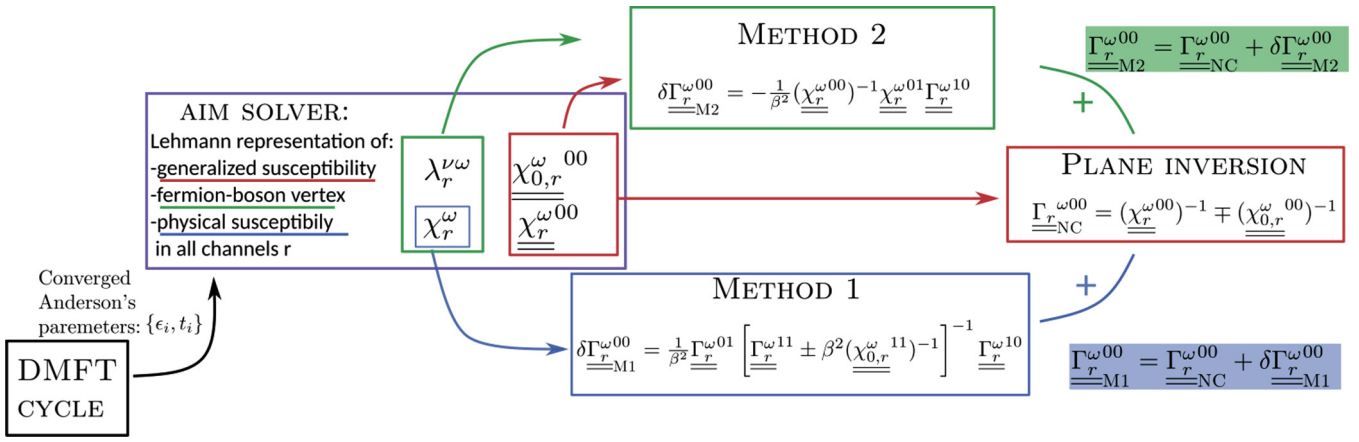

FIG. 1. Schematic representation of the proposed procedures to properly invert the BS equations by means of the two correction schemes. From the impurity solver, one has access to the asymptotic functions χ_r^{ω} and $\lambda_r^{\nu,\omega}$, which are used to construct the correction terms (method 1 in blue and method 2 in green) to the plane inversion of the generalized susceptibility (red). The results for the two methods as discussed in Sec. IV converge quickly for increasing low-frequency interval I_0.

B. Method 2: *F*'s asymptotics

The second method for calculating $\Gamma_r^{\nu\nu'\omega}$ in the low-frequency regime uses *exclusively* Eq. (16a). From this, one easily obtains

$$\frac{1}{\beta^2}\underline{\underline{\Gamma}}_r^{\omega 00} = \left(\underline{\underline{\chi}}_r^{\omega 00}\right)^{-1} \mp \left(\underline{\underline{\chi}}_{0,r}^{\omega\ 00}\right)^{-1} - \frac{1}{\beta^2}\left(\underline{\underline{\chi}}_r^{\omega 00}\right)^{-1}\underline{\underline{\chi}}_r^{\omega 01}\underline{\underline{\Gamma}}_r^{\omega 10}. \tag{19}$$

Similar to method 1, the first line corresponds to the calculation of $\Gamma_r^{\nu\nu'\omega}$ in the low-frequency regime, without the higher frequencies, while the term in the second line represents a correction from the high-frequency asymptotic contributions. The advantage of this approach w.r.t. the one described in the previous section is that it does not require an additional inversion of the high-frequency asymptotic contributions. On the other hand, it makes necessary the determination of the asymptotic functions for $\chi_r^{\nu\nu'\omega}$ (and not only for $\Gamma_r^{\nu\nu'\omega}$), including the evaluation of $\lambda_r^{\nu\omega}$. For a computation within DMFT this represents, as discussed above and detailed in Appendix B, not a real obstacle since these functions can be obtained relatively easily from the impurity solver.

IV. NUMERICAL RESULTS

In this section, we present our results for $\Gamma_r^{\nu\nu'\omega}$ obtained by the methods discussed in the previous Secs. III A and III B. For the sake of clarity, we will focus on the DMFT solution of the half-filled Hubbard model in $3d$ [see Eq. (1)] for which a comparison with numerically exact results is possible. Specifically, we consider the two values of the Hubbard interaction $U=1D$ and $1.75D$, respectively, at a temperature $T=0.02D$ with $D=2\sqrt{6}t$ (which correspond to twice the standard deviation of the $3d$ noninteracting density of states). The selected interaction strengths correspond to weak coupling ($U=1$) and to the highly relevant intermediate-to-strong coupling regime near the Mott MIT ($U=1.75$), respectively, which allow for a representative benchmark of our newly developed techniques.

For evaluating the performance of the new methods we have pursued the following strategy, which is illustrated in the flowchart in Fig. 1. We calculate the irreducible vertex $\Gamma_r^{\nu\nu'\omega}$ (for selected values of ω) in a (small) interval $I_0=[N_{\min},N_{\max}]$ of fermionic frequencies (see Sec. III) by means of Eq. (10) without any corrections, and compare it to the values obtained by correcting the latter results with method 1 [Eq. (18)] and method 2 [Eq. (19)] (here and in the following, all frequency values and intervals refer to the corresponding integer valued Matsubara indices). According to the discussion in Sec. III, we typically consider a frequency range for ν and ν' for which the main structures of the corresponding two-particle susceptibilities and vertices are centered (see also Ref. [37]), i.e., $N_{\max}+1=-N_{\min}\mp 2m=N_{\text{inv}}/2\mp m$ (for the ph and the pp channels, respectively), where N_{inv} denotes the total number of frequencies used for the matrix inversion in Eq. (10) and m is the index of the bosonic Matsubara frequency ω. An illustration of these frequency intervals is given in Fig. 2 (red block). The correction terms are obtained in the (much larger) frequency interval $I=[M_{\min},M_{\max}]$, which has been chosen in such a way that all results presented in the following are converged w.r.t. the size of I. Specifically, the χ_r^{ω}'s have

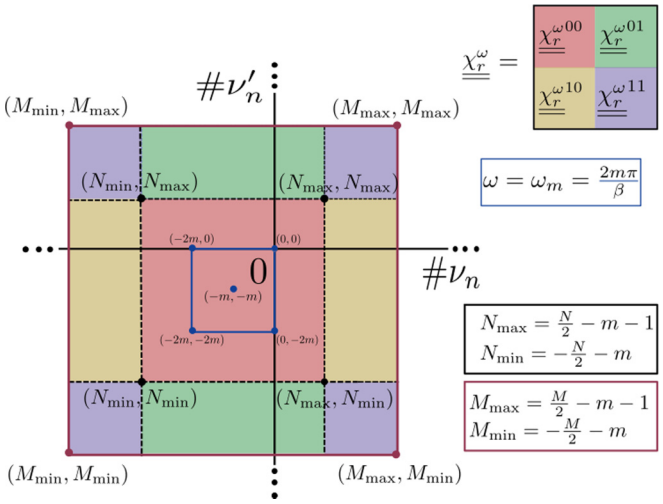

FIG. 2. Visual illustration of the block construction (see Sec. III).

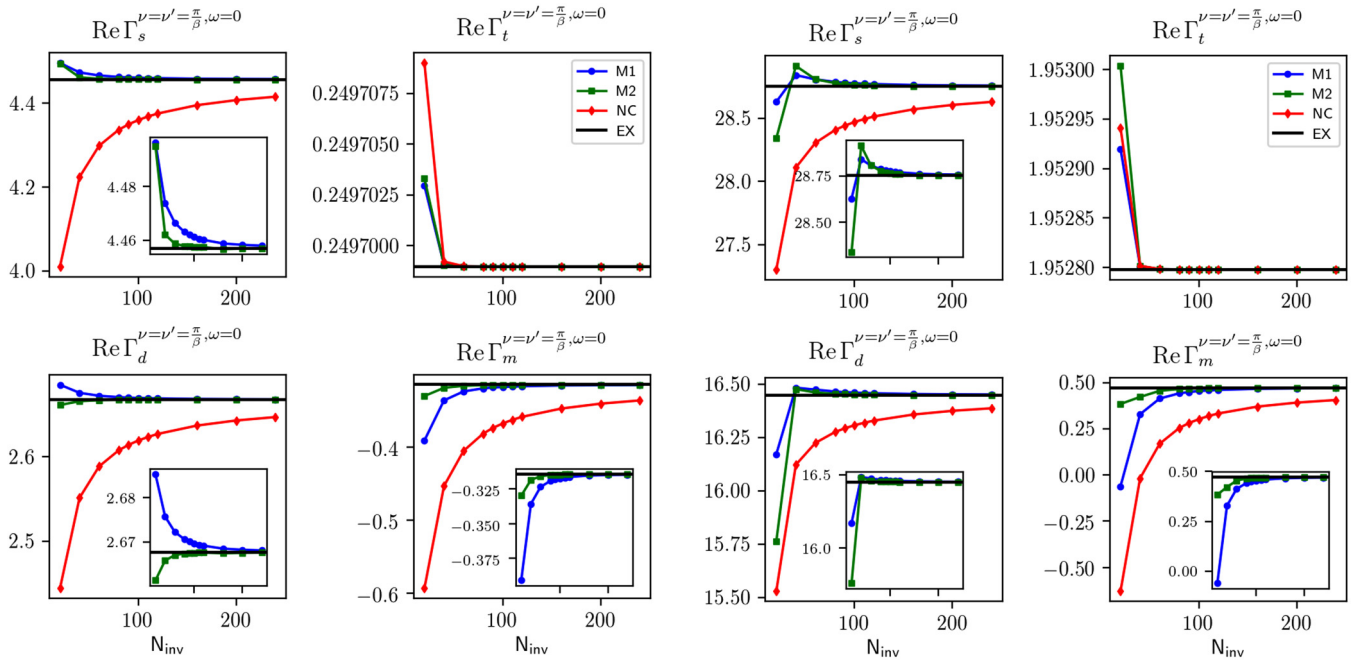

FIG. 3. $\Gamma_r^{\nu\nu'\omega}$ for $r = \{s,t,d,m\}$, evaluated at $\nu = \nu' = \pi/\beta$ and $\omega = 0$ as a function of the inversion range N_{inv}, for $U = 1$ (left panels) and $U = 1.75$ (right panels). Uncorrected results [red, first lines of Eqs. (18) and (19)] are compared to results corrected by method 1 [blue, second line of Eqs. (18)], method 2 [green, second line of Eqs. (19)] and the exact result (black). The insets provide a comparison between only the two correction methods on a smaller scale.

been calculated for 2001 bosonic ($M_{max} = -M_{min} = 1000$) Matsubara frequencies while the $\lambda_r^{\nu\omega}$'s have been evaluated for 240 fermionic ($M_{max}+1 = -M_{min} \mp 2m = 120 \mp m$, see Fig. 2) Matsubara frequencies where again the fermionic frequency interval has been centered around $\mp m$. Finally, the "exact" solution for $\Gamma_r^{\nu\nu'\omega}$, which serves as a benchmark for the performance of our new approaches, has been obtained from the plain inversion of Eq. (10) (i.e., without any corrections) for a very large frequency grid $I_L = [L_{min}, L_{max}]$ with $L_{max} + 1 = -L_{min} \mp 2m = L_{inv}/2 \mp m$ with $L_{inv} = 320$, and results have been extrapolated to $L \to \infty$. All calculations for obtaining $\chi_r^{\nu\nu'\omega}$, χ_r^{ω}, and $\lambda_r^{\nu\omega}$ have been carried out by means of an ED impurity solver[4] (see Ref. [25] and Appendix B) whereupon the AIM related to the DMFT solution of (1) has been parametrized by four bath sites.

Figure 3 shows $\Gamma_r^{\nu\nu'\omega}$ for fixed values of the Matsubara frequencies, i.e., $\nu = \nu' = \pi/\beta$, $\omega = 0$, as a function of the total number of fermionic frequencies N_{inv}, which have been used for the inversion of $\chi_r^{\nu\nu'\omega}$ in the 00 block [see first lines of Eqs. (10) and (14)]. The uncorrected values (red) are compared to the corresponding results of method 1 [blue, Eq. (18)] and method 2 [green, Eq. (19)] as well as the exact solution (black), for $U = 1$ (left panels) and $U = 1.75$ (right panels). We can see that even for a relatively large value of $N_{inv} = 240$ the noncorrected results substantially deviate from the corrected ones, which both converge rapidly to the exact value in all channels and for both values of U (up to a relative error lower than 10^{-3}). As expected, the noncorrected results are drastically affected by varying N_{inv}, with a (maximal) relative error of ∼100% for $U = 1$ and ∼200% for $U = 1.75$ w.r.t. the exact solution in the most sensitive magnetic channel for the lowest value of $N_{inv} = 20$.

In Fig. 4, we report an analogous analysis as in Fig. 3, but for a finite value of $\omega = 40\pi/\beta$. The overall picture is very similar as for $\omega = 0$ which confirms the applicability of the proposed

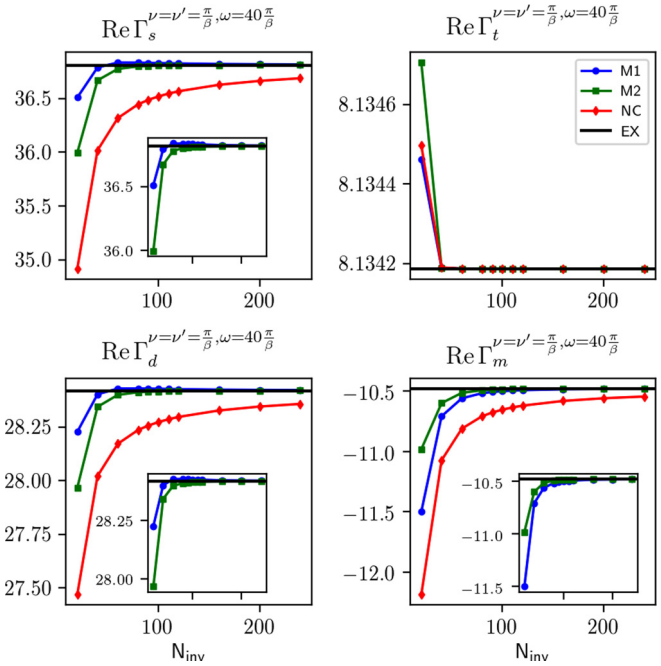

FIG. 4. Same as in Fig. 3 but for $\omega = 40\pi/\beta$ and $U = 1.75$ only.

[4]For the calculation of the full three-frequency dependent $\chi_r^{\nu\nu'\omega}$ the open source exact diagonalization (full-ED) code *pomerol* has been adopted, see Ref. [45].

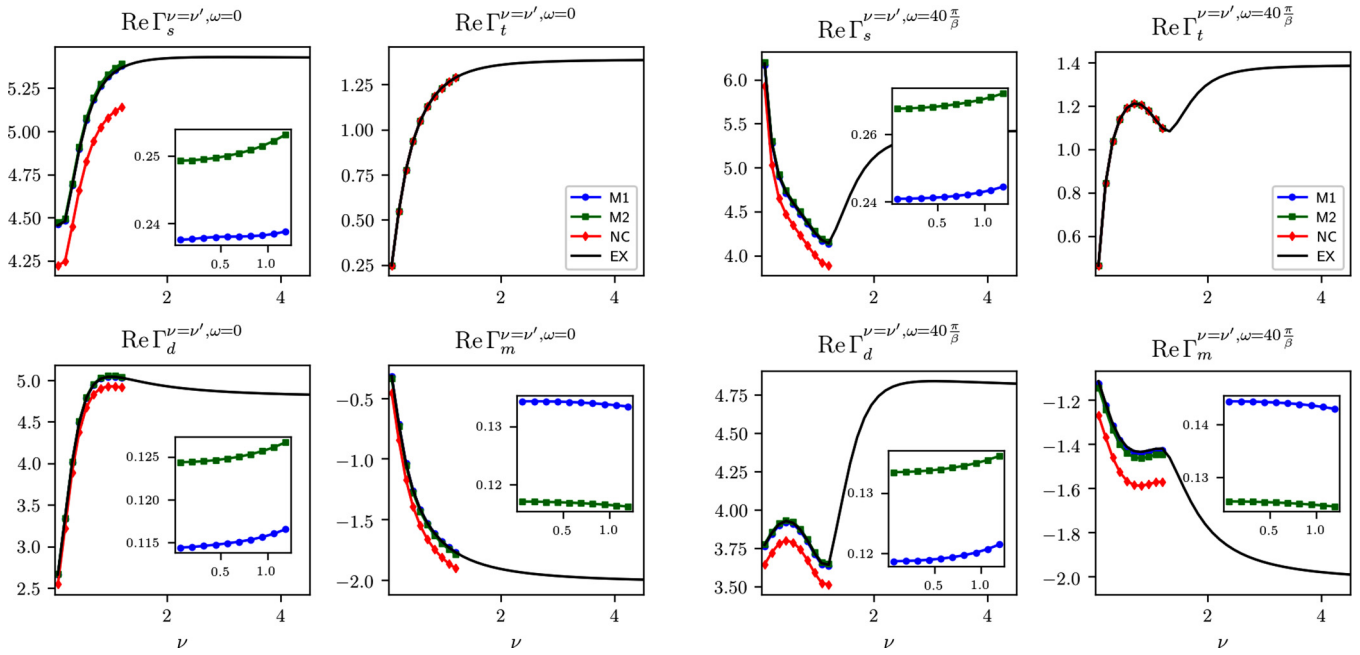

FIG. 5. $\Gamma_r^{\nu\nu'\omega}$ for $r=\{s,t,d,m\}$, evaluated along the positive diagonal $\nu=\nu'$ for $U=1$, $\omega=0$ (left panels) and $\omega=40\pi/\beta$ (right panels). Results of method 1 (blue) and method 2 (green) are compared to a plain inversion (red) of Eq. (10) for $N_{\mathrm{inv}}=40$ and the exact solution (black). Insets show the correction terms only.

methods for a finite bosonic transfer frequency. Interestingly, for both values of ω, the triplet channel is not affected by the correction terms and converges rapidly to the exact solution. This can be attributed to the fact that for the triplet vertices $\Gamma_t^{\nu\nu'\omega}$ and $F_t^{\nu\nu'\omega}$, respectively, the constant background proportional to U is absent. Hence, in their asymptotic high-frequency regime, the latter are dominated by the two diagonal structures [37,41] at $\nu=\nu'$ and $\nu=\omega-\nu'$, which originate from $\chi_{d/m}^{\nu'-\nu}$ and $\chi_{d/m}^{\omega-\nu-\nu'}$ [see Eqs. (11d) and (12d)]. Consequently, the actual inversion of the corresponding $\chi_t^{\nu\nu'\omega}$ depends only very weakly on the size of N_{inv}. More specifically, one can infer the (almost) vanishing of the correction terms for $\Gamma_t^{\nu\nu'\omega}$ in the second lines of Eqs. (18) and (19) also directly from the observation that the asymptotic contributions $\underline{\underline{\Gamma_t^{\omega 10}}}$ and $\underline{\underline{\Gamma_t^{\omega 10}}}$ are very small. In fact, they involve the physical susceptibilities $\chi_{d/m}^{\omega}$ for $\omega\neq 0$ in Eq. (11d),[5] while the latter are typically taking their maximum at $\omega=0$ and are rapidly decreasing with increasing ω.

In Fig. 5, we turn our attention to the frequency dependence of the correction terms obtained by the two methods. Specifically, we show $\Gamma_r^{\nu\nu'\omega}$ along the diagonal $\nu=\nu'$ for $\omega=0$ (left panels) and $\omega=40\pi/\beta$ (right panels) at $U=1$ (corresponding results for $U=1.75$ are given in Appendix D) where the uncorrected solution (red) has been obtained for $N_{\mathrm{inv}}=40$. As expected from the discussion above, the corrections from both methods 1 (blue) and 2 (green) are almost equivalent and provide a relevant improvement for the calculations of $\Gamma_r^{\nu\nu'\omega}$ for all channels apart from the triplet one ($r=t$), for which already the plain inversion yields an almost exact result. Interestingly, the corrections appear to have a weak dependence on (ν,ν') as can be seen in the insets in Fig. 5, which shows only the corrections provided by method 1 (blue line) and method 2 (green line). Indeed, one appreciates how the corrections given by both methods vary less then 1% along the diagonal $\nu=\nu'$ (for the case $U=1.75$ this is no longer true, see Appendix D). This can be explained by a similar argument as given for the vanishing of the corrections for the triplet vertex: rewriting, for instance, the correction term for method 1 in the second line of Eq. (18) into a more explicit form we obtain (apart from a prefactor $1/\beta^2$)

$$\sum_{\nu_1,\nu_2}\Gamma_{r,\mathrm{asym}}^{\nu\nu_1\omega}\left[\underline{\underline{\Gamma_r^{\omega 11}}}\pm\beta^2\left(\underline{\underline{\chi_{0,r}^{\omega 11}}}\right)^{-1}\right]^{-1}_{\nu_1\nu_2}\Gamma_{r,\mathrm{asym}}^{\nu_2\nu'\omega}, \tag{20}$$

where $\nu,\nu'\in I_0$ and the sums over ν_1 and ν_2 run over the high-frequency interval $I\backslash I_0$. Clearly, $\nu\neq\nu_1$ and $\nu'\neq\nu_2$ and the χ_r^{ω}'s in the asymptotic expressions for $\Gamma_{r,\mathrm{asym}}^{\nu\nu_1\omega}$ and $\Gamma_{r,\mathrm{asym}}^{\nu_2\nu'\omega}$ in Eqs. (11), which contribute here only for $\omega\neq 0$, are, hence, typically very small. Consequently, $\Gamma_{r,\mathrm{asym}}^{\nu\nu_1\omega}$ and $\Gamma_{r,\mathrm{asym}}^{\nu_2\nu'\omega}$ can be both approximated by the corresponding first terms in Eq. (11), which are just constants proportional to U. When we insert this approximation, i.e., $\Gamma_{r,\mathrm{asym}}^{\nu\nu_1\omega}=\Gamma_{r,\mathrm{asym}}^{\nu_2\nu'\omega}\sim U$, into the expression for the correction term of method 1 in Eq. (20), the latter obviously becomes frequency independent. An analogous argument explains also the frequency independence[6] of the correction term obtained in method 2 [second line of Eq. (19)] for which the above considerations also allow for a simplification

[5]Note that for the 10 and the 01 region in the $\nu-\nu'$ frequency plane $\nu\neq\pm\nu'(+\omega)$.

[6]For the correction term in second line of Eq. (19), we can actually prove only its ν' independence explicitly. However, for a system with time inversion symmetry, we have that $\Gamma_r^{\nu\nu'\omega}=\Gamma_r^{\nu'\nu\omega}$ (and the same for the corresponding asymptotic functions) and, consequently, the correction also does not depend on ν.

TABLE I. Differences $\delta\Gamma_r^{\eta}(\omega)$, with $\eta=$M1 for method 1 and $\eta=$M2 for method 2, between the noncorrected and the corrected results, as provided by the two different methods. The data are reported for different sizes of the frequency box N_{inv} used for the inversion, and for $\omega=0$ and $\omega=40\frac{\pi}{\beta}$. The upper panel refers to $U=1$, and the lower to $U=1.75$.

N_{inv}	$\delta\Gamma_s^{\text{M1}}$ $(\omega=0)$	$\delta\Gamma_s^{\text{M1}}$ $(\omega=40\frac{\pi}{\beta})$	$\delta\Gamma_s^{\text{M2}}$ $(\omega=0)$	$\delta\Gamma_s^{\text{M2}}$ $(\omega=40\frac{\pi}{\beta})$	N_{inv}	$\delta\Gamma_d^{\text{M1}}$ $(\omega=0)$	$\delta\Gamma_d^{\text{M1}}$ $(\omega=40\frac{\pi}{\beta})$	$\delta\Gamma_d^{\text{M2}}$ $(\omega=0)$	$\delta\Gamma_d^{\text{M2}}$ $(\omega=40\frac{\pi}{\beta})$	N_{inv}	$\delta\Gamma_m^{\text{M1}}$ $(\omega=0)$	$\delta\Gamma_m^{\text{M1}}$ $(\omega=40\frac{\pi}{\beta})$	$\delta\Gamma_m^{\text{M2}}$ $(\omega=0)$	$\delta\Gamma_m^{\text{M2}}$ $(\omega=40\frac{\pi}{\beta})$
40	−0.256	−0.276	−0.238	−0.246	40	−0.128	−0.137	−0.117	−0.123	40	−0.116	−0.124	−0.133	−0.142
80	−0.126	−0.129	−0.121	−0.122	80	−0.0631	−0.0643	−0.0598	−0.0607	80	−0.0619	−0.0631	−0.0662	−0.0673
120	−0.0842	−0.0850	−0.0814	−0.0818	120	−0.0421	−0.0425	−0.0406	−0.0408	120	−0.0418	−0.0422	−0.0437	−0.0440
160	−0.0631	−0.0634	−0.061	−0.0613	160	−0.0315	−0.0317	−0.0305	−0.0307	160	−0.0316	−0.0317	−0.0325	−0.0327
200	−0.0505	−0.0507	−0.0492	−0.0493	200	−0.0253	−0.0254	−0.0246	−0.0247	200	−0.0253	−0.0254	−0.0259	−0.0259
240	−0.0421	−0.0422	−0.0412	−0.04127	240	−0.0211	−0.0211	−0.0206	−0.0206	240	−0.0211	−0.0211	−0.0215	−0.0215
40	−0.759	−0.801	−0.706	−0.699	40	−0.374	−0.395	−0.344	−0.353	40	−0.345	−0.364	−0.436	−0.456
80	−0.382	−0.389	−0.357	−0.357	80	−0.190	−0.194	−0.176	−0.177	80	−0.188	−0.191	−0.211	−0.214
120	−0.257	−0.259	−0.243	−0.243	120	−0.128	−0.129	−0.121	−0.121	120	−0.127	−0.128	−0.138	−0.139
160	−0.193	−0.193	−0.183	−0.184	160	−0.0962	−0.0966	−0.0914	−0.0918	160	−0.0964	−0.0969	−0.102	−0.103
200	−0.154	−0.155	−0.148	−0.148	200	−0.0772	−0.0774	−0.0739	−0.0742	200	−0.0773	−0.0775	−0.0808	−0.0810
240	−0.129	−0.129	−0.124	−0.124	240	−0.0644	−0.0646	−0.0621	−0.0622	240	−0.0645	−0.0646	−0.0668	−0.0670

of the calculation procedure. Considering, e.g., for the density channel, that for the (off-diagonal) (10) frequency region $F_{d,\text{asym}}^{\nu\nu'\omega}\sim U+U^2\chi_d^{\omega}+U\lambda_d^{\nu\omega}$ [Eq. (12a)], we obtain for the correction term (apart from a prefactor $1/\beta^2$) approximately

$$\sum_{\nu_1}\left[\underline{\underline{\chi_d^{\omega 00}}}\right]^{-1}_{\nu\nu_1}G(\nu_1)G(\nu_1+\omega)\left[U+U^2\chi_d^{\omega}+U\lambda_d^{\nu_1\omega}\right]$$

$$\times\sum_{\nu_2}\frac{1}{i\nu_2}\frac{1}{i(\nu_2+\omega)}U,$$

where $[\underline{\underline{\chi_d^{\omega 00}}}]^{-1}$ represents the exact inversion of $\chi_d^{\nu\nu'\omega}$ in the small frequency interval I_0 and the (right) outer legs Green's functions of $\chi_d^{\nu_1\nu_2\omega}$, which depend on $\nu_2\in I\setminus I_0$, have been replaced by their asymptotic values (which allows the corresponding sum over ν_2 to be evaluated analytically).

Given the small dependence of the correction on the fermionic frequencies, one can extract the values of the corrections provided by the two methods at $\nu=\nu'=\pi/\beta$ $(n=n'=0)$ in order to give an estimation of the convergence with respect to N_{inv}. These are reported in Table I for two values of $U=1$ and 1.75 as well as $\omega=0$ and $40\pi/\beta$, for all channels but the triplet one, whose corrections can be assumed negligible (see previous discussion). The overall picture that can be obtained from Table I confirms the similarity of method 1 and method 2 regarding their results and predicts a relatively weak dependence of the corrections on the bosonic Matsubara frequency ω (as it is the case for the fermionic ones ν and

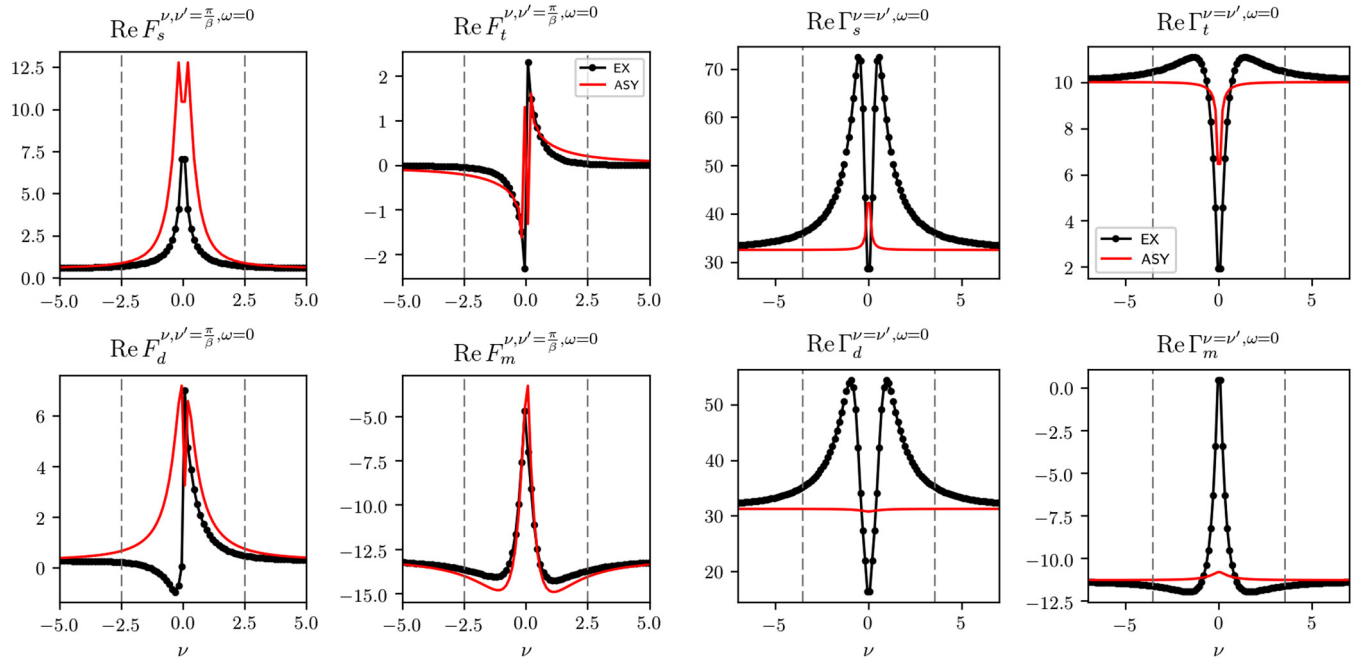

FIG. 6. (Left) (ED)DMFT full vertex $F_r^{\nu\nu'\omega}$ (black), with $r=\{s,t,d,m\}$ as a function of ν for $\nu'=\pi/\beta$, $\omega=0$, and $U=1.75$. (Right) "Exact" (see definition in the text) $\Gamma_r^{\nu\nu'\omega}$ (black), with $r=\{s,t,d,m\}$ evaluated for $\nu=\nu'$, $\omega=0$ and $U=1.75$. In both panels, the red line shows the behavior of the respective asymptotic functions [see Eq. (12)]. The dashed lines mark the edges of the (00) block for $N_{\text{inv}}=40$.

ν'). For the correction term of method 1 in the second line of Eq. (18), this observation can be ascribed to the fact that for a given bosonic frequency ω the calculation intervals I_0 and I are centered around $\nu,\nu' = \mp\omega/2$ for the ph ($r = d,m$) and the pp ($r = s,t$) channels, respectively. In fact, this centering can be also realized by performing the shift $\nu \to \nu \mp \omega/2$ and $\nu' \to \nu \mp \omega/2$ in $\Gamma^{\nu\nu'\omega}_{r,\mathrm{asym}}$ in Eq. (11), which renders the latter indeed independent[7] of ω. Although the mechanism responsible for the ω independence of the correction in method 2 is less transparent [$F^{\nu\nu'\omega}_{r,\mathrm{asym}}$ explicitly depends on ω, see Eq. (12)], it could rely on a mutual compensation of ω-dependent terms in the second line of Eq. (19), namely, $(\underline{\underline{\chi_r^{\omega 00}}})^{-1}$ and $\underline{\underline{\chi_r^{\omega 01}}}$.

Let us finally investigate the frequency structure of the asymptotic functions themselves. In Fig. 6, we compare $\Gamma^{\nu\nu'\omega}_{r,\mathrm{asym}}$ (right panels) and $F^{\nu\nu'\omega}_{r,\mathrm{asym}}$ (left panels) to the corresponding exact values for $\omega = 0$ at $U = 1.75$. At $\nu = 41\pi/\beta \sim 2.5$, the asymptotic functions (red lines) clearly deviate from the exact values (black lines) to which the former converge only for frequencies $\nu \sim 101\pi/\beta$. This is surprising since the former frequency ($\nu = 41\pi/\beta$) corresponds to the choice of the inner box (I_0) with $N_{\mathrm{inv}} = 40$ for which both correction methods have already converged to the exact results in Figs. 3–5. Hence our asymptotic correction techniques unexpectedly provide excellent results even for very small intervals I_0 for which the structures of the vertex functions have not yet decayed to their respective asymptotic values.

V. CONCLUSIONS

We have presented two different methods for improving the numerical treatment of the Bethe-Salpeter equations within a DMFT (as well an AIM) calculation and, in particular, for extracting the local irreducible vertex $\Gamma_r^{\nu\nu'\omega}$. The latter can be obtained via a matrix inversion of the generalized impurity susceptibilities $\chi_r^{\nu\nu'\omega}$ w.r.t. the fermionic Matsubara frequencies ν and ν'. In practice, however, the—in principle infinite—range of these frequencies has to be restricted to a finite interval I_0 of size N_{inv} in which $\chi_r^{\nu\nu'\omega}$ is calculated "exactly." Since the numerical effort for this task rapidly grows with the matrix size, the calculations are typically restricted to a relatively small I_0: this introduces an error in the determination of $\Gamma_r^{\nu\nu'\omega}$, which also affects the low-frequency sector ($|\nu|$, $|\nu'| < N_{\mathrm{inv}}/2$).

The two methods described in this work, which represent a significant extension of previous approaches [40], aim to mitigate—or even to completely remove—these inversion errors by downfolding the high-frequency contributions of $\chi_r^{\nu\nu'\omega}$ and $\Gamma_r^{\nu\nu'\omega}$ into the low-frequency interval I_0, and are formulated for being applicable to any scattering channel (r) and any value of the transfer bosonic frequency (ω). Both procedures lead to (additive) correction terms w.r.t. the plane inversion on I_0, which substantially improve the final result for $\Gamma_r^{\nu\nu'\omega}$. The important point exploited in these procedures is that the high-frequency functions $\Gamma^{\nu\nu'\omega}_{r,\mathrm{asym}}$ and $\chi^{\nu\nu'\omega}_{r,\mathrm{asym}}$ can be obtained numerically at a much lower cost (i.e., growing only linearly with the number of frequencies) compared to the respective exact expressions. In fact, they are defined by the physical response functions χ_r^{ω} and the fermion-boson vertices $\lambda_r^{\nu\omega}$, which depend on *only one* bosonic and (at most) only one fermionic Matsubara frequency.

Interestingly, the correction terms provided by both methods are essentially equivalent in size, allowing the users to freely choose the one which better matches their DMFT/AIM algorithm of choice. Furthermore, the computed corrections are almost independent of the fermionic frequencies ν and ν' as well as of the bosonic frequency ω. In fact, the error introduced by inverting $\chi_r^{\nu\nu'\omega}$ in a finite frequency range corresponds—to a large extent- to a rigid shift of the vertex function, which is properly compensated by using our newly introduced methods. Remarkably, the correction terms provide very accurate results even if the inner interval is restricted to frequencies where the two-particle correlation functions have not fully reached their asymptotic values.

As a testbed example, we have applied our method to the DMFT solution of a single band Hubbard model in parameter regimes, where numerically reliable results for $\Gamma_r^{\nu\nu'\omega}$ are available for comparison. The full strength of these methods will, however, become evident by considering more challenging situations, such as, e.g., calculations (i) in the low-T regime (where more Matsubara frequencies are needed) and (ii) of multiorbital systems (where the number of frequencies, for which $\chi_r^{\nu\nu'\omega}$ can be directly computed, is substantially limited). Moreover, our analysis allows for a generalization to treat the case of fully momentum-dependent BS equations for all systems with an instantaneous microscopic interaction. In this respect, our newly developed techniques will represent a valuable tool both for computing physical response functions at the DMFT level and for including nonlocal correlations effects by means of diagrammatic extensions of DMFT.

ACKNOWLEDGMENTS

The authors thank A. Antipov, E. Gull, C. Hille, P. Hansmann, K. Held, T. Schäfer, for valuable discussions, and the Wolfgang Pauli Institute for the kind hospitality. We acknowledge financial support from the Russian Science Foundation through Grant No. 16-42-01057, the Deutsche Forschungsgemeinschaft (DFG) through ZUK 63 and Projects No. AN 815/5-1 and No. AN 815/6-1, and the Austrian Science Fund (FWF) within the Project F41 (SFB ViCoM) and the Project I 2794-N35. Calculations were performed on the Vienna Scientific Cluster (VSC).

APPENDIX A: DERIVATION OF THE VERTEX ASYMPTOTICS

The diagrammatic techniques to analyze the high-frequency behavior of the vertex functions $F_r^{\nu\nu'\omega}$ and $\Gamma_r^{\nu\nu'\omega}$ have been developed and discussed extensively in Refs. [37,39,43]. In the following, we will only recall the basic concepts which are relevant for the present work. The key to the high-frequency behavior of the vertices relies on the following observation: if an external particle (hole) with an energy ν enters a (Feynman)

[7]The term $\chi^{\nu\nu'\omega}_{0,r}$ in the second line of Eq. (18) behaves like $\sim 1/[i\nu(i\nu \pm i\omega)]$, which, hence, exhibits only a very weak ω dependence if the interval I_0 is chosen considerably larger than ω, i.e., if $\nu,\nu' \gg \omega$.

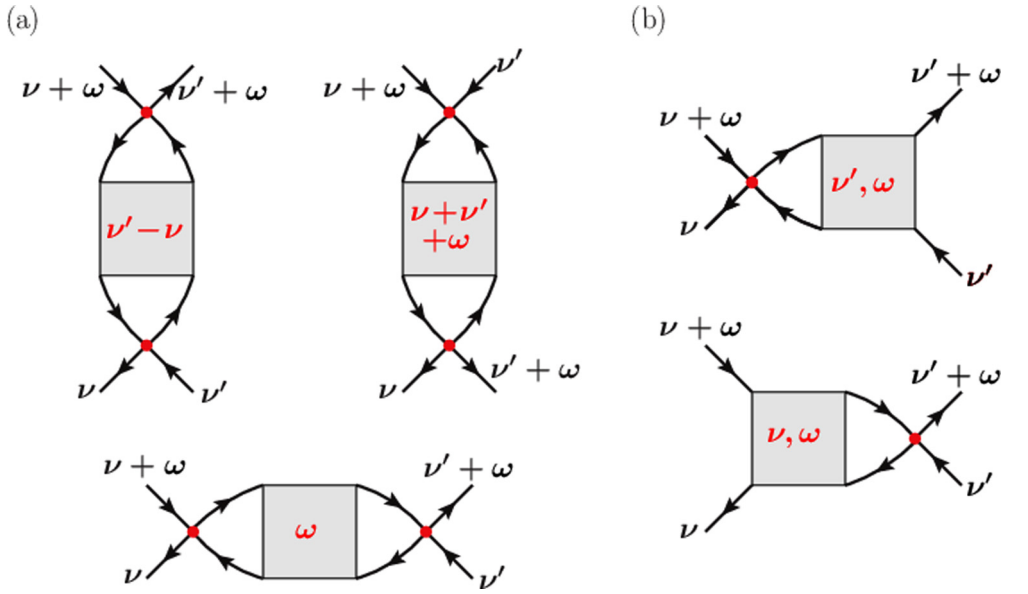

FIG. 7. Diagrams contributing to the full vertex $F_r^{\nu\nu'\omega}$. Red dots denote the bare Hubbard interaction U. The characteristic frequency combination on which the diagram depends is marked in red. If the gray box represents the full vertex $F_r^{\nu\nu'\omega}$ the diagrams in (a) correspond to the physical susceptibility [Eq. (5)], while the ones in (b) are related to the fermion-boson vertex [Eq. (7)].

diagram for the two-particle scattering amplitude at a vertex U, which is otherwise connected only to (three) internal propagators, the frequency ν will appear in one or more of the internal Green's functions. Consequently, the ν dependence of such a diagram will follow the ν dependence of these Green's functions and, hence, it decays for $\nu\to\infty$ at least as $1/i\nu$. The situation is different, if two external particles (or a particle and a hole) with frequencies ν_1 and ν_2 are scattered at the *same* bare vertex U. In this case, the diagram will depend only on the combination $\nu_1\pm\nu_2$. As a result, its contribution to the vertex functions will remain finite even when $\nu_1,\nu_2\to\infty$, as long as $\nu_1\pm\nu_2$ is kept fixed. This observation allows to classify [24,39] all Feynman diagrams for $F_r^{\nu\nu'\omega}$ and $\Gamma_r^{\nu\nu'\omega}$ in the following way: (i) the first class consists of all diagrams where *both* the two incoming and the two outgoing particles (holes) enter at the respective same bare vertices U, see Fig. 7(a). According to the considerations above, these diagrams, hence, depend only on a *single* (bosonic) combination of the incoming and outgoing frequencies, rather than on each of them independently. From Fig. 7(a), one can see, that the contribution of all diagrams of this type obviously corresponds to the physical susceptibilities defined in Eq. (5). (ii) For the second class of diagrams either the incoming *or* the outgoing lines enter at the same bare vertex, see Fig. 7(b). These diagrams depend only on one bosonic and one fermionic Matsubara frequency and can be related to a fermion-boson vertex [24,27,33,39] defined in Eq. (7). (iii) For the third class of diagrams, all four external particles enter at different bare vertices and for this reason the corresponding diagrams decay at large frequencies and do not contribute to the asymptotics.

The crucial point is now that all diagrams of class (i) and (ii)—which are responsible for the nontrivial high-frequency asymptotic behavior of the vertex—are reducible in one of the three channels (ph, $\overline{ph}$, pp). In fact, for two outer lines entering the same bare vertex U only two inner lines can be attached to it. As a consequence, when these two inner lines are cut the corresponding bare vertex gets separated from the rest of the diagram, which is, hence, (two-particle) reducible. Let us denote all diagrams reducible in a given channel r by the vertex function $\Phi_r^{\nu\nu'\omega}$, with $r=d,m,s,t$ (assuming the natural frequency notation, i.e., ph for $r=d,m$ and pp for $r=s,t,$). Obviously, the sum of all reducible and irreducible diagrams in a given channel yields all two-particle diagrams, i.e., $\Gamma_r^{\nu\nu'\omega}+\Phi_r^{\nu\nu'\omega}=F_r^{\nu\nu'\omega}$. Moreover, since each diagram is either (fully) two-particle irreducible or reducible in exactly one channel [37], $\Gamma_r^{\nu\nu'\omega}$ corresponds to the sum of all diagrams, which are either fully irreducible or reducible in a channel $r'\neq r$. From this follow the so-called parquet equations:

$$\Gamma_d^{\nu\nu'\omega} = \Lambda_d^{\nu\nu'\omega} - \tfrac{1}{2}\Phi_d^{\nu(\nu+\omega)(\nu'-\nu)} - \tfrac{3}{2}\Phi_m^{\nu(\nu+\omega)(\nu'-\nu)} + \tfrac{1}{2}\Phi_s^{\nu\nu'(\nu+\nu'+\omega)} + \tfrac{3}{2}\Phi_t^{\nu\nu'(\nu+\nu'+\omega)}, \tag{A1a}$$

$$\Gamma_m^{\nu\nu'\omega} = \Lambda_m^{\nu\nu'\omega} - \tfrac{1}{2}\Phi_d^{\nu(\nu+\omega)(\nu'-\nu)} + \tfrac{1}{2}\Phi_m^{\nu(\nu+\omega)(\nu'-\nu)} - \tfrac{1}{2}\Phi_s^{\nu\nu'(\nu+\nu'+\omega)} + \tfrac{1}{2}\Phi_t^{\nu\nu'(\nu+\nu'+\omega)}, \tag{A1b}$$

$$\Gamma_s^{\nu\nu'\omega} = \Lambda_s^{\nu\nu'\omega} + \tfrac{1}{2}\Phi_d^{\nu(\omega-\nu')(\nu'-\nu)} - \tfrac{3}{2}\Phi_m^{\nu(\omega-\nu')(\nu'-\nu)} + \tfrac{1}{2}\Phi_d^{\nu\nu'(\omega-\nu-\nu')} - \tfrac{3}{2}\Phi_m^{\nu\nu'(\omega-\nu-\nu')}, \tag{A1c}$$

$$\Gamma_t^{\nu\nu'\omega} = \Lambda_t^{\nu\nu'\omega} - \tfrac{1}{2}\Phi_d^{\nu(\omega-\nu')(\nu'-\nu)} - \tfrac{1}{2}\Phi_m^{\nu(\omega-\nu')(\nu'-\nu)} + \tfrac{1}{2}\Phi_d^{\nu\nu'(\omega-\nu-\nu')} + \tfrac{1}{2}\Phi_m^{\nu\nu'(\omega-\nu-\nu')}, \tag{A1d}$$

where $\Lambda_r^{\nu\nu'\omega}$ denotes the fully irreducible vertex which does not exhibit any dependence on the (irreducibility) channels ph, $\overline{ph}$, and pp. Hence, here, the index r labels—as for $F_r^{\nu\nu'\omega}$ and $\chi_r^{\nu\nu'\omega}$—only the spin combination and the frequency convention (ph for $r=d,m$ and pp for $r=s,t$) in which $\Lambda_r^{\nu\nu'\omega}$ is represented. Note that on a first glance it seems rather inconsistent that the vertices reducible in the density and spin (i.e., in the ph) channels, $\Phi_d^{\nu\nu'\omega}$ and $\Phi_m^{\nu\nu'\omega}$, contribute to the vertices which are irreducible exactly in the same channels ($\Gamma_d^{\nu\nu'\omega}$ and

$\Gamma_m^{\nu\nu'\omega}$). The reason for this contradiction is that these contributions originate from the transverse particle-hole channel ($\overline{ph}$), which, of course, contributes to $\Gamma_d^{\nu\nu'\omega}$ and $\Gamma_m^{\nu\nu'\omega}$. Considering crossing and SU(2) symmetry, $\Phi_{\overline{ph},\sigma\sigma'}^{\nu\nu'\omega}$ can be represented by the corresponding functions in the longitudinal (ph) channel by means of a frequency shift which explains the presence of $\Phi_d^{\nu(\nu+\omega)(\nu'-\nu)}$ and $\Phi_m^{\nu(\nu+\omega)(\nu'-\nu)}$ in Eqs. (A1a) and (A1b).

According to the discussion above, the asymptotic high-frequency behavior of $\Gamma_r^{\nu\nu'\omega}$ is determined by the asymptotic behavior of the reducible vertices Φ_r in Eqs. (A1). The latter in turn is given by the diagrams in Fig. 7(a) [for the ph ($r=d,m$) channels by the two upper and for the pp ($r=s,t$) channels by the upper left and the lower diagrams]. which can be expressed in terms of the physical susceptibilities [Eq. (5)] as

$$\Phi_{d,\text{asym}}^{\nu bc} = -U^2\chi_d^c, \tag{A2a}$$

$$\Phi_{m,\text{asym}}^{\nu bc} = -U^2\chi_m^c, \tag{A2b}$$

$$\Phi_{s,\text{asym}}^{\nu\nu'(\nu+\nu'+\omega)} = -2U^2\chi_{pp,\uparrow\downarrow}^{\nu+\nu'+\omega}, \tag{A2c}$$

$$\Phi_{t,\text{asym}}^{\nu\nu'(\nu+\nu'+\omega)} = 0, \tag{A2d}$$

where b and c represent the respective frequency arguments according to Eqs. (A1). Note that for the derivation of the asymptotic behavior of Φ_r in Eqs. (A2) the bosonic frequency ω (in the respective natural notation of the given channel) has been considered to be fixed. For this reason, no asymptotic contributions from fermion-boson diagrams [as given in Fig. 7(b)] can arise since the latter would be constant along lines in the three-dimensional frequency space which are not parallel to planes of constant ω. Inserting the high-frequency expressions for Φ_r in Eqs. (A2) into the parquet equations for Γ_r [Eqs. (A1)] yields the asymptotic high-frequency functions $\Gamma_{r,\text{asym}}^{\nu\nu'\omega}$ (for a fixed ω) given in Eq. (11) in Sec. II B.

For the determination of $F_{r,\text{asym}}^{\nu\nu'\omega}$, we use the fact $F_r^{\nu\nu'\omega} = \Gamma_r^{\nu\nu'\omega} + \Phi_r^{\nu\nu'\omega}$. Hence, in addition to the high-frequency behavior of $\Gamma_r^{\nu\nu'\omega}$ discussed above [and explicitly given in Eqs. (11)], we have to determine $\Phi_{r,\text{asym}}^{\nu\nu'\omega}$. Let us stress that the latter is different from the expressions given in Eq. (A2) due to the difference in the frequency arguments. Specifically, for $\Phi_{r,\text{asym}}^{\nu\nu'\omega}$ (i.e., without any shifts in the arguments) for $\nu,\nu'\to\infty$, one has to consider contributions of diagrams such as given in Fig. 7(b) which correspond to fermion-boson vertices [Eq. (7)]. Explicitly, we obtain

$$\Phi_{d,\text{asym}}^{\nu\nu'\omega} = U\lambda_d^{\nu\omega} + U\lambda_d^{\nu'\omega} + U^2\chi_d^{\omega}, \tag{A3a}$$

$$\Phi_{m,\text{asym}}^{\nu\nu'\omega} = U\lambda_m^{\nu\omega} + U\lambda_m^{\nu'\omega} + U^2\chi_m^{\omega}, \tag{A3b}$$

$$\Phi_{s,\text{asym}}^{\nu\nu'\omega} = 2U\lambda_{pp,\uparrow\downarrow}^{\nu\omega} + 2U\lambda_{pp,\uparrow\downarrow}^{\nu'\omega} + 2U^2\chi_{pp,\uparrow\downarrow}^{\omega}, \tag{A3c}$$

$$\Phi_{t,\text{asym}}^{\nu\nu'\omega} = 0, \tag{A3d}$$

where the terms χ_r^{ω} remove the double counting of contributions which are contained in both $\lambda_r^{\nu\omega}$ and $\lambda_r^{\nu'\omega}$ [cf. the two diagrams in Fig. 7, which both contain the lower diagram in Fig. 7(a)]. Adding the asymptotic contributions for $\Phi_{r,\text{asym}}^{\nu\nu'\omega}$ in Eq. (A3) to the corresponding ones of $\Gamma_{r,\text{asym}}^{\nu\nu'\omega}$ in Eq. (11) yields $F_{r,\text{asym}}^{\nu\nu'\omega}$ as given in Eq. (12).

APPENDIX B: NUMERICAL CALCULATION OF χ_r^{ω} AND $\lambda_r^{\nu\omega}$ IN ED

As mentioned in Sec. II, the asymptotic functions of the two-particle vertex, i.e., the susceptibility and the fermion-boson vertex, can be evaluated in the same way as the two-particle Green's function by means of the impurity solver used in our (ED)DMFT cycle. In fact, while the treatment of the full frequency dependence of the vertex is computationally challenging, valuable information of the two-particle scattering processes can be extracted from more manageable quantities whose parameter dependence is restricted to one or two frequencies [in our single-band SU(2) symmetric Hubbard model]. In this section, we explicitly derive their spectral representation, as implemented in our impurity solver.

1. Lehmann representation of $\lambda_r^{\nu\omega}$

In this section, we derive the Lehmann representation for the fermion-boson vertices $\lambda_r^{\nu'\omega}$. *First*, we present the equations for the ph channel, i.e., for $\lambda_{d/m}^{\nu'\omega} = \lambda_{ph,\uparrow\uparrow}^{\nu'\omega} \pm \lambda_{ph,\uparrow\downarrow}^{\nu\omega}$. Our starting point is the Fourier representation of the generalized susceptibility [25,46] $\chi_r^{\nu\nu'\omega}$ summed over one fermionic Matsubara frequency (ν)

$$\tilde{\lambda}_{ph,\sigma\sigma'}^{\nu'\omega} = \frac{1}{\beta}\sum_{\nu}\chi_{ph,\sigma\sigma'}^{\nu\nu'\omega} = \frac{1}{\beta}\sum_{\nu}\int_0^{\beta} d\tau_1 d\tau_2 d\tau_3\, e^{-i\nu\tau_1} e^{i(\nu+\omega)\tau_2} e^{-i(\nu'+\omega)\tau_3} \times [\langle T_\tau c_\sigma^\dagger(\tau_1)c_\sigma(\tau_2)c_{\sigma'}^\dagger(\tau_3)c_{\sigma'}(0)\rangle - \langle T_\tau c_\sigma^\dagger(\tau_1)c_\sigma(\tau_2)\rangle\langle T_\tau c_{\sigma'}^\dagger(\tau_3)c_{\sigma'}(0)\rangle], \tag{B1}$$

which is related to the fermion-boson vertices $\lambda_{ph,\sigma\sigma'}^{\nu'\omega}$ as (note the inversion of σ')

$$\lambda_{ph,\sigma\sigma'}^{\nu'\omega} = -\frac{\tilde{\lambda}_{ph,\sigma(-\sigma')}^{\nu'\omega}}{G(\nu')G(\nu'+\omega)} - \delta_{\sigma(-\sigma')}. \tag{B2}$$

Exchanging frequency summation and (imaginary) time integration in Eq. (B1), we obtain [$\frac{1}{\beta}\sum_\nu e^{-i\nu\tau} = \delta(\tau)$]

$$\tilde{\lambda}_{ph,\sigma\sigma'}^{\nu'\omega} = \int_0^{\beta} d\tau_1 d\tau_3\, e^{i\omega\tau_1} e^{-i(\nu'+\omega)\tau_3} [\langle T_\tau c_\sigma^\dagger(\tau_1)c_\sigma(\tau_1)c_{\sigma'}^\dagger(\tau_3)c_{\sigma'}(0)\rangle - \langle T_\tau c_\sigma^\dagger(\tau_1)c_\sigma(\tau_1)\rangle\langle T_\tau c_{\sigma'}^\dagger(\tau_3)c_{\sigma'}(0)\rangle]. \tag{B3}$$

Let us begin by calculating first term in the square brackets on the r.h.s. of Eq. (B3). Considering the time-ordering operator, we obtain the following two contributions:

$$\tilde{\lambda}^{\nu'\omega}_{ph,\sigma\sigma'} = \int_0^\beta d\tau_1 \left[\int_0^{\tau_1} d\tau_3 e^{i\omega\tau_1} e^{-i(\nu'+\omega)\tau_3} \langle c^\dagger_\sigma(\tau_1) c_\sigma(\tau_1) c^\dagger_{\sigma'}(\tau_3) c_{\sigma'}(0)\rangle \int_{\tau_1}^\beta d\tau_3 e^{i\omega\tau_1} e^{-i(\nu'+\omega)\tau_3} \langle c^\dagger_{\sigma'}(\tau_3) c^\dagger_\sigma(\tau_1) c_\sigma(\tau_1) c_{\sigma'}(0)\rangle \right]$$
$$= \tilde{\lambda}^{\nu'\omega}_{13,\sigma\sigma'} + \tilde{\lambda}^{\nu'\omega}_{31,\sigma\sigma'}. \tag{B4}$$

The first term can be transformed by inserting a complete basis of the Hilbert space ($\mathbb{1} = \sum_i |i\rangle\langle i|$) after each operator in the trace

$$\begin{aligned}
\tilde{\lambda}^{\nu'\omega}_{13,\sigma\sigma'} &= \int_0^\beta d\tau_1 \int_0^{\tau_1} d\tau_3 e^{i\omega\tau_1} e^{-i(\nu'+\omega)\tau_3} \langle n_\sigma(\tau_1) c^\dagger_{\sigma'} c_{\sigma'}(0)\rangle \\
&= \frac{1}{Z}\int_0^\beta d\tau_1 \int_0^{\tau_1} d\tau_3 e^{i\omega\tau_1} e^{-i(\omega+\nu')\tau_3} \sum_{i,j,k} \langle i|e^{-\beta H} e^{H\tau_1} n_\sigma e^{-H\tau_1}|j\rangle\langle j|e^{H\tau_3} c^\dagger_{\sigma'} e^{-H\tau_3}|k\rangle\langle k|c_{\sigma'}|i\rangle \\
&= \frac{1}{Z}\sum_{i,j,k}\int_0^\beta d\tau_1 \int_0^{\tau_1} d\tau_3 e^{i\omega\tau_1} e^{-i(\omega+\nu')\tau_3} e^{-\beta E_i} e^{E_i\tau_1} e^{-E_j\tau_1} e^{E_j\tau_3} e^{-E_k\tau_3} \langle i|n_\sigma|j\rangle\langle j|c^\dagger_{\sigma'}|k\rangle\langle k|c_{\sigma'}|i\rangle \\
&= \frac{1}{Z}\sum_{i,j,k} \frac{\langle i|n_\sigma|j\rangle\langle j|c^\dagger_{\sigma'}|k\rangle\langle k|c_{\sigma'}|i\rangle}{i(\nu'+\omega)+E_k-E_j}\left[\frac{e^{-E_j\beta}-e^{-E_i\beta}}{i\omega+E_i-E_j} - \frac{e^{-E_k\beta}+e^{-E_i\beta}}{i\nu'+E_k-E_i}\right],
\end{aligned} \tag{B5}$$

where Z denotes the partition function (see Sec. II). Using the same procedure for $\tilde{\lambda}^{\nu'\omega}_{31,\sigma\sigma'}$ one obtains

$$\tilde{\lambda}^{\nu'\omega}_{31,\sigma\sigma'} = \frac{1}{Z}\beta\sum_{i,j,k} \frac{\langle i|c^\dagger_{\sigma'}|j\rangle\langle j|n_\sigma|k\rangle\langle k|c_{\sigma'}|i\rangle}{i(\nu'+\omega)+E_j-E_i}\left[\frac{e^{-E_k\beta}-e^{-E_j\beta}}{i\omega+E_j-E_k} + \frac{e^{-E_k\beta}+e^{-E_i\beta}}{i\nu'+E_k-E_i}\right]. \tag{B6}$$

Let us now consider the second term in the square brackets on the r.h.s. of Eq. (B3). It contains only one-particle correlation functions and can be rewritten as

$$\tilde{\lambda}^{\nu'\omega}_{0,ph,\sigma\sigma'} = \int_0^\beta d\tau_1 \int_0^\beta d\tau_3 e^{i\omega\tau_1} e^{-i(\nu'+\omega)\tau_3} \langle T_\tau c^\dagger_\sigma(\tau_1) c_\sigma(\tau_1)\rangle\langle T_\tau c^\dagger_{\sigma'}(\tau_3) c_{\sigma'}(0)\rangle = \delta_{\omega 0}\langle n_\sigma\rangle G_{\sigma'}(\nu'), \tag{B7}$$

where $\langle n_\sigma\rangle$ is the local electron density which, at half filling and in the SU(2) symmetric case, simplifies to $\langle n_\sigma\rangle = 1/2$.

In the *second* step, we present the derivation of $\lambda^{\nu'\omega}_{pp,\sigma\sigma'}$. This can be easily achieved by using the frequency transformation between *ph* and *pp* channels. As in the *ph* case, we define a quantity

$$\begin{aligned}
\tilde{\lambda}^{\nu'\omega}_{pp,\sigma\sigma'} &= \frac{1}{\beta}\sum_\nu \chi^{\nu\nu'\omega}_{pp,\sigma\sigma'} \equiv \frac{1}{\beta}\sum_\nu \chi^{\nu\nu'(\omega-\nu-\nu')}_{ph,\sigma\sigma'} \\
&= \int_0^\beta d\tau_1 d\tau_2 e^{i(\omega-\nu')\tau_2} e^{-i\omega\tau_1} [\langle T_\tau c^\dagger_\sigma(\tau_1) c_\sigma(\tau_2) c^\dagger_{\sigma'}(\tau_1) c_{\sigma'}(0)\rangle - \langle T_\tau c^\dagger_\sigma(\tau_1) c_\sigma(\tau_2)\rangle\langle T_\tau c^\dagger_{\sigma'}(\tau_1) c_{\sigma'}(0)\rangle],
\end{aligned} \tag{B8}$$

which is related to $\lambda^{\nu'\omega}_{pp,\sigma\sigma'}$ via $\lambda^{\nu'\omega}_{pp,\sigma\sigma'} = \tilde{\lambda}^{\nu'\omega}_{pp,\sigma\sigma'}/[G(\nu')G(\omega-\nu')]$. In analogy to the previous derivation, one can express the first term of the second line of Eq. (B8) as a sum of two contributions:

$$\tilde{\lambda}^{\nu'\omega}_{pp,\sigma\sigma'} = \tilde{\lambda}^{\nu'\omega}_{12,\sigma\sigma'} + \tilde{\lambda}^{\nu'\omega}_{21,\sigma\sigma'}, \tag{B9}$$

with $\tau_1 > \tau_2$ and $\tau_2 > \tau_1$, respectively (we omitted the *pp* label on the r.h.s. to simplify the notation). The explicit expressions then read

$$\tilde{\lambda}^{\nu'\omega}_{12,\sigma\sigma'} = \frac{1}{Z}\beta\sum_{i,j,k} \frac{\langle i|\Delta^*_{\sigma\sigma'}|j\rangle\langle j|c_\sigma|k\rangle\langle k|c_{\sigma'}|i\rangle}{i(\omega-\nu')+E_j-E_k}\left[\frac{e^{-E_i\beta}-e^{-E_j\beta}}{i\omega+E_j-E_i} - \frac{e^{-E_k\beta}+e^{-E_i\beta}}{i\nu'+E_k-E_i}\right], \tag{B10a}$$

$$\tilde{\lambda}^{\nu'\omega}_{21,\sigma\sigma'} = -\frac{1}{Z}\beta\sum_{i,j,k} \frac{\langle i c_\sigma|j\rangle\langle j|\Delta^*_{\sigma\sigma'}|k\rangle\langle k|c_{\sigma'}|i\rangle}{i(\omega-\nu')+E_i-E_j}\left[\frac{e^{-E_k\beta}-e^{-E_j\beta}}{i\omega+E_k-E_j} - \frac{e^{-E_k\beta}+e^{-E_i\beta}}{i\nu'+E_k-E_i}\right], \tag{B10b}$$

with $\Delta^{(*)}_{\sigma\sigma'} = c^{(\dagger)}_\sigma c^{(\dagger)}_{\sigma'}$ representing the pair annihilation (creation) operator. The second term of Eq. (B8), in the following referred as $\tilde{\lambda}^{\nu'\omega}_{0,pp,\sigma\sigma'}$, can be expressed by means of single-particle propagators:

$$\tilde{\lambda}^{\nu'\omega}_{0,pp,\sigma\sigma'} = \int_0^\beta d\tau_1 d\tau_2 e^{i(\omega-\nu')\tau_2} e^{-i\omega\tau_1} G_\sigma(\tau_1-\tau_2) G_{\sigma'}(\tau_1) = G(\nu')G(\omega-\nu'). \tag{B11}$$

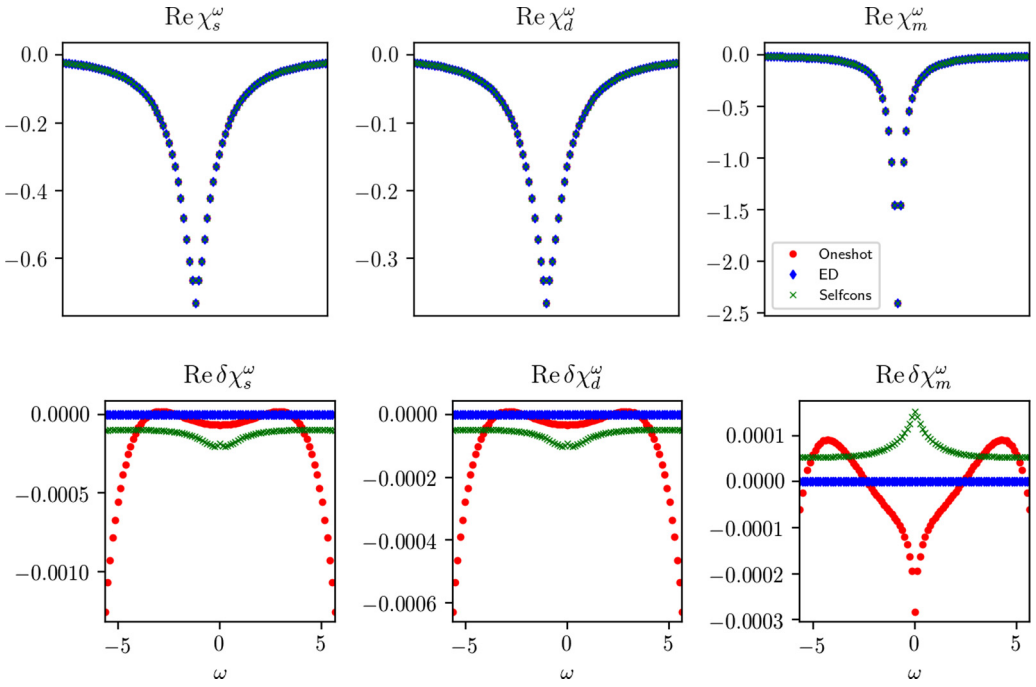

FIG. 8. Comparison of the physical susceptibilities acquired by means of the ED impurity solver (blue diamonds), by means of the self-consistent procedure (green crosses) and by directly summing the generalized susceptibilities $\chi_r^{\nu\nu'\omega}$ over ν and ν' (red dots). The first row shows the susceptibilities in the physical channels for $U = 1$, while the second one displays the correspondent difference to the exact results.

2. Lehmann representation of χ_r^ω

In this section, we derive the spectral representation for the susceptibilities (5). In particular, we consider its building blocks

$$\chi^\omega_{ph/pp,\sigma\sigma'} = \frac{1}{\beta^2}\sum_{\nu\nu'}\chi^{\nu\nu'\omega}_{ph/pp,\sigma\sigma'}. \tag{B12}$$

We start by analyzing the particle-hole channel:

$$\chi^\omega_{ph,\sigma\sigma'} = \frac{1}{\beta^2}\sum_{\nu\nu'}\int_0^\beta d\tau_1 d\tau_2 d\tau_3 e^{-i\nu\tau_1}e^{i(\nu+\omega)\tau_2}e^{-i(\nu'+\omega)\tau_3}[\langle T_\tau c^\dagger_\sigma(\tau_1)c_\sigma(\tau_2)c^\dagger_{\sigma'}(\tau_3)c_{\sigma'}(0)\rangle - \langle T_\tau c^\dagger_\sigma(\tau_1)c_\sigma(\tau_2)\rangle\langle T_\tau c^\dagger_{\sigma'}(\tau_3)c_{\sigma'}(0)\rangle]$$

$$= \int_0^\beta d\tau e^{i\omega\tau}[\langle T_\tau c^\dagger_\sigma(\tau)c_\sigma(\tau)c^\dagger_{\sigma'}(0)c_{\sigma'}(0)\rangle - \langle n_\sigma(\tau)\rangle\langle n_{\sigma'}(0)\rangle], \tag{B13}$$

The actual derivation of the spectral representation is now completely analogous to the one for the fermion-boson vertex illustrated above and we obtain

$$\chi^\omega_{ph,\sigma\sigma'} = \frac{1}{Z}\sum_{i,j}\frac{\langle i|n_\sigma|j\rangle\langle j|n_{\sigma'}|i\rangle}{i\omega + E_i - E_j}(e^{-E_j\beta} - e^{-E_i\beta}) - \beta\langle n_\sigma\rangle^2\delta_{\omega 0}, \tag{B14}$$

where we have used that in the SU(2) symmetric case $\langle n_\uparrow\rangle = \langle n_\downarrow\rangle$. For the particle-particle channel one finds

$$\chi^\omega_{pp,\sigma\sigma'} = \frac{1}{Z}\sum_{i,j}\frac{\langle i|\Delta^*_{\sigma\sigma'}|j\rangle\langle j|\Delta_{\sigma\sigma'}|i\rangle}{i\omega + E_j - E_i}(e^{-E_i\beta} - e^{-E_j\beta}). \tag{B15}$$

Let us finally emphasize the simplicity of the above expressions with respect to the Lehmann representation of the full (not summed) three-frequency two-particle propagator. The equal time evaluation significantly reduces the number of permutations due to the time-ordering. In addition, the reduced variable dependence cuts down the huge computational cost of evaluating the two-particle propagators.

APPENDIX C: SELF-CONSISTENT EVALUATION OF χ_r^ω AND $\lambda_r^{\nu\omega}$

We remark that although the spectral representation of χ_r^ω and $\lambda_r^{\nu\omega}$ represents a computationally straightforward task for the ED impurity solver, alternative schemes to acquire the asymptotics of the vertex function are available. Besides the implementations used by other impurity solvers as quantum Monte Carlo (QMC) [47], we recall here another approach, which turns out to be feasible for different vertex-based solvers as the DΓA [25,27,48], the parquet approximation [49–51], and the functional renormalization group (fRG) [31,39,52,53]. This technique, which has been proposed in Ref. [39], is based

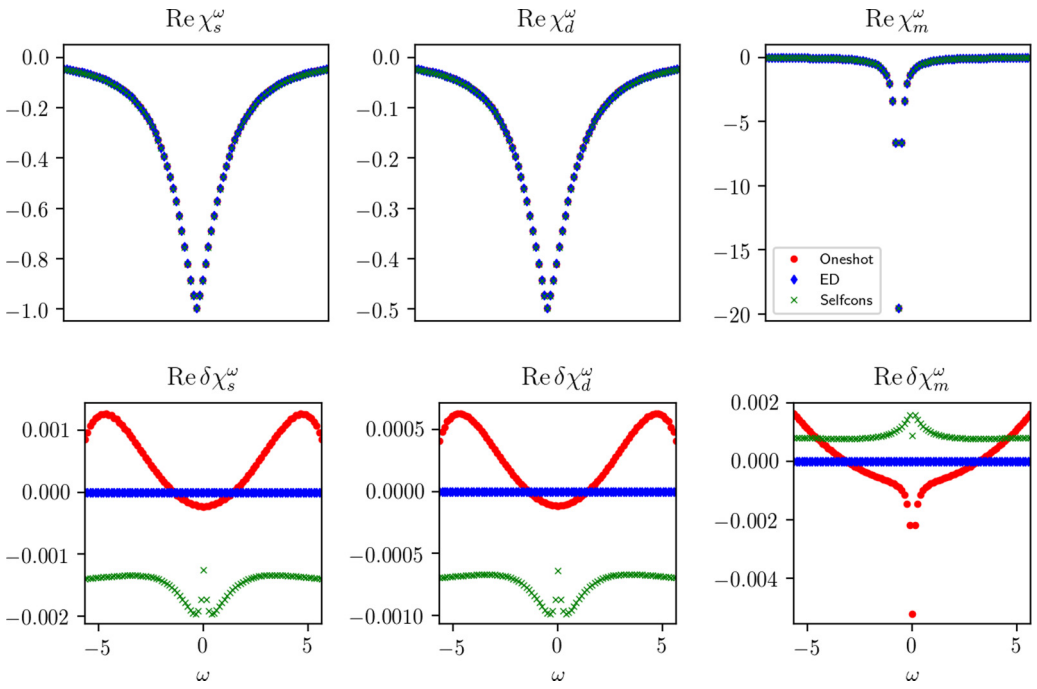

FIG. 9. Same as in Fig. 8 for $U = 1.75$.

on a self-consistent determination of the asymptotic functions from the low-frequency data for the two-particle Green's function (see, in particular, Appendix C in Ref. [39]). In Figs. 8–11, we show converged results which exhibit deviations to the exact value at most of the order of $\delta \sim 10^{-3}$ (relative error). Nevertheless, one should note that this approach presents some intrinsic drawbacks which may become pathological in certain parameter regimes, in particular for too small frequency ranges which do not capture the entire low-frequency structures of the two-particle correlation functions.

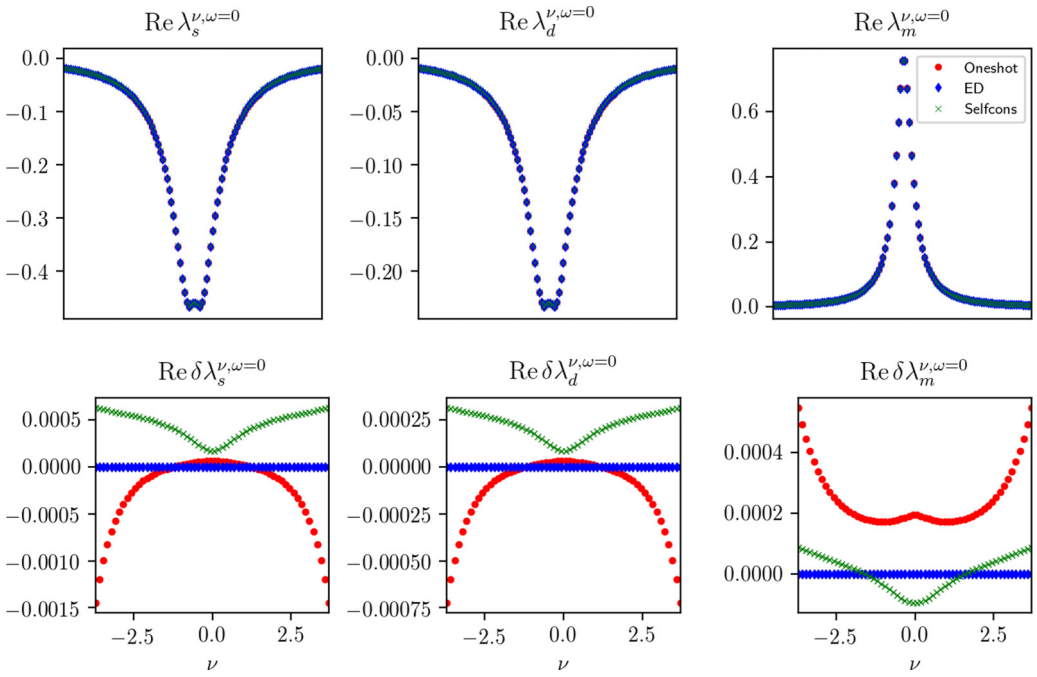

FIG. 10. Comparison of the fermi-boson vertices acquired by means of the ED impurity solver (blue diamonds), by means of the self-consistent procedure (green crosses) and by directly summing the generalized susceptibilities $\chi_r^{\nu\nu'\omega}$ over ν' (red dots). Here, $\lambda^{\nu\omega}$ is plotted as a function of the fermionic frequency ν and for a fixed bosonic frequency $\omega = 0$. The first row shows $\lambda^{\nu\omega=0}$ in the physical channels for $U = 1$, while the second one displays the corresponding difference to the exact results.

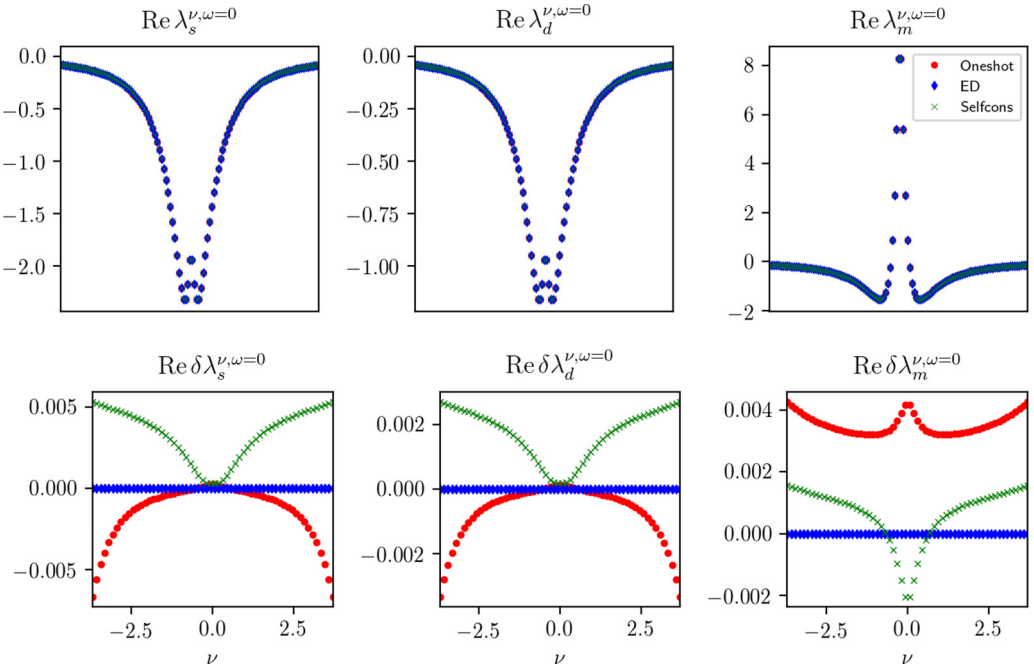

FIG. 11. Same as in Fig. 10 for $U = 1.75$.

APPENDIX D: COMPARISON OF THE TWO METHODS FOR $U = 1.75$

In this Appendix, we report the behavior of $\Gamma^{\nu\nu'\omega}$ for $U = 1.75$ (see Fig. 12). We compare the data obtained by the two methods to correct the inversion of the Bethe-Salpeter equations with to the "noncorrected" result. Differently from the case $U = 1$, one observes, for the singlet and the density channels, a non-negligible fermionic frequency structure of the corrections provided by the two methods. Albeit quite relevant for the case $N_{\rm inv} = 40$, this structure has been shown to became negligible going to higher values of $N_{\rm inv}$. By looking at the fermionic frequency dependence provided by the second line of Eq. (18) (method 1) and Eq. (19) (method 2), one can deduce (see discussion in Sec. IV) that this is originated by the asymptotics of $\Gamma_{r,\rm asym}$ in Eq. (11). In the intermediate regime, one would expect the low-frequency structure of Γ_r (not captured

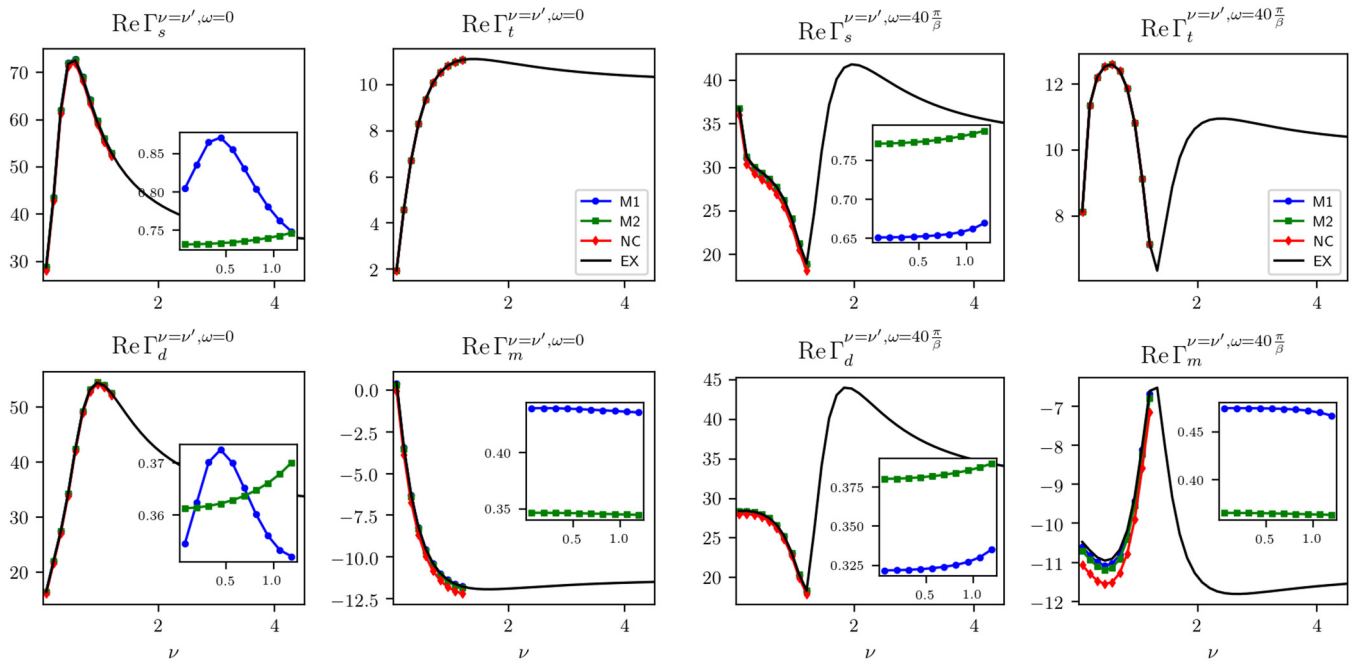

FIG. 12. $\Gamma_r^{\nu\nu'\omega}$ for $r = \{s,t,d,m\}$, evaluated along the diagonal $\nu = \nu'$ for $U = 1.75$, $\omega = 0$, (left) and $\omega = 40\pi/\beta$ (right). Results of method 1 (blue) and method 2 (green) are compared to a plain inversion (red) of Eq. (10) for $N_{\rm inv} = 40$ and the exact solution (black). Insets show the corrections terms only.

by the asymptotics) to become particularly pronounced in the density and the singlet channels [54,55]. Possibly, this creates a cancellation with the (fermionic) frequency-dependent terms of $\Gamma_{r,\mathrm{asym}}$ in the regime where the low-frequency structure in not fully decayed. As one can see in Fig. 6 the latter are not fully decayed for $N_{\mathrm{inv}}=40$. This can explain the (fermionic)frequency structure shown in the insets if Fig. 12, which can be reduced by considering a bigger N_{inv} range.

[1] E. Rutherford, Philos. Mag. **21**, 669 (1911).
[2] G. Aad, T. Abajyan, B. Abbott, J. Abdallah, S. A. Khalek, A. Abdelalim, O. Abdinov, R. Aben, B. Abi, M. Abolins *et al.*, Phys. Lett. B **716**, 1 (2012).
[3] N. F. Mott, Rev. Mod. Phys. **40**, 677 (1968).
[4] D. B. McWhan, T. M. Rice, and J. P. Remeika, Phys. Rev. Lett. **23**, 1384 (1969).
[5] J. G. Bednorz and K. A. Müller, Z. Phys. B: Condens. Matter **64**, 189 (1986).
[6] P. A. Lee, N. Nagaosa, and X.-G. Wen, Rev. Mod. Phys. **78**, 17 (2006).
[7] W. Metzner and D. Vollhardt, Phys. Rev. Lett. **62**, 324 (1989).
[8] A. Georges and G. Kotliar, Phys. Rev. B **45**, 6479 (1992).
[9] A. Georges, G. Kotliar, W. Krauth, and M. J. Rozenberg, Rev. Mod. Phys. **68**, 13 (1996).
[10] G. Kotliar, S. Y. Savrasov, K. Haule, V. S. Oudovenko, O. Parcollet, and C. A. Marianetti, Rev. Mod. Phys. **78**, 865 (2006).
[11] K. Held, Adv. Phys. **56**, 829 (2007).
[12] A. Toschi, R. Arita, P. Hansmann, G. Sangiovanni, and K. Held, Phys. Rev. B **86**, 064411 (2012).
[13] E. Pavarini, *Linear Response Functions* (Verlag des Forschungszentrum Jülich, Jülich, Germany, 2014), Vol. 4, Chap. 6.
[14] L. Boehnke, Ph.D. thesis, University of Hamburg, 2015.
[15] K. Steiner, S. Hoshino, Y. Nomura, and P. Werner, Phys. Rev. B **94**, 075107 (2016).
[16] S. Hoshino and Y. Kuramoto, Phys. Rev. Lett. **112**, 167204 (2014).
[17] S. Hoshino and P. Werner, Phys. Rev. Lett. **115**, 247001 (2015).
[18] S. Hoshino and P. Werner, Phys. Rev. B **93**, 155161 (2016).
[19] O. Gunnarsson, T. Schäfer, J. P. F. LeBlanc, E. Gull, J. Merino, G. Sangiovanni, G. Rohringer, and A. Toschi, Phys. Rev. Lett. **114**, 236402 (2015).
[20] G. Kotliar, S. Y. Savrasov, G. Pálsson, and G. Biroli, Phys. Rev. Lett. **87**, 186401 (2001).
[21] M. H. Hettler, A. N. Tahvildar-Zadeh, M. Jarrell, T. Pruschke, and H. R. Krishnamurthy, Phys. Rev. B **58**, R7475 (1998).
[22] M. H. Hettler, M. Mukherjee, M. Jarrell, and H. R. Krishnamurthy, Phys. Rev. B **61**, 12739 (2000).
[23] T. Maier, M. Jarrell, T. Pruschke, and M. H. Hettler, Rev. Mod. Phys. **77**, 1027 (2005).
[24] G. Rohringer, H. Hafermann, A. Toschi, A. A. Katanin, A. E. Antipov, M. I. Katsnelson, A. I. Lichtenstein, A. N. Rubtsov, and K. Held, Rev. Mod. Phys. **90**, 025003 (2018).
[25] A. Toschi, A. A. Katanin, and K. Held, Phys. Rev. B **75**, 045118 (2007).
[26] A. Toschi, G. Rohringer, A. Katanin, and K. Held, Ann. Phys. **523**, 698 (2011).
[27] G. Rohringer and A. Toschi, Phys. Rev. B **94**, 125144 (2016).
[28] A. N. Rubtsov, M. I. Katsnelson, and A. I. Lichtenstein, Phys. Rev. B **77**, 033101 (2008).
[29] G. Rohringer, A. Toschi, H. Hafermann, K. Held, V. I. Anisimov, and A. A. Katanin, Phys. Rev. B **88**, 115112 (2013)
[30] A. N. Rubtsov, M. I. Katsnelson, and A. I. Lichtenstein, Ann. Phys. **327**, 1320 (2012).
[31] C. Taranto, S. Andergassen, J. Bauer, K. Held, A. Katanin, W. Metzner, G. Rohringer, and A. Toschi, Phys. Rev. Lett. **112**, 196402 (2014).
[32] T. Ayral and O. Parcollet, Phys. Rev. B **92**, 115109 (2015).
[33] T. Ayral and O. Parcollet, Phys. Rev. B **93**, 235124 (2016).
[34] T. Ayral and O. Parcollet, Phys. Rev. B **94**, 075159 (2016).
[35] N. Bickers, in *Theoretical Methods for Strongly Correlated Electrons*, CRM Series in Mathematical Physics, edited by D. Sénéchal, A.-M. Tremblay, and C. Bourbonnais (Springer, New York, 2004), pp. 237–296.
[36] V. Janiš, Phys. Rev. B **64**, 115115 (2001).
[37] G. Rohringer, A. Valli, and A. Toschi, Phys. Rev. B **86**, 125114 (2012).
[38] G. Li, N. Wentzell, P. Pudleiner, P. Thunström, and K. Held, Phys. Rev. B **93**, 165103 (2016).
[39] N. Wentzell, G. Li, A. Tagliavini, C. Taranto, G. Rohringer, K. Held, A. Toschi, and S. Andergassen, arXiv:1610.06520.
[40] J. Kuneš, Phys. Rev. B **83**, 085102 (2011).
[41] G. Rohringer, Ph.D. thesis, Vienna University of Technology, 2014.
[42] A. A. Abrikosov, *Methods of Quantum Field Theory in Statistical Physics*, Dover Books on Physics (Dover, UK, 1975).
[43] S. Hummel, Master's thesis, Vienna University of Technology, 2014.
[44] M. Kinza and C. Honerkamp, Phys. Rev. B **88**, 195136 (2013).
[45] A. E. Antipov and I. Krivenko, POMEROL: 1.1 (2015), http://doi.org/10.5281/zenodo.17900.
[46] H. Hafermann, C. Jung, S. Brener, M. I. Katsnelson, A. N. Rubtsov, and A. I. Lichtenstein, Europhys. Lett. **85**, 27007 (2009).
[47] J. Kaufmann, P. Gunacker, and K. Held, Phys. Rev. B **96**, 035114 (2017).
[48] A. Valli, T. Schäfer, P. Thunström, G. Rohringer, S. Andergassen, G. Sangiovanni, K. Held, and A. Toschi, Phys. Rev. B **91**, 115115 (2015).
[49] C.-X. Chen and N. E. Bickers, Solid State Commun. **82**, 311 (1992).
[50] N. E. Bickers, Int. J. Mod. Phys. B **5**, 253 (1991).
[51] K.-M. Tam, H. Fotso, S.-X. Yang, T.-W. Lee, J. Moreno, J. Ramanujam, and M. Jarrell, Phys. Rev. E **87**, 013311 (2013).
[52] W. Metzner, M. Salmhofer, C. Honerkamp, V. Meden, and K. Schönhammer, Rev. Mod. Phys. **84**, 299 (2012).
[53] C. J. Halboth and W. Metzner, Phys. Rev. Lett. **85**, 5162 (2000).
[54] T. Schäfer, G. Rohringer, O. Gunnarsson, S. Ciuchi, G. Sangiovanni, and A. Toschi, Phys. Rev. Lett. **110**, 246405 (2013).
[55] P. Chalupa, P. Gunacker, T. Schäfer, K. Held, and A. Toschi, Phys. Rev. B **97**, 245136 (2018).

III Multiloop functional renormalization group for the two-dimensional Hubbard model: Loop convergence of the response functions

Multiloop functional renormalization group for the two-dimensional Hubbard model: Loop convergence of the response functions

A. Tagliavini[1,2], C. Hille[2*], F. B. Kugler[3], S. Andergassen[2], A. Toschi[1], C. Honerkamp[4,5]

1 Institute for Solid State Physics, Vienna University of Technology, 1040 Vienna, Austria
2 Institut für Theoretische Physik and Center for Quantum Science, Universität Tübingen, Auf der Morgenstelle 14, 72076 Tübingen, Germany
3 Physics Department, Arnold Sommerfeld Center for Theoretical Physics, and Center for NanoScience, Ludwig-Maximilians-Universität München, Theresienstrasse 37, 80333 Munich, Germany
4 Institute for Theoretical Solid State Physics, RWTH Aachen University, D-52056 Aachen, Germany
5 JARA - Fundamentals of Future Information Technology
* cornelia.hille@uni-tuebingen.de

August 8, 2018

Abstract

We present a functional renormalization group (fRG) study of the two dimensional Hubbard model, performed with an algorithmic implementation which lifts some of the common approximations made in fRG calculations. In particular, in our fRG flow; (i) we take explicitly into account the momentum and the frequency dependence of the vertex functions; (ii) we include the feedback effect of the self-energy; (iii) we implement the recently introduced multiloop extension which allows us to sum up *all* the diagrams of the parquet approximation with their exact weight. Due to its iterative structure based on successive one-loop computations, the loop convergence of the fRG results can be obtained with an affordable numerical effort. In particular, focusing on the analysis of the physical response functions, we show that the results become *independent* from the chosen cutoff scheme and from the way the fRG susceptibilities are computed, i.e., either through flowing couplings to external fields, or through a "post-processing" contraction of the interaction vertex at the end of the flow. The presented substantial refinement of fRG-based computation schemes paves a promising route towards future quantitative fRG analyses of more challenging systems and/or parameter regimes.

Contents

1 Introduction

Over the last two decades, functional renormalization group (fRG) methods have been broadly used for analyzing two-dimensional (2D) lattice electron systems (for reviews, see Refs. [1,2]). The main advantage of the fRG lies in the exploration of the leading low-energy correlations and instabilities towards long-range ordered states, similar to what has been investigated earlier for one-dimensional systems [3, 4]. However, in one dimension, other methods like Bethe-Ansatz, bosonization [5, 6] and DMRG [7] exist, which are for certain aspects more controlled. Hence, assessing the precision of RG methods in one-dimensional systems was not really in the foreground. The situation evidently changes for two- and three-dimensional systems, where the specific simplifications associated to the peculiar one-dimensional geometry are not applicable. At the same time, spatial correlations in 2D are strong enough to induce qualitative corrections [8, 9] with respect to another class

of rigorous many-body approaches, such as the Dynamical Mean-Field Theory (DMFT) [10–12] which allows one to include all purely local dynamical correlations.

In fact, due to the intrinsic complexity of the many-electron problem in 2D, the development of unbiased quantitative methods applicable to a wide energy range from electronic structures on the scale of a few eV down to, e.g., ground state ordering in the (sub-)meV region, is still on the wishlist. This goal has motivated, in the last decade, the development of several algorithmic schemes for treating electronic correlations in 2D from different perspectives [1, 13, 14]. In this context, the fRG has already unveiled quite promising features: The fRG has the potential of resolving band structures and Fermi surface details *and* to treat competing orders on low energy scales in a rather unbiased way, since it does not require preliminary assumptions about dominating scattering channels. Recent applications range from studies of cuprate high-T_c superconductors [15–18] over iron superconductors [2, 19] to few-layer graphene systems [20, 21], to cite a few.

We also note that, while the current applicability of the fRG is generally restricted to the weak to intermediate coupling regimes, its combination [22, 23] with the DMFT might allow one, in the future, to access much more strongly correlated parameter regions, including the ones in proximity of the Mott-Hubbard metal-insulator transition. This is achieved by constructing a fRG flow starting from the DMFT solution of the considered lattice problem to the exact solution, i.e., in practice, using the DMFT to determine the initial conditions for the fRG flow [22]. Similarly to other diagrammatic extensions [14] of DMFT, such as the Dynamical Vertex Approximation (DΓA) [24] or the Dual Fermion [25] approach, one might work either with the physical degrees of freedom (as in the so-called DMF^{2}RG [22]) or in the space of auxiliary (dual) fermions [26], introduced by means of a suitable [14, 25] Hubbard-Stratonovich transformation.

Yet, what is hitherto missing is a thorough analysis of the *quantitative* reliability of the fRG for a well-defined test case. More precisely this would require to clarify how much the fRG results, going beyond the correct estimation of general physical trends, depend on the approximations inherent in the used fRG scheme. This study within the fRG would then also provide a solid basis for future comparisons with other numerical techniques.

The mentioned approximations can be grouped in three categories:
(i) *Momentum/frequency discretization*: As the fRG algorithm typically exploits the flow of vertex functions that depend continuously on multiple momenta and frequencies, various approximations are performed to mitigate numerical and memory costs. Early on, N-patch discretizations of the momentum dependencies through the Brillouin zone were used. Later, it was noticed that channel-decompositions in conjunction with form factor expansions [27–29] lead to physically appealing approximations featuring advantageous momentum resolution and numerical performance [30]. Clever prescriptions for the treatment of the high-frequency tails of the vertex function have been devised [31–33] which are also used in this work.

(ii) *Self-energy feedback*: In many applications of the fRG the self-energy and its feedback on the flow of the n-particle ($n > 1$) vertex functions has *not* been accounted for. While there are arguments that the self-energy may be important mainly when the interactions are close to a flow to strong coupling (see Appendix in Ref. [34]), more quantitative results should overcome this deficit. In fact, neglecting the self-energy feedback was mainly motivated by the disregarded frequency dependence of the interactions in earlier fRG studies: Within a static treatment the self-energy lacks the effects of quasiparticle degradation, so that its inclusion became less important. Within the current frequency-dependent fRG treatments, the self-energy feedback can be included in a meaningful way. A number of works have already investigated the self-energy effects in the flows to strong coupling in Hubbard-type models [28, 35–43], mainly exploring the quantitative effects,

besides signatures of pseudogap openings [38, 39] and non-Fermi liquid behavior [28] in particular cases.
(iii) *Truncation of the flow equation hierarchy*: Finally, one should also consider the truncation of the hierarchy of flow equations for the n-point one-particle irreducible (1PI) vertex functions. This is usually done at "level-II" as defined in Ref. [1], also referred to as one-loop (1ℓ) approximation, i.e., the 1PI six-point vertex is set to zero. Due to this truncation, the final result of an fRG flow might depend –to a certain degree– on the cutoff scheme adopted for the calculation.

In this perspective, it was noticed by Katanin [44] that replacing the so-called single-scale propagator in the loops on the r.h.s. of the flow equation for the four-point vertex by a scale-derivative of the full Green's function allows this scheme to become equivalent to one-particle self-consistent (a.k.a. mean-field) theories in reduced models, and then to go beyond such self-consistent approximations in more general models. Another significant comparison can be made with the parquet-based approaches [45, 46], such as the parquet approximation (PA) [32, 33, 47–49]. The latter represents the "lowest order" solution of the parquet equations, where the two-particle irreducible vertex is approximated by the bare interaction. In fact, although the diagrams summed in the 1ℓ truncation of the fRG are topologically the same as in the PA, the way the single contributions are generated during the flow leads in general to differences with respect to the PA [33, 50]. This is due to some internal-line combinations, e.g., in particle-hole corrections to the particle-particle channel, which are suppressed by the cutoff functions attached to the propagators and not fully reconstructed during the flow because of the truncation. A quantitative analysis of this effect has been performed for the single impurity Anderson model in Ref. [33]. These differences are absent for single-channel summations (e.g. RPA), but could lead to more pronounced quantitative errors in presence of channel coupling, e.g., in the generation of superconducting pairing through spin fluctuations. Furthermore, while the Mermin-Wagner theorem is fulfilled within the PA [51], it is typically violated by 1ℓ fRG calculations. First steps to remedy this shortcoming were undertaken in various works [42, 52, 53], but only recently a comprehensive path of how the PA contributions can be recovered in full extent was presented within the multiloop extension of the fRG (mfRG) [54–56]. The mfRG flow equations incorporate all contributions of the six-point vertex that complement the derivative of diagrams already part of the 1ℓ flow, as organized by their loop structure. A key insight in this approach is that the higher-loop contributions can be generated by computing 1ℓ flows for scale-differentiated vertices, with an effort growing only linearly with the loop order that is fully kept. The multiloop corrections stabilize the flow by enabling full screening of competing two-particle channels, ultimately recovering the self-consistent structure of the PA. As the PA corresponds to a well-defined subset of diagrams, a converged mfRG flow able to reproduce the PA is by construction independent of the adopted cutoff.

In this paper, we present a fRG study of the 2D Hubbard model performed with an algorithm combining the most recent progress on all three approximation levels. We use (i) the so-called "truncated unity" fRG [30] (TUfRG) formalism to describe the momentum dependence of the vertex and, in addition, keep the full frequency dependence as a function of three independent frequencies. Differently from the approach adopted in Ref. [43], we employ a refined scheme to treat the high-frequency asymptotics [33] that allows us to reduce the numerical effort considerably. Within this scheme, we can consistently include (ii) the (frequency-dependent) self-energy feedback in our fRG flow equations. Finally, we present (iii) first data for the 2D Hubbard model computed with the multiloop extension proposed by Kugler and von Delft [54]. In this context, we have also generalized the multiloop formalism to compute the flow of the response functions, and illustrated the

loop convergence of the fRG results for the 2D Hubbard model. In particular, we show that including up to 8 loops in the fRG flow yields a clear convergence of the data with the loop order and the final results are independent of the cutoff. This represents an important check and illustrates that fRG flows can be brought in quantitative control for 2D problems. Finally, our multiloop analysis of the response functions demonstrates that the two different ways to compute susceptibilities in the fRG, either by tracking the renormalization group flow of the couplings to external fields [1] or by contracting the final interaction vertex (see, e.g., Ref. 22), converge to the same value with increasing loop order. This confirms that the output of this improved fRG scheme can indeed be trusted on a quantitative level.

The paper is organized as follows: The formalism and theory of the linear response functions and their computation by mfRG flow equations are introduced in Section 2. In Section 3 we present the actual implementation scheme for the full momentum- and frequency-dependent fRG. In Section 4 we show the results for the 2D Hubbard model, with a detailed analysis of the effects of the different approximation levels and in particular of the convergence with the loop order. A conclusion and outlook is provided in Section 5.

2 Theory and formalism

2.1 Definitions and formalism

In this section we provide the definitions of the linear response functions to an external field, before describing their computation with the fRG. We focus on correlation functions of fermionic bilinears. In particular, in a time-space translational-invariant system, we consider the charge (density) and spin (magnetic) bilinears, both charge invariant,

$$\rho_{\mathrm{d}}^{n}(q) = \sum_{\sigma} \int dp\, \bar{\psi}_{\sigma}(p) f_n(p,q) \psi_{\sigma}(p+q) \;, \tag{1a}$$

$$\rho_{\mathrm{m}}^{n}(q) = \sum_{\sigma} (-1)^{\sigma} \int dp\, \bar{\psi}_{\sigma}(p) f_n(p,q) \psi_{\sigma}(p+q) \;, \tag{1b}$$

and the non-charge invariant pairing (superconducting) bilinears

$$\rho_{\mathrm{sc}}^{n}(q) = \int dp\, \psi_{\downarrow}(q-p) f_n^{*}(p,q) \psi_{\uparrow}(p) \;, \tag{2a}$$

$$\rho_{\mathrm{sc}}^{n\,*}(q) = \int dp\, \bar{\psi}_{\uparrow}(p) f_n(p,q) \bar{\psi}_{\downarrow}(q-p) \;, \tag{2b}$$

where ψ and $\bar{\psi}$ represent the Grassman variables and p (q) a fermionic (bosonic) quadri-momentum $p = \{i\nu_o, \mathbf{p}\}$ ($q = \{i\omega_l, \mathbf{q}\}$). The integral includes a summation over the Matsubara frequencies ($i\nu_o$), normalized by the inverse temperature β, and an integral over the first Brillouine Zone normalized by its volume $\mathcal{V}_{\mathrm{BZ}}$. The function $f_n(p,q)$, determines the momentum and frequency structure of the bilinears in the different physical channels. In the present case we restrict ourselves to a static external source field, such that the function $f_n(p,q) = f_n(\mathbf{p})$ acquires only a momentum dependence, whose structure is specified by the subscript n and explicitly shown in Table 1 (in the present work we will mostly focus on the s- as well as d-wave momentum structure). Note that, when using a different frequency-momentum notation, centered in the center of mass of the scattering process (see "symmetrized" notation in Appendix A), one should account for an additional shift of the momentum dependence $\mathbf{p}$ by means of the momentum transfer $\mathbf{q}$.

After a reshift of the operators in Eq. (1) with respect to their average value $\rho^n_{\mathrm{d/m}} \to \rho^n_{\mathrm{d/m}} - \langle\rho^n_{\mathrm{d/m}}\rangle$, we can now define the correlation functions of these bilinears in the three channels

$$\chi^{nn'}_{\mathrm{d/m}}(q) = \frac{1}{2}\langle\rho^n_{\mathrm{d/m}}(q)\rho^{n'*}_{\mathrm{d/m}}(q)\rangle \tag{3a}$$

$$\chi^{nn'}_{\mathrm{sc}}(q) = \langle\rho^n_{\mathrm{sc}}(q)\rho^{n'*}_{\mathrm{sc}}(q)\rangle\ . \tag{3b}$$

In linear response theory, these correlation functions correspond to the physical susceptibilities in the corresponding channels. Divergences in $\chi^{nn'}_\eta(q)$, with $\eta = \{\mathrm{d},\mathrm{m},\mathrm{sc}\}$, indicate spontaneous ordering tendencies or instabilities of the system. The above definition encodes not only the real-space pattern or wavevector with which the system starts ordering, but also the symmetry of the order parameter associated to the instability. In the 2D Hubbard model study presented here (see Section 4) we detect various response functions growing considerably towards low T, such as the spin-density wave (SDW) response, characterized by the isotropic s-wave magnetic susceptibility at $\mathbf{q} = (\pi,\pi)$, as well as s- and d-wave pairing response functions at $\mathbf{q} = (0,0)$ and Pomeranchuk instabilities [57]. Inserting Eq. (1) or Eq. (2) into Eq. (3), the susceptibilities appear as two-particle Green's functions. In particular, they can be determined from the two-particle vertex γ_4 by

$$\chi^{nn'}_{\mathrm{d/m}}(q) = \frac{1}{2}\sum_{\sigma\sigma'}\int dpdp' f_n(\mathbf{p})f^*_{n'}(\mathbf{p}')\boldsymbol{\sigma}^{0/3}_{\sigma\sigma}\boldsymbol{\sigma}^{0/3}_{\sigma'\sigma'}\big[\Pi_{\mathrm{d/m};\sigma,\sigma'}(q,p,p') + \tag{4a}$$

$$\Pi_{\mathrm{d/m};\sigma\sigma}(q,p,p)\gamma_{4;\sigma\sigma\sigma'\sigma'}(p,p+q,p'+q,p')\Pi_{\mathrm{d/m};\sigma'\sigma'}(q,p',p')\big] \tag{4b}$$

$$\chi^{nn'}_{\mathrm{sc}}(q) = \int dpdp' f_n(\mathbf{p})f^*_{n'}(\mathbf{p}')\big[\Pi_{\mathrm{sc};\uparrow\downarrow}(q,p,p') + \tag{4c}$$

$$\Pi_{\mathrm{sc};\uparrow\downarrow}(q,p,p)\gamma_{4;\uparrow\uparrow\downarrow\downarrow}(p,p',q-p,q-p')\Pi_{\mathrm{sc};\uparrow\downarrow}(q,p',p')\big]\ , \tag{4d}$$

where $\boldsymbol{\sigma}^{0/3}$ represent the Pauli matrices ($\boldsymbol{\sigma}^0 = \mathbb{1}$) and we made use of the spin conservation. Eqs. (4) can be considerably simplified by making use of the SU(2) symmetry. The "bare bubbles" Π_η appearing in (4) read

$$\Pi_{\mathrm{d/m};\sigma\sigma'}(q,p,p') = -\beta\mathcal{V}_{\mathrm{BZ}}\delta_{\sigma,\sigma'}\delta_{p,p'}G_\sigma(p)G_\sigma(p+q)\ , \tag{5a}$$

$$\Pi_{\mathrm{sc};\uparrow\downarrow}(q,p,p') = \beta\mathcal{V}_{\mathrm{BZ}}\delta_{p,p'}G_\uparrow(p)G_\downarrow(q-p)\ . \tag{5b}$$

By exploiting the SU(2) symmetry,

$$G_\sigma(p) = G_{\bar\sigma}(p) = G(p)\ , \tag{6}$$

we can drop the spin dependencies for the bare bubbles. In presence of the above symmetries, we can introduce the following definitions for (spin-independent) channels of the two-particle vertex

$$\gamma_{4,\mathrm{d}}(q,p,p') = \frac{1}{2}\sum_{\sigma,\sigma'}\gamma_{4;\sigma\sigma\sigma'\sigma'}(p,p+q,p'+q,p') \tag{7a}$$

$$\gamma_{4,\mathrm{m}}(q,p,p') = \frac{1}{2}\sum_{\sigma,\sigma'}(-1)^{\epsilon_{\sigma\sigma'}}\gamma_{4;\sigma\sigma\sigma'\sigma'}(p,p+q,p'+q,p') \tag{7b}$$

$$\gamma_{4,\mathrm{sc}}(q,p,p') = \gamma_{4;\uparrow\uparrow\downarrow\downarrow}(p,p',q-p,q-p')\ , \tag{7c}$$

with ϵ the Levi-Civita symbol. The resulting spin-independent expression of the physical susceptibilities reads

$$\chi^{nn'}_\eta(q) = \int dpdp' f_n(\mathbf{p})f^*_{n'}(\mathbf{p}')\big[\Pi_\eta(q,p,p') + \Pi_\eta(q,p,p)\gamma_{4,\eta}(q,p,p')\Pi_\eta(q,p',p')\big]\ . \tag{8}$$

We conclude this section by recalling the definition of the so-called fermion-boson vertex [58], which, for the considered symmetries, reads

$$\gamma^n_{3,\mathrm{d/m};\sigma\sigma}(q,p) = \Pi^{-1}_{\mathrm{d/m}}(q,p,p)\boldsymbol{\sigma}^{0/3}_{\sigma\sigma}\langle\bar{\psi}_\sigma(p)\psi_\sigma(p+q)\rho^{n\,*}_{\mathrm{d/m}}(q)\rangle \tag{9a}$$

$$\gamma^n_{3,\mathrm{sc};\downarrow\uparrow}(q,p) = \Pi^{-1}_{\mathrm{sc}}(q,p,p)\langle\psi_\downarrow(p)\psi_\uparrow(q-p)\rho^{n\,*}_{\mathrm{sc}}(q)\rangle\ . \tag{9b}$$

Similarly to the susceptibility, one can rewrite Eqs. (9a) and (9b) in a form where the two-particle vertex $\gamma_{4,\eta}$ appears explicitly

$$\gamma^n_{3,\eta}(q,p) = f_n(\mathbf{p}) + \int dp' f_n(\mathbf{p}')\gamma_{4,\eta}(q,p,p')\Pi_\eta(q,p',p')\ , \tag{10}$$

where, because of the SU(2) symmetry, we dropped the spin dependence of the fermion-boson vertices

$$\gamma^n_{3,\mathrm{d/m};\sigma\sigma} = \gamma^n_{3,\mathrm{d/m};\bar{\sigma}\bar{\sigma}} = \gamma^n_{3,\mathrm{d/m}} \tag{11a}$$

$$\gamma^n_{3,\mathrm{sc};\downarrow\uparrow} = \gamma^n_{3,\mathrm{sc};\uparrow\downarrow} = \gamma^n_{3,\mathrm{sc}}\ . \tag{11b}$$

2.2 Flow equations for the response functions

In this section we derive the mfRG [54] flow equations of the response functions and discuss the improvement with respect to the 1ℓ version [1]. Note that one could analogously provide a formal analytical derivation [59] in the same spirit of the approach used in Ref. [56]. In the following we provide the main steps of the derivation in the 1PI formulation [1, 60] (see also Ref. [57] for the Wick-ordered formulation), for the details we refer to Appendix B. Following the review of Metzner et al. [1], we introduce the coupling of the density operators in Eqs. (1) and (2), shifted with respect to their average values, i.e. $\rho^n_\eta \to \rho^n_\eta - \langle\rho^n_\eta\rangle$, to the external field J_η by defining the following scalar product

$$(J^n_{\mathrm{d/m}}, \rho^n_{\mathrm{d/m}}) = \int dq J^n_{\mathrm{d/m}}(q)\rho^n_{\mathrm{d/m}}(q)\ , \tag{12a}$$

$$(J^n_{\mathrm{sc}}, \rho^{n\,*}_{\mathrm{sc}}) + (J^{n\ *}_{\mathrm{sc}}, \rho^n_{\mathrm{sc}}) = \int dq\big[J^n_{\mathrm{sc}}(q)\rho^{n\,*}_{\mathrm{sc}}(q)\ + J^{n\ *}_{\mathrm{sc}}(q)\rho^n_{\mathrm{sc}}(q)\big]\ . \tag{12b}$$

We note that, although J^n_η appears as a functional dependence in our derivation, it is not an integration variable since our system is fully fermionic (for an fRG formulation of coupled fermion-boson systems, see Refs. [1, 61–63]).

By expanding the scale-dependent effective action Γ^Λ in powers of the fermionic fields, as well as of the external bosonic source field, we obtain

$$\begin{aligned}\Gamma^\Lambda[J_\eta,\bar{\psi},\psi] = \Gamma^\Lambda[\bar{\psi},\psi] &+ \sum_\eta\sum_{y_1,y_2}\frac{\partial^{(2)}\Gamma^\Lambda[J_\eta,\bar{\psi},\psi]}{\partial J_\eta(y_1)\partial J^*_\eta(y_2)}\bigg|_{\substack{\psi=\bar{\psi}=0\\J=0}} J_\eta(y_1)J^*_\eta(y_2) - \\ &\sum_{\eta'=\ \mathrm{d,m}}\sum_{y,x,x'}\frac{\partial^{(3)}\Gamma^\Lambda[J_\eta,\bar{\psi},\psi]}{\partial J_{\eta'}(y)\partial\bar{\psi}(x')\psi(x)}\bigg|_{\substack{\psi=\bar{\psi}=0\\J=0}} J_{\eta'}(y)\bar{\psi}(x')\psi(x) - \\ &\sum_{y,x,x'}\frac{\partial^{(3)}\Gamma^\Lambda[J_\eta,\bar{\psi},\psi]}{\partial J_{\mathrm{sc}}(y)\partial\bar{\psi}(x')\partial\bar{\psi}(x)}\bigg|_{\substack{\psi=\bar{\psi}=0\\J=0}} J_{\mathrm{sc}}(y)\bar{\psi}(x')\bar{\psi}(x) + ...\end{aligned} \tag{13}$$

Note that the index $x = \{\sigma, k\}$ combines the spin index σ and the fermionic quadrivector $k = (i\nu_l, \mathbf{k})$ (here we disregard additional quantum dependencies, e.g., orbital), while $y = \{n, q\}$ refers to the momentum structure of the coupling to the bilinears, n, and to

the bosonic quadrivector $q = \{i\omega_l, \mathbf{q}\}$. In Eq. (13) the first term on the r.h.s. represents the expansion of the effective action in absence of external field (see Section 3), while the functional derivatives in the following terms represent the Λ-dependent susceptibility and the fermion-boson vertex in the different channels. Taking the derivative with respect to the scale parameter Λ (see Appendix B), yields the following flow equations for the susceptibility and fermion-boson vertex (assuming SU(2) symmetry and momentum-frequency as well as spin conservation)

$$\begin{aligned}\partial_\Lambda \chi^{nn',\Lambda}_{\mathrm{d/m}}(q) = \int dk \, \big[&- S^\Lambda(k)\tilde{\gamma}^{nn',\Lambda}_{4,\mathrm{d/m}}(q,k) - \\ &\gamma^{n,\Lambda}_{3,\mathrm{d/m}}(q,k)[G^\Lambda(k)S^\Lambda(q+k) \; + (S \leftrightarrow G)]\gamma^{n',\Lambda,\dagger}_{3,\mathrm{d/m}}(q,k)\big] \qquad (14a)\\ \partial_\Lambda \chi^{nn',\Lambda}_{\mathrm{sc}}(q) = \int dk \, \big[&- S^\Lambda(k)\tilde{\gamma}^{nn',\Lambda}_{4,\mathrm{sc}}(q,k) + \\ &\gamma^{n,\Lambda}_{3,\mathrm{sc}}(q,k)[G^\Lambda(k)S^\Lambda(q-k) + (S \leftrightarrow G)]\gamma^{n',\Lambda,\dagger}_{3,\mathrm{sc}}(q,k)\big] \qquad (14b)\end{aligned}$$

and respectively

$$\begin{aligned}\partial_\Lambda \gamma^{n,\Lambda}_{3,\mathrm{d/m}}(q,k) = \int dk' \, \big[&-S^\Lambda(k)\gamma^{n,\Lambda}_{5,\mathrm{d/m}}(q,k,k') \\ &\gamma^{n,\Lambda}_{3,\mathrm{d/m}}(q,k')[G^\Lambda(k')S^\Lambda(q+k') \; + (S \leftrightarrow G)]\gamma^{\Lambda}_{4,\mathrm{d/m}}(q,k',k)\big] \qquad (15a)\\ \partial_\Lambda \gamma^{n,\Lambda}_{3,\mathrm{sc}}(q,k) = \int dk' \, \big[&-S^\Lambda(k)\gamma^{n,\Lambda}_{5,\mathrm{sc}}(q,k,k') + \\ &\gamma^{n,\Lambda}_{3,\mathrm{sc}}(q,k')[G^\Lambda(k')S^\Lambda(q-k') \; + (S \leftrightarrow G)]\gamma^{\Lambda}_{4,\mathrm{sc}}(q,k',k)\big] \; , \qquad (15b)\end{aligned}$$

where

$$S^\Lambda = \; \partial_\Lambda G^\Lambda|_{\Sigma=\mathrm{const}} \qquad (16)$$

represents the single-scale propagator. The function $\tilde{\gamma}_4$, differently from the (fermionic) two-particle vertex γ_4, represents a mixed bosonic-fermionic vertex, i.e., with two bosonic and two fermionic legs where we summed over its spin dependences

$$\tilde{\gamma}^{nn',\Lambda}_{4,\eta}(q,k) = \sum_\sigma \tilde{\gamma}^{nn',\Lambda}_{4,\eta;\sigma\sigma}(q,k) \; , \qquad (17)$$

while the spin-independent form for γ_5 used in Eqs. (15) reads

$$\begin{aligned}\gamma^{n,\Lambda}_{5,\mathrm{d/m}}(q,k,k') &= \sum_{\sigma'} \boldsymbol{\sigma}^{0/3}_{\sigma\sigma}\gamma^{n,\Lambda}_{5,\mathrm{d/m};\sigma\sigma\sigma'\sigma'}(q,k,k') \qquad (18a)\\ \gamma^{n,\Lambda}_{5,\mathrm{sc}}(q,k,k') &= \sum_{\sigma'} \gamma^{n,\Lambda}_{5,\mathrm{sc};\sigma\bar{\sigma}\sigma'\sigma'}(q,k,k') \; . \qquad (18b)\end{aligned}$$

The conventional approximations [1,57,60] disregard the first terms on the r.h.s. of Eqs. (14) and (15). This 1ℓ approximation is consistent with the corresponding approximation of γ^Λ_4 (see Appendix C) and justified in the weak-coupling regime. Using the notation of Refs. [44, 54], one can rewrite the 1ℓ approximation of Eqs. (14) and (15) in a more concise tensor-form

$$\begin{aligned}\dot{\boldsymbol{\chi}}^{\Lambda(1)}_\eta &= \; \boldsymbol{\gamma}^\Lambda_{3,\eta} \circ \dot{\mathbf{\Pi}}^\Lambda_{S,\eta} \circ \boldsymbol{\gamma}^{\Lambda,\dagger}_{3,\eta} \qquad (19a)\\ \dot{\boldsymbol{\gamma}}^{\Lambda(1)}_{3,\eta} &= \; \boldsymbol{\gamma}^\Lambda_{3,\eta} \circ \dot{\mathbf{\Pi}}^\Lambda_{S,\eta} \circ \boldsymbol{\gamma}^\Lambda_{4,\eta} \; . \qquad (19b)\end{aligned}$$

where

$$\dot{\Pi}^{\Lambda}_{S,\mathrm{d/m}(ph)}(q,k) = -G^{\Lambda}(k)S^{\Lambda}(q+k) + (S \leftrightarrow G) \tag{20a}$$

$$\dot{\Pi}^{\Lambda}_{S,\mathrm{sc}(pp)}(q,k) = G^{\Lambda}(k)S^{\Lambda}(q-k) + (S \leftrightarrow G)\ . \tag{20b}$$

We here introduced also the subscript ph and pp indicating the diagrammatic channels that will be referred to in Sec. 3.

So far we pinpointed two possible ways to compute the susceptibility and fermion-boson vertex from an fRG calculation: (i) Solving Eqs. (14) and (15) alongside the ones for Σ and γ_4 (at the same level of approximation), and (ii) by means of Eqs. (8) and (10) at the end of the fRG flow, using $\Sigma^{\Lambda_{\mathrm{final}}}$ and $\gamma_4^{\Lambda_{\mathrm{final}}}$, later referred to as "post-processing". These two procedures are non-equivalent in the presence of approximations, e.g., if one restricts oneself to the 1ℓ level. This leads to an ambiguity in practical implementations of the fRG. In fact, as shown in Appendix D, the two results deviate at $\mathcal{O}((\gamma_4^{\Lambda})^2)$ for the 1ℓ case (for a larger number of loops the deviations occur at higher orders in the effective interaction γ_4^{Λ}). In order to solve this ambiguity we note that the exact relations (8) and (10) are fulfilled in the PA. At the same time, the recently introduced multiloop extension allows one to sum up all parquet diagrams. Hence, generalizing the multiloop flow to the computation of the response functions recovers the equivalence of the two procedures.

In order to derive the mfRG equations for the response functions, we first recall the channel-decomposition of the two-particle vertex as known from the parquet formalism. The latter divides γ_4 in the two-particle reducible vertex ϕ (all diagrams that can be divided into two separate ones by removing two internal fermionic propagators) and the two-particle irreducible vertex I (which can be not be divided). Depending on the direction of the propagation lines the diagrams are reducible in either parallel, longitudinal antiparallel or transverse antiparallel, corresponding to the particle-particle, particle-hole, and particle-hole crossed channel, respectively. Besides this diagrammatic channel decomposition, there is also a distinct physical channel decomposition that identifies the components $\eta = \{\mathrm{d}, \mathrm{m}, \mathrm{sc}\}$ and which we will use in the following. Inserting this decomposition into the flow equation for the two-particle vertex, we obtain

$$\partial_{\Lambda}\gamma^{\Lambda}_{4,\eta} = \partial_{\Lambda} I^{\Lambda}_{\eta} + \partial_{\Lambda}\phi^{\Lambda}_{\eta}\ . \tag{21}$$

While the usual diagrammatic channel decomposition [64] leads to simple expressions for the two-particle irreducible vertex I^{Λ}_{η}, the latter assumes a more complicated form in the physical channels

$$\begin{aligned} I^{\Lambda}_{\mathrm{d}}(q,k,k') = {} & -U - \frac{1}{2}\phi^{\Lambda}_{\mathrm{d}}(k'-k,k,k+q) - \frac{3}{2}\phi^{\Lambda}_{\mathrm{m}}(k'-k,k,k+q) + 2\phi^{\Lambda}_{\mathrm{sc}}(q+k+k',k,k') \\ & - \phi^{\Lambda}_{\mathrm{sc}}(q+k+k',k,q+k) \end{aligned} \tag{22a}$$

$$I^{\Lambda}_{\mathrm{m}}(q,k,k') = U - \frac{1}{2}\phi^{\Lambda}_{\mathrm{d}}(k'-k,k,k+q) + \frac{1}{2}\phi^{\Lambda}_{\mathrm{m}}(k'-k,k,k+q) - \phi^{\Lambda}_{\mathrm{sc}}(q+k+k',k,k+q) \tag{22b}$$

$$I^{\Lambda}_{\mathrm{sc}}(q,k,k') = -U - \phi^{\Lambda}_{\mathrm{m}}(k'-k,k,q-k') + \frac{1}{2}\phi^{\Lambda}_{\mathrm{d}}(q-k-k',k,k') - \frac{1}{2}\phi^{\Lambda}_{\mathrm{m}}(q-k-k',k,k') \tag{22c}$$

where we approximated the fully two-particle irreducible vertex by its first-order contribution in the interaction $\sim U$, which is known as PA.

We now derive the mfRG flow equations for the response functions, which mimic the effect of the mixed fermion-boson vertices $\tilde{\gamma}^{\Lambda}_4$ and γ^{Λ}_5 in the exact flow Eqs. (14) and (15). First, one performs the so-called Katanin substitution [44] $S^{\Lambda} \to \partial_{\Lambda} G^{\Lambda}$, which implies

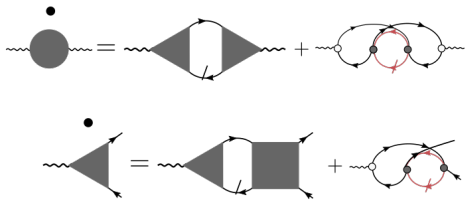

Figure 1: Multiloop corrections (beyond 1ℓ) for $\gamma^{\Lambda}_{3,\mathrm{d/m}}$ (top) and $\chi^{\Lambda}_{\mathrm{d/m}}$ (bottom) at the leading order in the bare interaction (filled black dot). The empty dot represents the bare fermion-boson vertex $\gamma^{n}_{3,\eta,0}(q,k) = f_n(\mathbf{k})$.

$\dot{\mathbf{\Pi}}^{\Lambda}_{S,\eta} \to \dot{\mathbf{\Pi}}^{\Lambda}_{\eta}$ in the 1ℓ flow equations (19). One observes that all differentiated lines in these flow equations come from $\dot{\mathbf{\Pi}}^{\Lambda}_{\eta}$. Secondly, differentiated lines from the other channels are contained in the higher-loop terms of the expansion

$$\partial_\Lambda \boldsymbol{\chi}^{\Lambda}_{\eta} = \sum_{\ell \geqslant 1} \dot{\boldsymbol{\chi}}^{\Lambda(\ell)}_{\eta} \tag{23a}$$

$$\partial_\Lambda \boldsymbol{\gamma}^{\Lambda}_{3,\eta} = \sum_{\ell \geqslant 1} \dot{\boldsymbol{\gamma}}^{\Lambda(\ell)}_{3,\eta} \,. \tag{23b}$$

Using the channel decomposition (21), we can directly write down the 2ℓ correction to the flow of the fermion-boson vertex, which accounts for the leading-order diagrams of the effective interaction and stem from γ^{Λ}_{5} in Eq. (15) (see Appendix B)

$$\dot{\boldsymbol{\gamma}}^{\Lambda(2)}_{3,\eta} = \boldsymbol{\gamma}^{\Lambda}_{3,\eta} \circ \mathbf{\Pi}^{\Lambda}_{\eta} \circ \dot{\mathbf{I}}^{\Lambda(1)}_{\eta} \,. \tag{24}$$

On the three- and higher-loop level, we can now use $\dot{\mathbf{I}}^{\Lambda(\ell)}_{\eta}$ in an analogous way. In addition, we have to consider the vertex corrections to the right of the differentiated lines, yielding

$$\dot{\boldsymbol{\gamma}}^{\Lambda(\ell+2)}_{3,\eta} = \boldsymbol{\gamma}^{\Lambda}_{3,\eta} \circ \mathbf{\Pi}^{\Lambda}_{\eta} \circ \dot{\mathbf{I}}^{\Lambda(\ell+1)}_{\eta} + \boldsymbol{\gamma}^{\Lambda}_{3,\eta} \circ \mathbf{\Pi}^{\Lambda}_{\eta} \circ \dot{\mathbf{I}}^{\Lambda(\ell)}_{\eta} \circ \mathbf{\Pi}^{\Lambda}_{\eta} \circ \boldsymbol{\gamma}^{\Lambda}_{4,\eta} \,. \tag{25}$$

Considering the 1ℓ flow equation of the susceptibility (19a), we see that the fermion-boson vertices provide vertex corrections on both sides of the differentiated lines in $\dot{\mathbf{\Pi}}^{\Lambda}_{\eta}$. Hence, for all higher-loop corrections we can simply connect $\dot{\mathbf{I}}^{\Lambda(\ell)}_{\eta}$ to both fermion-boson vertices, thereby raising the loop order by two. We obtain $\dot{\boldsymbol{\chi}}^{\Lambda(2)}_{\eta} = 0$, as well as

$$\dot{\boldsymbol{\chi}}^{\Lambda(\ell+2)}_{\eta} = \boldsymbol{\gamma}^{\Lambda}_{3,\eta} \circ \mathbf{\Pi}^{\Lambda}_{\eta} \circ \dot{\mathbf{I}}^{\Lambda(\ell)}_{\eta} \circ \mathbf{\Pi}^{\Lambda}_{\eta} \circ \boldsymbol{\gamma}^{\Lambda,\dagger}_{3,\eta} \,. \tag{26}$$

For a schematic representation of Eqs. (25) and (26) at the leading order in the bare interaction, see Fig. 1. The above equations, together with the multiloop flow of the fermionic two-particle vertex (see Section 3.2) allow us to sum up all differentiated parquet diagrams of $\boldsymbol{\gamma}^{\Lambda}_{3}$ and $\boldsymbol{\chi}^{\Lambda}$. As a consequence, the aforementioned two ways of computing the response functions within the fRG become equivalent. We finally note that for a consistent fRG scheme, it is important to adopt the same level of approximation (truncating the sums in Eq. (23a) to a certain finite ℓ-loop level) for all flowing quantities.

3 Numerical implementation

3.1 Full frequency and momentum parametrization

In order to illustrate the fRG algorithm adopted in the present work, let us start from the flow equations for the 1PI fermionic vertex in the 1ℓ fRG approximation. In the following, the SU(2), spin conserving symmetry will be always assumed. Exploiting this symmetry, the self-energy and two-particle fermionic vertices can be written as

$$\Sigma_{\sigma\sigma'}(k) = \delta_{\sigma,\sigma'}\Sigma_{\sigma}(k) = \delta_{\sigma,\sigma'}\Sigma(k) \tag{27}$$

$$\gamma_{4,\sigma_1\sigma_2\sigma_3\sigma_4}(k_1,k_2,k_3) = [-\delta_{\sigma_1,\sigma_4}\delta_{\sigma_2,\sigma_3}\gamma_4(k_1,k_4,k_3) + \delta_{\sigma_1,\sigma_2}\delta_{\sigma_3,\sigma_4}\gamma_4(k_1,k_2,k_3)] \,, \tag{28}$$

where the fourth argument of γ_4 is determined by $k_4 = k_1 + k_3 - k_2$ in a momentum and energy conserving system. The spin-independent flow equation for the self-energy reads

$$\dot{\Sigma}^{\Lambda}(k) = -\int dp S^{\Lambda}(p) \left[2\,\gamma_4^{\Lambda}(k,k,p) - \gamma_4^{\Lambda}(p,k,k)\right] , \tag{29}$$

where $S^{\Lambda}(p)$ represents the single-scale propagator specified in Eq. (16). We formulate the flow equation for γ_4 in the channel decomposed form suggested by Husemann and Salmhofer [27]

$$\dot{\gamma}_4^{\Lambda}(k_1,k_2,k_3) = \mathcal{T}_{pp}^{\Lambda}(k_1+k_3,k_1,k_4) + \mathcal{T}_{ph}^{\Lambda}(k_2-k_1,k_1,k_4) + \mathcal{T}_{\overline{ph}}^{\Lambda}(k_3-k_2,k_1,k_2) \,, \tag{30}$$

where the diagrammatic channel index $r = \{pp, ph, \overline{ph}\}$ distinguishes between particle-particle, particle-hole and particle-hole exchange diagrams, and the first dependence of the functions $\mathcal{T}_r^{\Lambda}$ refers to the bosonic four-momentum transfer in the internal loop of their corresponding equations

$$\begin{aligned}
\mathcal{T}_{pp}^{\Lambda}(k_1+k_3,k_1,k_4) = &\int dp\, \gamma_4^{\Lambda}(k_1,k_1+k_3-p,k_3)\gamma_4^{\Lambda}(p,k_2,k_1+k_3-p)\times \\
&\left[S^{\Lambda}(p)G^{\Lambda}(k_1+k_3-p) + (S\leftrightarrow G)\right] , \qquad (31a)\\
\mathcal{T}_{ph}^{\Lambda}(k_2-k_1,k_1,k_4) = &-\int dp \left[2\,\gamma_4^{\Lambda}(k_1,k_2,k_2-k_1+p)\;\gamma_4^{\Lambda}(p,k_2-k_1+p,k_3) - \right. \\
&\gamma_4^{\Lambda}(k_1,p,k_2-k_1+p)\;\gamma_4^{\Lambda}(p,k_2-k_1+p,k_3) - \\
&\left.\gamma_4^{\Lambda}(k_1,k_2,k_2-k_1+p)\;\gamma_4^{\Lambda}(p,k_2,k_3)\right]\times \\
&\left[S^{\Lambda}(p)G^{\Lambda}(k_2-k_1+p) + (S\leftrightarrow G)\right] , \qquad (31b)\\
\mathcal{T}_{\overline{ph}}^{\Lambda}(k_3-k_2,k_1,k_2) = &\int dp\, \gamma_4^{\Lambda}(k_1,p,k_3-k_2+p)\gamma_4^{\Lambda}(p,k_2,k_3)\times \\
&\left[S^{\Lambda}(p)G^{\Lambda}(k_3-k_2+p) + (S\leftrightarrow G)\right] . \qquad (31c)
\end{aligned}$$

Each of the above equations depends, besides the aforementioned bosonic transfer dependence (k_1+k_3, k_2-k_1 and k_3-k_2), on two fermionic dependencies. Such mixed 'bosonic-fermonic' notation, referred to as 'non-symmetrized' notation, has been substituted in some work (e.g., in Ref. [30]) by a different notation where the dependencies of the four fermionic propagators involved in the scattering process have been chosen symmetrically with respect to the bosonic four-momentum transfer. This symmetrized notation simplifies the implementation of the symmetries exploited in the fRG code (see Appendix

F and Ref. [30]) but leads to less compact flow equations. The equation (31) generates the two-particle reducible vertices $\mathcal{T}_r = \dot{\phi}_r$ of the diagrammatic parquet decomposition

$$\gamma_4(k_1, k_2, k_3) \approx U + \phi_{pp}(k_1 + k_3, k_1, k_4) + \phi_{ph}(k_2 - k_1, k_1, k_4) + \phi_{\overline{ph}}(k_3 - k_2, k_1, k_2) \ . \tag{32}$$

The two-particle fermionic vertex can be reconstructed by using Eq. (32). The use of a mixed 'bosonic-fermonic' notation allows us to identify the bosonic transfer four-momentum as the strongest dependence, while the two fermionic dependencies can be treated with controllable approximations. In the following we illustrated two efficient ways to simplify the treatment of both momentum and frequency dependencies.

3.1.1 Truncated Unity fRG

The approximation for the fermionic momentum dependencies in TUfRG [30] is done by the expansion of the fermionic momentum dependencies in form factors, illustrated here for the *pp* channel

$$\phi_{pp}(\mathbf{q}, \mathbf{k}, \mathbf{k}') = \sum_{n,n'} f_n(\mathbf{k}) f^*_{n'}(\mathbf{k}') P_{n,n'}(\mathbf{q}) \ , \tag{33}$$

while the expansion of the ϕ_{ph} and $\phi_{\overline{ph}}$ analogously defines $D_{n,n'}(\mathbf{q})$ and $C_{n,n'}(\mathbf{q})$. Following the conventions introduced in previous works [27, 28, 30, 40, 65, 66], we choose the form factors such that they correspond to a specific shell of neighbors in the real space lattice. The unity inserted in the flow equations contains a complete basis set of form factors

$$\mathbb{1} = \int d\mathbf{p}' \sum_n f^*_n(\mathbf{p}') f_n(\mathbf{p}) \ . \tag{34}$$

Converged results can be obtained already with a small set of form factors [30]. For a fast convergence it is convenient to include one shell after another, starting from the constant local form factor and increasing the distance of neighbors taken into account. The form factors used in this paper are listed in Table 1.

A major difficulty in this approach is the feedback of the different channels into each other. In addition to the dressing of the objects by the form factors, the translation of the notation in momentum and frequency from one to another channel has to be considered. Computationally time consuming integrations in momentum space can be avoided by Fourier transformation and evaluation in real space. Furthermore the expression of the projection in terms of a matrix multiplication allows for the precalculation of the projection matrices which can be found in the Appendix F.

3.1.2 Dynamical fRG

In frequency space, we adopt the simplifications proposed in Refs. [32, 33]. For all systems with an instantaneous microscopic interaction one can use diagrammatic arguments to prove that, in the high-frequency regime, the fermionic two-particle vertex exhibits a simplified asymptotic structure. In this region one can reduce the three-dimensional frequency dependence of γ_4 using functions with a simplified parametric dependence. It is straightforward to see that, sending all three frequencies to infinity, γ_4 reduces to the instantaneous microscopic interaction, which in the present case is represented by the Hubbard on-site U. The contribution of the reducible vertices ϕ_r to γ_4 becomes non-negligible if the bosonic frequency transfer is kept finite, while sending the two secondary fermionic frequencies to infinity. This contribution, depending on a single bosonic frequency transfer in a given channel r, is denoted by $\mathcal{K}_{1,r}(i\omega_l, q)$. For models with an instantaneous and

local microscopic interaction, one observes that the momentum dependencies disappear alongside the frequency dependencies when performing such limits. In the limit where just one fermionic frequency is sent to infinity, the vertex ϕ_r can be parametrized by the function $\mathcal{K}_{2,r}(i\omega_l, i\nu_o, q, k)+\mathcal{K}_{1,r}(i\omega_l, q)$. By subtracting the asymptotic functions from the full object ϕ_r we obtain the so-called [33],"rest-function" $\mathcal{R}(i\omega_l, i\nu_o, i\nu_{o'}, q, k, k')$ which decays to zero within a small frequency box. The parametrization in terms of $\mathcal{K}_{1/2}$ allows us to reduce the numerical cost of computing and storing the fermionic two-particle vertices. In fact, for any of the three channels, we calculate the fRG flow of the three-frequency dependent function $\mathcal{R}$ on a small low-frequency region and add the information on the high frequencies by computing the flow of the functions $\mathcal{K}_1$ and $\mathcal{K}_2$ which are numerically less demanding. The full two-particle reducible vertex ϕ_r is then recovered by

$$\begin{aligned}\phi_r(i\omega_l, i\nu_o, i\nu_{o'}, \mathbf{q}, \mathbf{k}, \mathbf{k}') = \mathcal{R}_r(i\omega_l, i\nu_o, i\nu_{o'}, \mathbf{q}, \mathbf{k}, \mathbf{k}')+ \\ \mathcal{K}_{2,r}(i\omega_l, i\nu_o, \mathbf{q}, \mathbf{k}) + \bar{\mathcal{K}}_{2,r}(i\omega, i\nu_{o'}, \mathbf{q}, \mathbf{k}') + \mathcal{K}_{1,r}(i\omega_l, \mathbf{q}),\end{aligned} \tag{35}$$

where $\bar{\mathcal{K}}_{2,r}$ can be obtained from $\mathcal{K}_{2,r}$ by exploiting the time reversal symmetry (see Appendix A.3).

3.1.3 Flow equations for the TU-dynamical fRG

Finally, applying the aforementioned projection on the form-factor basis we can write matrix-like 1ℓ fRG flow equations for the self-energy, the two-particle vertex, the fermion-boson vertex and the susceptibility:

$$\dot{\Sigma}^\Lambda(k) = -\int dp\, S^\Lambda(p)\Big[2\,\gamma_4^\Lambda(k,k,p) - \gamma_4^\Lambda(p,k,k)\Big] \tag{36a}$$

$$\dot{\mathbf{P}}^\Lambda(q, i\nu_o, i\nu_{o'}) = \frac{1}{\beta}\sum_{i\nu_{n''}} \boldsymbol{\gamma}^\Lambda_{4,P}(q, i\nu_o, i\nu_{n''})\dot{\mathbf{\Pi}}^\Lambda_{S,pp}(q, i\nu_{n''})\boldsymbol{\gamma}^\Lambda_{4,P}(q, i\nu_{n''}, i\nu_{o'}) \tag{36b}$$

$$\begin{aligned}\dot{\mathbf{D}}^\Lambda(q, i\nu_o, i\nu_{o'}) = \frac{1}{\beta}\sum_{i\nu_{n''}} \dot{\mathbf{\Pi}}^\Lambda_{S,ph}(q, i\nu_{n''})\Big[2\boldsymbol{\gamma}^\Lambda_{4,D}(q, i\nu_o, i\nu_{n''})\boldsymbol{\gamma}^\Lambda_{4,D}(q, i\nu_{n''}, i\nu_{o'}) - \\ \boldsymbol{\gamma}^\Lambda_{4,C}(q, i\nu_o, i\nu_{n''})\boldsymbol{\gamma}^\Lambda_{4,D}(q, i\nu_{n''}, i\nu_{o'}) - \boldsymbol{\gamma}^\Lambda_{4,D}(q, i\nu_o, i\nu_{n''})\boldsymbol{\gamma}^\Lambda_{4,C}(q, i\nu_{n''}, i\nu_{o'})\Big]\end{aligned} \tag{36c}$$

$$\dot{\mathbf{C}}^\Lambda(q, i\nu_o, i\nu_{o'}) = -\frac{1}{\beta}\sum_{i\nu_{n''}} \boldsymbol{\gamma}^\Lambda_{4,C}(q, i\nu_o, i\nu_{n''})\dot{\mathbf{\Pi}}^\Lambda_{S,ph}(q, i\nu_{n''})\boldsymbol{\gamma}^\Lambda_{4,C}(q, i\nu_{n''}, i\nu_{o'}) \tag{36d}$$

$$\dot{\boldsymbol{\gamma}}^\Lambda_{3,\eta}(q, i\nu_o) = \frac{1}{\beta}\sum_{i\nu_{n'}} \boldsymbol{\gamma}^\Lambda_{3,\eta}(q, i\nu_{n'})\dot{\mathbf{\Pi}}^\Lambda_{S,\eta}(q, i\nu_{n'})\boldsymbol{\gamma}^\Lambda_{4,\eta}(q, i\nu_{n'}, i\nu_o) \tag{36e}$$

$$\dot{\boldsymbol{\chi}}^\Lambda_{\eta}(q) = \frac{1}{\beta}\sum_{i\nu_{n}} \boldsymbol{\gamma}^\Lambda_{3,\eta}(q, i\nu_{n})\dot{\mathbf{\Pi}}^\Lambda_{S,\eta}(q, i\nu_{n})\boldsymbol{\gamma}^\Lambda_{3,\eta}(q, i\nu_{n})\ , \tag{36f}$$

where the multiplication of bold symbols has here to be understood as matrix multiplications with respect to the form factors. For a schematic visualization of the practical implementation of these equations, see Fig. 2. We note that, in order to derive Eqs. (36), we inserted the unity (34), truncated to a finite number of form factors, in Eqs. (19) as well as in (31). The full vertex $\gamma_{4,r}$, with $r = \{P, D, C\}$ represents the fermionic two-particle vertex in the channel-specific mixed 'bosonic-fermionic' notations, while $\gamma_{4,\eta}$ with

$\eta = \{\mathrm{sc}, \mathrm{d}, \mathrm{m}\}$ is given by

$$\boldsymbol{\gamma}_{4,\mathrm{d}} = 2\boldsymbol{\gamma}_{4,D} - \boldsymbol{\gamma}_{4,C} \tag{37a}$$

$$\boldsymbol{\gamma}_{4,\mathrm{m}} = -\boldsymbol{\gamma}_{4,D} \tag{37b}$$

$$\boldsymbol{\gamma}_{4,\mathrm{sc}} = \boldsymbol{\gamma}_{4,P} \ . \tag{37c}$$

The 1ℓ-fRG flow consists in integrating the coupled differential equations in (36) with the following initial conditions:

$$\Sigma^{\Lambda_{\mathrm{init}}} = 0 \tag{38a}$$

$$\boldsymbol{\gamma}_{4,P}^{\Lambda_{\mathrm{init}}} = \boldsymbol{\gamma}_{4,D}^{\Lambda_{\mathrm{init}}} = \boldsymbol{\gamma}_{4,C}^{\Lambda_{\mathrm{init}}} = U\delta_{n,0}\delta_{n',0} \tag{38b}$$

$$\boldsymbol{\chi}_{\eta}^{\Lambda_{\mathrm{init}}} = 0 \tag{38c}$$

$$\boldsymbol{\gamma}_{3,\eta}^{\Lambda_{\mathrm{init}}} = \delta_{n,n'} \ . \tag{38d}$$

Finally, $\dot{\boldsymbol{\Pi}}_{S,\eta}$ relative to the particle-hole $\eta = \{\mathrm{d/m}(ph)\}$ and to the particle-particle channels $\eta = \{\mathrm{sc}(pp)\}$, are defined as

$$\dot{\Pi}^{\Lambda}_{S,\mathrm{d/m}(ph)}(i\omega_l, i\nu_o, \mathbf{q})_{n,n'} = -\int d\mathbf{p} f^*_n(\mathbf{p}) f_{n'}(\mathbf{p})\ \dot{\Pi}^{\Lambda}_{S,\mathrm{d/m}(ph)}(i\omega_l, i\nu_o, \mathbf{q}, \mathbf{p}) \ , \tag{39a}$$

$$\dot{\Pi}^{\Lambda}_{S,\mathrm{sc}(pp)}(i\omega_l, i\nu_o, \mathbf{q})_{n,n'} = \int d\mathbf{p} f^*_n(\mathbf{p}) f_{n'}(\mathbf{p})\ \dot{\Pi}^{\Lambda}_{S,\mathrm{sc}(pp)}(i\omega_l, i\nu_o, \mathbf{q}, \mathbf{p}) \ , \tag{39b}$$

where $\dot{\Pi}^{\Lambda}_{S,\eta}(q,k)$ is defined in Eq. (20). In order to perform the momentum integration in Eqs. (39) we adopt a strategy which, exploiting the convolution theorem, represents a numerically convenient alternative to the use of adaptive integration algorithms. The latter is described in the following section.

3.1.4 Calculation of the fermionic particle-hole and particle-particle excitation

We here present a numerically convenient way of calculating the fermionic particle-hole and particle-particle bubbles in the flow equations of the vertex (36), defined in Eqs. (39). Since the integral over momenta is very sensitive on the momentum mesh resolution near the Fermi surface and a refined adaptive integration is computationally time consuming, we rewrote the integrals in such a way to use the convolution theorem. The Green's function can then be transformed via the Fast-Fourier-Transform (FFT) to real space, where the real-space expression of the form factors is provided in Table 1. After some algebraic steps, we find an expression without momentum integration

$$\begin{aligned}\dot{\Pi}_{S,ph}(i\omega_l, i\nu_o, \mathbf{q})]_{n,n'} = -\sum_{\mathbf{R}} e^{i\mathbf{R}\mathbf{q}} W_{n,n'}(\mathbf{R}) \ \times \\ \mathcal{F}\Big[S(i\nu_o, -\tilde{\mathbf{R}})G(i\omega_l + i\nu_o, \tilde{\mathbf{R}} - \mathbf{R}) + (S \leftrightarrow G)\Big](\mathbf{q}) \ ,\end{aligned} \tag{40a}$$

$$\begin{aligned}\dot{\Pi}_{S,pp}(i\omega_l, i\nu_o, \mathbf{q})]_{n,n'} = \sum_{\mathbf{R}} e^{-i\mathbf{R}\mathbf{q}} W_{n,n'}(\mathbf{R}) \ \times \\ \mathcal{F}\Big[S(i\nu_o, \tilde{\mathbf{R}})G(i\omega_l - i\nu_o, \tilde{\mathbf{R}} + \mathbf{R}) + (S \leftrightarrow G)\Big](\mathbf{q}) \ ,\end{aligned} \tag{40b}$$

where $\mathcal{F}\Big[f(\tilde{R})\Big](\mathbf{k})$ is the Fourier transform which can be determined by using FFT-methods and the weight $W_{n,n'}(R)$ is defined as

$$W_{n,n'}(\mathbf{R}) = \sum_{\mathbf{R}'} f^*_n(\mathbf{R}') f_{n'}(\mathbf{R} + \mathbf{R}') \ . \tag{41}$$

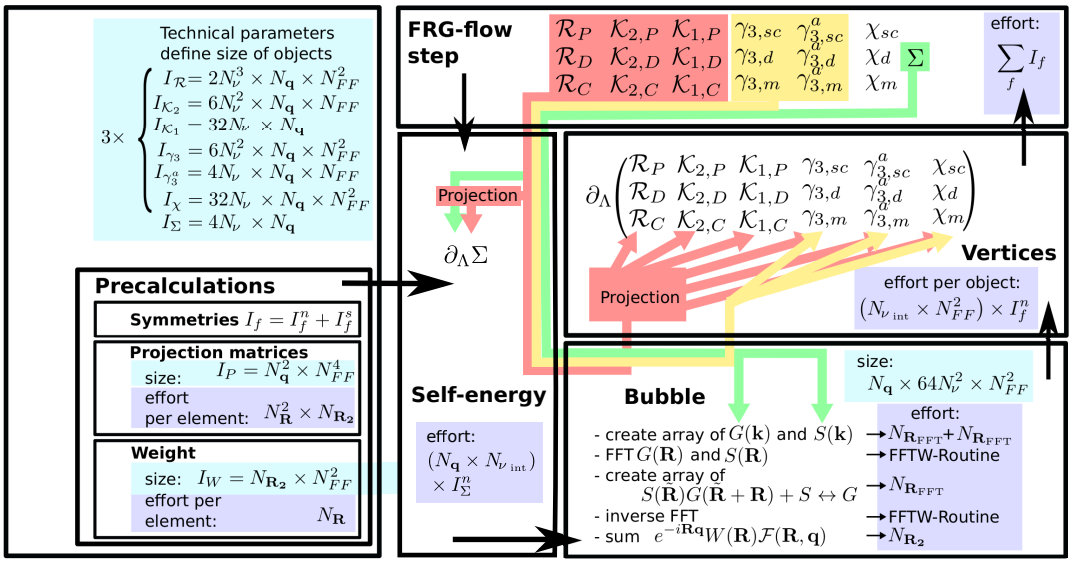

Figure 2: Schematic code structure specifying the array sizes and the numerical effort of the single steps. I_f denotes the number of elements of the object f. N_ν is the number of fermionic frequencies of the rest function, $N_{\mathbf{q}}$ the number of bosonic momentum patches, N_{FF} the number of form factors, $N_{\mathbf{R}_{\mathrm{FFT}}}$ and $N_{\nu_{\mathrm{int}}}$ the number of frequencies over which the internal fermionic bubble is integrated. The symmetries reduce the total number of elements I_f to I_f^n independent elements which have to be calculated and to I_f^s which can be obtained by using symmetry relations. The arrows indicate the feedback of the different parts, namely the two-particle fermionic vertices (red), fermion-boson vertex (yellow), and the self-energy (green).

The infinite sum of the lattice points in Eqs. (40b), (40a), and (41) is restricted by the finite range of the form factors for a specific truncation. For instance the sum in Eq. (41) is limited to the maximal shell taken into account by the form factors. Hence, the weight has a nonzero contribution only inside a shell twice as large the maximal shell of the form factors and therefore the sum in Eq. (40a) can be constrained to twice the distance of the maximal form factor shell.

The momentum and real space grid for the Fourier transformations needed in the bubbles has to be chosen fine enough, especially at low temperatures. The convergence in terms of FFT-grid points $N_{\mathbf{R}_{\mathrm{FFT}}}$ has to be checked separately from the bosonic momentum grid of the vertex. Recent works using the TUfRG [30, 66] have demonstrated that, if needed, both low temperatures and high wavevector resolutions can be achieved by means of an adaptive integration scheme.

3.1.5 Diagrammatic and lattice related symmetries

Further numerical simplifications come from the extensive use of symmetries related to diagrammatic arguments and lattice-specific properties, which can be found in Appendix A.

3.2 The mfRG implementation

The mfRG flow introduced in Ref. [54] ameliorates the approximation induced by the truncation of the fRG hierarchy of flow equations as it incorporates all contributions from the

six-point vertex γ_6 that can be computed at the same cost as the 1ℓ flow considered so far. In fact, it includes all contributions coming from γ_6 that can be computed in an iterative 1ℓ construction of four-point objects; hence, the numerical effort grows only linearly in the number of loops retained. It has been shown [54] that the multiloop prescription fully sums up all parquet diagrams. This gives rise to a number of advantageous properties, the most important of which are (i) that the multiloop corrections restore the independence on the choice of regulator, and (ii) that the multiloop flow fully accounts for the interplay between different two-particle channels and thus hampers spurious vertex divergences coming from ladder diagrams in the individual channels.

Let us briefly recall the multiloop vertex flow employing the same line of arguments as used for the flow of the response functions in Section 2.2. We consider the reducible vertices in the physical channels $\phi_{\eta=\{\mathrm{sc,d,m}\}}$. At first, one performs the Katanin substitution [44] $S^\Lambda \to \partial_\Lambda G^\Lambda$ ($\dot{\Pi}_{S,\eta} \to \dot{\Pi}_\eta$) in the 1ℓ flow equation

$$\dot{\boldsymbol{\phi}}_\eta^{\Lambda,(1)} = \boldsymbol{\gamma}_{4,\eta}^\Lambda \circ \dot{\boldsymbol{\Pi}}_\eta^\Lambda \circ \boldsymbol{\gamma}_{4,\eta}^\Lambda \,, \tag{42}$$

and finds that, for every channel $\boldsymbol{\phi}_\eta^\Lambda$, all differentiated lines come from $\dot{\boldsymbol{\Pi}}_\eta^\Lambda$. Differentiated lines from the other channels are contained in higher-order terms of the loop expansion

$$\partial_\Lambda \boldsymbol{\phi}_\eta^\Lambda = \sum_{\ell\geq 1} \dot{\boldsymbol{\phi}}_\eta^{\Lambda,(\ell)} \,. \tag{43}$$

Using the channel decomposition (21), one has the two-loop correction

$$\dot{\boldsymbol{\phi}}_\eta^{\Lambda,(2)} = \boldsymbol{\gamma}_{4,\eta}^\Lambda \circ \boldsymbol{\Pi}_\eta^\Lambda \circ \dot{\mathbf{I}}_\eta^{\Lambda,(1)} + \dot{\mathbf{I}}_\eta^{\Lambda,(1)} \circ \boldsymbol{\Pi}_\eta^\Lambda \circ \boldsymbol{\gamma}_{4,\eta}^\Lambda \,, \tag{44}$$

where, according to Eq. (22), $\dot{\mathbf{I}}_\eta^{\Lambda,(\ell)}$ can be determined from the $\dot{\boldsymbol{\phi}}_{\eta'}^{\Lambda,(\ell)}$ of the complementary channels $\eta' \neq \eta$. All higher-loop terms are obtained in a similar fashion where one additionally accounts for vertex corrections to both sides of $\dot{\mathbf{I}}_\eta^{\Lambda,(\ell)}$

$$\begin{aligned}\dot{\boldsymbol{\phi}}_\eta^{\Lambda,(\ell+2)} &= \boldsymbol{\gamma}_{4,\eta}^\Lambda \circ \boldsymbol{\Pi}_\eta^\Lambda \circ \dot{\mathbf{I}}_\eta^{\Lambda,(\ell+1)} + \dot{\mathbf{I}}_\eta^{\Lambda,(\ell+1)} \circ \boldsymbol{\Pi}_\eta^\Lambda \circ \boldsymbol{\gamma}_{4,\eta}^\Lambda + \boldsymbol{\gamma}_{4,\eta}^\Lambda \circ \boldsymbol{\Pi}_\eta^\Lambda \circ \dot{\mathbf{I}}_\eta^{\Lambda,(\ell)} \circ \boldsymbol{\Pi}_\eta^\Lambda \circ \boldsymbol{\gamma}_{4,\eta}^\Lambda \\ &= \big(\dot{\boldsymbol{\phi}}_\eta^{\Lambda,(\ell+2)}\big)_{\mathrm{R}} + \big(\dot{\boldsymbol{\phi}}_\eta^{\Lambda,(\ell+2)}\big)_{\mathrm{L}} + \big(\dot{\boldsymbol{\phi}}_\eta^{\Lambda,(\ell+2)}\big)_{\mathrm{C}} \,,\end{aligned} \tag{45}$$

where in the last line the subscripts $\{\mathrm{R},\mathrm{L},\mathrm{C}\}$ refer to the diagrammatic position of $\dot{\mathbf{I}}^\Lambda$, i.e., right, left and central, respectively. Using Eq. (21) one can easily deduce the multiloop flow of the vertices $\boldsymbol{\gamma}_{4,\eta}$

$$\partial_\Lambda \boldsymbol{\gamma}_{4,\eta}^\Lambda = \sum_{\ell\geq 1} \dot{\boldsymbol{\gamma}}_{4,\eta}^{\Lambda,(\ell)} = \sum_{\ell\geq 1} \big(\dot{\boldsymbol{\phi}}_\eta^{\Lambda,(\ell)} + \dot{\mathbf{I}}_\eta^{\Lambda,(\ell)}\big) \,. \tag{46}$$

In Ref. [54], it has further been pointed out that corrections to the self-energy flow (29) are necessary in order to generate all differentiated diagrams of the parquet self-energy. These corrections are included in the central part of the vertex flow $\boldsymbol{\gamma}_{4,\eta} \circ \boldsymbol{\Pi}_\eta \circ \dot{\mathbf{I}}_\eta \circ \boldsymbol{\Pi}_\eta \circ \boldsymbol{\gamma}_{4,\eta}$ and read

$$\partial_\Lambda \Sigma^\Lambda = \dot{\Sigma}^\Lambda + \delta\dot{\Sigma}_1^\Lambda + \delta\dot{\Sigma}_2^\Lambda \,, \tag{47}$$

with $\dot{\Sigma}$ given by Eq. (36a) and

$$\delta\dot{\Sigma}_1^\Lambda(k) = -\int dp\, G^\Lambda(p) \Big[2\big(\dot{\phi}_{\bar{D}}^\Lambda\big)_{\mathrm{C}}(k,p,k) - \big(\dot{\phi}_{\bar{D}}^\Lambda\big)_{\mathrm{C}}(p,k,k)\Big] \tag{48a}$$

$$\delta\dot{\Sigma}_2^\Lambda(k) = -\int dp\, \delta S^\Lambda(p) \Big[2\boldsymbol{\gamma}_4^\Lambda(k,p,k) - \boldsymbol{\gamma}_4^\Lambda(p,k,k)\Big] \,, \tag{48b}$$

	n	$f_n(\mathbf{k})$	$f_n(r_i, r_j)$
loc	0	$\frac{1}{2\pi}$	$\delta_{j,i}$
1NN	1	$\frac{1}{\sqrt{2}\pi}\cos(k_x)$	$\frac{1}{\sqrt{2}}(\delta_{j,i+x}+\delta_{j,i-x})$
	2	$\frac{1}{\sqrt{2}\pi}\cos(k_y)$	$\frac{1}{\sqrt{2}}(\delta_{j,i+y}+\delta_{j,i-y})$
	3	$\frac{1}{\sqrt{2}\pi}\sin(k_x)$	$\frac{i}{\sqrt{2}}(\delta_{j,i+x}-\delta_{j,i-x})$
	4	$\frac{1}{\sqrt{2}\pi}\sin(k_y)$	$\frac{i}{\sqrt{2}}(\delta_{j,i+y}-\delta_{j,i-y})$

Table 1: Local and first nearest-neighbor form factors both in momentum and real space presentation. For each calculation we specify which form factors are used. A pure s-wave calculation restricts to the first line corresponding to the local form factor, the d-wave accounts for the first two nearest neighbors form factors, and a calculation with all nearest neighbors form factors includes all five form factors shown here.

where the central part (see Eq. (45)) for the differentiated reducible vertices $\dot{\boldsymbol{\phi}}_{r=\{P,C,D\}} = \{\dot{\mathbf{P}}, \dot{\mathbf{D}}, \dot{\mathbf{C}}\}$ is defined by

$$\left(\dot{\phi}_{\bar{D}}^{\Lambda}\right)_{\mathrm{C}}(k_1,k_2,k_3) = \sum_{\ell\geq 1}\sum_{n,n'}\left[f_n(\mathbf{k}_1)f^*_{n'}(\mathbf{k}_4)\,\left(\dot{\boldsymbol{\phi}}_P^{\Lambda,(\ell)}\right)_{\mathrm{C}}^{n,n'}(\nu_1+\nu_3,\nu_1,\nu_4,\mathbf{k}_1+\mathbf{k}_3) + \right.$$
$$\left. f_n(\mathbf{k}_1)f^*_{n'}(\mathbf{k}_3-\mathbf{k}_2+\mathbf{k}_1)\,\left(\dot{\boldsymbol{\phi}}_C^{\Lambda,(\ell)}\right)_{\mathrm{C}}^{n,n'}(\nu_3-\nu_2,\nu_1,\nu_3-\nu_2+\nu_1,\mathbf{k}_3-\mathbf{k}_2)\right], \tag{49}$$

and $\delta S^{\Lambda}(p) = G^{\Lambda}(p)\delta\dot{\Sigma}_1^{\Lambda}(p)G^{\Lambda}(p)$.

4 Numerical results

In this section we show fRG numerical results obtained with the formalism and code described in the previous sections. After introducing our test system, namely the 2D Hubbard model at half-filling, we will test our full momentum-frequency resolved fRG implementation, together with the inclusion of the self-energy feedback, and study the effect of including multiloop corrections to the 1ℓ approximated flow equations. If not specified differently, we will make use of a "smooth" frequency-dependent regulator throughout this work:

$$G_0^{\Lambda}(k) = \frac{\nu^2}{\nu^2+\Lambda^2}G_0(k) \tag{50}$$

where G_0 specifies the non-interacting Green's function of the 2D Hubbard model. The fRG scheme associated to such a regulator is referred to as Ω-flow [28].

4.0.1 2D Hubbard model at half filling as test system

As test model we consider the single-band two-dimensional (2D) Hubbard model on the square lattice. Its Hamiltonian reads

$$\hat{\mathcal{H}} = -t\sum_{\langle ij\rangle,\sigma}\hat{c}^{\dagger}_{i\sigma}\hat{c}_{j\sigma} + U\sum_i \hat{n}_{i\uparrow}\hat{n}_{i\downarrow} - \mu\sum_{i,\sigma}\hat{n}_{i\sigma}\,, \tag{51}$$

where $\hat{c}^{(\dagger)}_{i\sigma}$ annihilates (creates) an electron with spin σ at the lattice site $\mathbf{R}_i$ ($\hat{n}_{i\sigma} = \hat{c}^{\dagger}_{i\sigma}\hat{c}_{i\sigma}$), t is the hopping amplitude for electrons between neighboring sites, μ the chemical potential and $U > 0$ the repulsive on-site Coulomb interaction. In the present study, we consider $U = 2t$, $\mu = U/2$ and different temperature regimes. Since the present model has been extensively studied in the theoretical literature (see, e.g., Refs. [10, 13, 14, 45, 67–70]) as

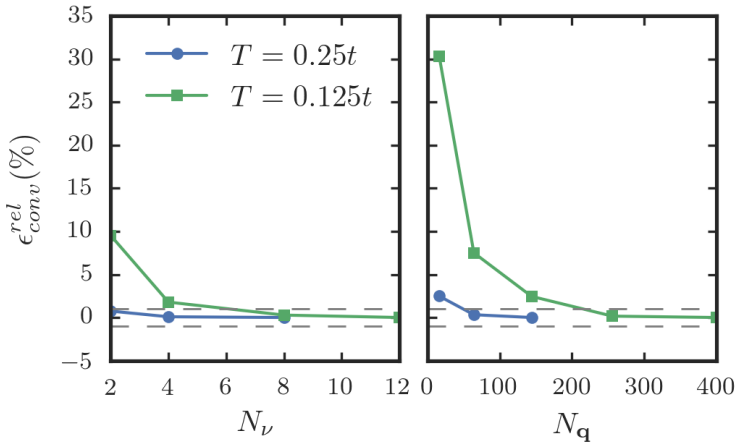

Figure 3: Relative error $\epsilon^{rel}_{conv} = -(\chi - \chi_{conv})/\chi_{conv}$ of the (1ℓ) AF susceptibilities as a function of the number of fermionic frequencies N_ν (left) and the number of bosonic momentum patching points $N_{\mathbf{q}}$ (right), for $U = 2t$ and different values of T. All calculations are performed with only local (s-wave) form factors. In the left panel, $N_{\mathbf{q}}$=144 and $N_{\mathrm{FFT}} = 24 \times 24 = 576$ momentum patching points for the fast Fourier transform. In the right panel, $N_{\mathbf{R}_{\mathrm{FFT}}} = \max(576, 4 \times N_{\mathbf{q}})$ and $N_\nu = 4$ for $T = 0.25$ and $N_\nu = 8$ for $T = 0.125$ respectively. The dashed line corresponds to our tolerance limit of 1%.

well as in fRG (for a review, see Ref. [1]), it constitutes a reference system to test our novel fRG implementation. Furthermore, the 2D Hubbard model constitutes a delicate case in the context of the Mermin-Wagner theorem [71], which prevents the onset of the antiferromagnetic ordering at finite temperature. Whereas the 1ℓ fRG results exhibit a pseudocritical Néel temperature (T_{pc}), the inclusion of the multiloop corrections to the standard fRG flow should, from a theoretical perspective, recover the parquet solution, which is known to fulfill the Mermin-Wagner theorem [72]. Therefore, we expect T_{pc} to be moved down to 0 in the (converged) multiloop fRG scheme. Despite the rich phase diagram of the 2D Hubbard model out of particle-hole symmetry, we restrict this study to the half-filled particle-hole symmetric case, in order to reduce the numerical efforts.

Let us stress that the bosonic momentum discretization of the first Brillouin zone (BZ) has been chosen such that one obtains a uniform grid along the x- and y- directions. This represents, though, not the unique choice of resolving the reciprocal space and one could adopt some sophisticated "patching" schemes [43], which should be accounted in future optimization of our code.

4.0.2 Convergence and stability study on the TUfRG-implementation

In the previous section 3.1, we presented an efficient parameterization of the vertex which combines the TUfRG scheme [30] for treating momenta and the dynamical fRG implementation proposed in Ref. [33]. In order to illustrate the efficiency of such merge, we have performed a convergence study of the (dominant) antiferromagnetic (AF) susceptibility, ($\chi_{\mathrm{AF}} = \chi^{00}_{\mathrm{m}}(i\omega_l = 0, \mathbf{q} = (\pi, \pi))$, by means of Eq. (36f), as a function of the number of Matsubara frequencies, momenta and form factors, used in our algorithm. The convergence tests have been performed at temperatures $T = 0.25t \gg T_{\mathrm{pc}}$ and $T = 0.125t \sim T_{\mathrm{pc}}$.

Let us first consider the convergence in the number of fermionic frequencies N_ν at which

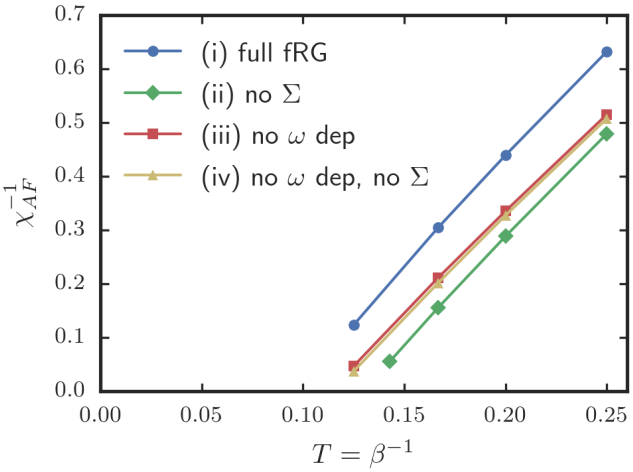

Figure 4: Inverse (1ℓ) AF susceptibility at $\mathbf{q} = (\pi, \pi)$ as a function of temperature, for $U = 2t$. Only local (s-wave) form factors are used, but including the nearest-neighbor form factors does not change the results within the accuracy. Besides the curve obtained using the full TU dynamical fRG scheme (i) (blue dots, "full fRG"), different approximations are shown: approximation (ii) (green diamonds, "no Σ"), (iii) (red squares, "no ω dep") and (iv) (yellow triangles, "no ω dep, no Σ").

the low-frequency structure of the rest-function $\mathcal{R}$ is captured. For $T = 0.25t$ in Fig. 3 (left panel) one observes that the susceptibility does not show significant changes as a function of N_ν. In fact, it is known that, in weakly correlated electron systems, the frequency dependence of the vertex is less important because of power counting arguments [57, 73] and as shown by numerics for small numbers of fermionic Matsubara frequencies, e.g., in Ref. [41]. At $T = 0.125t$ the convergence with respect to N_ν is slower. According to our tolerance of 1% we get convergence at $N_\nu = 8$. Secondly, we analyze the dependence of the AF-susceptibility on the number of bosonic patching points, $N_\mathbf{q}$, as shown in Fig. 3. The data at $T = 0.25t$ are already converged at $N_\mathbf{q} = 64$, while at $T = 0.125t$ we need $N_\mathbf{q} = 256$. In the latter case, one sees that the convergence is more sensitive to $N_\mathbf{q}$ than to N_ν. This can be ascribed to the presence of a finite pseudocritical temperature since for $T \to T_{\mathrm{pc}}$ the AF fluctuations become long-ranged, requiring an increasingly finer momentum resolution. At the same time, the size of the objects to handle is only linear in $N_\mathbf{q}$ while it is expected to scale up to cubic in N_ν, depending on the quantity considered (see Fig. 2). Moreover, the number of independent momentum patching points can be substantially reduced by exploiting point-group symmetries of the lattice.

Last but not least, we have also verified that, for all T considered, the AF response function is fully converged with respect to the number of form factors (not shown).

4.0.3 Effects of different approximations

In our fRG scheme, we can choose different approximation levels regarding the treatment of the frequency dependence of the interactions and the self-energy. This allows us to gain a better understanding of the interplay of the different interaction channels and the role of the self-energy.

Here we define four approximation levels (i) to (iv) with decreasing rigor. Approximation (i) represents the fRG treatment described in Sec. (3) which merges the TUfRG

scheme with an efficient inclusion of the vertex dynamics; (ii) denotes the flow with a frequency-dependent effective interaction but without the flow and feedback of the self-energy; (iii) is the frequency-independent (static) approximation for the effective interaction and the self-energy, in which the fermion-fermion, fermion-boson and boson-boson vertices are approximated by their value at zero frequency; and (iv) combines the neglect of the self-energy feedback with a static approximation for the vertices.

Approximation (iv) has been the standard one adopted in many previous works, as those reviewed in Ref. [1]. Various other fRG works have already explored the changes occurring by using better approximations like (i) to (iii) introduced above. Earlier studies of the self-energy without explicit frequency dependence of the effective interaction pointed to the possibility of non-Fermi liquid behavior [38,74]. Later, channel-decomposed fRG [28,40] and N-patch fRG [41] were used to explore the effects of a frequency-dependent effective interaction and of the self-energy feedback. In the following, we rediscover some of their findings, with a more refined momentum- and frequency-dependent self-energy. Eberlein [42] used a channel-decomposed description of the interaction where each exchange propagator was allowed to depend on one bosonic frequency. He found that in the presence of antiferromagnetic hot spots on the Fermi surface, antiferromagnetic fluctuations lead to a flattening of the Fermi surface and increase the critical scales. Most recently, Vilardi et al. [43] presented a refined 1ℓ study of the role of the various frequency structures in the interaction, parametrized by three frequencies, albeit with a reduced set of form factors. They argued that a one-frequency parametrization can in some cases lead to spurious instabilities. Our study differs from this work by the ability of taking into account more form factors, using a more economic description of the higher frequencies, and by implementing the multiloop corrections.

In Fig. 4 we show how differently the approximations affect the results for the AF susceptibility. More precisely, we plot the inverse AF susceptibility which decreases quite linearly, i.e., Curie-Weiss-like, upon lowering T. The intersection of the curve with the abscissa marks the pseudocritical temperature which, violating the Mermin-Wagner theorem, assumes a finite value in the 1ℓ fRG scheme. One can observe that the full TU-dynamic fRG approach (i) leads to larger inverse AF susceptibilities, or smaller χ_{AF}, than the other three approximations, shifting $T_{\rm pc}$ to a smaller value.

Let us first compare the full calculation (i) with the calculation without self-energy but frequency-dependent interactions (ii). It is to be expected that the self-energy renormalizes the leading vertices and therefore also susceptibilities, as has also been observed in fRG studies [28, 43]. This explains why the calculations without self-energy flow diverge at higher $T_{\rm pc}$ with respect to scheme (i).

The flow variants with static interactions (iii) and (iv) differ only slightly. Compared to the fRG flow using scheme (ii), the AF tendencies in these static flows are somewhat weaker as their suppression by particle-particle processes increases when the pairing channel is approximated by its static part, for which it assumes the maximum value. The downward-shift in the inverse AF susceptibility from (iii) and (iv) to (ii) with the inclusion of the frequency dependence of the couplings is however overcompensated by the inclusion of the dynamical self-energy in (i).

Finally, we consider the pseudocritical temperature and the AF susceptibility for the combined approximation of no self-energy and no frequency dependence (iv). Without the screening effect of the self-energy, the pseudocritical temperature increases a little bit more with respect to the static approximation (iii). This has been already observed in Ref. [41]. The small difference may come from the real part of the self-energy that can be understood as upward-renormalization of the hopping parameter, or equivalently a downward-renormalization of the density of states. This is consistent with the self-energy

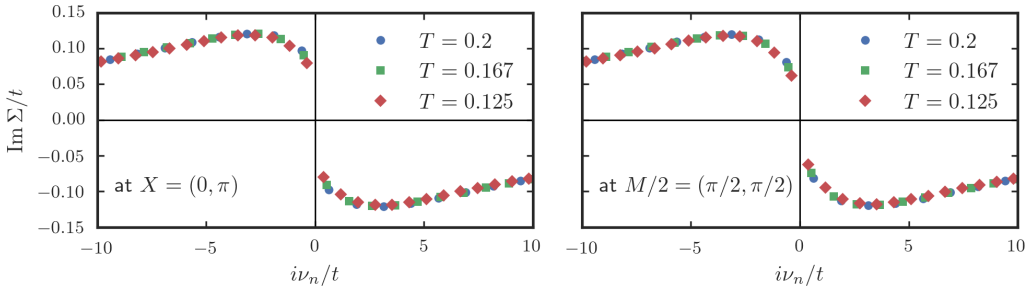

Figure 5: Imaginary part of the self-energy as a function of the Matsubara frequency, at X=$(0, \pi)$ and M/2=$(\pi/2, \pi/2)$, for $U = 2t$ and different temperatures $T = 0.2t$ (blue dots), $T = 0.167t$ (green squares) and $T = 0.125t$ (red diamonds).

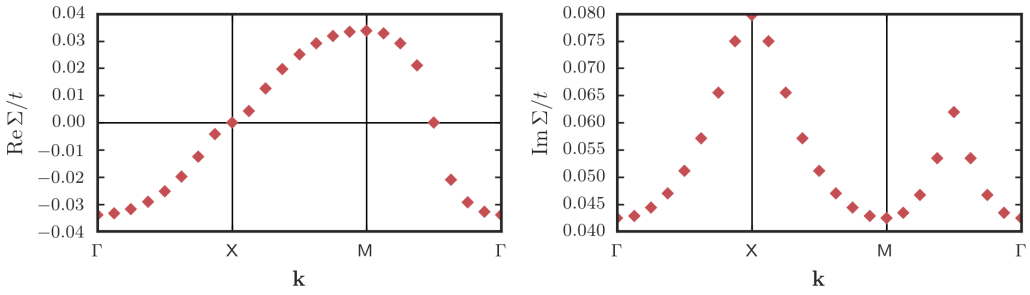

Figure 6: Real (right) and imaginary (left) part of the self-energy $\Sigma(-i\pi/T)$ as a function of the bosonic transfer momentum, for $U = 2t$ and $T = 0.125t$.

shown below in Fig. 6. For a detailed discussion on the pseudocritical temperatures on a wider range of parameters, we refer the reader to Ref. [40].

4.0.4 Computation of the self-energy

As already implied above, the implementation presented in Sec. 3.1 allows one to compute a frequency and momentum dependence of self-energy during the flow according to Eq. (36a). In Figs. 5 and 6, we present the results for the frequency- and momentum-dependence of the self-energy for different temperatures and momentum points. For the fermionic momentum patching we use the same momentum grid as for the bosonic transfer momentum of the vertex. In the results shown in Fig. 6 (left panel), we subtracted the Hartree contribution, which represents a rigid $U/2$ energy shift at half-filling. By looking at Fig. 5, we notice that the frequency dependence of the imaginary part of the self-energy is consistent with a Fermi-liquid, yet without any remarkable difference at different temperatures. As the slope of these curves determines the quasiparticle weight Z, we arrive at the conclusion that Z does not decrease steeply when we lower T towards the AF pseudocritical temperature, as already observed in Refs. [41, 42]. Figure 6 shows the momentum dependence of the real and imaginary part of the self-energy along a path in the first BZ defined by $\Gamma = (0, 0)$, $X = (0, \pi)$ and $M = (\pi, \pi)$. The fermionic frequency is set to the first fermionic Matsubara frequency. The real part is positive at M and negative at Γ, while at X and Y it is zero. At lowest order, this momentum structure can be approximated by a positive nearest-neighbor hopping renormalization, which increases the bandwidth. The imaginary part of the self-energy shows two peaks around X and

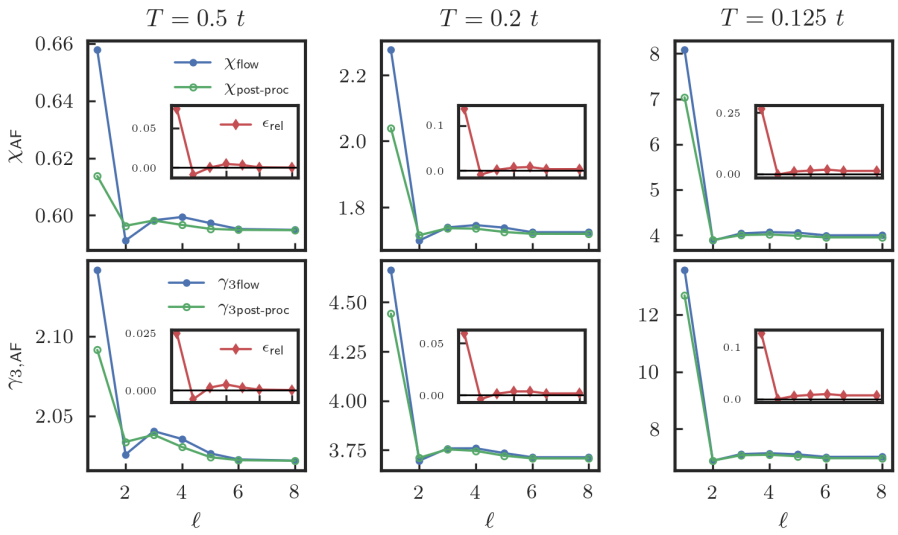

Figure 7: AF susceptibility (upper panels) and fermion-boson vertex (lower panel) at ($\mathbf{q} = (\pi, \pi)$) as a function of the number of loops, for $U = 2t$ and $T = 0.5t, 0.2t, 0.125t$ (from left to right). The susceptibility is evaluated at $\omega = 0$ and the fermion-boson vertex at $\omega = 0$ and $\nu = \pi/\beta$. The blue line shows the behavior of the integrated Eq. (23a) up to $\ell = 8$, while the green line the one obtained from the post-processed calculation by means of Eq. (8) for χ and of (10) for γ_3). The insets show the relative difference between the blue and the green lines, defined for the susceptibility as $\epsilon_{\mathrm{rel}} = (\chi^{\ell}_{\mathrm{flow}} - \chi^{\ell}_{\mathrm{post\text{-}proc}})/\chi^{\ell=8}_{\mathrm{post\text{-}proc}}$.

M/2= $(\pi/2, \pi/2)$. This corresponds to a maximal scattering on the nested Fermi surface and minimal on the points Γ and M, which are at maximal distance from the Fermi surface. Note that this refers to the self-energy at small fixed imaginary frequency and not at real frequency equal to the excitation energy, i.e., this behavior does not contradict the typical behavior that the scattering rates for quasiparticles rise with distance from the Fermi surface.

4.0.5 Effect of the multiloop implementation

Let us now investigate the effect of including multiloop corrections to the flow equations of the susceptibility and the fermion-boson vertex as in Eq. (23a). As previously discussed, the inclusion of the multiloop corrections should allow us to recover the full derivative of Eq. (8) and (10) with respect to the scale parameter Λ. This means that the integration of the multiloop fRG flow equations should converge, by increasing the number of loops, to Eq. (8) and (10), as well as to the parquet equations for γ_4 and Σ as discussed in Ref. [54].

Although, in the half-filled case, the numerical effort is already reduced compared to the non-particle-hole symmetric situation, calculations for $T < 0.5t$ are already quite demanding if a multiloop cycle is included. Therefore, the only calculations involving more than one form factor (i.e., s-wave) that will be presented here were performed at a rather high temperature of $T = 0.5t$. Despite this restriction, since the physics of the single band Hubbard model at half-filling is dominated by the AF fluctuations, the fRG

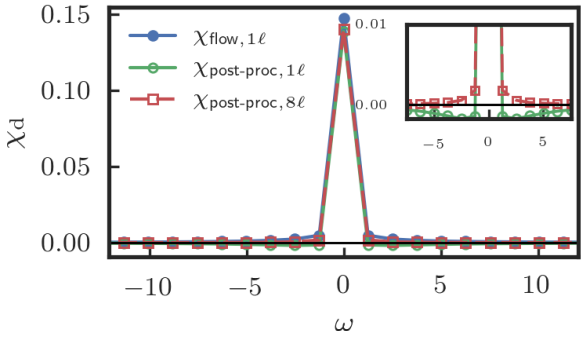

Figure 8: s-wave density susceptibility evaluated at $\mathbf{q} = (0, 0)$ as a function of bosonic Matsubara frequencies, for $U = 2t$ and $T = 0.2t$. The blue and green lines represent the flow and post-processed values for 1ℓ, while the red dashed line corresponds to the post-processed mfRG result for 8ℓ. The zoom in the inset shows that the post-processed 1ℓ data assume unphysical negative values at finite frequencies.

results are already converged in the form factor numbers. Nevertheless, a meaningful part of the d-wave susceptibilities is still accessible, as it will be shown in the following, via the s-wave two-particle vertex.

In Fig. 7 we show the s-wave susceptibility χ (fermion-boson vertex γ_3) in the upper (lower) panels in the magnetic channel for $i\omega_l = 0$ ($i\omega_l = 0$ and $i\nu_o = \pi/\beta$ for γ_3) and $\mathbf{q} = (\pi, \pi)$ as a function of the number of loops considered in the mfRG calculation, for three selected temperatures $T = \{0.5t, 0.2t, 0.125t\}$ (left to right). The blue lines show the value of χ and γ_3 calculated by the integration of Eq. (23a). On the other hand, the green lines show χ (γ_3) acquired at the end of the ℓ-loop fRG flow ($\Lambda = \Lambda_{\text{fin}}$) by means of Eq. (8) ((10)), where we inserted on the r.h.s $\gamma_4^{\Lambda_{\text{fin}}}$ and $G^{\Lambda_{\text{fin}}}$, referred to in Section 2.2 as "post-processed" method. In the present case, one sees how the convergence of the two lines is achieved after 8ℓ for all temperatures presented. Thus, we have a dual convergence: as a function of the loop number and between two ways of computing the same quantity. Clearly, by decreasing the temperature and approaching the 1ℓ fRG pseudocritical temperature (see Fig. 10), the antiferromagnetic (AF) susceptibility and $\gamma^{00}_{3,\text{m}}(\omega = 0, \nu = \pi/\beta, \mathbf{q} = (\pi, \pi)) = \gamma_{3,\text{AF}}$ increase and the green and blue lines for the two ways to compute the susceptibility exhibit the largest relative difference at $\ell = 1$ of $\sim 25\%$. This difference decreases by increasing the loop number down to less then 1% for $\ell = 8$.

It is interesting to see the main effect of the multiloop corrections occurs already at the 2ℓ level, where the 1ℓ results experience the strongest screening effect. Furthermore, as explicitly argued in Ref. [33] the inclusion of the two-loop corrections to the flow of the interaction allows to substantially enrich the virtual excitation content of the fRG equations. By looking at Fig. 7 one could deduce that, performing a post-processed evaluation of the susceptibility, as well as of the fermi-boson vertex, brings them closer to the converged values than the corresponding results coming from the fRG flow (blue curves). However, it has to be stressed that the convergence trend observed in the magnetic channel for the post-processed χ and γ_3 does not apply in general. Counterexamples can be observed, for instance, in the s-wave secondary channels (i.e., charge and superconducting), where the post-processed evaluation of the 1ℓ susceptibility not only leads to an overscreening (i.e., an underestimation with respect to the converged result), but, e.g., in the charge channel,

to even unphysical results, as can be observed in Fig. 8. Here, the s-wave susceptibility in the density channel is plotted at $\mathbf{q} = (0, 0)$ as a function of the bosonic Matsubara frequencies. One observes negative values of the post-processed susceptibility (green line) at finite bosonic frequencies, which are restored to positive values by the multiloop corrections (red line). An attempt to explain this different trend between the dominant (magnetic) and the secondary channels (density and superconducting) is extensively discussed in Appendix D and summarized in the following observations.

As explicitly derived in Appendix D, the Λ-derivative of the formal definition for the susceptibility reported in Eq. (8) (as well as Eq. (10) for γ_3), after substituting the derivative of γ_4 and Σ by their 1ℓ fRG flow equations, leads to additional terms with respect to the standard 1ℓ flow equations for χ in Eq. (19a) (for γ_3 in Eq. (19b)). These terms, besides self-energy derivative corrections (which are generally introduced starting from the second loop-order under the name of *Katanin* corrections [52]), have a 3ℓ-like topological diagrammatic form (see Eq. (26)). The internal loops of $\dot{\mathbf{I}}_\eta^{\Lambda,(1)}$ (marked in red in Fig. 14) contained in such terms act as a screening effect provided by the complementary channels (η') to the one considered ($\eta \neq \eta'$). Because of the imbalance between the 1ℓ approximation for the two-particle vertex γ_4 and Σ, and the 3ℓ diagrams included in the modified "post-processed flow equation" for the susceptibility (see Appendix D), this screening effect ends up being overestimated. Nonetheless, it represents a minor effect on the dominant (magnetic) channel, where the imbalance effect is still governed by the large 1ℓ antiferromagnetic contribution. It could however lead to major changes in the secondary channels, which are affected by the strong screening effect of the magnetic channel appearing on the 3ℓ-like terms. The overscreening affects all frequencies, because of the internally summed diagrams. Therefore, it is particularly severe at nonzero frequencies where the susceptibility assumes small values. This explains the unphysical negative values of the density susceptibility in Fig. 8.

By applying different fRG cutoff schemes, we obtain further tests of the reconstruction of the full derivative of Eq. (8) provided by the multiloop approach. In Fig. 9 we compare the results shown already in Fig. 7 (central upper panel) for $T = 0.2t$ using a frequency-dependent regulator (Ω-flow) with the results for χ at the same temperature obtained by a trivial or flat regulator, also known as interaction or U-cutoff [75]. Differently from the Ω-flow, the U-flow just multiplies the bare propagator with a scale factor that is increased from 0 to 1. Hence, it does not provide any cutoff in energy during the fRG flow so that all energy scales are treated on an equal footing. The insertion of the multiloop corrections into the fRG flow equations, as already observed in a different system in Ref. [55], makes the mfRG calculation almost independent, at high enough loop-order, from the specific regulator considered. A more detailed analysis of our results revealed a persisting small discrepancy even for higher loops. Since it vanishes in absence of self-energy corrections, we attribute it to the truncation of the form factor basis in the vertex flow which prevents the reconstruction of the full derivative of the self-energy.

The substantial reduction of the pseudocritical temperature (T_{pc}) provided by the multiloop corrections is shown in Fig. 10. Here, the inverse 1ℓ fRG antiferromagnetic susceptibility (blue line) is plotted as a function of temperature and compared to the one computed with 8ℓ mfRG calculation (green line). We note that, in principle, the formal equivalence between the mfRG and the parquet approximation should even guarantee the fulfillment of the Mermin-Wagner theorem [71] as this is fulfilled by the parquet approximation [64].

Hence, a frequency-momentum converged mfRG calculation should yield a complete suppression of the pseudocritical temperature down to zero. It is, however, very hard to prove this result numerically, due to the quasi-long-range nature of the spatial fluctuations

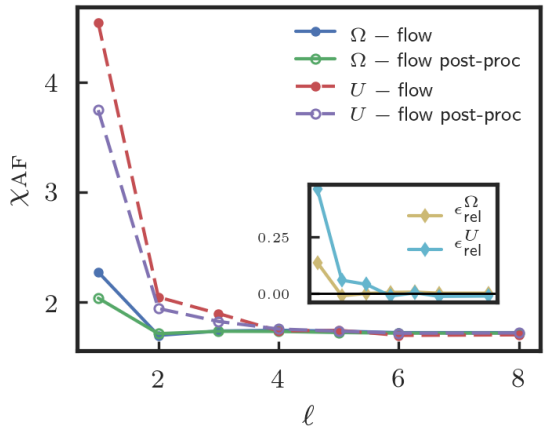

Figure 9: Comparison of two cutoff schemes, the U-flow and the Ω-flow, for the AF susceptibility as a function of the number of loops, for $U = 2t$ and $T = 0.2t$. *Inset*: Relative difference with respect to the converged value $(\chi^{\ell}_{\rm AF} - \chi^{\text{post-proc},\ell}_{\rm AF})/\chi^{8\ell}_{\rm AF}$.

responsible for the Mermin-Wagner theorem. In fact, the avoided onset of a true long-range antiferromagnetism at finite temperature T is associated with the appearance of antiferromagnetic fluctuations with an exponential growing correlation length (see, e.g, discussion in Ref. [72]). Their occurrence has been indeed explicitly verified in several many-body calculations [8,72,76–79] compatible with the Mermin-Wagner theorem. While these low-temperature exponentially extended correlations make the overall physics of our system very similar to that of a true AF ordered phase [80], being associated with a rapid crossover towards a low-temperature insulating behavior, they also make it numerically impossible to access the $T \to 0$ limit, because of the finiteness of any momentum grid discretization. In fact, in the temperature range where we could achieve a satisfactory momentum-convergence of our 8ℓ results the antiferromagnetic susceptibility does not show yet any evidence of the exponential behavior expected in the low-temperature regime. This finding is, however, fully consistent with the most recent estimates of the temperature range, below which the exponential behavior of $\chi_{\rm AF}$ should become visible: According to the most recent DΓA and Dual Fermion studies [8,14,79,81] such a "crossover" temperature would be *lower* than the ordering temperature of DMFT. The latter, for $U = 2$ is $T_N^{DMFT} \sim 0.05$ ($\beta = 20$), i.e., already twice smaller than the lowest temperature considered in the present work.

To conclude this section, we analyze the effect of the fRG multiloop corrections on some d-wave physical susceptibilities which, although suppressed in the particle-hole symmetric case, play an important role in describing the phase diagram of the 2D Hubbard model, most notably away from half filling [27,35,57,82,83]. In particular we analyze the static ($\omega = 0$) d-wave susceptibility in the superconducting channel for $\mathbf{q} = (0,0)$ (dSC), as well as the static d-wave susceptibility in the charge channel for a bosonic momentum transfer $\mathbf{q} = (0,0)$ (dPom), which would become dominant in the case of the so-called "Pomeranchuk" instability. The staggered d-wave charge density wave (dCDW) susceptibility for $\mathbf{q} = (\pi,\pi)$ has not been shown because of its degeneracy with the correspondent d-wave superconducting one. In fact, one can formally demonstrate that in a SU(2) and particle-hole symmetric case, where the system becomes invariant under pseudospin rotation, the pairing susceptibility at $\mathbf{q} = (0,0)$ associated to a specific symmetry of the order parameter is degenerate with the staggered ($\mathbf{q} = (\pi,\pi)$) CDW associated to that specific symmetry. In Fig. 11 we display the result of a fRG calculation where, in addition to the

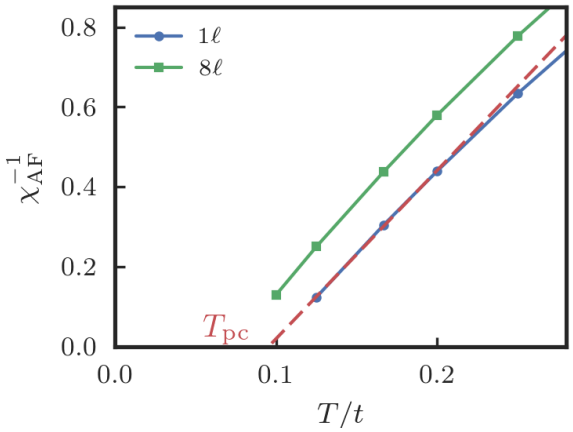

Figure 10: Inverse AF susceptibility as a function of temperature, for $U = 2t$.

s-wave form factor, the form factors indicated as 1 and 2 in Table 1 have been used. As in Fig. 7, the blue line indicates the fRG result obtained by the integration of Eq. (23a) up to a specific ℓ-loop order, alongside the corresponding (ℓ-loop) mfRG equations for Σ and γ_4. The green line represents the post-processed result for the d-wave susceptibilities calculated from a s+d-wave ℓ-loop order mfRG results for the self-energy (Σ) and the two-particle vertex (γ_4). The red line has been obtained, similarly to the green one, from a s-wave ℓ-order mfRG results for Σ and γ_4. One notices that, differently to the antiferromagnetic case, the relative difference between blue and green lines with respect to the convergence value is, at the 1ℓ-level, of the order of few percents and lowers even down to less then $1‰$ at 8ℓ. Interestingly, the post-processed susceptibilities obtained from the s-wave fRG results (red curve) are almost on top of the correspondent ones where both s- and d-wave form factors have been considered during the fRG flow. This shows clearly that, as already known from previous studies on the single-band 2D Hubbard model, the d-wave tendencies in pairing and charge channels are triggered by the antiferromagnetic fluctuations of onsite (s-wave) spin bilinears. However, according to our data for the Fermi surface and the temperature considered, the flow of d-wave pairing and charge channels, which are not captured if only s-wave interactions flow, does not seem to be particularly relevant. This means that in the full system where all channels (s-wave, d-wave, etc.) are allowed to flow, the d-wave attractions triggered by the s-wave AF fluctuations would not fall on a too fertile ground at $T = 0.5t$, i.e., they would not flow strongly in their 'native' d-wave channels. Going to lower T and in particular out of half-filling, this will likely change, as the particle-particle diagrams will enhance any attractive pairing component. Therefore, it is a priori not clear if the d-wave susceptibilities computed at lower T by projecting the vertex made up from s-wave bilinears could provide satisfactory physical results. Nevertheless, we argue that they serve as useful theoretical test objects for the convergence in the order of the multiloop corrections. This is because the effective d-wave interactions captured this way can be understood as two-particle irreducible (2PI) interactions in the d-wave pairing or charge channels, generated purely by s-wave one-loop processes. These 2PI d-wave quantities are non-singular but zero at lowest order in U in typical cases. Hence they can be expected to be dominated by diagrams of finite order in U that should exhibit stronger multiloop effects. In contrast with these terms, the missing boosts in the respective native channels, e.g., in the pairing channel, would just be a higher-order ladder summation of, for $T \to 0$, increasingly singular one-loop diagrams. Hence, if multiloop convergence is reached in the two-particle irreducible interactions, it

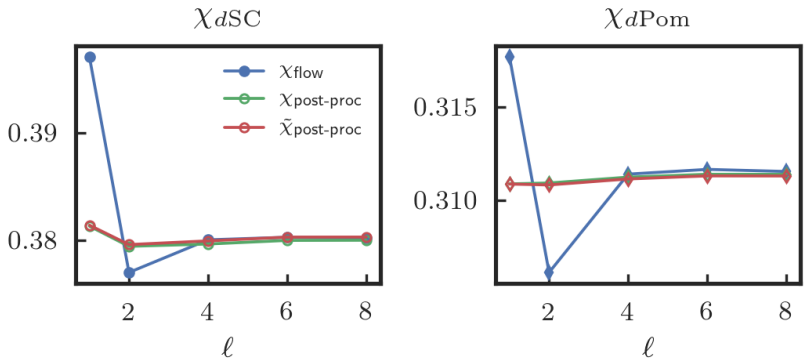

Figure 11: d-wave susceptibililties dSC, dPomeranchuk ($\mathbf{q} = (0,0)$) at $i\omega_m = 0$ as a function of the number of loops, for $U = 2t$ and $T = 0.5t$. The red line has been evaluated by means of Eq. (8), by inserting the two-particle vertex computed from a single (s-wave) form factor.

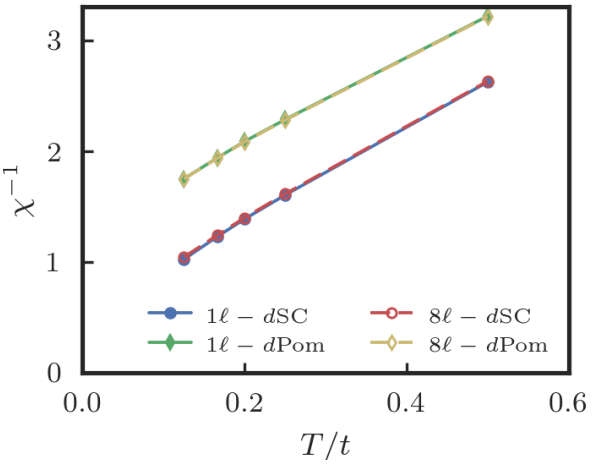

Figure 12: Inverse d-wave susceptibilities, computed by post-processing, as a function of temperature, for $U = 2t$ (fRG flow with only s-wave bilinear interactions).

is likely that the same degree of convergence would be found in the true susceptibilities. This idea leads us to consider the data shown in Fig. 12.

As already visible for $T = 0.5t$ in Fig. 11, the post-processing calculations exhibit a weak dependence on the loop number (with a relative fluctuation less then 1‰). This is confirmed in Fig. 12 where the post-processed inverse d-wave susceptibilities in the aforementioned channels are calculated out of an s-wave 1ℓ (blue and green lines) and 8ℓ (red and yellow dashed lines) fRG flow. As it is apparent in the figure, the effects of the multiloop corrections are insignificant compared to the variation of the inverse susceptibilities in temperature.

5 Conclusions

We have presented a comprehensive study of forefront algorithmic implementations of the fRG for interacting fermions on 2D lattices. While we focused on the 2D Hubbard model, the methodological improvements discussed here can provide a useful guidance for the

generalization to other systems.

Our main goal is to illustrate the progress achieved when going beyond the approximations routinely made in most previous fRG computations. In particular, we have worked on the following aspects: (i) an accurate and converged treatment of both the momentum and frequency dependence of the vertex function together with its asymptotic structures; (ii) the inclusion of the self-energy and its feedback in the fRG flow; (iii) the implementation of the multiloop corrections beyond the standard 1ℓ.

Regarding the first aspect (i), we have kept the more general dependence of the two-particle vertex on all *three* Matsubara frequencies. We extend previous works [40,43,83–86] by exploiting an "economic" description [33] provided by an efficient parametrization of the high frequency asymptotics [31]. We could show that this parametrization can be brought to convergence in the number of frequencies employed, i.e. it the results do not change if more frequencies are used. We combined this treatment of the frequency dependence with the truncated-unity technique for the momentum dependence, whose form-factor expansion was also shown to converge quickly for our test case [30].

With a frequency-dependent flowing interaction, we could also compute a momentum- and frequency-dependent self-energy, which has been fed back into the flow of the two-particle vertex. Through a systematic analysis of specific observables – in particular of the response functions – we could assess the effects of the improved algorithmic implementation with respect to previous results and demonstrate how, for the parameters studied, the fRG results can be converged in the number of considered frequencies. An analogous convergence could be also established for the 2D momentum dependence.

The major advancement achieved in this work is, however, the implementation of the multiloop corrections both for the flow of the two-particle vertex as well as for the flow of the coupling to external fields and the corresponding susceptibilities. The multiloop extension, so far only tested for a (prototypical) toy model [55], adds more virtual excitations to the flow of the two-particle vertex compared to the previously used 1ℓ truncation. As it was diagrammatically shown [54, 55], if truncated fRG results are converged with respect to the loop order, they exactly reproduce the parquet approximation (PA), not only concerning the topology of the summed diagrams, but also – quantitatively – their precise weight. This has been also recently confirmed by a formal analytical derivation of the multiloop fRG equations [56]. From this property, it follows that the results of a loop-converged fRG algorithm become completely independent from the employed cutoff scheme, at least if all modes are integrated out at sufficiently high temperature.

Previously, it was not clear how the contributions missing in the 1ℓ truncation would influence the results quantitatively. On the numerical level, the effort for including the multiloop corrections to order ℓ only rises linearly in ℓ, i.e. the situation is far better than if one really had to compute all higher-loop diagrams. Our studies show that the multiloop corrections can be included also in 2D up to rather high orders of $\ell = 8$. We find that the observables converge quite nicely when the multiloop order is increased. While it is not obvious that this quick convergence will hold for all model parameters and for all models of interest, our study shows that these checks can be performed with feasible numerical efforts. This adds an new important degree of quantitative control to the fRG, at least in the weak to intermediate coupling regime where the PA can be considered accurate. At stronger coupling, where low-frequency vertex corrections beyond the PA might appear [31, 49, 87–89], the mfRG could provide a much better [14] setup for the proposed combination with the DMFT [22, 26]. The loop convergence of our fRG results is also reflected in the progressive reduction of the dependence of our fRG results on the chosen cutoff scheme, which appears completely suppressed at the 8ℓ level.

The incorporation of the multiloop contributions has also another rather appealing and

quantitatively important aspect, giving rise to an additional very useful type of convergence. It has been known that response functions can be computed in two different ways in RG approaches and that the results differ due to the involved approximations. One way is to consider the flow of couplings of 'composite operator' bilinears in the primary degrees of freedom to external fields of appropriate type. Then the response function is obtained as renormalization of the propagator of the external field.

The other way, referred to as post-processing, is to compute the response functions by means of their diagrammatic expression, evaluated from the dressed bare fermion bubbles and the two-particle vertex at the end of the flow. In fact, in some cases arguments were made (see, e.g., Ref. 90 and references therein) that the external field methods should give more controlled results, i.e., that composite operators should be renormalized separately, because, at the level of the approximations made, the post-processed quantities, which involve the integration over all energies and momenta, are more afflicted by approximation errors. In our study, the multiloop extension of the response function flow allows us to show that *also* the flow of the response functions becomes an exact scale derivative of the post-processed response function. This establishes the formal equivalence of the two ways to compute response functions on the multiloop level. This formal equivalence is remarkably reflected by our numerical results, which exhibit a clear convergence of the two approaches: If the multiloop convergence is achieved, and frequency and momentum dependencies as well as the self-energy feedback are included appropriately, the fRG results for the response functions are unambiguous. The corresponding data can be used for quantitative studies and directly compared with other numerical techniques or with experiments, if the effective modelling of the problem is sufficiently realistic.

In summary, our study shows how the fRG algorithms for two-dimensional fermionic lattice models can be brought to a quantitatively reliable level at weak to moderate couplings, as long as the parquet approximation is appropriate. This goal has been reached by means of an economic, but accurate, treatment of the momentum and frequency dependencies which takes into account the asymptotic structure of the two-particle vertex and the self-energy during the fRG flow. This fRG framework has been supplemented with the implementation of the multiloop corrections to the 1ℓ truncation scheme.

The algorithmic implementation presented in this paper can be applied to other model Hamiltonians, and - within the framework of the 2D Hubbard model - to broader parameter regimes in future works. For instance, if the Fermi surface displays a given curvature, due to the inclusion of, e.g., more hopping terms or changes of the band filling, the dominance of the AF channel will be weakened and the pseudo-critical scales will become smaller. For such cases the convergences of the different approximation might possibly vary. In particular, since the generation of d-wave pairing tendencies in third order of the bare coupling involves 2ℓ diagrams that are only partially captured in the 1ℓ truncation, we would expect the impact of the multiloop corrections to become more noticeable.

Acknowledgements

The authors thank A. Eberlein, J. Ehrlich, P. Hansmann, J. Lichtenstein, W. Metzner, T. Reckling, D. Sanchez de la Pena, G. Schober, C. Taranto, J. von Delft, D. Vilardi, and N. Wentzell for valuable discussions, D. Rohe (FZ Jülich) for major help on the parallelization of the code, and W. Metzner for a careful reading of the manuscript.

Author information A. Tagliavini and C. Hille contributed equally to this work.

Funding information We acknowledge financial support from the Deutsche Forschungsgemeinschaft (DFG) through ZUK 63, RTG 1995, HO 2422/11-1, and Projects No. AN 815/5-1 and No. AN 815/6-1, and the Austrian Science Fund (FWF) within the Project F41 (SFB ViCoM) and I2794-N35. Calculations were performed on the Vienna Scientific Cluster (VSC) and at Jülich Supercomputing Centre (JSC) in the frame of project jjsc28.

A Symmetries and symmetrized notation

Here we illustrate how diagrammatic and lattice related symmetries can be expressed in an easy way and how they are implemented in our code. Directly related to the symmetries is the question if one uses the symmetrized or the non-symmetrized notation for the momentum and frequency dependence of the channels. In Section 3.1 we argued that the non-symmetrized notation leads to more readable flow equations, bubbles and projection matrices. Therefore we adopted primarily this notation. The symmetries, however, are much easier to express in the symmetrized notation. While in the non-symmetrized notation, simple relations like the crossing relation involve multiple form factor combinations, in the symmetrized notation we find a one-to-one correspondence. Therefore we here use for both momentum and frequency the symmetrized notation (s), which is related to the non-symmetrized (ns) by

$$\phi^s_{ph}(q,k,k') = \phi^{ns}_{ph}\left(-q, k+\frac{q}{2}, k'+\frac{q}{2}\right) \tag{52a}$$

$$\phi^s_{\overline{ph}}(q,k,k') = \phi^{ns}_{\overline{ph}}\left(-q, k+\frac{q}{2}, k'+\frac{q}{2}\right) \tag{52b}$$

$$\phi^s_{pp}(q,k,k') = \phi^{ns}_{pp}\left(q, k+\frac{q}{2}, k'+\frac{q}{2}\right) \ . \tag{52c}$$

A.1 Lattice related symmetries

First we specify how lattice related symmetries are reflected in the form factor expansion of the channels in the symmetrized notation. The lattice symmetries always depend on the system and we here focus on the 2D Hubbard model on a square lattice, where we have for example the rotation of $\pi/2$ around the z-axis and the mirroring at the y-axis as independent symmetry operations. Under any of these operations, or combinations of them, applied simultaneously to all momentum dependencies, the expressions of the channels are invariant. This can be translated into the form factor expansion by

$$\begin{aligned}\hat{P}[F]_{n,n'}(\mathbf{q}) &= \int d\mathbf{k}d\mathbf{k}' f^*_n(\mathbf{k}) f_{n'}(\mathbf{k}') F(\mathbf{q},\mathbf{k},\mathbf{k}') \\ &= \int d\mathbf{k}d\mathbf{k}' f^*_n(\mathbf{k}) f_{n'}(\mathbf{k}') F(\hat{R}(\mathbf{q}),\hat{R}(\mathbf{k}),\hat{R}(\mathbf{k}')) \\ &= \int d\mathbf{k}d\mathbf{k}' f^*_n(\hat{R}^{-1}(\mathbf{k})) f_{n'}(\hat{R}^{-1}(\mathbf{k}')) F(\hat{R}(\mathbf{q}),\mathbf{k},\mathbf{k}') \ ,\end{aligned} \tag{53}$$

where F is any of the channels D, C or P. The frequency dependence is not affected and is therefore omitted. We here exploited the symmetry under consideration and introduced a variable change. If the form factors are chosen in such a way that under this symmetry operation any form factor is related to a linear combination of others, described by the matrix $\mathbf{M}_{\hat{R}^{-1}}(\mathbf{k})$, it holds in addition

$$\hat{P}[F]_{n,n'}(\mathbf{q}) = \int d\mathbf{k}d\mathbf{k}' \sum_m f^*_m(\mathbf{k}) M_{\hat{R}^{-1}}(\mathbf{k})_{mn} \sum_{m'} M_{\hat{R}^{-1}}(\mathbf{k}')_{n'm'} f_{m'}(\mathbf{k}') F(\hat{R}(\mathbf{q}),\mathbf{k},\mathbf{k}') \ . \tag{54}$$

If moreover, the symmetry operation on every form factor yields a single other form factor expressed by the vector $\mathbf{V}_{\hat{R}^{-1}}$, the above relation simplifies to

$$\hat{P}[F]_{n,n'}(\mathbf{q}) = \hat{P}[F]_{V_{\hat{R}^{-1}}(n)V_{\hat{R}^{-1}}(n')}(\mathbf{q}) S_{V_R(n)} S_{V_R(n')} \ , \tag{55}$$

where the only difference is a possible sign change taken into account by $S_{V_R(n)}$. These assumptions hold for the form factors used in the present implementation (see Table 1), but are not necessarily valid for an arbitrary choice of form factors.

A.2 Diagrammatic symmetries

In addition to the lattice related symmetries, there are diagrammatic symmetries which are independent of the geometry of the system. Considering a two-particle fermionic vertex, we can apply the crossing symmetry simultaneously to the annihilation and the creation operators, recovering the following relations:

$$F_{\sigma_1,\sigma_2,\sigma_3}(i\nu_{o_1}, i\nu_{o_2}, i\nu_{o_3}, k_1, k_2, k_3) = F_{\sigma_3,\sigma_4,\sigma_1}(i\nu_{o_3}, i\nu_{o_4}, i\nu_{o_1}, k_3, k_4, k_1) \tag{56}$$

time reversal

$$F_{\sigma_1,\sigma_2,\sigma_3}(i\nu_{o_1}, i\nu_{o_2}, i\nu_{o_3}, k_1, k_2, k_3) = F_{\sigma_2,\sigma_1,\sigma_4}(i\nu_{o_2}, i\nu_{o_1}, i\nu_{o_4}, k_2, k_1, k_4) \tag{57}$$

and complex conjugation

$$F^*_{\sigma_1,\sigma_2,\sigma_3}(i\nu_{o_1}, i\nu_{o_2}, i\nu_{o_3}, k_1, k_2, k_3) = F_{\sigma_2,\sigma_1,\sigma_4}(-i\nu_{o_2}, -i\nu_{o_1}, -i\nu_{o_4}, k_2, k_1, k_4) \tag{58}$$

for which we refer to Ref. [91]. In the SU(2) symmetric case, by projecting the vertex ϕ to the form factor basis and adopting the symmetrized notation, one has that Eq. (56) gives

$$P_{n,n'}(i\omega_m, i\nu_o, i\nu_{o'}, \mathbf{q}) = \Pi_n \Pi_{n'} P_{n,n'}(i\omega_m, -i\nu_o, -i\nu_{o'}, \mathbf{q}) \tag{59a}$$
$$D_{n,n'}(i\omega_m, i\nu_o, i\nu_{o'}, \mathbf{q}) = D_{n,n'}(-i\omega_m, i\nu_{o'}, i\nu_o, -\mathbf{q}) \tag{59b}$$
$$C_{n,n'}(i\omega_m, i\nu_o, i\nu_{o'}, \mathbf{q}) = C_{n,n'}(-i\omega_m, i\nu_{o'}, i\nu_o, -\mathbf{q}) \tag{59c}$$

where Π_m is the parity associated to the momentum inversion of the form factor m defined as

$$f_n(-\mathbf{k}) = \Pi_n f_n(\mathbf{k}) \ . \tag{60}$$

The time reversal symmetry reads

$$P_{n,n'}(i\omega_m, i\nu_o, i\nu_{o'}, \mathbf{q}) = P_{n',n}(i\omega_m, i\nu_{o'}, i\nu_o, \mathbf{q}) \tag{61a}$$
$$D_{n,n'}(i\omega_m, i\nu_o, i\nu_{o'}, \mathbf{q}) = D_{n,n'}(-i\omega_m, i\nu_o, i\nu_{o'}, -\mathbf{q}) \tag{61b}$$
$$C_{n,n'}(i\omega_m, i\nu_o, i\nu_{o'}, \mathbf{q}) = C_{n',n}(i\omega_m, i\nu_{o'}, i\nu_o, \mathbf{q}) \tag{61c}$$

and the complex conjugation

$$P^*_{n,n'}(i\omega_m, i\nu_o, i\nu_{o'}, \mathbf{q}) = P_{n',n}(-i\omega_m, -i\nu_{o'}, -i\nu_o, \mathbf{q}) \tag{62a}$$
$$D^*_{n,n'}(i\omega_m, i\nu_o, i\nu_{o'}, \mathbf{q}) = D_{n,n'}(i\omega_m, -i\nu_o, -i\nu_{o'}, -\mathbf{q}) \tag{62b}$$
$$C^*_{n,n'}(i\omega_m, i\nu_o, i\nu_{o'}, \mathbf{q}) = C_{n',n}(-i\omega_m, -i\nu_{o'}, -i\nu_o, \mathbf{q}) \ . \tag{62c}$$

A.3 Connection between $\mathcal{K}_2$ and $\bar{\mathcal{K}}_2$

In Section 3.1.2 we argued that $\bar{\mathcal{K}}_2$ can be obtained from $\mathcal{K}_2$ by symmetry. For the pp and $\overline{ph}$ channel the time reversal symmetry exchanges the two fermionic dependencies while keeping the transfer frequency and momentum fixed. The same holds for the ph-channel by using the combination of the crossing and the time reversal symmetry. Taking the limit of large frequencies for the first and second fermionic frequency respectively, we obtain trivially

$$\mathcal{K}_{2,P,n}(i\omega_m, i\nu_o, \mathbf{q}) = \bar{\mathcal{K}}_{2,P,n}(i\omega_n, i\nu_o, \mathbf{q}) \tag{63a}$$
$$\mathcal{K}_{2,D,n}(i\omega_m, i\nu_o, \mathbf{q}) = \bar{\mathcal{K}}_{2,D,n}(i\omega_n, i\nu_o, \mathbf{q}) \tag{63b}$$
$$\mathcal{K}_{2,C,n}(i\omega_m, i\nu_o, \mathbf{q}) = \bar{\mathcal{K}}_{2,C,n}(i\omega_n, i\nu_o, \mathbf{q}) \ . \tag{63c}$$

B Formal derivation of the fRG flow equations for χ and γ_3

In this section we provide an explicit derivation of the flow equations for the response functions. As anticipated in Sec. 2.2, we start by coupling the fermionic bilinears to an external source field J, by adding the following scalar product

$$(J_\eta^n, \rho_\eta^n) = \int dk J_\eta^n(k)\rho_\eta^n(k) \ , \tag{64}$$

where n indicates the momentum structure of the fermionic bilinears coupled to the field J_η^n. Since the density is in general not charge conserving, it is convenient to use the Nambu formalism that allows for a more concise derivation of the flow equations of the physical response functions. We rewrite Eqs. (1) and (2) in the Nambu basis [92, 93]

$$\rho_\eta^n(q) = \sum_{s,s'=\pm} \alpha_{s,s'}^\eta \int dp \bar{\phi}_s(p-q) f_n(\mathbf{p}) \phi_{s'}(p) \tag{65}$$

where $s = \pm$ represents the Nambu index and

$$\phi_+(k) = \psi_\uparrow(k) \qquad \bar{\phi}_+(k) = \bar{\psi}_\uparrow(k)$$
$$\phi_-(k) = \bar{\psi}_\downarrow(-k) \qquad \bar{\phi}_-(k) = \psi_\downarrow(-k) \ .$$

The matrices $\boldsymbol{\alpha}^\eta$ (with $\eta = \{\mathrm{d}, \mathrm{m}, \mathrm{sc}\}$), which define the Nambu index structure in the different physical channels, are given by

$$\boldsymbol{\alpha}^{\mathrm{d}} = \begin{pmatrix} 1 & 0 \\ 0 & -1 \end{pmatrix} \quad \boldsymbol{\alpha}^{\mathrm{m}} = \begin{pmatrix} 1 & 0 \\ 0 & 1 \end{pmatrix} \quad \boldsymbol{\alpha}^{\mathrm{sc}} = \begin{pmatrix} 0 & 1 \\ -1 & 0 \end{pmatrix} \ . \tag{66}$$

In order to derive the flow equations for the fermion-boson vertex of Eq. (15) and the susceptibility of Eq. (14) we start from the so-called Wetterich equation [94]

$$\partial_\Lambda \Gamma^\Lambda[J_\eta, \phi] = -(\bar{\phi}, \dot{Q}_0^\Lambda \phi) - \frac{1}{2}\mathrm{tr}\{\dot{\mathbf{Q}}_0^\Lambda (\mathbf{\Gamma}^{(2)\Lambda}[J_\eta, \phi])^{-1}\} \ , \tag{67}$$

where Γ^Λ represents the scale-dependent effective action, which is a function of the functional variable J_η and the Nambu field ϕ, Q_0^Λ is the inverse non-interacting Green's function and the dot denotes the derivative with respect to the flow parameter Λ. Further, the matrix $\mathbf{Q}_0^\Lambda = \mathrm{diag}(Q_0^\Lambda, -Q_0^{\Lambda,t})$ and

$$\mathbf{\Gamma}^{(2)\Lambda}[J_\eta, \phi] = \begin{pmatrix} \bar{\partial}\partial\Gamma^\Lambda[J_\eta, \phi] & \bar{\partial}\bar{\partial}\Gamma^\Lambda[J_\eta, \phi] \\ \partial\partial\Gamma^\Lambda[J_\eta, \phi] & \partial\bar{\partial}\Gamma^\Lambda[J_\eta, \phi] \end{pmatrix} \tag{68}$$

were we used, where ∂ and $\bar{\partial}$ applied to the effective action Γ^Λ are a shorthand notation for the functional derivative of with respect to ϕ and $\bar{\phi}$, respectively. Following the derivation of Ref. [2], we introduce the matrix

$$\mathbf{U}^\Lambda[J_\eta,\phi] = (\mathbf{G}^\Lambda)^{-1} - \mathbf{\Gamma}^{(2)\Lambda}[J_\eta,\phi] \; . \tag{69}$$

Thus, we can recast $(\mathbf{\Gamma}^{(2)\Lambda}[J_\eta,\phi])^{-1} = (\mathbf{1} - \mathbf{G}^\Lambda\mathbf{U}^\Lambda)^{-1}\ \mathbf{G}^\Lambda$ and expand the inverse matrix in a geometric series

$$(\mathbf{\Gamma}^{(2)\Lambda}[J_\eta,\phi])^{-1} = \sum_{n=0}^{\infty}(\mathbf{G}^\Lambda\mathbf{U}^\Lambda)^n\ \mathbf{G}^\Lambda \; . \tag{70}$$

We can now insert Eq. (70) in Eq. (67). Expanding up to second order yields

$$\partial_\Lambda\Gamma^\Lambda[J_\eta,\phi] = -(\bar{\phi},\dot{Q}_0^\Lambda\phi) - \frac{1}{2}\mathrm{tr}\{\dot{\mathbf{Q}}_0^\Lambda\mathbf{G}^\Lambda\} - \frac{1}{2}\mathrm{tr}\{\mathbf{S}^\Lambda\mathbf{U}^\Lambda\} - \frac{1}{2}\mathrm{tr}\{\mathbf{S}^\Lambda\mathbf{U}^\Lambda\mathbf{G}^\Lambda\mathbf{U}^\Lambda\} + ... \tag{71}$$

where $\mathbf{S}^\Lambda = \mathbf{G}^\Lambda\mathbf{Q}_0^\Lambda\mathbf{G}^\Lambda = \mathrm{diag}(S^\Lambda, -S^{\Lambda,t})$ represents the matrix diagonal form of the single scale propagator, and we exploited the cyclic property of the trace. After applying the trace to the matrices in the curly brackets, we can expand the effective action in powers of the fermionic Nambu fields and the external bosonic source field

$$\begin{aligned}\Gamma^\Lambda[J_\eta,\phi] = &\sum_{m_1,n_1=0}^{\infty}\frac{(-1)^{m_1}}{n_1!\ (m_1!)^2}\times \\ &\sum_{\substack{x_1...x_{m_1}\\ x'_1...x'_{m_1}\\ y_1...y_{n_1}}}\frac{\partial^{(2m_1+n_1)}\Gamma^\Lambda[J_\eta,\phi]}{\partial J_\eta(y_1)...\partial J_\eta(y_{n_1})\partial\bar{\phi}(x'_1)...\partial\bar{\phi}(x'_{m_1})\partial\phi(x_{m_1})...\phi(x_1)}\Big|_{\phi=J_\eta=0}\times \\ &J_\eta(y_1)...J_\eta(y_{n_1})\bar{\phi}(x'_1)...\bar{\phi}(x'_{m_1})\phi(x_{m_1})...\phi(x_1) \qquad (72a)\\ = &\sum_{m_1,n_1=0}^{\infty}\frac{(-1)^{m_1}}{n_1!\ (m_1!)^2}\sum_{\substack{x_1...x_{m_1}\\ x'_1...x'_{m_1}\\ y_1...y_{n_1}}}\gamma^\Lambda_{2m_1+n_1,y_1..y_{n_1},x'_1..x'_{m_1},x_1..x_{m_1}}\times \\ &J_\eta(y_1)...J_\eta(y_{n_1})\bar{\phi}(x'_1)...\bar{\phi}(x'_{m_1})\phi(x_{m_1})...\phi(x_1) \; . \qquad (72b)\end{aligned}$$

Note that the index $x = \{s,k\}$ combines the Nambu index s and the fermionic quadrivector $k = (\nu,\mathbf{k})$ (here we disregard additional quantum numbers, as e.g., orbital), while $y = \{n,q\}$ combines the momentum structure of the coupling to the bilinears, n, with the bosonic quadrivector $q = (\omega,\mathbf{q})$. Inserting this expansion in Eq. (71), we compare the expansion coefficient related to the same order on the fields on both sides of the equation.

For $n_1 = 0$ we recover the standard fermionic hierarchy of flow equations [1, 2]. For $n_1 > 0$ we can derive the flow equations for the fermion-boson vertex ($n_1 = 1$, $m_1 = 1$) as well as for the boson-boson vertices or susceptibilities ($n_1 = 2$, $m_1 = 0$). In Nambu notation, the flow equation for the susceptibility reads

$$\begin{aligned}\partial_\Lambda\chi^\Lambda(y,y') = &\sum_{\substack{x_1,x'_1\\ x_2,x'_2}}\gamma_3^\Lambda(y,x'_1,x_1)[G^\Lambda(x_1,x'_2)S^\Lambda(x_2,x'_1) + (S\leftrightarrow G)]\gamma_3^{\Lambda\dagger}(y',x_2,x'_2) + \\ &\sum_{x_1,x'_1}S^\Lambda(x_1,x'_1)\tilde{\gamma}_4^\Lambda(y,y',x'_1,x_1) \; ,\end{aligned} \tag{73}$$

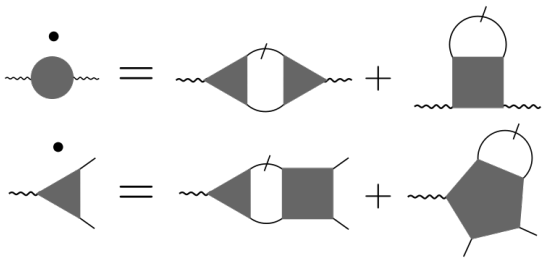

Figure 13: Simplified diagrammatic representation of the flow equations for the susceptibily (first line) and the fermi-boson vertex (second line) illustrating the topological structure of the diagrams. The circle, triangle and the square represent the susceptibility χ, the fermi-boson vertex γ_3, and the two-particle vertex γ_4, respectively.

and the one for the fermion-boson vertex is

$$\partial_\Lambda \gamma_3^\Lambda(y,x',x) = \sum_{x_1,x_1'} S^\Lambda(x_1,x_1')\gamma_5^\Lambda(y,x',x_1',x_1,x) + \sum_{\substack{x_1,x_1'\\x_2,x_2'}} \gamma_3^\Lambda(y,x_1',x_1)[G^\Lambda(x_1,x_2')S^\Lambda(x_2,x_1') + (S\leftrightarrow G)]\gamma_4^\Lambda(x',x_2,x_2',x)\,. \tag{74}$$

In the second term on the r.h.s. of Eq. (73), $\gamma^\Lambda_{2m_1+n_1} = \tilde{\gamma}^\Lambda_{2+2}$ represents the functional derivative of the effective action with respect to two bosonic and two fermionic Nambu fields. The two Eqs. (73) and (74) are schematically shown in Fig. 13. If one neglects the second term in both r.h.s., they correspond to the 1ℓ fRG equations for the response functions. Both γ_3 and χ do not feed back into the flow equations for γ_4 and Σ.

C Connection between the vertex asymptotics and the response functions

In this appendix we demonstrate that the integration of the fRG flow equations for the so-called kernel functions $\mathcal{K}_1$ and $\mathcal{K}_2$ mentioned in Section 3, coincide with the s-wave susceptibility and fermion-boson vertex resulting from the flow.

Let us write explicitly the flow equation for the asymptotics $\boldsymbol{\mathcal{K}}^\Lambda_{1,\eta}$ and $\bar{\boldsymbol{\mathcal{K}}}^\Lambda_{2,\eta}$, with $\eta = \{\mathrm{sc,d,m}\}$, obtained from Eq. (43) in the limit of infinite fermionic Matsubara frequencies ν and ν'

$$\lim_{\substack{\nu\to\infty\\ \nu'\to\infty}} \dot{\boldsymbol{\phi}}^\Lambda_\eta = \dot{\boldsymbol{\mathcal{K}}}^\Lambda_{1,\eta} = (\boldsymbol{\gamma}^0_{4,\eta} + \boldsymbol{\mathcal{K}}^\Lambda_{1,\eta} + \bar{\boldsymbol{\mathcal{K}}}^\Lambda_{2,\eta}) \circ \dot{\boldsymbol{\Pi}}^\Lambda_\eta \circ (\boldsymbol{\gamma}^0_{4,\eta} + \boldsymbol{\mathcal{K}}^\Lambda_{1,\eta} + \boldsymbol{\mathcal{K}}^\Lambda_{2,\eta}) + (\boldsymbol{\gamma}^0_{4,\eta} + \boldsymbol{\mathcal{K}}^\Lambda_{1,\eta} + \bar{\boldsymbol{\mathcal{K}}}^\Lambda_{2,\eta}) \circ \boldsymbol{\Pi}^\Lambda_\eta \circ \dot{\mathbf{I}}^\Lambda_\eta \circ \boldsymbol{\Pi}^\Lambda_\eta \circ (\boldsymbol{\gamma}^0_{4,\eta} + \boldsymbol{\mathcal{K}}^\Lambda_{1,\eta} + \boldsymbol{\mathcal{K}}^\Lambda_{2,\eta}) \tag{75}$$

and

$$\lim_{\nu\to\infty} \dot{\boldsymbol{\phi}}^\Lambda_\eta = \dot{\boldsymbol{\mathcal{K}}}^\Lambda_{1,\eta} + \dot{\bar{\boldsymbol{\mathcal{K}}}}^\Lambda_{2,\eta} = (\boldsymbol{\gamma}^0_{4,\eta} + \boldsymbol{\mathcal{K}}^\Lambda_{1,\eta} + \bar{\boldsymbol{\mathcal{K}}}^\Lambda_{2,\eta}) \circ \dot{\boldsymbol{\Pi}}^\Lambda_\eta \boldsymbol{\gamma}^\Lambda_{4,\eta} + (\boldsymbol{\gamma}^0_{4,\eta} + \boldsymbol{\mathcal{K}}^\Lambda_{1,\eta} + \bar{\boldsymbol{\mathcal{K}}}^\Lambda_{2,\eta}) \circ \boldsymbol{\Pi}^\Lambda_\eta \circ \dot{\mathbf{I}}^\Lambda_\eta + (\boldsymbol{\gamma}^0_{4,\eta} + \boldsymbol{\mathcal{K}}^\Lambda_{1,\eta} + \bar{\boldsymbol{\mathcal{K}}}^\Lambda_{2,\eta}) \circ \boldsymbol{\Pi}^\Lambda_\eta \circ \dot{\mathbf{I}}^\Lambda_\eta \circ \boldsymbol{\Pi}^\Lambda_\eta \circ \boldsymbol{\gamma}^\Lambda_{4,\eta}\,, \tag{76}$$

where $\dot{\boldsymbol{\phi}}_\eta^\Lambda$ is given by

$$\dot{\boldsymbol{\phi}}_{\mathrm{sc}}^\Lambda = \dot{\boldsymbol{P}}^\Lambda \tag{77a}$$

$$\dot{\boldsymbol{\phi}}_{\mathrm{d}}^\Lambda = 2\dot{\boldsymbol{D}}^\Lambda - \dot{\boldsymbol{C}}^\Lambda \tag{77b}$$

$$\dot{\boldsymbol{\phi}}_{\mathrm{m}}^\Lambda = -\dot{\boldsymbol{C}}^\Lambda \,, \tag{77c}$$

the bare vertex $\boldsymbol{\gamma}_{4,\eta}^0 = \mp U$ corresponds to the Hubbard interaction (with the minus sign for $\eta = \mathrm{sc}, \mathrm{d}$ and the plus sign for $\eta = \mathrm{m}$), and the asymptotic vertex function $\bar{\boldsymbol{\mathcal{K}}}_{2,\eta}^\Lambda$ is related to $\boldsymbol{\mathcal{K}}_{2,\eta}^\Lambda$ by symmetry (see Appendix A). For local bare interactions, the only non-zero elements of the matrices $\dot{\boldsymbol{\mathcal{K}}}_{1,\eta}^\Lambda$ and $\boldsymbol{\gamma}_{4,\eta}^0$ correspond to both form factors being equal to zero, and of $\boldsymbol{\mathcal{K}}_{2,\eta}^\Lambda$ ($\bar{\boldsymbol{\mathcal{K}}}_{2,\eta}^\Lambda$) to a vanishing second (first) form factor.

The connection between the vertex asymptotics and the response function is shown by induction using the assumption

$$\boldsymbol{\gamma}_{4,\eta}^0 + \boldsymbol{\mathcal{K}}_{1,\eta}^\Lambda + \bar{\boldsymbol{\mathcal{K}}}_{2,\eta}^\Lambda = \alpha \boldsymbol{\gamma}_{3,\eta}^\Lambda(\omega, \nu, \mathbf{q}) \,. \tag{78}$$

For the initial condition, it holds $\boldsymbol{\gamma}_{3,\eta}^{\Lambda_{\mathrm{init}}} = \boldsymbol{\gamma}_{3,\eta}^0 = \mathbb{1}$. Since $\mathcal{K}_1^{\Lambda_{\mathrm{init}}}$ and $\mathcal{K}_2^{\Lambda_{\mathrm{init}}}$ both vanish, one has $\alpha = \boldsymbol{\gamma}_{4,\eta}^0 = \mp U \delta_{n,0}\delta_{n',0}$. Considering $(\boldsymbol{\gamma}_{4,\eta}^0 + \boldsymbol{\mathcal{K}}_{1,\eta}^\Lambda + \bar{\boldsymbol{\mathcal{K}}}_{2,\eta}^\Lambda)$ for an arbitrary value of Λ, we can identify the flow equation of the asymptotics with the one of γ_3, see Eq. (23a). Therefore Eq. (78) applies also for the following Λ step. As a consequence we can extract the fermion-boson vertex from the vertex asymptotics. Finally, inserting Eq. (78) into (75), we obtain the flow equation for the susceptibility (23a).

The s-wave fRG results for the susceptibility and the fermion-boson vertex can be extracted from the asymptotic vertex functions $\boldsymbol{\mathcal{K}}_{1,\eta}^\Lambda$ and $\bar{\boldsymbol{\mathcal{K}}}_{2,\eta}^\Lambda$ by dividing the s-wave form factor component by the bare interaction $\mp U$. Since $\boldsymbol{\gamma}_{4,\eta}^0$ vanishes for all other form factor combinations, other than s-wave response functions cannot be recovered by the asymptotics. This observation simplifies the fRG implementation, where the flow equations for χ and γ_3 can be omitted if only their s-wave components are needed.

D "Post-processed" flow equations for γ_3 and χ

In this section we explicitly provide the scale derivative of Eqs. (8) and (10) for the case in which the Σ and γ_4 entering the r.h.s. are obtained from the integration of the corresponding 1ℓ flow equations. We first consider Eq. (10) and, after introducing a Λ-dependence of the Green's functions and of γ_4 on the r.h.s., perform the full derivative with respect to Λ. For simplicity we here consider the magnetic vertex as example, which is directly related to the particle-hole crossed vertex by

$$\gamma_{4,\mathrm{m}}(q,k,k') = \gamma_{4,ph,\uparrow\uparrow}(q,k,k') - \gamma_{4,ph,\uparrow\downarrow}(q,k,k') = \gamma_{4,ph,\bar{\uparrow}\downarrow}(k'-k,k,k+q) = -\gamma_{4,\overline{ph},\uparrow\downarrow}(q,k,k') \,, \tag{79}$$

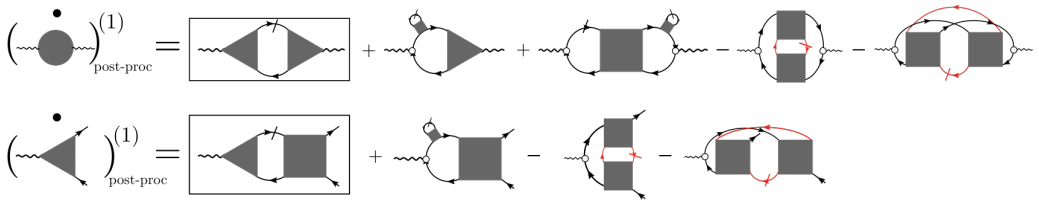

Figure 14: Diagrammatic representation of Eqs. (80) (first line) and (82) (second line), where the boxes indicate the conventional 1ℓ approximation. The internal loops in red provide the particle-hole and particle-particle contributions respectively. The empty dot represents the bare AF fermion-boson vertex $(\gamma^0_{3,\mathrm{m}})_{n,m} = \delta_{n,m}$.

where we used the SU(2) and crossing symmetries [31]. The derivative of the fermion-boson vertex with respect to Λ, as obtained from Eq. (10), reads

$$\begin{aligned}
\partial_\Lambda \left(\boldsymbol{\gamma}^\Lambda_{3,\mathrm{m}}\right)^{(1)}_{\text{post-proc}} =& \partial_\Lambda \left(\boldsymbol{\gamma}^0_{3,\mathrm{m}} + \boldsymbol{\gamma}^0_{3,\mathrm{m}} \circ \boldsymbol{\Pi}^\Lambda_{\mathrm{m}} \circ \boldsymbol{\gamma}^\Lambda_{4,\mathrm{m}}\right) \\
=& \boldsymbol{\gamma}^0_{3,\mathrm{m}} \circ \left(\dot{\boldsymbol{\Pi}}^{\Lambda,(1)}_{S,\mathrm{m}} + \dot{\tilde{\boldsymbol{\Pi}}}^{\Lambda,(1)}_{\mathrm{m}}\right) \circ \boldsymbol{\gamma}^\Lambda_{4,\mathrm{m}} + \boldsymbol{\gamma}^0_{3,\mathrm{m}} \circ \boldsymbol{\Pi}^\Lambda_{\mathrm{m}} \circ \dot{\boldsymbol{\gamma}}^{\Lambda,(1)}_{4,\mathrm{m}} \\
=& \boldsymbol{\gamma}^0_{3,\mathrm{m}} \circ \left(\dot{\boldsymbol{\Pi}}^{\Lambda,(1)}_{S,\mathrm{m}} + \dot{\tilde{\boldsymbol{\Pi}}}^{\Lambda,(1)}_{\mathrm{m}}\right) \circ \boldsymbol{\gamma}^\Lambda_{4,\mathrm{m}} - \\
& \boldsymbol{\gamma}^0_{3,\mathrm{m}} \circ \boldsymbol{\Pi}^\Lambda_{\mathrm{m}} \circ \left(\dot{\boldsymbol{C}}^{\Lambda,(1)} - \hat{\boldsymbol{C}}[\dot{\phi}^{\Lambda,(1)}_{ph}] - \hat{\boldsymbol{C}}[\dot{\phi}^{\Lambda,(1)}_{pp}]\right) \\
=& \boldsymbol{\gamma}^\Lambda_{3,\mathrm{m}} \circ \dot{\boldsymbol{\Pi}}^{\Lambda,(1)}_{S,\mathrm{m}} \circ \boldsymbol{\gamma}^\Lambda_{4,\mathrm{m}} + \boldsymbol{\gamma}^0_{3,\mathrm{m}} \circ \dot{\tilde{\boldsymbol{\Pi}}}^{\Lambda,(1)}_{\mathrm{m}} \circ \boldsymbol{\gamma}^\Lambda_{4,\mathrm{m}} - \boldsymbol{\gamma}^0_{3,\mathrm{m}} \circ \boldsymbol{\Pi}^\Lambda_{\mathrm{m}} \circ \hat{\boldsymbol{C}}[\dot{\phi}^{\Lambda,(1)}_{ph}] - \\
& \boldsymbol{\gamma}^0_{3,\mathrm{m}} \circ \boldsymbol{\Pi}^\Lambda_{\mathrm{m}} \circ \hat{\boldsymbol{C}}[\dot{\phi}^{\Lambda,(1)}_{pp}] \,, \qquad (80)
\end{aligned}$$

where for sake of conciseness we used a tensor-product form. In contrary to the definition in Sec. 3.2, the bubble $\boldsymbol{\Pi}^\Lambda_{S,\mathrm{m}}$ does not have the Katanin substitution [44] and we define $\dot{\tilde{\boldsymbol{\Pi}}}_{\mathrm{m}} = \dot{\boldsymbol{\Pi}}_{S\to G\dot{\Sigma}G,\mathrm{m}}$ in order to take care of the scale derivative in the self-energy. Further $\boldsymbol{\gamma}^0_{3,\mathrm{m}} = \mathbb{1}$, and $\hat{\boldsymbol{C}}[\dot{\phi}_\eta]$ stands for

$$\hat{C}[\dot{\phi}^\Lambda_{ph}]_{n,n'} = \int d\mathbf{k} d\mathbf{k}' f^*_n(\mathbf{k})\ f_{n'}(\mathbf{k}')\dot{\phi}^\Lambda_{ph}(k'-k,k,k+q) \qquad (81a)$$

$$\hat{C}[\dot{\phi}^\Lambda_{pp}]_{n,n'} = \int d\mathbf{k} d\mathbf{k}' f^*_n(\mathbf{k})\ f_{n'}(\mathbf{k}')\dot{\phi}^\Lambda_{pp}(q+k+k',k,k+q)\,. \qquad (81b)$$

The superscript (1) indicates that flowing objects (Σ and the ϕ's) are computed within 1ℓ from their corresponding differential equations. From the second to the third line of Eq. (80) we used Eq. (79) and the parquet decomposition in Eq. (32). The diagrammatic representation of the last line of Eq. (80) is shown in the first line of Fig. 14.

Let us now turn to Eq. (8) for the susceptibility, where we again restrict ourselves to the magnetic channel. Following the derivation of Eq. (80) one obtains

$$\begin{aligned}
\partial_\Lambda \left(\boldsymbol{\chi}^\Lambda_{\mathrm{m}}\right)^{(1)}_{\text{post-proc}} =& \partial_\Lambda \left(\boldsymbol{\gamma}^0_{3,\mathrm{m}} \circ \boldsymbol{\Pi}^\Lambda_{\mathrm{m}} \circ \boldsymbol{\gamma}^{\dagger,0}_{3,\mathrm{m}} + \boldsymbol{\gamma}^0_{3,\mathrm{m}} \circ \boldsymbol{\Pi}^\Lambda_{\mathrm{m}} \circ \boldsymbol{\gamma}^\Lambda_{4,\mathrm{m}} \circ \boldsymbol{\Pi}^\Lambda_{\mathrm{m}} \circ \boldsymbol{\gamma}^{\dagger,0}_{3,\mathrm{m}}\right) \\
=& \boldsymbol{\gamma}^\Lambda_{3,\mathrm{m}} \circ \dot{\boldsymbol{\Pi}}^{\Lambda,(1)}_{S,\mathrm{m}} \circ \boldsymbol{\gamma}^{\Lambda,\dagger}_{3,\mathrm{m}} + \\
& \boldsymbol{\gamma}^0_{3,\mathrm{m}} \circ \dot{\tilde{\boldsymbol{\Pi}}}^{\Lambda,(1)}_{\mathrm{m}} \circ \boldsymbol{\gamma}^{\Lambda,\dagger}_{3,\mathrm{m}} + \boldsymbol{\gamma}^0_{3,\mathrm{m}} \circ \boldsymbol{\Pi}^\Lambda_{\mathrm{m}} \circ \boldsymbol{\gamma}^\Lambda_{4,\mathrm{m}} \circ \dot{\tilde{\boldsymbol{\Pi}}}^{\Lambda,(1)}_{\mathrm{m}} \circ \boldsymbol{\gamma}^{\dagger,0}_{3,\mathrm{m}} - \\
& \boldsymbol{\gamma}^0_{3,\mathrm{m}} \circ \boldsymbol{\Pi}^\Lambda_{\mathrm{m}} \circ \hat{\boldsymbol{C}}[\dot{\phi}^{\Lambda,(1)}_{ph}] \circ \boldsymbol{\Pi}^\Lambda_{\mathrm{m}} \circ \boldsymbol{\gamma}^{\dagger,0}_{3,\mathrm{m}} - \\
& \boldsymbol{\gamma}^0_{3,\mathrm{m}} \circ \boldsymbol{\Pi}^\Lambda_{\mathrm{m}} \circ \hat{\boldsymbol{C}}[\dot{\phi}^{\Lambda,(1)}_{pp}] \circ \boldsymbol{\Pi}^\Lambda_{\mathrm{m}} \circ \boldsymbol{\gamma}^{\dagger,0}_{3,\mathrm{m}} \,, \qquad (82)
\end{aligned}$$

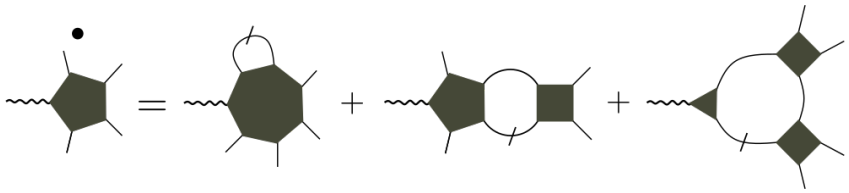

Figure 15: Simplified diagrammatic representation of the flow equation for γ_5^Λ illustrating the topological structure of the diagrams.

with the diagrammatic representation is provided in Fig. 14 (second line). One observes the appearance of additional terms on the r.h.s. of the post-processing flow equations for γ_3 and χ with respect to their standard 1ℓ equations, indicated by the boxes in Fig. 14. Besides the terms containing the Λ derivative of the self-energy (which are included in the Katanin corrections [44]), let us draw the attention to the last two diagrams appearing on the r.h.s. for both $\partial_\Lambda(\gamma_3^\Lambda)_{\text{post-proc}}$ and $\partial_\Lambda(\chi^\Lambda)_{\text{post-proc}}$. The diagrammatic structure in terms of loops is of second order for γ_3 and of third for χ. The integration of these post-processed flow equations, along with the 1ℓ flow equations for Σ and γ_4, would generate the last two diagrams already at the first integration step $\Lambda_{\text{init}} + d\Lambda$ (with $d\Lambda < 0$ in the Ω-flow), providing the following contribution to $\dot{\boldsymbol{\chi}}_{\text{m}}^{\Lambda_{\text{init}}}$

$$-\boldsymbol{\gamma}_{3,\text{m}}^{0} \circ \left(\boldsymbol{\Pi}_{\text{m}}^{\Lambda_{\text{init}}} \circ \hat{\boldsymbol{C}}[\dot{\phi}_{ph}^{\Lambda_{\text{init}}}] \circ \boldsymbol{\Pi}_{\text{m}}^{\Lambda_{\text{init}}} + \boldsymbol{\Pi}_{\text{m}}^{\Lambda_{\text{init}}} \circ \hat{\boldsymbol{C}}[\dot{\phi}_{pp}^{\Lambda_{\text{init}}}] \circ \boldsymbol{\Pi}_{\text{m}}^{\Lambda_{\text{init}}} \right) \circ \boldsymbol{\gamma}_{3,\text{m}}^{\dagger,0} \,. \tag{83}$$

The first term vanishes due to the Pauli principle ($\dot{\phi}_{ph}^{\Lambda_{\text{init}}} = 0$, see Ref. [33]), and the last one provides a negative contribution which reduces the 1ℓ term. In fact, the unscreened particle-particle bubble entering $\hat{C}[\dot{\phi}_{pp}^{\Lambda_{\text{init}}}]_{n,m}$ has the same sign of the unscreened (magnetic) $S-G$ bubble. This overall suppression by the additional 3ℓ-like terms is a general feature of the post-processed fRG scheme. The unbalance between the 1ℓ γ_4 flow, which topologically cuts part of the parquet diagrams, and the additional 3ℓ-like diagrams of the susceptibility flow, leads to an artificial overscreening of the conventional 1ℓ calculation. Analogous conclusions can be drawn for the density and superconducting channels. Thus one expects a pronounced effect in the secondary channels because the dominant channel enters the internal loop of one of the two 3ℓ-like additional diagrams, resulting in a reduction with respect to the converged data. In contrast, the dominant channel will not be affected that strongly, presenting only a slight overestimation of the post-processed susceptibility at the 1ℓ level (see Fig. 7). Moreover, since this overscreening affects all frequencies, it may be responsible for the unphysical negative value of the density susceptibility observed at finite frequencies in Fig. 8. In particular, since the parquet diagrams disregarded in the 1ℓ approximation depend on the cutoff, the detected unphysical results in the secondary channels were observed to be more severe for the interaction flow. We finally note that this opposite effect of the density and the superconducting channels with respect to the dominant magnetic channel has been observed also in Ref. [95] by analyzing the effect of the parquet decomposition of the vertex on the self-energy.

E Two-loop approximation for γ_3's flow equation

We here provide the derivation of the 2ℓ corrections to the conventional 1ℓ truncated flow equations. The derivation follows the scheme adopted for the flow equation of the two-particle vertex as reported in Ref. [16]. Our goal is to include the feedback of γ_5^Λ onto

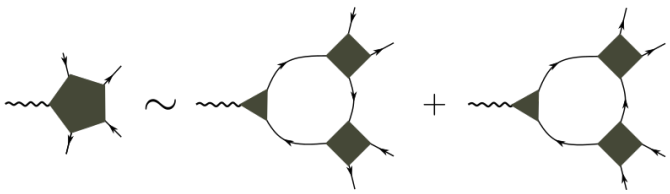

Figure 16: Diagrammatic contributions for γ_5^Λ up to the second oder in the effective interaction γ_4^Λ.

the flow equation for γ_3^Λ, see Eq. (74), at the second order in the effective interaction. From the derivation provided in Appendix B, one sees that the differential equation for γ_5^Λ is given by the sum of all diagrams which have the topological structure depicted in Fig. 15. The first and the second diagrams on the r.h.s. are at least of third order in the effective interaction since γ_7^Λ (depicted by a heptagon) and γ_5 (depicted by a pentagon) are at least $O((\gamma_4^\Lambda)^3)$ and $O((\gamma_4^\Lambda)^2)$, respectively. Therefore, we can restrict ourselves to diagrams with a topological structure of the third one. Its contribution can be obtained by taking the following functional derivative evaluated at zero fields

$$\partial_\Lambda \gamma_5^\Lambda(y, x_1', x_2, x_1, x_2) = \frac{\partial^5}{\partial J_\eta(y)\partial\bar{\phi}(x_1')\partial\bar{\phi}(x_2')\partial\phi(x_2)\partial\phi(x_1)} \Big[\frac{1}{3}\partial_{\Lambda,S}\mathrm{tr}\big(G^\Lambda\bar{\partial}\partial\Gamma^\Lambda G^\Lambda\bar{\partial}\partial\Gamma^\Lambda G^\Lambda\bar{\partial}\partial\Gamma^\Lambda\big) - \partial_{\Lambda,S}\mathrm{tr}\big(G^\Lambda\bar{\partial}\partial\Gamma^\Lambda G^\Lambda\bar{\partial}\bar{\partial}\Gamma^\Lambda G^{\Lambda,t}\partial\partial\Gamma^\Lambda\big)\Big]|_{J=\phi=0} \tag{84}$$

where $x = \{s, k\}$, $y = \{\eta, q\}$ and $\partial_{\Lambda,S}$ acts only on G^Λ and returns the single-scale propagator S^Λ. At this point we integrate the r.h.s. which is an easy operation once we take into account that i) one can replace $S^\Lambda = \partial_{\Lambda,S}G^\Lambda$ by the full derivative $\partial_\Lambda G^\Lambda$ since their difference due the derivative of the self-energy is of higher order in the effective interaction γ_4^Λ, and ii) one can let the scale derivative act also on γ_4^Λ since its derivative is at least of order $O((\gamma_4^\Lambda)^2)$. According to these arguments, the r.h.s. of Eq. (84) can be approximated by the total derivative with respect to the Λ and integrated to

$$\gamma_5^\Lambda(y, x_1', x_2, x_1, x_2) = \frac{\partial^5}{\partial J_\eta(y)\partial\bar{\phi}(x_1')\partial\bar{\phi}(x_2')\partial\phi(x_2)\partial\phi(x_1)} \Big[\frac{1}{3}\mathrm{tr}\big(G^\Lambda\bar{\partial}\partial\Gamma^\Lambda G^\Lambda\bar{\partial}\partial\Gamma^\Lambda G^\Lambda\bar{\partial}\partial\Gamma^\Lambda\big) - \mathrm{tr}\big(G^\Lambda\bar{\partial}\partial\Gamma^\Lambda G^\Lambda\bar{\partial}\bar{\partial}\Gamma^\Lambda G^{\Lambda,t}\partial\partial\Gamma^\Lambda\big)\Big]|_{J=\phi=0}\,. \tag{85}$$

The only terms surviving the functional derivative are all connected diagrams composed by two two-particle vertices γ_4^Λ and one fermion-boson vertex γ_3^Λ. What distinguishes the first and the second contributions of Eq. (85) is the position of γ_3^Λ which can be inserted at all $\bar{\partial}\partial$ in the first line, while is restricted to a single $\bar{\partial}\partial$ in the second one because of the conservation of Nambu particles. Moreover, the first term accounts for two-particle vertices whose external lines are always a particle and a hole, whereas in the second term they are attached to two particles $\partial\partial\Gamma^\Lambda$ and two holes $\bar{\partial}\bar{\partial}$, respectively. The topological structure of these two contributions is schematically shown in Fig. 16.

The last step consists in closing these diagrams in all possible ways by means of the single-scale propagator and adding them to the flow equation of γ_3^Λ. Hence, one obtains 2ℓ approximated flow equations for γ_3^Λ which contain terms of the order $O((\gamma_4^\Lambda)^2)$ in the

effective interaction. We can classify [16, 39] the 2ℓ corrections according to theit topological structure, with overlapping loops (Fig. 17 (b)) and non-overlapping loops (Fig. 17 (a)). We observe that the latter can be included in the 1ℓ equations by using the Katanin correction [44] where $S^\Lambda \to S^\Lambda + G^\Lambda \dot{\Sigma}^\Lambda G^\Lambda$. The remaining 2ℓ corrections have as building block the 1ℓ diagrams of the flow equation of γ_4^Λ. Translating our Nambu formalism to the physical fields, those corrections yield Eq. (24).

F Implementation details

Here we provide the explicit form of $\boldsymbol{\gamma}_{4,\{P,D,C\}}$ appearing on the r.h.s. of Eq. (36). By using the parquet decomposition in the diagrammatic channels (see Eq. (32)), the first contribution of the projections of the four-point vertex onto the different channels, is the projection of the fully two-particle irreducible vertex, approximated by its first order in the on-site Hubbard interaction U, onto the form-factor basis. The projected bare interaction is

$$\begin{aligned}[\hat{P}[U](i\omega_l, i\nu_o, i\nu_{o'}, \mathbf{q})]_{n,n'} &= [\hat{D}[U](i\omega_l, i\nu_o, i\nu_{o'}, \mathbf{q})]_{n,n'} \\ &= [\hat{C}[U](i\omega_l, i\nu_o, i\nu_{o'}, \mathbf{q})]_{n,n'} = -U\delta_{n,0}\delta_{n',0} \,. \end{aligned} \tag{86}$$

Secondly, every channel, written in its natural bosonic-fermionic notation on the l.h.s. of Eq. (36), need to be projected onto the complementary channels. The projection of one channel ϕ_r to another leads to a linear combination of its frequency arguments (see Eq. (22) for the physical channels and Eq. (90a) to Eq. (90f) for the diagrammatic channels). In momentum space, the projection is more involved due to the form factor dependence. Following the procedure of Ref. [30], we identify the projection matrices which describe the momentum translation from one channel to another using a matrix multiplication

$$[\hat{B}[\phi_{B'}](i\omega_l, i\nu_o, i\nu_{o'}, \mathbf{q})]_{n,n'} = \sum_{m,m',\mathbf{l}} A^{B,B'}_{n,n',m,m'}(\mathbf{l}, \mathbf{q}) B'_{m,m'}(\ldots, \mathbf{l}) \,, \tag{87}$$

where $\ldots$ stands for the channel specific translation of the frequency dependencies.

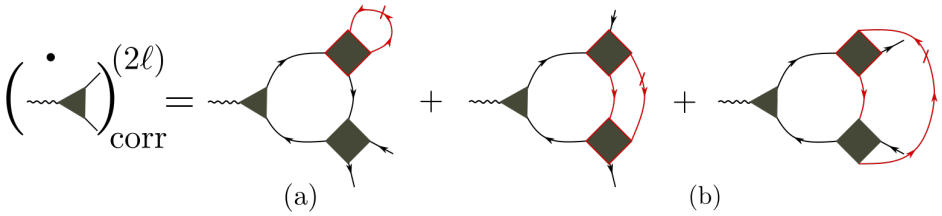

Figure 17: Simplified diagrammatic representation of the 2ℓ correcting diagrams for the flow equation of γ_3^Λ illustrating the topological structure of the diagrams. Diagram (a) can be reabsorbed in the single-scale propagator according to the "Katanin correction", while the second and the third contributions (b) represent the so-called "overlapping-diagrams".

We exemplify the projection for the channel D to P. In momentum space, it reads

$$\begin{aligned}[\hat{P}[\phi_{ph}](i\omega_l, i\nu_o, i\nu_{o'}, \mathbf{q})]_{n,n'} = &\int d\mathbf{k}d\mathbf{k}' f_n^*(\mathbf{k})\ f_{n'}(\mathbf{k}')\times \\ &\phi_{ph}\Big(i\omega_l - i\nu_{o'}, i\nu_o, i\nu_{o'}, \mathbf{q}-\mathbf{k}'-\mathbf{k}, \mathbf{k}, \mathbf{k}'\Big) \\ = &\sum_{m,m'}\int d\mathbf{k}d\mathbf{k}' f_n^*(\mathbf{k})\ f_{n'}(\mathbf{k}')\ f_m(\mathbf{k})\ f_{m'}^*(\mathbf{k}')\times \\ &D_{m,m'}(i\omega_l - i\nu_{o'}, i\nu_o, i\nu_{o'}, \mathbf{q}-\mathbf{k}'-\mathbf{k})\ . \end{aligned} \tag{88}$$

We now transform the form factors to real space and shift the momentum dependence in order to get the matrix form of (87)

$$\begin{aligned}[\hat{P}[\phi_{ph}](i\omega_l, i\nu_o, i\nu_{o'}, \mathbf{q})]_{n,n'} = \sum_{m,m'}\int_{-\pi}^{\pi} d\mathbf{K} \sum_{\mathbf{R}\mathbf{R_1}\mathbf{R_2}} e^{i\mathbf{l}\mathbf{R}-i\mathbf{q}\mathbf{R}} f_n^*(\mathbf{R}_1-\mathbf{R}) f_{n'}(\mathbf{R}_2+\mathbf{R})\times \\ f_m(\mathbf{R}_1) f_{m'}^*(\mathbf{R}_2) D_{m,m'}\Big(i\omega_l - i\nu_{o'} - i\nu_o, i\nu_o, i\nu_{o'}, \mathbf{l}\Big)\ . \end{aligned} \tag{89}$$

The same procedure for every channel projection leads to the matrix equations

$$[\hat{P}[\phi_{ph}](i\omega_l, i\nu_o, i\nu_{o'}, \mathbf{q})]_{n,n'} = \sum_{m,m',\mathbf{l}} A^{P,D}_{n,n',m,m'}(\mathbf{l},\mathbf{q}) D_{m,m'}\Big(i\omega_l - i\nu_{o'} - i\nu_o, i\nu_o, i\nu_{o'}, \mathbf{l}\Big) \tag{90a}$$

$$[\hat{P}[\phi_{\overline{ph}}](i\omega_l, i\nu_o, i\nu_{o'}, \mathbf{q})]_{n,n'} = \sum_{m,m',\mathbf{l}} A^{P,C}_{n,n',m,m'}(\mathbf{l},\mathbf{q}) C_{m,m'}\Big(-i\nu_o + i\nu_{o'}, i\nu_o, i\omega_l - i\nu_{o'}, \mathbf{l}\Big) \tag{90b}$$

$$[\hat{D}[\phi_{pp}](i\omega_l, i\nu_o, i\nu_{o'}, \mathbf{q})]_{n,n'} = \sum_{m,m',\mathbf{l}} A^{D,P}_{n,n',m,m'}(\mathbf{l},\mathbf{q}) P_{m,m'}\Big(i\omega_l + i\nu_o + i\nu_{o'}, i\nu_o, i\nu_{o'}, \mathbf{l}\Big) \tag{90c}$$

$$[\hat{D}[\phi_{\overline{ph}}](i\omega_l, i\nu_o, i\nu_{o'}, \mathbf{q})]_{n,n'} = \sum_{m,m',\mathbf{l}} A^{D,C}_{n,n',m,m'}(\mathbf{l},\mathbf{q}) C_{m,m'}\Big(i\nu_{o'} - i\nu_o, i\nu_o, i\nu_o + i\omega_l, \mathbf{l}\Big) \tag{90d}$$

$$[\hat{C}[\phi_{pp}](i\omega_l, i\nu_o, i\nu_{o'}, \mathbf{q})]_{n,n'} = \sum_{m,m',\mathbf{l}} A^{C,P}_{n,n',m,m'}(\mathbf{l},\mathbf{q}) P_{m,m'}\Big(i\omega_l + i\nu_o + i\nu_{o'}, i\nu_o, i\omega_l + i\nu_o, \mathbf{l}\Big) \tag{90e}$$

$$[\hat{C}[\phi_{ph}](i\omega_l, i\nu_o, i\nu_{o'}, \mathbf{q})]_{n,n'} = \sum_{m,m',\mathbf{l}} A^{C,D}_{n,n',m,m'}(\mathbf{l},\mathbf{q}) D_{m,m'}\Big(i\nu_{o'} - i\nu_o, i\nu_o, i\nu_o + i\omega_l, \mathbf{l}\Big) \tag{90f}$$

with the following projection matrices for the non-symmetrized notation

$$A^{P,D}_{n,n',m,m'}(\mathbf{l},\mathbf{q}) = \sum_{\mathbf{R}\mathbf{R_1}\mathbf{R_2}} e^{i\mathbf{l}\mathbf{R}-i\mathbf{q}\mathbf{R}} f^*_n(\mathbf{R}_1-\mathbf{R}) f_{n'}(\mathbf{R}_2+\mathbf{R}) f_m(\mathbf{R}_1) f^*_{m'}(\mathbf{R}_2) \tag{91a}$$

$$A^{P,C}_{n,n',m,m'}(\mathbf{l},\mathbf{q}) = \sum_{\mathbf{R}\mathbf{R_1}\mathbf{R_2}} e^{i\mathbf{l}\mathbf{R}+i\mathbf{q}\mathbf{R}_2} f^*_n(\mathbf{R}_1-\mathbf{R}) f_{n'}(-\mathbf{R}_2-\mathbf{R}) f_m(\mathbf{R}_1) f^*_{m'}(\mathbf{R}_2) \tag{91b}$$

$$A^{D,P}_{n,n',m,m'}(\mathbf{l},\mathbf{q}) = \sum_{\mathbf{R}\mathbf{R_1}\mathbf{R_2}} e^{i\mathbf{l}\mathbf{R}-i\mathbf{q}\mathbf{R}} f^*_n(\mathbf{R}_1+\mathbf{R}) f_{n'}(\mathbf{R}_2-\mathbf{R}) f_m(\mathbf{R}_1) f^*_{m'}(\mathbf{R}_2) \tag{91c}$$

$$A^{D,C}_{n,n',m,m'}(\mathbf{l},\mathbf{q}) = \sum_{\mathbf{R}\mathbf{R_1}\mathbf{R_2}} e^{i\mathbf{l}\mathbf{R}+i\mathbf{q}\mathbf{R}_2} f^*_n(\mathbf{R}_1-\mathbf{R}_2-\mathbf{R}) f_{n'}(-\mathbf{R}) f_m(\mathbf{R}_1) f^*_{m'}(\mathbf{R}_2) \tag{91d}$$

$$A^{C,P}_{n,n',m,m'}(\mathbf{l},\mathbf{q}) = \sum_{\mathbf{R}\mathbf{R_1}\mathbf{R_2}} e^{i\mathbf{l}\mathbf{R}+i\mathbf{q}(\mathbf{R_2}-\mathbf{R})} f^*_n(\mathbf{R}_1-\mathbf{R}) f_{n'}(\mathbf{R}-\mathbf{R}_2) f_m(\mathbf{R}_1) f^*_{m'}(\mathbf{R}_2) \tag{91e}$$

$$A^{C,D}_{n,n',m,m'}(\mathbf{l},\mathbf{q}) = \sum_{\mathbf{R}\mathbf{R_1}\mathbf{R_2}} e^{i\mathbf{l}\mathbf{R}+i\mathbf{q}\mathbf{R}_2} f^*_n(\mathbf{R}_1-\mathbf{R}_2-\mathbf{R}) f_{n'}(-\mathbf{R}) f_m(\mathbf{R}_1) f^*_{m'}(\mathbf{R}_2)\ . \tag{91f}$$

References

[1] W. Metzner, M. Salmhofer, C. Honerkamp, V. Meden and K. Schönhammer, *Functional renormalization group approach to correlated fermion systems*, Rev. Mod. Phys. **84**, 299 (2012), doi:10.1103/RevModPhys.84.299.

[2] C. Platt, W. Hanke and R. Thomale, *Functional renormalization group for multi-orbital Fermi surface instabilities*, Adv. Phys. **62**, 453 (2013), doi:10.1080/00018732.2013.862020.

[3] J. Sólyom, *The Fermi gas model of one-dimensional conductors*, Adv. Phys. **28**, 201 (1979), doi:10.1080/00018737900101375.

[4] C. Bourbonnais, B. Guay and R. Wortis, *Renormalization group technique for quasi-one-dimensional interacting Fermion systems at finite temperature*, eprint ArXiv:cond-mat/0204163 (2002).

[5] J. von Delft and H. Schoeller, *Bosonization for beginners — refermionization for experts*, Ann. Phys. **7**, 225 (1998), doi:10.1002/(SICI)1521-3889(199811)7:4<225::AID-ANDP225>3.0.CO;2-L.

[6] T. Giamarchi, *Quantum physics in one dimension*, Internat. Ser. Mono. Phys. Clarendon Press, Oxford (2004).

[7] E. Jeckelmann, *Ground-state phase diagram of a half-filled one-dimensional extended Hubbard model*, Phys. Rev. Lett. **89**, 236401 (2002), doi:10.1103/PhysRevLett.89.236401.

[8] T. Schäfer, F. Geles, D. Rost, G. Rohringer, E. Arrigoni, K. Held, N. Blümer, M. Aichhorn and A. Toschi, *Fate of the false Mott-Hubbard transition in two dimensions*, Phys. Rev. B **91**, 125109 (2015), doi:10.1103/PhysRevB.91.125109.

[9] G. Rohringer and A. Toschi, *Impact of nonlocal correlations over different energy scales: A dynamical vertex approximation study*, Phys. Rev. B **94**, 125144 (2016), doi:10.1103/PhysRevB.94.125144.

[10] A. Georges, G. Kotliar, W. Krauth and M. J. Rozenberg, *Dynamical mean-field theory of strongly correlated fermion systems and the limit of infinite dimensions*, Rev. Mod. Phys. **68**, 13 (1996), doi:10.1103/RevModPhys.68.13.

[11] G. Kotliar, S. Y. Savrasov, K. Haule, V. S. Oudovenko, O. Parcollet and C. A. Marianetti, *Electronic structure calculations with dynamical mean-field theory*, Rev. Mod. Phys. **78**, 865 (2006), doi:10.1103/RevModPhys.78.865.

[12] K. Held, *Electronic structure calculations using dynamical mean field theory*, Adv. Phys. **56**, 829 (2007), doi:10.1080/00018730701619647.

[13] T. Maier, M. Jarrell, T. Pruschke and M. H. Hettler, *Quantum cluster theories*, Rev. Mod. Phys. **77**, 1027 (2005), doi:10.1103/RevModPhys.77.1027.

[14] G. Rohringer, H. Hafermann, A. Toschi, A. A. Katanin, A. E. Antipov, M. I. Katsnelson, A. I. Lichtenstein, A. N. Rubtsov and K. Held, *Diagrammatic routes to nonlocal correlations beyond dynamical mean field theory*, Rev. Mod. Phys. **90**, 025003 (2018), doi:10.1103/RevModPhys.90.025003.

[15] S. Uebelacker and C. Honerkamp, *Multiband effects on superconducting instabilities driven by electron-electron interactions*, Phys. Rev. B **85**, 155122 (2012), doi:10.1103/PhysRevB.85.155122.

[16] A. Eberlein, *Fermionic two-loop functional renormalization group for correlated fermions: Method and application to the attractive Hubbard model*, Phys. Rev. B **90**, 115125 (2014), doi:10.1103/PhysRevB.90.115125.

[17] A. Eberlein and W. Metzner, *Superconductivity in the two-dimensional t-t$'$-Hubbard model*, Phys. Rev. B **89**, 035126 (2014), doi:10.1103/PhysRevB.89.035126.

[18] A. Eberlein, W. Metzner, S. Sachdev and H. Yamase, *Fermi surface reconstruction and drop in the Hall number due to spiral Antiferromagnetism in high-T_c cuprates*, Phys. Rev. Lett. **117**, 187001 (2016), doi:10.1103/PhysRevLett.117.187001.

[19] J. Lichtenstein, S. A. Maier, C. Honerkamp, C. Platt, R. Thomale, O. K. Andersen and L. Boeri, *Functional renormalization group study of an eight-band model for the iron arsenides*, Phys. Rev. B **89**, 214514 (2014), doi:10.1103/PhysRevB.89.214514.

[20] M. M. Scherer, S. Uebelacker and C. Honerkamp, *Instabilities of interacting electrons on the honeycomb bilayer*, Phys. Rev. B **85**, 235408 (2012), doi:10.1103/PhysRevB.85.235408.

[21] M. M. Scherer, S. Uebelacker, D. D. Scherer and C. Honerkamp, *Interacting electrons on trilayer honeycomb lattices*, Phys. Rev. B **86**, 155415 (2012), doi:10.1103/PhysRevB.86.155415.

[22] C. Taranto, S. Andergassen, J. Bauer, K. Held, A. Katanin, W. Metzner, G. Rohringer and A. Toschi, *From infinite to two dimensions through the functional renormalization group*, Phys. Rev. Lett. **112**, 196402 (2014), doi:10.1103/PhysRevLett.112.196402.

[23] W. Metzner, *Functional renormalization group approach to interacting fermi systems: DMFT as a booster rocket. Chapter 11*, vol. 4, Verlag des Forschungszentrum Jülich (2015).

[24] A. Toschi, A. Katanin and K. Held, *Dynamical vertex approximation: A step beyond dynamical mean-field theory*, Phys. Rev. B **75**, 45118 (2007), doi:10.1103/PhysRevB.75.045118.

[25] A. N. Rubtsov, M. I. Katsnelson and A. I. Lichtenstein, *Dual fermion approach to nonlocal correlations in the Hubbard model*, Phys. Rev. B **77**, 033101 (2008), doi:10.1103/PhysRevB.77.033101.

[26] N. Wentzell, C. Taranto, A. Katanin, A. Toschi and S. Andergassen, *Correlated starting points for the functional renormalization group*, Phys. Rev. B **91**, 045120 (2015), doi:10.1103/PhysRevB.91.045120.

[27] C. Husemann and M. Salmhofer, *Efficient parametrization of the vertex function, Ω scheme, and the t, t' Hubbard model at van Hove filling*, Phys. Rev. B **79**, 195125 (2009), doi:10.1103/PhysRevB.79.195125.

[28] K.-U. Giering and M. Salmhofer, *Self-energy flows in the two-dimensional repulsive Hubbard model*, Phys. Rev. B **86**, 245122 (2012), doi:10.1103/PhysRevB.86.245122.

[29] W.-S. Wang, Z.-Z. Li, Y.-Y. Xiang and Q.-H. Wang, *Competing electronic orders on kagome lattices at van Hove filling*, Phys. Rev. B **87**, 115135 (2013), doi:10.1103/PhysRevB.87.115135.

[30] J. Lichtenstein, S. Sanchez de la Peña, D. Rohe, E. Di Napoli, C. Honerkamp and S. Maier, *High-performance functional renormalization group calculations for interacting fermions*, Comput. Phys. Commun. **213**, 100 (2017), doi:10.1016/j.cpc.2016.12.013.

[31] G. Rohringer, A. Valli and A. Toschi, *Local electronic correlation at the two-particle level*, Phys. Rev. B **86**, 125114 (2012), doi:10.1103/PhysRevB.86.125114.

[32] G. Li, N. Wentzell, P. Pudleiner, P. Thunström and K. Held, *Efficient implementation of the parquet equations: Role of the reducible vertex function and its kernel approximation*, Phys. Rev. B **93**, 165103 (2016), doi:10.1103/PhysRevB.93.165103.

[33] N. Wentzell, G. Li, A. Tagliavini, C. Taranto, G. Rohringer, K. Held, A. Toschi and S. Andergassen, *High-frequency asymptotics of the vertex function: Diagrammatic parametrization and algorithmic implementation*, eprint ArXiv:cond-mat/1610.06520 (2016).

[34] C. Honerkamp, M. Salmhofer, N. Furukawa and T. M. Rice, *Breakdown of the Landau-Fermi liquid in two dimensions due to umklapp scattering*, Phys. Rev. B **63**, 035109 (2001), doi:10.1103/PhysRevB.63.035109.

[35] Zanchi, D., *Angle-resolved loss of Landau quasiparticles in 2D Hubbard model*, Europhys. Lett. **55**, 376 (2001), doi:10.1209/epl/i2001-00413-7.

[36] C. Honerkamp, *Electron-doping versus hole-doping in the 2D t-t' Hubbard model*, Eur. Phys. J. B **21**, 81 (2001), doi:10.1007/PL00011117.

[37] C. Honerkamp and M. Salmhofer, *Flow of the quasiparticle weight in the N-patch renormalization group scheme*, Phys. Rev. B **67**, 174504 (2003), doi:10.1103/PhysRevB.67.174504.

[38] D. Rohe and W. Metzner, *Pseudogap at hot spots in the two-dimensional Hubbard model at weak coupling*, Phys. Rev. B **71**, 115116 (2005), doi:10.1103/PhysRevB.71.115116.

[39] A. A. Katanin, A. P. Kampf and V. Y. Irkhin, *Anomalous self-energy and Fermi surface quasisplitting in the vicinity of a ferromagnetic instability*, Phys. Rev. B **71**, 085105 (2005), doi:10.1103/PhysRevB.71.085105.

[40] C. Husemann, K.-U. Giering and M. Salmhofer, *Frequency-dependent vertex functions of the (t,t') Hubbard model at weak coupling*, Phys. Rev. B **85**, 075121 (2012), doi:10.1103/PhysRevB.85.075121.

[41] S. Uebelacker and C. Honerkamp, *Self-energy feedback and frequency-dependent interactions in the functional renormalization group flow for the two-dimensional Hubbard model*, Phys. Rev. B **86**, 235140 (2012), doi:10.1103/PhysRevB.86.235140.

[42] A. Eberlein, *Self-energy effects in functional renormalization group flows of the two-dimensional $t-t'$ Hubbard model away from van Hove filling*, Phys. Rev. B **92**, 235146 (2015), doi:10.1103/PhysRevB.92.235146.

[43] D. Vilardi, C. Taranto and W. Metzner, *Nonseparable frequency dependence of the two-particle vertex in interacting fermion systems*, Phys. Rev. B **96**, 235110 (2017), doi:10.1103/PhysRevB.96.235110.

[44] A. A. Katanin, *Fulfillment of Ward identities in the functional renormalization group approach*, Phys. Rev. B **70**, 115109 (2004), doi:10.1103/PhysRevB.70.115109.

[45] N. E. Bickers, *Self-consistent many-body theory for condensed matter systems*, pp. 237–296, Springer New York, New York, NY, ISBN 978-0-387-21717-8, doi:10.1007/0-387-21717-7_6 (2004).

[46] V. Janiš , *Stability of self-consistent solutions for the Hubbard model at intermediate and strong coupling*, Phys Rev. B **60**, 11345 (1999), doi:10.1103/PhysRevB.60.11345.

[47] S. X. Yang, H. Fotso, J. Liu, T. A. Maier, K. Tomko, E. F. D'Azevedo, R. T. Scalettar, T. Pruschke and M. Jarrell, *Parquet approximation for the 4×4 Hubbard cluster*, Phys. Rev. E **80**, 046706 (2009), doi:10.1103/PhysRevE.80.046706.

[48] K.-M. Tam, H. Fotso, S.-X. Yang, T.-W. Lee, J. Moreno, J. Ramanujam and M. Jarrell, *Solving the parquet equations for the Hubbard model beyond weak coupling*, Phys. Rev. E **87**, 013311 (2013), doi:10.1103/PhysRevE.87.013311.

[49] A. Valli, T. Schäfer, P. Thunström, G. Rohringer, S. Andergassen, G. Sangiovanni, K. Held and A. Toschi, *Dynamical vertex approximation in its parquet implementation: Application to Hubbard nanorings*, Phys. Rev. B **91**, 115115 (2015), doi:10.1103/PhysRevB.91.115115.

[50] C. Taranto, *Diagrammatic methods beyond DMFT*, Ph.D. thesis, Vienna University of Technology (2014).

[51] N. E. Bickers and D. J. Scalapino, *Critical behavior of electronic parquet solutions*, Phys. Rev. B **46**, 8050 (1992), doi:10.1103/PhysRevB.46.8050.

[52] A. A. Katanin, *Two-loop functional renormalization group approach to the one- and two-dimensional Hubbard model*, Phys. Rev. B **79**, 235119 (2009), doi:10.1103/PhysRevB.79.235119.

[53] S. A. Maier and C. Honerkamp, *Effective three-particle interactions in low-energy models for multiband systems*, Phys. Rev. B **85**, 064520 (2012), doi:10.1103/PhysRevB.85.064520.

[54] F. B. Kugler and J. von Delft, *Multi-loop functional renormalization group for general models*, Phys. Rev. B **97**, 035162 (2018), doi:10.1103/PhysRevB.97.035162.

[55] F. B. Kugler and J. von Delft, *Multiloop functional renormalization group that sums up all parquet diagrams*, Phys. Rev. Lett. **120**, 057403 (2018), doi:10.1103/PhysRevLett.120.057403.

[56] F. B. Kugler and J. von Delft, *Derivation of exact flow equations from the self-consistent parquet relations*, eprint arXiv:cond-mat/1807.02898 (2018).

[57] C. J. Halboth and W. Metzner, *Renormalization-group analysis of the two-dimensional Hubbard model*, Phys. Rev. B **61**, 7364 (2000), doi:10.1103/PhysRevB.61.7364.

[58] T. Ayral and O. Parcollet, *Mott physics and spin fluctuations: A unified framework*, Phys. Rev. B **92**, 115109 (2015), doi:10.1103/PhysRevB.92.115109.

[59] F. Kugler and J. von Delft, Unpublished (2018).

[60] M. Salmhofer and C. Honerkamp, *Fermionic renormalization group flows technique and theory*, Progr. Theor. Exp. Phys. **105**, 1 (2001), doi:10.1143/PTP.105.1.

[61] P. Kopietz, L. Bartosch and F. Schütz, *Introduction to the Functional Renormalization Group (Lecture Notes in Physics)*, Springer, Berlin, ISBN 364205093X (2010).

[62] F. Schütz, L. Bartosch and P. Kopietz, *Collective fields in the functional renormalization group for fermions, Ward identities, and the exact solution of the Tomonaga-Luttinger model*, Phys. Rev. B **72**, 035107 (2005), doi:10.1103/PhysRevB.72.035107.

[63] F. B. Kugler and J. von Delft, *Fermi-edge singularity and the functional renormalization group*, J. Phys. Condens. Matter **30**, 195501 (2018), doi:10.1088/1361-648X/aaba2e.

[64] N. E. Bickers, *Parquet equations for numerical self-consistent-field theory*, Int. J. Mod. Phys. B **05**, 253 (1991), doi:10.1142/s021797929100016x.

[65] S. A. Maier, J. Ortloff and C. Honerkamp, *Multiorbital effects in the functional renormalization group: A weak-coupling study of the Emery model*, Phys. Rev. B **88**, 1 (2013), doi:10.1103/PhysRevB.88.235112.

[66] D. S. de la Peña, J. Lichtenstein and C. Honerkamp, *Competing electronic instabilities of extended Hubbard models on the honeycomb lattice: A functional renormalization group calculation with high wavevector resolution*, Phys. Rev. B **95**, 085143 (2016), doi:10.1103/PhysRevB.95.085143.

[67] A. Auerbach, *Interacting electrons and quantum magnetism*, Springer-Verlag (1994).

[68] P. Fazekas, *Lecture notes on electron correlation and magnetism*, World Scientific (1999).

[69] S. White, D. Scalapino, R. Sugar, E. Y. Loh, J. Gubernatis and R. Scalettar, *Numerical study of the two-dimensional Hubbard model*, Phys. Rev. B **40** (1989), doi:10.1103/PhysRevB.40.506.

[70] J. P. F. LeBlanc, A. E. Antipov, F. Becca, I. W. Bulik, G. K.-L. Chan, C.-M. Chung, Y. Deng, M. Ferrero, T. M. Henderson, C. A. Jiménez-Hoyos, E. Kozik, X.-W. Liu *et al.*, *Solutions of the two-dimensional Hubbard model: Benchmarks and results from a wide range of numerical algorithms*, Phys. Rev. X **5**, 041041 (2015), doi:10.1103/PhysRevX.5.041041.

[71] N. D. Mermin and H. Wagner, *Absence of ferromagnetism or antiferromagnetism in one- or two-dimensional isotropic Heisenberg models*, Phys. Rev. Lett. **17**, 1133 (1966), doi:10.1103/PhysRevLett.17.1133.

[72] Y. M. Vilk and A.-M. S. Tremblay, *Non-perturbative many-body approach to the Hubbard model and single-particle pseudogap*, J. Phys. I France **7**, 1309 (1997), doi:10.1051/jp1:1997135.

[73] D. Zanchi and H. J. Schulz, *Weakly correlated electrons on a square lattice: Renormalization-group theory*, Phys. Rev. B **61**, 13609 (2000), doi:10.1103/PhysRevB.61.13609.

[74] A. A. Katanin and A. P. Kampf, *Quasiparticle anisotropy and pseudogap formation from the weak-coupling renormalization group point of view*, Phys. Rev. Lett. **93**, 106406 (2004), doi:10.1103/PhysRevLett.93.106406.

[75] C. Honerkamp, D. Rohe, S. Andergassen and T. Enss, *Interaction flow method for many-fermion systems*, Phys. Rev. B **70**, 235115 (2004), doi:10.1103/PhysRevB.70.235115.

[76] Y. M. Vilk and A.-M. S. Tremblay, *Destruction of Fermi-liquid quasiparticles in two dimensions by critical fluctuations*, EPL **33**, 159 (1996), doi:10.1209/epl/i1996-00315-2.

[77] K. Borejsza and N. Dupuis, *Antiferromagnetism and single-particle properties in the two-dimensional half-filled Hubbard model: A nonlinear sigma model approach*, Phys. Rev. B **69**, 085119 (2004), doi:10.1103/PhysRevB.69.085119.

[78] J. Otsuki, H. Hafermann and A. I. Lichtenstein, *Superconductivity, antiferromagnetism, and phase separation in the two-dimensional Hubbard model: A dual-fermion approach*, Phys. Rev. B **90**, 235132 (2014), doi:10.1103/PhysRevB.90.235132.

[79] T. Schäfer, A. A. Katanin, K. Held and A. Toschi, *Quantum criticality with a twist - interplay of correlations and Kohn anomalies in three dimensions*, Phys. Rev. Lett. **119**, 046402 (2017), doi:10.1103/PhysRevLett.119.046402.

[80] T. Baier, E. Bick and C. Wetterich, *Temperature dependence of antiferromagnetic order in the Hubbard model*, Phys. Rev. B **70**, 125111 (2004), doi:10.1103/PhysRevB.70.125111.

[81] E. G. C. P. van Loon, H. Hafermann and M. I. Katsnelson, *Precursors of the insulating state in the square-lattice Hubbard model*, Phys. Rev. B **97**, 085125 (2018), doi:10.1103/PhysRevB.97.085125.

[82] C. J. Halboth and W. Metzner, *d-Wave superconductivity and Pomeranchuk instability in the two-dimensional Hubbard model*, Phys. Rev. Lett. **85**, 5162 (2000), doi:10.1103/PhysRevLett.85.5162.

[83] C. Honerkamp, H. C. Fu and D.-H. Lee, *Phonons and d-wave pairing in the two-dimensional Hubbard model*, Phys. Rev. B **75**, 014503 (2007), doi:10.1103/PhysRevB.75.014503.

[84] C. Karrasch, R. Hedden, R. Peters, T. Pruschke, K. Schönhammer and V. Meden, *A finite-frequency functional renormalization group approach to the single impurity Anderson model*, J. Phys. Condens. Matter **20**, 345205 (2008), doi:10.1088/0953-8984/20/34/345205.

[85] K.-M. Tam, S.-W. Tsai, D. K. Campbell and A. H. Castro Neto, *Retardation effects in the Holstein-Hubbard chain at half filling*, Phys. Rev. B **75**, 161103 (2007), doi:10.1103/PhysRevB.75.161103.

[86] K.-M. Tam, S.-W. Tsai, D. K. Campbell and A. H. Castro Neto, *Phase diagram of the Holstein-Hubbard two-leg ladder using a functional renormalization-group method*, Phys. Rev. B **75**, 195119 (2007), doi:10.1103/PhysRevB.75.195119.

[87] T. Schäfer, G. Rohringer, O. Gunnarsson, S. Ciuchi, G. Sangiovanni and A. Toschi, *Divergent precursors of the Mott-Hubbard transition at the two-particle level*, Phys. Rev. Lett. **110**, 246405 (2013), doi:10.1103/PhysRevLett.110.246405.

[88] T. Schäfer, S. Ciuchi, M. Wallerberger, P. Thunström, O. Gunnarsson, G. Sangiovanni, G. Rohringer and A. Toschi, *Nonperturbative landscape of the Mott-Hubbard transition: Multiple divergence lines around the critical endpoint*, Phys. Rev. B **94**, 235108 (2016), doi:10.1103/PhysRevB.94.235108.

[89] P. Chalupa, P. Gunacker, T. Schäfer, K. Held and A. Toschi, *Divergences of the irreducible vertex functions in correlated metallic systems: Insights from the Anderson impurity model*, Phys. Rev. B **97**, 245136 (2018), doi:10.1103/PhysRevB.97.245136.

[90] S. Andergassen, T. Enss, V. Meden, W. Metzner, U. Schollwöck and K. Schönhammer, *Functional renormalization group for Luttinger liquids with impurities*, Phys. Rev. B **70**, 075102 (2004), doi:10.1103/PhysRevB.70.075102.

[91] G. Rohringer, *New routes towards a theoretical treatment of nonlocal electronic correlations*, Ph.D. thesis, Vienna University of Technology (2013).

[92] M. Salmhofer, C. Honerkamp, W. Metzner and L. Oliver, *Renormalization group flows into phases with broken symmetry*, Prog. Theor. Phys. **112**, 943 (2004), doi:10.1143/PTP.112.943.

[93] R. Gersch, C. Honerkamp and W. Metzner, *Superconductivity in the attractive Hubbard model: Functional renormalization group analysis*, New J. Phys. **10**, 045003 (2008), doi:10.1088/1367-2630/10/4/045003.

[94] C. Wetterich, *Exact evolution equation for the effective potential*, Phys. Lett. B **301**, 90 (1993), doi:10.1016/0370-2693(93)90726-X.

[95] O. Gunnarsson, T. Schäfer, J. P. F. LeBlanc, J. Merino, G. Sangiovanni, G. Rohringer and A. Toschi, *Parquet decomposition calculations of the electronic self-energy*, Phys. Rev. B **93**, 245102 (2016), doi:10.1103/PhysRevB.93.245102.

IV Detecting a preformed pair phase: Response to a pairing forcing field

Detecting a preformed pair phase: Response to a pairing forcing field

A. Tagliavini,[1] M. Capone,[2] and A. Toschi[1]
[1]*Institute for Solid State Physics, Vienna University of Technology, 1040 Vienna, Austria*
[2]*International School for Advanced Studies (SISSA), Via Bonomea 265, I-34136 Trieste, Italy*
(Received 9 May 2016; revised manuscript received 9 September 2016; published 10 October 2016)

The normal state of strongly coupled superconductors is characterized by the presence of "preformed" Cooper pairs well above the superconducting critical temperature. In this regime, the electrons are paired, but they lack the phase coherence necessary for superconductivity. The existence of preformed pairs implies the existence of a characteristic energy scale associated with a pseudogap. Preformed pairs are often invoked to interpret systems where some signatures of pairing are present without actual superconductivity, but an unambiguous theoretical characterization of a preformed-pair system is still lacking. To fill this gap, we consider the response to an external pairing field of an attractive Hubbard model, which hosts one of the cleanest realizations of a preformed pair phase, and a repulsive model where s-wave superconductivity cannot be realized. Using dynamical mean-field theory to study this response, we identify the characteristic features which distinguish the reaction of a preformed pair state from a normal metal without any precursor of pairing. The theoretical detection of preformed pairs is associated with the behavior of the *second* derivative of the order parameter with respect to the external field, as confirmed by analytic calculations in limiting cases. Our findings provide a solid test bed for the interpretation of state-of-the-art calculations for the normal state of the doped Hubbard model in terms of d-wave preformed pairs and, in perspective, of nonequilibrium experiments in high-temperature superconductors.

DOI: 10.1103/PhysRevB.94.155114

I. INTRODUCTION

In many complex materials and quantum systems we witness the persistence of fingerprints of superconductivity well above the critical temperature and clearly distinct from fluctuation phenomena. This often leads to a possible interpretation in terms of electron pairs which are formed at very large temperature but they can condense only at a much lower critical temperature due to the phase fluctuations of their wave function. Yet, the unambiguous detection of preformed pairs is elusive, as it does not correspond to an actual phase transition and it cannot be unambiguously associated with a direct observable quantity.

The prototypical realization of this physics takes place in model systems with strong pairing interaction, which drives the formation of tightly bound pairs with a reduced phase coherence. In this regime, superconductivity occurs as a Bose-Einstein condensation (BEC) of composite bosons formed by the bound pairs of fermions. When the pairing strength is tuned from weak to strong coupling one observes a continuous crossover from the familiar BCS [1] pairing to this regime.

This BCS-BEC crossover [2–6] has been intensively studied, both in the context of cold atoms trapped in optical lattices [7] and in high-temperature superconductivity, where a preformed pair regime has been invoked [8–12] for the pseudogap state [13,14] of underdoped cuprates.

In this work we use the attractive Hubbard model as a theoretical device to set a *practical protocol* to confirm or disprove the existence of preformed pairs in a specific system under analysis. Comparing regimes where s-wave preformed pairs are certainly present or certainly absent, we identify which properties of the system are so sensitive to their presence to be exploited for their detection. Such an identification will also be applicable to interpret existing analyses of the pseudogap phase in the cuprates [15–17].

We have structured our paper as follows: In Sec. II, we briefly discuss the modelization of the problem, in terms of the single-band (attractive) Hubbard Hamiltonian, and briefly review some of the previous dynamical mean-field theory (DMFT) studies in the absence of an external field. In Sec. III, we report our DMFT results in the presence of a forcing field at different temperatures and interactions, comparing explicitly the attractive and repulsive models. The physical interpretation of our numerical results in terms of the underlying ground-state properties is given in Sec. IV. In Sec. V we discuss the implication of this criterion in a broader context, while in Sec. VI we present our conclusions.

II. MODELIZATION OF THE PROBLEM

Throughout this paper we will consider a simple Hubbard model in the presence of an external field driving an s-wave superconducting order parameter:

$$H = -t \sum_{\langle ij\rangle\sigma} c^{\dagger}_{i\sigma} c_{j\sigma} + U \sum_{i} n_{i\uparrow} n_{i\downarrow} - \mu \sum_{i\sigma} n_{i\sigma} - \eta \sum_{i} (c^{\dagger}_{i\uparrow} c^{\dagger}_{i\downarrow} + \text{H.c.}). \quad (1)$$

Here, t represents the nearest-neighbor amplitude, μ is the chemical potential, and the effective interaction U is negative for the *attractive* and positive for the *repulsive* Hubbard model. The last contribution in Eq. (1) represents the coupling of the system to a forcing, time-independent pairing field η, which is assumed to be positive and isotropic (s wave).

In more than two dimensions the attractive Hubbard model displays a low-temperature s-wave superconductivity, smoothly evolving from a weak-coupling (BCS) regime to a strong-coupling BEC regime with increasing U [18]. In the latter regime, pairs are formed at a very high temperature of order U, while they can only condense at a much lower temperature $T = T_c \propto \frac{1}{U}$ because of the large phase fluctuations which contrast the formation of a coherent condensate [2]. In the BCS regime, superconductivity is stabilized by a potential energy

gain, while the superconductor has a (slightly) higher kinetic energy than the normal state. In the BEC regime the energetic balance is the opposite: The superconductor is stabilized by a kinetic energy gain with a slight potential energy loss with respect to the normal state [18].

Given the s-wave nature of the pairs and the local nature of the interactions, much of the physics for $d > 2$ can be well captured by dynamical mean-field theory (DMFT) [19], an approach where spatial fluctuations are frozen, but the local dynamics is included nonperturbatively at every value of the interaction strength. DMFT becomes formally exact in the limit of infinite coordination [20] of the lattice but it can be used as an approximation in finite dimensions, where it provides a fully nonperturbative description. This represents a major advantage to analyze weak- and strong-coupling regimes on equal footing. Previous DMFT studies [18,21–23] have focused on spectral, thermodynamic properties, and even on some nonequilibrium properties [24]. Here we consider a different aspect, namely the response to an external stimulus which drives a superconducting s-wave pairing, also beyond the linear-response regime.

For the sake of definiteness we consider a semicircular density of states $N(\epsilon) = \frac{2}{\pi D^2}\sqrt{D^2 - \epsilon^2}$ (D being its half-bandwidth) which is suitable to represent a finite-bandwidth system in DMFT. To solve the auxiliary impurity problem of DMFT we adopted an exact diagonalization (ED) solver with $n_s = 5$ sites (one impurity and $n_b = 4$ bath electronic sites), and tested the stability of the results by increasing the number of sites in the most relevant intermediate-coupling/low-temperature regime. Obviously, due to the external pairing field in Eq. (1), the DMFT treatment has to be extended to the broken-symmetry phase, by recasting DMFT in Nambu formalism (see, e.g., [22]).

In this section we set up the stage by presenting refined results for the unperturbed attractive Hubbard model. In this way we identify concretely weak-, intermediate-, and strong-coupling regions whose definition will be helpful to guide the discussion of the following sections.

Figure 1 shows the energy difference between the superconducting and the normal state $\Delta E_{tot} = E_S - E_N$ (resolved in its kinetic and potential energy components) in different interaction regimes for two significant choices of the electron density: $n = 1$ (half filling) and $n = 0.5$ (quarter filling). We consider a low value of the temperature $\beta = 50D^{-1}$ which is significantly below T_c for the broad range of $|U|$ used in the figure. Moreover, we verified that discretization effects associated with a finite bath size of the ED solver are negligible.

Our findings are summarized by the different colors in the diagrams, which mark the different regimes (BCS: blue; intermediate: violet; BEC: red). Figure 1 shows that a qualitative change of the energetic balance with respect to BCS only takes place when $U \simeq 2D$, where a narrow intermediate region, in which the superconductor gains both potential and kinetic energy, starts. At $U \simeq 2.5D$ a BEC regime is established. This evolution of the energetic balance tracks the progressive formation of preformed pairs in the normal state. These results provide a more accurate determination of the boundaries found in Ref. [18]. We also notice that the results for $n = 1$ and $n = 0.5$ are remarkably similar. This observation shows how weakly the physics of the attractive

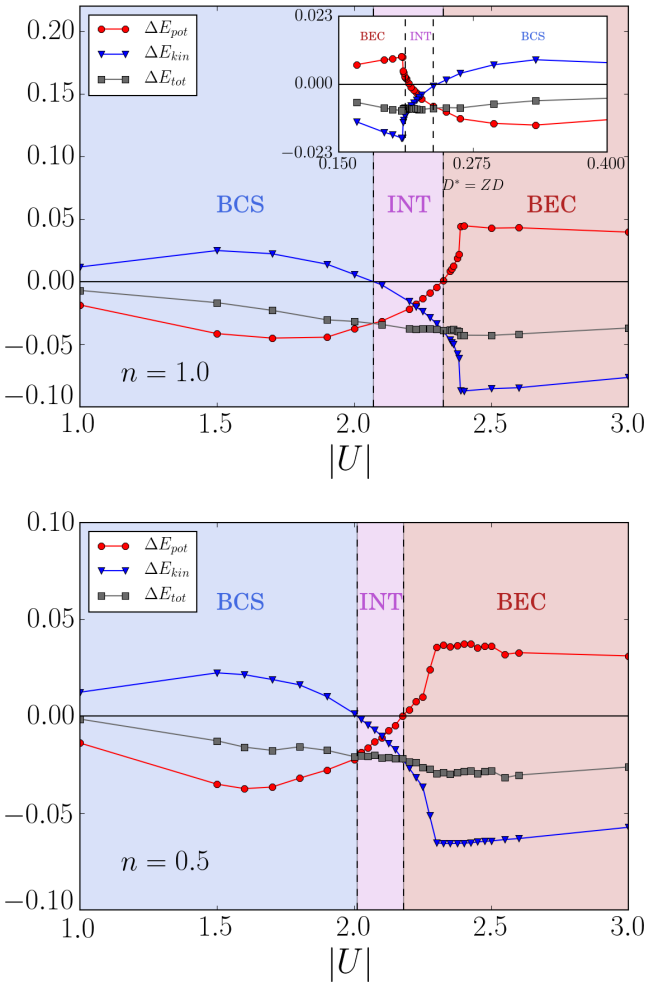

FIG. 1. Energy balance $\Delta E_{tot} = E_S - E_N$ (and its kinetic and potential components) computed in the superconducting region at $\beta = 50D^{-1}$ as a function of the attractive interaction U. The upper panel refers to the half-filled ($n = 1$) case, while the lower panel refers to the electron density $n = 0.5$. Inset: The same but for the Hamiltonian of Eq. (2), where the energies have been scaled in order to keep the attractive interaction constant ($\lambda = -0.5$) and let the bandwidth vary as a more realistic effect of the correlation and/or doping.

Hubbard model depends on doping. For this reason we will mainly focus in the following on the half-filled case, which has an important practical advantage for our calculations, which are performed in the grand-canonical ensemble, where the chemical potential is the independent variable. The half-filling condition is indeed obtained by enforcing particle-hole symmetry, which corresponds to $\mu = U/2$. For any other filling, the corresponding chemical potential and its dependence on U are not known analytically and they must be found numerically. We however show explicitly that our findings are general by performing a set of calculations for $n = 0.5$. Analogous DMFT characterizations also hold for magnetic phases, in particular for the "sibling" crossover from a Slater to an Heisenberg antiferromagnet, as explicitly shown by recent DMFT [25] and dynamical cluster approximation (DCA) [26] results.

In this work the attractive Hubbard is not introduced as a microscopic description of any realistic material, but as a simple tool for the detection of preformed pairs. However, the energetic analysis we just summarized was suggested as a possible explanation of the spectral weight changes observed in the optical conductivity on the cuprates [27–38]. Evidently any attempt in this direction must include at least qualitatively the effect of strong repulsive correlations, which mainly control the doping dependence of the cuprate phase diagram. Thus, if one wanted to use Eq. (1) with $U = -\lambda < 0$ for a rough investigation of these specific features in the cuprate physics, one should account for the doping dependence of the quasiparticle properties. This can be achieved by renormalizing the kinetic term by means of the quasiparticle weight Z, while leaving at first approximation the effective attractive interaction unchanged:

$$H = -Z\,t \sum_{\langle ij\rangle,\sigma} c^{\dagger}_{i\sigma} c_{j\sigma} - \lambda \sum_{i} n_{i\uparrow} n_{i\downarrow} - \mu \sum_{i} (n_{i\uparrow} + n_{i\downarrow}). \tag{2}$$

Here the effective bandwidth $D^* = 2Zt$ decreases as we reduce the hole doping and vanishes at the Mott transition $Z \to 0$ as $x \to 0$, while the attractive interaction λ is taken as a constant. Such a simple assumption is explicitly realized, e.g., in realistic modeling of the strongly correlated superconductivity in fullerides [39,40]. As for the energetic balance this amounts to a rescaling in the previous plot, whose effects are reported in the inset of Fig. 1: The results of this a "more physical" approach to the problem do not change the qualitative picture, making, however, the energetic balance between the BCS and the BEC regimes overall more symmetric.

III. DMFT RESULTS IN THE PRESENCE OF A FORCING FIELD

In this section we will apply a "theoretical probe" to investigate the preformed pair physics: We will study the superconducting response induced by a *finite* forcing pairing field, also *beyond* the linear response regime. We will compute by means of DMFT the s-wave superconducting order parameter $\Delta = \frac{1}{N}\sum_i \langle c_{i\downarrow} c_{i\uparrow}\rangle$ as a function of the external field η at different interaction couplings (U) and inverse temperatures ($\beta = 1/T$). We detail our analysis in the half-filling case, where particle-hole symmetry strongly reduces the time required by the calculations, and then we extend our investigation to a less symmetric case away from half filling, specifically for $n = 0.5$ (quarter filling).

A. Half-filling study ($n = 1.0$)

As a first step, we follow the evolution of $\Delta(\eta)$ in the attractive case ($U < 0$) across the critical temperature at weak- and strong-coupling regimes (according to the classification of Sec. II). This evolution shows the expected appearance of a finite Δ for $\eta = 0$ below T_c and the divergence of the slope of $\Delta(\eta)$ for $\eta \to 0^+$ (which coincides with the linear-response pairing susceptibility) approaching T_c from above (see Fig. 2).

These obvious features are a direct consequence of a second-order phase transition and could, thus, hide the preformed-pair physics. Hence, in the following analysis, we will choose a sufficiently high temperature $T = 1/7D$ (i.e., $T \gg T_c$ for the selected U) to be safely in the normal state and to mitigate the impact of the underlying phase transition on the low-η behavior of $\Delta(\eta)$.

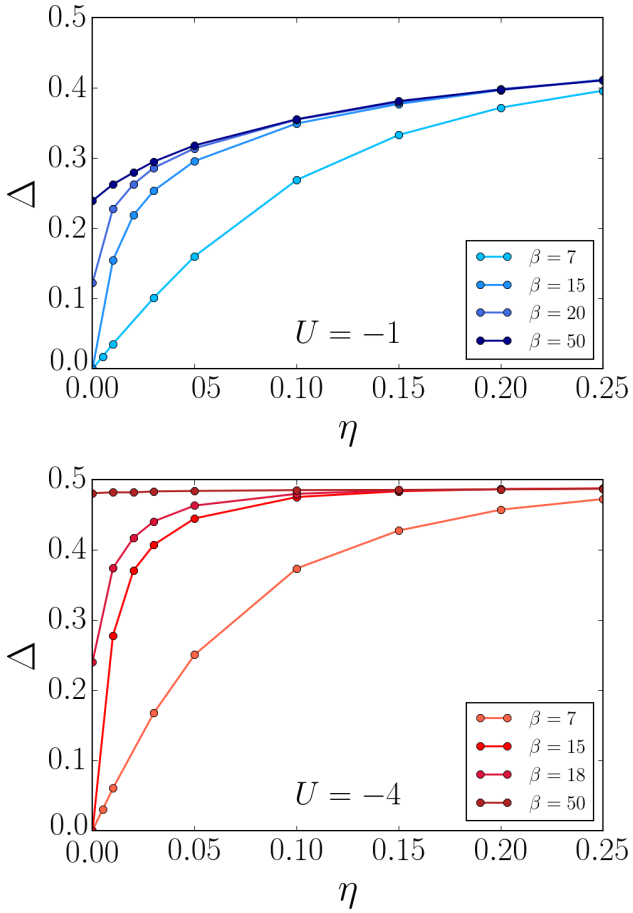

FIG. 2. Superconducting s-wave order parameter for two different values of the on-site attractive interaction, namely, $U = -1$ and $U = -4$, and for different β values at half filling.

The corresponding results are shown in Fig. 3 (left panel), where the exact result for the atomic limit ($t = 0$) is also reported for comparison. For all U values from weak to strong coupling and in the atomic limit $\Delta(\eta)$ saturates to 1/2 by increasing η. Physically, this reflects the fact that, due to the attractive interaction in the s-wave channel, the system responds promptly to the forcing pairing field: the slope of $\Delta(\eta)$ assumes the largest value for $\eta \to 0^+$ and decreases monotonically with η.

Mathematically, this means that $\Delta(\eta)$ is a *concave* function for the whole interval $\eta \in (0,\infty)$, i.e.,

$$\frac{d^2\Delta(\eta)}{d\eta^2} < 0 \quad \forall\, \eta > 0. \tag{3}$$

We note that this general property is totally unaffected by the specific behavior of the linear response regime (slope for $\eta \to 0^+$), whose quantitative change as a function of U mostly reflects a different proximity to T_c, which is maximum at intermediate coupling [18,41], very close to the reported

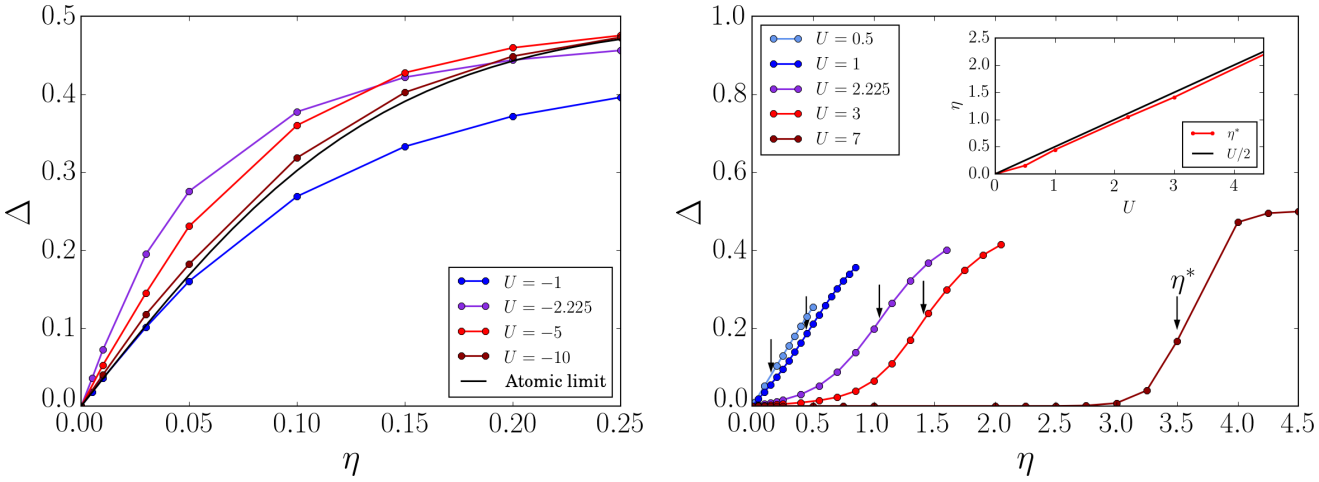

FIG. 3. Superconducting s-wave order parameter $\Delta = \frac{1}{N}\sum_i \langle c_{i\downarrow} c_{i\uparrow}\rangle$ as a function of the forcing pairing field η in the attractive (left panel) and the repulsive (right panel) Hubbard model (half-filling case). Here all the quantities are expressed in units of the half-bandwidth D. The black line on the right panel refers to the analytic behavior in the atomic limit at $\beta = 7$ [see Eq. (9)].

value of $U/D = -2.225$. This is exemplified in Fig. 4 where we perform the same analysis but for a *local* pairing field η_{loc} and detecting the local order parameter. Here the small-η slope, being proportional to the local pairing susceptibility, is unaffected by the proximity to the second-order phase transition, and it monotonically approaches the atomic limit result. Nevertheless, the curvature of the second-order derivative is the same as the one of the uniform-field case.

In order to understand the physical meaning of Eq. (3), and to exploit it for a preformed-pairs probing beyond our work, we provide a comparative DMFT study of the opposite situation, where our external pairing field η contrasts the underlying spontaneously ordered phase of the system at low T. This can be realized repeating the same analysis for the *repulsive* ($U > 0$) Hubbard model. The corresponding results are shown in Fig. 3 (right panel), where—as before—the s-wave superconducting order parameter is plotted as a function

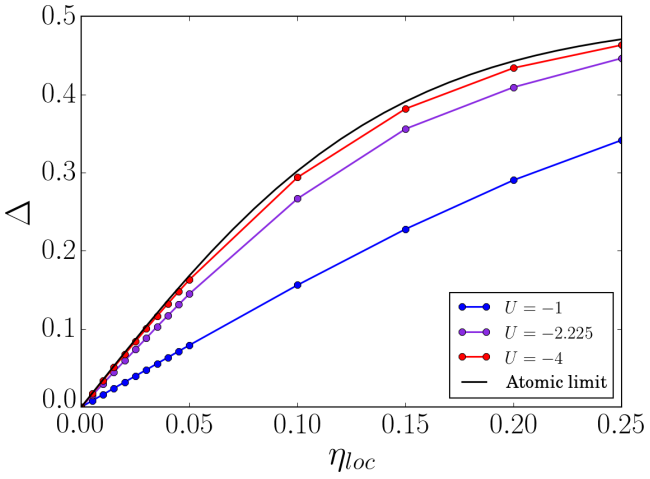

FIG. 4. Local superconducting s-wave order parameter $\Delta = \frac{1}{N}\sum_i \langle c_{i\downarrow} c_{i\uparrow}\rangle$ as a function of the local forcing pairing field η_{loc} in the attractive Hubbard model. The black line provides the analytic behavior in the atomic limit case at $U = -7$ and $\beta = 7$ [see Eq. (9)].

of the pairing field η for the same high temperature ($\beta = 7D^{-1}$). The DMFT behavior of $\Delta(\eta)$ shows quantitative and qualitative differences between the attractive and the repulsive case. The first difference concerns the linear response to the pairing field, which is progressively suppressed by increasing the strength of the repulsive interaction.

Yet, this difference should be considered—from our perspective—only quantitative: Since the linear response is crucially affected by the proximity to the second-order phase transition, it *always* becomes progressively smaller going farther away from the transition (e.g., for the attractive case by increasing T, or for the repulsive case by increasing U). Hence, its absolute value is not *per se* informative about the presence of preformed pairs in the system.

The behavior of the second derivative of $\Delta(\eta)$, instead, is qualitatively richer than in the attractive case (Fig. 3): For small values of η, the second derivative has a positive sign [i.e., $\Delta(\eta)$ is a *convex* function], up to an inflection point η^* (marked by a vertical arrow in the picture). For $\eta > \eta^*$ the curvature becomes negative and $\Delta(\eta)$ becomes concave, approaching eventually the regime value $\Delta = 0.5$.

As a first, heuristic interpretation of this difference, we observe that the appearance of a region with a *convex* curvature at low η reflects the *defiance* of the ($U > 0$) system against the formation of the s-wave pairs induced by the field. Very large fields instead simply override the repulsive interaction leading to the formation of pairs.

This implies a quite general rule of thumb: If, by applying a finite pairing field η to a system of interest, one observes an initial *convex* curvature of the corresponding superconducting response, the presence of an underlying preformed pair physics (with the same symmetry of the pairing field) can be ruled out. In fact, on the basis of our model results, an inspection of sign changes of the second derivative of $\Delta(\eta)$ should provide a good test for detecting the *absence* of preformed pair physics. This rule of thumb, which represents one of the main outcomes of our study, will be applied to the more realistic d-wave pairing in the pseudogap regime of the Hubbard model in Sec. V.

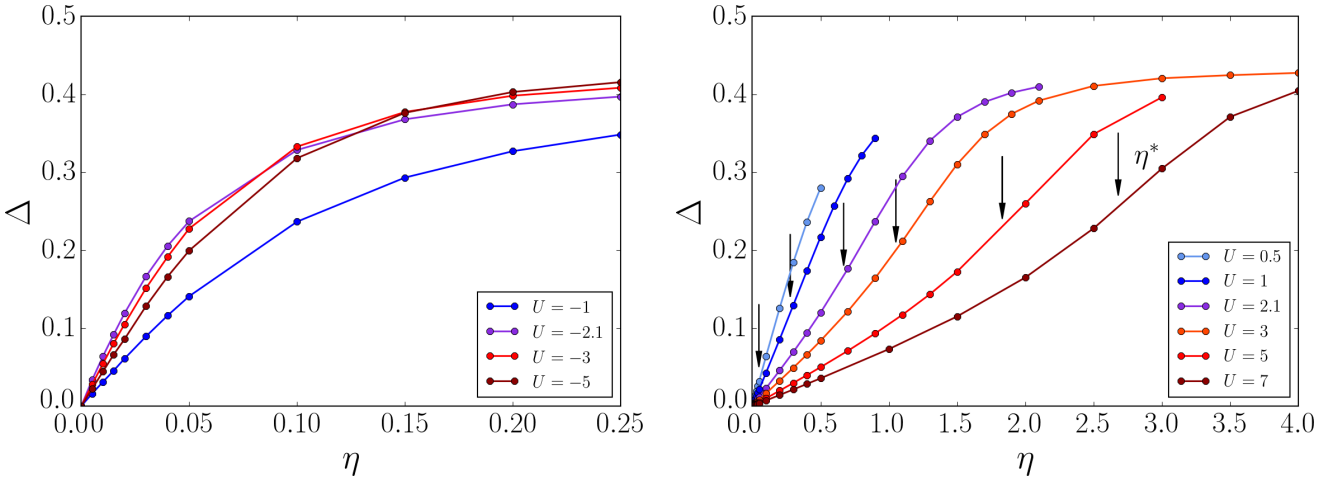

FIG. 5. Superconducting s-wave order parameter $\Delta = \frac{1}{N}\sum_i \langle c_{i\downarrow} c_{i\uparrow}\rangle$ as a function of the forcing pairing field η in the attractive (left panel) and the repulsive (right panel) Hubbard model (at quarter filling). The values of the pairing field corresponding to the inflection point are marked by black arrows.

Before proceeding, however, we should recall that only the first derivative of $\Delta(\eta)$ (and, rigorously, only in the limiting case of $\eta \to 0^+$) has a standard interpretation within the linear response theory. Hence, we need to formalize our heuristic understanding of the curvature of $\Delta(\eta)$ more precisely. This will be done in the next section by investigating explicitly, in relevant limiting cases, the relation between the nature of the ground state of the system and its "defying" response to the pairing field.

B. Quarter-filling study ($n = 0.5$)

The calculations we have presented so far have been performed on the half-filled model. In this section, we repeat the same analysis in the "less symmetric", but more generic, situation of quarter filling ($n = 0.5$).

In Fig. 5 we show the evolution of the s-wave superconducting order parameter Δ as a function for the external field η in the attractive (left panel) and the repulsive (right panel) Hubbard model. In both cases, we observe the same qualitative behavior found at half filling in Fig. 3, with an overall concave $\Delta(\eta)$ for $U < 0$, and an inflection point at η^* for $U > 0$.

The differences with respect to the half-filling case are merely qualitative: For $U < 0$, a weakened response at small η is observed, which is consistent with the suppression of the superconducting order at low densities and with the corresponding atomic limit analysis in Appendix B. For $U > 0$, we find a reduction of η^* with respect to half filling, also consistent with our atomic limit analysis, and coherent with the expected progressive reduction of the effects of the electronic repulsion away from half filling.

Thus, our DMFT analysis at $n = 0.5$, supported by the corresponding atomic limit study in Appendix B, confirms the robustness of the behavior of $\Delta(\eta)$ in a broad range of model parameters and, consequently, the validity of our study also away from the particle-hole symmetric case.

IV. ANALYSIS OF LIMITING CASES

Aiming at extracting the physical information encoded in the second derivative of the superconducting order parameter, we perform an investigation of the simplest limiting cases, i.e., noninteracting ($U = 0$), atomic limit ($t = 0$), and the two-site model, where a full analytical treatment is possible.

We start with the noninteracting case which can be diagonalized in momentum space:

$$H = \sum_{\mathbf{k}\sigma} \epsilon_{\mathbf{k}} c^\dagger_{\mathbf{k}\sigma} c_{\mathbf{k}\sigma} - \eta \sum_{\mathbf{k}} (c^\dagger_{\mathbf{k}\uparrow} c^\dagger_{-\mathbf{k}\downarrow} + c_{-\mathbf{k}\downarrow} c_{\mathbf{k}\uparrow}), \qquad (4)$$

where $\epsilon_{\mathbf{k}}$ represents the free-particle energy dispersion. Because of the presence of the static field η, one immediately recognizes the formal analogy with the BCS mean field. After a few algebraic steps (see Appendix A), one obtains

$$\Delta(\eta) = \frac{\eta}{\pi D^2} \int_{-D}^{D} d\epsilon \frac{\sqrt{D^2 - \epsilon^2}}{\sqrt{\epsilon^2 + \eta^2}} \tanh\left(\frac{\beta\sqrt{\epsilon^2 + \eta^2}}{2}\right). \qquad (5)$$

While this integral can be computed numerically, it is insightful to study its behavior in the zero and high-temperature regimes for a small pairing field ($\eta \ll 1$ and $\beta\sqrt{\eta^2 + \epsilon^2} \ll 1$). In the first case, we have

$$\Delta(\eta)|_{T=0} = \frac{2\eta}{\pi}\left[\int_0^\eta d\epsilon \frac{\sqrt{1-\epsilon^2}}{\sqrt{\epsilon^2+\eta^2}} + \int_\eta^1 d\epsilon \frac{\sqrt{1-\epsilon^2}}{\sqrt{\epsilon^2+\eta^2}}\right] \simeq \frac{2\eta}{\pi}\left[\frac{\eta^2}{2} + \ln(2) - \ln(\eta)\right]. \qquad (6)$$

Hence, at $T = U = 0$, the first derivative exhibits a positive logarithmic divergence as $\eta \to 0$, which is readily understood by looking at the noninteracting problem in the limit of vanishing interaction ($U/D \to 0$). Since T_c decreases exponentially as $U \to 0$ [1], the noninteracting pair susceptibility at $U = 0$ must diverge exactly at $T = 0$. In the opposite, high-temperature regime, the expansion of the Fermi function as $\beta\sqrt{\eta^2 + \epsilon^2} \ll 1$ yields

$$\Delta(\eta) \simeq \frac{\beta}{4}\eta - \frac{\beta^2\eta}{4\pi}\int_0^1 d\epsilon \sqrt{1-\epsilon^2}\sqrt{\epsilon^2+\eta^2}. \qquad (7)$$

As the second integral is always positive, we obtain an overall *negative* value of the second derivative of Δ, which vanishes

only for $\eta \to 0$. The study of the noninteracting case is not fully conclusive in itself, but it already indicates that a *negative* curvature of $\Delta(\eta)$ does not provide an unambiguous indication of an underlying preformed pair physics, certainly absent in our model for $U = 0$.

Further insights can be gained by considering the atomic limit ($t = 0$) of Eq. (1). Here, the superconducting order parameter assumes the following expression (see Appendix B):

$$\Delta(\eta) = \frac{\eta}{2\,\epsilon}\,\frac{\sinh(\beta\epsilon)}{\cosh(\beta\epsilon) + e^{\beta\frac{U}{2}}}, \tag{8}$$

where $\epsilon = \sqrt{\mu^2 + \eta^2}$. In particular, Eq. (8) further simplifies at half filling:

$$\Delta_{\text{att}}(\eta) = \frac{1}{2}\,\frac{\sinh(\beta\eta)}{\cosh(\beta\eta) + e^{-\beta\frac{|U|}{2}}}, \tag{9}$$

$$\Delta_{\text{rep}}(\eta) = \frac{1}{2}\,\frac{\sinh(\beta\eta)}{\cosh(\beta\eta) + e^{\beta\frac{|U|}{2}}}, \tag{10}$$

whose dependence on η, at different temperatures, is plotted in Fig. 6 both for the attractive and the repulsive case. By exploiting a (rather rough) resemblance of the $\Delta(\eta)$ curves to the corresponding DMFT results of Fig. 3, we progress in clarifying the physical meaning of the second derivative of $\Delta(\eta)$. In particular, let us now focus on the repulsive atomic case, whose $\Delta(\eta)$ displays an inflection point at $\eta^* = U/2$, in a somewhat similar fashion to the DMFT results. We observe that the inflection point η^* is exactly associated with a corresponding change of the ground state. By diagonalizing the Hamiltonian (see Appendix B), a crossing of energy levels occurs exactly at $\eta^* = U/2$: For $\eta < \eta^*$ the lowest energy eigenvalue is achieved in the (degenerate) subspace $\{|\uparrow\rangle, |\downarrow\rangle\}$ describing an (isolated) magnetic moment, while for $\eta > \eta^*$, the ground state becomes $\frac{|\uparrow\downarrow\rangle + |0\rangle}{\sqrt{2}}$, i.e., a doubly/empty occupied state. Hence, the curvature of the superconducting response, as a function of the pairing field, provides direct information about the ground-state properties of the system and, in particular, about the presence or the absence of pairs.

The simplest way to verify to what extent these results hold, also for *finite* electron hopping, is to consider a two-site model. Here the Hilbert space is spanned by 16 basis vectors and the matrix can be readily diagonalized (see Appendix C), allowing us to exactly compute the ground-state vector and Δ (Fig. 7) as a function of η.

The agreement with DMFT obviously improves with respect to the atomic limit and an inflection point at η^* remains well visible. The broadening around the inflection point is no longer just a mere effect of the temperature as in the atomic case, but it results from the interplay between the magnetic moment and pair formation tendencies of the ground state. Such interplay is—evidently—affected by the hopping term, as also happens for the DMFT results.

Also in this case we relate $\Delta(\eta)$, and specifically, the value of its inflection point η^*, to the corresponding evolution of the system's ground state. For the latter, in the presence of the pairing field η, we obtain

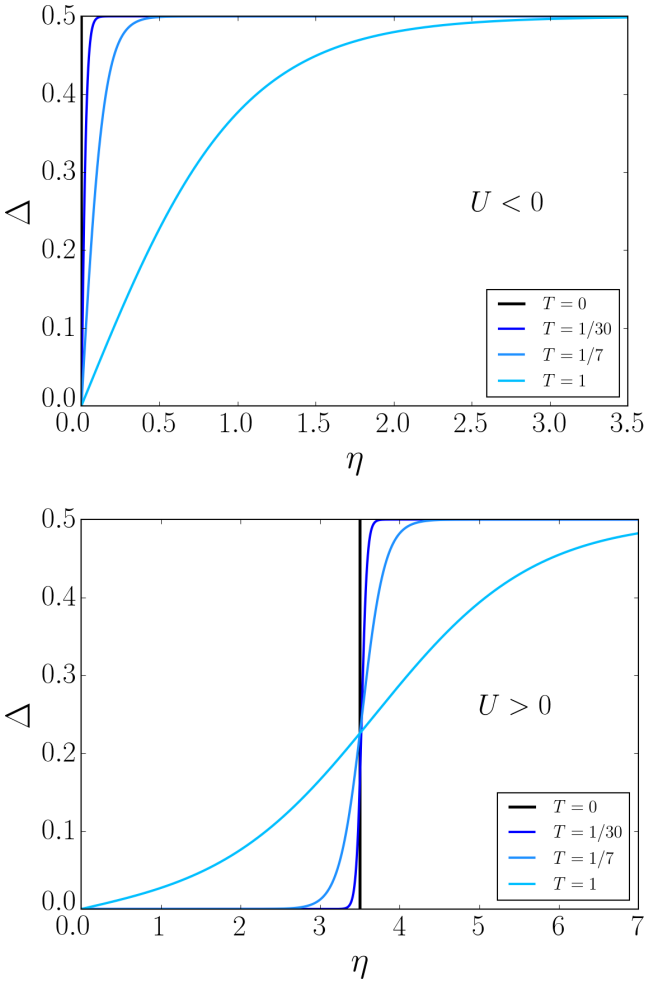

FIG. 6. Analytic behavior in the atomic limit of the superconducting order parameter $\Delta = \frac{1}{N}\sum_i \langle c_{i\downarrow} c_{i\uparrow}\rangle$ with respect to the forcing pairing field η in the attractive (upper panel) and in the repulsive (lower panel) Hubbard model for $U = -7$ (and $U = 7$ in the repulsive case) and different temperature values [see Eqs. (9) and (10)].

$$|\text{GS}\rangle = \alpha\left(\frac{|\uparrow,\downarrow\rangle - |\downarrow,\uparrow\rangle}{\sqrt{2}}\right) + \beta\left(\frac{|\uparrow\downarrow,0\rangle + |0,\uparrow\downarrow\rangle}{\sqrt{2}}\right) + \gamma\left(\frac{|0,0\rangle + |\uparrow\downarrow,\uparrow\downarrow\rangle}{\sqrt{2}}\right), \tag{11}$$

where the coefficients α, β, γ vary continuously as a function of the field η and the interaction strength U. The first term of Eq. (11) represents a singlet state over the two sites while the two remaining terms feature empty and double occupations. Intuitively, the singlet state could be linked to the presence of a localized magnetic moment (with antiferromagnetic tendency) in the ground state, while the other states contain localized ("preformed") pairs.

The explicit dependence of the squared amplitude of α, β, γ is shown in Fig. 8 as a function of the pairing field and for different values of the interaction U: The coefficients show a smooth evolution as a function of η which becomes sharper by increasing the interaction, before recovering the

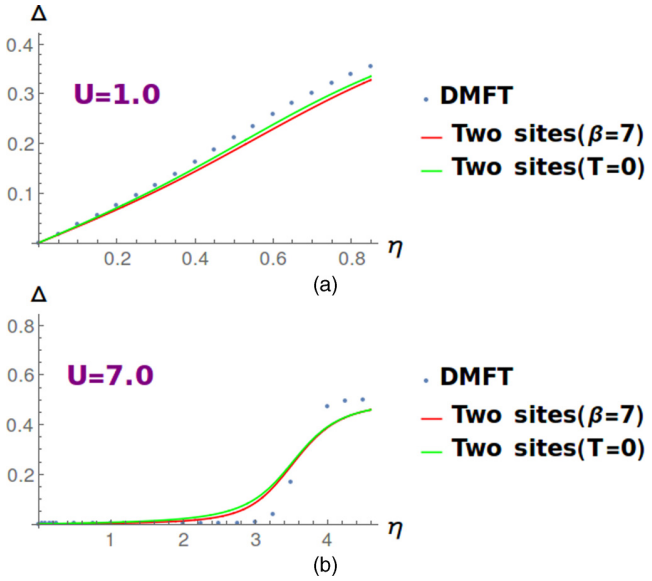

FIG. 7. Superconducting order parameter $\Delta(\eta) = \frac{1}{N}\sum_i \langle c_{i\downarrow} c_{i\uparrow}\rangle$ as a function of η: comparison between the DMFT results at $\beta = 7D^{-1}$ and the two-site results for $T = 0$ (green line) and $\beta = 7D^{-1}$ (red line).

step function of the atomic limit for $U \to \infty$. For any given value of U, $|\alpha|^2$ monotonically increases with η, while $|\beta|^2$ and $|\gamma|^2$ decrease, reflecting the progressively enhanced weight of "pairs" (doubly occupied sites) induced by the pairing field.

By reporting the corresponding values of the inflection point η^* (as extracted by the data of Fig. 7) we find that η^* occurs in correspondence of the value of $|\alpha|^2 = 0.5$ (marked by dashed line in the figure) in the intermediate- and strong-coupling regimes ($U = 3$ and $U = 7$). This reflects the fact that, *also* in the two-site model, the sign change of the second derivative of $\Delta(\eta)$ marks a change of the prevalent character of the ground state. This is dominated by localized magnetic moments ($|\alpha|^2 > 0.5 > |\beta|^2 + |\gamma|^2$) for $\eta < \eta^*$, i.e., where the curvature of $\Delta(\eta)$ is convex. On the other hand, local ("preformed") pairs prevail ($|\alpha|^2 < 0.5 < |\beta|^2 + |\gamma|^2$) for $\eta > \eta^*$, i.e., where a concave curvature of $\Delta(\eta)$ occurs. Our microscopic analysis confirms thus the link between the curvature of $\Delta(\eta)$ with the tendency of the system to contrast or to favor the driven superconducting state.

From a quantitative perspective, one should note that in the weak-coupling regime [$U = 1$, Fig. 8(a)], the inflection point η^* is slightly before the coefficient $|\alpha|^2$ crosses the value 0.5; i.e., at $\eta = \eta^*$ one finds an $|\alpha|^2$ slightly larger than 0.5. While this weak-coupling feature might be a specific result of the two-site model, its presence does not compromise the validity of our interpretation. This can be better understood looking at Fig. 10, where the physics of the two-site model with the pairing field is eventually summarized. Here, in a phase diagram U vs η (drawn at a fixed $T = 1/7D$), the values of η^* and of the loci where $|\alpha|^2 = 0.5$ are reported. Moreover, in the spirit of Sec. II, different region of the phase diagram could be defined, and classified in terms of the kinetic/potential energy gain/losses induced by the application of the (finite) pairing

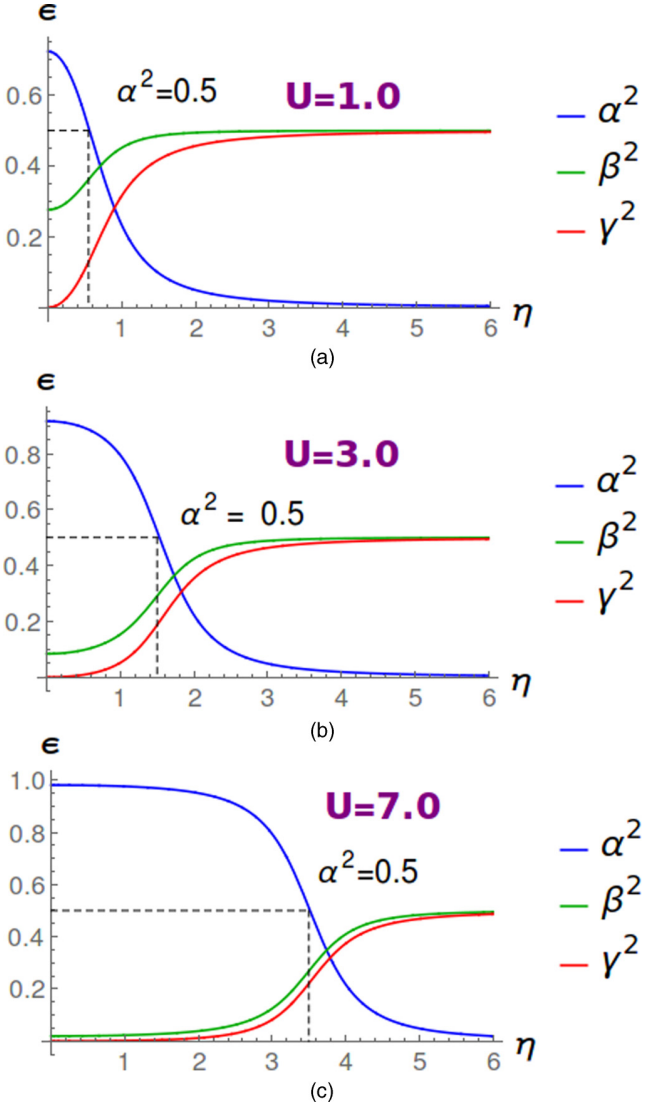

FIG. 8. Ground-state coefficients $|\alpha|^2$ (blue line), $|\beta|^2$ (green line), and $|\gamma|^2$ (red line) of the two-site model [Eq. (11)] for different U values as a function of the forcing field η.

field:

$$\begin{aligned} \langle H_{\rm K}\rangle_\eta - \langle H_{\rm K}\rangle_{\eta=0} &= -2\alpha\beta + \frac{2}{U}\left(1+\frac{4}{U^2}\right)^{1/2}, \\ \langle H_{\rm pot}\rangle_\eta - \langle H_{\rm pot}\rangle_{\eta=0} &= -U\alpha^2 - 4\eta\beta\gamma \\ &\quad + \frac{U}{2}\left[1+\left(1+\frac{4}{U^2}\right)^{-1/2}\right]. \end{aligned} \tag{12}$$

The energetic balance analysis of Fig. 10 confirms, hence, that the correspondence between η^* and the change of nature in the ground state of the two-site model is rather solid in the whole intermediate and BEC coupling regime (relevant for the preformed pair physics) with minor deviations occurring in the BCS regime. Moreover, we observe that in the BCS region for $\eta = \eta^*$, $|\alpha|^2$ is slightly larger than 0.5, indicating that a convex (=positive) curvature of $\Delta(\eta)$ is definitely *incompatible* with any preformed pair physics

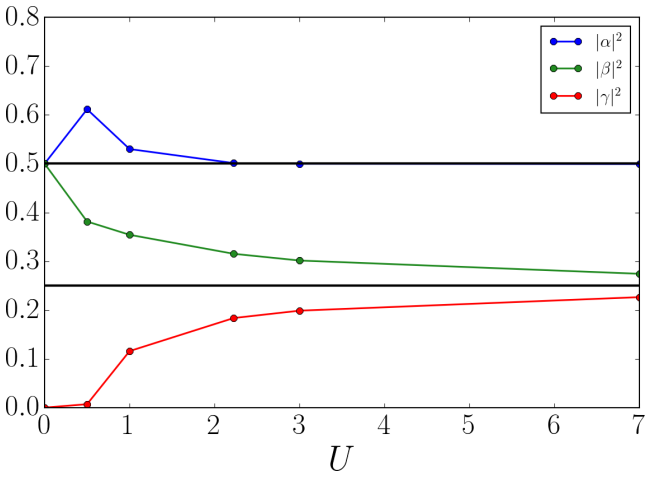

FIG. 9. Values of the coefficients $|\alpha|^2$, $|\beta|^2$, and $|\gamma|^2$ of Eq. (11) at η^* as a function of U.

in the ground state (see Figs. 9 and 10). We finally note that such criterion of "absence", usable to rigorously exclude the presence of preformed pairs, is also compatible with the analysis of the concave (=negative) curvature of $\Delta(\eta)$ in the noninteracting case, discussed at the beginning of the section.

V. IMPLICATIONS FOR OTHER STUDIES

By analyzing systematically the superconducting response (Δ) of simple models to an external s-wave pairing field (η), we have demonstrated that, whenever $\Delta(\eta)$ displays a *convex* curvature in the low-field limit, we can safely exclude preformed Cooper pairs. In this section, we discuss the relevance of this rule-of-thumb criterion to a wider range of systems. Through a unitary transformation, the pairing field and the superconducting order parameter in the attractive Hubbard model map onto the magnetic field and the magnetic

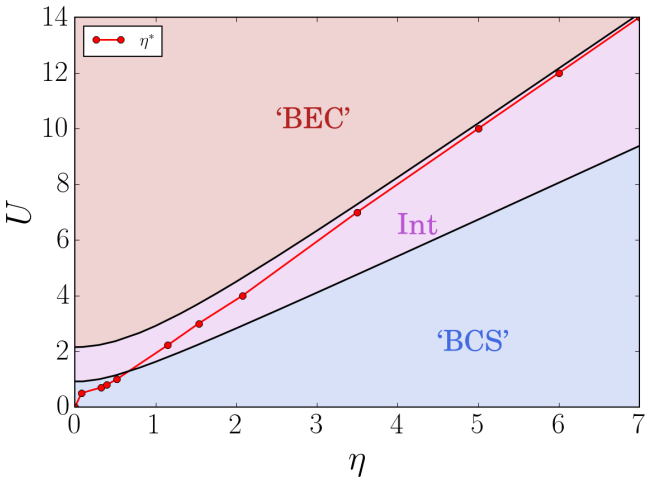

FIG. 10. U-η plane showing the different regimes obtained from an energy balance analysis in the two-site model. The blue, violet, and red regions indicate respectively the weak-, intermediate-, and strong-coupling regimes. The η^* behavior at different U values is shown by the red line.

moments in the correspondent repulsive counterpart [2]. This means that our findings apply also for detecting the presence/absence of preformed magnetic moments by means of an external magnetic field. This generalization of our results is particularly promising, because a measure of the magnetization as a function of the magnetic field is obviously not a pure theoretical probe and it can be directly exploited in various experiments (at least for the study of preformed moments in ferromagnetic compounds).

Since the presence and the role of preformed magnetic moments remain a debated issue for several correlated materials, ranging from simple metals such as Fe and Ni [42–45] to alloys (FeAl [46]) and iron-pnictides and chalcogenides [47,48], the clear-cut criterion proposed in this work may find widespread application in future experimental and theoretical studies of these materials.

One may also envisage further applications of our results as an idealized description of pump-probe experiments on superconductors. There, a transient state with an optical response, which is at least compatible with a superconductor, can be created by impulsive excitations inducing coherent phonon deformations, while leaving the temperature of the electrons unchanged [49–53]. Comparing experiments against our idealized calculations, one could analyze to which extent the impulsive excitation can be interpreted as an external field driving superconductivity (obviously in our calculations the driven superconductivity is static, as the external field does not depend on time).

One of the most natural applications of our results is, however, the possible presence of preformed d-wave pairs in the pseudogap phase of the two-dimensional Hubbard model. Indeed a closely related theoretical analysis has already been performed using the dynamical cluster approximation (DCA) [54], an extension of DMFT where the single impurity is replaced by a cluster of N_c sites. An external d-wave pairing field was applied and the resulting d-wave superconducting response $\Delta_{\mathbf{k}}$ was then computed [15]. Without driving fields, for $N_c = 8$ and $U > 1.5D$ (with $D = 4t$) the superconducting phase is replaced by the pseudogap state, where a strong spectral weight suppression is found at the antinodal point, without any superconducting long-range order. Clearly, the identification of the physical origin of this phase is also crucial to understand the debated underlying physics of the high-temperature superconductors. In this respect, the two main alternative interpretations describe the pseudogap either as the result of intrinsic interaction effects (spin fluctuations, Mott physics, or other) or as the signature of preformed d-wave pairs.

The results of Ref. [15] are reproduced in Fig. 11, which shows $\Delta_{\mathbf{k}}(\eta_{\mathbf{k}})|_{\mathbf{k}=(0,\pi)}$ as a function of the external d-wave pairing field field $\eta = \eta_d$. On the basis of these calculations the authors concluded that the superconducting response to a d-wave forcing field was "weak enough" to exclude a preformed pair origin of the pseudogap state in DCA. This statement is certainly reasonable, but it still lacks formal strength as it is not based on some precise criterion.

A closer look to the data of Fig. 11 shows that, besides an expected progressive suppression of the linear response moving away from the critical regime, one observes a sign change of the second derivative of $\Delta_{\mathbf{k}}(\eta_d)$, which starts

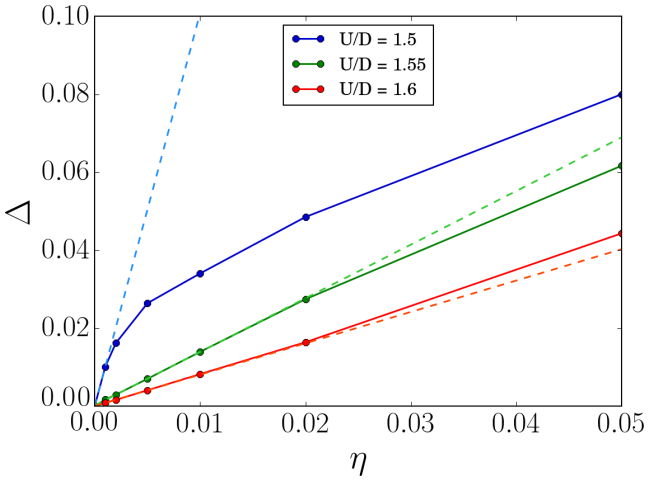

FIG. 11. (DCA data reproduced from Ref. [15].) The d-wave superconducting order parameter induced by the corresponding d-wave pairing field η_d: in a DCA calculation for a 2D Hubbard model at $\beta D = 240$ the order parameter $\Delta_{\mathbf{k}}$ is evaluated in the sector $\mathbf{k} = (0,\pi)$ and plotted as a function of η_d at doping $x = 0$ for interaction strengths indicated. The dashed lines, marking the slope of the (linear) response at $\eta_d \to 0^+$, make more easily noticeable the curvature change of $\Delta(\eta_d)$ occurring for the data set at $U = 1.6D$.

displaying a convex curvature for small fields at $U = 1.6D$. Hence, according to our criterion, we can now safely conclude that, once the system is sufficiently far from the superconducting instability, there are no well-defined preformed pairs which couple with the external pairing field in a parameter region where the pseudogap is observed in DCA. This excludes a preformed-pair origin of the pseudogap and it is rather suggestive of a major role played by the strong antiferromagnetic correlations or by nonlocal Mott physics. It is worth mentioning that the claim of a lack of preformed pairs of Ref. [15], made more rigorous by the present analysis, is not necessarily in contradiction with the claim, based on a different DCA study [16], of significant d-wave pairing fluctuations also far from T_c. The latter result indeed refers to *short-ranged* fluctuations both in space and time, while the (static) forcing-field analysis focuses on long-lived pairs. Indeed these results are perfectly compatible in view of the more recent study of Ref. [17], where it has been shown that well-defined spin fluctuations, emerging as the predominant pseudogap mechanism according to our analysis of the data of Ref. [15], show up as short-range/short-lived pairing fluctuating modes, if viewed from the perspective of the particle-particle scattering channel.

VI. CONCLUSIONS

This work has been devoted to the definition of an operative criterion to confirm or exclude the existence of preformed pairs in a non-superconducting state. This goal has been achieved by a systematic DMFT study of the response to an external s-wave pairing forcing field η in the controlled situation of a single band (attractive and repulsive) Hubbard model. For strong attractive interactions we are indeed certain of the existence of a preformed pair region, while the repulsive model does not host any s-wave pair.

By comparing the different regimes, we identified a clear-cut rule-of-thumb criterion for excluding a preformed pair physics: The latter are certainly absent, if the second derivative of $\Delta(\eta)$ is positive in a finite region of η from 0 to a finite value η^* [i.e., $\Delta(\eta)$ is a convex function at small fields]. This happens because the convexity of $\Delta(\eta)$ reflects the "reluctance" of the systems to respond to the pairing field. In other words, the positive second derivative indicates that the applied forcing field is not intense enough to *revert* the dominant nature of the ground state, which is opposed to the order induced by the probing field. Only if η is enough large to exceed any intrinsic property of the model, the curvature changes sign and becomes concave, leading, eventually, to a saturation to the maximum pairing amplitude. This behavior testifies to the absence of any intrinsic preformed pairing.

On the other hand, an overall concave curvature of $\Delta(\eta)$ is a necessary condition for the existence of preformed pairs, but it is not a sufficient condition. Therefore, the latter should be supplemented with further physical information, such as the energetic balance underlying superconductivity, as we also discuss in Sec. II of this paper.

Our results have a potential impact for several different aspects. Our rule of thumb can be indeed applied, as showed in the previous section, for improving the interpretation of cutting-edge DCA calculations [15], relevant for the cuprate physics, and—in particular—to exclude on a rigorous basis that the pseudogap state of DCA is originated by preformed pair fluctuations. Indeed, a related analysis has been proposed in Ref. [15], where, however, the physical interpretation of the results was mostly heuristic.

Moreover, it is quite natural to extend the conclusions of our analysis (and, in particular, our criterion) to cases of other, more physical, forcing fields: This would be, e.g., the case of a (finite) magnetic field exploited to detect preformed magnetic moments via the evolution of the magnetization as a function of magnetic field beyond linear response. Evidently, the latter analysis allows also for direct experimental realizations.

Finally, we notice that the study of regimes of external perturbation field, far away from the linear response, might provide important complementary information to interpret more challenging nonequilibrium phenomena. Comparing our results with pump-probe experiments where transient superconductivity is realized by coherently exciting phonon modes, we could study whether, and to which extent, these nonequilibrium phenomena can be interpreted in terms of a light-driven pairing field which favors pair formation.

ACKNOWLEDGMENTS

We thank E. Gull, O. Gunnarsson, C. Taranto, G. Sangiovanni, T. Schäfer, and G. Rohringer for insightful discussions. We acknowledge financial support for our research activities from the Austrian Science Fund (FWF) through the project I-610-N16 and the subproject I-1395-N16 as part of the German Research Foundation (DFG) research unit FOR 1346.

APPENDIX A: NONINTERACTING CASE

The half-filled noninteracting problem under a isotropic pairing forcing field η can be easily solved in $\mathbf{k}$ space. Here, the Hamiltonian assumes the following form:

$$H = \sum_{\mathbf{k}\sigma} \epsilon_{\mathbf{k}} c^{\dagger}_{\mathbf{k}\sigma} c_{\mathbf{k}\sigma} - \eta \sum_{\mathbf{k}} (c^{\dagger}_{\mathbf{k}\uparrow} c^{\dagger}_{-\mathbf{k}\downarrow} + c_{-\mathbf{k}\downarrow} c_{\mathbf{k}\uparrow}), \tag{A1}$$

where $\epsilon_{\mathbf{k}}$ represents the free particle energy dispersion. This Hamiltonian can be exactly diagonalized by exploiting the Bogoliubov transformations [1], which read

$$\begin{cases} \gamma^{\dagger}_{\mathbf{k},\uparrow} = u_{\mathbf{k}} c_{\mathbf{k},\sigma}{}^{\dagger} - v_{\mathbf{k}} c_{-\mathbf{k},\downarrow}, \\ \gamma_{-\mathbf{k},\downarrow} = u_{\mathbf{k}} c_{-\mathbf{k},\downarrow} + v_{\mathbf{k}} c_{\mathbf{k},\uparrow}{}^{\dagger}, \end{cases} \tag{A2}$$

where

$$\begin{cases} u_{\mathbf{k}}^2 = \frac{1}{2}\left(1 + \frac{\epsilon(\mathbf{k})}{E(\mathbf{k})}\right), \\ v_{\mathbf{k}}{}^2 = \frac{1}{2}\left(1 - \frac{\epsilon(\mathbf{k})}{E(\mathbf{k})}\right), \end{cases} \tag{A3}$$

and $E(\mathbf{k}) = \sqrt{\epsilon_{\mathbf{k}}{}^2 + \eta^2}$.

In order to evaluate the superconducting order parameter in real space, one has to perform the expectation value of the annihilation "pair operator" $b_{\mathbf{k}} = c_{-\mathbf{k}\downarrow} c_{\mathbf{k}\uparrow}$ and sum over the Brillouin zone:

$$\begin{aligned} \langle b_{\mathbf{k}} \rangle &= \langle c_{-\mathbf{k}\downarrow} c_{\mathbf{k}\uparrow} \rangle = u^*_{\mathbf{k}} v_{\mathbf{k}} (1 - \langle \gamma_{\mathbf{k}\uparrow}{}^{\dagger} \gamma_{\mathbf{k}\uparrow} \rangle - \langle \gamma_{\mathbf{k}\downarrow}{}^{\dagger} \gamma_{\mathbf{k}\downarrow} \rangle) \\ &= u^*_{\mathbf{k}} v_{\mathbf{k}} [1 - 2 f(E_{\mathbf{k}})], \end{aligned} \tag{A4}$$

where $f(E_{\mathbf{k}})$ represents the usual Fermi-Dirac thermal distribution for fermion-like excitations with energy $E_{\mathbf{k}}$. Hence, we finally end up with the following expression for the superconducting order parameter:

$$\begin{aligned} \Delta &= \sum_{\mathbf{k}} u^*_{\mathbf{k}} v_{\mathbf{k}} [1 - 2 f(E_{\mathbf{k}})] \\ &= \sum_{\mathbf{k}} \frac{\eta}{2E(\mathbf{k})} [1 - 2 f(E_{\mathbf{k}})] \\ &= \frac{\eta}{2} \int_{-D}^{D} d\epsilon \frac{D(\epsilon)}{E(\epsilon)} [1 - 2 f(E(\epsilon))]. \end{aligned} \tag{A5}$$

Explicitly substituting the DOS of the Bethe-lattice and the Fermi-Dirac thermal distribution, one gets Eq. (5).

APPENDIX B: ATOMIC LIMIT

In this section we explicitly derive the expression for the superconducting order parameter Δ in the atomic limit. We proceed in two steps: first we perform the unitary transformation to map the attractive Hubbard model onto the repulsive one; second we project the system onto the new principal axes and evaluate the expectation value $\langle c_{i\downarrow} c_{i\uparrow} \rangle$ in the starting (attractive) system. Note that the analogous procedure can be adopted for the repulsive case just by swapping the U sign.

Let us start from the attractive Hubbard model Hamiltonian, properly readjusted to emphasize the particle-hole symmetry:

$$\begin{aligned} H_{attr} = U \sum_i \left(n_{i\uparrow} - \frac{1}{2}\right)\left(n_{i\downarrow} - \frac{1}{2}\right) - \left(\mu - \frac{U}{2}\right) \\ \times \sum_i (n_{i\uparrow} + n_{i\downarrow}) - \eta \sum_i (c^{\dagger}_{i\uparrow} c^{\dagger}_{i\downarrow} + \text{H.c.}). \end{aligned} \tag{B1}$$

Here $U < 0$ and μ is the shifted chemical potential (note $\mu = U/2$ at half filling). By performing the unitary transformation to map the attractive Hubbard model onto the repulsive one [2],

$$\begin{cases} c_{i\downarrow} \to (-1)^{n_i} c^{\dagger}_{i\downarrow}, \\ c_{i\uparrow} \to c_{i\uparrow}, \end{cases} \tag{B2}$$

we end up with the corresponding repulsive Hubbard Hamiltonian:

$$\begin{aligned} H_{rep} = |U| \sum_i n_{i\uparrow} n_{i\downarrow} - \frac{|U|}{2} \sum_i (n_{i\uparrow} + n_{i\downarrow}) - \left(\mu + \frac{|U|}{2}\right) \\ \times \sum_i (n_{i\uparrow} - n_{i\downarrow}) - \eta \sum_i (-1)^{n_i} (c^{\dagger}_{i\uparrow} c_{i\downarrow} + c^{\dagger}_{i\downarrow} c_{i\uparrow}). \end{aligned} \tag{B3}$$

Notice that Eq. (B3) is nothing but a half-filled repulsive system with two external magnetic fields applied onto the z and the x axes. Since the first two terms are invariant under axis rotation, it is convenient to perform a unitary transformation of the operators, projecting the system along the principal axes in the (x,z) plane.

Diagonalizing the last two terms in the 4-state Hilbert space for the single site and making the proper transformations, we end up with to the following expression:

$$\begin{aligned} H_{rep} = |U| \sum_i n_{i\uparrow} n_{i\downarrow} - \frac{|U|}{2} \sum_i (n_{i\uparrow} + n_{i\downarrow}) \\ + \epsilon \sum_i (n_{i\uparrow} - n_{i\downarrow}), \end{aligned} \tag{B4}$$

where $\epsilon = \sqrt{(\mu + \frac{|U|}{2})^2 + \eta^2}$ is the effective magnetic field resulting from the μ and η terms.

In order to evaluate the superconducting order parameter Δ, we need to map the pairing operator $c_{i\downarrow} c_{i\uparrow}$ onto the corresponding repulsive system by projecting it along the principal axes. We obtain

$$\begin{aligned} \langle c_{i\downarrow} c_{i\uparrow} \rangle \to \frac{1}{4\eta\epsilon^2} \Bigg[-\frac{\left(\epsilon - \frac{|U|}{2} - \mu\right)}{a^2} \langle c^{\dagger}_{i\uparrow} c_{i\uparrow} \rangle \\ + \frac{\left(\epsilon + \frac{|U|}{2} + \mu\right)}{b^2} \langle c^{\dagger}_{i\downarrow} c_{i\downarrow} \rangle \Bigg], \end{aligned} \tag{B5}$$

where $a/b = [\eta^2 + (\mu \pm \frac{|U|}{2} \pm \epsilon)]^{-1/2}$.

Evaluating explicitly the expectation values in Eq. (B5) one obtains

$$\Delta(\eta) = \frac{\eta}{2\,\epsilon} \frac{\sinh(\beta\epsilon)}{\cosh(\beta\epsilon) + e^{-\beta\frac{|U|}{2}}}, \tag{B6}$$

which reduces to the simpler expression in the half-filling case:

$$\Delta_{\rm att}(\eta) = \frac{1}{2}\,\frac{\sinh(\beta\eta)}{\cosh(\beta\eta) + e^{-\beta\frac{|U|}{2}}}. \tag{B7}$$

Since this expression is typically applicable for large values of $|U|$, one can notice that the order parameter exhibits a weak dependence on the interacting constant. This also sets a minimum value for the slope in the limit $|U| \to +\infty$ at finite temperature:

$$\lim_{|U|\to+\infty} \frac{\partial\Delta_{\rm att}}{\partial\eta}\bigg|_{\eta=0} = \frac{\tanh\left(\beta\left|\mu + \frac{|U|}{2}\right|\right)}{2\left|\mu + \frac{|U|}{2}\right|}, \tag{B8}$$

which displays a maximum in the half-filling case:

$$\lim_{|U|\to+\infty} \frac{\partial\Delta_{\rm att}}{\partial\eta}\bigg|_{\eta=0,\mu=-\frac{|U|}{2}} = \frac{\beta}{2}. \tag{B9}$$

This means that, away from half-filling, the superconducting linear response of the system is progressively reduced and, thus, the regime value $\Delta = 0.5$ is approached more slowly if compared with the half-filling situation. This result is consistent with the DMFT data shown in Fig. 5 (left panel). A study on the second derivative $\partial^2\Delta_{\rm att}/\partial\eta^2$ shows that, for all $\eta > 0$, the superconducting order parameter exhibits a negative curvature in the attractive Hubbard model, as shown in Fig. 6 for the half-filling case (upper panel). The corresponding behavior for $U > 0$ (in the half-filling case) is shown in Fig. 6 (lower panel).

Ground state

As a final atomic limit analysis in the repulsive case, we can look at the ground-state evolution as a function of the external pairing field. The local, repulsive Hamiltonian has the following form:

$$H^i_{rep} = U\, n_{i\uparrow}n_{i\downarrow} - \frac{U}{2}\,(n_{i\uparrow} + n_{i\downarrow}) - \eta\,(c_{i\downarrow}c_{i\uparrow} + c^\dagger_{i\uparrow}c^\dagger_{i\downarrow}), \tag{B10}$$

where, for the sake of simplicity, we reduced at half filling.

By diagonalizing the 4×4 block matrix, we find three different eigenvalues: $-U/2$ (twofold degenerate), $\pm\eta$. Therefore, as soon as $\eta \to U/2$, the ground state of the system abruptly changes from the degenerate subspace to the eigenstate associated with $-\eta$, namely,

$$|-\eta\rangle = \frac{|\uparrow\downarrow\rangle + |0\rangle}{\sqrt{2}}. \tag{B11}$$

Out of half filling the condition for having this level crossing which changes abruptly the ground state of the system from singly occupied magnetic moment to $\frac{|\uparrow\rangle+|0\rangle}{\sqrt{2}}$ becomes

$$\sqrt{\eta^2 + \left(\mu - \frac{U}{2}\right)^2} = \frac{U}{2}. \tag{B12}$$

Although μ depends in general on the specific parameters of the system (e.g., temperature, electronic density, and external field η) and it must be determined self-consistently, it is clear from Eq. (B12) that the change of the ground state will occur at a smaller value of the pairing field η than the half-filled system. This trend is also coherent with the DMFT results in Fig. 5 (right panel).

APPENDIX C: TWO-SITE MODEL

In this section we target the solution of the repulsive Hubbard model taking into account just two sites. The two-site Hamiltonian reads

$$H = -t\sum_\sigma (c^\dagger_{1\sigma}c_{2\sigma} + c^\dagger_{2\sigma}c_{1\sigma}) + U\sum_{i=1,2}\left(n_{i\uparrow} - \frac{1}{2}\right) \times\left(n_{i\downarrow} - \frac{1}{2}\right) - \eta\sum_{i=1,2}(c^\dagger_{i\uparrow}c^\dagger_{i\downarrow} + c_{i\downarrow}c_{i\uparrow}), \tag{C1}$$

where t is the hopping integral, $U > 0$ is the interaction parameter, and η represents the external pairing field. Since we are working in the grand-canonical ensemble, the Hilbert space is spanned by 16 basis vectors, namely,

$$\{|\uparrow,\downarrow\rangle,|\downarrow,\uparrow\rangle,|\uparrow\downarrow,0\rangle,|0,\uparrow\downarrow\rangle,|\uparrow,\uparrow\rangle,|\downarrow,\downarrow\rangle\} \Rightarrow \text{ssp } n = 1, \tag{C2}$$

$$\{|\uparrow,0\rangle,|\downarrow,0\rangle,|0,\uparrow\rangle,|0,\downarrow\rangle\} \Rightarrow \text{ssp } n = 0.5, \tag{C3}$$

$$\{|\uparrow,\uparrow\downarrow\rangle,|\downarrow,\uparrow\downarrow\rangle,|\uparrow\downarrow,\uparrow\rangle,|\uparrow\downarrow,\downarrow\rangle\} \Rightarrow \text{ssp } n = 1.5, \tag{C4}$$

$$\{|\uparrow\downarrow,\uparrow\downarrow\rangle\} \Rightarrow \text{ssp } n = 2, \tag{C5}$$

$$\{|0,0\rangle\} \Rightarrow \text{ssp } n = 0, \tag{C6}$$

where each line indicates a specific subspace (ssp) characterized by an electron density n. By exploiting the symmetries of the system one can identify for which states the Hamiltonian is diagonal:

$$\left\{\frac{|\uparrow\downarrow,0\rangle - |0,\uparrow\downarrow\rangle}{\sqrt{2}}, \frac{|0,0\rangle - |\uparrow\downarrow,\uparrow\downarrow\rangle}{\sqrt{2}}\right\} \Rightarrow E_1 = 0, \tag{C7}$$

$$\left\{|\uparrow,\uparrow\rangle,|\downarrow,\downarrow\rangle, \frac{|\uparrow,\downarrow\rangle + |\downarrow,\uparrow\rangle}{\sqrt{2}}\right\} \Rightarrow E_2 = -U, \tag{C8}$$

while projecting the Hamiltonian on the 3-dimensional subspace $\{\frac{|0,0\rangle+|\uparrow\downarrow,\uparrow\downarrow\rangle}{\sqrt{2}}, \frac{|\uparrow\downarrow,0\rangle+|0,\uparrow\downarrow\rangle}{\sqrt{2}}, \frac{|\uparrow,\downarrow\rangle-|\downarrow,\uparrow\rangle}{\sqrt{2}}\}$ gives the following matrix:

$$M = \begin{pmatrix} -U & -2t & 0 \\ -2t & 0 & -2\eta \\ 0 & -2\eta & 0 \end{pmatrix}. \tag{C9}$$

One can demonstrate that this matrix has three distinguished real eigenvalues (E_3, E_4, and E_5) even if an explicit simple expression cannot be found analytically. Nevertheless, we are able to compute numerically eigenvalues and eigenvectors as a function of the interaction U and the pairing field η. The remaining states with an odd average number of particles span two equivalent 4-dimensional subspaces (one for each spin channel) whose Hamiltonian projection reads

$$M_1 = \begin{pmatrix} -\frac{U}{2} & -t & -\eta & 0 \\ -t & -\frac{U}{2} & 0 & -\eta \\ -\eta & 0 & -\frac{U}{2} & t \\ 0 & -\eta & t & -\frac{U}{2} \end{pmatrix}. \tag{C10}$$

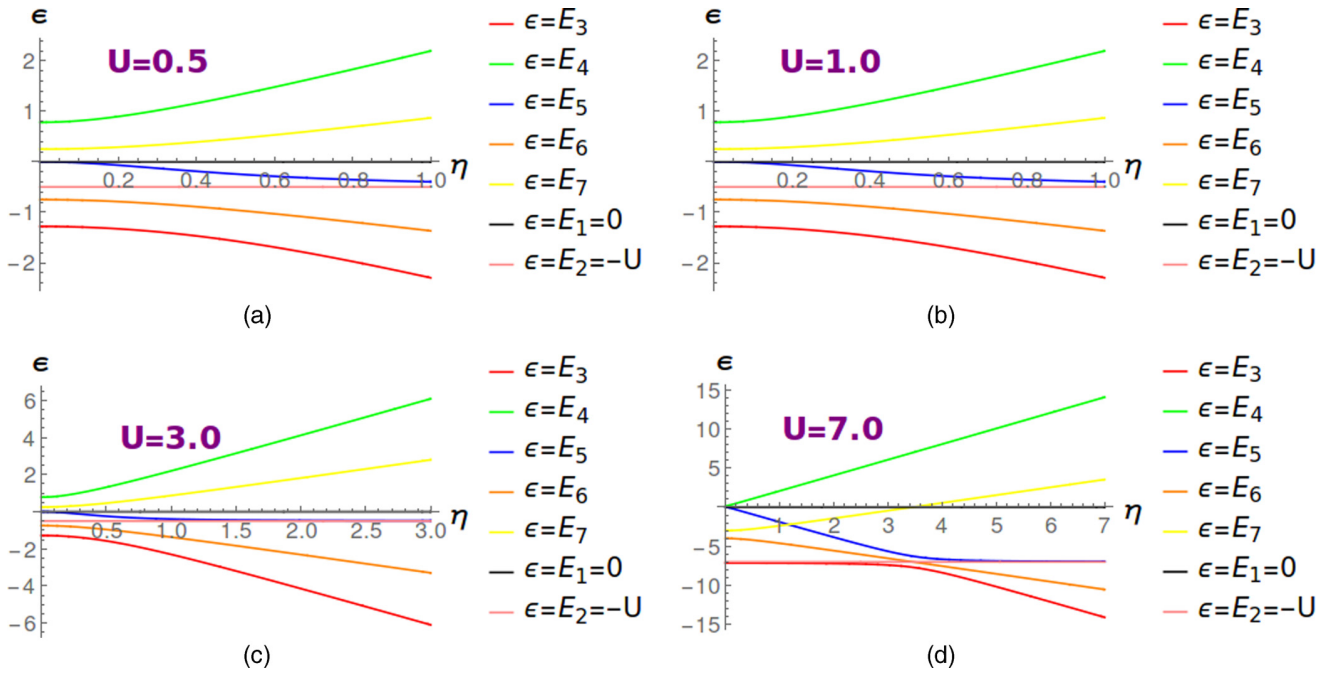

FIG. 12. Energy levels as a function of the pairing forcing field η for different values of U.

So we obtain the two eigenvalues E_6 and E_7 (each one four times degenerate) and the associated eigenvectors.

Figure 12 shows the seven eigenvalues as a function of η at different interaction values. Hence, it is possible to identify the state associated with E_3 to be the ground state of the system for any U and η values. This state lives in the subspace described by matrix M and can be written as follows:

$$|\mathrm{GS}\rangle = \alpha\left(\frac{|\uparrow,\downarrow\rangle - |\downarrow,\uparrow\rangle}{\sqrt{2}}\right) + \beta\left(\frac{|\uparrow\downarrow,0\rangle + |0,\uparrow\downarrow\rangle}{\sqrt{2}}\right) + \gamma\left(\frac{|0,0\rangle + |\uparrow\downarrow,\uparrow\downarrow\rangle}{\sqrt{2}}\right). \tag{C11}$$

Superconducting response at $T \neq 0$

The superconducting order parameter at finite temperature in the two-site model is readily computed as

$$\Delta = \frac{1}{2}\sum_i \frac{1}{Z}\mathrm{Tr}(e^{-\beta\hat{H}} c_{i\downarrow} c_{i\uparrow}) = \frac{1}{2}\frac{1}{Z}\sum_i \sum_{\tilde{n}\, n} e^{-\beta\epsilon_n} \langle \tilde{n}|c_{i_\downarrow}|n\rangle (\langle \tilde{n}|c^\dagger_{i\uparrow}|n\rangle)^*$$

$$= \frac{1}{Z}\{e^{-\beta E_6}(m_1 p_1 + m_2 p_2) + e^{-\beta E_7}(m_3 p_3 + m_4 p_4) + e^{-\beta E_3}(\beta_1\gamma_1) + e^{-\beta E_4}(\beta_2\gamma_2) + e^{-\beta E_5}(\beta_3\gamma_3)\}, \tag{C12}$$

where the coefficients m_i and p_i ($i = \{1,4\}$) are related to the eigenstates of M_1. Namely,

$$|E_6\rangle = l_{1(2)}|\uparrow,0\rangle + m_{1(2)}|0,\uparrow\rangle + n_{1(2)}|\uparrow,\uparrow\downarrow\rangle + p_{1(2)}|\uparrow\downarrow,\uparrow\rangle, \tag{C13}$$

$$|E_7\rangle = l_{3(4)}|\uparrow,0\rangle + m_{3(4)}|0,\uparrow\rangle + n_{3(4)}|\uparrow,\uparrow\downarrow\rangle + p_{3(4)}|\uparrow\downarrow,\uparrow\rangle, \tag{C14}$$

and the partition function is given by

$$Z = 3\,e^{\beta U} + 2 + e^{-\beta E_3} + e^{-\beta E_4} + e^{-\beta E_5} + 4e^{-\beta E_6} + 4e^{-\beta E_7}. \tag{C15}$$

Figure 7 shows the comparison between Eq. (C12) and the DMFT result for the superconducting order parameter.

[1] J. Bardeen, L. N. Cooper, and J. R. Schrieffer, Phys. Rev. **108**, 1175 (1957).

[2] R. Micnas, J. Ranninger, and S. Robaszkiewicz, Rev. Mod. Phys. **62**, 113 (1990).

[3] C. A. R. Sá de Melo, M. Randeria, and J. R. Engelbrecht, Phys. Rev. Lett. **71**, 3202 (1993).

[4] R. Haussmann, Z. Phys. B **91**, 291 (1993).

[5] F. Pistolesi and G. C. Strinati, Phys. Rev. B **53**, 15168 (1996).

[6] B. Kyung, S. Allen, and A.-M. S. Tremblay, Phys. Rev. B **64**, 075116 (2001).

[7] W. S. Bakr, J. I. Gillen, A. Peng, S. Fölling, and M. Greiner, Nature (London) **462**, 74 (2009).

[8] V. J. Emery and S. A. Kivelson, Nature (London) **374**, 434 (1995).

[9] Z. A. Xu, N. P. Ong, Y. Wang, T. Kakeshita, and S. Uchida, Nature (London) **406**, 486 (2000).

[10] Y. Wang, L. Li, M. J. Naughton, G. D. Gu, S. Uchida, and N. P. Ong, Phys. Rev. Lett. **95**, 247002 (2005).

[11] Y. Kosaka, T. Hanaguri, M. Azuma, M. Takano, J. C. Davis, and H. Takagi, Nat. Phys. **8**, 534 (2012).

[12] M. Norman, Nat. Phys. **10**, 357 (2014).

[13] T. Timusk and B. W. Statt, Rep. Prog. Phys. **62**, 61 (1999).

[14] J. C. Campuzano, M. R. Norman, and M. Randeria, *Physics of Superconductors*, Vol. II, edited by K. H. Bennemann and J. B. Ketterson (Springer, Berlin, 2004), pp. 167–273.

[15] E. Gull and A. J. Millis, Phys. Rev. B **86**, 241106 (2012).

[16] J. Merino and O. Gunnarsson, Phys. Rev. B **89**, 245130 (2014).

[17] O. Gunnarsson, T. Schäfer, J. P. F. LeBlanc, E. Gull, J. Merino, G. Sangiovanni, G. Rohringer, and A. Toschi, Phys. Rev. Lett. **114**, 236402 (2015).

[18] A. Toschi, M. Capone, and C. Castellani, Phys. Rev. B **72**, 235118 (2005).

[19] A. Georges, G. Kotliar, W. Krauth and M. J. Rozenberg, Rev. Mod. Phys. **68**, 13 (1996).

[20] W. Metzner and D. Vollhardt, Phys. Rev. Lett. **62**, 324 (1989).

[21] M. Keller, W. Metzner, and U. Schollwöck, Phys. Rev. Lett. **86**, 4612 (2001).

[22] A. Toschi, P. Barone, M. Capone, and C. Castellani, New J. Phys. **7**, 7 (2005).

[23] A. Garg, H. R. Krishnamurthy, and M. Randeria, Phys. Rev. B **72**, 024517 (2005).

[24] A. Amaricci and M. Capone, Phys. Rev. B **93**, 014508 (2016).

[25] C. Taranto, G. Sangiovanni, K. Held, M. Capone, A. Georges, and A. Toschi, Phys. Rev. B **85**, 085124 (2012).

[26] E. Gull, P. Werner, X. Wang, M. Troyer, and A. J. Millis, Europhys. Lett. **84**, 37009 (2008).

[27] H. J. A. Molegraaf *et al.*, Science **295**, 2239 (2002).

[28] A. F. Santander-Syro, R. P. S. M. Lobo, N. Bontemps, Z. Konstantinovic, Z. Li, and H. Raffy, Phys. Rev. Lett. **88**, 097005 (2002).

[29] A. F. Santander-Syro, R. P. S. M. Lobo, N. Bontemps, Z. Konstantinovic, Z. Z. Li, and H. Raffy, Europhys. Lett. **62**, 568 (2003).

[30] J. P. Carbotte and E. Schachinger, J. Low. Phys. **144**, 61 (2006).

[31] M. M. Qazilbash *et al.*, Nat. Phys. **5**, 647 (2009).

[32] L. Benfatto, S. Sharapov, and H. Beck, Eur. Phys. J. B **39**, 469 (2004).

[33] A. Toschi, M. Capone, M. Ortolani, P. Calvani, S. Lupi, and C. Castellani, Phys. Rev. Lett. **95**, 097002 (2005).

[34] L. Baldassarre *et al.*, Phys. Rev. B **77**, 113107 (2008).

[35] A. Toschi and M. Capone, Phys. Rev. B **77**, 014518 (2008).

[36] D. Nicoletti *et al.*, Phys. Rev. Lett. **105**, 077002 (2010).

[37] G. Deutscher, A. F. Santander-Syro, and N. Bontemps, Phys. Rev. B **72**, 092504 (2005).

[38] F. Carbone, A. B. Kuzmenko, H. J. A. Molegraaf, E. van Heumen, V. Lukovac, F. Marsiglio, D. van der Marel, K. Haule, G. Kotliar, H. Berger, S. Courjault, P. H. Kes, and M. Li, Phys. Rev. B **74**, 064510 (2006).

[39] M. Capone, M. Fabrizio, C. Castellani, and E. Tosatti, Science **296**, 2364 (2002).

[40] Y. Nomura, S. Sakai, M. Capone, and R. Arita, Sci. Adv. **1**, e1500568 (2015).

[41] G. Keller, K. Held, V. Eyert, D. Vollhardt, and V. I. Anisimov, Phys. Rev. B **70**, 205116 (2004).

[42] V. I. Anisimov, A. S. Belozerov, A. I. Poteryaev, and I. Leonov, Phys. Rev. B **86**, 035152 (2012).

[43] A. E. Antipov, I. S. Krivenko, V. I. Anisimov, A. I. Lichtenstein, and A. N. Rubtsov, Phys. Rev. B **86**, 155107 (2012).

[44] A. I. Lichtenstein, M. I. Katsnelson, and G. Kotliar, Phys. Rev. Lett. **87**, 067205 (2001).

[45] S. V. Vonsovsky, M. I. Katsnelson, and A. V. Trefilov, Phys. Met. Metallogr **76**, 247 (1993).

[46] A. Galler, C. Taranto, M. Wallerberger, M. Kaltak, G. Kresse, G. Sangiovanni, A. Toschi, and K. Held, Phys. Rev. B **92**, 205132 (2015).

[47] A. Toschi, R. Arita, P. Hansmann, G. Sangiovanni, and K. Held, Phys. Rev. B **86**, 064411 (2012).

[48] Z. P. Yin, K. Haule, and G. Kotliar, Nat. Phys. **7**, 294 (2011).

[49] D. Fausti, R. I. Tobey, N. Dean, S. Kaiser, A. Dienst, M. C. Hoffmann, S. Pyon, T. Takayama, H. Takagi, and A. Cavelleri, Science **331**, 189 (2012).

[50] C. Giannetti, M. Capone, D. Fausti, M. Fabrizio, F. Parmigiani, and D. Mihailovic, Adv. Phys. **65**, 58 (2016).

[51] R. Mankowsky, A. Subedi, M. Forst, S. O. Mariager, M. Chollet, H. T. Lemke, J. S. Robinson, J. M. Glownia, M. P. Minitti, A. Frano, M. Fechner, N. A. Spaldin, T. Loew, B. Keimer, A. Georges, and A. Cavalleri, Nature (London) **516**, 71 (2014).

[52] D. Fausti, F. Novelli, G. Giovannetti, A. Avella, F. Cilento, L. Patthey, M. Radovic, M. Capone, and F. Parmigiani, arXiv:1408.0888.

[53] M. Mitrano, A. Cantaluppi, D. Nicoletti, S. Kaiser, A. Perucchi, S. Lupi, P. Di Pietro, D. Pontiroli, M. Riccò, S. R. Clark, D. Jaksch, and A. Cavalleri, Nature (London) **530**, 461 (2016).

[54] T. Maier, M. Jarrell, T. Pruschke, and Matthias H. Hettler, Rev. Mod. Phys. **77**, 1027 (2005).

References

(1963). Electron correlations in narrow energy bands. *Proceedings of the Royal Society of London A: Mathematical, Physical and Engineering Sciences*, *276*(1365), 238–257.

URL http://rspa.royalsocietypublishing.org/content/276/1365/238

Abrikosov, A. A. A. A., Gor'kov, j. a., L. P. (Lev Petrovich), & Dzi□a□loshinskiĭ, j. a., I. E. (Igor' Ekhiel'evich) (1975). *Methods of quantum field theory in statistical physics*. New York : Dover Publications, rev. english ed. / translated and edited by richard a. silverman ed. Rev. English translation of Metody kvantovoĭ teorii poli□a□.

Alexander Altland, B. D. S. (2010). *Condensed Matter Field Theory*. Cambridge University Press.

Andergassen, S., Enss, T., & Meden, V. (2006). Kondo physics in transport through a quantum dot with luttinger-liquid leads. *Phys. Rev. B*, *73*, 153308.

URL https://link.aps.org/doi/10.1103/PhysRevB.73.153308

Andergassen, S., Enss, T., Meden, V., Metzner, W., Schollwöck, U., & Schönhammer, K. (2004). Functional renormalization group for luttinger liquids with impurities. *Phys. Rev. B*, *70*, 075102.

URL https://link.aps.org/doi/10.1103/PhysRevB.70.075102

Anisimov, V. I., Belozerov, A. S., Poteryaev, A. I., & Leonov, I. (2012). Rotationally invariant exchange interaction: The case of paramagnetic iron. *Phys. Rev. B*, *86*, 035152.

URL https://link.aps.org/doi/10.1103/PhysRevB.86.035152

Antipov, A. E., Krivenko, I. S., Anisimov, V. I., Lichtenstein, A. I., & Rubtsov, A. N. (2012). Role of rotational symmetry in the magnetism of a multiorbital model. *Phys. Rev. B*, *86*, 155107.

URL https://link.aps.org/doi/10.1103/PhysRevB.86.155107

Arsenault, L.-F., Neuberg, R., Hannah, L. A., & Millis, A. J. (2017). Projected regression method for solving fredholm integral equations arising in the analytic continuation problem of quantum physics. *Inverse Problems*, *33*(11), 115007.

URL http://stacks.iop.org/0266-5611/33/i=11/a=115007

Aryasetiawan, F., & Gunnarsson, O. (1998). The gw method. *Reports on Progress in Physics*, *61*(3), 237.

URL http://stacks.iop.org/0034-4885/61/i=3/a=002

Ayral, T., & Parcollet, O. (2015). Mott physics and spin fluctuations: A unified framework. *Phys. Rev. B*, *92*(11), 115109.

Ayral, T., & Parcollet, O. (2016). Mott physics and collective modes: An atomic approximation of the four-particle irreducible functional. *Phys. Rev. B*, *94*, 075159.

URL https://link.aps.org/doi/10.1103/PhysRevB.94.075159

Bardeen, J., Cooper, L. N., & Schrieffer, J. R. (1957). Microscopic theory of superconductivity. *Phys. Rev.*, *106*, 162–164.

URL https://link.aps.org/doi/10.1103/PhysRev.106.162

Baym, G., & Kadanoff, L. P. (1961). Conservation laws and correlation functions. *Phys. Rev.*, *124*, 287–299.

URL https://link.aps.org/doi/10.1103/PhysRev.124.287

Beach, K. S. D., Gooding, R. J., & Marsiglio, F. (2000). Reliable padé analytical continuation method based on a high-accuracy symbolic computation algorithm. *Phys. Rev. B*, *61*, 5147–5157.

URL https://link.aps.org/doi/10.1103/PhysRevB.61.5147

Bednorz, J. G., & Müller, K. A. (1986). Possible hightc superconductivity in the ba–la–cu–o system. *Zeitschrift für Physik B Condensed Matter*, *64*(2), 189–193.

URL https://doi.org/10.1007/BF01303701

Berges, J., Borsányi, S., Reinosa, U., & Serreau, J. (2005). Nonperturbative renormalization for 2pi effective action techniques. *Annals of Physics*, *320*(2), 344–398.

URL http://www.sciencedirect.com/science/article/pii/S0003491605001156

Berges, J., Tetradis, N., & Wetterich, C. (2002). Non-perturbative renormalization flow in quantum field theory and statistical physics. *Renormalization group theory in the new millennium. IV*, *363*(4), 223–386.

URL http://www.sciencedirect.com/science/article/pii/S0370157301000989

Bickers, N. E. (1991). Parquet equations for numerical self-consistent-field theory. *Int. J. Mod. Phys. B*, *05*(01n02), 253–270.

URL https://doi.org/10.1142/S021797929100016X

Binney, J. J., Dowrick, N. J., Fisher, A. J., & Newman, M. (1992). *The Theory of Critical Phenomena: An Introduction to the Renormalization Group*. New York, NY, USA: Oxford University Press, Inc.

Blaizot, J.-P., Pawlowski, J. M., & Reinosa, U. (2011). Exact renormalization group and Φ-derivable approximations. *Physics Letters B*, *696*(5), 523–528.

URL http://www.sciencedirect.com/science/article/pii/S0370269310014619

Boehnke, L., Hafermann, H., Ferrero, M., Lechermann, F., & Parcollet, O. (2011). Orthogonal polynomial representation of imaginary-time green's functions. *Phys. Rev. B*, *84*, 075145.

URL https://link.aps.org/doi/10.1103/PhysRevB.84.075145

Borejsza, K., & Dupuis, N. (2004). Antiferromagnetism and single-particle properties in the two-dimensional half-filled hubbard model: A nonlinear sigma model approach. *Phys. Rev. B*, *69*, 085119.

URL https://link.aps.org/doi/10.1103/PhysRevB.69.085119

Byczuk, K., Kollar, M., Held, K., Yang, Y.-F., Nekrasov, I. A., Pruschke, T., & Vollhardt, D. (2007). Kinks in the dispersion of strongly correlated electrons. *Nature Physics*, *3*, 168.

URL http://dx.doi.org/10.1038/nphys538

Capone, M., Fabrizio, M., Castellani, C., & Tosatti, E. (2002). Strongly correlated superconductivity. *Science*, *296*(5577), 2364–2366.

URL http://science.sciencemag.org/content/296/5577/2364

Chalupa, P., Gunacker, P., Schäfer, T., Held, K., & Toschi, A. (2018). Divergences of the irreducible vertex functions in correlated metallic systems: Insights from the anderson impurity model. *Phys. Rev. B*, *97*, 245136.

URL https://link.aps.org/doi/10.1103/PhysRevB.97.245136

Comanac, A., de' Medici, L., Capone, M., & Millis, A. J. (2008). Optical conductivity and the correlation strength of high-temperature copper-oxide superconductors. *Nature Physics*, *4*, 287.

URL http://dx.doi.org/10.1038/nphys883

Craco, L., Laad, M. S., Leoni, S., & Rosner, H. (2008). Normal-state correlated electronic structure of iron pnictides from first principles. *Phys. Rev. B*, *78*, 134511.

URL https://link.aps.org/doi/10.1103/PhysRevB.78.134511

Del Re, L., Capone, M., & Toschi, A. (2018). Dynamical vertex approximation for the attractive Hubbard model. *ArXiv e-prints*.

Eberlein, A. (2014). Fermionic two-loop functional renormalization group for correlated fermions: Method and application to the attractive hubbard model. *Phys. Rev. B*, *90*, 115125.

URL https://link.aps.org/doi/10.1103/PhysRevB.90.115125

Enss, T. (2005). *Renormalization, Conservation Laws and Transport in Correlated Electron Systems*. Ph.D. thesis, Max-Planck-Institut für Festkörperforschung.

Fausti, D., Tobey, R. I., Dean, N., Kaiser, S., Dienst, A., Hoffmann, M. C., Pyon, S., Takayama, T., Takagi, H., & Cavalleri, A. (2011). Light-induced superconductivity in a stripe-ordered cuprate. *Science*, *331*(6014), 189.

URL http://science.sciencemag.org/content/331/6014/189.abstract

Ferris-Prabhu, A. V., & Withers, D. H. (1973). Numerical analytic continuation using padé approximants. *Journal of Computational Physics*, *13*(1), 94–99.

URL http://www.sciencedirect.com/science/article/pii/0021999173901277

Fisk, Z., Ott, H.-R., & Thompson, J. (2009). Superconducting materials: What the record tells us. *Philosophical Magazine*, *89*(22-24), 2111–2115.

URL https://doi.org/10.1080/14786430902724962

Galler, A., Kaufmann, J., Gunacker, P., Pickem, M., Thunström, P., Tomczak, J. M., & Held, K. (2018). Towards ab initio calculations with the dynamical vertex approximation. *J. Phys. Soc. Jpn.*, *87*(4), 041004.

URL https://doi.org/10.7566/JPSJ.87.041004

Galler, A., Taranto, C., Wallerberger, M., Kaltak, M., Kresse, G., Sangiovanni, G., Toschi, A., & Held, K. (2015). Screened moments and absence of ferromagnetism in feal. *Phys. Rev. B*, *92*, 205132.

URL https://link.aps.org/doi/10.1103/PhysRevB.92.205132

Galler, A., Thunström, P., Gunacker, P., Tomczak, J. M., & Held, K. (2017). Ab initio dynamical vertex approximation. *Phys. Rev. B*, *95*, 115107.

URL https://link.aps.org/doi/10.1103/PhysRevB.95.115107

Georges, A., & Kotliar, G. (1992). Hubbard model in infinite dimensions. *Phys. Rev. B*, *45*, 6479–6483.

URL https://link.aps.org/doi/10.1103/PhysRevB.45.6479

Georges, A., Kotliar, G., Krauth, W., & Rozenberg, M. J. (1996). Dynamical mean-field theory of strongly correlated fermion systems and the limit of infinite dimensions. *Rev. Mod. Phys.*, *68*, 13–125.

URL https://link.aps.org/doi/10.1103/RevModPhys.68.13

Giering, K.-U., & Salmhofer, M. (2012). Self-energy flows in the two-dimensional repulsive hubbard model. *Phys. Rev. B*, *86*, 245122.

URL https://link.aps.org/doi/10.1103/PhysRevB.86.245122

Goldenfeld, N. (2018). *Lectures On Phase Transition And The Renormalization Group*. CRC Press.

Gubernatis, J. E., Jarrell, M., Silver, R. N., & Sivia, D. S. (1991). Quantum monte carlo simulations and maximum entropy: Dynamics from imaginary-time data. *Phys. Rev. B*, *44*, 6011–6029.

URL https://link.aps.org/doi/10.1103/PhysRevB.44.6011

Gull, E., & Millis, A. J. (2012). Energetics of superconductivity in the two-dimensional hubbard model. *Phys. Rev. B*, *86*, 241106.

URL https://link.aps.org/doi/10.1103/PhysRevB.86.241106

Gunacker, P., Wallerberger, M., Gull, E., Hausoel, A., Sangiovanni, G., & Held, K. (2015). Continuous-time quantum monte carlo using worm sampling. *Phys. Rev. B*, *92*, 155102.

URL https://link.aps.org/doi/10.1103/PhysRevB.92.155102

Gunnarsson, O., Schäfer, T., LeBlanc, J. P. F., Merino, J., Sangiovanni, G., Rohringer, G., & Toschi, A. (2016). Parquet decomposition calculations of the electronic self-energy. *Phys. Rev. B*, *93*, 245102.

URL https://link.aps.org/doi/10.1103/PhysRevB.93.245102

Hafermann, H., Li, G., Rubtsov, A. N., Katsnelson, M. I., Lichtenstein, A. I., & Monien, H. (2009). Efficient perturbation theory for quantum lattice models. *Phys. Rev. Lett.*, *102*, 206401.

URL https://link.aps.org/doi/10.1103/PhysRevLett.102.206401

Halboth, C. J., & Metzner, W. (2000). Renormalization-group analysis of the two-dimensional hubbard model. *Phys. Rev. B*, *61*(11), 7364–7377.

URL https://link.aps.org/doi/10.1103/PhysRevB.61.7364

Hansmann, P., Arita, R., Toschi, A., Sakai, S., Sangiovanni, G., & Held, K. (2010). Dichotomy between large local and small ordered magnetic moments in iron-based superconductors. *Phys. Rev. Lett.*, *104*, 197002.

URL https://link.aps.org/doi/10.1103/PhysRevLett.104.197002

Hansmann, P., Ayral, T., Tejeda, A., & Biermann, S. (2016). Uncertainty principle for experimental measurements: Fast versus slow probes. *Scientific Reports*, *6*, 19728.

URL http://dx.doi.org/10.1038/srep19728

Hansmann, P., Vaugier, L., Jiang, H., & Biermann, S. (2013). What about u on surfaces? extended hubbard models for adatom systems from first principles. *Journal of Physics: Condensed Matter*, *25*(9), 094005.

URL http://stacks.iop.org/0953-8984/25/i=9/a=094005

Haule, K., & Kotliar, G. (2009). Coherence–incoherence crossover in the normal state of iron oxypnictides and importance of hund's rule coupling. *New Journal of Physics*, *11*(2), 025021.

URL http://stacks.iop.org/1367-2630/11/i=2/a=025021

Haule, K., Shim, J. H., & Kotliar, G. (2008). Correlated electronic structure of $\mathrm{lao}_{1-x}\mathrm{f}_x\mathrm{FeAs}$. *Phys. Rev. Lett.*, *100*, 226402.

URL https://link.aps.org/doi/10.1103/PhysRevLett.100.226402

Hausoel, A., Karolak, M., Şaşıoğlu, E., Lichtenstein, A., Held, K., Katanin, A., Toschi, A., & Sangiovanni, G. (2017). Local magnetic moments in iron and nickel at ambient and earth's core conditions. *Nature Communications*, *8*, 16062.

URL http://www.ncbi.nlm.nih.gov/pmc/articles/PMC5510222/

Hedin, L. (1965). New method for calculating the one-particle green's function with application to the electron-gas problem. *Phys. Rev.*, *139*, A796–A823.

URL https://link.aps.org/doi/10.1103/PhysRev.139.A796

Held, K. (2014). *DMFT at 25: Infinite Dimensions Modeling and Simulation. Chapter 4*, vol. 4. Verlag des Forschungszentrum Jülich.

Held, K., Keller, G., Eyert, V., Vollhardt, D., & Anisimov, V. I. (2001a). Mott-hubbard metal-insulator transition in paramagnetic V_2O_3: An $lda + dmft(\mathrm{QMC})$ study. *Phys. Rev. Lett.*, *86*, 5345–5348.

URL https://link.aps.org/doi/10.1103/PhysRevLett.86.5345

Held, K., McMahan, A. K., & Scalettar, R. T. (2001b). Cerium volume collapse: Results from the merger of dynamical mean-field theory and local density approximation. *Phys. Rev. Lett.*, *87*, 276404.

URL https://link.aps.org/doi/10.1103/PhysRevLett.87.276404

Hettler, M. H., Mukherjee, M., Jarrell, M., & Krishnamurthy, H. R. (2000). Dynamical cluster approximation: Nonlocal dynamics of correlated electron systems. *Phys. Rev. B*, *61*, 12739–12756.

URL https://link.aps.org/doi/10.1103/PhysRevB.61.12739

Hirsch, J. E., & Fye, R. M. (1986). Monte carlo method for magnetic impurities in metals. *Phys. Rev. Lett.*, *56*, 2521–2524.

URL https://link.aps.org/doi/10.1103/PhysRevLett.56.2521

Honerkamp, C. (2008). Density waves and cooper pairing on the honeycomb lattice. *Phys. Rev. Lett.*, *100*, 146404.

URL https://link.aps.org/doi/10.1103/PhysRevLett.100.146404

Honerkamp, C., & Salmhofer, M. (2003). Flow of the quasiparticle weight in the n-patch renormalization group scheme. *Phys. Rev. B*, *67*, 174504.

URL https://link.aps.org/doi/10.1103/PhysRevB.67.174504

Honerkamp, C., Salmhofer, M., Furukawa, N., & Rice, T. M. (2001). Breakdown of the landau-fermi liquid in two dimensions due to umklapp scattering. *Phys. Rev. B*, *63*, 035109.

URL https://link.aps.org/doi/10.1103/PhysRevB.63.035109

Hummel, S. (2014). *Asymptotic behavior of two-particle vertex functions in dynamical mean-field theory*. Master's thesis, Technische Universität Wien.

Husemann, C., & Salmhofer, M. (2009). Efficient parametrization of the vertex function, Ω scheme, and the t, t' hubbard model at van hove filling. *Phys. Rev. B*, *79*, 195125.

URL https://link.aps.org/doi/10.1103/PhysRevB.79.195125

Janiš, V. (1999). Stability of self-consistent solutions for the hubbard model at intermediate and strong coupling. *Phys. Rev. B*, *60*, 11345–11360.

URL https://link.aps.org/doi/10.1103/PhysRevB.60.11345

Janiš, V., Kauch, A., & Pokorný, V. (2017). Thermodynamically consistent description of criticality in models of correlated electrons. *Phys. Rev. B*, *95*, 045108.

URL https://link.aps.org/doi/10.1103/PhysRevB.95.045108

Janiš, V., & Pokorný, V. (2014). Critical metal-insulator transition and divergence in a two-particle irreducible vertex in disordered and interacting electron systems. *Phys. Rev. B*, *90*, 045143.

URL https://link.aps.org/doi/10.1103/PhysRevB.90.045143

J.W. Negele, H. O. (1994). *Quantum Many-particle Systems (Frontiers in Physics)*. Perseus Books,U.S.

Kadanoff, L. P. (1966). Scaling laws for ising models near T_c. *Physics Physique Fizika*, *2*, 263–272.

URL https://link.aps.org/doi/10.1103/PhysicsPhysiqueFizika.2.263

Karrasch, C. (2010). *The Functional Renormalization Group for Zero-Dimensional Quantum Systems in and out of Equilibrium*. Ph.D. thesis, RWTH Aachen University.

Katanin, A. A. (2004). Fulfillment of ward identities in the functional renormalization group approach. *Phys. Rev. B*, *70*, 115109.

URL https://link.aps.org/doi/10.1103/PhysRevB.70.115109

Katanin, A. A. (2009). Two-loop functional renormalization group approach to the one- and two-dimensional hubbard model. *Phys. Rev. B*, *79*, 235119.

URL https://link.aps.org/doi/10.1103/PhysRevB.79.235119

Kaufmann, J., Gunacker, P., & Held, K. (2017). Continuous-time quantum monte carlo calculation of multiorbital vertex asymptotics. *Phys. Rev. B*, *96*, 035114.

URL https://link.aps.org/doi/10.1103/PhysRevB.96.035114

Khatami, E., Scalettar, R. T., & Singh, R. R. P. (2015). Finite-temperature superconducting correlations of the hubbard model. *Phys. Rev. B*, *91*, 241107.

URL https://link.aps.org/doi/10.1103/PhysRevB.91.241107

Khodas, M., & Chubukov, A. V. (2012). Interpocket pairing and gap symmetry in fe-based superconductors with only electron pockets. *Phys. Rev. Lett.*, *108*, 247003.

URL https://link.aps.org/doi/10.1103/PhysRevLett.108.247003

Kiesel, M. L., Platt, C., Hanke, W., Abanin, D. A., & Thomale, R. (2012). Competing many-body instabilities and unconventional superconductivity in graphene. *Phys. Rev. B*, *86*, 020507.

URL https://link.aps.org/doi/10.1103/PhysRevB.86.020507

Kiesel, M. L., Platt, C., Hanke, W., & Thomale, R. (2013a). Model evidence of an anisotropic chiral $d+id$-wave pairing state for the water-intercalated $\mathrm{na}_x\mathrm{coo}_2 \cdot y\mathbf{h}_2\mathbf{O}$ superconductor. *Phys. Rev. Lett.*, *111*, 097001.

URL https://link.aps.org/doi/10.1103/PhysRevLett.111.097001

Kiesel, M. L., Platt, C., & Thomale, R. (2013b). Unconventional fermi surface instabilities in the kagome hubbard model. *Phys. Rev. Lett.*, *110*, 126405.

URL https://link.aps.org/doi/10.1103/PhysRevLett.110.126405

Kinza, M. W. (2013). *Single Impurity Anderson Model and Dynamical Mean Field Theory A Functional Renormalization Group Study*. Ph.D. thesis, RWTH Aachen University.

Kotliar, G., Savrasov, S. Y., Pálsson, G., & Biroli, G. (2001). Cellular dynamical mean field approach to strongly correlated systems. *Phys. Rev. Lett.*, *87*, 186401.

URL https://link.aps.org/doi/10.1103/PhysRevLett.87.186401

Kraberger, G. J., Triebl, R., Zingl, M., & Aichhorn, M. (2017). Maximum entropy formalism for the analytic continuation of matrix-valued green's functions. *Phys. Rev. B*, *96*, 155128.

URL https://link.aps.org/doi/10.1103/PhysRevB.96.155128

Kugler, F. B., & von Delft, J. (2018a). Derivation of exact flow equations from the self-consistent parquet relations.

Kugler, F. B., & von Delft, J. (2018b). Multiloop functional renormalization group for general models. *Phys. Rev. B*, *97*(3), 035162.

Kugler, F. B., & von Delft, J. (2018c). Multiloop functional renormalization group that sums up all parquet diagrams. *Phys. Rev. Lett.*, *120*, 057403.

URL https://link.aps.org/doi/10.1103/PhysRevLett.120.057403

Kuneš, J. (2011). Efficient treatment of two-particle vertices in dynamical mean-field theory. *Phys. Rev. B*, *83*(8), 085102.

Li, G., Höpfner, P., Schäfer, J., Blumenstein, C., Meyer, S., Bostwick, A., Rotenberg, E., Claessen, R., & Hanke, W. (2013). Magnetic order in a frustrated two-dimensional atom lattice at a semiconductor surface. *Nature Communications*, *4*, 1620.

URL http://dx.doi.org/10.1038/ncomms2617

Li, G., Kauch, A., Pudleiner, P., & Held, K. (2017). The {\it victory} project v1.0: an efficient parquet equations solver. *ArXiv e-prints*.

Li, G., Wentzell, N., Pudleiner, P., Thunström, P., & Held, K. (2016). Efficient implementation of the parquet equations: Role of the reducible vertex function and its kernel approximation. *Phys. Rev. B*, *93*, 165103.

URL https://link.aps.org/doi/10.1103/PhysRevB.93.165103

Lichtenstein, A. I., Katsnelson, M. I., & Kotliar, G. (2001). Finite-temperature magnetism of transition metals: An ab initio dynamical mean-field theory. *Phys. Rev. Lett.*, *87*, 067205.

URL https://link.aps.org/doi/10.1103/PhysRevLett.87.067205

Lichtenstein, J., Sanchez de la Peña, S., Rohe, D., Di Napoli, E., Honerkamp, C., & Maier, S. (2017). High-performance functional renormalization group calculations for interacting fermions. *Computer Physics Communications*, *213*.

Lin, N., Gull, E., & Millis, A. J. (2012). Two-particle response in cluster dynamical mean-field theory: Formalism and application to the raman response of high-temperature superconductors. *Phys. Rev. Lett.*, *109*, 106401.

URL https://link.aps.org/doi/10.1103/PhysRevLett.109.106401

Löhneysen, H. v., Rosch, A., Vojta, M., & Wölfle, P. (2007). Fermi-liquid instabilities at magnetic quantum phase transitions. *Rev. Mod. Phys.*, *79*, 1015–1075.

URL https://link.aps.org/doi/10.1103/RevModPhys.79.1015

Luttinger, J. M., & Ward, J. C. (1960). Ground-state energy of a many-fermion system. ii. *Phys. Rev.*, *118*, 1417–1427.

URL https://link.aps.org/doi/10.1103/PhysRev.118.1417

Mahan, G. D. (2000). *Many-Particle Physics*. Springer.

Maier, T., Jarrell, M., Pruschke, T., & Hettler, M. H. (2005). Quantum cluster theories. *Rev. Mod. Phys.*, *77*, 1027–1080.

URL https://link.aps.org/doi/10.1103/RevModPhys.77.1027

Mazin, I. I., Singh, D. J., Johannes, M. D., & Du, M. H. (2008). Unconventional superconductivity with a sign reversal in the order parameter of $\mathrm{lafeaso}_{1-x}\mathrm{f}_x$. *Phys. Rev. Lett.*, *101*, 057003.

URL https://link.aps.org/doi/10.1103/PhysRevLett.101.057003

Mermin, N. D., & Wagner, H. (1966). Absence of ferromagnetism or antiferromagnetism in one- or two-dimensional isotropic heisenberg models. *Phys. Rev. Lett.*, *17*, 1133–1136.

URL https://link.aps.org/doi/10.1103/PhysRevLett.17.1133

Metzner, W., Salmhofer, M., Honerkamp, C., Meden, V., & Sch□□nhammer, K. (2012). Functional renormalization group approach to correlated fermion systems. *Rev. Mod. Phys.*, *84*.

Metzner, W., & Vollhardt, D. (1989). Correlated lattice fermions in $d = \infty$ dimensions. *Phys. Rev. Lett.*, *62*, 324–327.

URL https://link.aps.org/doi/10.1103/PhysRevLett.62.324

Micnas, R., Ranninger, J., & Robaszkiewicz, S. (1990). Superconductivity in narrow-band systems with local nonretarded attractive interactions. *Rev. Mod. Phys.*, *62*, 113–171.

URL https://link.aps.org/doi/10.1103/RevModPhys.62.113

Mishchenko, A. S., Prokof'ev, N. V., Sakamoto, A., & Svistunov, B. V. (2000). Diagrammatic quantum monte carlo study of the fröhlich polaron. *Phys. Rev. B*, *62*, 6317–6336.

URL https://link.aps.org/doi/10.1103/PhysRevB.62.6317

Nicoletti, D., Limaj, O., Calvani, P., Rohringer, G., Toschi, A., Sangiovanni, G., Capone, M., Held, K., Ono, S., Ando, Y., & Lupi, S. (2010). High-temperature optical spectral weight and fermi-liquid renormalization in bi-based cuprate superconductors. *Phys. Rev. Lett.*, *105*, 077002.

URL https://link.aps.org/doi/10.1103/PhysRevLett.105.077002

Ornstein, L., & Zernike, F. (1914). Accidental deviations of density and opalescence at the critical point of a single substance. *Proceeding of Akademic Science (Amsterdam)*, *17*, 793–806.

Otsuki, J., Hafermann, H., & Lichtenstein, A. I. (2014). Superconductivity, antiferromagnetism, and phase separation in the two-dimensional hubbard model: A dual-fermion approach. *Phys. Rev. B*, *90*, 235132.

URL https://link.aps.org/doi/10.1103/PhysRevB.90.235132

Park, H., Haule, K., & Kotliar, G. (2011). Magnetic excitation spectra in $\mathrm{bafe_2as_2}$: A two-particle approach within a combination of the density functional theory and the dynamical mean-field theory method. *Phys. Rev. Lett.*, *107*, 137007.

URL https://link.aps.org/doi/10.1103/PhysRevLett.107.137007

Platt, C., Hanke, W., & Thomale, R. (2013). Functional renormalization group for multi-orbital fermi surface instabilities. *Advances in Physics*, *62*(4-6), 453–562.

URL https://doi.org/10.1080/00018732.2013.862020

Platt, C., Thomale, R., Honerkamp, C., Zhang, S.-C., & Hanke, W. (2012). Mechanism for a pairing state with time-reversal symmetry breaking in iron-based superconductors. *Phys. Rev. B*, *85*, 180502.

URL https://link.aps.org/doi/10.1103/PhysRevB.85.180502

Rentrop, J. F., Meden, V., & Jakobs, S. G. (2016). Renormalization group flow of the luttinger-ward functional: Conserving approximations and application to the anderson impurity model. *Phys. Rev. B*, *93*, 195160.

URL https://link.aps.org/doi/10.1103/PhysRevB.93.195160

Ribic, T., Rohringer, G., & Held, K. (2016). Nonlocal correlations and spectral properties of the falicov-kimball model. *Phys. Rev. B*, *93*, 195105.

URL https://link.aps.org/doi/10.1103/PhysRevB.93.195105

Rohringer, G. (2014). *New routes toward a theoretical treatment of nonlocal electronic correlations*. Ph.D. thesis, Technische Universitaät Wien.

Rohringer, G., Hafermann, H., Toschi, A., Katanin, A. A., Antipov, A. E., Katsnelson, M. I., Lichtenstein, A. I., Rubtsov, A. N., & Held, K. (2018). Diagrammatic routes to nonlocal correlations beyond dynamical mean field theory. *Rev. Mod. Phys.*, *90*, 025003.

URL https://link.aps.org/doi/10.1103/RevModPhys.90.025003

Rohringer, G., & Toschi, A. (2016). Impact of nonlocal correlations over different energy scales: A dynamical vertex approximation study. *Phys. Rev. B*, *94*, 125144.

URL https://link.aps.org/doi/10.1103/PhysRevB.94.125144

Rohringer, G., Toschi, A., Hafermann, H., Held, K., Anisimov, V. I., & Katanin, A. A. (2013). One-particle irreducible functional approach: A route to diagrammatic extensions of the dynamical mean-field theory. *Phys. Rev. B*, *88*, 115112.

URL https://link.aps.org/doi/10.1103/PhysRevB.88.115112

Rohringer, G., Toschi, A., Katanin, A., & Held, K. (2011). Critical properties of the half-filled hubbard model in three dimensions. *Phys. Rev. Lett.*, *107*, 256402.

URL https://link.aps.org/doi/10.1103/PhysRevLett.107.256402

Rohringer, G., Valli, A., & Toschi, A. (2012). Local electronic correlation at the two-particle level. *Phys. Rev. B*, *86*(12), 125114.

Rubtsov, A., Katsnelson, M., & Lichtenstein, A. (2012). Dual boson approach to collective excitations in correlated fermionic systems. *Annals of Physics*, *327*(5), 1320 – 1335.

URL http://www.sciencedirect.com/science/article/pii/S0003491612000164

Rubtsov, A. N., Katsnelson, M. I., & Lichtenstein, A. I. (2008). Dual fermion approach to nonlocal correlations in the hubbard model. *Phys. Rev. B*, *77*, 033101.

URL https://link.aps.org/doi/10.1103/PhysRevB.77.033101

Rubtsov, A. N., Savkin, V. V., & Lichtenstein, A. I. (2005). Continuous-time quantum monte carlo method for fermions. *Phys. Rev. B*, *72*, 035122.

URL https://link.aps.org/doi/10.1103/PhysRevB.72.035122

Salmhofer, M., & Honerkamp, C. (2001). Fermionic renormalization group flowstechnique and theory. *Progress of Theoretical Physics*, *105*(1), 1–35.

URL http://dx.doi.org/10.1143/PTP.105.1

Salmhofer, M., Honerkamp, C., Metzner, W., & Oliver (2004). Renormalization Group Flows into Phases with Broken Symmetry. *Prog. Theor. Phys.*, *112*, 943–970.

Sandvik, A. W. (1998). Stochastic method for analytic continuation of quantum monte carlo data. *Phys. Rev. B*, *57*, 10287–10290.

URL https://link.aps.org/doi/10.1103/PhysRevB.57.10287

Sangiovanni, G., Toschi, A., Koch, E., Held, K., Capone, M., Castellani, C., Gunnarsson, O., Mo, S.-K., Allen, J. W., Kim, H.-D., Sekiyama, A., Yamasaki, A., Suga, S., & Metcalf, P. (2006). Static versus dynamical mean-field theory of mott antiferromagnets. *Phys. Rev. B*, *73*, 205121.

URL https://link.aps.org/doi/10.1103/PhysRevB.73.205121

Savrasov, S. Y., Kotliar, G., & Abrahams, E. (2001). Correlated electrons in δ-plutonium within a dynamical mean-field picture. *Nature*, *410*, 793.

URL http://dx.doi.org/10.1038/35071035

Scalapino, D. J. (2012). A common thread: The pairing interaction for unconventional superconductors. *Rev. Mod. Phys.*, *84*, 1383–1417.

URL https://link.aps.org/doi/10.1103/RevModPhys.84.1383

Schäfer, T. (2016). *Classical and quantum phase transitions in strongly correlated electron systems*. Ph.D. thesis, Technischen Universität Wien.

Schäfer, T., Ciuchi, S., Wallerberger, M., Thunström, P., Gunnarsson, O., Sangiovanni, G., Rohringer, G., & Toschi, A. (2016). Nonperturbative landscape of the mott-hubbard transition: Multiple divergence lines around the critical endpoint. *Phys. Rev. B*, *94*, 235108.

URL https://link.aps.org/doi/10.1103/PhysRevB.94.235108

Schäfer, T., Geles, F., Rost, D., Rohringer, G., Arrigoni, E., Held, K., Blümer, N., Aichhorn, M., & Toschi, A. (2015). Fate of the false Mott-Hubbard transition in two dimensions. *Phys. Rev. B*, *91*(12), 125109.

Schäfer, T., Rohringer, G., Gunnarsson, O., Ciuchi, S., Sangiovanni, G., & Toschi, A. (2013). Divergent precursors of the mott-hubbard transition at the two-particle level. *Phys. Rev. Lett.*, *110*, 246405.

URL https://link.aps.org/doi/10.1103/PhysRevLett.110.246405

Schiller, A., & Ingersent, K. (1995). Systematic $1/d$ corrections to the infinite-dimensional limit of correlated lattice electron models. *Phys. Rev. Lett.*, *75*, 113–116.

URL https://link.aps.org/doi/10.1103/PhysRevLett.75.113

Schütz, F., Bartosch, L., & Kopietz, P. (2005). Collective fields in the functional renormalization group for fermions, ward identities, and the exact solution of the tomonaga-luttinger model. *Phys. Rev. B*, *72*, 035107.

URL https://link.aps.org/doi/10.1103/PhysRevB.72.035107

Shiba, H. (1972). Thermodynamic properties of the one-dimensional half-filled-band hubbard model. iiapplication of the grand canonical method. *Progress of Theoretical Physics*, *48*(6), 2171–2186.

URL http://dx.doi.org/10.1143/PTP.48.2171

Silver, R. N., Sivia, D. S., & Gubernatis, J. E. (1990). Maximum-entropy method for analytic continuation of quantum monte carlo data. *Phys. Rev. B*, *41*, 2380–2389.

URL https://link.aps.org/doi/10.1103/PhysRevB.41.2380

Skornyakov, S. L., Katanin, A. A., & Anisimov, V. I. (2011). Linear-temperature dependence of static magnetic susceptibility in lafeaso from dynamical mean-field theory. *Phys. Rev. Lett.*, *106*, 047007.

URL https://link.aps.org/doi/10.1103/PhysRevLett.106.047007

Smith, R. A. (1992). Planar version of baym-kadanoff theory. *Phys. Rev. A*, *46*, 4586–4597.

URL https://link.aps.org/doi/10.1103/PhysRevA.46.4586

Strinati, G. C., Pieri, P., Röpke, G., Schuck, P., & Urban, M. (2018). The bcs-bec crossover: From ultra-cold fermi gases to nuclear systems. *The BCS-BEC crossover: From ultra-cold Fermi gases to nuclear systems*, *738*, 1–76.

URL http://www.sciencedirect.com/science/article/pii/S0370157318300267

Taranto, C., Andergassen, S., Bauer, J., Held, K., Katanin, A., Metzner, W., Rohringer, G., & Toschi, A. (2014). From infinite to two dimensions through the functional renormalization group. *Phys. Rev. Lett.*, *112*, 196402.

URL https://link.aps.org/doi/10.1103/PhysRevLett.112.196402

Taranto, C., Sangiovanni, G., Held, K., Capone, M., Georges, A., & Toschi, A. (2012). Signature of antiferromagnetic long-range order in the optical spectrum of strongly correlated electron systems. *Phys. Rev. B*, *85*, 085124.

URL https://link.aps.org/doi/10.1103/PhysRevB.85.085124

Teschl, G. (2012). *Ordinary Differential Equations and Dynamical Systems*, vol. 140. American Mathematical Society.

Thomale, R., Platt, C., Hanke, W., & Bernevig, B. A. (2011a). Mechanism for explaining differences in the order parameters of feas-based and fep-based pnictide superconductors. *Phys. Rev. Lett.*, *106*, 187003.

URL https://link.aps.org/doi/10.1103/PhysRevLett.106.187003

Thomale, R., Platt, C., Hanke, W., Hu, J., & Bernevig, B. A. (2011b). Exotic d-wave superconducting state of strongly hole-doped $\mathbf{k}_x\mathrm{ba}_{1-x}\mathrm{fe}_2\mathrm{as}_2$. *Phys. Rev. Lett.*, *107*, 117001.

URL https://link.aps.org/doi/10.1103/PhysRevLett.107.117001

Thomale, R., Platt, C., Hu, J., Honerkamp, C., & Bernevig, B. A. (2009). Functional renormalization-group study of the doping dependence of pairing symmetry in the iron pnictide superconductors. *Phys. Rev. B*, *80*, 180505.

URL https://link.aps.org/doi/10.1103/PhysRevB.80.180505

Thunström, P., Gunnarsson, O., Ciuchi, S., & Rohringer, G. (2018). Analytical investigation of singularities in two-particle irreducible vertex functions of the Hubbard atom. *ArXiv e-prints*.

Toschi, A., Arita, R., Hansmann, P., Sangiovanni, G., & Held, K. (2012). Quantum dynamical screening of the local magnetic moment in fe-based superconductors. *Phys. Rev. B*, *86*, 064411.

URL https://link.aps.org/doi/10.1103/PhysRevB.86.064411

Toschi, A., Capone, M., Castellani, C., & Held, K. (2009). Kinks in the electronic specific heat. *Phys. Rev. Lett.*, *102*, 076402.

URL https://link.aps.org/doi/10.1103/PhysRevLett.102.076402

Toschi, A., Capone, M., Ortolani, M., Calvani, P., Lupi, S., & Castellani, C. (2005). Temperature dependence of the optical spectral weight in the cuprates: Role of electron correlations. *Phys. Rev. Lett.*, *95*, 097002.

URL https://link.aps.org/doi/10.1103/PhysRevLett.95.097002

Toschi, A., Katanin, A. A., & Held, K. (2007). Dynamical vertex approximation: A step beyond dynamical mean-field theory. *Phys. Rev. B*, *75*, 045118.

URL https://link.aps.org/doi/10.1103/PhysRevB.75.045118

Uebelacker, S., & Honerkamp, C. (2012). Self-energy feedback and frequency-dependent interactions in the functional renormalization group flow for the two-dimensional hubbard model. *Phys. Rev. B*, *86*, 235140.

URL https://link.aps.org/doi/10.1103/PhysRevB.86.235140

Valli, A., Schäfer, T., Thunström, P., Rohringer, G., Andergassen, S., Sangiovanni, G., Held, K., & Toschi, A. (2015). Dynamical vertex approximation in its parquet implementation: Application to hubbard nanorings. *Phys. Rev. B*, *91*, 115115.

URL https://link.aps.org/doi/10.1103/PhysRevB.91.115115

Vidberg, H. J., & Serene, J. W. (1977). Solving the eliashberg equations by means ofn-point padé approximants. *Journal of Low Temperature Physics*, *29*(3), 179–192.

URL https://doi.org/10.1007/BF00655090

Vilardi, D., Taranto, C., & Metzner, W. (2017). Nonseparable frequency dependence of the two-particle vertex in interacting fermion systems. *Phys. Rev. B*, *96*, 235110.

URL https://link.aps.org/doi/10.1103/PhysRevB.96.235110

Vilk, Y. M., & Tremblay, A.-M. S. (1996). Destruction of fermi-liquid quasiparticles in two dimensions by critical fluctuations. *EPL (Europhysics Letters)*, *33*(2), 159.

URL http://stacks.iop.org/0295-5075/33/i=2/a=159

Vilk, Y. M., & Tremblay, A.-M. S. (1997). Non-perturbative many-body approach to the hubbard model and single-particle pseudogap. *J. Phys. I France*, *7*(11), 1309–1368.

URL https://doi.org/10.1051/jp1:1997135

Vučičević, J., Wentzell, N., Ferrero, M., & Parcollet, O. (2018). Practical consequences of the luttinger-ward functional multivaluedness for cluster dmft methods. *Phys. Rev. B*, *97*, 125141.

URL https://link.aps.org/doi/10.1103/PhysRevB.97.125141

Wang, F., & Lee, D.-H. (2011). The electron-pairing mechanism of iron-based superconductors. *Science*, *332*(6026), 200.

URL http://science.sciencemag.org/content/332/6026/200.abstract

Wang, W. L., Yazyev, O. V., Meng, S., & Kaxiras, E. (2009). Topological frustration in graphene nanoflakes: Magnetic order and spin logic devices. *Phys. Rev. Lett.*, *102*, 157201.

URL https://link.aps.org/doi/10.1103/PhysRevLett.102.157201

Wang, W.-S., Li, Z.-Z., Xiang, Y.-Y., & Wang, Q.-H. (2013). Competing electronic orders on kagome lattices at van hove filling. *Phys. Rev. B*, *87*, 115135.

URL https://link.aps.org/doi/10.1103/PhysRevB.87.115135

Werner, P., & Millis, A. J. (2006). Hybridization expansion impurity solver: General formulation and application to kondo lattice and two-orbital models. *Phys. Rev. B*, *74*, 155107.

URL https://link.aps.org/doi/10.1103/PhysRevB.74.155107

Wilson, K. G. (1971). Renormalization group and critical phenomena. i. renormalization group and the kadanoff scaling picture. *Phys. Rev. B*, *4*, 3174–3183.

URL https://link.aps.org/doi/10.1103/PhysRevB.4.3174

Yang, S. X., Fotso, H., Liu, J., Maier, T. A., Tomko, K., D'Azevedo, E. F., Scalettar, R. T., Pruschke, T., & Jarrell, M. (2009). Parquet approximation for the 4×4 hubbard cluster. *Phys. Rev. E*, *80*, 046706.

URL https://link.aps.org/doi/10.1103/PhysRevE.80.046706

Zanchi, D. (2001). Angle-resolved loss of landau quasiparticles in 2d hubbard model. *Europhys. Lett.*, *55*(3), 376–382.

URL https://doi.org/10.1209/epl/i2001-00413-7